UNIVERSIDAD COMPLUTENSE DE MADRID

FACULTAD DE CIENCIAS FÍSICAS
DEPARTAMENTO DE ASTROFÍSICA Y CIENCIAS DE LA ATMÓSFERA

Multi-wavelength analysis of the physical properties of distant galaxies

Análisis multi-longitud de onda de las propiedades físicas de galaxias lejanas

Dirigida por:

Dr. Pablo G. Pérez González
Profesor Titular
UCM

Dr. Jesús Gallego Maestro
Profesor Titular
UCM

Memoria presentada por
D. Guillermo Barro Calvo
para aspirar al grado de
Doctor en Ciencias Físicas
Madrid, Mayo 2011

What is the relevance of accidentally finding a hunk of rock that's been traipsing around the Universe for billions of years?.. You didn't discover it, you merely noticed it was there!.

Dr. Sheldon Cooper, *The Big Bang Theory*

...Bienvenido a mi mundo.

Dr. P.G. Pérez-González, *Real life*

Contents

Agradecimientos

Me gustaría agradecer en estas líneas a las muchas personas que me han ayudado y animado durante el proceso de investigación y redacción de esta tesis. En primer lugar, quisiera agradecer a mis directores por su inestimable apoyo y guia durante todo el doctorado. Dado que esta tesis se presenta en formato de artículos deseo agradecer también a todos los co-autores por sus detalladas revisiones y comentarios constructivos. Gracias también a todos aquellos que me han ayudado ha revisar esta tesis incontables veces, por su paciencia infinita y su ayuda a la hora de cumplir los plazos de tiempo. Por último, agradecer también al Departamento de Astrofísica y C.C. de la atmósfera de la Universidad Complutense de Madrid que me ha brindado la oportunidad y los medios para realizar esta tesis.

1

Introducción

1.1 Comprendiendo la evolución general de las galaxias

El desarrollo científico de la última década que mas ha influido en los estudios de formación y evolución de galaxias es el firme establecimiento del modelo cosmológico ΛCDM de energía y materia oscuras. En este modelo, el Universo se compone de un 70% de energía oscura, un 25% de materia oscura y tan sólo el 5% de materia ordinaria (barionica). Desarrollado a comienzo de la década de los 80 (Peebles 1982), el éxito del modelo ΛCDM subyace en su capacidad para explicar simultáneamente la naturaleza y estructura de la radiación de fondo de microondas (CMB, Cosmic Microwave Background, Smoot et al. 1992), la expansión de el Universo, así como la estructura a gran escala observacional en la que las galaxias están dispuestas (la telaraña cósmica; véase panel izquierdo de la Figura 1.1).

El firme establecimiento de este paradigma ha supuesto un cambio en los objetivos prioritarios de los estudios de población de galaxias, pasando de tratar de determinar con precisión los valores de los parámetros cosmológicos a centrarse en caracterizar los procesos que controlan la formación y evolución de galaxias. Dado que ahora conocemos los valores de la mayoría de los parámetros cosmológicos fundamentales con mucha precisión (Spergel et al. 2003; Komatsu et al. 2010), nos encontramos en una nueva era de cosmología de alta precisión donde el reto más importante es entender la formación de galaxias.

Dentro del paradigma cosmológico actual ΛCDM, nuestra idea de cómo funcionan los mecanismos de formación de galaxias se basa en la idea de que tan sólo una pequeña fracción de la masa total de una galaxia es materia luminosa. Por el contrario, la mayoría de su masa se encuentra localizada en un halo de materia oscura no barionica que contiene la materia ordinaria y en ultima instancia controla su evolución (White & Rees 1978; Davis et al. 1985; White & Frenk 1991). El modelo ΛCMD ha proporcionado un contexto teórico que es muy eficiente a la hora de caracterizar el comportamiento de estos halos de materia oscura. Hoy en día, la evolución de estos halos puede ser modelada con gran precisión mediante la ejecución de grandes, simulaciones de N-cuerpos que describen su crecimiento a partir de fluctuaciones primordiales que detectamos en la radiación de fondo de microondas. (Somerville & Primack 1999; Cole et al. 2000; De Lucia et al. 2004; Springel et al. 2005b; Bower et al. 2006; Croton et al. 2006). No obstante, a pesar de sus importantes logros a la hora de explicar la formación de estructuras, todavía existen bastantes desafíos para explicar con precisión el crecimiento jerárquico de las galaxias. Por ejemplo, mientras que los modelos ΛCMD predicen con éxito los resultados observacionales sobre distribución a gran escala las galaxias, las simulaciones parecen predecir un exceso de pequeños halos de materia oscura que no coinciden con el número de galaxias satélites enanas observadas en el Grupo Local

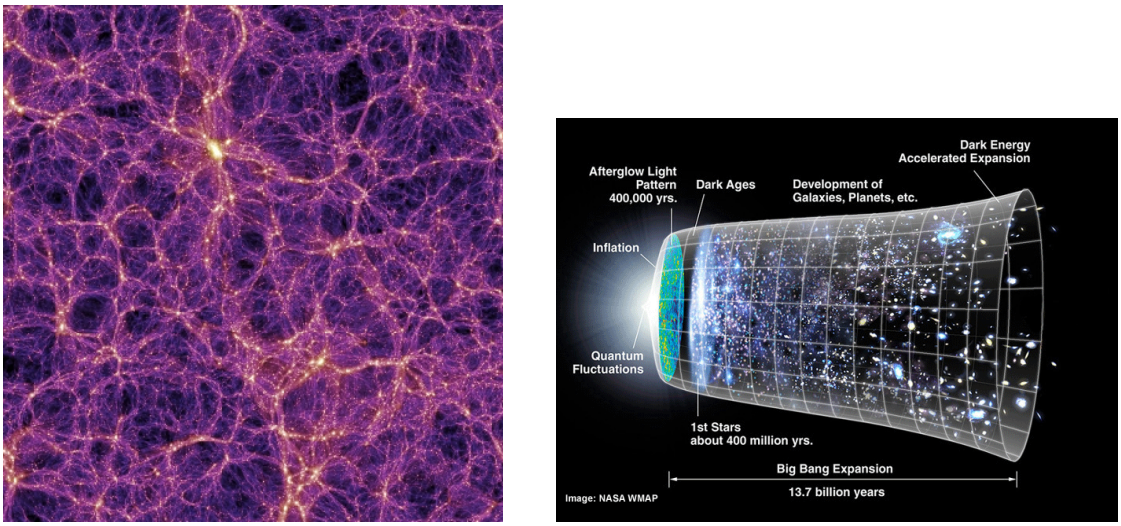

Figure 1.1: Izquierda: La telaraña cósmica tal y como aparece en los modelos ΛCDM. El código de colores indica la densidad de materia oscura a escalas de Gigaparsecs. Los colores brillantes y oscuros muestran las zonas de mayor y menor densidad, respectivamente. El grueso de la formación estelar sucede en las áreas más brillantes. Derecha: Visión esquemática de la evolución del Universo desde las fluctuaciones primordiales en el CMB, que aparecen poco después del Big Bang, hasta la gran variedad de tipos de galaxias que se aprecian en el Universo local.

(Kauffmann et al. 1993; Mateo 1998; Moore et al. 1999). Además, los procesos fundamentales que regulan la evolución de las galaxias dentro de estos halos: las acreción de gas, la formación estelar y el "feedback" (el efecto de transmisión de energía de una generación de estrellas a la siguiente) son extremadamente complejos, y por tanto aun no han sido caracterizados con suficiente detalle (Kauffmann & Haehnelt 2000; Granato et al. 2004; Springel et al. 2005a).

Sin embargo, a pesar de estos problemas a la hora de modelar la física de las interacciones a escala galáctica (la mayoría de las veces asociadas con limitaciones en la resolución máxima de los modelos), las simulaciones numéricas son herramienta muy potentes que nos proporcionan mucha información sobre las primeras etapas de la formación de galaxias. Dentro del paradigma del ΛCDM, podríamos decir que la evolución galáctica (simplificada) sigue un proceso de dos fases (véase, por ejemplo el resumen detallado de Baugh 2006): En primer lugar, el mecanismo de inestabilidad gravitacional da lugar a los halos de materia oscura a través de un colapso no disipativo. En esta fase comienzan a desarrollarse las primeras estructuras como consecuencia del enfriamiento radiativo de bariones. En segundo lugar, la condensación de grandes masas de gas prístino estabiliza las proto-galaxias frente a las disrupciones causadas por las fusiones de los halos evitando que estas se difuminen. Es en este momento cuando comienzan los primeros brotes de formación estelar dentro de las semillas primordiales suficientemente masivas, dando comienzo al proceso global evolución química (incluyendo la formación de metales y polvo). Mas adelante, sera necesaria la intervención de los mecanismos de *feedback* para hacer que las galaxias mas pequeñas sean mas difusas (menos compactas) y por tanto menos eficientes manteniendo su estabilidad estructural durante los procesos de fusión de halos, evitando así la producción de un numero mayor de galaxias más débiles que el observado. A escala global, estas estrellas y las galaxias primordiales llevaran a cabo un reionización gradual del gas neutro (opaco) que constituye la mayor parte de la materia barionica del Universo instantes después del Big Bang (véase por ejemplo Loeb & Barkana 2001). Este sencillo modelo se repetirá continuamente a gran escala y finalmente, un complicado equilibrio entre estos procesos de acreción de gas, enfriamiento de

bariones y fusión de galaxias dará lugar a la escenario local que se observamos hoy en día. El panel de la derecha de la figura 1.1 muestra un esquema simplificado del proceso evolutivo general.

Con todo, gran parte del éxito reciente explicando los procesos de formación de galaxias habría sido imposible sin una mejora sustancial en la calidad de los resultados observacionales, que nos ha proporcionado evidencias directa de como se comporta el universo a alto *redshift*. La sinergia entre teoría y observaciones nos permite integrar las observaciones de galaxias a diferentes edades del universo en un marco coherente. Al mismo tiempo, este proceso de integración plantea nuevas preguntas y hace predicciones que pueden ser contrastadas con datos.

En última instancia, el propósito de estudiar la evolución de las galaxias es determinar los procesos que llevaron a las fluctuaciones primordiales en el CMB a convertirse en la gran variedad de galaxias de distintos tipos (galaxias de disco, galaxias elípticas, etc.) que observamos hoy en día. Sin embargo, esta pregunta general puede resumirse en varias preguntas clave mas concretas:

- ¿Cuando se formaron las primeras galaxias?
- ¿Cómo y cuándo comenzaron las galaxias a formar sus estrellas?
- ¿Qué comienza los episodios formación estelar a escala de galáctica y qué los termina?
- ¿Cuál es el papel del entorno en el proceso de formación de galaxias?

La evolución de las galaxias a partir de semillas primordiales hasta convertirse en sistemas masivos ya maduros depende de la respuesta a cada una de estas preguntas. Por lo tanto, **para realizar un análisis detallado es necesario usar grandes muestras de galaxias a diferentes edades del Universo**. Sólo si comprendemos la evolución temporal de los procesos que controlan la formación de las galaxias podremos obtener una imagen sólida de la evolución a escala global.

Aunque es igualmente importante estudiar galaxias en todas las épocas del Universo, desde el punto de vista observacional, hay diferencias significativas en la manera de enfocar los *surveys* de galaxias cuando éstos se centran en el estudio de galaxias locales (dentro de unos pocos Mpc) o en galaxias muy distantes a diferentes tiempos cósmicos ($z \gtrsim 0.05$-0.1). Mientras que los primeros usan a menudo datos tomados en todo el cielo (o una gran zona), los últimos se centran en la observaciones muy profundas de regiones relativamente pequeñas. En las secciones siguientes nos centraremos preferentemente en estos *surveys*, que están más estrechamente relacionados con el tema central de esta tesis. En particular, explicaremos cual es la motivación para llevar a cabo estos *surveys* y cuales son sus principales características dentro de un contexto histórico. Daremos por tanto una descripción de su evolución desde los primeros estadíos de su desarrollo hasta su estado actual. A continuación, describiremos también algunos de los principales resultados que podemos obtener a partir de estos *surveys*.

1.2 La búsqueda de galaxias lejanas

1.2.1 Los primeros *surveys* de galaxias

De manera similar a lo que sucedió con las formulaciones iniciales de los modelos cosmológicos, las ideas fundamentales detrás de los métodos de búsqueda sistemática de las galaxias primiti-

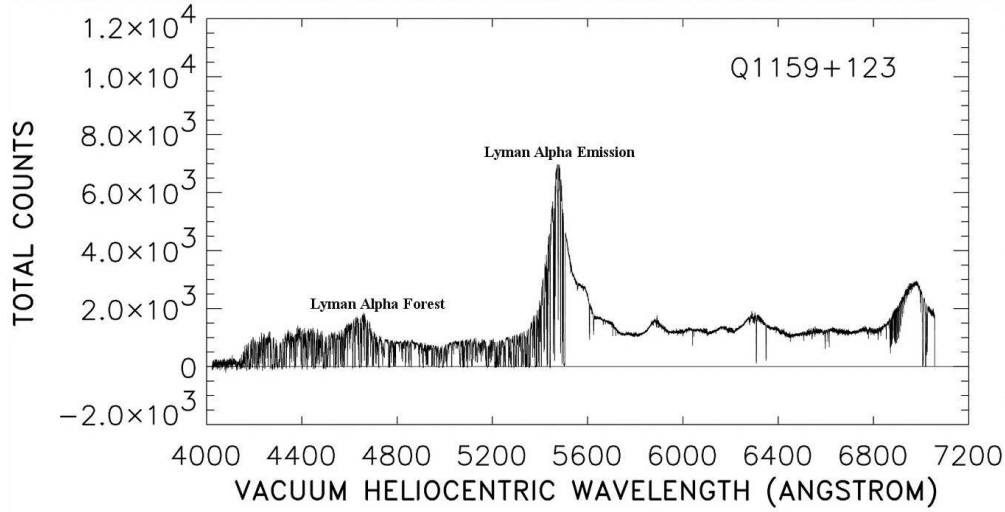

Figure 1.2: Espectro óptico de una galaxia a *redshift* z=3.52 mostrando el UV en reposo (adaptada de Pahre&Djorgovski 1995). El espectro muestra la línea de emisión Lyman-α, a 1216 Å en reposo, junto con el Lyman-α forest, causado por la absorción de fotones Lyman (aquellos emitidos a λ<1216 Å en reposo) en galaxias a *redshifts* mas bajos que el del objeto.

vas también fueron desarrollados relativamente pronto. Partridge & Peebles (1967a,b) fueron los primeros en discutir las distribuciones espectrales de energía (SED del ingles Spectral Energy Distribution) en el ultravioleta lejano de galaxias con formación estelar y la metodología general para explotar la detección de ciertas características en ese rango de longitud de onda, por ejemplo la linea de emisión Lyman-α (1216 Å; Gunn & Peterson 1965) o el limite de Lyman a 912 Å como un indicador fiable para detectar galaxias lejanas (ver Figura 1.2). Esencialmente, la idea detrás de esta técnica es detectar estas características espectrales en diferentes bandas fotométricas observadas como resultado del desplazamiento al rojo cosmológico (*redshift*). Por desgracia, los primeros *surveys* fotométricos basados en estos trabajos teóricos pioneros resultaron infructuosos, debido principalmente a las limitaciones técnicas de los detectores fotográficos y fotoeléctricos (e incluso de los primeros CCDs; Koo & Kron 1980) disponibles en aquel momento (Davis & Wilkinson 1974).

De hecho, la primera muestra significativa de galaxias distantes (z$>$ 1.5) se detectaron por medio de observaciones en longitudes de onda no óptica. Fue el seguimiento espectroscópico de objetos detectados a longitudes de onda radio en el tercer catálogo de Cambridge (3CR, Bennett 1962) el que permitió la confirmación de unos pocos cientos de galaxias a alto *redshift* a través de la detección de lineas de emisión bien caracterizadas (Spinrad & Djorgovski 1984a,b; Spinrad et al. 1985). En los años siguientes se encontraron algunos objetos mas basados en la búsqueda sistemática de la linea espectral Lyman-α en galaxias cercanas a algunos quasares previamente conocidos. (por ejemplo, Schneider et al. 1986, Hu & Cowie 1987). Debido al éxito de estas búsquedas, hasta hace poco, las galaxias a alto *redshift* eran sinónimo de radio galaxias. Sin embargo, otros *surveys* llevados a cabo en esa época, y centrados en detectar en esa linea con técnicas de filtros estrechos o espectroscopia de rendija larga fueron relativamente infructuosos. (Lowenthal et al. 1990, de Propris et al. 1993, Thompson et al. 1995) y los pocos que tuvieron éxito, demostraron que estas observaciones sólo son sensibles a los objetos mas brillantes, que son bastante escasos y por tanto bastante raros de encontrar en esos *surveys*.

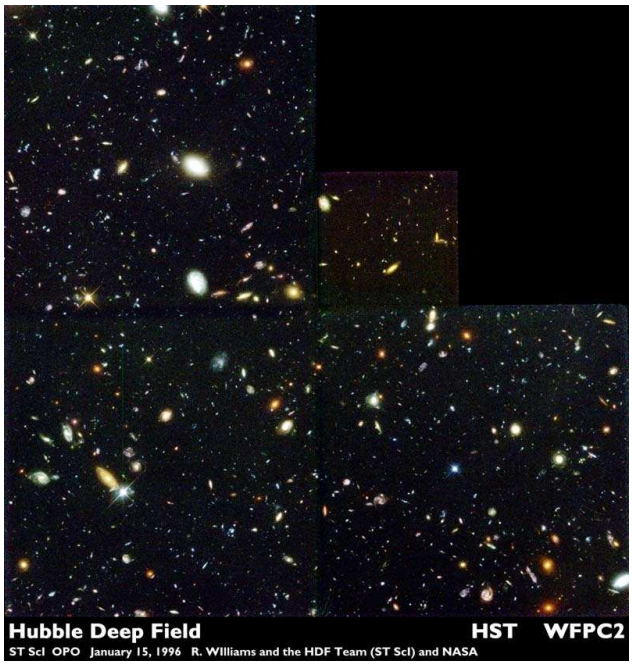

Figure 1.3: Imágen original del Hubble Deep Field tomada con la Wide Field and Planetary Camera 2 (WFPC2) abordo del telescopio espacial Hubble (Williams et al. 1996). La imágen se compone de 342 exposiciones diferentes tomadas en 10 dias consecutivos durante diciembre de 1995. El campo fue observado un total de $\sim$30h en 4 filtros anchos diferentes a una longitud de onda de 300 nm, 450 nm, 606 nm and 814 nm. La imágen de color se obtuvo combinando los datos tomados en 3 de estos filtros anchos.

1.2.2 *Surveys* fotométricos modernos

El comienzo de los *surveys* fotométricos modernos, que encuentran habitualmente miles de objetos a alto *redshift*, tuvo que esperar hasta la década de 1990. El lanzamiento del Telescopio Espacial Hubble (HST 1990), la puesta en marcha de los primeros telescopios de clase 8-10 metros (Keck, 1993; SUBARU 1999) y las mejoras en la tecnología de detectores CCD, proporcionando alta sensibilidad y gran área, abrió las puertas a la explotación sistematica de las técnicas fotométricas de búsqueda de galaxias lejanas. De hecho, el primer avance importante en la caracterización del universo lejano fue el producido a raíz de los resultados obtenidos en el Hubble Deep Field (Williams et al. 1996, ver Figura 1.3). La profundidad sin precedentes alcanzada en la pequeña imagen (2,5 'x2.5') del telescopio espacial consiguió identificar miles de galaxias simultáneamente (caracterizadas además con una resolución espacial muy alta) y explotar de manera eficiente la técnica (previamente poco exitosa) de detección del *Lyman-break* para aislar galaxias a alto *redshift* ($z > 3$; LBGs del ingles Lyman-break galaxies) (Steidel et al. 1996, ver Figura 1.4).

Tras la identificación espectroscópica de los primeros candidatos a LBGs, el seguimiento sistemático de estos objetos con el primer espectrógrafo multi objeto, funcionando en el telescopio de 10 metros Keck, permitió la confirmación de más de un millar de galaxias a $z>3$ (Steidel et al. 1999). Al mismo tiempo, *surveys* fotométricos complementarios basados en la combinación de observaciones desde telescopios terrestres y desde el HST permitieron llevar la búsqueda de galaxias lejanas a redshifts mas altos, a la vez que aumentaban rápidamente el numero de candidatos a LBGs. Con este objetivo en mente, pronto nuevos *surveys* comenzaron a llevar a cabo observaciones multicolor (en múltiples bandas fotométricas) ultra-profundas en lugares clave del cielo,

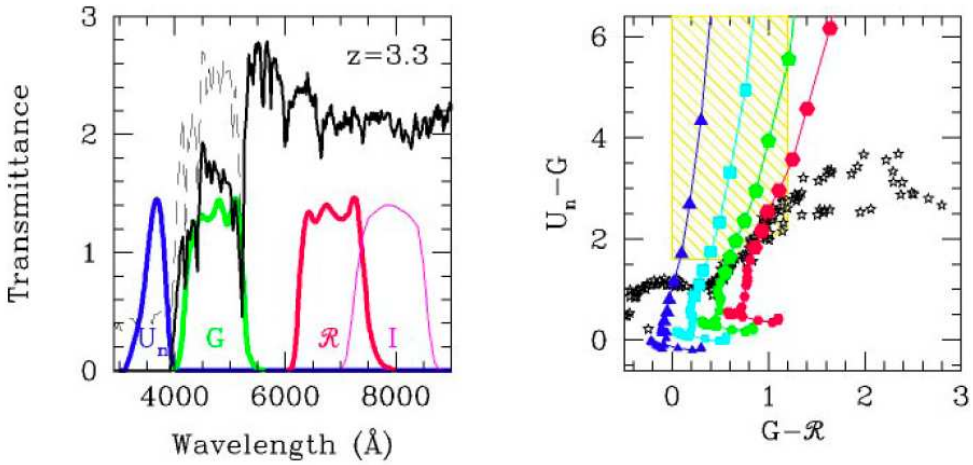

Figure 1.4: *Izquierda:* Las líneas azul, verde y roja muestran el conjunto de filtros anchos (U_n,G,R) usados en Steidel et al. (1996) para identificar LBGs a z∼3. La línea negra muestra el espectro sintético de una galaxia con formación estelar continua (Bruzual & Charlot 1993) en la que se puede apreciar el Lyman break a 912 Å en reposo. *Derecha:* Criterio color-color empleado para seleccionar candidatos a galaxias LBG. Las curvas representan magnitudes sintéticas de galaxias (con formación estelar continua) situadas a *redshifts* progresivamente crecientes comenzando a z=0.5 con pasos de z=0.1. Los 4 recorridos corresponden con diferentes cantidades de extinción por polvo variando entre extinción nula (azul) y A(V)=2 mag (rojo). El grueso de los colores estelares típicos se muestran como estrellas. Las áreas sombreadas corresponden con criterio de selección de galaxias a z∼3.

marcando así el comienzo de una nueva era de explotación fructífera de los denominados *blank surveys*.

La disponibilidad de grandes telescopios, instalaciones dedicadas y observaciones del espacio supuso un gran paso adelante para la búsqueda de galaxias distantes. Junto con las LBGs, nuevas técnicas fotométricas comenzaron a prosperar a mediados de 1990. Las más relevantes de estas estrategias se pueden resumir brevemente en dos categorías principales:

- Las técnicas **LBG** o **drop-out**, que seleccionan galaxias en un intervalo de *redshift* determinado mediante la detección de una discontinuidad importante en la emisión de continuo de la galaxia usando fotometría en varios filtros fotométricos (a veces sólo dos, pero por lo general más). La generalización de este método de detección de características prominentes en la SED de una galaxia, se conoce a menudo como técnica de selección por colores.

- Búsqueda de **líneas de emisión**, dirigida a emisores Lyman-α (LAEs; del ingles Lyman-α emiters) o de otras galaxias que presentan fuertes líneas de emisión, como Hα o [OII]. Utilizando técnicas fotométricas hay básicamente dos técnicas similares que pueden ser utilizadas para identificar dichas líneas: 1) imágenes de filtro estrecho: basada en el uso de una combinación de un filtro de banda ancha y uno de banda estrecha ($\Delta\lambda$=10-50 Å) para detectar el exceso de flujo que presentarían las galaxias con lineas de emisión a un *redshift* específico (véase el panel derecho de la Figura 1.5); 2) filtros sintonizables: basado esencialmente en la misma técnica, pero trabajando con un rango de longitud de onda variable que permite ampliar la búsqueda de una linea de emisión a un intervalo de *redshift* más amplio.

De acuerdo a un censo de Bouwens et al. (2006), en ese momento, la técnica de **drop-out**

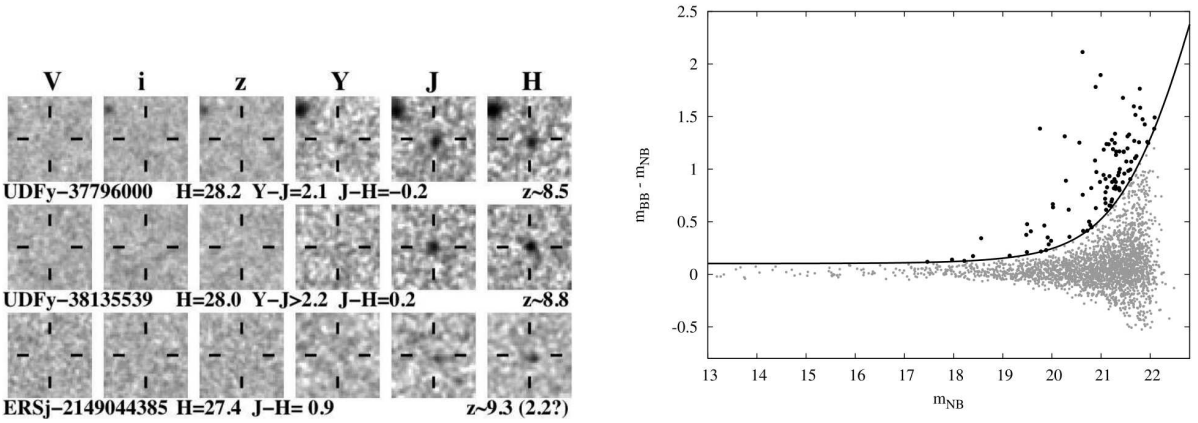

Figure 1.5: Izquierda: Imágenes de 3 galaxias candidatas a encontrarse a *redshifts* z∼8.5-9 identificadas con la técnica LBG en las imágenes ultra-profundas HUDF tomadas en el infrarrojo con WFC3 (Bouwens et al. 2010b). Ninguno de los candidatos se detecta en las imágenes profundas de ACS (BViz) y al menos dos de ellos son *drop-outs* en banda Y indicando que el break de Lyman se ha desplazado a bandas infrarrojas como resultado del (alto) *redshift* de estas galaxias. Derecha: Diagrama color magnitud para los candidatos a galaxias con líneas de emisión a z=0.84 (negro) detectados con la técnica del filtro estrecho en Villar et al. (2008). Un exceso en el color de filtro estrecho frente a filtro ancho en las galaxias para ciertas galaxias indica que el filtro estrecho esta detectando una señal adicional que no procede del continuo de la galaxia si no de una línea de emisión. En este ejemplo, la línea de emisión Hα a 6563Å en reposo se detecta en el filtro estrecho a $\lambda_{\rm eff}$=1.20 μm en galaxias a z=0.84.

había identificado en torno a: 4000 galaxias a z∼4 (B-drop), 1000 galaxias a z∼5 (V-drop), y 500 galaxias a z∼6 (i-drop). Hoy en día, la disponibilidad de observaciones ultra profundas en el infrarrojo cercano (NIR) permite la confirmación fiable de galaxias a z∼7 (z-drop) y extiende la técnica del *drop-out* hasta z∼10 (J-drop), hasta tan sólo 500 millones de años después del Big Bang (Bouwens et al. 2010a,b, ver panel izquierdo de la Figura 1.5).

1.2.3 Sesgos observacionales y observaciones multi-longitud de onda

Aunque todas las técnicas descritas anteriormente son muy eficientes para seleccionar muestras de galaxias a alto *redshift*, es fundamental tener en cuenta que cada uno de estos métodos proporciona siempre una visión parcial del Universo lejano, es decir, ninguno de ellos está exento su propio sesgo observacional. Por ejemplo, la técnica LBG está destinada a seleccionar galaxias jóvenes con formación estelar activa y que están relativamente libres de polvo. Esto implica que está muy sesgado en contra de galaxias polvorientas y galaxias con poblaciones estelares rojas que presentan SEDs mas rojas, lo que probablemente causará ambigüedades a la hora de estimar su *redshift* (por ejemplo, Reddy et al. 2005). Del mismo modo, los LAEs, y en general los objetos seleccionados por líneas de emisión, tienen un sesgo observacional claro pero difícil de caracterizar. Esto se debe a que además del requisito de que formen estrellas activamente , estos *surveys* presentan dos umbrales de sensibilidad, uno al nivel de flujo y otro a la anchura equivalente de la linea (sólo galaxias con una anchura equivalente lo suficientemente grande pueden ser detectadas independientemente del brillo en el continuo), además el intervalo de *redshift* que seleccionan es relativamente estrecho, lo que hace que habitualmente sean *surveys* menos completos que aquellos basados en la detección del continuo.

Con el fin de superar estos problemas de sesgos observacionales, se han desarrollado otros

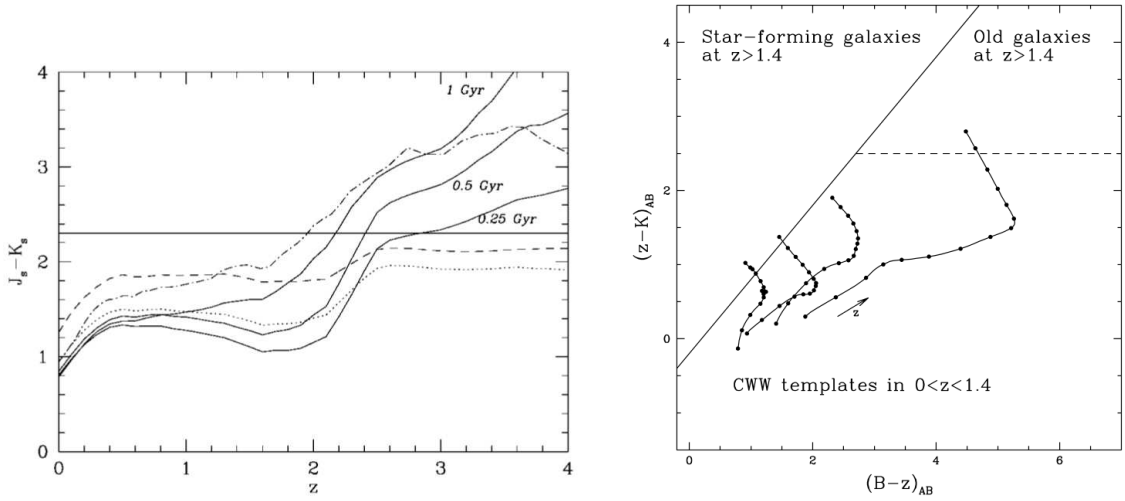

Figure 1.6: Izquierda: Color $J-K_s$, empleado para identificar DRGs en función del *redshift*, para varios espectros sintéticos de galaxias (Franx et al. 2003). Las líneas solidas indican poblaciones estelares simples (una sola población) con edades de 0.25, 0.5, y 1 Gyr. El color excede un valor de $J-K_s$>2.3 solo para galaxias a z>2 como resultado del desplazamiento del Balmer break/4000Å a la banda J observada. Derecha: Color B−z frente a z−K empleado en el criterio BzK (Daddi et al. 2004) para una serie de *templates* de galaxias locales de varios tipos Coleman et al. (1980). Los modelos se muestran para el intervalo de *redshift* 0<z<1.4 y se puede apreciar que ninguna de estas galaxias alcanzan las regiones donde se situan las galaxias con formación estelar y quiescentes en el intervalo de *redshift* 1.4<z<2.5.

métodos selección que detectan características en la forma del continuo en longitudes de onda ópticas (en reposo) de galaxias *normales* en lugar de en el ultravioleta (UV) de galaxias con formación estelar. Muchas de estas técnicas se basan en la detección de la discontinuad de Balmer y el *break* de 4000 usando colores en el infrarrojo cercano (NIR) para identificar los sistemas masivos y típicamente más evolucionados que aquellos de las muestras seleccionadas en el UV; ejemplos representativos de estos métodos son: EROS, IEROS, DRG, BzKs (véase, por ejemplo, Elston et al. 1988; Yan et al. 2004; Franx et al. 2003; Daddi et al. 2004; ver Figura 1.6). Sin embargo, de manera similar a lo que sucede con las técnicas *drop-out* en el óptico, estos métodos no han podido ofrecer resultados significativos hasta la reciente mejora en la calidad de los detectores en el NIR (a principios de los 2000),que los llevó a niveles de eficiencia y cobertura en área similares a los de los CCDs ópticos. Más recientemente, la disponibilidad del Telescopio Espacial *Spitzer*, que observa las longitudes de onda infrarrojas entre 3.6-8.0μm, ha permitido la detección de estos sistemas masivos hasta z$\sim$4 (Pérez-González et al. 2008). Evidentemente, las técnicas de color NIR también presentan sus propios sesgos. De todos ellos, quizás, el más notable es la degeneración a la hora de distinguir objetos que presentan colores muy rojos, y que podrían ser o bien objetos muy oscurecidos por el polvo o bien objetos con poblaciones estelares muy viejas (véase, por ejemplo, Papovich et al. 2006).

Estudios complementarios que permitan romper esta degeneración requieren observaciones de galaxias a longitudes de onda mayores (en el infrarrojo medio-lejano, sub-milímetro o en radio) que muestreen la radiación infrarroja re-emitida por el polvo caliente en galaxias con formación estelar fuertemente oscurecidas. Este tipo de *surveys*, como aquellos realizados con JCMT / SCUBA (sub-mm), VLA (radio), Spitzer / MIPS (FIR) y ahora Herschel, ofrecen los datos necesarios para complementar la visión sesgada de las galaxias a alto z que nos proporcionan los *surveys* centra-

dos sólo en longitud de onda UV y óptica. Desafortunadamente, sólo las muestras mas recientes seleccionadas en estas longitudes de onda son capaces de proporcionar un número suficientemente grande (estadísticamente representativo) de galaxias.

Impulsados por el rápido desarrollo de la instrumentación astronómica, nuevos *surveys* llevados a cabo en múltiples longitudes de onda nos ofrecen con frecuencia nuevos y sorprendentes resultados. Esto es posible gracias al uso de instrumentos e instalaciones astronómicas punteras que permiten mejoras significativas sobre los trabajos anteriores. Sin embargo, muchos de estos estudios a menudo afirman haber encontrado una nueva población de galaxias, bautizada con unas nuevas siglas, y no siempre está claro en qué medida estas poblaciones son realmente nuevas o si en realidad son complementarios a otras anteriores. Como se indica recientemente en el libro blanco de objetivos para la próxima década, *Esta es una situación sintomática de que el tema está todavía en su infancia. Durante la próxima década, las búsquedas de galaxias a alto redshift deben tratar de unificar todas estas clases de galaxias diferente, con el fin de formular una visión coherente de la evolución de galaxias desde el Universo a alto redshift hasta las galaxias que observamos hoy* (Bell et al. 2009). En la práctica, la forma más eficaz para evitar los sesgos observacionales introducidos por el uso de una técnica fotométricas concreta es la combinación de varias de estos técnicas, o por lo menos contar con volumen de datos suficientemente largo y preciso que permita analizar con suficiente precisión las SEDs de las galaxias a lo largo de un amplio rango de longitudes de onda.

Evidentemente, este tipo de esfuerzo no es factible para un un observador individual. Por lo tanto, los *surveys* extra-galácticos más relevantes suelen ser aquellos llevados a cabo por una colaboración a nivel mundial en la que varios grupos unen sus esfuerzos para observar un mismo campo cielo (los llamados campos cosmológicos), lo que a la larga garantiza que esas regiones cuentan con una caracterización multi-longitud de onda muy extensa. Este tipo de grandes colaboraciones también asegura la disponibilidad de proyectos de tiempo garantizado capaces de cumplir los exigentes requisitos observaciones necesarios para dotar estos campos con observaciones en diferentes longitudes de onda. La colaboración más ambiciosa de este tipo hasta la fecha es la de Great Observatories Origins Deep Survey (GOODS; Giavalisco et al. 2004), que cuenta con dos campos clave, uno en el hemisferio norte, centrado en la localización del HDF-N original , y otro en el hemisferio sur. No obstante, muchos otras colaboraciones han seguido a GOODS, como el *survey* de gran área (COSMOS; Scoville et al. 2007), o el Extended Groth Strip (EGS; Davis et al. 2007), que cuenta con uno de los mayores coberturas espectroscópicas disponibles. Reunir grandes conjuntos de datos que incluyan no sólo fotometría, sino también espectroscopia óptica e infrarroja o imágenes de alta resolución, convierte a estos campos en activos clave para poder realizar una amplia gama de objetivos astronómicos.

1.2.4 *Surveys* espectroscópicos de galaxias

Una visión general de los *surveys* de galaxias estaría claramente incompleta si no mencionáramos los seguimientos espectroscópicos. Aunque estos no son el tema principal de esta tesis, se mencionan aquí brevemente debido a su papel fundamental en los estudios de evolución de las galaxias. De hecho, los *surveys* espectroscópicos a *redshifts* bajo e intermedio son el puente entre los estudios a alto *redshift* (fundamentalmente fotométricos) y los estudios locales. Esta conexión es de critica importancia, ya que, así como los modelos ΛCDM nos ofrecen un marco teórico para poner en contexto las observaciones, este cuadro estaría incompleto completo sin la conexión entre los

entre los resultados de estudios del Universo primitivo y del Universo local.

Ejemplos representativos de *surveys* espectroscópicos a bajo *redshift* incluyen el Sloan Digital Survey Sky (SDSS; York et al. 2000) o el Two-Degree Field Galaxy Redshift Survey (2dfGRS; Cole et al. 2001). Ambos *surveys* tienen como objetivo caracterizar las propiedades de la población de galaxias y su relación con el entorno hasta un *redshift* de z$<$0.2, basándose en observaciones espectroscópicas de casi un millón de galaxias. A *redshifts* intermedios (z$<$1.5), existen tres *surveys* principales llevándose a cabo. Estos *surveys* hacen uso de espectrógrafos multi-objeto muy eficientes funcionando en grandes telescopios: El Deep Evolutionary Extragalactic Probe (DEEP; Davis et al. 2003), utilizando LRIS y Deimos en Keck ($>$ 120 noches; Faber et al 2003.), y zCOSMOS (80 noches; Lilly et al 2007) y VIMOS VLT Deep Survey (VVDS; $>$ 70 noches; Le Fèvre et al, 2005.), utilizando VIMOS (Le Fèvre et al. 2003) en el VLT. En los últimos 5 años, estos *surveys* han acumulado unas cuantas decenas de miles de espectros ópticos de galaxias hasta z$\sim$1.

La cantidad y la calidad de la información proporcionada por los datos espectroscópicos es muy superior a lo que puede lograrse inclusos con varias bandas fotométricas. Sin embargo, la debilidad extrema en el brillo de las fuentes mas lejanas, por una parte, y la falta de líneas espectrales detectables, por otra, evita que los *surveys* espectroscópicos continúen su seguimiento exhaustivo en el intervalo de *redshift* entre z$\sim$1.4 y 3 (el llamado *redshift* desierto). A *redshifts* mas altos, galaxias con fuerte emisión en Lyman-α pueden ser detectadas, pero éstas constituyen sólo una pequeña fracción de la población total de galaxias en ese *redshift*. Por lo tanto, los *surveys* espectroscópicos sistemáticos a *redshifts* más altos tendrán que esperar a la próxima generación de instrumentos (espectrógrafos multi-objeto en el NIR) y los telescopios (30m, el JWST), que podrán observar galaxias distantes muy débiles obteniendo espectros en el NIR que muestreen las longitudes de onda ópticas en reposo donde se pueden identificar líneas de emisión intensas.

1.3 Resultados principales de los *surveys* de galaxias

En una época en que las observaciones van un paso por delante de los modelos teóricos, y su aportación es indispensable para el avance de los esfuerzos teóricos, los estudios de evolución de las galaxias proporcionar información no sólo acerca de los componentes principales de la Universo, sino también acerca de las propiedades del Universo en su conjunto.

Ya hemos mencionado algunas de las áreas clave de interés en los estudios de evolución de las galaxias (§ 1.1). A continuación hacemos un breve resumen de dos de los temas de investigación más relevantes en este ámbito, que son comunes a la gran parte de los *surveys* de galaxias actuales.

Crecimiento global en masa

Como mencionamos anteriormente, los modelos actuales de formación de estructura predicen que los halos de materia oscura, ensamblados de manera jerárquica, controlan el proceso general de formación de galaxias. Como consecuencia, la formación de las galaxias deben haber seguido un desarrollo jerárquico similar, dejando huellas de su patrón de crecimiento a través del tiempo cósmico. Por lo tanto, a fin de poner a prueba los modelos teóricos, los estudios del crecimiento en masa se centran en el análisis de muestras de galaxias a diferentes redshifts agrupados por su masa estelar. Esto nos permite realizar el seguimiento de la épocas de formación de las galaxias en función de su masa. Uno de los ingredientes clave de este análisis, es el estudio de la

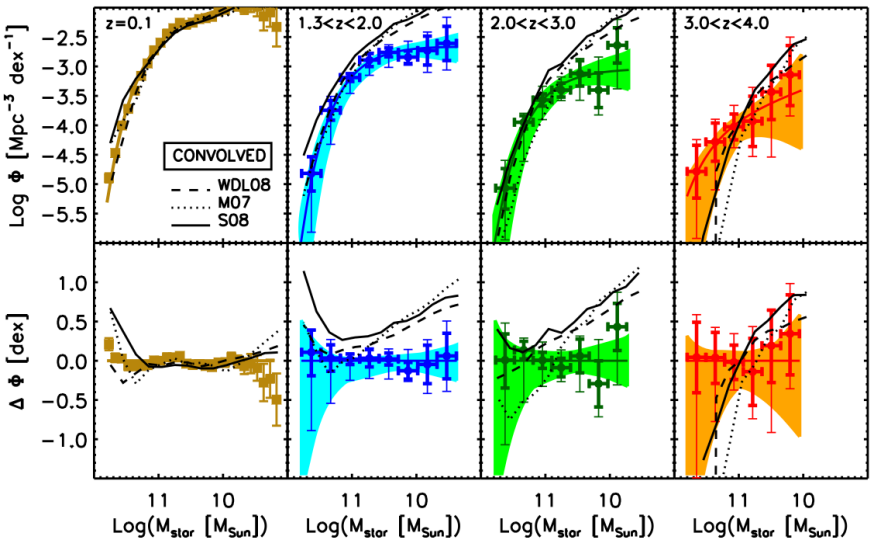

Figure 1.7: Comparación entre las SMF estimadas a partir de datos observacionales y aquellas calculadas con modelos semi-analíticos a diferentes *redshifts* extraídas del trabajo de Marchesini et al. (2009). Las SMF teóricas se representan en color negro: línea solida para Somerville et al. (2008), punteada para Monaco et al. (2007), y discontinua para Wang et al. (2008). Los círculos rellenos en rojo, verde y azul representan las SMFs estimadas con datos observacionales; las barras de error gruesas incluyen errores Poisonianos, varianza cósmica y las incertidumbres en los redshifts fotométricos; las barras delgadas muestran las incertidumbres sistemáticas.

densidad de galaxias en función de su masa estelar a diferentes *redshifts* (es decir, las funciones de masa estelar). La integración de cada una de estas funciones de masa en diferentes intervalos de *redshift* nos permite estimar una densidad de masa estelar (SMD, del ingles Stellar Mass Density) en función del tiempo cósmico, lo que nos proporciona información sobre el ritmo al que se produce en crecimiento en masas de las galaxias.

Estudios recientes que exploran el crecimiento de la masa estelar en el intervalo de *redshift* desde z=3-4 (cuando la primeras galaxias completamente formadas empiezan a detectarse) a z=0.5 (cuando la mayoría de las galaxias más masivas, $M \gtrsim 10^{11} M_{\odot}$, ya se han formado) demuestran que aproximadamente la mitad de la masa estelar en las actuales galaxias se formo en intervalo de tiempo entre 1<z<4 (por ejemplo, Fontana et al. 2006; Pérez-González et al. 2008; Elsner et al. 2008; Marchesini et al. 2009), mientras que el crecimiento en masa restante se llevo a cabo a z<1 (Bell et al. 2004; Faber et al. 2007) impulsado por una ubicua tasa de formación estelar intensa, aunque también afectados de forma significativa por una gran tasa fusión de galaxias, especialmente en los sistemas masivos (Conselice et al. 2003, 2008, 2009; Feldmann et al. 2008).

De hecho, la evolución global de las galaxias parece haber seguido un escenario de *downsizing* (Cowie et al. 1996), consistente en un crecimiento diferencial de la densidad masa estelar, de modo que las galaxias mas masivas se formaron antes y más rápidamente que aquellas de baja masa. Sin embargo, el escenario de *downsizing* sigue siendo un punto de fricción importante entre los modelos y las observaciones. A pesar del acuerdo general sobre el proceso general de crecimiento en masa, los modelos siguen sin poder reproducir los efectos del *downsizing* (o al menos el *downsizing* en masa; Drory & Alvarez 2008; Fontanot et al. 2009) y mas concretamente resultados observacionales como la densidad de galaxias masivas a z=2. Para los modelos, estos objetos evolucionados aparecen en etapas demasiado tempranas de la formación de galaxias (Kriek et al. 2006; Cimatti et al. 2008; Salimbeni et al. 2008; Fontana et al. 2009) y parecen haber conclu-

ido su crecimiento muy pronto (Pozzetti et al. 2003; Arnouts et al. 2007; Ferreras et al. 2009), manifestando un crecimiento en masa mas similar a un colapso monolítico que a un crecimiento jerárquico.

En búsca de una mayor convergencia, las últimas versiones de los modelos de ΛCDM han mejorado su habilidad para el reproducir el extremo mas masivo de las funciones de masa mediante la introducción de una serie de recetas empíricas que suprimen la formación estelar en galaxias primitivas, por ejemplo, las supernovas o el *feedback* de los núcleos galácticos activos (AGN, del ingles Active Galactic Nuclei) (ver por ejemplo, Croton et al. 2006; Bower et al. 2006; De Lucia et al. 2006; Somerville et al. 2008). Además, las simulaciones hidrodinámicas muestran que la gran cantidad de gas presente a alto *redshift* puede conducir a la formación de galaxias esferoidales a edades relativamente tempranas (Naab et al. 2007; Dekel et al. 2009). Existen también importantes incertidumbres sistemáticas en las estimaciones de las masas estelares para galaxias individuales que, en su conjunto, pueden hacer que la forma de la función de masas, especialmente a alto *redshift*, presente grandes incertidumbres (ver por ejemplo, Marchesini et al. 2009). Un re-análisis de las predicciones teóricas teniendo en cuenta estas incertidumbres, muestra que los modelos son capaces de reproducir la evolución de la densidad espacial de las galaxias mas masivas cuando sus predicciones tienen en cuenta estimaciones mas realistas de los errores observacionales en las masas estelares (Fontanot et al. 2009).

Aunque el acuerdo cualitativo entre entre los datos y los modelos es prometedor, algunas discrepancias siguen estando presentes. Por lo tanto, grandes muestras de galaxias caracterizadas con propiedades físicas precisas son fundamentales a la hora de determinar de forma robusta los mecanismos de formación de galaxias.

La densidad de tasa de formación estelar del Universo

El análisis de la evolución con el tiempo cósmico de densidad de tasa de formación estelar (SFRD del ingles Star Formation Rate Density) proporciona una visión complementaria a los estudios de la SMD, trazando la época en que las galaxias formaban activamente la mayor parte de su contenido estelar, que es responsable en última instancia de su crecimiento en masa (o por lo menos del crecimiento de la componente bariónica).

Al igual que las funciones de masa, el calculo de funciones de luminosidad (LF del ingles Luminosity Functions; la densidad de galaxias en función de su luminosidad a diferentes *redshifts* y longitudes de onda) ha madurado rápidamente en los últimos años (Faber et al. 2007; Marchesini et al. 2007; Arnouts et al. 2007). Una ventaja de las LFs es que, bajo ciertos supuestos, la luminosidad de las galaxias esta relacionada con la cantidad de formación estelar en curso, por ejemplo, en el UV una fracción significativa de la luminosidad total es emitida por las estrellas recién formadas, las cuales son tambien responsables de la ionización del gas neutro y por tanto de las líneas de emisión. Así pues, el estudio de las LFs ofrece una medida directa de como evoluciona la densidad espacial de la tasa de formación estelar (SFR; del ingles Star Formation Rate) en las galaxias, lo que nos permite caracterizar la historia de formación estelar global (Lilly et al. 1996; Madau et al. 1996).

La última década ha sido testigo de importantes avances en nuestra comprensión de la historia de la formación estelar. Hoy en día, es posible encontrar varios cientos de estimaciones de la densidad de tasa de formación de estelar calculada a partir de observaciones de galaxias en diferentes longitudes de onda y abarcando un amplio intervalo de tiempo cósmico (por ejemplo,

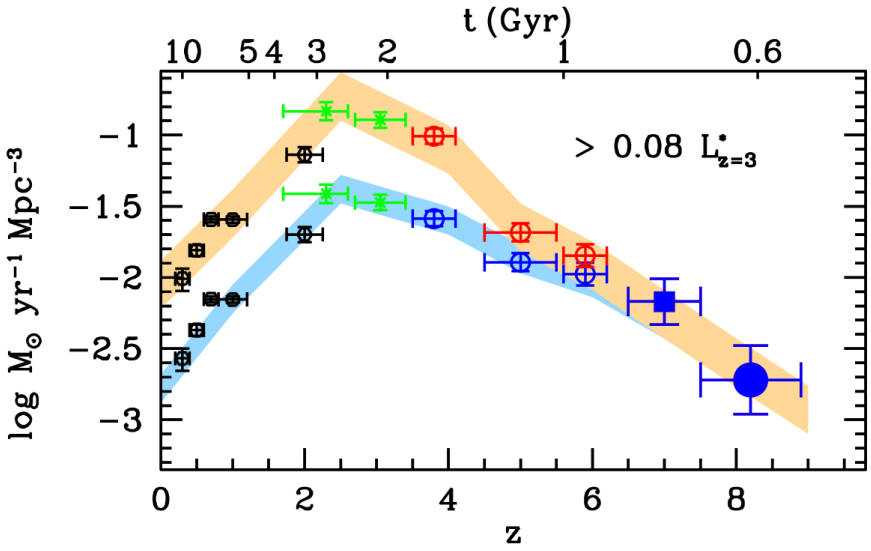

Figure 1.8: Estimaciones de la densidad de luminosidad en el UV y la densidad de SFR a diferentes *redshifts* mostrando los resultados de diferentes autores, extraído de (Bouwens et al. 2010). Los círculos rojos grandes muestran las estimaciones a z∼8 obtenidas a partir de objetos seleccionados con la técnica *drop-out* en las imágenes en banda Y obtenidas con *HST*/WFC3. El conjunto de puntos más bajo (y la región en azul) muestran la densidad de SFR inferida directamente a partir de datos en el UV, mientras que los puntos superiores (y región naranja) muestran el valor que se obtendría corrigiendo las medidas anteriores de los efectos de extinción del polvo estimados a partir de la pendiente del continuo UV.

Hopkins & Beacom 2006). En conjunto, estas observaciones sugieren un rápido aumento en la SFRD desde la época de la reionización hasta z=2-3 (Bouwens et al. 2010a). A partir de ese momento, la SFRD ha disminuido gradualmente durante los últimos 10 millones de años (Schiminovich et al. 2005; Arnouts et al. 2005) hasta su valor actual (Gallego et al. 1995), que es al menos un factor de 10 bajo que en la época de máxima actividad. Este panorama global es frecuentemente explicado en el contexto de un crecimiento jerárquico de pequeños bloques constituyentes con grandes reservas de gas en épocas tempranas del Universo, que agotan o pierden este material (a través de Supernovas o AGNs) en épocas mas tardías.

Sin embargo, aunque esta caracterización de la historia de formación estelar es correcta groso modo, hay varios detalles importantes que aún no están bien determinados, lo que causa ciertas controversias a la hora de interpretar los resultados. Algunos de estos problemas surgen de la discrepancia sustancial en las medidas de la SFRD derivadas a partir de observaciones a diferentes longitudes de onda, sobre todo entre la estimación basada en el UV (Schiminovich et al. 2005; Salim et al. 2007; Reddy et al. 2008), líneas de emisión (Villar et al. 2008; Sobral et al. 2009), y aquellas obtenidas a partir de medidas en el infrarrojo y sub-mm (Le Floc'h et al. 2005; Pérez-González et al. 2005; Caputi et al. 2007). Así pues, a pesar de los esfuerzos por reunir grandes cantidades de datos, las incertidumbres en los factores de conversión entre luminosidad y SFR (véase, por ejemplo, Kennicutt 1998 o Moustakas et al. 2006), la cantidad de oscurecimiento debida al polvo, o el sesgo introducido por los diferentes criterios de selección de cada *survey* son todavía una fuente potencial de discrepancias. Una forma mas fiable de estimar la SFRD consistiría en la comparación de dos o más indicadores de la tasa de formación estelar para un mismo grupo de objetos. No obstante, mientras que los nuevos *surveys* de galaxias proporcionan grandes muestras de objetos con las que uno puede llevar a cabo diversos estudios, las muestras de las galaxias para

las cuales contamos con más de un indicador de la tasa de formación estelar no es necesariamente tan grande.

Otro problema potencial para el análisis de la formación de galaxias es el desacuerdo entre la SFRD y SMD a alto *redshift* ($z \gtrsim 2$). Varios estudios revelan que la integración con respecto al tiempo de las estimaciones de la SFRD tienden a sobre-estimar la SMD a bajo *redshift* (Eke et al. 2005; Hopkins & Beacom 2006; Pérez-González et al. 2008). Estas diferencias sugieren que o bien las estimaciones de la masa estelar son incorrectas o bien la historia de formación estelar está sobre estimada, o quizás ambos (Wilkins et al. 2008). Soluciones alternativas podrían ser que las tasas de formación estelar a alto *redshift* pudieran ser el resultado de una evolución de la función inicial de masa (IMF; van Dokkum et al. 2008; Meurer at al. 2009), lo que sin embargo tendría repercusiones significativas en otros observables (ver por ejemplo, Fardal et al. 2007), otra posibilidad es que hubiera una cantidad considerable de la masa total a alto-z que estuviera encerrada dentro de una población de galaxias poco brillantes y poco masivas, que podrían perderse en una muestra seleccionada en masa. Estas tendrían que ser lo suficientemente numerosas para variar sensiblemente con total de la masa estelar (Reddy & Steidel 2009).

Una vez más, estas discrepancias entre parámetros estimados observacionalmente, pone de relieve la necesidad de que el análisis de la historia de la formación estelar y la evolución de la SMD se lleven a cabo a partir de estudios que combinen diferentes indicadores basados en datos multi-longitud de onda reduciendo los sesgos observacionales los máximo posible.

1.4 Apuntes sobre *surveys* de galaxias

De las discusiones llevadas a cabo en las secciones anteriores se deduce que, para resolver las controversias actuales sobre evolucion de galaxias, son necesarias grandes muestras de galaxias que cuenten con una cobertura multi-banda exhaustiva. Sólo entonces seremos capaces de caracterizar con precisión las propiedades físicas de las galaxias de manera que estas nos garanticen la obtención de resultados significativos sobre su evolución.

En ese sentido, los *surveys* modernos ofrecen capacidades extraordinarias para examinar las propiedades de miles de galaxias de forma simultánea y coherente. Sin embargo, sin una adecuada combinación y modelización de la gran cantidad de datos espectro-fotométricos un análisis detallado de sus propiedades globales no puede llevarse a cabo. Por lo tanto, un paso fundamental para aprovechar plenamente las posibilidades de grandes conjuntos de datos es conectar de manera eficiente los heterogéneos recursos observacionales (datos crudos) y las propiedades intrínsecas de las galaxias.

La mayoría de los estudios actuales basados en grandes muestras de galaxias tienen que lidiar con esta situación de alguna manera. Paradójicamente, a pesar del continuo crecimiento de recursos observacionales, un proyecto a veces puede a veces sufrir un exceso de datos. En ese caso, es la gran cantidad de información la que causa un cuello de botella que nos impiden extraer información valiosa sobre las galaxias individuales observadas en las imágenes.

La tarea de combinar todos los datos disponibles de manera eficiente para obtener cantidades significativas de una galaxia en particular implica varios pasos, por lo que no es un procedimiento sencillo. En primer lugar debemos realizar identificación multi-banda de cada objeto y calcular una

fotometría consistente para cada fuente en cada una de estas bandas. Después, se ha de modelar la fotometría combinada de forma que podamos estimar las propiedades intrínsecas de cada objeto. Todo ello debe realizarse además, teniendo en cuenta los posibles sesgos observacionales no deseados o los errores sistemáticos que se puedan introducir a raíz de las limitaciones del método usado. Por ejemplo, los errores derivados de la falta de suficientes datos fotométricos a ciertas longitudes de onda, o de las asunciones realizadas durante la estimación estimación de las propiedades físicas.

1.5 Objetivos de la tesis

El objetivo principal de esta tesis es utilizar datos fotométricos multi-longitud de onda para obtener las estimaciones mas fiables de importantes parámetros físicos para galaxias a *redshifts* intermedios-altos. Esto nos proporcionara información sobre los procesos de formación y evolución de galaxias a lo largo de la mayor parte del tiempo de Hubble. Más concretamente, en este trabajo de tesis se ha creado una gran muestra de galaxias que abarca un amplio intervalo de *redshift* y hace uso de: fotometría óptica e infrarroja para caracterizar sus propiedades físicas mas relevantes; fotometría en el infrarrojo medio-y-lejano para caracterizar la tasa de formación estelar de estas galaxias a través del análisis de la emisión del polvo; datos espectroscópicos para determinar con precisión su *redshift*, consiguiendo así una mejor caracterización de sus propiedades en reposo (luminosidades, colores, etc.). El análisis simultaneo de todas estas propiedades nos permitirá caracterizar su crecimiento y evolución con el tiempo cósmico.

Para lograr estos objetivos, en primer lugar nos centramos en la obtención de una amplia muestra de galaxias seleccionadas en una imagen de *Spitzer*/IRAC (que abarca el rango espectral de 3.6 a 8.0 micras) del campo cosmológico Extended Groth Strip (EGS), el cual es uno de los campos profundos mas importantes. Este campo se ha observado usando observatorios terrestres y espaciales, por lo que presenta una gran cantidad de datos espectro-fotométricos de muy alta calidad y en múltiples longitudes de onda. En el **Capítulo 2** nos centraremos en los detalles técnicos de **la creación de la muestra de galaxias y la obtención de un catálogo fotométrico multi-longitud de onda** consistente basado en todos estos datos. Este catálogo servirá de base para la posterior modelización de las SED de las galaxias desde el UV hasta el infrarrojo lejano, lo que nos permitirá estimar sus propiedades físicas. Además, en el capítulo 2 se presentan también los resultados mas relevantes sobre las propiedades fotométricas en el UV, óptico e infrarrojo lejano de la muestra seleccionada en el NIR (IRAC). En particular, se discutira el método de de-convolución empleado para reducir los efectos de confusión de fuentes en las bandas IRAC, que son de critica importancia para obtener densidades de fuentes realistas o estudiar la distribución espacial de las galaxias. A continuación se presenta un resumen detallado de los objetivos principales de los capítulos 2:

- **Capítulo 2:** reunir un conjunto de datos espectro-fotométricos exhaustivos en el campo EGS; combinar los datos de diferentes *surveys* reduciendo y catalogando los datos cuando sea necesario; crear una muestra seleccionada en IRAC caracterizando su nivel de completitud, identificar las contrapartidas multi-banda de las fuentes IRAC, dotar al catalogo de fotometría multi-longitud de onda consistente teniendo en cuenta las diferencias en profundidad y resolución espacial, análizar la propiedades multi-banda del catalogo (es decir, el número de bandas en las que se detectan las fuentes IRAC) en función de la magnitud y redshift; identificar la naturaleza estelar o galáctica de las fuentes.

Entre las múltiples posibilidades científicas del catalogo multi-longitud de onda, el objetivo inmediato y a largo plazo de esta tesis se centra en estudiar de forma global el proceso de crecimiento en masa en galaxias a diferentes edades del Universo. Con este objetivo, la muestra de galaxias está seleccionada en el infrarrojo cercano (próximo a una selección en masa) y una fracción significativa del trabajo se dedicara a calcular **masas estelares** precisas y a analizar en detalle las incertidumbres asociadas. Igualmente importante para caracterizar el crecimiento de las galaxias es determinar el ritmo al que cada galaxia incrementa su masa (es decir, la cantidad de estrellas que contiene). Por lo tanto, los métodos y los posibles sesgos en la estimación de **SFRs** precisas serán también ampliamente discutidos en esta tesis. Junto con los **redshifts** fotométricos, sin los cuales no podríamos estudiar la evolución con el tiempo cósmico, la estimación y análisis de las masas estelares y las SFRs serán la pieza central del **Capítulo 3**. A continuación se presenta un resumen detallado de los principales objetivos de este capítulo:

- *Capítulo 3:* caracterizar la SED desde el óptico al infrarrojo cercano para todas las galaxias de la muestra mediante el ajuste de la fotometría observada a *templates* sintéticos calculados con modelos de síntesis de poblaciones estelares; estimar *redshifts* fotométricos y masas estelares a partir de este ajuste; cuantificar la calidad general de los *redshifts* fotométricos mediante la comparación frente a *redshifts* espectroscópicos y otros *redshifts* fotométricos publicados previamente; evaluar la precisión de las masas estelares mediante la exploración de posibles efectos sistemáticos derivados de la utilización de diferentes supuestos en el modelado de las poblaciones estelares; estudiar la bondad de las masas estelares comparándolas con las estimaciones de otros autores, caracterizar la SED de las galaxias en el rango espectral del infrarrojo medio a lejano mediante el ajuste de la fotometría a diferentes templates de emisión del polvo; estimar SFRs con trazadores UV e IR basadas en el ajuste completo de la SED para todas las galaxias; estimar las incertidumbres aleatorias y sistemáticas típicas de las SFR en el infrarrojo comparando los valores obtenidos con diferentes conjuntos de modelos y estudiando el efecto de trabajar con una cantidad reducida de datos IR.

Explotar todos los datos espectro-fotométrico disponibles en los campos cosmológicos es el punto de partida habitual en los estudios actuales basados en el análisis de fuentes extra-galácticas. Por tanto, es importante subrayar que el objetivo fundamental de esta tesis no solo es la creación de un catálogo como medio para resolver un problema científico específico, si no el desarrollo de la herramienta lo más general posible, obteniendo para ello la más amplia gama de propiedades fundamentales de las galaxias que nos servirán para múltiples propósitos. Por esta razón, en esta tesis nos centraremos no sólo en la **obtención de múltiples propiedades físicas** sino también de **asegurar su calidad y precisión**. Esto incluye la comprobación de los posibles sesgos observacionales y limitaciones del método en si, de manera que los resultados obtenidos con estos datos proporcionen conclusiones científicas sólidas.

La calidad y cantidad de parámetros estimados para miles de galaxias en el campo cosmológico EGS permitirá llevar a cabo múltiples proyectos científicos diferentes. Por ello, un objetivo fundamental de esta tesis es hacer que todos los datos procesados y los parámetros estimados en este catalogo estén a disposición de toda la comunidad astronómica. Para ello, nuestro objetivo sera desarrollar un **interfaz web multi-funcional que permita a los usuarios el acceso a todos los datos para las galaxias en EGS**. La herramienta resultante aumentará significativamente el legado de los *surveys* observacionales que han empleado una cantidad significativa de

recursos para ser llevados a cabo. Una descripción de nuestro trabajo en este sentido se detalla en el **Capítulo 2** y también en el **Apéndice 1**.

A largo plazo, este catálogo será la semilla para múltiples estudios de la evolución de las galaxias. Sin embargo, para presentar algunas de las numerosas posibilidades de este y otros catálogos similares, en esta tesis se discuten varios estudios destinados responder preguntas científicas más concretas. La mayor parte de los esfuerzos en este sentido se detallan en el **Capítulo 4**, que constituye el objetivo principal de esta tesis después de la creación del catálogo en si. En este capítulo nos centramos en investigar la relación existente entre la magnitud observada y la distribución en *redshift* para una muestra seleccionada en el infrarrojo cercano (banda K). En particular, estudiaremos si **las características observadas en la forma del número de cuentas de galaxias (NCs del ingles Number Counts; la densidad observada de galaxias en función de la magnitud) están relacionadas con una evolución temporal en la distribución intrínseca en luminosidad (funciones de luminosidad) de estas galaxias**. A continuación presentamos un resumen de los principales objetivos de este capítulo:

- *Capítulo 4:* investigar las causas que hacen que la forma de las cuentas de galaxias de la banda K sea diferente de las cuentas de galaxias en bandas óptica; determinar la naturaleza de las galaxias que constituyen el grueso del número de cuentas hasta $K = 19$, explorando la contribución relativa de las galaxias a diferentes *redshifts*; realizar un análisis de la forma funcional del número de cuentas en términos de las funciones de luminosidad (LF) a distintos *redshifts*; calcular LFs a diferentes *redshifts* para la muestra seleccionada en banda K; estimar el número de cuentas de galaxias en la banda K a partir de LFs en diferentes bandas en reposo; explicar la características más relevantes en la forma del número de cuentas en banda K en términos de la evolución con el *redshift* de los parametros clave de las LFs.

Numerosos **trabajos liderados por otros autores se han beneficiado directamente del procesado de datos y el calculo de parámetros realizado en esta tesis**. A continuación presentamos una lista de estos trabajos que se han publicado en revistas arbitradas y de los que soy co-autor. En el **Capítulo 5 se presenta un resumen detallado de una selección de estos trabajos** (los marcados en negrita a continuación), poniendo de relieve los resultados más relevantes de cada uno.

- *Colaboraciones:*

- **Exploring the Evolutionary Paths of the Most Massive galaxies**. Pérez-González, Pablo G., Trujillo, Ignacio, Barro, Guillermo, Gallego, Jesus, Zamorano, Jaime, & Conselice, Christopher J. 2008, The Astrophysical Journal.

- *Spitzer View on the Evolution of Star-forming Galaxies from z= 0 to z∼3*. Pérez-González, Pablo G., Rieke, George H., Egami, Eiichi, Alonso-Herrero, Almudena, Dole, Hervé, Papovich, Casey, Blaylock, Myra, Jones, Jessica, Rieke, Marcia, Rigby, Jane, Barmby, Pauline, Fazio, Giovanni G., Huang, Jiasheng, & Martin, Christopher 2005, The Astrophysical Journal.

- **The Stellar Mass Assembly of Galaxies from z = 0 to z = 4: Analysis of a Sample Selected in the Rest-Frame Near-Infrared with Spitzer**. Pérez-González, Pablo G., Rieke,

George H., Villar, Victor, Barro, Guillermo, Blaylock, Myra, Egami, Eiichi, Gallego, Jesús, Gil de Paz, Armando, Pascual, Sergio, Zamorano, Jaime, & Donley, Jennifer L. 2008, The Astrophysical Journal.

- **The Spitzer's Contribution to the AGN Population**. Donley, J. L., Rieke, G. H., Pérez-González, P. G., & Barro, G. 2008, The Astrophysical Journal.

- *The Minor Role of Gas-Rich Major Mergers in the Rise of Intermediate-Mass Early Types at $z \lesssim 1$*. López-Sanjuan, Carlos, Balcells, Marc, Pérez-González, Pablo G., Barro, Guillermo, García-Dabó, César Enrique, Gallego, Jesús, & Zamorano, Jaime 2010, The Astrophysical Journal.

- *The galaxy major merger fraction to z=1* López-Sanjuan, C., Balcells, M., Pérez-González, P. G., Barro, G., García-Dabó, C. E., Gallego, J., & Zamorano, J. 2009, Astronomy and Astrophysics.

- *Characterization of Active Galactic Nuclei and Their Hosts in the Extended Groth Strip: A Multiwavelength Analysis*. Ramos Almeida, C., Rodríguez Espinosa, J. M., Barro, G., Gallego, J., & Pérez-González, P. G. 2009, The Astronomical Journal.

- **Infrared Excess sources: Compton thick QSOs, low-luminosity Seyferts or starbursts?**. Georgakakis, A., Rowan-Robinson, M., Nandra, K., Digby-North, J., Pérez-González, P. G., & Barro, G. 2010, Monthly Notices of the Royal Astronomical Society.

- *The Hα-based Star Formation Rate Density of the Universe at z= 0.84*. Villar, Víctor, Gallego, Jesús, Pérez-González, Pablo G., Pascual, Sergio, Noeske, Kai, Koo, David C., Barro, Guillermo, & Zamorano, Jaime 2008, The Astrophysical Journal.

Esta tesis se presenta como una recopilación de artículos. En particular, el material que abarca los Capítulos 2, 3 ha sido publicado en Astrophysical Journal Supplement (2011ab), y el Capítulo 4 ha sido publicado en Astronomy and Astrophysics (2009). Además, en el Capítulo 5 se resumen los resultados de varios artículos publicados en diferentes revistas con arbitro (ver mas arriba). Para facilitar la comprensión y de poner los capítulos en el contexto general de la tesis, cada uno de ellos incluye una breve introducción que proporciona información básica sobre los temas abordados más adelante en los artículos. Por último, la tesis es precedida y concluida por un traducción completa de la Introducción y conclusiones generales.

Nótese que los resultados de los Capítulos 2 a 5 no se presentan en estricto orden cronológico, si no siguiendo una estructura más lógica. Esto se debe a que el análisis presentado en los Capítulos 2-3 se centra en la caracterización de las propiedades de una muestra de galaxias, mientras que los Capítulos 4 y 5 se centran en cómo utilizar las cantidades derivadas de tales caracterizaciones para abordar las cuestiones más concretas. Además, como se mencionó anteriormente, los Capítulos 2 y 3 constituyen el grueso de trabajo desarrollado para esta tesis, y se les da así más relevancia. Como consecuencia de ello, el Capítulo 4 no sigue estrictamente los resultados de la capítulos anteriores, sino más bien al contrario. De hecho, el objetivo principal del estudio presentado en el Capítulo 4 fue realizado con éxito utilizando una versión reducida (en tamaño y profundidad) de la muestra de galaxias presentada en los capítulos 2 y 3. No obstante, las conclusiones de este trabajo nos indicaron la necesidad de obtener una muestra de galaxias más ambicioso. En particular, una basada en unos datos que cuenten con una área observada superior y una mayor profundidad

(como por ejemplo la que nos proporciona *Spitzer*/ IRAC), que aumente la sinergias con todos los otros datos disponibles y nos permita llevar cabo un análisis científico más ambicioso, como los presentados en el Capítulo 5.

1

Introduction

1.1 Understanding the global galaxy evolution

The scientific development of the last decade which most impacted the study of galaxy formation was the establishment of the Λ-Cold Dark Matter (ΛCDM) concordance cosmological model. In this model the Universe consists of ∼70% dark energy, ∼25% dark matter and only ∼5% of ordinary matter. Early developed in the 1980s (Peebles 1982), the success of these ΛCDM lies in its capability to simultaneously explain the nature and structure of the cosmic microwave background (CMB; the remnant of the Bing Bang; Smoot et al. 1992), the expansion of the Universe, as well as the observed large scale structure in which galaxies are arranged (the cosmic web; see left panel of Figure 1.1).

The firm establishment of this paradigm has shifted the focus of galaxy population studies from constraining cosmological parameters to characterizing the processes which drive the formation and evolution of galaxies. Knowing the values of most of the fundamental cosmological parameters with very high accuracy (Spergel et al. 2003; Komatsu et al. 2010), we find ourselves in a new era of precision cosmology, where the most important challenge is understanding the formation of the galaxies themselves.

Within the ΛCDM cosmological framework our present knowledge of how galaxies formed is based upon the idea that only a small subset of the total mass of a galaxy is traceable by their light. On the contrary, most of the mass is contained by a surrounding halo of dark, non-baryonic, matter that ultimately drives the evolution of the baryons contained within (White & Rees 1978; Davis et al. 1985; White & Frenk 1991). ΛCMD has provided a successful theoretical background for characterizing the behavior of these dark matter halos. Nowadays, their evolution can be modeled to high accuracy by running large N-body simulations, that describe their growth from the initial fluctuations detected in the cosmic microwave background (Somerville & Primack 1999; Cole et al. 2000; De Lucia et al. 2004; Springel et al. 2005b; Bower et al. 2006; Croton et al. 2006). However, in spite of some significant achievements explaining the formation of cosmic structures, there are still many challenges in explaining the hierarchical growth of real galaxies. For example, while the models are quite successful in matching the observed large-scale distribution of galaxies, simulations appear to predict an excess of dark matter sub-halos that do not match the number of dwarf satellites observed within the Local Group (Kauffmann et al. 1993; Mateo 1998; Moore et al. 1999) . In addition, and more fundamentally, the crucial processes that regulate galaxy evolution within the haloes: gas accretion, star formation and “feedback” (the effect of the energy input from one generation of sources to the next) are extremely complex, and thus still poorly understood (Kauffmann & Haehnelt 2000; Granato et al. 2004; Springel et al. 2005a).

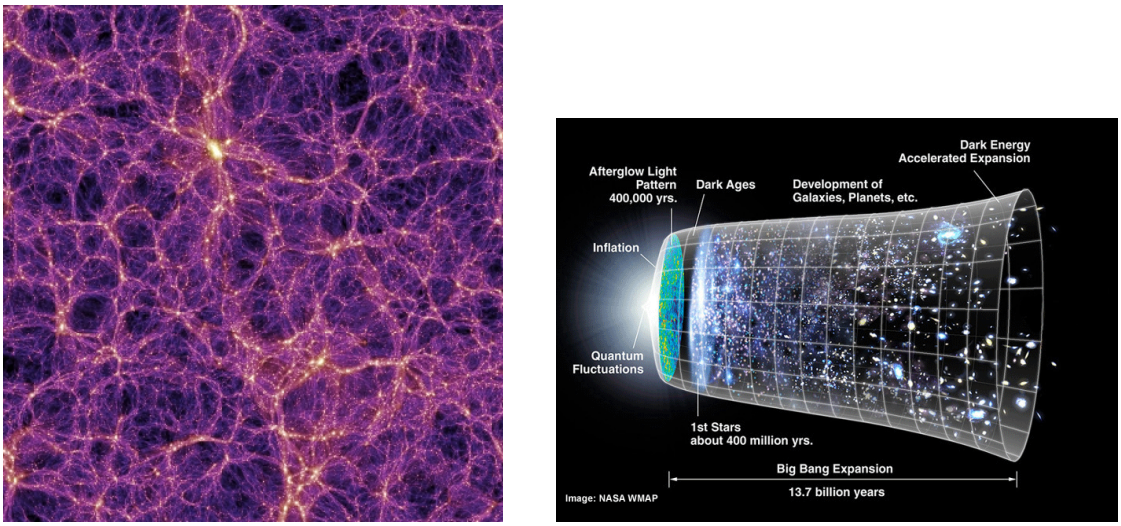

Figure 1.1: Left: The Cosmic Web as pictured by ΛCDM models. The color code depicts the dark matter density field on a Gpc scale. The bright and dark colors indicate the highest and lowest density regions, respectively. The bulk of the galaxy formation takes place in the brightest areas. Right: Schematic view of the evolution of the Universe from the primordial fluctuations of the CMB formed shortly after the Big Bang, to the wide variety of galaxy types observed in the local Universe.

Nevertheless, despite these issues modeling the physics of the interactions (most of the times associated with the limited resolution of the models), numerical simulations are powerful tools that provide a great insight into the early stages of galaxy formation. Within the ΛCDM paradigm, the (simplified) picture of galaxy evolution follows a two stage process (see e.g., Baugh 2006 for a detailed review) : First, driven by a mechanism of gravitational instability, dark haloes form in a dissipation-less, gravitational collapse. In this phase the first structures start to develop following the radiative cooling of baryons. Second, the condensation of the large masses of pristine gas stabilizes the proto-galaxies against the disruption caused by the merging of the haloes. Then, within these primordial seeds, star formation triggers in sufficiently massive halos starting the sequence of global chemical evolution (including metals and dust formation). Later on, additional feedback process are required to make small galaxies more diffuse and less successful at surviving the merging process, thus avoiding the production of more faint galaxies than are observed. On a global scale, these primeval stars and galaxies would gradually reionize the (opaque) neutral gas that populates the universe from shortly after the Big Bang (see e.g., Loeb & Barkana 2001 and references therein). After that, this oversimplified pattern will essentially replicate itself at large scales and eventually the complicated balance between gas accretion, cooling, and merging will lead to the local scenario that we observe today. The right panel of Figure 1.1 shows a simplified scheme of the whole evolutive process.

All in all, much of the recent success in understanding galaxy formation would not have been possible without a corresponding similar improvement in the quality of the observational astrophysics, that has provided direct evidence of the high redshift universe. The synergy between theory and observations allows to integrate the observations of galaxies at different ages of the Universe in a consistent framework. At the same time, this process also raises several questions and make predictions that can be put to test with the data.

Ultimately, the purpose of studying the evolution of galaxies is determining how galaxies

evolved from the primordial fluctuations in the CMB to the diverse population of disk and elliptical galaxies that we observe today?. However, this general question which can be summarized into several other key questions:

- When did the first galaxies form?
- How and when did galaxies assemble their stars?
- What triggers episodes of galaxy-scale star formation? What shuts them off?
- What is the role of environment in driving galaxy formation to its present scenario?

The evolution of galaxies from primordial seeds to mature massive systems depends on the answer to such questions. Therefore, **in order to perform a detailed analysis we need to assemble large samples of galaxies at different ages of the Universe**. Only by understanding the evolution with cosmic time of the process that drives the formation of galaxies could we derive a robust picture of the whole process.

Although the study of galaxies at different epochs of the Universe are equally important, from the observer point of view, there are significant differences in the approach to galaxy surveys when these are focus on the study of local galaxies (within a few Mpc) or distant galaxies at different cosmic times ($z \gtrsim 0.05$-0.1). Whereas the first frequently involve whole sky (or a very large area) surveys, the latter focus on deep observations of relatively small regions. In the next sections we will focus on these surveys which are more closely related with the topic of this thesis. In particular, we will explain their motivation and main characteristics from a historical context, describing them from their early developments to their actual state. Then, we will describe some of the main results that we can obtain from them.

1.2 The search of distant galaxies

1.2.1 The first galaxy surveys

Similarly to what happened with the initial formulations of the cosmological models, the fundamental ideas behind the systematic search of primeval galaxies were also soon developed. Partridge & Peebles (1967a,b) were the first to discuss the expected far-UV spectral energy distribution (SED) of star-forming galaxies and the general methodology of how to exploit the features present in this wavelength range, such as the 1216 Å, Lyman-α emission line (and Lyα forest; Gunn & Peterson 1965) or the 912 Å Lyman limit, as observational flag poles to identify distant galaxies (see Figure 1.2). The idea behind this technique is the detection of these strong features in different observed bands as a result of the cosmological redshift. Unfortunately, the first photometric surveys following these pioneering theoretical works proved to be unsuccessful, mainly due to the limitations of the available photographic and photoelectric detectors (Davis & Wilkinson 1974) and even the first modern CCDs (Koo & Kron 1980).

In fact, the first handful of galaxies at significant redshifts ($z > 1.5$) were detected using observations at non-optical wavelengths. The systematic spectroscopic follow-up of the hosts of radio sources from the revised 3rd Cambridge catalog (3CR; Bennett 1962), led to the confirmation of

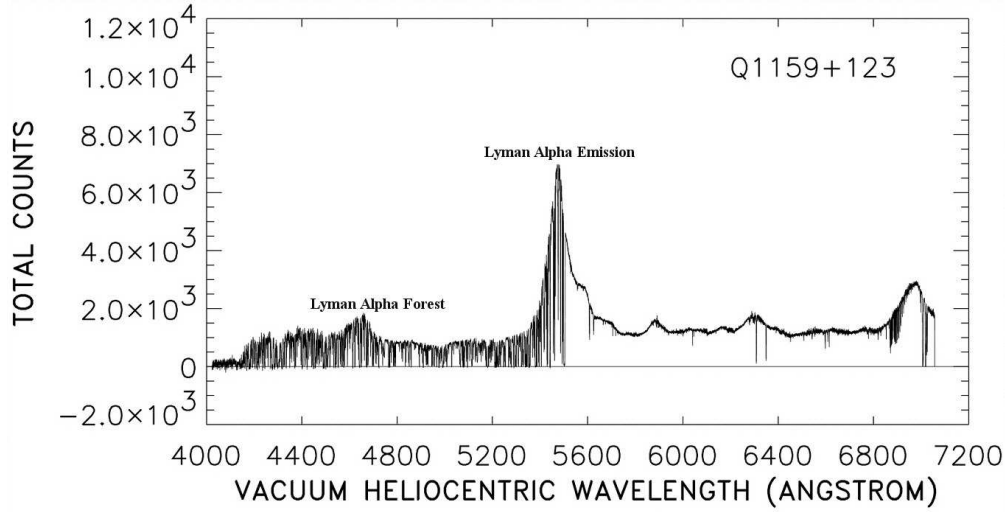

Figure 1.2: Optical spectra of a galaxy at redshift z=3.52 depicting the rest-frame UV. The spectra shows the Lyman-α line, emitted at 1216 Å rest-frame, jointly with the Lyman-α forest, caused by the absorption of Lyman photons (those emitted at λ<1216 Å rest-frame) in galaxies at lower redshifts. Adapted from Pahre & Djorgovski (1995).

a few hundreds high redshift galaxies showing well-characterized emission lines (Spinrad & Djorgovski 1984a,b; Spinrad et al. 1985). In the following years a few more detections were reported based on Lyman-α detections targeted around some of these known QSOs, and looking for companions at the same redshift as the quasars (e.g., Schneider et al. 1986, Hu & Cowie 1987). Due to the success of these searches, up until recently, high redshift galaxies was synonym for radio galaxies. Nevertheless, other early surveys using both narrow-band and long-slit techniques to detect this emission line find essentially no detections (Lowenthal et al. 1990, de Propris et al. 1993, Thompson et al. 1995) and the few that succeeded, demonstrated that these observations were only sensitive to the few brightest, and thus rarest objects in the fields.

1.2.2 Modern photometric surveys

The dawn of *modern* photometric surveys, routinely returning thousands of high redshift galaxies, had to wait until the 1990's. The launch of the Hubble Space Telescope (HST 1990), the commissioning of the first 8 to 10 meter-class telescopes (Keck 1993; SUBARU 1999) and the improvements in detector technologies, providing high sensitivity and large area CCDs, opened the door to a full systematic exploitation of the galaxy search techniques. Indeed, the first major breakthrough in the characterization of the high redshift universe was perhaps the observations of the Hubble Deep Field (Williams et al. 1996, Figure 1.3). The unprecedented faint imaging (2.5'x2.5') containing literally thousands of galaxies (depicted with extremely high spatial resolution) held the key for the success of the previously under-performing Lyman-break dropout technique to isolate high redshift (z>3; LBGs) galaxies (Steidel et al. 1996, see Figure 1.4).

Following the spectroscopic identification of the initial LBGs candidates, the first multi-object spectrograph, mounted in the Keck telescope, allowed the systematic confirmation of more than a thousand galaxies at $z \gtrsim 3$ (Steidel et al. 1999). At the same time, complementary surveys making use of combined ground-based and HST observations allowed to push the search to higher redshifts, while rapidly expanding the number of photometric candidates. With this aim, new sur-

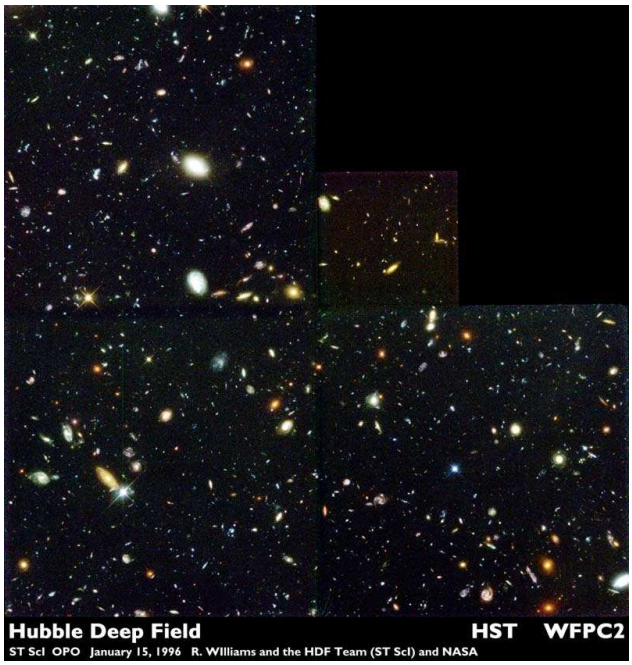

Figure 1.3: The original Hubble Deep Field taken with the Wide Field and Planetary Camera 2 (WFPC2) on board the Hubble Space Telescope (Williams et al. 1996). The image is composed of 342 different exposures taken in 10 consecutive days in December of 1995. The field was observed for $\sim$30h in 4 different broad band filters at 300 nm, 450 nm, 606 nm and 814 nm. The color image was obtained by combining the data taken in 3 different broad band filters.

veys started ultra-deep multicolor observations at key locations of the sky, signaling the beginning of the fruitful exploitation of *blank* surveys.

The availability of large telescopes, dedicated facilities and space-based observations supposed a great leap forward in the search for distant galaxies. Along with the LBGs, some other photometric techniques began to prosper during the mid 1990's. The most relevant of these blind search techniques, can be briefly classified in essentially two categories.

- The **LBG** or **drop-out** techniques, which selects galaxies over a certain redshift interval by measuring a strong discontinuity in the continuum based on the detection of the galaxy in several (sometimes only 2, but generally more) broadband filters. The generalization of this method by measuring prominent features in the galaxy SED, other than the Lyman break, is often referred as a **color** selection technique.

- **Emission line** searches, targeting Lyman-α emitters (LAEs) or other galaxies showing strong emission lines, such as Hα or [OII]. Basically, two similar photometric techniques may be used to identify the lines: 1) Narrow Band imaging, based on the use of a combination of a broad band filter and a narrow band ($\Delta\lambda$=10-50 Å) to detect the excess flux of a specific at a certain redshift (see right panel of Figure 1.5); 2) Tunable filter imaging, based essentially on the same technique but working on customizable wavelength range that allows to expand the line search on a wider redshift interval.

According to a census by Bouwens et al. (2006), by that time, the **drop-out** technique had already identified around: 4000 z$\sim$4 galaxies (B-dropout), 1000 z$\sim$5 galaxies (V-dropout), and

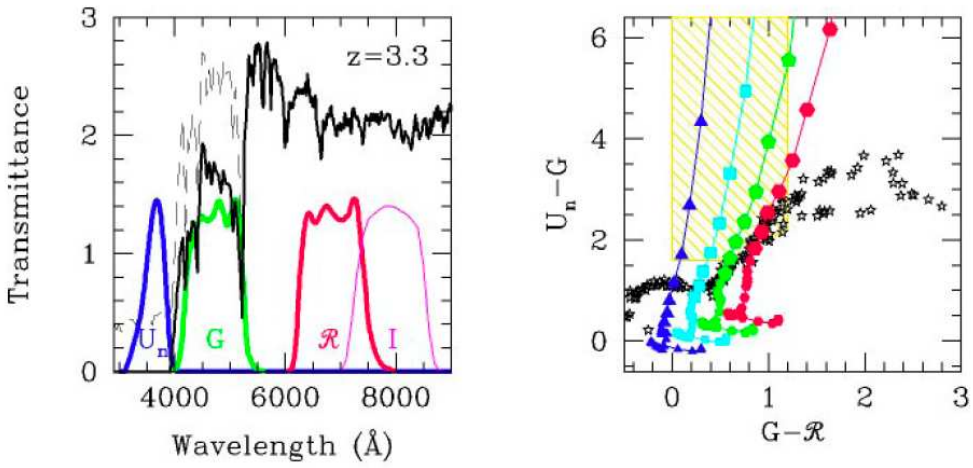

Figure 1.4: Left: The blue, green and red lines depict the set of broad band filters (U_n,G,R) used by Steidel et al. (1996) to identify LBGs at z$\sim$3. The black line shows a synthetic galaxy spectra of continuous star formation (Bruzual & Charlot 1993) featuring the Lyman break at 912 Å rest-frame. Right: Color-Color criteria used to select the LBG candidates. The curves represent synthetic galaxies (with continuous star formation) placed at progressively higher redshifts, starting at z=0.5 with step z=0.1. The four tracks correspond to different amounts of dust obscuration ranging from zero extinction (blue) to A(V)=2 mag (red). The locus of stellar colors is shown as stars. The shaded areas correspond to the selection criteria at z$\sim$3. Both figures are extracted from Giavalisco et al. (2002)

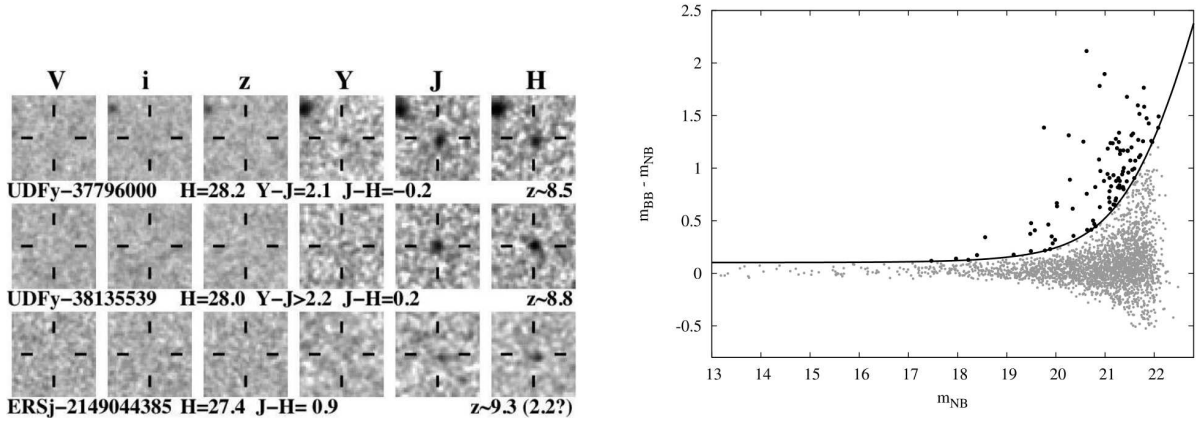

Figure 1.5: Left: Image cutouts of three z$\sim$8.5-9 galaxy candidates identified in the ultra-deep HUDF WFC3/IR observations with the LBG technique (adapted from Bouwens et al. 2010b). None of the candidates is detected in the deep ACS BV iz observations, and at least two of them are Y-band drop-outs indicating, i.e., the lyman break shifted to the NIR bands due to the (high) redshift of the galaxies. Right: Color-magnitude diagram for candidates to emission line galaxies at z=0.84 (black) detected with a narrow-band filter technique in Villar et al. (2008). An excess in the narrow band vs. broad band color indicates that the narrow band filter is picking up an additional contribution to the flux due to an emission line. In this case, the Hα emission at 6563Å rest-frame is detected in the narrow-band filter at $\lambda_{\rm eff}$=1.20 μm for galaxies at z=0.84.

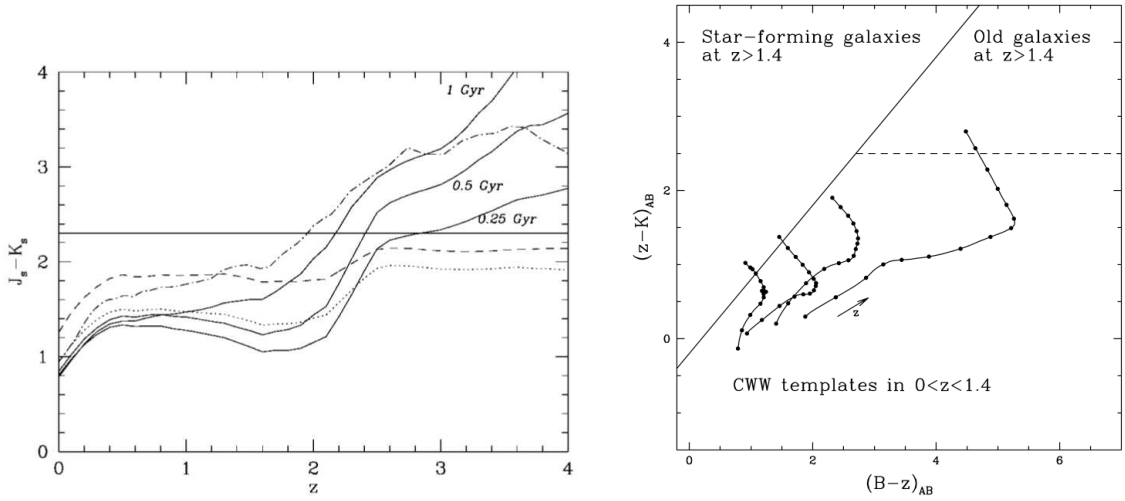

Figure 1.6: Left: $J-K_s$ color used to identify DRGs as a function of redshift for several synthetic galaxy spectra (adapted from Franx et al. 2003). The solid curves indicate single-age stellar populations with ages of 0.25, 0.5, and 1 Gyr. The colors exceed $J-K_s$>2.3 only for z>2 as a result of the Balmer break/4000Å break moving into the J band. Right: B−z versus z−K color used in the BzK criteria (Figure as shown in Daddi et al. 2004) for the local templates of various galaxy types from Coleman et al. (1980). The models are plotted for the range 0<z<1.4 and do not reach the regions where star-forming and quiescent galaxies at 1.4<z<2.5 are located.

500 z∼6 galaxies (i-dropout). Nowadays, the availability of ultra deep NIR observations allows a robust confirmation of z∼7 (z-dropouts) and extends the drop-out technique all the way up to z∼10 (J-dropout), merely 500 Myr after the Big Bang (Bouwens et al. 2010a,b, see left panel of Figure 1.5).

1.2.3 Observational biases and multi-band observations

Although all the techniques described above are extremely efficient at providing high redshift galaxy samples, it is critical to bear in mind that each of these method provides a shaded view of the extragalactic Universe, i.e., none of them are exempt from their own observational bias. For example, the LBG technique is intended to select young, star-forming, relatively dust free galaxies, which implies that it is severely biased against dust enshrouded galaxies and older populations that would redden the observed spectral energy distributions and likely lead to redshift ambiguities (e.g. Reddy et al. 2005). Similarly, LAEs, and in general emission line searches, have a clear but uncertain observational bias. This is because, in addition to the star-forming requirement, these surveys present two sensitivity thresholds, of flux level and equivalent width (only galaxies with relatively large equivalent can be detected no matter how bright the continuum), and a very narrow redshift range that causes them to be generally less complete than those based on continuum emission.

In order to overcome the issues regarding the observational biases on these techniques, other methods has been developed targeting at continuum features in rest-frame optical wavelengths of *normal* galaxies (observed in the NIR) instead of the UV of star-forming galaxies. Many of these techniques are based on the detection of the Balmer and the 4000 Å break using NIR colors to identify massive systems, more evolved than the UV selected samples, e.g., EROS, IEROS, DRG, BzKs (see e.g., Elston et al. 1988; Yan et al. 2004; Franx et al. 2003; Daddi et al. 2004; see

Figure 1.6). Nevertheless, similarly to what happens with the optical-dropout techniques, these methods could not start to provide significant results until the recent improvement in NIR detectors (in the early 2000's), that brought them to the efficiency levels and area coverage of the optical CCDs. More recently, the availability of the *Spitzer* Space Telescope, probing the 3.6-8.0μm range, has allowed the detection of these massive systems up to z$\sim$4 (Pérez-González et al. 2008). Evidently, NIR color techniques also present their own biases. Perhaps, the most remarkable is the degeneracy in red optical colors that do not allow to robustly distinguish between old stellar populations and dusty starbursts (see e.g., Papovich et al. 2006).

Complementary studies that allow to break this degeneracy require observations at longer wavelengths (in the mid-to-far IR, sub-mm or radio) that probe IR radiation re-emitted by the dust in heavily obscured star-forming systems. These kind of surveys, such us those performed with JCMT/SCUBA(sub-mm), VLA(radio), Spitzer/MIPS(FIR) and now Herschel, offer the necessary data to complement the biased vision of high-z galaxy populations that we obtain from surveys focused only on UV/optical wavelength ranges. Unfortunately, it is only recently that the samples selected at longer wavelengths are able to provide a statistically representative number of galaxies.

Guided by the rapid development of astronomical instrumentation, new surveys at multiple wavelengths are frequently presenting new and and sometimes ground-breaking results. This is possible thanks to state-of-the-art instruments and facilities that allow significant improvements over the previous works. Nevertheless, many of these surveys often claim to have find a new galaxy population, named with its own acronym, and it is not always clear to what degree these groups are orthogonal or complementary to the previous ones. As it is stated in the recent 2010 decadal white paper, *This situation is symptomatic of a subject that is still in its infancy. Over the next decade, high redshift observers will attempt to unify these different galaxy classes, in order to formulate a coherent evolutionary picture connecting galaxies in the high redshift Universe to galaxies today* (Bell et al. 2009). In practice, the most efficient way to avoid the selection biases introduced by the single photometric techniques is to combine several of these methods, or at least count with a body of data large and accurate enough to analyze the SEDs of the galaxies in a broad wavelength range.

Evidently, this kind of endeavor is not feasible for single observers. Therefore, the most relevant galaxy surveys are always conducted by world-wide collaborations that join their efforts by targeting the same well-characterized fields in the sky (the so-called cosmological fields). Large collaborations also ensure the availability of guaranteed time projects capable of fulfilling the very demanding observations required to survey these fields with several instruments at different wavelengths. The most ambitious collaboration of this kind to date is the Great Observatories Origins Deep Survey (GOODS; Giavalisco et al. 2004), which count with two key fields in the northern, centered at the location of the original HDF-N, and southern hemispheres. However, many others have followed, such as the large area (COSMOS; Scoville et al. 2007) or the Extended Groth Strip (EGS; Davis et al. 2007), which count with one of the largest spectroscopic follow-up observations. The gathering of exhaustive data-sets including not only photometry, but also optical and NIR spectroscopy, and high resolution imaging, turn these fields into key assets to achieve a broad range of astronomical goals.

1.2.4 Spectroscopic galaxy surveys

An overview of the most relevant galaxy surveys would be clearly incomplete without mentioning the exhaustive spectroscopic surveys. Although these are not the main topic of this thesis, we briefly mention them because of the their fundamental role in the studies of galaxy evolution. Indeed, spectroscopic surveys at the low and intermediate redshift regimes bridges the (mostly photometric) studies at higher redshifts to the local studies. This is of critical importance because, as much as the ΛCDM models offer a framework to put observations into context, the whole picture of galaxy evolution could not be sustained without a proper linking between the surveys of early universe and the local ones.

Representative examples of spectroscopic surveys at low redshifts are the Sloan Digital Sky Survey (SDSS; York et al. 2000) or the Two-Degree Field Galaxy Redshift Survey (2dfGRS; Cole et al. 2001). Both of these surveys aim at characterizing the properties of the general galaxy population and their relationship with the galaxy environment to a distance of about $z \lesssim 0.2$, based on spectroscopic observations of nearly a million galaxies. At intermediate redshifts ($z<1.5$), there are three main surveys currently being conducted, that take advantage of very efficient multi-object spectrographs in large telescope facilities: the Deep Evolutionary Extragalactic Probe (DEEP; Davis et al. 2003), using LRIS and DEIMOS at Keck ($>$120 nights; Faber et al. 2003), and zCOSMOS ($\sim$80 nights; Lilly et al. 2007) and VIMOS VLT Deep Survey (VVDS; $>$70 nights; Le Fèvre et al. 2005), using VIMOS(Le Fèvre et al. 2003) at the VLT. Over the past 5 years, these surveys have amassed a few tens of thousands of optical spectra of galaxies up to $z\sim1$.

The amount of information and the quality of the data provided by a spectra is far superior to what can be achieved from multi-band photometry. Nevertheless, the extreme faintness of distant sources on the one hand, and the lack of measurable spectral lines on the other, prevent spectroscopic redshift surveys to continue their exhaustive task in the redshift range between $z\sim1.4$ and $z=3$ (the so-called redshift-desert). At higher redshifts, galaxies with strong Lyman-α emission can be picked up, but these constitute only a small fraction of the galaxy population at that redshifts. Therefore, systematic spectroscopic surveys at the highest redshifts would have to wait for the next generation of instruments (NIR multi-object spectrographs) and telescopes (30m, JWST) that will be able to observe very faint distant galaxies obtaining NIR spectra that probe the rest-frame optical emission lines.

1.3 Insights from galaxy surveys

In an epoch where observations have a leading edge over theoretical models, and their input is indispensable to the advance of theoretical efforts, studies of galaxy evolution provide information not only about the main constituents of the Universe but also about the properties of the Universe as a whole.

We have already mentioned some of the key areas of interest in studies of galaxy evolution (§ 1.1). Here we will briefly outline two of the most relevant research topics in this area, that are common to all current galaxy surveys.

The global Mass Assembly

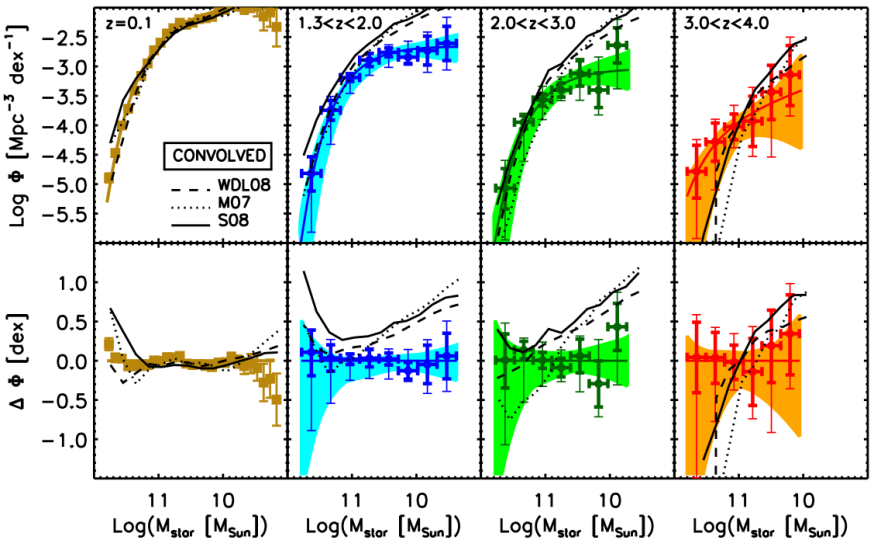

Figure 1.7: Comparison between the observed SMFs and the semianalytic model-predicted SMFs at different redshifts from the work of Marchesini et al. (2009). The predicted SMFs are represented by black curves: solid for the Somerville et al. (2008) model, dotted for the Monaco et al. (2007) model, and dashed for the Wang et al. (2008) model. Red, green, and blue filled circles represent the SMFs; the thick error bars include Poisson errors, cosmic variance, and the uncertainties from photometric redshift random errors; the thin error bars include the systematic uncertainties.

As it has already been introduced, current models of structure formation predict that dark matter halos, built up in a hierarchical *bottom-up* fashion, drive the process of galaxy formation. Consequently, the formation of galaxies must have followed a similar hierarchical development, leaving traces of their growth pattern across cosmic time. Thus, in order to put theoretical models to the test, studies of mass assembly focus on the analysis of galaxy samples at different redshift intervals and grouped by stellar mass. This allows us to track the assembly of mass with cosmic time and to trace the formation epochs of galaxies as a function of their mass. One of the key ingredients in these analysis, is the study of the density of galaxies as a function of the stellar mass at different redshifts (i.e., the stellar mass functions). The integration of each of these mass functions in different redshift intervals allows us to estimate a stellar mass density (SMD) as a function of loop-back time, which provides information on the rate of global mass assembly.

Recent studies exploring the build up of the stellar mass in the key interval from z$\sim$3-4 (when the first fully assembled galaxies are detected) to z$\sim$0.5 (when the majority of the most massive galaxies, $M \gtrsim 10^{11} M_{\odot}$, are already in place) have shown that about half the stellar mass in present day galaxies was assembled in the 1<z<4 interval (e.g., Fontana et al. 2006; Pérez-González et al. 2008; Elsner et al. 2008; Marchesini et al. 2009), whereas the remaining mass growth takes place at z<1 (Bell et al. 2004; Faber et al. 2007) driven by a widespread intense star formation rate, but also significantly affected by a large fraction of galaxy mergers, specially in massive systems (Conselice et al. 2003, 2008, 2009; Feldmann et al. 2008). In fact, the evolution of galaxies seems to have followed a *downsizing* scenario (Cowie et al. 1996), consisting of a differential growth of the stellar mass density, such that massive galaxies are assembled earlier and more rapidly than low mass galaxies. Nevertheless, the downsizing scenario is still a frictional point between models and observations. Despite the overall agreement in the global picture of mass assembly, models still fail to reproduce the downsizing trend (or at least mass downsizing; Drory & Alvarez 2008; Fontanot et al. 2009), and more precisely, the density of massive galaxies at z$\gtrsim$2. In theory, these objects

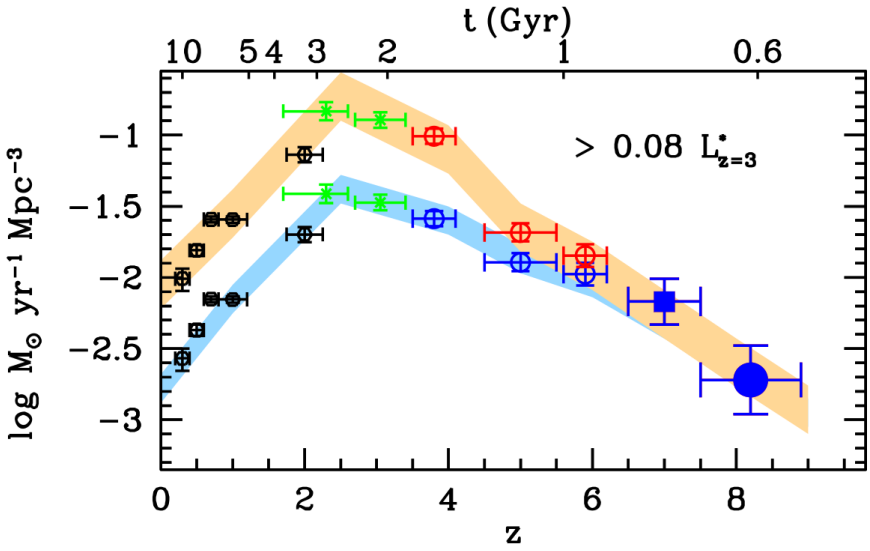

Figure 1.8: Determinations of the UV luminosity density and SFR density at different redshifts showing results from several authors (adapted from Bouwens et al. 2010). The large red circle shows the constraints at z∼8 from the dropout search conducted at the WFC3 Y-band observations. The lower set of points (and blue region) show the SFR density determination inferred directly from the UV light, and the upper set of points (and orange region) show what one would infer using dust corrections inferred from the UV-continuum slope measurements.

are first spotted at too early stages of galaxy formation (Kriek et al. 2006; Cimatti et al. 2008; Salimbeni et al. 2008; Fontana et al. 2009) and seems to finish their build up too soon (Pozzetti et al. 2003; Arnouts et al. 2007; Ferreras et al. 2009), which is more similar to a monolithic collapse than to a hierarchical growth.

In the seek of convergence, the latest versions of the ΛCDM models have improved their ability to reproduce the massive end of the mass function by introducing empirical recipes that suppress star formation in primeval galaxies, e.g., the supernovae or Active Galactic Nuclei (AGN) feedback (Croton et al. 2006; Bower et al. 2006; De Lucia et al. 2006; Somerville et al. 2008). Also, hydrodynamic simulations show that the large amount of dense gas present at high redshift can lead to the formation of spheroid-dominated galaxies at relatively early epoch (Naab et al. 2007; Dekel et al. 2009). In addition, there are substantial systematic uncertainties in the stellar mass determinations for individual galaxies that causes the shape of the mass function, specially at high redshift, to be poorly constrained, adding another potential source for disagreement (see e.g., Marchesini et al. 2009). A re-analysis of the theoretical predictions taking these issues into account, shows that models roughly reproduce the evolution of the space density of massive galaxies when their predictions are convolved with a realistic estimate for the observational error on stellar masses (Fontanot et al. 2009).

While the overall qualitative agreement between the data and the models is promising, some discrepancies are still present. Thus, large samples of galaxies characterized with accurate physical properties and redshifts are necessary in order to robustly determine the mechanisms of galaxy assembly.

The star formation rate density of the Universe

The analysis of the evolution with cosmic time of the star formation rate density (SFRD)

provides a complementary view to the studies of the SMD, tracing back the epoch when galaxies where actively forming the bulk of their stellar content, that it is ultimately responsible for the build up of their mass (or at least the baryonic component).

Similarly to the stellar mass functions, measurement of galaxy luminosity functions (LF; i.e., the density of galaxies as a function of their luminosity at different redshifts and wavelengths) has rapidly matured in the past few years (Faber et al. 2007; Marchesini et al. 2007; Arnouts et al. 2007). An advantage of LFs it that, under certain assumptions, the luminosity of galaxies can be related to the amount of ongoing star formation, e.g., in the UV a large fraction of the total luminosity is emitted by the newly formed stars, which are also responsible for ionizing the neutral gas and causing the emission lines. Therefore, the study of LFs offers a direct probe on how the space density of the galaxy star formation rate (SFR) evolves, allowing us to constraint the global star formation history (Lilly et al. 1996; Madau et al. 1996).

The last decade has seen significant advances in our understanding of the history of star formation. Nowadays, one can find several hundred determinations of the star formation rate density estimated from observations at many wavelengths across a large range of lookback time (e.g., Hopkins & Beacom 2006). Taken together, these observations suggest a rapid increase in the SFRD from the epoch of reionization to $z\sim2-3$ (Bouwens et al. 2010a). After that time, the SFRD steadily decreased over the last 10 billion years (Schiminovich et al. 2005; Arnouts et al. 2005) down to its actual value (Gallego et al. 1995), which is at least a factor of $\sim$10 lower than at the epoch of maximum activity. The global picture is generally understood in the context of a hierarchical growth of small building blocks with large gas reservoirs at early times, and gas exhaustion or heating through self regulated process (such as supernovas or AGNs) at late times. However, while this characterization of the Star Formation History is broadly accepted, there are several key details that still are poorly determined, thus leading to controversies in this interpretation. Some of these issues arise from the substantial disagreement in the measurements of the SFRD derived at different wavelengths, most notably between the UV (Schiminovich et al. 2005; Salim et al. 2007; Reddy et al. 2008), emission line indicators (Villar et al. 2008; Sobral et al. 2009) and those in the FIR and sub-mm (Le Floc'h et al. 2005; Pérez-González et al. 2005; Caputi et al. 2007) domain. Thus, despite our increased capabilities to gather large amounts of data, the uncertainties in the conversion factors from luminosity to SFR (see e.g., Kennicutt 1998 or Moustakas et al. 2006), the amount of dust obscuration or the bias introduced by the different selection criteria of each survey are still a potential source of discrepancies. A more reliable evaluation of the SFRD can be achieved by comparing two or more star formation indicators for the same set of objects. While new galaxy surveys provide large (statistically significant) samples with which one can attempt such studies, the samples of galaxies for which more than a single star formation indicator can be applied are not necessarily that large.

Another potential problem for the analysis of galaxy assembly is the disagreement between SFRD and SMD at high redshifts $z\gtrsim2$. A number of studies reveal that, upon integration with time, the current estimates of the SFRD tend to over-predict the stellar mass density at low redshift (Eke et al. 2005; Hopkins & Beacom 2006; Pérez-González et al. 2008). These discrepancies suggests that either stellar mass estimates are incorrect or the Star Formation History is overestimated, or perhaps both (Wilkins et al. 2008). Alternative solutions are that the larger star formation rates at high redshift could be explained by an evolution of the stellar initial mass function (IMF; van Dokkum 2008; Meurer et al. 2009), which nonetheless would have significant implications in other observables (e.g., Fardal et al. 2007), or that there is a sizable amount of total mass at high-z

that it is locked up inside a population of UV-faint (low mass) galaxies that may escape stellar mass selected samples but, even with their low stellar masses, are sufficiently numerous to add appreciably to the total budget of stellar mass (Reddy & Steidel 2009).

Again, this discrepancies between observationally derived measurements, highlights the necessity that the analysis of Star Formation History and the evolution of the SMD are carried out from studies that combine different indicators based on multi-wavelength data reducing the observational biases as much as possible.

1.4 Remarks on galaxy surveys

It follows from the discussion in previous sections that, in order to the tackle the actual controversies on galaxy evolution, we require large (statistically significant) samples of galaxies counting with a exhaustive multi-band coverage. Only then we would be able to accurately characterize the physical properties of the galaxies to obtain meaningful results on galaxy evolution.

In this regard modern galaxy surveys offer extraordinary capabilities to examine the properties of thousands of galaxies simultaneously and consistently. Nonetheless, without a proper merging and modeling of the vast amount of spectro-photometric data, a detailed analysis of the global galaxy properties is not possible. Thus, a critical step to fully exploit the possibilities of large datasets is filling the gap between the large set of heterogeneous resources and the intrinsic properties of galaxies. The majority of the current studies based on large galaxy samples have to deal with this situation somehow. Paradoxically, in spite of our continuous requirements of new data, a project can sometimes face an excess of resources. In that cases, the large amount of data causes a bottleneck that prevent us from extracting valuable information on the individual galaxies observed in the images.

The task of efficiently merging the data to derive meaningful quantities on a galaxy-by-galaxy basis involves a combination of several steps, and thus it is not straightforward procedure. First we must perform the multi-band identification and compute consistent photometry for each source, then we model the merged photometry for each galaxy to estimate their intrisic properties. In addition, one must be aware of unintended selection effects an deal with possible systematic biases introduced by limitations of the method. For example, those arising from the lack of sufficient data at certain wavelengths, or from the assumptions made to estimate of the physical properties.

1.5 Aims of this thesis

The main purpose of this thesis is to use multi-wavelength photometric data to obtain the most reliable estimates of important physical parameters of intermediate- and high-redshift galaxies, which will give us an insight into the formation and evolution of galaxies throughout (most of) the Hubble time. More precisely, this thesis work has gathered a large sample of galaxies spanning a wide redshift interval and make use of: optical to NIR photometry to characterize their most relevant physical properties, mid-to-far IR photometry to characterize the ongoing star formation on these galaxies through the analysis of their dust emission, spectroscopic data to robustly determine their redshift and thus obtaining a better characterization of their rest-frame properties (luminosities,

colors, etc). The simultaneous analysis of all these properties will allow us to characterize their growth and evolution with cosmic time.

To accomplish these goals, we first focus on the assembly of a large sample of *Spitzer*/IRAC (covering the 3.6-to-8.0 μm spectral range) selected galaxies in the cosmological field Extended Groth Strip (EGS), which is one of the most important cosmological deep fields. It has been observed by ground and space based observatories alike, presenting a vast amount of high quality spectro-photometric data in multiple wavelengths. In **Chapter 2** we focus on the technical details of the assembly of the galaxy sample and **the develop of a consistent merged multi-band catalog** based on these data. This catalog will be the basis for the subsequent modeling of the UV-to-FIR SEDs of the galaxies, that will allow us to estimate their physical properties. In addition, Chapter 2 also present relevant results on the UV, optical and FIR properties of the NIR (IRAC) selected sample. In particular, we discuss the de-blending method used to alleviate the source confusion issues in the IRAC bands, which are of critical importance to obtain reliable source densities or studying the spatial distribution of galaxies. A detailed summary of the main objectives of Chapters 2:

- *Chapter 2:* gathering a comprehensive spectro-photometric dataset in the EGS; combining the data products of multiple surveys reducing and mosaicking data when necessary; creating an IRAC selected sample characterizing its completeness level; identifying the multi-band counterparts of the IRAC sources; computing a consistent merged photometric catalog overcoming differences in depth and spectral resolution; analyzing the overall multi-band coverage of the sources (i.e., the number of bands in which they are detected) as a function of the magnitude and redshift; identifying stellar or galactic nature the sources.

Among the multiple scientific possibilities of the multi-wavelength galaxy catalog, the inmediate and long term goal this thesis is aimed at studying the global process of mass assembly in galaxies at different epochs of the Universe. For that matter, the sample of galaxies is selected in the NIR (closer to selection in mass) and a significant fraction of the work is devoted to compute accurate **stellar masses** analyzing in detail the associated uncertainties. Equally important to characterize the growth of galaxies is determining the rate at which each galaxy increases its mass content (the number of existing stars). Therefore, the methods and possible biases in the estimate of robust **SFRs** are also extensively discussed in this thesis. Along with the **photometric redshifts**, without which the evolution with cosmic time can not be addressed, the estimate and analysis of stellar masses and SFRs are the central piece of **Chapter 3**. A detailed summary of the main objectives of this Chapter follows:

- *Chapter 3:* characterizing the optical-to-NIR SEDs of the galaxies by fitting the observed photometry to synthetic templates modeled with stellar population synthesis models; estimating photometric redshifts and stellar masses out this fitting procedure; quantifying the overall quality of the photometric redshifts from the comparison to spectroscopic redshifts and other previously published photo-z estimates; evaluating the accuracy of the stellar mass estimates by exploring possible systematic effects arising from the use of different assumptions in the modeling of the stellar populations; studying the goodness of the stellar mass estimates comparing them against the estimates of other authors; characterizing the mid-to-fir SEDs of the galaxies by fitting the observed photometry to different models of dust

emission; estimating UV- and IR-based SFRs for all galaxies based on the full fitting of the SED; estimating the typical random and systematic uncertainties of the IR-based SFRs comparing the values obtained using different sets of models and the studying the effects of working with limited IR data.

Exploiting all the available spectro-photometric data in cosmological fields is the common starting point in current studies based on the analysis of extra-galactic sources. Consequently, it is important to stress that the fundamental aim of this thesis is not creating a catalog as a means to address just one specific problem, but developing the most general tool possible, obtaining a wide range of fundamental properties that will serve to multiple purposes. For this reason, we will focus not only on **obtaining several physical properties but also on ensuring their quality and accuracy**. This includes checking for possible biases or limitations of the method so that the results based on this compilation of data led to robust scientific conclusions.

The breadth and quality of the estimated parameters obtained for thousands of galaxies in the EGS allows to pursue multiple scientific projects. For that matter, a fundamental goal of this thesis is to make all the processed data-set and estimated parameters of the catalog publicly available. To that end, we aim to develop multi-functional **web-interface that allows the whole scientific the access to all the data products for the EGS galaxies**. The resulting tool will significantly increase the legacy of all the surveys that observed the field spending a significant amount of resources. A description of our work in this context is presented in Chapter 2 and **Appendix 1**.

In the long term this catalog will be the seed for multiple studies of galaxy evolution. However, to reveal the numerous possibilities of this and similar catalogs, this thesis discuss several studies aimed at addressing specific scientific questions. Most of the efforts in this regard are detailed in **Chapter 4** which constitute the main goal of this thesis after the creation of the catalog. In this Chapter we focus on investigating relation between the observed magnitude and redshift distribution for a NIR (K-band) selected galaxy sample. In particular, we study if the observed features in **the shape of galaxy number counts (the observed density as a function of magnitude) are related with an evolution with cosmic time of the intrinsic distribution in luminosity (luminosity functions) of the galaxies**. A detailed summary of the main objectives of this Chapter follows:

- *Chapter 4:* investigating the causes for the different shape of the K-band number counts compared to optical number counts; determining the nature of the galaxies that constitute the bulk of the number counts up to K =19, exploring the relative contribution of galaxies at different redshifts; performing an analysis of the functional form of the number counts in terms of the luminosity functions (LFs) and the redshift; computing LFs at different redshift intervals from a K-band selected sample; estimating number counts in the K-band using LFs at different rest-frame bands; explaining the most relevant features in the shape of the K-band number counts in terms of the evolution with redshift of the key parameters of the LFs.

Many other **works led by other authors have directly benefited from the data processing performed in this thesis**. Here we present a list of these works, where I am a co-author, that has been published in refereed journals. **Chapter 5 presents a detailed summary of a selection of these works** (those marked in boldface), highlightning the most relevant results of each work.

- *Colaborations:*

- **Exploring the Evolutionary Paths of the Most Massive galaxies**. Pérez-González, Pablo G., Trujillo, Ignacio, Barro, Guillermo, Gallego, Jesus, Zamorano, Jaime, & Conselice, Christopher J. 2008, The Astrophysical Journal.

- *Spitzer View on the Evolution of Star-forming Galaxies from z= 0 to z∼3*. Pérez-González, Pablo G., Rieke, George H., Egami, Eiichi, Alonso-Herrero, Almudena, Dole, Hervé, Papovich, Casey, Blaylock, Myra, Jones, Jessica, Rieke, Marcia, Rigby, Jane, Barmby, Pauline, Fazio, Giovanni G., Huang, Jiasheng, & Martin, Christopher 2005, The Astrophysical Journal.

- **The Stellar Mass Assembly of Galaxies from z = 0 to z = 4: Analysis of a Sample Selected in the Rest-Frame Near-Infrared with Spitzer**. Pérez-González, Pablo G., Rieke, George H., Villar, Victor, Barro, Guillermo, Blaylock, Myra, Egami, Eiichi, Gallego, Jesús, Gil de Paz, Armando, Pascual, Sergio, Zamorano, Jaime, & Donley, Jennifer L. 2008, The Astrophysical Journal.

- **The Spitzer's Contribution to the AGN Population**. Donley, J. L., Rieke, G. H., Pérez-González, P. G., & Barro, G. 2008, The Astrophysical Journal.

- *The Minor Role of Gas-Rich Major Mergers in the Rise of Intermediate-Mass Early Types at $z\lesssim1$*. López-Sanjuan, Carlos, Balcells, Marc, Pérez-González, Pablo G., Barro, Guillermo, García-Dabó, César Enrique, Gallego, Jesús, & Zamorano, Jaime 2010, The Astrophysical Journal.

- *The galaxy major merger fraction to z=1* López-Sanjuan, C., Balcells, M., Pérez-González, P. G., Barro, G., García-Dabó, C. E., Gallego, J., & Zamorano, J. 2009, Astronomy and Astrophysics.

- *Characterization of Active Galactic Nuclei and Their Hosts in the Extended Groth Strip: A Multiwavelength Analysis*. Ramos Almeida, C., Rodríguez Espinosa, J. M., Barro, G., Gallego, J., & Pérez-González, P. G. 2009, The Astronomical Journal.

- **Infrared Excess sources: Compton thick QSOs, low-luminosity Seyferts or starbursts?**. Georgakakis, A., Rowan-Robinson, M., Nandra, K., Digby-North, J., Pérez-González, P. G., & Barro, G. 2010, Monthly Notices of the Royal Astronomical Society.

- *The Hα-based Star Formation Rate Density of the Universe at z= 0.84*. Villar, Víctor, Gallego, Jesús, Pérez-González, Pablo G., Pascual, Sergio, Noeske, Kai, Koo, David C., Barro, Guillermo, & Zamorano, Jaime 2008, The Astrophysical Journal.

This thesis is presented as a compilation of papers. In particular, the material comprising Chapters 2, 3 has been published in the Astrophysical Journal Supplement (2011ab), and Chapter 4 has been published in Astronomy and Astrophysics (2009). In addition, Chapter 5 summarizes the results of several papers published in different journals, listed above. In order to facilitate the comprehension and to put the Chapters into the general context of the thesis, each one includes a brief introduction that provides some basic information on the subjects addressed later in the papers. Finally, the thesis is preceded and concluded by a complete translation of the general Introduction and Conclusions.

Note that the results in Chapters 2 to 5 are not presented following a strict chronological order but following a more logic structure. The reason for this is that the analysis in Chapter 2-3 is focused on characterizing the general properties of a galaxy sample, while Chapters 4 and 5 shows how to use the quantities derived from such characterizations to address more concise questions. In addition, as mentioned above, Chapters 2 and 3 constitute the majority of the work developed for this thesis and thus we give them more relevance. As a result, Chapter 4 does not strictly follows the results of the previous chapters, but rather the contrary. Indeed, the main purpose of the study presented in Chapter 4 was successfully accomplished using a reduced version (both in size and depth) of the larger galaxy sample presented in Chapters 2 and 3. Nonetheless, the conclusions of that work highlighted the necessity for a more ambitious galaxy sample. In particular, one based on a survey with a higher area/depth product (such as that of *Spitzer*/IRAC), that increases the synergies with all other photometric resources available and allowed us to carry more insightful scientific analysis such us those introduced in Chapter 5.

2

Multi-wavelength SEDs of *Spitzer*/IRAC galaxies in EGS

2.1 Introduction

As we have explained in Chapter 1, recent years have seen a dramatic progress in our understanding of galaxy evolution thanks to the observational study of high redshift galaxies. Nowadays, surveys of distant galaxies frequently rely on carefully-designed color selection techniques that requires only a few bands to identify the candidate galaxies. However, although such selection techniques are able to isolate large samples of galaxies in a well-defined redshift range, diagnostic information about individual galaxies or about the range of properties spanned by the whole sample requires further analysis of their SEDs over a large wavelength range. Characterizing the full SED of the galaxies provides a deeper insight into the properties of the galaxies. Thus allowing us to perform sample selections directly based on the intrinsic properties of the galaxies, such as the redshift or the stellar mass, instead of using only few colors that are prone to larger uncertainties and systematic effects.

In this context, **we will present in this Chapter a multi-wavelength characterization of the SEDs of a *Spitzer*/IRAC selected sources in the EGS**. To perform this task we will: (1) gather a large amount of spectro-photometric resources in the field obtained by multiple surveys, (2) analyze the overall properties of these data, such as depth, area or image quality, focusing mainly on the characteristics of the IRAC data, (3) extract all the sources detected in the IRAC mosaic, (4) perform a cross-identification of these sources to each other dataset based on their sky-coordinates, (5) perform a multi-band photometric measurement using *Rainbow* (Pérez-González et al. 2005, 2008), a custom method that takes into account the strong differences in image resolution, and the non-detection of a source in some bands.

After producing a catalog containing the multi-wavelength SEDs for each galaxy, we will analyze in some detail overall properties such us the overall multi-band identification or the photometric quality in different areas. We will conclude carrying a classification of all the sources in the catalog as galaxies or stars aided by the large amount of information on the sources contained in their SEDs. Note that the choice of a NIR selection as reference sample is done with the aim of creating a catalog that is particularly suitable for studies on the stellar mass content of the galaxies, but it is also appropiate for the detection of the most distant galaxies, which progressively *drop-out* of the optical bands as the Lyman break shifts into the NIR (See Chapter 1). In this and the following Chapters we will elaborate more on the importance of the NIR wavelength range for the study of distant galaxies.

A significant fraction of the efforts to obtain robust SEDs relies on the use of *Rainbow*. For that matter, an important goal of this thesis consisted on improving the already existing version of *Rainbow* developing new features that allow us to overcome specific issues intrinsic to the procedures of SEDs characterization. Some examples that are fully described in this Chapter include:

- A re-calibration of the local astrometric solution to improve the accuracy of the cross-matching procedure. This is critical to ensure that the photometric aperture used to measure the flux not only match the same size in all bands but also is accurately positioned.
- The addition of a secondary reference band in the process of multi-band identification to alleviate miss-match issues. This feature is most useful in the case of high-z NIR bright sources that can be wrongly cross-identifed to other optically bright objects nearby (being the real counterpart un-detected in the optical).
- Characterizing the accuracy of the de-convolution procedure required to match un-resolved IRAC sources to other optical/NIR detections. In spite of the very depth limiting magnitudes of the IRAC catalogs, the slightly worse resolution of the image could cause that introducing a bias in our measurement of the density of galaxies if these are not appropriately de-blended.
- Developing additional photometric measurements for un-detected sources, e.g., forced measurements (for galaxies missed in the source extraction) or sky measurements (to be used as limiting magnitudes). The multi-wavalength identification of the sources in the IRAC catalog is based on a cross-match to the source catalog in other bands. This implies that very faint sources missing in those catalogs would not be associated to the corresponding IRAC sources. To solve that problem include the forced/sky photometry that attempt a flux meassurement even when the IRAC sources does not have a counterpart in the other catalog.

In addition to the technical procedures and the discussion on catalog properties outlined above, in this Chapter we will also present the *Rainbow* database (DB) and the associated query web-interface *Rainbow Navigator*, which also discussed in Appendix I. The *Rainbow* DB is meant to be a permanent repository that keeps record of all the data products resulting from the processing of the imaging data in a cosmological field (in this particular case the EGS), as well as the final photometric catalog. In addition to the data-products obtained in this Chapter, the *Rainbow* DB stores the values of the physical properties for each galaxy that we will be estimated using different SED modeling techniques (this will be described in Chapter 3). As it happened with the part of *Rainbow* devoted to compute the SEDs, an important fraction of the this thesis has been devoted to technical tasks related with the DB, i.e., creating new structures within the *Rainbow* DB pipeline. This includes developing new programs and scripts that comply with the existing data structure. For example, in order for *Rainbow* to compute the SEDs all the datasets must be processed in the DB following a standard data flow that requires several steps. A particularly relevant development is *Rainbow Navigator*, a user-friendly web-interface to the DB featuring additional data-handling possibilities. This application was entirely created from scratch for this thesis. This effort was aimed at making all the results obtained for the source in EGS available for the whole astrophysical community so that they could benefit of these resources for new independent analysis.

In summary, this Chapter is thus focused on the use of integrated multi-band SEDs as primary source of information on the properties of distant galaxies. Indeed, all the different physical

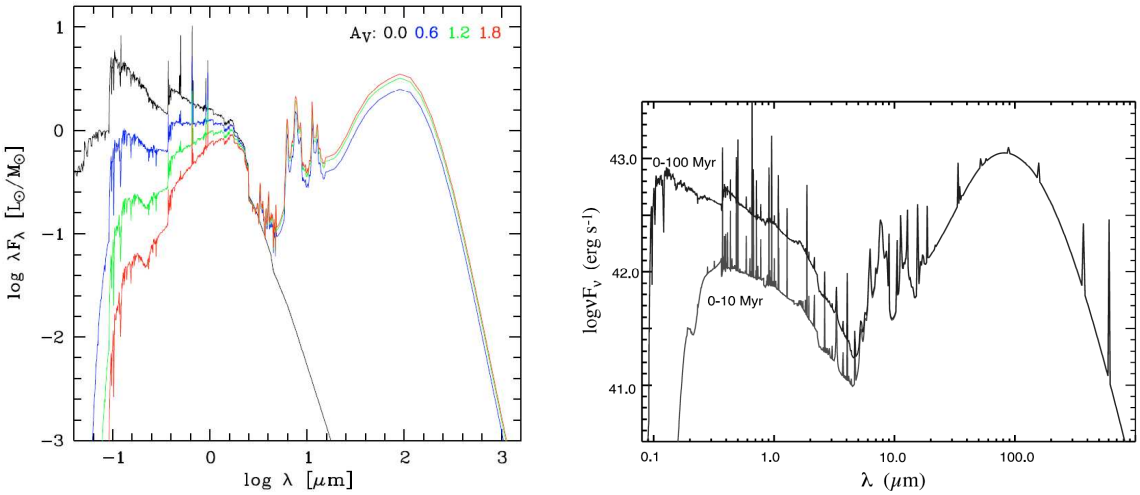

Figure 2.1: *Left:* UV-to-FIR SEDs of galaxies modeled with the code CIGALE (Noll et al. 2009), featuring different degrees of dust attenuation, A(V)=0-1.8, affecting most significantly to the UV wavelength range. It can also be seen how the different amounts of dust attenuation affects the emissivity in the IR wavelengths. Intense emission lines in the optical and NIR are also featured. *Right:* Synthetic model of the SED of a starburst galaxy in two different evolutive stages: in the peak of star-formation event and after the intensity of the burst has significantly diminish (Grooves et al. 2008)

processes occurring in galaxies leave their imprint on the shape of the spectrum, each dominating at different wavelengths. Consequently, a detailed analysis of the SED of a galaxy should in principle allow us to consistently link multiple physical properties of the galaxy, in contrast to searching a single feature, that could constrain a single parameter (e.g., the use of the Hα line to derive the star formation rate, SFR). Along this introduction we will briefly describe the most relevant elements that gives place to the galaxy SED and we will discuss the properties of the galaxy that can be estimated from different spectral features. Finally, we will conclude with a description of some relevant databases widely used in extragalactic astronomy. This would help us to put into context the relevance of the *Rainbow* DB. In particular, the public version developed for this thesis.

2.2 Key contributors to the global UV-to-FIR SED of a galaxy

Galaxies emit radiation across all the electromagnetic spectrum (Figure 2.1), and for the majority of them, the ultraviolet to infrared spectra arises mostly from stellar light, either directly or reprocessed by the gas and dust of the surrounding interstellar medium (ISM). An exception to this rule are galaxies where the emission is dominated by an active black hole in their nucleus (AGNs; e.g., Polletta et al. 2007).

In a simplified scenario, the SED of a galaxy is essentially the result of combining the contribution of just a few components, namely stars, gas and dust. The relative importance of each contribution depends on the spectral range and on the strength of the interactions between them. The basic and most relevant ingredient are the **stars** (e.g., Tinsley 1972; Searle et al. 1973), which basically ranges from numerous, low-luminosity, low-mass stars, to bright, short-lived, massive OB stars. On a closer examination, these stars are distributed in both metallicity and age (Girardi et al. 2000; Lejeune & Schaerer 2001), therefore producing distinct global SEDs for galaxies. Sec-

ond in importance is the interstellar **gas** from which stars are formed. The gas is predominantly in its atomic form and it is one of the critical opacity sources (next to dust) for the UV emission, reprocessing this light into strong emission lines in the UV, optical and IR (e.g., Hummer et al. 1995; Leitherer et al. 1999). Molecular gas is only a noticeable source of attenuation in specific spectral features or in galaxies dominated by nuclear (or heavily obscured) sources (AGNs, Ultra Luminous Infrared Galaxies; ULIRGs), and emits predominantly at longer wavelengths (MIR and longer; see e.g., Young & Scoville 1991). Finally, the **dust** component, whose relevance varies strongly between galaxy types, is essentially composed of carbonaceous and silicate-like grains, attenuates the galaxy radiation differentially as a function of wavelength, being more severe in the UV-optical range, and almost negligible in the IR (see e.g., Calzetti 1997; Pei et al. 1999). Nonetheless, there can be significant exceptions such as the strong silicate absorption at 10 μm (Smith et al. 2007). By absorbing the radiation emitted by the stars, the dust increases its temperature and re-emits the light in the MIR-FIR wavelengths, following essentially a black body curve determined by the average dust temperature (see e.g., Draine 2003).

In Chapter 3 we will provide a more detailed description on the origin and the effects of the energy emitted by each of the different components briefly described above. In the following we focus on describing some of the key spectral features observed in galactic SEDs (at different wavelength ranges) that can be linked to some of these components and the physical properties of the galaxy. The description will mainly focus on the UV-to-FIR wavelength range, which is the central part this thesis. Following a qualitative, not sharp, definition, these SED encompasses: ultraviolet (UV) for λ <3500 Å, optical for 3500< λ <10,000 Å, near infrared (NIR) 1.0< λ <3.0 μm, mid infrared (MIR) 3.0< λ <25 μm, far-infrared (FIR) and sub-mm 25< λ < 1mm, and radio λ >1 mm.

As mentioned in the previous Chapter, an intrinsic problem of tracking particular features of a galaxy SED emitted at a certain wavelength is that these are observed at a different wavelengths due to the redshift. For example, at z$\sim$2 the rest-frame optical shifts into the observed NIR (see e.g. Figure 1.6). In the following, we describe some relevant features at their rest-frame wavelengths.

2.3 Inferences of galaxy properties from multi-wavelength data.

- **Ultraviolet (UV)**

  In Chapter I we described the Lyman Break as a strong feature in the UV spectra of galaxies originated by the concentration of neutral hydrogen in the ISM. The presence of neutral gas even in relatively low density columns causes the radiation at higher energies than 912 Å to be almost completely absorbed. As a result, the gas becomes ionized and creates a break in the continuum beyond the Lyman limit (the termination of the Lyman series in the Hydrogen). The position of the break moves into longer observed wavelengths with redshift, (1+z)·912 Å, providing a highly efficient technique to track high-z galaxies.

  In young star-forming galaxies, which count with strong ionization fields (E>13.6 eV) a significant fraction of the energy radiated in the extreme UV(λ <912 Å), is re-emitted through Hydrogen recombination lines (see e.g., Leitherer et al. 1999). One of the strongest lines observed in the UV is Lyman-α (Lyα; a transition from n=2 to the fundamental level; λ=1216 Å). The intensity and equivalent width of the line depends on the metallicity, and it

can become the dominant cooling line of the gas when few metals are present, i.e., emitting a large fraction of the bolometric luminosity.

The strong UV emission in these young galaxies is in general dominated by the most massive and short-lived stars (M>10M$_\odot$, $t \sim 10^6 yr$) in the star-formation region, which in turn represent only a small fraction of the total number of stars. For these galaxies, the UV luminosity offers a relatively direct tracer of the star formation rate (SFR). Several calibrations have been published in order to estimate the SFR from the luminosity in the wavelength range between 1250-2500 Å (Buat et al. 1989; Leitherer & Heckman 1995; Madau et al. 1998), which is longward of the Lyα forest but short enough to minimize contamination from absorption lines that originate in the atmospheres of older stellar populations (e.g; MgII at λ=2800 Å).

These calibrations are often based on a certain number of hyphotesis, such us the distribution in mass of newly formed stars (or initial mass function; IMF) or the assumption that the SFR remained constant during the first $\sim$100 Myr of activity, while the number of massive stars (and the UV emission) was still increasing (Kennicutt 1998). The latter assumption makes this estimates more sensitive to the star-formation history (SFH) of the galaxy, whereas the values derived from recombination lines, such as Lyα, provide a nearly instantaneous measure of the SFR.

The UV is also the wavelength range most severely affected by dust attenuation (see Figure 2.1). This implies that all of the above SFR indicators, based on observed UV fluxes, render useless without a proper estimate of the dust attenuation. The most reliable extinction estimators are based on the measurement of the total-IR to UV flux ratio (Meurer et al. 1999; Gordon et al. 2000), because it tackles the energy balance between the two key ingredients: The IR emission of dust, and the unobscured UV radiation which carries the imprint of the extinction. Calibrating this ratio to a UV observable in large galaxy samples allows to derive empirical recipes that can used when IR data is not available, e.g., the well known TIR/UV $-$ β - A(V) relation (Meurer et al. 1999; Buat et al. 2005), where β is the slope of the UV continuum in the range 1300$<\lambda<$2600Å) and A(V) is the attenuation in the V-band.

- **Optical**

  While the UV luminosity is the most commonly used SFR indicator, the luminosity at the U-band ($\lambda \sim$3600Å) is similarly dominated by young stellar populations in starburst galaxies, and it present the advantage that this band can be observed from ground-based observatories. Therefore, in the absence of UV measurements, the luminosity in this band may be used as SFR indicator (Glazebrook et al. 1999; Sullivan et al. 2000). Another advantage of the U-band over the other UV measurements is that it suffers from less dust attenuation. However, the U-band luminosity also depends on the recent SFH of the galaxy, and its sensitivity as SFR indicator may be compromised by the flux contribution of evolved (>100 Myr) stellar populations in this range (e.g., Hopkins et al. 2003).

  Some of the strongest and most relevant emission lines that arise from the re-combination (or collisionally excited states) of Hydrogen and other heavier elements (He, O, N, C, etc.) that are present in the interstellar gas, are visible in the optical (see Figure 2.1). Re-combination lines are linked to the extreme UV radiation from massive stars, and therefore, similarly to the Lyα line, provides a measure of the ongoing SFR. Furthermore, optical lines are less affected by dust extinction. Among these lines, those in the Balmer series (Hα,Hβ) are more easily detected due to the comparatively higher density of Hydrogen (with respect

to other metals). Furthermore, these lines present a relatively minimal dependence on the physical conditions of the ionized gas and radiation field (Kennicutt 1998; Schaerer et al. 2000). Galaxy surveys based on the Hα line have been successfully used to study the SFR at different redshifts (Gallego et al. 1995, Pascual et al. 2001, Villar et al. 2008). Other nebular lines such as [OII], [OIII] has also been used as alternative SFR tracers (Martin et al. 2000; Drozdovsky et al. 2005). However, these lines requires a more careful calibration of the chemical abundance and excitation state of the ionized gas, being less reliable. The main reason for attempting the use of [OII] (λ =3727Å) is that it can be observed in the optical up to higher redshifts than Hα and Hβ, approximately to z$\gtrsim$1.4, the beginning of the so-called spectroscopic redshift desert. In addition to the studies of SFR, emission lines are also powerful tools to analyze other properties of the gas (see e.g., Stasińska et al. 2004), and hence the galaxy, such as the extinction (from the Balmer decrement Hα/Hβ), the metallicity (from [OII]+[OIII]/Hβ; R_{23}) or even diagnostic analysis of the primary source of ionization, either if it is star forming regions or AGNs (e.g., the BPT diagram, Baldwin et al. 1981).

Another remarkable feature in the optical SEDs is the Balmer/4000 Å break. These are often treated as one feature, due to their similar locations and the fact that they partially overlap (see left panel of Figure 2.2, top and bottom SEDs). However, the breaks originate from different physical processes and present a different evolution with age of the stellar population. The 4000 Å arises because of an accumulation of absorption lines of mainly ionized metals. As the opacity increases with decreasing stellar temperature, the 4000 Å break gets larger with older ages, being largest for old and metal-rich stellar populations (Bruzual & Charlot 2003). There are several definitions to quantify the strength of this break (e.g., Bruzual A. 1983). Balogh et al. (1999) defined a new index Dn(4000) that is based on small continuum regions at both sides of the break (3850–3950 Å and 4000–4100 Å) to minimize the effect of dust reddening. The Balmer break, at 3646 Å marks the termination of the hydrogen Balmer series and it is strongest in A-type stars. Therefore, the break strength does not monotonically increase with age, but reaches a maximum in stellar populations of intermediate ages (0.3–1 Gyr). The strength of the Balmer sequence can be best measured from the individual Balmer lines, such as Hγ (e.g., Kauffmann et al. 2003). The 4000 Å break is used in several color-color criteria to identify old stellar populations at high-z (e.g., ERO, DRGs).

- **Near IR (NIR)**

  The NIR spectral region is especially interesting for studies of the galaxy stellar population. While the UV-optical range is dominated by younger populations, making it an excellent indicator of the recent star formation, the contribution of young stars frequently outshines that of the underlying older stellar population, which constitutes the bulk of the stellar mass of the system. On the contrary, in the NIR, the flux contribution from young OB stars and emission lines emission from ionized gas is minimized. The H (1.6μm) and K (2.2μm) bands are in the Rayleigh-Jeans part of the spectrum for even the coldest stellar photospheres (e.g., M type stars peak in this range). Therefore, the relative contribution of hot-to-cold stars is significantly reduced, making the longer-lived, cooler stars better represented and providing a meaningful indicator of mass and age. NIR light is also less attenuated by interstellar dust than optical light, which reduces the assumptions and uncertainties required in the estimate of the intrinsic luminosities.

  Assuming that these old stars dominate the NIR, this range will reflect the underlying stellar

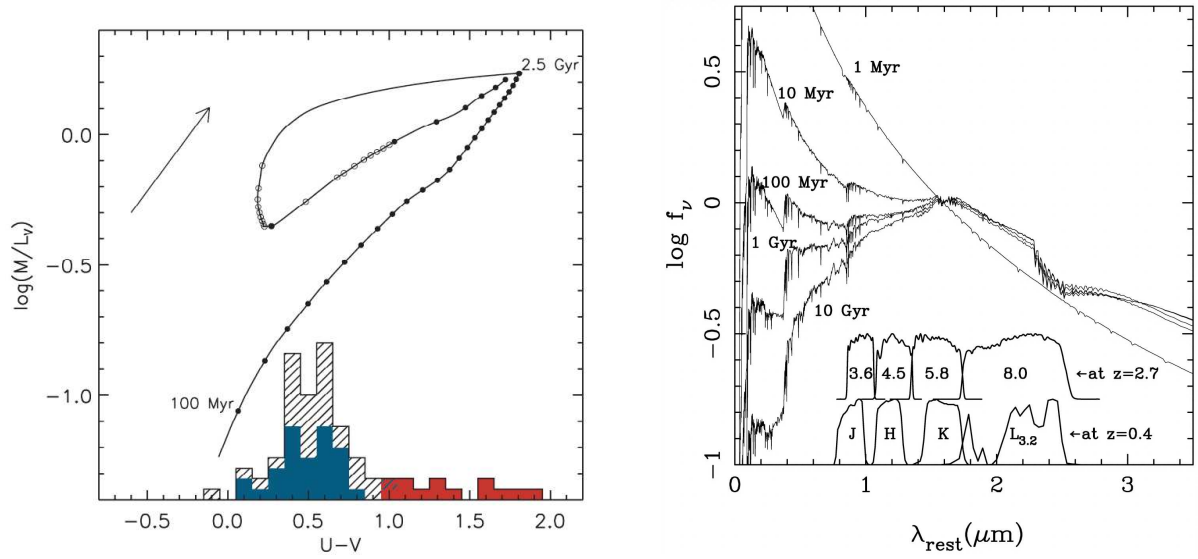

Figure 2.2: *Left:* Evolution of galaxy in a mass-to-light against color plot (M/L_V vs. U−V) as a function of time (adapted from Wuyts et al. 2007). The age track starts as an exponentially declining star formation model (from Bruzual&Charlot 2003). Filled circles mark age steps of 100 Myr. Open circles represent 10 Myr age steps for secondary burst in 2.5 Gyr. *Right:* Model SEDs (Bruzual&Charlot 2003) at different ages normalized at 1.6 μm (adapted from sawicki et al. 2002). The 1.6 μm bump is particularly prominent in all but the very youngest stellar populations.

mass distribution. Then, making simple yet physically motivated assumptions, the stellar mass of a galaxy can be estimated by multiplying the luminosity in a given band by a mass-to-light (M/L) ratio, that can be estimated from one (or more) color (see e.g., Bell et al. 2001; also Figure 2.2). The color is in fact a probe into the physical properties of the stellar population. Therefore, it is a good idea to search for a reference band that minimizes the effects of M/L variations due to stellar populations (age, metallicity, chemical abundances) and dust absorption. Several optical and NIR M/L calibrations has been proposed over the last decade, but the general agreement is that those based on NIR are more robust against the effects of the assumed SFH of the galaxies (Brinchmann & Ellis 2000; Bell & de Jong 2001; Rudnick et al. 2003; Wuyts et al. 2007). Nonetheless, the NIR is not exempt from some uncertainties, in particular from those arising from issues in the modeling of some particularly unstable and short lived phases of stellar evolution (e.g., the thermally pulsing asymptotic giant branch stars, TP-AGB; see Maraston 2005).

Similarly to the other wavelength ranges, the NIR range also presents a characteristic spectral feature that can be easily identified with an appropriate band coverage of the SED. A peak (or bump) in the emission of the stellar component at 1.6 μm imprints itself in the SEDs of cool stars due to a minimum in the opacity of the H^- ion present in their photospheres. Consequently, the SEDs of composite stellar populations that contain significant numbers of such stars can be expected to possess the same spectral imprint. As illustrated in Figure 2.2, the 1.6 μm bump is easily discernible in all but the extremely young ($<$1 Myr) stellar populations, where it is swamped by the power-law spectra of hot massive young stars. Given the strength of this feature it can also be efficiently exploited in the search for distant galaxies (Simpson & Eisenhardt 1999; Egami et al. 2004).

Finally, it has been pointed out that the balance between optical and NIR emission could

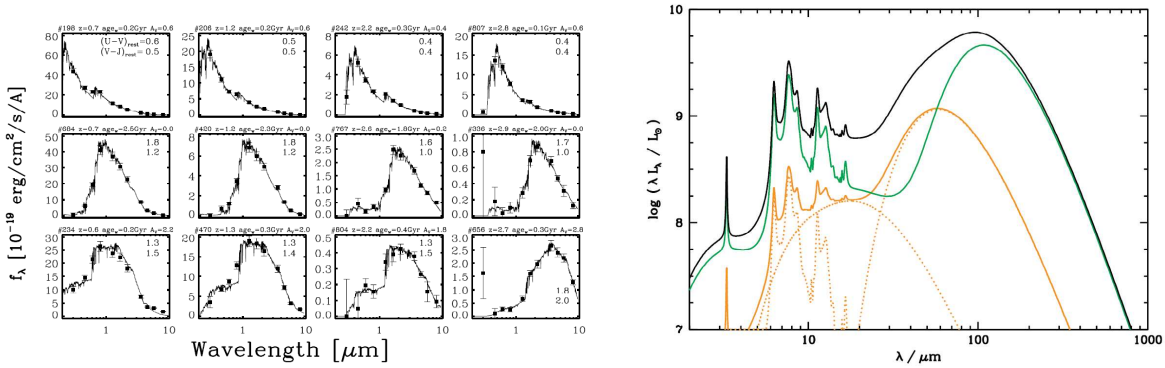

Figure 2.3: *Left:* U-to-8 μm SEDs of galaxies at 0.7<z<3 (adapted from Wuyts et al. 2007). Each column shows (top-to-bottom) the SEDs of: a) a young star-forming galaxy with little dust attenuation, A(V)=0.6; b) an old-quiescent galaxy with no attenuation; c) a young star-forming galaxy presenting high dust obscuration, A(V)$\sim$2. *Right:* IR emission of cold and warm dust components (green and orange, respectively) plus contribution from the PAH emission (adapted from da Cunha et al. 2008).

be and efficient probe to estimate the amount of dust attenuation, complementary to UV+IR analysis. Wutys et al. (2007) and showed that the V-J$_{rest}$ could be able to measure the effect of dust on the strength of the 4000 Å break, efficiently discriminating between the dusty and old systems when accurate photometry is available in the rest-frame NIR (see e.g., Brammer et al. 2009; also left panel of Figure 2.3).

- **Mid-to-Far IR**

  Beyond the NIR wavelengths, the stellar radiation arises almost exclusively from the the Rayleigh-Jeans part of their spectrum, which is rapidly decreasing. The majority of the light in this range originates from the dust component (if present in the galaxy) which is essentially re-radiating the ionizing photons of young stars that heated the grains. Dust emission in the FIR and sub-mm is most commonly represented by a single black body or a simple sum over a limited (2–3) number of these (see right panel of Figure 2.3). This forms assumes that one or several dust components are in thermal equilibrium at different temperatures. In general, two modified black-bodies are sufficient to model these wavelengths, encompassing the idea of warm and cold components of the ISM (see e.g., Popescu et al. 2002; Hippelein et al. 2003; Sauvage et al. 2005). However, simple black bodies might not be sufficient to accurately represent the SEDs in the 5-20μm range. This is due to the presence of broad emission features originated in Polycyclic Aromatic Hydrocarbons (PAHs; see e.g., Smith et al. 2007) and strong silicate absorptions. PAHs can be considered either the largest molecular species or the smallest dust. Thus, the shape of the emission features is usually modeled combining the stretching modes of the large aromatic molecules and the stochastic heating processes that become important for smaller dust grains.

  One of the most commonly extracted galaxy properties from the IR is the SFR. As recently formed stellar populations tend to be more obscured (from their own parental cloud) a large fraction of their luminosity is absorbed in the UV, and thus dust emission is in principle a good tracer of recent star formation (Kennicutt 1998). Nonetheless, the assumptions upon which SFR empirical calibrations are derived are also affected by some uncertainties characteristic of this spectral range. For example, a range of ages (not only young stars) can contribute to dust heating (Cortese et al. 2008; Kennicutt et al. 2009). In addition, the star

forming regions can suffer from a different range of dust extinctions, from totally obscured (ULIRGs) to unobscured (blue dwarfs), meaning that caution must be exercised when using these IR-SFR calibrations. Finally, as mentioned before, the FIR emission provides a robust estimate of the dust extinction when combined to UV measurements, and if sufficiently detailed data are available (frequently only for local galaxies), it can also be used to estimate the total dust mass (e.g.,Dale & Helou 2002; Draine et al. 2007) or to discriminate the dominant energy source in IR bright galaxies (starburts vs. AGN), especially ultra luminous IR galaxies (ULIRGs; see e.g., Rowan-Robinson 2003).

- **Other wavelengths**

  At wavelengths outside the regime considered here, such as the X-ray and radio wavelengths, non-stellar processes (or at least those not directly associated with stellar light) such as shocks, accretion into black holes, etc. dominate the SED. These processes require a higher order of complexity and their study can be associated with the SFH of a galaxy (e.g. supernova rate and recent star formation). Some examples of the properties that can be inferred from the data observed at the these wavelengths include the Radio-FIR correlation for star-forming galaxies (e.g., Condon 1992; Garrett 2002; Bell 2003), or the use of Hard and Soft X-ray detections as probes for presence of an active black hole or ongoing star-formation (e.g., White et al. 1983;Fabbiano 1989; Persic & Rephaeli 2002).

2.4 Examples of multi-band surveys and the importance of galaxy survey databases.

Due to the key role of multi-wavelength data in our capabilities to analyze in detail the physical properties of the galaxies, many world-wide astronomical communities have joined their efforts in order to obtain complementary multi-band observations. These groups count with people from many different areas of expertise, which allows the group to lead multiple proposals to different astronomical facilities gathering large dataset in a coordinated manner. For evident reasons, these efforts are often located in just a few selected areas of the sky (the so-called cosmological fields) which count with the most exhaustive coverage available. Some of the most relevant of these world-wide collaborations are GOODS (Giavalisco et al. 2004), COSMOS (Scoville et al. 2007), or AEGIS (Davis et al. 2007).

As a result of these efforts, the number of public datasets potentially useful for SED analysis in large samples of galaxies is truly impressive. In fact, many science projects can be carried out without ever writing an observing proposal, just by exploiting the already existing data. A clear sign that the capabilities of galaxy databases extent well beyond a sum of catalogs. A paradigmatic example of the scientific possibilities of these databases is the Sloan Digitalized Sky Survey (SDSS; York et al. 2000). To date, countless works with hundreds of citations have been produced (are still being written) out of SDSS data only.

Nonetheless, in an era of large telescope facilities and technological development, where individual surveys detecting millions of sources produce data sets measured in disk space of the order of Terabytes, we are not yet exploiting the full potential of these resources due ti processing issues. For example, a lot of these resources, although publicly available, are hard to find and access in the practice. While a multitude of archives and data depositories do exist, the resources

are frequently scattered in the web, and must be accessed individually one at a time, downloading only modest amounts of data from each of them. In addition, the growth in data volume, inevitably leads to an increase in data complexity, and generally also in quality and homogeneity. Thus, even downloading all the existing data sets the analysis is not straightforward. The user must first face the difficulties associated with the construction of robust SEDs from the observed multi-band photometry, e.g., noting that the observed flux depends on the spectral response of the instruments (+filter), or that the real shape of the source is spatially redistributed over the point spread function (PSF) of the instrument. In addition, in order to robustly identify the multi-band counterparts of each source, it is necessary to join data from different instruments overcoming the differences in spatial resolution and accounting for non-detections in some bands.

Altogether, the difficulties mentioned above highlights the importance of assembling unified multi-band catalogs which process the data in a consistent manner, and offering a clearly organized access to final data products. Nowadays, stellar and (local) extragalactic studies are benefiting from recent improvements in the world-wide community of the Virtual Observatory (www.ivoa.net), or already developed resources like the NASA Extragalactic Database (NED), the Multimission Archive at STScI (MAST), or the smaller GoldMINE (Gavazzi et al. 2003) or HyperLEDA (Paturel et al. 2003). However, the resources at high redshift are often more heterogeneous and the efforts are only focused in characterizing individual blank fields, providing multi-band catalogs or photometric redshifts (COMBO-17, Wolf et al. 2003; GOODS-MUSIC Grazian et al. 2006, etc.). Modest efforts have been developed so that all the available resources in different selected fields can be unified. This kind of works would largely improve the legacy of the data, enabling further scientific exploitation to be done in a reasonable and practical amounts of time.

2.5 Barro et al. (2011a) ApJS, 193, 13B

The Astrophysical Journal Supplement Series, 193:13 (24pp), 2011 March doi:10.1088/0067-0049/193/1/13

UV-TO-FIR ANALYSIS OF *SPITZER*/IRAC SOURCES IN THE EXTENDED GROTH STRIP. I. MULTI-WAVELENGTH PHOTOMETRY AND SPECTRAL ENERGY DISTRIBUTIONS

Guillermo Barro[1], P. G. Pérez-González[1,5], J. Gallego[1], M. L. N. Ashby[2], M. Kajisawa[3], S. Miyazaki[4], V. Villar[1], T. Yamada[3], and J. Zamorano[1]
[1] Departamento de Astrofísica, Facultad de CC. Físicas, Universidad Complutense de Madrid, E-28040 Madrid, Spain
[2] Harvard-Smithsonian Center for Astrophysics, 60 Garden Street, Cambridge, MA 02138, USA
[3] Astronomical Institute, Tohoku University, Aramaki, Aoba, Sendai 9808578, Japan
[4] National Astronomical Observatory of Japan, Mitaka, Tokyo 181-8588, Japan
Received 2010 May 21; accepted 2011 January 14; published 2011 March 1

ABSTRACT

We present an IRAC 3.6+4.5 μm selected catalog in the Extended Groth Strip (EGS) containing photometry from the ultraviolet to the far-infrared and stellar parameters derived from the analysis of the multi-wavelength data. In this paper, we describe the method used to build coherent spectral energy distributions (SEDs) for all the sources. In a forthcoming companion paper, we analyze those SEDs to obtain robust estimations of stellar parameters such as photometric redshifts, stellar masses, and star formation rates. The catalog comprises 76,936 sources with [3.6] $\leqslant$ 23.75 mag (85% completeness level of the IRAC survey in the EGS) over 0.48 deg^2. For approximately 16% of this sample, we are able to deconvolve the IRAC data to obtain robust fluxes for the multiple counterparts found in ground-based optical images. Typically, the SEDs of the IRAC sources in our catalog count with more than 15 photometric data points, spanning from the ultraviolet wavelengths probed by *GALEX* to the far-infrared observed by *Spitzer*, and going through ground- and space-based optical and near-infrared data taken with 2–8 m class telescopes. Approximately 95% and 90% of all IRAC sources are detected in the deepest optical and near-infrared bands. These fractions are reduced to 85% and 70% for S/N $>$ 5 detections in each band. Only 10% of the sources in the catalog have optical spectroscopy and redshift estimations. Almost 20% and 2% of the sources are detected by MIPS at 24 and 70 μm, respectively. We also cross-correlate our catalog with public X-ray and radio catalogs. Finally, we present the *Rainbow Navigator* public Web interface utility, designed to browse all the data products resulting from this work, including images, spectra, photometry, and stellar parameters.

Key words: galaxies: high-redshift – galaxies: photometry – galaxies: starburst – infrared: galaxies

Online-only material: machine-readable tables

1. INTRODUCTION

Multi-wavelength observations of blank fields provide a fertile ground for studies of the evolution of galaxies from the early universe. Indeed, in the past decade we have advanced amazingly in our knowledge about the formation of galaxies thanks to deep field imaging and spectroscopic surveys. The extraordinary success of these surveys is sustained by the coordinated effort of several telescope facilities, institutions, and research groups that gather large collections of multi-wavelength photometry and spectroscopy, providing the entire scientific community with a vast pool of data to analyze. Remarkable examples of this kind of projects are the Hubble Deep Field (HDF) observations (Williams et al. 1996), the Classifying Objects by Medium-Band Observations project (COMBO17; Wolf et al. 2001), Great Observatories Optical Deep Survey (GOODS; Giavalisco et al. 2004), VIMOS-VLT Deep Survey (VVDS; Le Fèvre et al. 2005), All-wavelength Extended Groth strip International Survey (AEGIS; Davis et al. 2007), or Cosmic Evolution Survey (COSMOS; Scoville et al. 2007).

Nevertheless, the full scientific exploitation of these surveys unavoidably needs a consistent merging of the data coming from heterogeneous sources (with different depths and resolutions) to build catalogs of galaxies characterized with panchromatic photometry and spectroscopy. Although substantial effort has been devoted to create homogeneously processed multi-wavelength catalogs for the most important fields (e.g., Chandra Deep Field South, Wolf et al. 2001; Hubble Deep Field North, Steidel et al. 2003, Capak et al. 2004; Extended Groth Strip (EGS), Coil et al. 2004, Ilbert et al. 2006), many of these catalogs are selected in the optical bands (i.e., rest-frame ultraviolet (UV) at high redshift) and lack near-infrared (NIR) imaging (an important data set for the studies of galaxy populations at high redshift) reaching depths that match the optical observations. Fortunately, the proliferation of deep and wide NIR surveys has supported the publication of an increasing number of multi-band samples selected in the *K* band (Grazian et al. 2006; Quadri et al. 2007; Wuyts et al. 2008) or Infrared Array Camera (IRAC) bands (Rowan-Robinson et al. 2008; Pérez-González et al. 2005, 2008, hereafter PG05 and PG08). A detailed UV-to-NIR coverage of the spectral energy distribution (SED) improves the estimates of important stellar parameters, such as the mass, age, extinction, or star formation rate (SFR; see, e.g., Walcher et al. 2008; Salim et al. 2007). Moreover, in order to obtain the most reliable stellar mass estimates for $z \sim$ 2–3 galaxies, and to distinguish young dusty starburst from quiescent galaxies at these redshifts, we need to obtain data probing the rest-frame NIR for these populations (Bundy et al. 2006; Pozzetti et al. 2007; Wuyts et al. 2007; Williams et al. 2009; Muzzin et al. 2009). This became possible with the launch of *Spitzer* and the use of one of its instruments, IRAC (Fazio et al. 2004), which covers the 3.6-to-8.0 μm spectral range.

[5] Associate Astronomer at Steward Observatory, The University of Arizona.

The power of multi-band catalogs is significantly enhanced when optical and NIR data are complemented with mid-IR ($>5\,\mu$m) to radio fluxes, such as those from *Spitzer*/MIPS, SCUBA, VLA, or *Herschel* surveys. These data directly probe the emission of the dust component of galaxies (Santini et al. 2009; Wuyts et al. 2008). Actively star-forming galaxies harbor large amounts of dust, which cause that a fraction of the UV emission, directly related to the ongoing star formation, is extincted and re-emitted in the IR. Thus, modeling the IR emission offers not only a complementary approach to estimate the SFR of a galaxy but also an improved measurement of the intrinsic UV extinction (Reddy et al. 2006; Daddi et al. 2007; Salim et al. 2007; Iglesias-Páramo et al. 2007). The IR approach to studies of the star formation becomes particularly relevant at higher redshifts, where the number of luminous infrared galaxies (whose integrated IR luminosity is $L(\mathrm{IR}) > 10^{11}\ L_{\odot}$) and their contribution to the cosmic SFR density increase significantly (Chary & Elbaz 2001; PG05; Caputi et al. 2007).

The downside to having an exceptional data pool available in many regions of the sky is that the data quality is largely heterogeneous. Unfortunately, the high-redshift community still lacks the existence of a unified database that facilitates the access to the multiple data sets and resources, similar to local extragalactic databases such as the NASA Extragalactic Database (NED) or the Sloan Digitalized Sky Survey (SDSS; York et al. 2000) database.

The purpose of this work is to present an NIR-selected sample of galaxies with well-sampled SEDs and analyze their properties maximally benefiting from the panchromatic data. To do this, we have built an IRAC 3.6+4.5 μm selected photometric and spectroscopic catalog including data from X-ray to radio wavelengths for 76,936 galaxies at $0 < z \lesssim 4$ in the EGS.

The EGS has been intensively observed as a part of the AEGIS (Davis et al. 2007) collaboration in order to assemble an exceptional multi-wavelength data set, including deep optical imaging from the Canada–France–Hawaii Telescope (CFHT) Legacy Survey (CFHTLS), *HST* coverage in two bands, UV data from *Galaxy Evolution Explorer* (*GALEX*), and mid-IR and far-IR photometry from *Spitzer*. In addition, the EGS is the key field for the DEEP2 survey, one of the largest and deepest spectroscopic surveys to date (Davis et al. 2003), with more than 10,000 optical spectra down to $R \sim 24$. This vast data set converts the EGS in one of the main fields for the study of galaxy evolution at different epochs of the lifetime of the universe. Our goal is get advantage of this impressive multi-wavelength data collection and use it to build UV-to-FIR SEDs, whose analysis will allow us to obtain estimations of interesting parameters, such as the photometric redshifts, stellar masses, and SFRs.

The photometric catalog along with the photometric redshifts and the inferred stellar parameters are intended to become a multi-purpose resource useful for many different scientific goals. Some of them will be presented in forthcoming papers. We make all the catalogs publicly available through our Web site and through a dedicated Web interface, dubbed *Rainbow Navigator*, conceived to facilitate the access to the data, but also to serve as a permanent repository for updates in these catalogs, or similar catalogs in other cosmological fields (e.g., those presented in PG08 for the GOODS fields).

In this paper, we concentrate on the description of the data set and the methods developed to measure the merged photometry for the IRAC sample in the EGS. We also analyze the multi-band properties of the sample to understand the main properties of the *Spitzer* surveys. All the multi-wavelength photometry is released in a public database, conceived to allow the astronomical community to access all the results from our work and use them for their own purposes. In a forthcoming companion paper (hereafter Paper II), we will present our methodology to fit the SEDs presented in this paper and to estimate photometric redshifts, stellar masses, and SFRs out of them. We will also assess the quality of the inferred parameters, analyzing in detail their intrinsic systematic and random uncertainties.

The outline of this paper follows. In Section 2, we present the available data sets that we have compiled for this paper. In Section 3, we present the techniques developed to extract the IRAC 3.6+4.5 μm selected sample and we discuss the properties of the IRAC photometry of the sample. In Section 4, we present the methods developed to build the merged multi-band photometric catalog. In Section 5, we describe in detail the photometric properties and reliability of the catalog. In Section 6, we describe the format of the published catalogs, the database built to allow an easy access and handling of those, baptized as the *Rainbow* Cosmological Surveys Database, and the publicly available Web interface to surf the database, *Rainbow Navigator*.

Throughout this paper we use AB magnitudes. We adopt the cosmology $H_0 = 70\,\mathrm{km^{-1}\,s^{-1}\,Mpc^{-1}}$, $\Omega_m = 0.3$, and $\Omega_\lambda = 0.7$.

2. DATA DESCRIPTION

The EGS ($\alpha = 14^{\mathrm{h}}17^{\mathrm{m}}$, $\delta = +52^{\circ}30'$) is one of the most targeted cosmological deep fields. Noticeably, a comprehensive panchromatic data set has been compiled in this field within the AEGIS collaboration (Davis et al. 2007).

The sample of galaxies studied in this paper is based on an IRAC 3.6+4.5 μm selection. This choice obeys to several reasons. First, the IRAC bands are specially tailored to probe the rest-frame near-infrared (NIR) fluxes of distant galaxies, thus being the perfect tool for studies of massive galaxies at high-z (e.g., Rodighiero et al. 2007; Mancini et al. 2009). Second, the quality, depth, and ubiquity of the IRAC observations in the so-called cosmological fields favor the assembly of coherent flux limited catalogs over large cosmological volumes (e.g., PG08), which is the cornerstone of the observational cosmology. The IRAC bands offer an alternative to the less efficient NIR ground-based surveys and provide a starting point to consistently anchor surveys at longer wavelengths (*Spitzer*/MIPS, *Herschel*, ALMA). Despite its lower spatial resolution (FWHM $\sim 2''$; Fazio et al. 2004) compared to optical/NIR ground-based surveys, the image quality of IRAC is very stable and several authors have been able to perform deblending techniques successfully merging IRAC catalogs into their panchromatic data sets (PG05; PG08; Grazian et al. 2006; Ilbert et al. 2009).

In the rest of this section, we describe the multi-wavelength data sets in EGS compiled for this paper to characterize the IRAC-selected sample. Table 1 summarizes the main characteristics of these data sets, including the depth, the area, and the image quality. Figure 1 shows the footprints of the various surveys, highlighting the area with higher band coverage.

2.1. X-ray Data

The EGS region has been observed in the X-ray (0.5–10 keV) using *Chandra*/*ACIS* during two observation cycles in 2002 and 2005. The AEGIS-X survey covers an area of 0.67 deg^2 in eight pointings ($\sim 17' \times 17'$ each), completely overlapping

Table 1
Properties of the Data Set in the EGS

Band (1)	$\lambda_{\rm eff}$ (2)	$m_{\rm lim}$[AB] (3)	FWHM (4)	Area (5)	Surf. Dens. ($\times 10^3$) (6)	Source (7)
Hard X-Ray[a]	0.31 nm (2–10 keV)	3.8×10^{-16} erg cm^2 s^{-1}	0.5″–6″	0.67	1.102	*Chandra*/ACIS; Laird et al. (2009)
Soft X-Ray[a]	1.24 nm (0.5–2 keV)	5.3×10^{-17} erg cm^2 s^{-1}	0.5′–4′	0.67	1.540	*Chandra*/ACIS; Laird et al. (2009)
FUV	153.9 nm	25.6	5.″5	1.13	10.5	*GALEX* GTO
NUV	231.6 nm	25.6	5.″5	1.13	24.7	*GALEX* GTO
u'	362.5 nm	26.1	1.″0	0.77	148.2	MMT/Megacam
u^*	381.1 nm	25.7	0.″9	1	152.5	CFHTLS/MegaCam
B	439.0 nm	25.7	1.″2	1.31	101.7	CFHT-12k
g	481.4 nm	26.7	1.″3	0.77	203.8	MMT/MegaCam
g'	486.3 nm	26.5	0.″9	1	163.4	CFHTLS/MegaCam
V_{606}	591.3 nm	26.9	0.″2	0.197	440.7	*HST*/ACS
r'	625.8 nm	26.3	0.″8	1	363.9	CFHTLS/MegaCam
R	651.8 nm	26.1	0.″7	1	220.0	Subaru/SuprimeCam
R	660.1 nm	25.3	1.″0	1.31	144.3	CFHT-12k
i'	769.0 nm	25.9	0.″8	1	341.1	CFHTLS/MegaCam
i	781.5 nm	25.3	1.″0	0.77	275.8	MMT/MegaCam
I	813.2 nm	24.9	1.″1	1.31	117.0	CFHT-12k
i_{814}	807.3 nm	26.1	0.″2	0.197	452.1	*HST*/ACS
z'	887.1 nm	24.7	0.″8	1	179.0	CFHTLS/Megacam
z	907.0 nm	25.3	1.″2	0.77	214.0	MMT/Megacam
J_{110}	1.10 μm	23.5	0.″7	0.0128	252.0	*HST*/NICMOS
J	1.21 μm	22.9	1.″0	0.195	67.0	CAHA-Ω2*k*
H_{160}	1.59 μm	24.2	0.″8	0.0128	252.0	*HST*/NICMOS
J[a]	1.24 μm	21.9	1″	0.30	30.0	Palomar-WIRC; Bundy et al. (2006)
K_s	2.11 μm	20.7	1.″5	0.20	18.6	CAHA-Ω′
K_s	2.15 μm	23.7	0.″6	0.09	124.0	Subaru MOIRCS
K[a]	2.16 μm	22.9	1″	0.70	34.0	Palomar-WIRC; Bundy et al. (2006)
IRAC 3.6	3.6 μm	23.9	2.″1	0.48	315.0	*Spitzer* GTO
IRAC 4.5	4.5 μm	23.9	2.″1	0.48	274.4	*Spitzer* GTO
IRAC 5.8	5.8 μm	22.3	2.″2	0.48	129.7	*Spitzer* GTO
IRAC 8.0	8.0 μm	22.3	2.″2	0.48	115.2	*Spitzer* GTO
MIPS 24	23.7 μm	19.5 (60 μJy)	5″	0.79	30.0	*Spitzer* GTO
MIPS 70	71.4 μm	15 (3.5 mJy)	19″	0.69	6.0	*Spitzer* GTO
Radio 20 cm[a]	20 cm	100 μJy beam^{-1}	4.″2	0.73	1.538	VLA; Ivison et al. (2007)
R, redshift[a]	640–910 nm	24.1	···	1.31	10.343	DEEP2

Notes. Column 1: name of the observing band. Column 2: effective wavelength of the filter calculated by convolving the Vega spectrum (Colina & Bohlin 1994) with the transmission curve of the filter+detector. Column 3: limiting AB magnitude (except for the X-ray catalogs) of the image estimated as the magnitude of an S/N = 5 detection (see Section 4 for details on the measurement of the photometric errors). Column 4: median FWHM of the PSF in arcseconds measured in a large number of stars (see Section 5.4). Column 5: area covered by the observations in deg^2. Column 6: source density per square degree up to the limiting magnitude given in Column 3. Column 7: source from where the data were obtained.
[a] Data drawn from a catalog.

with the region covered by IRAC. The nominal exposure time of the frames is 200 ks per pixel, reaching limiting fluxes of 5.3×10^{-17} and 3.8×10^{-16} erg cm^2 s^{-1} in the soft (0.5–2 keV) and hard (2–10 keV) bands, respectively. In this work, we use the data reduction and point source catalogs published in Laird et al. (2009; see also Nandra et al. 2005 for a first version of the catalogs). The two-band (soft and hard) merged catalog comprises 1325 sources with <1.5% spurious detections. The authors identified optical and NIR counterparts for 1013 and 830 sources, respectively, from the CFHTLS optical catalog (see Section 2.3.1), and the *Spitzer*/IRAC catalog of Barmby et al. (2008). The cross-match is based on maximum likelihood method with a search radius of 2″ (more than a factor of 1.5 the rms of their astrometric accuracy).

2.2. Ultraviolet Data

The *GALEX* (Martin et al. 2005) observed the EGS over three consecutive years providing deep UV data in two channels (FUV at 153 nm, and NUV at 231 nm) on a 1.13 deg^2 circular area around $\alpha = 14^{\rm h}20^{\rm m}$, $\delta = +52^\circ47'$. The total exposure times for the composite stacks are 58 ks and 120 ks in the FUV and NUV filters, respectively. The approximate limiting magnitude in both bands is ∼25.1 mag.

2.3. Optical Data

2.3.1. CFHTLS/CFHT12K

A $1^\circ \times 1^\circ$ square region centered on the coordinates $\alpha = 14^{\rm h}19^{\rm m}27^{\rm s}$, $\delta = +52^\circ40'56''$ was observed within the CFHTLS (sector D3). Using the MEGACAM camera on the CFHT, imaging data were obtained in five broadband filters over the wavelength range 350 nm < λ < 940 nm: u^*, g', r', i', z'. The overall exposure times range from 4 hr to 40 hr (for the u^* and z' bands, respectively), reaching limiting magnitudes between 26 and 27 mag. The reduced images have gone through several releases. The data used in this paper are part of the CFHTLS "T0004" release produced at the TERAPIX data center (Gwyn et al. 2011[6]). Although the total mosaicked area covers 1 deg^2, the overlap with the IRAC observations is just 0.35 deg^2.

[6] http://www.astro.uvic.ca/∼gwyn/cfhtls/

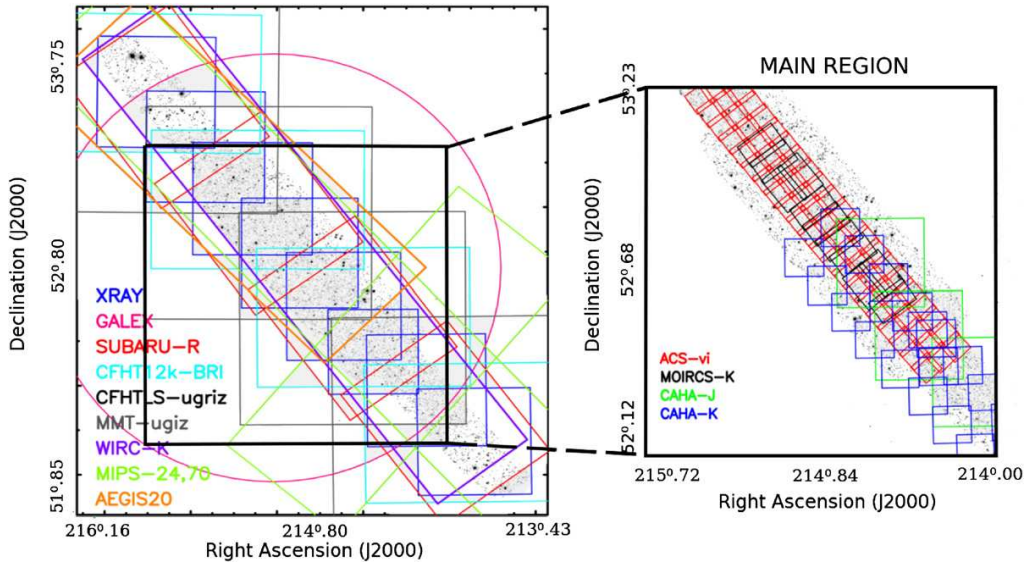

Figure 1. Layout of all the imaging surveys covering the EGS. The background gray-scale image shows the IRAC 3.6 μm mosaic. The black square depicts the CFHTLS pointing. The intersection of both footprints defines the region of higher photometric coverage (magnified on the right panel), which is referred as "main region" throughout the text (see Section 5) and contains the highest resolution *HST* data. The cyan and red rectangles show the CFHT12k-*BRI* and SUBARU *R*-band coverage, respectively. The gray and purple squares show the MMT-$u'giz$ and *Chandra*/ACIS pointings, respectively. The magenta circle shows the *GALEX* survey footprint. The green rectangles show the *Spitzer*/MIPS coverage. The orange rectangle shows VLA 20 cm coverage. In the main region, magnified on the right side of the figure, the red tiles depict the *HST*/ACS footprints (the NICMOS images overlap with this area). Black rectangles show the MOIRCS K_s-band imaging, and the green and purple lines delimit the CAHA *J*- and K_s-band surveys.

In addition to the CFHTLS data, shallower images were acquired in the *B*, *R*, and *I* bands over a larger area, using the wide-field 12K mosaic camera on CFHT. These observations were intended to provide optical coverage for the DEEP2 spectroscopic survey, extending through the whole EGS in four different pointings. The observing times were 3–6 hr, to achieve a limiting magnitude of ∼25 mag. The photometric catalogs were published within the DEEP2 DR1 (Coil et al. 2004), and the raw (non-reduced) images can be retrieved from the CADC archive.[7] We downloaded the raw and calibrations files from the archive to perform our own data reduction and cataloging. This reduction was carried out with the IRAF[8] task *mscred*. The photometric calibration was performed using the *BRI* public catalogs. The average dispersion of the photometry comparison is smaller than 0.03 mag.

2.3.2. MMT/Megacam

The EGS was observed with the Megacam camera (McLeod et al. 2006) on the MMT in the $u'giz$ bands during several campaigns from 2006 to 2009. Four pointings of the $24' \times 24'$ Megacam field of view were arranged to cover the full extension of the 2 deg long IRAC mosaic.

The MMT/Megacam imaging data were reduced with a combination of standard IRAF/`mscred` routines and custom software. Final mosaics were calibrated against the coextensive SDSS photometry with appropriate color corrections. The 5σ limiting magnitudes within a $2''$ diameter aperture for point sources vary among the four different pointings but are approximately 26.5, 27.2, 26.0, and 26.0 mag in the u', g, i, and z bands, respectively. The effective seeing in the final mosaics is roughly $1''$ FWHM or slightly better in some bands.

2.3.3. HST/ACS

As a part of a GO program (PI: Davis), the *HST* Advanced Camera for Surveys (ACS) acquired deep imaging of EGS in two optical bands: $F606W$ and $F814W$ (hereafter the V_{606} and i_{814} images). The ACS survey covers an area of ∼710.9 arcmin^2 ($10\farcm1 \times 70\farcm5$) on 63 contiguous tiles following the direction of the IRAC mosaic, covering approximately 50% of the total area surveyed by IRAC, and ∼80% of the area overlapping with the CFHTLS observations. The fully reduced, drizzled frames and calibration products were released by the AEGIS Team (Lotz et al. 2008). Each science image has an approximate exposure time of ∼0.6 hr per pixel and a limiting magnitude of ∼28 mag.

2.3.4. Subaru Suprime-Cam

Ground based *R*-band imaging of the EGS was carried out with the Subaru Telescope as a part of the Subaru Suprime-Cam Weak-Lensing Survey (Miyazaki et al. 2007). The Suprime-Cam field of view is 0.25 deg^2 in size, covering the whole IRAC map in four pointings. The total exposure time was 30 minutes for each pointing, taken in four 7.5 minute exposures, in a dithering pattern with $\sim 1'$ spacing. The approximate limiting magnitude is $R = 26$ mag. These data were downloaded from the SMOKA database and reduced with the Suprime-Cam pipeline (SDFRED, v1.0).

2.4. Near-infrared Data

2.4.1. HST/NICMOS

Simultaneously to the ACS observations, the Near-Infrared Camera and Multi-Object Spectrometer (NICMOS) covered

[7] http://www4.cadc-ccda.hia-iha.nrc-cnrc.gc.ca/cadcbin/cfht/wdbi.cgi/cfht/wdbi.cgi/cfht/quick/form
[8] http://iraf.noao.edu/

parallel fields in the $F110W$ and $F160W$ bands (hereafter J_{110} and H_{160} bands, respectively), with a similar exposure time and a limiting magnitude of 23.5 and 24.2, respectively. The observations were designed to maximize the overlap between both *HST* surveys. Virtually all (58 out of the 63) NICMOS frames lie within the area covered by the ACS primary imaging. However, the smaller field of view of NICMOS ($\sim 1' \times 1'$) leads to a total NIR coverage of only 0.0128 deg^2, with a 90% overlap with the area covered by ACS but less than a 4% with that covered by IRAC.

2.4.2. Subaru MOIRCS

In addition to the optical imaging, NIR observations of the EGS were also obtained with the Multi-Object InfraRed Camera and Spectrograph (MOIRCS) on five nights during 2006 April–May (PIs: Fukugita, Yamada) and a complementary run on 2007 June 25. The data set comprises 11 pointings covering a total of 0.09 deg^2 oriented along the original strip within $52.^\circ5 < \delta < 53.^\circ0$ and completely overlapping with the *HST*-ACS and CFHTLS imaging. The median exposure time per frame is $\sim$1 hr for an approximate limiting magnitude of $K_s \sim$ 23–24 mag. The data were reduced using dedicated scripts developed by the MOIRCS team involving the IRAF task MSCRED, plus an additional de-fringing process (see, e.g., Kajisawa et al. 2009).

2.4.3. Palomar and Calar Alto Imaging

Given the importance of having a continuous band coverage for any kind of study regarding galaxy populations (Wuyts et al. 2007), we have incorporated in our data compilation the POWIR NIR catalog (Bundy et al. 2006). These data were acquired between 2002 September and 2005 October using the WIRC camera in the Palomar 5 m telescope. The total surveyed area in the EGS field is 2165 arcmin^2 (0.6 deg^2) in the K band and $\sim$1/3 of that area in the J band. The approximate limiting magnitudes are $K \sim 22.9$ and $J \sim 21.9$. Note that no images were publicly available for this data set, so we only use the catalogs.

In addition, we also make use of the NIR imaging obtained by the Galaxy evolution and Young Assembly (GOYA[9]) project. Two photometric campaigns were carried out to obtain NIR data of the original Groth Strip $\alpha = 14^{\rm h}17^{\rm m}43^{\rm s}$, $\delta = 52^\circ28'41''$ (Cristóbal-Hornillos et al. 2003) and flanking fields (Barro et al. 2009). Here we make use of the K-band images of the flanking fields, observed with the Ω' instrument in the 3.5 m telescope at Calar Alto Spanish-German Astronomical Center (CAHA). The frames cover a total area of $\sim$0.24 deg^2 to a limiting magnitude of $K_s \sim 20.7$.

Finally, we have also included data in the J band from the narrowband survey of Hα emitters described in Villar et al. (2008). Three $15' \times 15'$ pointings centered at $\alpha = 14^{\rm h}17^{\rm m}31^{\rm s}$, $\delta = 52^\circ28'11''$, $\alpha = 14^{\rm h}17^{\rm m}31^{\rm s}$, $\delta = 52^\circ28'11''$ and $\alpha = 14^{\rm h}18^{\rm m}14^{\rm s}$, $\delta = 52^\circ42'15''$ were observed in CAHA using the $\Omega 2k$ instrument in the 3.5 m telescope. The combined pointings cover an area of 0.19 deg^2 to a limiting magnitude of $J = 22.9$.

2.5. Mid-to-far IR Data

2.5.1. Spitzer/IRAC

Our sample is drawn from *Spitzer* near/mid-IR data obtained as part of the Guaranteed Time Observations (GTO; PI: Fazio) and presented in Barmby et al. (2008). We also included additional data from the GO program with ID 41023 (PI: K. Nandra). The GTO IRAC imaging data at 3.6, 4.5, 5.8, and 8.0 μm were obtained over two epochs (2003 December and 2004 June/July). The data set comprises 52 different pointings that cover a $2^\circ \times 10'$ strip with approximately the same depth. To achieve this homogeneous coverage and due to scheduling issues, the width of the mosaic is slightly variable along the strip, ranging from $10'$ to $17'$. The average exposure time per pixel is 2.5 hr (9100 s) in the four channels. An area of 1440 arcmin^2 was observed for 1900 s, 930 arcmin^2 for 9100 s, and $\sim$100 arcmin^2 for >11,500 s (Barmby et al. 2008). The additional GO data are located in two strips of width $\sim 3.'5$ flanking the original strip and covering the declination range $52.^\circ35 < \delta < 53.^\circ25$. All the data were reduced with the general *Spitzer* pipeline, which provides Basic Calibrated Data, and then mosaicked with *Mopex* using a pixel scale half of the original ($\sim$0.61 arcsec pixel^{-1}). The details of the image quality are discussed in Section 3.2.

2.5.2. Spitzer/MIPS 24 μm and 70 μm

Complementary to the IRAC observations, MIR and FIR observations were also obtained with the Multiband Imaging Photometer for *Spitzer* (MIPS; Rieke et al. 2004) as part of the GTO and the Far-Infrared Deep Extragalactic Legacy Survey (FIDEL). For this paper, we use the whole GTO+FIDEL data set, reduced and mosaicked with the *Spitzer* pipeline and MOPEX+GeRT software. The surveyed area covers approximately the entire $2^\circ \times 10'$ strip, being slightly wider on the upper and lower edges. The MIPS mosaic overlaps with the deepest part of the IRAC observations. The mean exposure time at 24 μm is $\sim$7200 s per pixel, while for the 70 μm channel it is approximately 3800 s. The approximate limiting fluxes are 60 μJy and 3.5 mJy, respectively.

2.6. Radio Data

A radio survey at 1.4 GHz (20 cm) of the northern half of the EGS ($\sim$50% of the IRAC mosaic) was conducted with the Very Large Array (VLA) in its B configuration during 2003–2005. The AEGIS20 survey covers 0.73 deg^2 down to 130 μJy beam^{-1} including a smaller region of 0.04 deg^2 with a 50 μJy detection limit (5σ). The data reduction and the source catalog, comprising 1123 sources, were presented in Ivison et al. (2007).

2.7. Keck Optical Spectra

EGS has also been the target of an exhaustive and unique spectroscopic follow-up. As one of the DEEP2 fields, optical multi-object spectroscopy has been carried out from 2003 to 2005 with the Deep Imaging Multi-Object Spectrograph (DEIMOS; Faber et al. 2003) on the Keck II telescope. The observations cover the spectral range 640 nm $< \lambda <$ 910 nm with a resolution of 0.14 nm. The DEEP2 DR3[10] contains spectroscopic redshifts for 13,867 sources at $0 < z < 1.4$ with a median redshift $z = 0.75$. The targets were selected from the CFHT12k-*BRI* images (within 1.31 deg^2) in the magnitude range $18.5 \leqslant R \leqslant 24.1$. The spectroscopic redshifts for around 70% of the sources are labeled with a high-quality flag (values of 3 and 4, meaning >95% success rate). Lower quality flags are considered unreliable and will be excluded from our analysis here and in Paper II.

[9] http://www.astro.ufl.edu/GOYA/home.html

[10] http://deep.berkeley.edu/DR3/dr3.primer.html

The Astrophysical Journal Supplement Series, 193:13 (24pp), 2011 March

We complemented the DEEP2 spectroscopy of $z < 1.4$ galaxies with redshifts for $z \sim 3$ sources from the Lyman Break Galaxy (LBG) survey of Steidel et al. (2003). This survey covers a total area of 0.38 deg^2 divided in several fields, one of them centered in the EGS. The observations in EGS consist of a single $15' \times 15'$ mask centered at $\alpha = 14^h17^m43^s$, $\delta = 52°28'48''$ observed with the Low Resolution Imaging Spectrometer (LRIS; Oke et al. 1995) on Keck. The spectra cover the 400–700 nm range with a median resolution of 0.75 nm. The targets were pre-selected based on the LBG color–color criteria (Steidel et al. 1996) including only candidates brighter than $R = 25.5$. The EGS catalog contains a total of 334 LBG candidates in the surveyed area. Out of them, 193 are spectroscopically confirmed to be at $z \sim 3$. Unfortunately, the overlap with the IRAC frame is not complete (and some of the galaxies are extremely faint in the IRAC bands), and we were only able to identify 243 (72% of the spectroscopic sample) LBGs in our 3.6 + 4.5 μm selected catalog (we give more details on these sources in Paper II).

3. DESCRIPTION OF THE SAMPLE SELECTION

The data set described in the previous section was used to obtain UV-to-FIR SEDs for all the sources detected in the EGS IRAC survey. This merged photometric catalog was built following the procedure described in PG05 and PG08. Here we review all the basic steps of the method, emphasizing the improvements introduced for this paper concerning the extraction of the IRAC catalog and the band merging procedure.

3.1. The IRAC 3.6 μm+4.5 μm Selection

The source detection in the IRAC data was carried out separately in the 3.6 μm and 4.5 μm images using SExtractor (Bertin & Arnouts 1996). The complementary detection in the slightly shallower 4.5 μm band helps to alleviate the source confusion problems arising from the point-spread function (PSF) size and the remarkable depth of the IRAC data. Both catalogs were cross-matched using a 1″ search radius to remove repeated sources. This produces a master IRAC-selected catalog containing the sources detected in any of the two channels. Eventually, most sources are simultaneously detected in both channels.

The average survey depth is remarkably homogeneous across the strip, $t_{exp} \sim 10$ ks, with the exception of two small areas with lower exposure at the top ($\delta > 53.°525$) and bottom ($\delta < 52.°025$) of the mosaic. We took into account the lower exposure times near the edges of the images by defining two different areas: a shallower region with exposure time shorter than 3800 s (N(frames) $\leqslant 20$), and a deeper region covering the majority of the strip. The detection was carried out with different SExtractor parameters in each region, using a more conservative configuration for the shallower region. Then, we used this (more restrictive) catalog to purge some low significance detections in the other catalog within an overlapping area between them (N(frames) = 18–25). The purged catalog restricted to the area with N(frames) > 20 constitutes our master photometric catalog, and it covers an area of 0.50 deg^2.

After the detection of sources, we removed spurious sources in the wings of bright stars (where the PSF shows bright knots). For that purpose, first we made a preliminary detection of star-like sources based on the IRAC color–color criteria of Eisenhardt et al. (2004; see Section 5.4). Then, we eliminated detections within the typical distance where the contamination from the star is significant (typically ∼9″ for the typical star magnitudes and depth of the EGS observations). After masking the regions around stars, the total area covered by the catalog is 0.48 deg^2.

Aperture photometry for all 3.6 μm + 4.5 μm detected sources was measured with our own dedicated software (which takes into account pixel fractions appropriately; see PG08) in all four IRAC images, previously registered to the same World Coordinate System (WCS). The flux is measured in the four IRAC bands simultaneously. If a source is undetected in the shallower bands (i.e., [5.8] and [8.0]) we still measure an upper limit flux as three times the rms of the sky. The majority of the IRAC sources are unresolved in the 3.6 μm image (FWHM $\sim$ 2″). However, most of them are not point-like, but slightly extended. Consequently, PSF fitting is not effective and photometry is best measured with small circular apertures (PG08; Barmby et al. 2008; Wuyts et al. 2008; Ilbert et al. 2009). The flux measurement in all bands was carried out at the positions specified in the IRAC master catalog. We used a 2″ radius aperture and applied aperture corrections for each band derived from the PSF growth curves. The values of the correction are [0.32 ± 0.03,0.36 ± 0.02,0.53 ± 0.02, 0.65 ± 0.02] mag at [3.6,4.5,5.8,8.0] μm. The errors account for the typical WCS alignment uncertainties. For a small number of extended sources (∼2% of the total catalog, and 75% of them presenting [3.6] < 22.3), the 2″ aperture tend to underestimate the total magnitudes (by more than a 10%). These sources are typically bright nearby galaxies whose Kron (1980) radius is larger than ∼4.″5. The flux measurement for these sources was performed in larger apertures enclosing the full object and applying the extended source aperture corrections given in the *Spitzer*/IRAC cookbook.

The uncertainties in the IRAC photometry were computed taking into account the contributions from the sky emission, the readout noise, the photon counting statistics, the uncertainties in the aperture corrections, and a 2% uncertainty from the zero-point absolute calibration (Reach et al. 2005). We did not assume the uncertainties resulting from SExtractor flux measurement. Instead, we used a more realistic method to determine the background noise that takes into account the effects of pixel-to-pixel signal correlation. This procedure has also been applied to measure the photometric uncertainties in all the bands and is outlined in Section 4.3. Nevertheless, a straightforward comparison to the SExtractor errors indicates that the noise correlation does not introduce a significant contribution to the flux uncertainties at bright magnitudes, leading to a median increment $\leqslant$0.02 mag up to [3.6,4.5] ∼ 23.75.

A detailed comparison of our IRAC catalog of the EGS survey to the one published by Barmby et al. (2008) is presented in Section 3.3, including a discussion on the source confusion levels.

3.2. Completeness and Limiting Magnitude of the IRAC Catalog

We estimated the completeness of the IRAC catalog by analyzing the recovery of simulated sources added in the mosaicked images. The simulations were carried out in the central regions of the mosaic where the coverage is uniform ($t_{exp} \geqslant 10$ ks). Artificial sources spanning a wide range of sizes (from 1″ to 6″) and brightnesses ([3.6] = 16–25 mag) were created on the IRAC images at random locations. The number of simulated sources was chosen to be representative

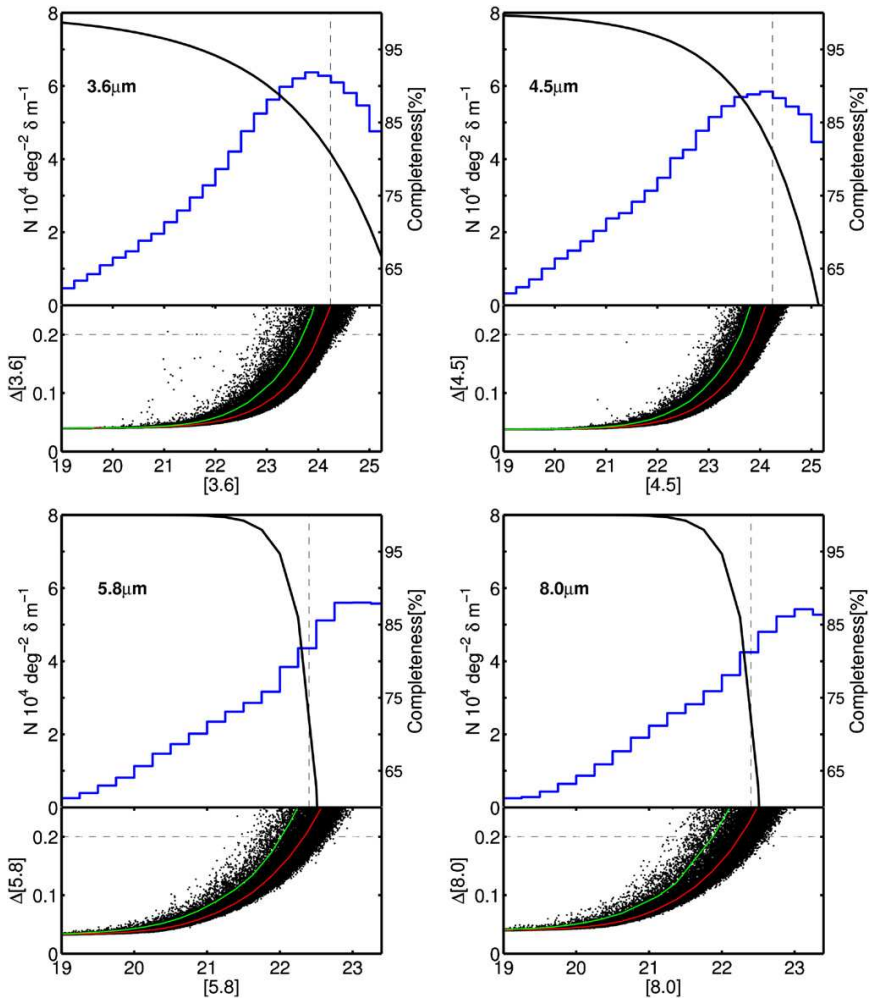

Figure 2. Upper panel of each quadrant shows the histogram of IRAC magnitudes for the sources in our sample selected in the IRAC 3.6 μm+4.5 μm data. The histograms are shown up to the 2σ limiting magnitude in each band. The blacks continuous curve depicts the detection efficiency as estimated from recovery rate of simulated punctual sources. The vertical dashed lines represent five times the median sky rms (5σ) measured in a large number of 2″ radius apertures. The lower panels in each quadrant show the distribution of photometric uncertainties as a function of the magnitude in each IRAC band. The red and green lines indicate the median and 90% of the error distribution as a function of magnitude, respectively. The horizontal dashed line shows the S/N $\sim$ 5 limit; the intersection with the red line indicates the values quoted in Table 1 for the IRAC bands. Note that these values are slightly lower than the 5σ sky rms.

of the Poisson uncertainty in the observed number densities. The source detection and photometry was performed again in the simulated images keeping the same SExtractor parameters as in the original frames. The success rate recovering the simulated sources allows us to estimate the completeness level as a function of magnitude. Figure 2 summarizes the completeness analysis in the four channels. For simplicity, we show results only for point-like sources. The completeness for extended sources is typically $\sim$10% lower at faint magnitudes, however, these sources represent a very small fraction of the catalog at these magnitudes. Figure 2 also shows the source density as function of the magnitude in each band. We find that the catalog is 85% complete for point sources with [3.6,4.5] = 23.75 mag and 75% complete at [3.6,4.5] = 24.75 mag. In the two other channels, the detection efficiency is significantly lower, with 85% completeness at [5.8,8.0] = 22.25, and the completeness dropping rapidly beyond that magnitude. Note that the forced photometric measurement in these bands provides a significant number of $<5\sigma$ (vertical dashed lines in Figure 2) detections that would be missed otherwise.

The lower panels of Figure 2 show the photometric uncertainties as a function of magnitude in the four IRAC bands. The red and green lines indicate the median and the level enclosing 90% of the distribution, respectively. For the region with the deepest coverage, we estimated a 3σ limiting magnitude of [3.6,4.5] $\sim$ 24.75 and [5.8,8.0] $\sim$ 22.90 from the median value of the sky rms in our default photometric apertures (2″ radius).

The 3.6+4.5 μm catalog contains 70,048 and 99,618 sources with [3.6] $<$ 23.75 and [3.6] $<$ 24.75, respectively. The median magnitude of the sample up to [3.6] $<$ 24.75 is [3.6] = 23.14, and 75% of the sources present [3.6] $<$ 23.96. Note that these numbers correspond to the IRAC 3.6+4.5 μm catalog before applying the deblending technique discussed in Section 5. Consequently, the number of sources quoted above is lower than in the final catalog (see Table 2).

Table 2
Number of Sources in the IRAC 3.6+4.5 μm Catalog

Sample	[3.6] $\leqslant$ 23.75[a]	[3.6] $\leqslant$ 24.75[b]
Prior to deblending	70,048	99,618
After deblending	76,936[c]	113,023[d]
Main[e]/Flanking regions	53,030/23,906	77,607/35,416

Notes.
[a] 85% completeness level.
[b] 3σ limiting magnitude.
[c] Only these sources have been included in the final catalog presented in Section 6.
[d] A larger, although less complete, sample including all the sources down to [3.6] $<$ 24.75 can be accessed through the Web interface *Rainbow Navigator* (Section 6.3).
[e] The main region is defined as: $52\overset{\circ}{.}16 < \delta < 53\overset{\circ}{.}20$ and $214\overset{\circ}{.}04 < \alpha < 215\overset{\circ}{.}74$. The flanking regions consist of the remaining area.

3.3. Comparison to Barmby et al. IRAC-selected Catalog

Here we compare our IRAC photometric catalog to that published by Barmby et al. (2008, hereafter BAR08). BAR08 used the same data set (except for the GO flanking regions) and obtained final mosaics in all four IRAC bands with a very similar reduction to ours. Concerning the source detection, our method is slightly different from BAR08 since we detect galaxies in both the 3.6 and 4.5 μm channel instead of only using the bluer band. Our dual detection technique helps to alleviate the source confusion problems arising from the PSF size and the remarkable depth of the IRAC data. In addition, we measure fluxes in the four channels simultaneously, obtaining upper limit values for undetected sources in the shallower bands ([5.8] and [8.0]). Note also that we have increased the resolution of our catalog by deconvolving blended sources using higher resolution information from ground-based observations (Section 4.1). However, for the sake of clarity, we compare here the BAR08 catalog with ours before carrying out the deblending procedure.

BAR08 measured aperture photometry with SExtractor. The publicly available catalog[11] includes MAG_AUTO and MAG_ISO measurements, jointly with aperture magnitudes for several radii corrected to total magnitudes with empirical PSF corrections. We compare our photometry to the magnitudes measured in the 3.5 pixel aperture ($2\overset{''}{.}1$) by BAR08. Their aperture corrections agree with our measurements for the $4''$ diameter aperture within the errors (due to alignment uncertainties).

BAR08 and our catalog are cross-correlated in the region of highest exposure ($t_{\rm exp} > 4$ ks) using a $1''$ radius. The comparison of the WCS between the two mosaics is in very good agreement, with an rms of $<0\overset{''}{.}05$. We find 41,514 and 52,130 sources in common up to [3.6] $<$ 23.75 and [3.6] $<$ 24.75, respectively.

Attending to the density of sources per unit area, we find that our catalog includes 11% $\pm$ 5% and 18% $\pm$ 7% more sources than the catalog published by BAR08 at [3.6] $<$ 23.75 mag and [3.6] $<$ 24.75 mag, respectively. The uncertainties in these measurements were estimated by comparing number counts in 0.5 mag bins, including Monte Carlo simulations on the photometric errors.

The different source densities are a consequence of their more conservative SExtractor detection threshold. We have carefully chosen the SExtractor parameters differentiating between the regions with high/low coverage (Section 3.1), trying to push down the detection limits as much as possible without degrading the reliability of the entire catalog. As a consequence, our catalog recovers a larger number of sources at fainter magnitudes, and the completeness of our catalog is larger than BAR08 for the same magnitude. For example, they quoted a $\leqslant$50% completeness for point-like sources at [3.6] = 23.75 mag, compared to our estimated 85%. Unfortunately, lowering the detection threshold inevitably increases the number of spurious detections. However, in the context of a merged multi-band photometric catalog, spurious detections can be efficiently identified as sources only detected by IRAC (cf. N(band) $<$ 5), and we will show that the reliability is $>$ 97%, with false detections located almost uniquely around very bright sources (see Section 5.3).

Figure 3 shows the comparison of the photometric magnitudes in the four bands for both catalogs. In both cases, the flux was measured on circular apertures and corrected to total magnitudes using aperture corrections. We have corrected the comparison by a constant value of -0.05 mag in [3.6] and [4.5] and by -0.04 mag and -0.03 mag in [5.8] and [8.0], respectively. Such small offsets are attributed to slight differences in the data reduction (final absolute calibration, frame stacking, registering, and mosaicking) and in the aperture corrections. Despite the small offsets, the overall results in the four IRAC bands are in good agreement. Note that the average photometric error in our catalog for each magnitude bin (green bars) encloses 1σ of the values around the median difference (red and cyan lines).

The lower panel of each plot in Figure 3 shows the comparison of the photometric errors in BAR08 and in our catalog. Our quoted photometric uncertainties tend to differ from BAR08, specially at faint magnitudes. In contrast with that paper, we have considered zero-point and WCS uncertainties, resulting in slightly larger uncertainties ($\sim$0.05 mag) in our catalog for bright sources up to [3.6][4.5] $\sim$ 21 mag and [5.8][8.0] $\sim$ 19 mag. At fainter magnitudes, the photometric uncertainties increase with magnitude at a faster rate in the catalog of BAR08. The cause for this difference is the procedure to measure the background noise. Similarly to BAR08, we estimated this value from the sky variance measured in circular apertures at different locations of the images that are empty of sources (Section 4.3). However, the definition of an empty region depends on the limits of source detection. Therefore, given our higher detection fraction, our *sky* regions would contain, in principle, lower signal pixels effectively decreasing the rms. In addition, our photometric procedure estimates uncertainties on a source-by-source basis studying the background around each object in a independent way, while BAR08 relied on SExtractor photometric errors and applied a correction to them based on the average properties of the mosaic. Nevertheless, our estimates of the photometric errors are consistent with the observed scatter of the comparison between our photometry and that measured by BAR08.

4. MULTI-WAVELENGTH PHOTOMETRY: THE *RAINBOW* CATALOG

Using the whole data set available in the EGS field, we created a multi-wavelength photometric catalog for the IRAC-selected sample described in the previous section. For that purpose, we used the *Rainbow* software package, described in detail in PG05 and PG08. This software was created to: (1) cross-correlate multi-band catalogs and obtain consistent (aperture matched) photometry on the different bands to build a UV-to-FIR SED and (2) estimate stellar parameters, such as photometric redshifts, stellar masses, and SFRs from those SEDs. In the rest of this

[11] http://www.cfa.harvard.edu/irac/egs/

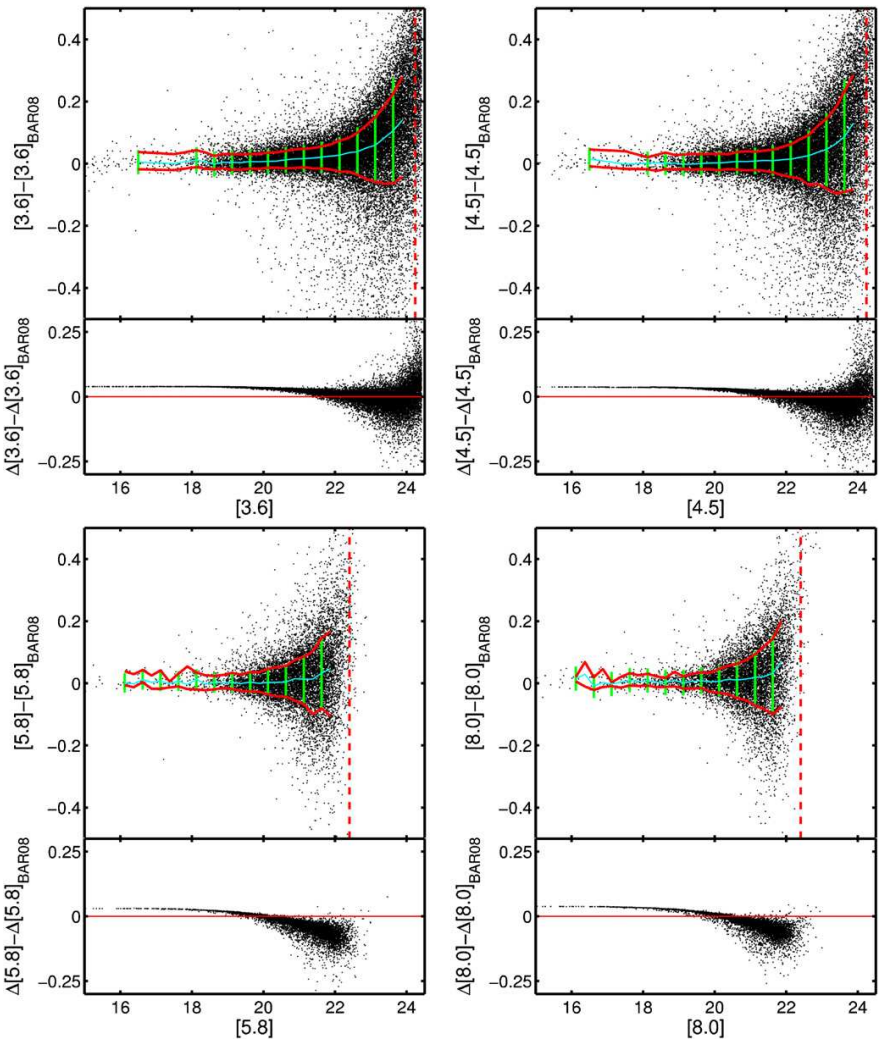

Figure 3. Comparison of the observed magnitudes (upper panels) and the photometric errors (lower panels) in the four IRAC bands for the sources in common between our IRAC 3.6+4.5 μm catalog and BAR08 catalog. The cyan line shows the median value of the magnitude difference as a function of magnitude. We have corrected the comparisons by a constant value of -0.05 mag in [3.6] and [4.5] and by -0.04 mag and -0.03 mag in [5.8] and [8.0], respectively. Such small offsets can be attributed to slight differences in the data reduction and aperture corrections. The green bars indicate the average photometric errors per magnitude bin in our catalog. The red lines enclose 1σ of the distribution centered in the median value (cyan line). The vertical dashed line indicate the 5σ limiting magnitude in our catalog. The photometry in the four bands is consistent up to the ∼85% completeness limit. The uncertainties in BAR08 are 5% to 10% larger at faint magnitudes, probably as a result of the slightly different procedure applied to measure the sky background.

section we will describe the photometry procedure, and in Paper II we will present the methods to estimate photometric redshifts, stellar masses, and SFRs out the SEDs.

4.1. Cross-correlation and Source Deblending

The *Rainbow* code starts from a primary selection catalog (in our case, IRAC selected) and obtains merged photometry and spectroscopy in other bands. The first step is to identify the counterparts of the IRAC sources in the other bands, where SExtractor catalogs have been built following typical procedures. These catalogs are cross-correlated to the 3.6+4.5 μm positions using a 2″ search radius. An exception to this rule are the MIPS, radio, and X-ray catalogs. For the MIPS and radio bands, we used a 2.″5 and 3″ radius, respectively, recognizing possible alignment and center estimation problems of the order of one pixel. For the latter, instead of using the WCS of the X-ray sources, we cross-matched to the positions of the IRAC counterparts (given in Laird et al. 2009) using a 1″ radius. These authors used as reference the IRAC catalog of BAR08, which covers a slightly lower area than ours. Thus, for sources outside of the BAR08 mosaic we cross-matched to the X-ray coordinates using a 2″ radius (see Section 5.2 for more details).

The IRAC sources are identified in this way with objects in all the other catalogs. One of the optical catalogs (typically the deepest; in the EGS, the Subaru *R*-band data) is used as a reference to narrow the following cross-correlations and alleviate confusion problems present in the IRAC images. As the cross-correlation to the catalog of spectroscopic redshifts is done to the coordinates of the counterpart in the reference (optical) band, it is possible to choose a more reliable 0.″75 search radius for this catalog.

Before the cross-matching procedure is carried out between a pair of images, these are re-aligned locally within a $4' \times 4'$ square region using the positions of several sources (typically more than 20) as reference. The mean rms between the central coordinates of matched sources in optical/NIR images is typically $\leqslant 0\farcs1$ and $\leqslant 0\farcs2$ between the IRAC and the ground-based images. This procedure allows to overcome small misalignment problems between the frames and assures a reliable identification of counterparts and an accurate positioning of the photometric aperture in all bands. It also allows to obtain reliable photometry (in the appropriate aperture) even if the source is very faint and/or undetected in an individual image.

The combination of the remarkable depth and the $\sim 2''$ FHWM of the IRAC observations inevitably leads to issues of source confusion, specially around crowded environments. However, based on the (ground-based) reference image, it is possible to deblend IRAC sources which have not been separated by SExtractor in the original IRAC images and lie at least $1''$ away (half the FWHM, chosen as our resolution criterion). *HST* images reveal that the multiplicity is larger, but the deconvolution of sources separated by less than $1''$ is very uncertain. When multiple counterparts are found in the optical/NIR images during the cross-matching, the IRAC photometry is recomputed following a deconvolution method similar to that used in Grazian et al. (2006), Wuyts et al. (2008), Williams et al. (2009), or Wang et al. (2010).

In our case, first, the coordinates of the photometric aperture are re-positioned to that of the optical/NIR counterparts. Then, the PSF of the higher resolution image is convolved to the IRAC PSF, and the flux of each source is scaled to match that of the real IRAC sources measured in $0\farcs9$ apertures (after re-centering to the positions of the optical counterparts). Finally, total magnitudes are computed applying an aperture correction of [1.30 ± 0.07,1.02 ± 0.08,1.2 ± 0.10,1.44 ± 0.14] mag in the [3.6,4.5,5.8,8.0] μm bands, respectively. Figure 4 illustrates the deconvolution procedure using an *HST*/ACS image as reference. The red and green apertures depict the *standard* $2''$ aperture (for isolated sources) and the $0\farcs9$ aperture, respectively. Pixel-by-pixel variations in the residual from subtracting the model PSF do not exceed a 5% within the $0\farcs9$ and $2''$ apertures. We also checked that the average rms ($\sim$3%) is well within the photometric error of the sources. The analysis of an average PSF, derived from observed sources across the image, indicates that for the typical separation between blended sources, $\sim 2\farcs2$ ($>1\farcs8$ for 75% of them), the flux contamination from the nearby neighbor does not exceed a 10% for sources with a flux ratio around 1:2–3. Approximately 75% of the blended sources present flux ratios lower than 1:3.5.

After applying the deblending method, our IRAC-selected catalog contains 76,936 (113,023) sources to [3.6] $<$ 23.75 (24.75). This means that we were able to deblend 8% of the sources in the original IRAC catalog built with SExtractor (presented in Section 3.1), and 16% of the final catalog of 76,936 sources were deblended (typically, each blended sources was a combination of two sources). We find no significant difference in the brightness distribution of the blended sources compared to the resolved sources.

In the following sections, and in Paper II, we will analyze the SEDs and physical properties of the IRAC sources, concentrating in the sample with [3.6] $<$ 23.75 mag, which count with more accurate IRAC photometry (S/N $\gtrsim$ 8). Therefore, this will be the working sample for the rest of the paper unless explicitly stated otherwise. Nonetheless, all the procedures discussed in the following are also applied to the sources down to [3.6] $<$ 24.75 mag. Although these objects are not included in the accompanying catalog (presented in Section 6, restricted to the most reliable detections), it is possible to retrieve their data through our online database (see Section 6.3).

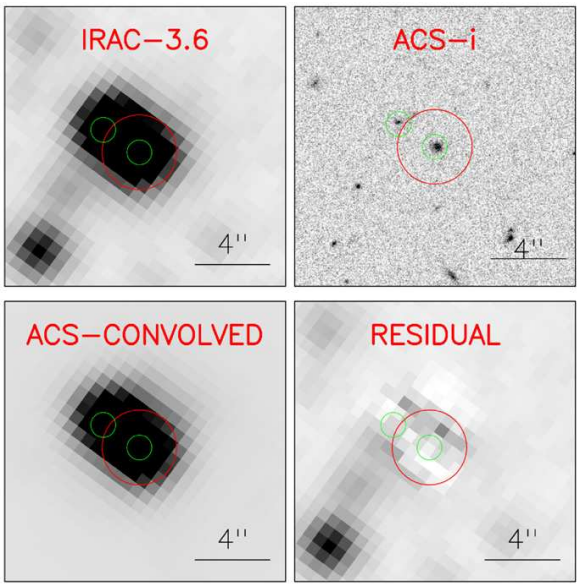

Figure 4. Example of the deconvolution procedure for unresolved sources in IRAC images. After the deblending, the unique IRAC source (irac164074) becomes two separate sources (irac164074 _1 and _2). Top left (a): IRAC 3.6 μm image ($0\farcs61$ pixel^{-1}) showing a blended source. The red circle depicts a $2''$ radius aperture (our default aperture for isolated sources). The green circles show $0\farcs9$ apertures centered at the positions of sources in the reference image. Top right (b): *HST*/ACS reference image ($0\farcs02$ pixel^{-1}) after applying a $4' \times 4'$ local WCS re-alignment, showing the individual sources. Bottom left (c): model of the blended source obtained by convolving the PSF of *HST*/ACS to the PSF of IRAC 3.6 μm in (b), registering it to image (a) and scaling each source to the flux in the $0\farcs9$ apertures (green) in (a). Bottom right (d): residual from the subtraction of the model and science images (c–a).

4.2. Merged Photometry

The photometry is carried out in the same (Kron) elliptical aperture in all bands. The parameters of that aperture are obtained from a reference image (the same as for the cross-matching procedure) whose resolution is representative of the entire data set. Normally, this reference image is a ground-based optical/NIR frame with a PSF of approximately $1''$–$1\farcs5$, which is easy to translate to other ground-based images avoiding aperture issues.

The bands are sorted according to depth to facilitate the cross-match to the optical bands. The typical aperture band for the majority of the sources (83% of the sample) is the Subaru R band, followed by the CFHTLS i' band (4%), MMT $-i$,$-z$ (3% each) and MOIRC-K (2%). For the remaining 5% of the sources, the aperture is computed from other bands (CFHTLS-r, i_{814}, V_{505}) that account for less than 1% of the total. The Subaru imaging was preferred to the CFHTLS as primary aperture band due to the uniform coverage of the whole IRAC mosaic (the CFHTLS frames cover only $\sim$60% of the IRAC survey). In order to ensure that the aperture radius is always large enough to enclose the full PSF profile in all ground-based images, we established a minimum aperture radius equal to the worst

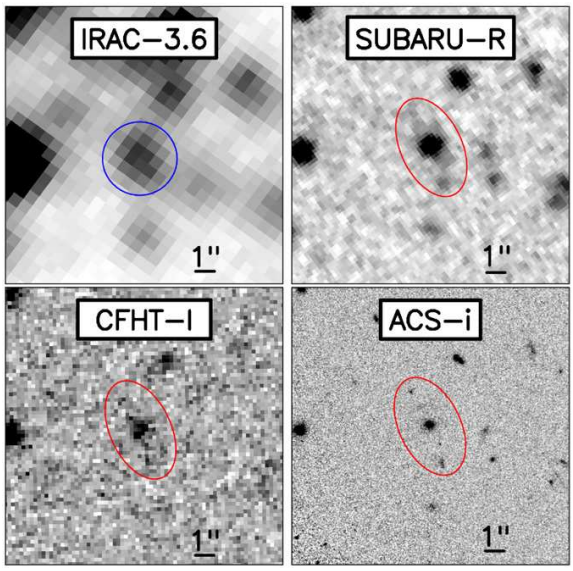

Figure 5. Multi-band images of an IRAC-selected source (irac096525) in the [3.6], *R*, *I*, and i_{814} bands (from left to right and top to bottom). The size of the frames is $15'' \times 15''$. In the three optical bands, the flux is measured in elliptical apertures (red) whose parameters are determined in the *R*-band image. Note that, despite the different image resolutions (and multiple *HST* counterparts), the accurate WCS re-centering (rms $< 0.''15$) allows to place the aperture correctly, recovering the flux of all sources. For the IRAC bands, we use fixed circular apertures of $2''$ radius (blue) and we apply a correction to the total magnitude.

value of the seeing ($1.''5$). Once the best photometric aperture is defined, if no counterpart is found in one band but data exist at that position, the flux is measured within the same aperture. Note that the local WCS re-centering of the images allows an accurate positioning of that aperture. In this way, we recover fluxes for very faint sources whose detection was missed by SExtractor. When the counter-part source is too faint to be detected, the sky-*rms* value is stored to be used as an upper limit in the SED analysis.

Some bands are deliberately excluded from the merged photometric measurement described above due to a significant difference of the resolution compared with the reference band or because images are not available. For all these bands, the photometry is obtained differently and later incorporated in the merged catalog during the cross-correlation procedure. For the four IRAC channels, the optical/NIR Kron apertures are typically not large enough to enclose the entire PSF. Therefore, we keep the values measured in Section 3.1 with aperture photometry. Given the comparatively large PSFs of the MIPS (24 μm, 70 μm) and *GALEX* (FUV, NUV) images, the flux measurement in these bands was carried with IRAF-DAOPHOT and SExtractor, respectively (see PG05; PG08). Figure 5 illustrates the different resolutions and aperture sizes involved in the photometric measurement (see also the captions in Figures 9–12).

The *HST* -ACS bands were included in the general photometric procedure. Although the much higher resolution may lead to multiple cross identifications even when compared with the optical ground based images, the high spatial resolution (after the local re-alignment described above) allows a reliable cross-matching within $0.''15$ (rms of the local WCS solution for *HST* images). As shown in Figure 5, apertures were placed correctly even when multiple counterparts are identified, and the photometry includes the fluxes from all of them. We have conducted an additional test to check the accuracy of the ACS photometry measured with this method. We compared the observed photometry to synthetic magnitudes derived from SED templates fitted to the multi-band photometry (except ACS) of spectroscopically confirmed galaxies. We find a very small offset ($\leqslant$0.02 mag) and a scatter consistent with the typical photometric errors in the bands (see Section 3.1.3 of Paper II for more details).

The NIR source catalog of the Palomar/WIRC survey (Bundy et al. 2006) is also included in the merged photometric catalog, although no images are available to match apertures. In this case, we use the SExtractor MAG_AUTO value of the closest neighbor in the *J* and *K* bands.

4.3. Photometric Uncertainties

The uncertainties in the photometry are derived simultaneously to the process of flux measurement in each individual band. As mentioned in Section 3.1, the photometric errors obtained using SExtractor often underestimate the true background noise due to signal correlation on adjacent pixels (Labbé et al. 2003; Gawiser et al. 2006). In order to properly account for this effect, we estimated the flux uncertainties in three different ways, as described in PG08 (Appendix A). First, we measured the background noise in a circular corona of $5''$ width around each source. This procedure is similar to that used by SExtractor and provides uncertainties $\sigma_{\rm AP} \propto N_{\rm pixels}^{1/2}$. In addition, we measured the average sky signal on non-connected artificial apertures built with random pixels around each source, with the same size as the photometric aperture, and containing only *pure* sky pixels (rejecting pixels $>5\sigma$ the rms obtained with the first method). Finally, we also estimated the background noise following the method by Labbé et al. (2003). The flux measured on several photometric apertures around the source, identical to the one employed for the photometry, is fitted to a Gaussian function to yield the rms background fluctuation. The sky background is set to the resulting average value of the three methods, and the final photometric uncertainty is set to the largest estimate, typically, the one measured with the second method.

5. PROPERTIES OF THE MERGED PHOTOMETRIC CATALOG

The exposure time of the IRAC mosaics in the four channels is remarkably homogeneous across the mosaic. However, the coverage of the strip at other wavelengths is patchy and discontinuous (see Figure 1). For the remaining of this section and in Paper II, we will differentiate between the region of the IRAC image covered by the CFHTLS, and the rest. The CFHTLS/IRAC common region ($52.^\circ16 < \delta < 53.^\circ20$ and $214.^\circ04 < \alpha < 215.^\circ74$) has been also surveyed with Subaru, the CFHT12k instrument, MMT/Megacam, *HST*/ACS, *HST*/NICMOS, and *GALEX*, so it constitutes the zone with the highest data quality (hereafter main region), where the SEDs are sampled with the highest band coverage. The area of this region is 0.35 deg^2 ($\sim$68% of the total) and contains 53,030 (76,936) sources down to [3.6] $<$ 23.75 (24.75). The 0.13 deg^2 outside the main region (hereafter flanking regions) also present a solid SED coverage, relying mostly in the MMT and SUBARU bands. Nevertheless, it lacks some of the best-quality data (taken with ACS and MOIRCS), and the fraction of surveyed area by the WIRC-*JK* bands is $\sim$15% lower. There are 23,906 (35,416) sources in the flanking regions with [3.6] $<$ 23.75

Table 3
The IRAC 3.6+4.5 μm Sample: Detection Efficiency in Each Band and Region

Band	$\lambda_{\rm eff}$	Main Region (0.35 deg^2)					Flanking Regions (0.13 deg^2)				
		Area	[3.6] < 23.75 [53,030]		[3.6] < 24.75 [77,607]		Area	[3.6] < 23.75 [23,906]		[3.6] < 24.75 [35,416]	
			Stats	All/S/N > 5(%)	Stats	All/S/N > 5(%)		Stats	All/S/N > 5(%)	Stats	All/S/N > 5(%)
(1)	(2)	(3)	(4)	(5)	(6)	(7)	(8)	(9)	(10)	(11)	(12)
X-ray[a]	0.31,1.24 nm	0.97	...	717 (1.3%)	...	718 (1.3%)	0.93	...	307 (1.2%)	...	307 (1.2%)
FUV	0.154	0.99	$27.90^{29.45}_{25.78}$	58.8/7.9	$28.03^{29.55}_{26.19}$	57.4/6.1	0.15	$27.71^{29.27}_{25.94}$	59.6/7.7	$27.83^{29.34}_{26.27}$	58.3/6.8
NUV	0.232	0.99	$26.28^{28.16}_{24.47}$	74.2/25.8	$26.60^{28.35}_{24.78}$	70.8/20.2	0.15	$26.26^{28.11}_{24.44}$	75.2/26.7	$26.57^{28.33}_{24.81}$	72.5/23.7
u'	0.363	1.00	$25.53^{27.01}_{24.29}$	88.4/52.8	$25.85^{27.25}_{24.61}$	86.1/44.1	1.00	$25.39^{26.78}_{24.15}$	89.6/64.3	$25.69^{27.03}_{24.45}$	88.0/57.8
u^*	0.381	1.00	$25.30^{26.68}_{24.13}$	88.2/53.9	$25.60^{26.93}_{24.43}$	85.2/44.2	...	...	...	...	...
CFH-*B*	0.440	1.00	$25.03^{26.26}_{23.82}$	89.6/55.2	$25.33^{26.56}_{24.16}$	87.1/45.6	1.00	$24.94^{26.20}_{23.73}$	87.3/53.1	$25.27^{26.48}_{24.05}$	83.7/43.0
g	0.481	1.00	$25.08^{26.31}_{23.85}$	96.1/85.1	$25.44^{26.64}_{24.23}$	95.0/80.3	1.00	$25.12^{26.40}_{23.76}$	96.6/84.9	$25.49^{26.71}_{24.14}$	95.5/80.5
g'	0.486	1.00	$24.86^{26.05}_{23.65}$	95.4/83.6	$25.20^{26.34}_{24.01}$	94.0/78.2	...	...	...	...	...
V_{606}	0.592	0.56	$24.58^{25.71}_{23.23}$	94.7/83.5	$24.92^{26.00}_{23.66}$	93.9/78.7	...	...	...	...	...
r'	0.626	1.00	$24.50^{25.56}_{23.08}$	97.1/89.3	$24.85^{25.93}_{23.52}$	96.0/84.2	...	...	...	...	...
R	0.652	1.00	$24.44^{25.45}_{23.00}$	97.0/88.5	$24.80^{25.82}_{23.44}$	95.8/82.5	1.00	$24.36^{25.44}_{22.81}$	97.4/87.7	$24.74^{25.80}_{23.27}$	96.5/81.9
CFH-*R*	0.660	1.00	$24.49^{25.58}_{22.98}$	95.3/71.5	$24.85^{25.96}_{23.45}$	93.1/60.2	1.00	$24.36^{25.50}_{22.73}$	91.6/73.7	$24.76^{25.90}_{23.22}$	88.4/63.0
i'	0.769	1.00	$24.00^{25.14}_{22.43}$	95.3/85.4	$24.41^{25.52}_{22.92}$	94.2/78.3	...	...	...	...	...
i	0.782	1.00	$24.09^{25.15}_{22.52}$	97.4/90.3	$24.51^{25.62}_{23.01}$	96.1/83.8	1.00	$24.13^{25.31}_{22.25}$	96.4/81.1	$24.54^{25.87}_{22.80}$	94.6/70.2
i_{814}	0.807	0.56	$24.12^{25.23}_{22.49}$	96.7/80.7	$24.52^{25.68}_{23.00}$	94.7/69.3	...	...	...	...	...
CFH-*I*	0.813	1.00	$24.03^{25.23}_{22.34}$	94.1/68.6	$24.45^{25.70}_{22.83}$	90.1/54.5	1.00	$23.97^{25.25}_{22.07}$	89.2/61.1	$24.43^{25.70}_{22.58}$	84.1/47.5
z'	0.887	1.00	$23.79^{24.98}_{22.17}$	93.3/66.2	$24.23^{25.48}_{22.61}$	89.1/51.2	...	...	...	...	...
z	0.907	1.00	$23.96^{25.18}_{22.30}$	96.0/77.7	$24.44^{25.66}_{22.75}$	92.7/64.9	1.00	$23.95^{25.25}_{22.15}$	97.5/85.5	$24.44^{25.73}_{22.65}$	95.3/75.4
J_{110}	1.10	0.04	$23.87^{24.94}_{22.38}$	84.6/65.4	$24.25^{25.48}_{22.79}$	88.9/55.6	...	...	...	...	...
$\Omega 2k$-*J*	1.21	0.40	$23.29^{24.50}_{21.81}$	93.7/38.5	$23.74^{25.01}_{22.21}$	88.4/27.1	...	...	...	...	...
WIRC-*J*	1.24	0.42	$22.43^{23.47}_{20.90}$	62.8/16.6	$22.49^{23.59}_{20.96}$	46.1/11.7	0.32	$22.31^{23.41}_{20.69}$	57.9/20.4	$22.35^{23.46}_{20.73}$	41.1/14.1
H_{160}	1.59	0.04	$24.71^{25.84}_{23.19}$	92.3/80.8	$25.18^{26.52}_{23.61}$	91.7/69.4	...	...	...	...	...
$\Omega' - K_s$	2.11	0.46	$22.43^{23.73}_{20.89}$	75.8/6.7	$22.74^{23.98}_{21.38}$	67.0/4.6	0.26	$22.17^{23.46}_{20.72}$	67.3/7.3	$22.39^{23.76}_{21.04}$	59.6/5.0
Ks	2.15	0.26	$24.64^{25.77}_{23.03}$	95.5/73.8	$25.14^{26.42}_{23.44}$	89.8/52.9	...	...	...	...	...
WIRC-*K*	2.17	0.97	$21.76^{22.74}_{20.21}$	62.6/27.1	$21.82^{22.81}_{20.26}$	42.6/16.3	0.80	$21.42^{22.50}_{19.86}$	45.3/18.4	$21.45^{22.55}_{19.89}$	42.4/14.4
IRAC 36	3.56	1.00	$22.54^{23.41}_{20.97}$	100.0/99.2	$23.18^{24.25}_{21.43}$	100.0/84.5	1.00	$22.52^{23.40}_{20.87}$	100.0/97.8	$23.17^{24.24}_{21.39}$	100.0/80.6
IRAC 45	4.51	1.00	$22.62^{23.55}_{21.05}$	99.8/95.3	$23.26^{24.44}_{21.51}$	98.9/75.3	1.00	$22.63^{23.61}_{21.00}$	99.3/91.1	$23.27^{24.49}_{21.44}$	97.1/70.5
IRAC 58	5.69	1.00	$22.50^{23.73}_{21.04}$	89.7/41.1	$22.89^{24.28}_{21.33}$	78.4/28.0	1.00	$22.45^{23.71}_{20.95}$	87.1/38.6	$22.80^{24.20}_{21.22}$	75.5/26.4
IRAC 80	7.96	1.00	$22.62^{23.89}_{21.14}$	85.8/34.4	$22.97^{24.33}_{21.37}$	73.8/23.5	1.00	$22.51^{23.83}_{21.05}$	82.6/32.9	$22.83^{24.26}_{21.29}$	71.1/22.6
MIPS 24	23.84	0.91	$19.58^{20.59}_{18.44}$	31.5/20.2	$19.71^{20.72}_{18.50}$	29.7/18.1	0.93	$19.36^{20.39}_{18.35}$	29.9/19.1	$19.49^{20.53}_{18.42}$	25.2/15.1
MIPS 70	72.49	0.80	$15.79^{16.37}_{15.23}$	13.1/1.5	$15.81^{16.35}_{15.25}$	7.5/5.7	0.86	$15.57^{16.24}_{14.86}$	13.6/1.2	$15.57^{16.24}_{14.87}$	6.7/4.7
VLA[a]	2E06	0.74	...	380 (<1%)	...	380 (<1%)	0.42	...	210 (<1%)	...	210(<1%)
			[3.6] < 23.75 [53,030]		[3.6] < 24.75 [77,607]			[3.6] < 23.75 [23,906]		[3.6] < 24.75 [35,416]	
Redshifts[a]	0.64–0.91	0.94	6191	12.0%	6420	8.4%	0.84	1445	6.0%	1481	4.2%

Notes. Detection efficiency for the sources IRAC 3.6+4.5 μm sample in the different bands compiled for this work. The analysis is divided in two zones: the main region, defined as the overlapping area between the IRAC and the CFHTLS mosaics ($52.^\circ16 < \delta < 53.^\circ20$ and $\alpha > 214.^\circ04$), and the flanking region. (1) Band name. (2) Effective wavelength of the bands in microns. (3) Fraction of the main region covered by the observations in each band. (4, 6) Median and quartiles of the magnitude distribution in each band for main region sources with [3.6] < 23.75 and [3.6] < 24.75, respectively. (5, 7) Percentage of IRAC sources in the main region detected in each band at any magnitude (All) and with S/N > 5. These values are computed in areas fully covered by both the IRAC mosaic and the observations in each band. (8) Same as (3) in the flanking regions. (9, 11) Same as (4,6) in the flanking regions. (10, 12) Same as (5,7) in the flanking regions.
[a] For these catalogs, we quote only the number of sources detected in IRAC, and the percentage of total IRAC sample that they represent.

(24.75). Table 2 summarizes the number of sources in the catalog according to different limiting magnitudes and area constraints.

Note that the bulk of the optical SED coverage is based on CFHTLS and MMT data (the CFHT12k-*BRI* data are ~2 mag shallower). On average numbers, their respective filter sets cover a similar wavelength range with comparable data quality (see Tables 1 and 3). Also, the subtle differences in the shape of the u- and z-band filters of each survey improve the quality of the SED coverage for the sources in the main region. The most remarkable difference between the two surveys is found in the homogeneity of data; whereas the CFHTLS presents a nearly uniform data quality across the mosaic, the MMT data show larger variations between the four pointings (e.g., $\Delta g(5\sigma) =$ 26–25 mag, ΔFWHM = 1.″0–1.″6; see Zhao et al. 2009 for more details). Unfortunately, the lowest quality pointings (shallower data and highest seeing) are precisely those covering the flanking regions (mainly the north region, $\delta > 53.^\circ20$). Furthermore, a small area in the north and south regions of the MMT mosaic

(<10% of the total) is not observed in the g and u bands, respectively. Thus, comparatively, the average data quality in the flanking regions is slightly lower than in the main region.

5.1. Multi-band Detection and Color Properties

Table 3 shows the fraction of the entire IRAC catalog detected in the different bands compiled for this work. We give specific values for different sub-samples divided as a function of brightness in the selection band, detection level (S/N), and location in the IRAC mosaic. The majority of sources are detected in the four IRAC channels. However, while most sources (>90%) have reliable detections at 3.6 and 4.5 μm, only half of the sample is detected with S/N > 5 at the two longer wavelengths. Note that the photometry at 5.8 and 8.0 μm was not performed independently (see Section 3.1).

The fraction of IRAC sources detected in the optical bands is also elevated (∼95%) for the majority of the bands. However, cutting the measurements at S/N > 5, the efficiency decreases to ∼85% for the deepest CFHTLS, MMT, Subaru and ACS bands, and to 50%–60% for the u and z bands (in both CFHTLS and MMT data) and the shallower CFHT *BRI* bands. For the *GALEX* data, the detection is typically lower than 10% and 25% in the FUV and NUV bands, respectively. Around 12% and 6% of the sources are matched to high-quality spectroscopic redshift estimates in the main and flanking regions, respectively. The lower efficiency in the flanking regions is caused by the inhomogeneous DEEP2 coverage of the IRAC mosaic.

The NIR coverage of the strip surveyed by IRAC is also discontinuous. The WIRC catalog provides the most uniform coverage, including 40% and ∼100% of the area in the main region in the J and K bands, respectively. The fraction of IRAC sources detected in each band is very similar, ∼50%–60% (∼20% with S/N > 5). The deepest NIR observations are those taken in CAHA-J and Subaru-MOIRCS-K_s bands. The latter covers ∼1/4 of the main region up to 1 mag deeper than the WIRC-K data, presenting a much higher detection fraction, ∼90% (70% with S/N > 5). The CAHA-J data cover 40% of the main region recovering ∼30% (S/N > 5) of the IRAC detections, a slightly larger fraction than WIRC-J.

We note that for most bands, the fraction of sources detected with S/N < 5 can be significantly higher than the overall value. In the shallowest bands, this is caused by the higher photometric uncertainties (e.g., the WIRC J and K bands). However, for most bands this is the result of the enhanced detection achieved with the forced photometric measurement. For each IRAC source undetected in a given image, but having a counterpart in any other band, we still measure the flux in the same aperture at the position of the counterpart. With this method, we increase the detection efficiency at fainter magnitudes recovering sources that would be missed otherwise. However, given the extreme faintness of these sources, some of the measurements produce low significance detections (S/N < 2). As a precaution, to preserve the overall quality of the SED, we do not include these values (photometric uncertainties >0.4 mag) in the SED fitting procedure, nor in the estimate of the physical parameters in Paper II. Nevertheless, we keep these values as they can be useful as upper limits. Another estimate of the limiting magnitude in each band is obtained from the value of the sky rms in failed forced measurements (i.e., those for which the measured flux in the aperture is negative).

Figure 6 illustrates the characteristics of the different flux measurements in four bands probing representative wavelengths in the UV-to-NIR range. The central panel of each plot shows a color–magnitude diagram in [3.6] versus u^*Ri' and K, respectively. The gray-scale density map depicts the distribution of *standard* (non-forced) photometric measurements, typically detected with S/N > 5 (magenta line). Forced detections for which we obtain a valid flux or a sky-rms value are shown as green and blue dots, respectively. The cyan markers are sources detected in IRAC only (for which we assign arbitrary magnitudes in each band). For the deep R and i' bands, which present the highest detection efficiency, forced measurements account for less than 5% of the flux measurements and present a median S/N $\lesssim$ 2 (black line). In the u^* band, the source density for a similar limiting magnitude is much lower, and consequently the fraction of forced detections is higher, around 20%.

The upper panels in each quadrant of Figure 6 show the fraction of undetected sources in each band. In the R and i' bands, these sources make up for <4% of the total sample. Most of them are IRAC-only sources (plotted in cyan), whereas the rest are at least marginally detected in one other (typically red) band, but the forced measurement fails for the particular band shown in the plot (blue). The fraction of undetected sources in the u^* band (and other shallower optical bands, e.g., CHFT12K *BRI*) increases to 10%, being in this case dominated by failed forced measurements at the positions of R or i' detections. These kinds of measurement are also predominant for undetected sources in the K band.

Note that some of the IRAC-only sources are relatively bright, 21 < [3.6] < 22. Most of them are detected in deep K-band observations. However, there are a few galaxies detected only in the IRAC bands (typically the faintest ones). The nature of these interesting sources, potential candidates to massive high-redshift galaxies, will be explored in a future paper.

Figure 6 also shows the color distribution of IRAC sources in bins of [3.6] mag (right panels in each quadrant) and spectroscopically confirmed galaxies in several redshift bins (red ellipses and dots in the central panels). The general trend with color in the R and i' bands is that faint IRAC sources are on average bluer than brighter ones. The median colors for the faintest [3.6] bin, 22.50 < [3.6] < 23.75, are $R-[3.6]=1.6$ and $i'-[3.6]=1.4$. These colors are similar to those of galaxies at $1<z<1.5$. This is consistent with the fact that the median redshift for the IRAC 3.6+4.5 μm magnitude limited sample ([3.6] < 23.75) is $z\sim1$ (see Paper II and PG08). Note also that most of the forced detections in the R band would qualify as IRAC extremely red objects (by the criteria of Yan et al. 2004, $R-[3.6]>4.0$) that target dusty starbursts or passively evolving galaxies at $z>1.5$.

In general, all galaxies tend to become redder in optical−IRAC colors with increasing redshifts. Indeed, for a typical galaxy SED, the observed optical bands shift into the (fainter) UV whereas the [3.6] mag becomes brighter as it approaches the stellar bump at 1.6 μm rest frame (for $z\lesssim1.2$). Therefore, it is not surprising that the $u^*-[3.6]$ median color is redder ($u^*-[3.6]=2.1$, typical of a $z\sim1$ galaxy) than the median color involving the $Ri'K$ bands. Note also that the observed UV progressively shifts into the Lyman break, producing the large fraction of $z>2.5$ (red dots in the top left quadrant of Figure 6) galaxies that are u-dropouts. Finally, we find that the $K-[3.6]$ color presents an almost constant value as a function of [3.6] mag for a given redshift range, becoming progressively redder as we move to higher redshifts: $K-[3.6]<0$ at $z<0.5$ and $K-[3.6]>0$ at $z>1$. Again, this is

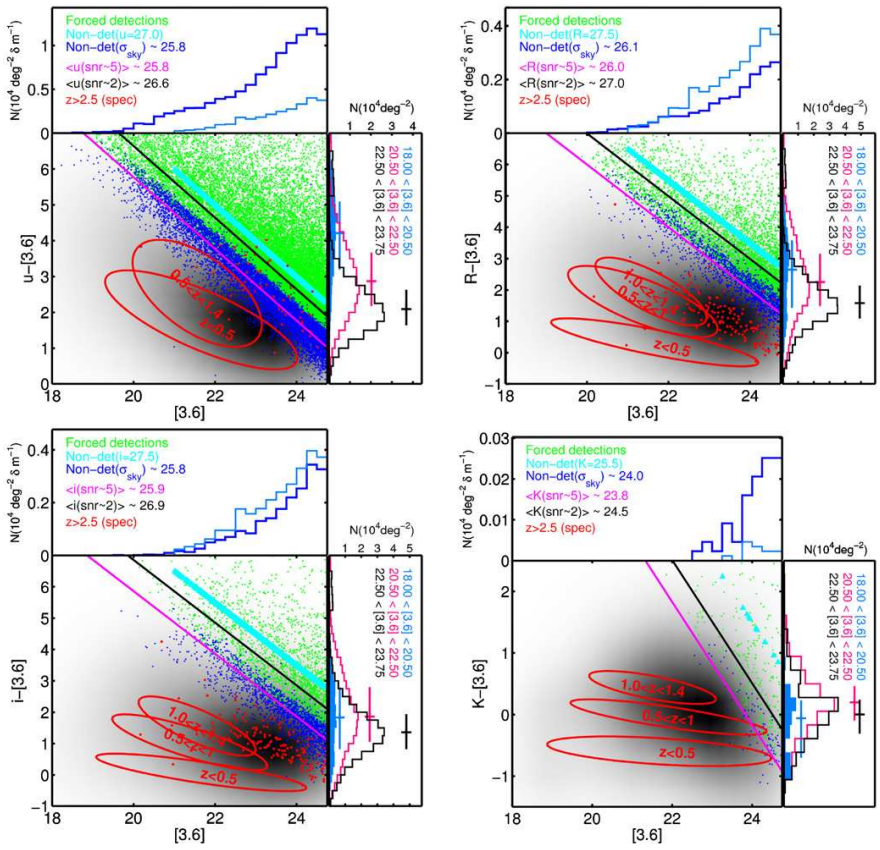

Figure 6. Central panel in each plot shows the color magnitude diagrams in the u^*, R, i', and K bands with respect to [3.6] (top to bottom, left to right). The density map in gray scale shows the distribution of IRAC sources detected in each band. For sources missing (not detected by SExtractor) in a given band but detected in any other, we force a flux measurement at the position of the existing source using the same Kron aperture. The green dots depict sources for which we are able to recover a positive flux in this forced measurement. The blue dots depict the value of the sky rms in the apertures where the forced measurement failed (i.e., the integrated flux was negative). The cyan triangles are sources undetected in any other band but IRAC. For these sources, we set an upper limiting magnitude ∼0.5–1 mag fainter than the typical magnitude for a source with S/N = 2 (black line). The magenta solid line indicates the median magnitude of the sources with S/N ∼ 5. The red dots depict galaxies with spectroscopic redshift $z > 2.5$. The red ellipses show the median and quartiles of the color–magnitude distribution for galaxies in different bins of redshift within $0 < z < 1.5$. The upper panel of each quadrant shows the [3.6] brightness distribution of undetected sources (blue and cyan markers in the central panel) in each band. The right panel of each quadrant shows the color distribution of detected sources (histogram, median, and quartiles) in three bins of the [3.6] magnitude.

consistent with the fact that both K and [3.6] transit through the peak of the stellar bump for $z < 1$, changing their relative positions (see, e.g., Huang et al. 2004). An interesting consequence of the red $K - [3.6]$ colors of high-z galaxies is that IRAC 3.6 μm observations are equivalent, in terms of source densities, to a K-selected sample down to slightly deeper limiting magnitudes.

Figure 7 shows the density map (central panel) and histograms (right panel) of the number of photometric bands with measured fluxes, N(band), in the main (left) and flanking regions (right). Typically, the SED of a galaxy in the main region has a median of 19 photometric data points. The average spectral coverage is ∼8 bands larger than in the flanking regions, mainly due to the lack of data from the CFHTLS and NIR surveys. Galaxies with an available spectroscopic redshift ($R \lesssim 24$ mag; green dots) typically present the highest band coverage (∼22 and ∼14 bands in the main and flanking regions, respectively), since they are relatively bright in the optical. Interestingly, the faintest IRAC sources, $[3.6] > 23.75$ mag (red histogram), present a relatively high band coverage, N(band) = 17 in the main region. In most of the cases, these are low significance detections in the deepest optical/NIR bands where the forced photometric measurement (see Section 4.2) is able to recover a flux (see, e.g., Figure 9). On the opposite side, there is a non-negligible number of IRAC-faint but optically bright sources with more than 19 photometric data points. These constitute a population of blue dwarf galaxies at intermediate redshift easily detected in the optical but with faint IRAC counterparts (i.e., not very massive).

The upper panel of Figure 7 shows the [3.6] magnitude distribution for the full sample (black) and for sources with poor spectral coverage (N(band) < 5; blue histogram). The latter defines a clearly isolated group in the density contours (central panel) and in the histograms (right panel) of Figure 7. These sources represent less than 3%(4%) of the sample up to [3.6] < 23.75 (24.75). Most of them are clear IRAC-only detections (as the ones discussed in Figure 6) relatively bright in [3.6,4.5]. However, some of the faintest sources can be affected by contamination of spurious sources (we give more details on these sources in Section 5.3).

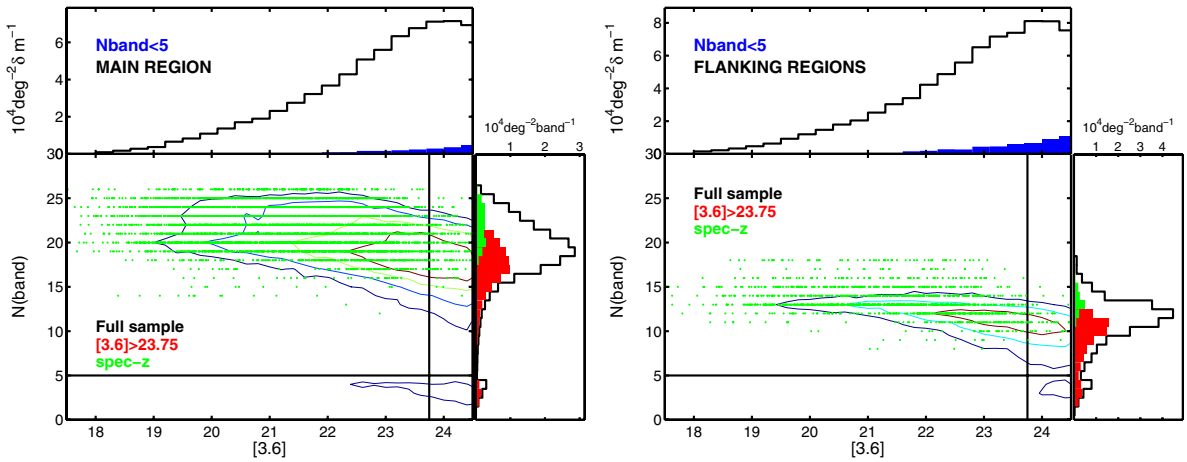

Figure 7. Central panel in each plot depicts the source density as function of the number of bands in which the source was detected (a positive flux was measured), *N*(band), and the magnitude in the [3.6] channel, for the main region (left) and the flanking regions (right). The color contours contain (from the inside out) approximately 25%, 50%, 75%, and 90% of the sources. The green dots mark galaxies with a spectroscopic redshift. The black lines indicate the 85% completeness limit of the catalog ([3.6] < 23.75, vertical) and the band coverage limit *N*(band) = 5 (horizontal), respectively. The histograms on top show the brightness distribution for the full sample (black) and for sources with *N*(band) < 5 (blue). The histograms to the right show the *N*(band) distribution of the full sample (black line), IRAC faint sources ([3.6] > 23.75; red area) and galaxies with spectroscopic redshifts (green area).

5.2. FIR, X-Ray, and Radio Counterparts

Table 3 shows the fraction of IRAC sources in our sample ([3.6] < 23.75) detected in the X-ray, FIR, and radio surveys within the overlapping area. About 30% (20% with S/N > 5 detections) of the IRAC sources are detected at 24 μm (S/N = 5 reached at ∼60 μJy), 10% (2% with S/N > 5) at 70 μm (S/N = 5 reached at ∼3.5 mJy), 1% in the X-rays, and $\leqslant$1% at 20 cm. For the radio and X-ray surveys, we cross-matched our sample to the catalogs of Ivison et al. (2007) and Laird et al. (2009), respectively. As explained in Section 4, the cross-match to the radio catalog was performed using a 3″ radius, whereas for the X-ray catalog we followed a two-step identification. First, we divided the X-ray sample attending to the availability of pre-identified IRAC counterparts (Laird et al. used the IRAC catalog of BAR08 as reference). For the galaxies identified in IRAC, we used a 1″ cross-matching radius, whereas for the other we used a more conservative 2″ radius. With this procedure, we found 848 out of the 882 galaxies with IRAC counterparts in their catalog (815 among the 830 with high reliability flag; see Laird et al. 2009 for more details). The remaining galaxies were either outside of the *N*(frame) > 20 region or too close to a bright star. In addition, we were able to identify 175 additional X-ray sources in the area of our mosaic not covered by the data of BAR08, i.e., we recover a total of 1023 out of 1325 X-ray sources from the catalog of Laird et al. For the MIPS 24 μm and 70 μm and radio surveys, we identify 10758, 868, and 590 (out of 1122) sources, respectively. Noticeably, about 20% and 54% of the sources detected in MIPS 24 μm and 70 μm present a multiple IRAC counterparts (typically 2–3) and ∼6% in X-ray and Radio.

All of these surveys cover an area larger than the IRAC observations, but none of them fully cover the IRAC strip (although the X-ray and MIPS 24 μm data cover >90% of the area). Table 4 shows the total area covered by the X-ray, MIPS, and radio surveys, the fraction that area in common with the IRAC mosaic, and the number of sources with an IRAC counterpart in our catalog. All the sources in the different surveys located within the area covered by IRAC are detected in our catalog (with the exception of a few objects too close to bright stars).

Table 4
Detection Efficiency of X-ray, FIR, and Radio Sources

Source (1)	Area (2)	Fraction (3)	Total (4)
Chandra/ACIS[a]	0.67 deg^2	0.70	1023 (77%)
MIPS 24 μm (f > 60 μJy)[b]	0.53 deg^2	0.59	10771
MIPS 70 μm (f > 3500 μJy)[b]	0.50 deg^2	0.61	868
VLA 20 cm[c]	0.73 deg^2	0.46	590 (52%)

Notes. (1) Name of the band. (2) Total area of the survey. (3) Fraction of the survey area overlapping with the IRAC mosaic. (4) Number of sources with IRAC counterparts ([3.6] < 23.75) and fraction of recovered sources from the whole catalog.
[a] Sources drawn from Laird et al. (2009). These include 815 high reliability identifications (based on a previous match to the IRAC catalog of BAR08) and 175 previously unidentified sources.
[b] The area of the survey refers to the GTO+FIDEL observations reduced for this paper.
[c] Sources drawn from Ivison et al. (2007).

Note that despite the larger area of the VLA observations, this survey covers only ∼40% of the region surveyed by IRAC. In fact the data are limited only to the upper region of the IRAC mosaic (δ > 53°.10; see Figure 1).

5.3. Catalog Reliability

In this section, we analyze in more detail the sources with a poor spectral coverage to asses the reliability of the IRAC catalog as a function of the magnitude in the [3.6] band.

First, we test the reliability with the widely used method of comparing the number of detections at faint levels in the original and a negative image. This test reveals that only ∼1% of the sources up to [3.6] < 23.75 mag are spurious.

However, this procedure is conceived to detect faint spurious sources based on the assumption of a symmetric noise, whereas most of the spurious detections are concentrated around bright regions as a consequence of PSF and saturation artifacts and an

excessive deblending. Therefore, we chose to follow a different approach to analyze the reliability of the catalog based on the fact that faint [3.6, 4.5] detections lacking a measurable counterpart in other bands are potential candidates for spurious detections.

As discussed in Section 5, we find a nearly isolated group of sources detected in N(band) $\leqslant 4$. Most of these sources are IRAC-only detections (cyan histogram of Figure 6) that, in the absence of low significance optical detections to validate them, could be artifacts of the source extraction procedure.

The visual inspection of galaxies with N(band) $\leqslant 4$ reveals a clear dichotomy. We find that these sources are either strongly clustered around bright stars and extended sources (typically low-z galaxies), or uniformly distributed across the image. Most of the sources in the first group are easily identified as spurious, whereas for the isolated sources, their high S/N (∼5–10) and the visual inspection seem to favor that they are real. We dealt with the reliability of sources with N(band) < 4 by considering spurious all detections in a 20″–30″ radius region around the brightest objects ([3.6] = 16–15 mag). Up to [3.6] $\leqslant$ 23.75, approximately half of the N(band) $\leqslant 4$ sources are spurious by this criteria, accounting for less than 2% of the total sample. Nevertheless, even for the more conservative scenario, the sum of all N(band) $\leqslant 4$ detections constitutes less than ∼4% of the sample in the main region. Finally, we also check the reliability of these sources by studying how many of them are simultaneously detected at both 3.6 and 4.5 μm. Unfortunately, we find that some real detections are missed at 4.5 μm due to the slightly worse image quality, while some of the spurious sources are detected in both images in regions where the density of artifacts is larger (i.e., around bright stars).

Summarizing, we conclude that the overall reliability of the catalog is very high (>97%) and that the contamination by spurious sources is strictly restricted to the surrounding areas of very bright sources. For the sake of completeness, we do not remove the sources with N(band) $\leqslant 4$ from the sample. Instead, we include in the data catalog (Table 6) both the number of bands in which the source was detected (N(band)) and a flag indicating if the source is located in the vicinity of a bright object (see Section 6.2).

5.4. Star–Galaxy Separation

Following PG08, we used eight different photometric and morphological criteria to identify stars in the merged photometric catalog: (1) the average of SExtractor star/galaxy separation parameter (stellarity) for all bands where the source is detected; (2) when available, the stellarity parameter and FWHM of the source in the *HST* images are also considered as an independent, more reliable, criterion; (3, 4) the IRAC-based color–magnitude criteria of Eisenhardt et al. (2004) and Barmby et al. (2004); (5) the concentration parameter (i.e., the difference of the [3.6] mag measured in a 3″ radius aperture and the SExtractor MagAuto); (6) the color–color and (7) color–magnitude criteria of Eisenhardt et al. (2004; this time based on optical and NIR bands); and (8) the *BzK* criteria of Daddi et al. (2004). In spite of using multiple stellarity criteria, the heterogeneous band coverage makes difficult the simultaneous application of the eight criteria (e.g., the *HST* data cover only ∼40% of the full area). For this reason, we chose the bulk of the criteria to be based on IRAC or optical colors, which are available for the majority of the sources independently of the region in which they are located. We verify that at least five criteria can be estimated for 86% of the sources with [3.6] < 23.75.

A source was identified as a star if three or more of the stellarity criteria are satisfied. Based on this method, we found 2913 stars. Among them, we are able to identify 69% of the spectroscopically confirmed stars. The rest of them satisfy at least one or two of the stellarity criteria. Figure 8 illustrates the efficiency of the IRAC morphological criteria by Eisenhardt et al. (2004) and the *BzK* criteria of Daddi et al. (2004). Red dots indicate sources with N(criteria) $\geqslant 3$. Clearly, the *BzK* criterion is more efficient identifying stars over a wider magnitude range. Note that, as discussed in PG08, an IRAC-selected catalog down to [3.6] < 23.75 only includes a minor fraction of stars (less than 5% at all magnitudes), the majority of them at bright magnitudes (∼40% at [3.6] < 18). At the faintest magnitudes, the overall dimming of the objects could lead us to identify some stars as galaxies due to the lack of applicable criteria. However, we find that both the galactic and stellar number counts in the IRAC bands are in good agreement with those presented in Fazio et al. (2004) down to our limiting magnitude. From the relative distribution of galaxies and stars, we also find that the fraction of stars makes up for only 3% of all sources at magnitudes fainter than the median of the sample ([3.6] = 22.4).

6. DATA CATALOGS AND DATABASE ACCESS

The catalog with the multi-band photometry for all the IRAC 3.6+4.5 μm selected sample in the EGS is presented in Table 5. Additional information regarding the photometry of the sources and other properties described in the paper are given in Table 6. Furthermore, we also present here a Web-based interface to access our database containing all the results presented in this and the companion paper. The Web tool is publicly available for the entire astronomical community.

As explained in Section 3.2, the catalogs presented in this paper are restricted to the 76,936 sources with [3.6] < 23.75, the ∼85% completeness level, which count with accurate IRAC photometry (S/N > 8). As explained in Section 3, our sample is extracted from the area of the IRAC mosaic counting with a frame coverage larger than 20 ($t_{\rm exp} \sim 4$ ks in the IRAC 3.6 μm band). Nevertheless, a deeper, although less complete, catalog without any magnitude restriction can be accessed through the online database (Section 6.3). In the following subsections, we describe the contents of Tables 5 and 6 and present *Rainbow Navigator*.

6.1. Table 5: Photometric Catalog

These are the fields included in Table 5.

1. *Object*. Unique object identifier starting with irac000001. Objects labeled with an underscore plus a number (e.g., irac000356_1) are those identified as a single source in the IRAC catalog built with SExtractor, but deblended during the photometric measurement carried out with the *Rainbow* software (see Section 4.1). Note that, although the catalog contains 76,936 elements, the identifiers do not follow the sequence irac000001 to irac076185. This is because the catalog is extracted from a larger reference set by imposing coordinate and magnitude constraints. The table is sorted according to this unique identifier.
2. α, δ. J2000.0 right ascension and declination in degrees.
3. *zspec*. Spectroscopic redshift determination drawn from the DEEP2 spectroscopic survey or the catalog of LBGs of Steidel et al. (2003).

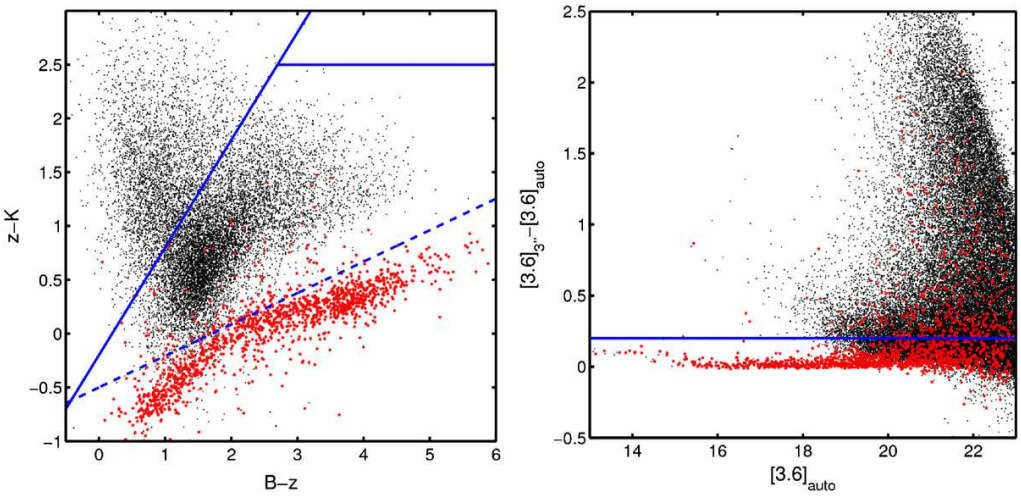

Figure 8. Example of two of the stellarity criteria used in this paper to separate galaxies from stars. Left: *B*-*z* vs. *z*-*K* for all sources in the catalog. The dashed line depicts the *BzK* criteria of Daddi et al. (2004) to isolate stars. The solid lines delimit the regions where high-redshift galaxies are located. The red dots indicate sources satisfying three or more stellarity criteria. Right: comparison of the magnitude in a 3″ radius aperture ($[3.6]_{3''}$) and SExtractor MagAuto ($[3.6]_{\rm auto}$), i.e., the concentration parameter, vs. $[3.6]_{\rm auto}$ for all sources in the catalog. The criterion of Eisenhardt et al. (2004) identifies stars with $-0.25 < [3.6]_{3''} - [3.6]_{\rm auto} < 0.2$ and $[3.6]_{\rm auto} < 17.80$.

4. *qflag*. Spectroscopic redshift quality flag from 1 to 4. Sources with *qflag* > 3 have a redshift reliability larger than 80%.
5. *FUV, NUV,u′*,.... Effective wavelengths (in nanometers), magnitudes, and uncertainties (in the AB system) for each of the 30 photometric bands compiled for this paper. The bandpasses are *GALEX* FUV and NUV, CFHTLS $u^*g'r'i'z'$, MMT $u'giz$, CFHT12k *BRI*, ACS V_{606} and i_{814}, Subaru *R*, NICMOS J_{110}, H_{160}, MOIRCS K_s, WIRC *JK*, CAHA-JK_s IRAC 3.6-8.0, and MIPS 24 μm and 70 μm. The bands are sorted according to the effective wavelength of the filter. We refer to Section 3 for details on the photometric measurement and error calculation. The magnitudes do not include zero-point corrections (see Paper II, Section 3.1.3). A value of the magnitude equal to −99.0 with error equal to 0.0 indicates a not valid photometric measurement. A negative error indicates that the source was undetected by SExtractor but a positive flux was obtained when forcing the measurement at that position using the appropriate aperture (see Section 4.2). An error equal to 0.0 indicates that the source was undetected and the forced measurement returned a negative flux. In this case, the value of the magnitude is an upper limit equal to the sky *rms* (1σ) in the photometric aperture (see Section 4.2).

6.2. Table 6: Photometric Properties Catalog

These are the fields included in Table 6.

1. *Object*. Unique object identifier (the same as in the photometric catalog in Table 5).
2. α, δ. J2000.0 right ascension and declination in degrees.
3. *N(bands,detect)*. Number of UV-to-NIR in which the source is detected.
4. *N(bands,forced)*. Number of UV-to-NIR in which the source is a priori undetected, but the forced photometry is able to recover a valid flux.
5. *Flag*. Quality flag indicating that the source is located in the vicinity of a bright object. Sources detected only in the IRAC bands (*N*(band) < 5) and close to a bright ([3.6] > 16) source are likely to be spurious (see Section 5.3). The values of the flag indicate: (5) source within 70″–100″ of the brightness saturated stars in the field, (4) source within 30″ of a [3.6] < 15 source, (3) source within 20″ of a 15 < [3.6] < 16 source, (2) source within 15″ of a 16 < [3.6] < 17 source, (1) source within 10″ of a 17 < [3.6] < 18 source, and (0) source unflagged.
6. *Stellarity*. Total number of stellarity criteria satisfied (see Section 5.4). A source is classified as a star if it satisfies three or more criteria. (Section 5.4).
7. *Region*. Region of the field in which the source is located (Section 5): A value of 1 or 0 indicates that the source is in the main or flanking region, respectively. The main region is defined as the area of the IRAC mosaic within 52.16 < δ < 53.20 and α > 214.04, the flanking regions are those containing the remaining area.

6.3. Rainbow Database and Navigator

The photometric catalog presented here and the inferred stellar parameters discussed in Paper II are obtained using the *Rainbow* software (see PG05; PG08). The program includes different sub-routines for each task, and the output of each step serves as the input for the next. After the data processing, both the input (images, spectra, templates) and the resulting catalogs are stored in a database with individual sources as building blocks. On doing so, we achieve several goals: (1) each object is fully characterized with all the available information; (2) the data can be easily sorted and retrieved according to several criteria; (3) the data are homogeneously stored, which allows a straightforward combination with data from other *Rainbow* fields and projects (such as those in PG05 or PG08).

In order to provide worldwide access to the data stored in our database, we have developed a publicly available Web interface, dubbed *Rainbow Navigator*.[12] Here we briefly describe the main

[12] http://rainbowx.fis.ucm.es

Table 5
The IRAC 3.6+4.5 μm Sample: Multi-band Photometry

Object	α	δ	zspec	qflag	FUV	NUV	u'	u^*	B	g	g'	V_{606}	r'	R	CFH-R	i'	i	i_{814}	I
					$\lambda_{\rm eff}$	$\lambda_{\rm eff}$	$\lambda_{\rm eff}$	$\lambda_{\rm eff}$	$\lambda_{\rm eff}$	$\lambda_{\rm eff}$	$\lambda_{\rm eff}$	$\lambda_{\rm eff}$	$\lambda_{\rm eff}$	$\lambda_{\rm eff}$	$\lambda_{\rm eff}$	$\lambda_{\rm eff}$	$\lambda_{\rm eff}$	$\lambda_{\rm eff}$	$\lambda_{\rm eff}$
					(mag)	(mag)	(mag)	(mag)	(mag)	(mag)	(mag)	(mag)	(mag)	(mag)	(mag)	(mag)	(mag)	(mag)	(mag)
					(err)	(err)	(err)	(err)	(err)	(err)	(err)	(err)	(err)	(err)	(err)	(err)	(err)	(err)	(err)
					z'	z	J_{110}	H_{160}	$\Omega 2k$-J	WIRC-J	Ω'-K_s	WIRC-K	Ks	[3.6]	[4.5]	[5.8]	[8.0]	[24]	[70]
					$\lambda_{\rm eff}$	$\lambda_{\rm eff}$	$\lambda_{\rm eff}$	$\lambda_{\rm eff}$	$\lambda_{\rm eff}$	$\lambda_{\rm eff}$	$\lambda_{\rm eff}$	$\lambda_{\rm eff}$	$\lambda_{\rm eff}$	$\lambda_{\rm eff}$	$\lambda_{\rm eff}$	$\lambda_{\rm eff}$	$\lambda_{\rm eff}$	$\lambda_{\rm eff}$	$\lambda_{\rm eff}$
					(mag)	(mag)	(mag)	(mag)	(mag)	(mag)	(mag)	(mag)	(mag)	(mag)	(mag)	(mag)	(mag)	(mag)	(mag)
					(err)	(err)	(err)	(err)	(err)	(err)	(err)	(err)	(err)	(err)	(err)	(err)	(err)	(err)	(err)
(1)	(2)	(3)	(4)	(5)	(6)	(7)	(8)	(9)	(10)	(11)	(12)	(13)	(14)	(15)	(16)	(17)	(18)	(19)	(20)
					(21)	(22)	(23)	(24)	(25)	(26)	(27)	(28)	(29)	(30)	(31)	(32)	(33)	(34)	(35)
					(36)	(37)	(38)	(39)	(40)	(41)	(42)	(43)	(44)	(45)	(46)	(47)	(48)	(49)	(50)
irac003270_1	215.43892696	53.08455063	0.00000	2	153.9	231.6	362.6	381.1	439.0	481.4	486.3	592.4	625.8	651.8	660.0	769.0	781.5	807.3	813.3
					26.370	25.785	24.068	24.028	23.629	23.959	23.712	−99.000	23.423	23.404	23.401	22.905	22.862	−99.000	22.824
					0.000	−0.127	0.079	0.033	0.051	0.039	0.018	0.000	0.017	0.036	0.040	0.018	0.040	0.000	0.034
					887.1	907.0	1103.3	1593.2	1209.4	1235.5	2114.6	2145.3	2161.3	3561.2	4509.6	5689.4	7957.6	23844.0	72493.7
					22.467	22.718	−99.000	−99.000	−99.000	−99.000	−99.000	−99.000	22.197	21.593	21.853	22.810	22.378	19.545	−99.000
					0.028	0.045	0.000	0.000	0.000	0.000	0.000	0.000	0.380	0.051	0.044	0.263	0.189	0.238	0.000
irac003278	215.42614011	53.09447161	0.00000	0	153.9	231.6	362.6	381.1	439.0	481.4	486.3	592.4	625.8	651.8	660.0	769.0	781.5	807.3	813.3
					27.016	25.598	23.354	22.688	21.342	20.683	20.461	−99.000	19.216	19.434	18.969	18.041	17.870	−99.000	17.928
					−0.633	−0.295	0.071	0.015	0.041	0.029	0.010	0.000	0.011	0.019	0.030	0.010	0.029	0.000	0.029
					887.1	907.0	1103.3	1593.2	1209.4	1235.5	2114.6	2145.3	2161.3	3561.2	4509.6	5689.4	7957.6	23844.0	72493.7
					17.583	17.661	−99.000	−99.000	−99.000	−99.000	−99.000	−99.000	17.303	18.011	18.417	18.841	19.341	−99.000	−99.000
					0.010	0.029	0.000	0.000	0.000	0.000	0.000	0.000	0.010	0.038	0.036	0.033	0.046	0.000	0.000
irac003291_1	215.44043562	53.08128671	0.85700	4	153.9	231.6	362.6	381.1	439.0	481.4	486.3	592.4	625.8	651.8	660.0	769.0	781.5	807.3	813.3
					29.948	27.232	25.312	25.157	24.623	24.680	24.423	−99.000	23.579	23.457	23.350	22.529	22.463	−99.000	22.390
					−4.101	−0.624	0.196	0.092	0.114	0.055	0.031	0.000	0.021	0.034	0.036	0.014	0.036	0.000	0.032
					887.1	907.0	1103.3	1593.2	1209.4	1235.5	2114.6	2145.3	2161.3	3561.2	4509.6	5689.4	7957.6	23844.0	72493.7
					22.130	22.295	−99.000	−99.000	−99.000	−99.000	−99.000	−99.000	20.449	20.391	20.721	21.007	21.247	18.860	−99.000
					0.021	0.041	0.000	0.000	0.000	0.000	0.000	0.000	0.106	0.050	0.054	0.054	0.067	0.118	0.000
irac003310	215.42129738	53.09430607	0.00000	0	153.9	231.6	362.6	381.1	439.0	481.4	486.3	592.4	625.8	651.8	660.0	769.0	781.5	807.3	813.3
					22.626	22.577	21.787	21.681	21.104	20.817	20.706	−99.000	20.323	20.344	20.301	20.033	19.985	−99.000	19.978
					0.026	−0.017	0.053	0.012	0.041	0.029	0.010	0.000	0.014	0.020	0.030	0.013	0.029	0.000	0.030
					887.1	907.0	1103.3	1593.2	1209.4	1235.5	2114.6	2145.3	2161.3	3561.2	4509.6	5689.4	7957.6	23844.0	72493.7
					19.983	20.085	−99.000	−99.000	−99.000	−99.000	−99.000	−99.000	19.779	20.339	20.757	21.294	19.695	19.436	−99.000
					0.013	0.030	0.000	0.000	0.000	0.000	0.000	0.000	0.063	0.039	0.039	0.102	0.045	0.165	0.000
irac003313	215.43553774	53.08200958	0.00000	0	153.9	231.6	362.6	381.1	439.0	481.4	486.3	592.4	625.8	651.8	660.0	769.0	781.5	807.3	813.3
					25.415	25.293	24.750	24.473	24.155	24.501	24.269	−99.000	24.029	23.998	24.069	23.517	23.433	−99.000	23.539
					0.000	−0.147	0.131	0.067	0.082	0.044	0.024	0.000	0.035	0.056	0.072	0.023	0.048	0.000	0.067
					887.1	907.0	1103.3	1593.2	1209.4	1235.5	2114.6	2145.3	2161.3	3561.2	4509.6	5689.4	7957.6	23844.0	72493.7
					23.198	23.437	−99.000	−99.000	−99.000	−99.000	−99.000	−99.000	−99.000	21.783	21.891	22.385	22.479	−99.000	16.266
					0.043	0.054	0.000	0.000	0.000	0.000	0.000	0.000	0.000	0.048	0.057	0.403	0.383	0.000	1.282

Notes. (1) Object unique identifier in the catalog. The catalog is sorted by this field. (2, 3) Right ascension and declination (J2000) in degrees. (4) Spectroscopic redshift determination drawn from (Davis et al. 2007; ∼8000 galaxies) and (Steidel et al. 2003; LBGs at $z \gtrsim 3$). (5) Quality flag of the spectroscopic redshift (4 => 99.5%, 3 => 90%, 2 = uncertain, 1 = bad quality). Only redshifts with qflag > 2 have been used in the analysis. (6–50) Effective wavelength of the FUV NUV $u^*g'r'i'z'$ $u'gRiz$ BRI V_{606} i_{814} $J_{110}H_{160}$ JK [3.6]-[8.0] [24] [70] bands in nanometer. Observed magnitude with the associated uncertainty as measured in the apertured matched procedure (see Section 4). All magnitudes refer to the AB photometric system. Negative values of the photometric uncertainty are for forced photometric detections. Magnitudes >0 with uncertainty equal to 0.00 are non-detections; for these bands the photometry indicates the magnitude of $\sigma_{\rm sky}$ (see Section 4.2).

(This table is available in its entirety in a machine-readable form in the online journal. A portion is shown here for guidance regarding its form and content.)

Table 6
The IRAC 3.6+4.5 μm Sample: Photometric Properties

Object (1)	α (2)	δ (3)	N(bands,detect) (4)	N(bands,forced) (5)	Flag (6)	Stellarity (7)	Region (8)
irac003270_1	215.43910540	53.08468920	18	1	0	0	1
irac003278	215.42614011	53.09447161	18	2	0	7	1
irac003291_1	215.44058360	53.08123980	18	2	0	0	1
irac003310	215.42129738	53.09430607	19	1	1	0	1
irac003313	215.43553774	53.08200958	17	1	0	1	1

Notes. (1) Object unique identifier in the catalog. The catalog is sorted by this field. (2, 3) Right ascension and declination (J2000) in degrees. (4) Number of optical-to-NIR bands (with effective wavelengths below 8.0 μm) in which the object is detected. (5) Number of optical-to-NIR bands (with effective wavelengths below 8.0 μm) in which the object is a priori undetected, but the forced photometry (see Section 4.2) recovers a valid flux. (6) Quality flag indicating the proximity of a very bright source in the vicinity of the source. Sources detected in very few bands (N(band) < 5) and located nearby a bright source are likely to be spurious detections (see Section 3.2). (7) Sum of all the stellarity criteria satisfied (see Section 5.4). A source is classified as star for Stellarity > 2. (8) Region of the field in which the source is located: 1 for the main region, 0 for the flanking region.

(This table is available in its entirety in a machine-readable form in the online journal. A portion is shown here for guidance regarding its form and content.)

features of the utility. A detailed description of its capabilities can be found at the Web site.

Rainbow Navigator is essentially a user-friendly Web interface to a database containing all the data products resulting from the process of creating and analyzing the IRAC-selected catalog presented in these two papers, from the initial source detection to the estimate of the stellar parameters.

As many other astronomical query interfaces (e.g., NED, SIMBAD), *Rainbow Navigator* allows to retrieve the information for single sources searching for the source name or by coordinates. It also allows to create subsets of the complete catalog based on multiple constraints over the multi-band photometry, the redshifts or the stellar parameters. In addition, we have incorporated a cross-matching tool that allows to compare catalogs uploaded by the user to the IRAC-selected sample stored in the database, returning the sources in common. *Rainbow Navigator* also has an on-the-fly utility to create sky maps of a selected area, including point-and-click access to the individual sources.

Furthermore, an interesting feature that we do not include in the public catalog for the sake of simplicity is the possibility of retrieving observed and rest-frame synthetic magnitudes over a predefined grid of 52 different filters covering the whole spectral range from the UV to the radio wavelengths. These values are computed by convolving the best-fitting template (see Paper II) for each source with the appropriate filter transmission curve.

Each source of the catalog has its own data sheets that provide all the available information including not only the photometry, the redshifts, or the stellar parameters but also detailed information of the stellarity, synthetic magnitudes, and the multiplicity in other bands, jointly with the unique identification and coordinates of the counterparts in each given band. The tool also provides postage stamps of the source in each of the available bands that can be modified on-the-fly or combined to create simple false color images. Furthermore, each page includes a figure depicting the full SED showing the fit of the optical and IR data jointly with the best-fitting templates.

Figures 9–12 show examples of the multi-band postage stamps, the UV-to-FIR SED and fitting templates, and the clickable map utility for a few galaxies at different redshifts. The postage stamps also illustrate the different photometric measurements in each band (aperture matched and circular apertures) and the forced detections for very faint sources (see, e.g., the source in Figure 11).

Rainbow Navigator has been conceived to serve as a permanent repository for future versions of the catalogs containing improvements over the previous results (the present version is data release 1), and also to similar data products in other cosmological fields (such as GOODS-N and GOODS-S, presented in PG08). Currently, it provides public access to the IRAC-selected catalog in the EGS presented in this paper, and also a similar release of the data described in PG08 for a small piece of the central region of the GOODS-S region.

7. SUMMARY

We presented an IRAC 3.6+4.5 μm selected catalog in the EGS characterized with multi-wavelength photometry. The sample contains 76,936 sources with [3.6] < 23.75 (85% completeness of the sample) covering an area of 0.48 deg^2. The IRAC sources are characterized with FUV NUV $u^*g'r'i'z'$ $u'gRiz$ *BRI* V_{606} i_{814} $J_{110}H_{160}$ *JK* [3.6]-[8.0] photometry. In addition, we have cross-correlated the sample with X-ray data (Laird et al. 2009, AEGIS-X), *Spitzer*/MIPS 24 μm and 70 μm FIR photometry, and VLA 20 cm radio data (AEGIS20; Ivison et al. 2007). Secure spectroscopic redshifts are also included in the catalog for 7636 sources with [3.6] < 23.75 obtained from the DEEP2 Survey and Steidel et al. (2003; LBGs at $z \gtrsim 3$). The data described in this paper are publicly available, and will be part of future extended analysis and projects. The main results of this work are summarized below.

1. The extraction of the IRAC sample presented in this paper was limited to a region with exposure times >4 ks. The average survey depth is $t_{\rm exp} \sim 10$ ks. Aperture photometry was performed in the four IRAC bands simultaneously allowing us to obtain upper limit fluxes for undetected sources in the [5.8] and [8.0] bands. We removed spurious detections masking areas around bright stars. The estimated 85% completeness level for point sources is [3.6,4.5] ~ 23.75 and [4.5,5.8] ~ 22.25. The 3σ limiting magnitude estimated from the sky rms is [3.6,4.5] ~ 24.75 and [4.5,5.8] ~ 22.90. We also validated the quality of the photometry by comparing our results with the catalog of Barmby et al. (2008), finding good agreement in both magnitudes ($\lesssim 0.05$ mag) and uncertainties (Section 3.3). Some small systematics were found in this comparison, which can be attributed to the slightly different

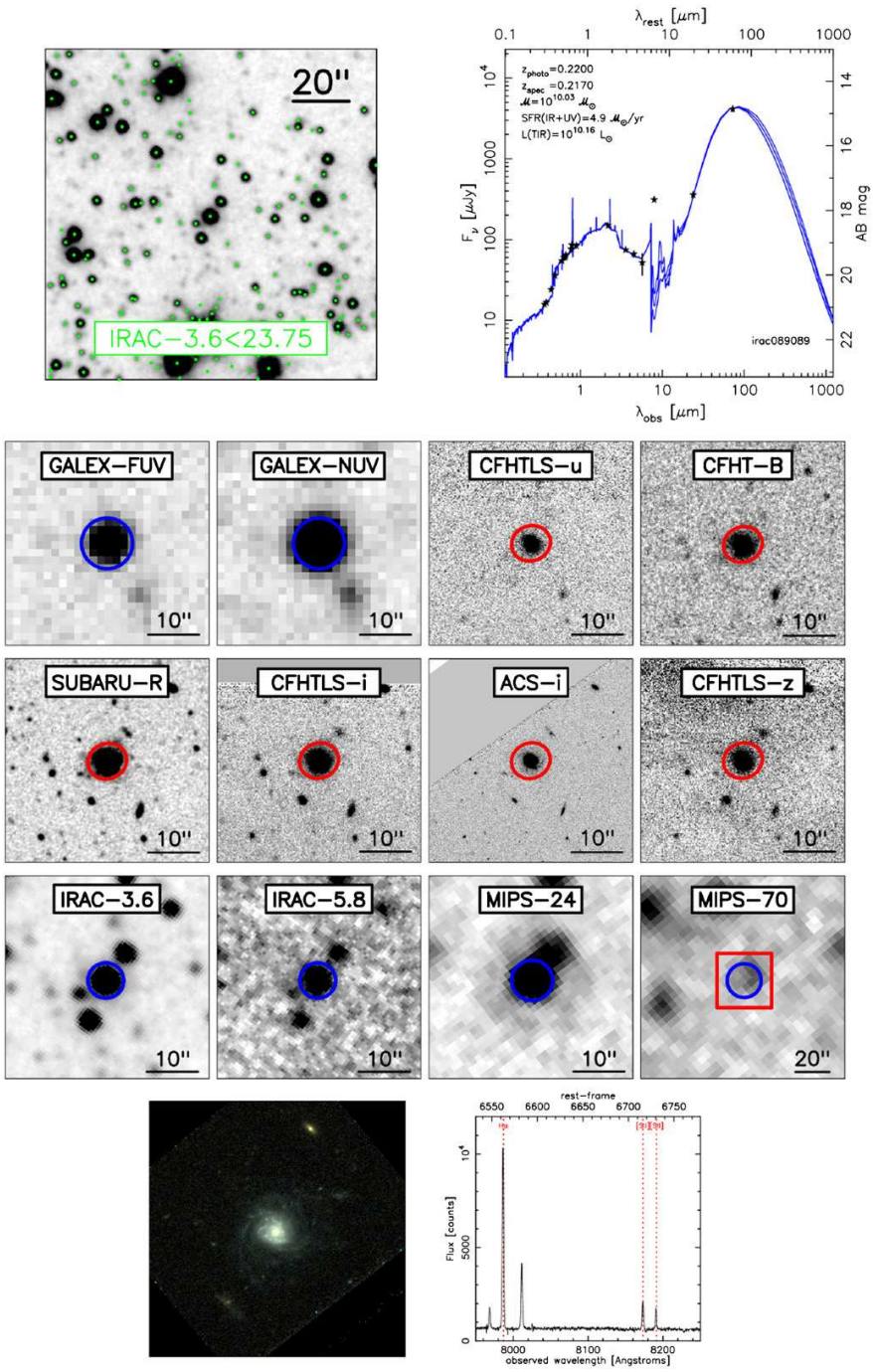

Figure 9. Example of the results available for each IRAC source in the *Rainbow* database, accessible through the *Rainbow Navigator* interface. This source is irac089089, a galaxy at $z = 0.2170$. Top left: map ($2' \times 2'$) of the sky area around the source. The green dots in the map depict sources in our IRAC catalog with [3.6] < 23.75. By clicking on any of the sources, the interface presents an individual Web site with all the available information for that source. Top right: full UV-to-FIR SED of the central galaxy in the sky map, a source at $z = 0.21$. The UV-to-NIR data are fitted to a stellar population model, while the IR-part of the SED is fitted to the models of CE01, DH02. A summary of the estimated stellar parameters, such us the stellar mass or the global SFR, is shown in the upper-left corner of the figure. Middle panels: gray-scale postage stamps (with size $40'' \times 40''$, except for the MIPS 70 image, whose size is $2' \times 2'$, same as the map in the top left figure) of the galaxy in some of the available bands, covering different wavelength ranges. The Kron aperture used to measure consistent photometry in optical/NIR bands and the circular aperture used in bands with significantly lower resolution are shown in all panels (red and blue, respectively). Bottom left: RGB color stamp obtained by combining images in the ACS-V_{606}, i_{814} bands. The *Rainbow Navigator* Web interface allows to produce on-the-fly monochromatic and RGB images changing the cuts interactively. Bottom right: DEEP2 1-D spectra of the galaxy depicting some of the identified lines. The wavelength range and the redshift can be modified interactively.

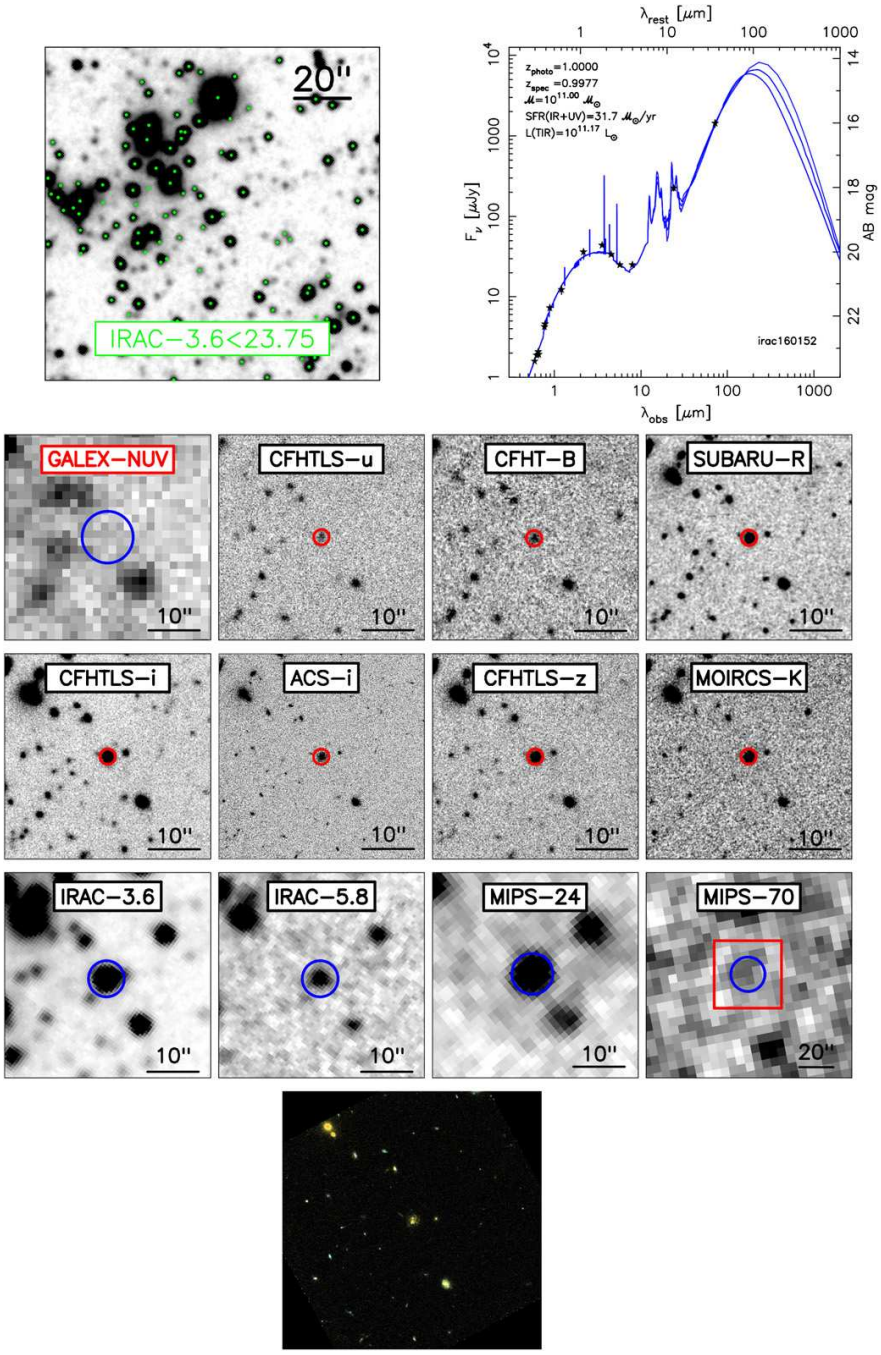

Figure 10. Same as Figure 9 for the galaxy irac160152 at $z = 0.99$. The band label shown in red in the *GALEX*-NUV postage stamps indicates a non-detection. For each of these bands, $\sigma_{\rm sky}$ is depicted in the UV-to-FIR SED as red arrow. Green name labels indicate forced detections (see Section 4.2). These bands are shown as green stars in the SED plot.

reduction versions and the limiting depth of the source extractions.

2. We described in detail our custom photometric procedure *Rainbow*, developed to measure photometry in multi-wavelength data in a consistent way. The main steps followed by our photometry software are: (a) re-calibration of the local ($5' \times 5'$) astrometric solution for each pair of images, improving the accuracy of the cross-identification of sources to a limit below $0\farcs1$ ($0\farcs2$) between optical-NIR (IRAC-ground based) images. (b) Deconvolution of blended IRAC sources ($\sim$16% of the entire catalog) separated by more than $1''$, using the positions of the

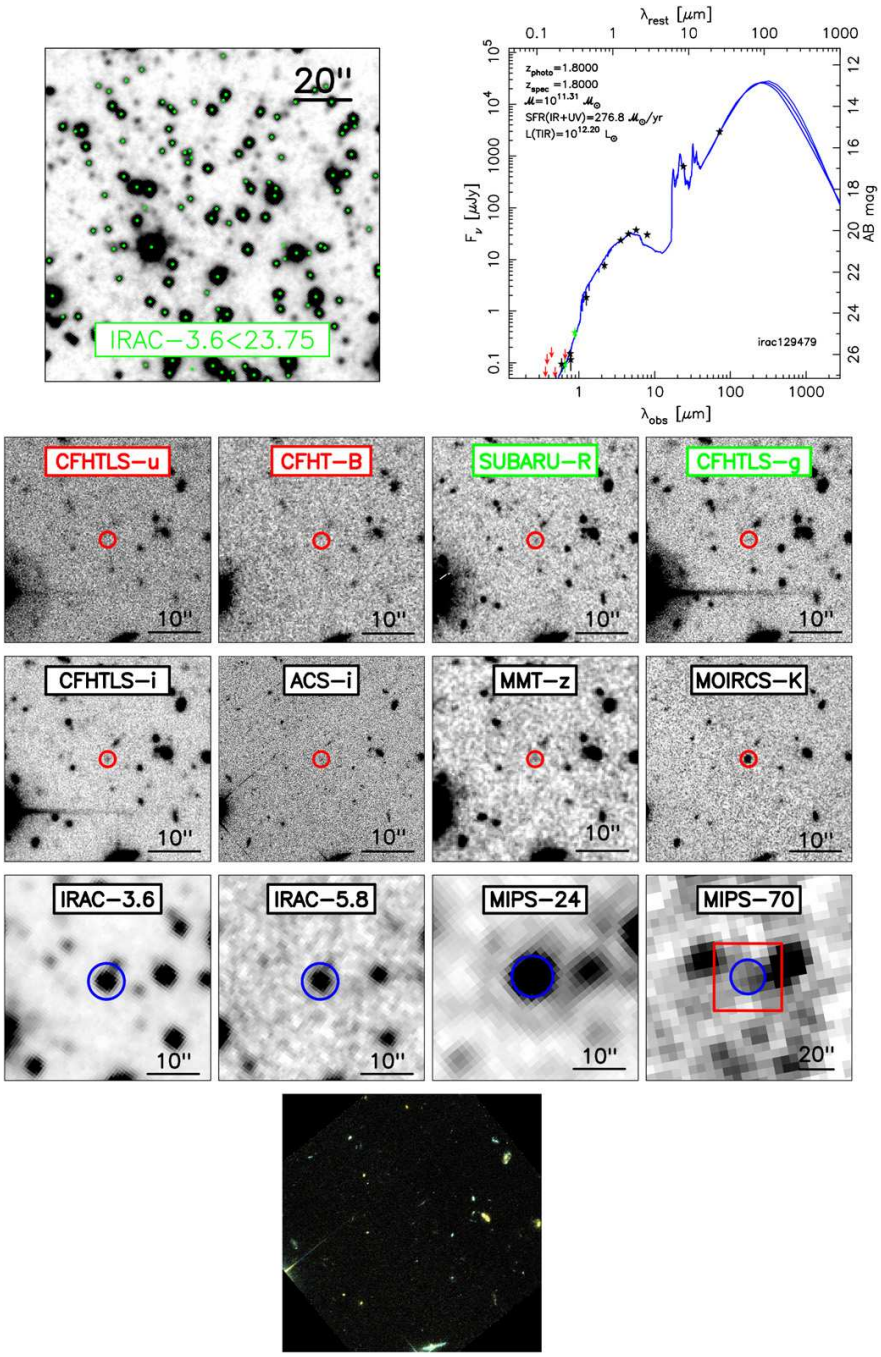

Figure 11. Same as Figure 9 for irac129479, an IR-bright galaxy at $z = 1.8$. This galaxy corresponds to source EGS11 in the paper of Huang et al. (2009). Band labels in red in the gray-scale postage stamps indicate non-detections. For each of these bands, σ_{sky} is depicted in the UV-to-FIR SED as red arrow. Band labels in green indicate forced photometric measurements (see Section 4.2). These bands are shown as green stars in the SED plot.

optical/NIR counterparts as reference. The IRAC photometry of deblended sources is accurate to 0.03–0.10 mag, depending on the flux ratio between neighbors (Section 4.1). (c) Measurement of consistent aperture matched photometry for a wide range of ground- and space-based observations, with different depths and resolutions (Section 4.2). (d) Obtaining (forced) flux measurements and upper limits for faint, undetected (in a direct analysis of each image) sources (Section 4.2). (e) Computing robust photometric errors that take into account variations in the sky rms and signal correlation (Section 4.3).

3. The inhomogeneous multi-wavelength coverage of the region covered by IRAC and the differences in depth of the various data sets justify the split of the complete sample

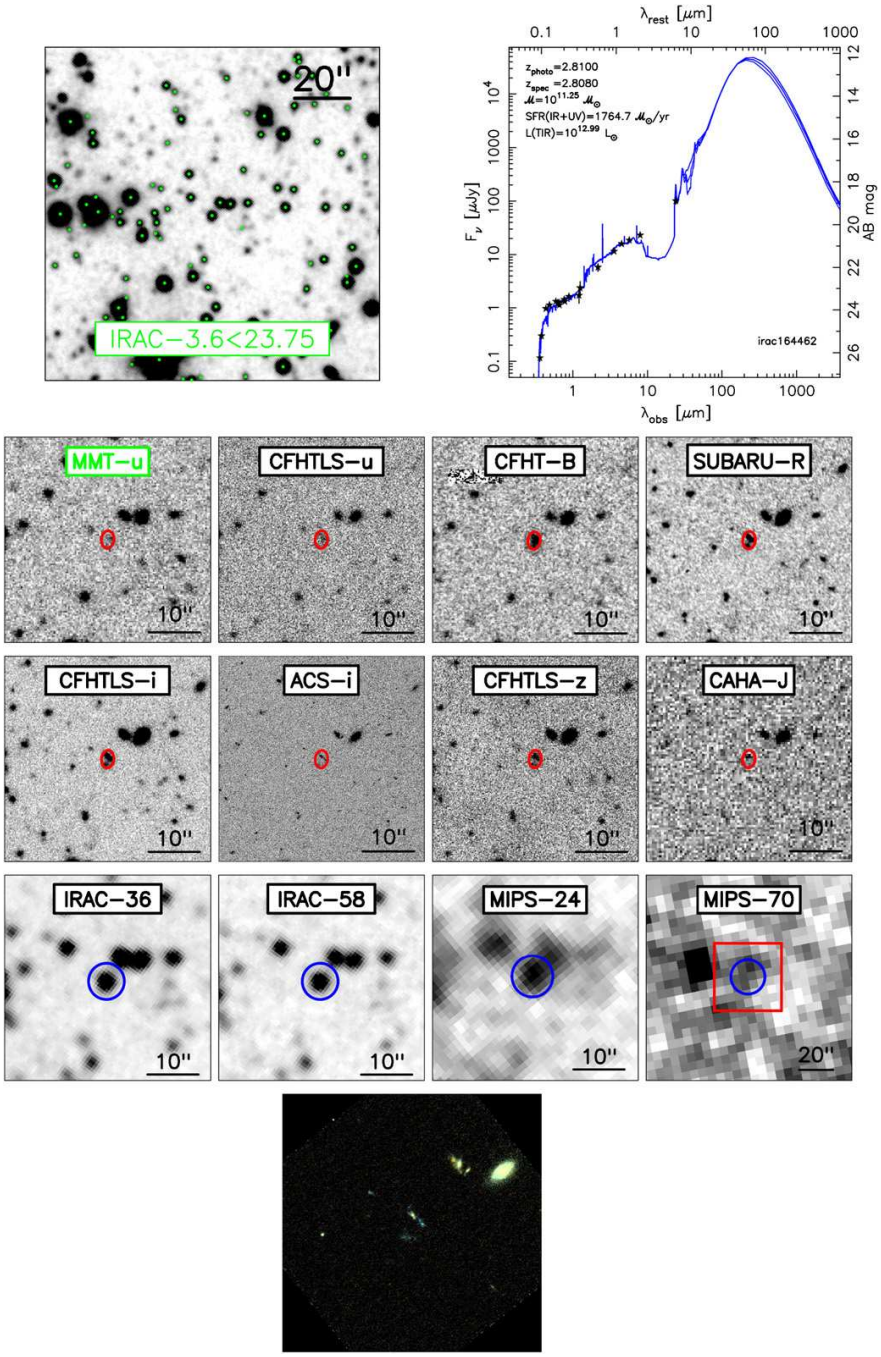

Figure 12. Same as Figure 11 for irac164462, an LBG at $z = 2.8$. Band labels in red in the gray-scale postage stamps indicate non-detections. For each of these bands, σ_{sky} is depicted in the UV-to-FIR SED as red arrow. Band labels in green indicate forced photometric measurements (see Section 4.2). These bands are shown as green stars in the SED plot.

in two complementary regions. The main region (covering 0.35 deg^2), delimited by the footprint of the CFHTLS image, constitutes the region with the highest data quality. Here the SEDs present a median coverage of 19 bands, including high-resolution imaging from *HST* (for ∼50% of the region) and deep NIR data from Subaru-MOIRCS (for ∼25% of the region). Nearly ∼70% of the complete sample presented in this paper is located in the main region. In the flanking regions (0.13 deg^2), the optical-to-NIR coverage is still robust, but the median-band coverage is reduced to 11 bands, lacking the high-resolution *HST* data and the deepest NIR observations.

4. The overall detection efficiency of counterparts for the IRAC sources ([3.6] < 23.75) in other bands is high: more than 85% of the sources are detected (with S/N > 5) in the deepest optical data (R or i' bands) and 70% in the deepest (MOIRCS) K_s-band images. Our method to perform (forced) photometric measurements for a priori undetected sources allows us to recover 10%–20% additional sources in the shallowest images. Despite the large fraction of IRAC sources detected in all other bands, we find that ∼2% of the sample is detected in IRAC only, some of them at relatively bright magnitudes 21 < [3.6] < 22 and with high S/N.
5. Around 10% of the sample counts with reliable spectroscopic redshifts. Nearly 20% and 2% of the sources are detected in the MIPS 24 μm and MIPS 70 μm data, respectively. This allows a detailed analysis of their IR-based SFRs. In addition, we recover 1023 of the X-ray sources in the catalog published by Laird et al. (2009; 77% of their complete catalog) and 590 radio sources from the catalog published by Ivison et al. (2007; 52% of their entire sample).
6. We presented the publicly available Web interface, *Rainbow Navigator*, for the database containing all the data products from this and the forthcoming companion paper (Paper II). The interface allows the access to the data using customizable queries on the photometry and derived parameters. Furthermore, it provides additional capabilities to inspect the data, such as the creation of on-the-fly clickable sky maps or the cross-match of the IRAC sample presented here to a user-provided catalog. We have made a significant effort to develop a useful and accessible tool that maximizes the legacy value of our catalogs in the EGS, and the future *Rainbow* based projects in other relevant fields (e.g., PG08). The online version of the catalog (IRAC-DR1) contains a deeper, although less complete, sample limited to [3.6] < 25.
7. In Paper II, we make use of the very detailed UV-to-FIR SEDs presented here to estimate photometric redshifts, stellar masses, and SFRs.

We acknowledge support from the Spanish Programa Nacional de Astronomía y Astrofísica under grant AYA2009-10368. P.G.P.-G. acknowledges support from the Ramón y Cajal Program financed by the Spanish Government and the European Union. Partially funded by the Spanish MICINN under the Consolider-Ingenio 2010 Program grant CSD2006-00070: First Science with the GTC. Support was also provided by NASA through contract no. 1255094 issued by JPL/Caltech. This work is based in part on observations made with the *Spitzer* Space Telescope, which is operated by the Jet Propulsion Laboratory, Caltech under NASA contract 1407. Observations reported here were obtained at the MMT Observatory, a joint facility of the Smithsonian Institution and the University of Arizona. *GALEX* is a NASA Small Explorer launched in 2003 April. We gratefully acknowledge NASA's support for construction, operation, and scientific analysis of the *GALEX* mission. This research has made use of the NASA/IPAC Extragalactic Database (NED) which is operated by the Jet Propulsion Laboratory, California Institute of Technology, under contract with the National Aeronautics and Space Administration. Based in part on data collected at Subaru Telescope and obtained from the SMOKA, which is operated by the Astronomy Data Center, National Astronomical Observatory of Japan.

REFERENCES

Barmby, P., et al. 2004, ApJS, 154, 97
Barmby, P., et al. 2008, ApJS, 177, 431
Barro, G., et al. 2009, A&A, 494, 63
Bertin, E., & Arnouts, S. 1996, A&AS, 117, 393
Bundy, K., et al. 2006, ApJ, 651, 120
Capak, P., et al. 2004, AJ, 127, 180
Caputi, K. I., et al. 2007, ApJ, 660, 97
Chary, R., & Elbaz, D. 2001, ApJ, 556, 562
Coil, A. L., et al. 2004, ApJ, 617, 765
Colina, L., & Bohlin, R. C. 1994, AJ, 108, 1931
Cristóbal-Hornillos, D., et al. 2003, ApJ, 595, 71
Daddi, E., et al. 2004, ApJ, 617, 746
Daddi, E., et al. 2007, ApJ, 670, 156
Davis, M., et al. 2003, Proc. SPIE, 4834, 161
Davis, M., et al. 2007, ApJ, 660, L1
Eisenhardt, P. R., et al. 2004, ApJS, 154, 48
Faber, S. M., et al. 2003, Proc. SPIE, 4841, 1657
Fazio, G. G., et al. 2004, ApJS, 154, 39
Gawiser, E., et al. 2006, ApJS, 162, 1
Giavalisco, M., et al. 2004, ApJ, 600, L93
Grazian, A., et al. 2006, A&A, 449, 951
Gwyn, S., et al. 2011, arXiv:1101.1084
Huang, J., et al. 2004, ApJS, 154, 44
Huang, J., et al. 2009, ApJ, 700, 183
Iglesias-Páramo, J., et al. 2007, ApJ, 670, 279
Ilbert, O., et al. 2006, A&A, 457, 841
Ilbert, O., et al. 2009, ApJ, 690, 1236
Ivison, R. J., et al. 2007, ApJ, 660, L77
Kajisawa, M., et al. 2009, ApJ, 702, 1393
Kron, R. G. 1980, ApJS, 43, 305
Labbé, I., et al. 2003, AJ, 125, 1107
Laird, E. S., et al. 2009, ApJS, 180, 102
Le Fèvre, O., et al. 2005, A&A, 439, 845
Lotz, J. M., et al. 2008, ApJ, 672, L177
Mancini, C., et al. 2009, A&A, 500, 705
Martin, D. C., et al. 2005, ApJ, 619, L1
McLeod, B., et al. 2006, in Scientific Detectors for Astronomy 2005, ed. J. E. Beletic, J. W. Beletic, & P. Amico (Berlin: Springer), 337
Miyazaki, S., et al. 2007, ApJ, 669, 714
Muzzin, A., et al. 2009, ApJ, 701, 1839
Nandra, K., et al. 2005, MNRAS, 356, 568
Oke, J. B., et al. 1995, PASP, 107, 375
Pérez-González, P. G., et al. 2005, ApJ, 630, 82
Pérez-González, P. G., et al. 2008, ApJ, 675, 234
Pozzetti, L., et al. 2007, A&A, 474, 443
Quadri, R., et al. 2007, AJ, 134, 1103
Reach, W. T., et al. 2005, PASP, 117, 978
Reddy, N. A., Steidel, C. C., Erb, D. K., Shapley, A. E., & Pettini, M. 2006, ApJ, 653, 1004
Rieke, G. H., et al. 2004, ApJS, 154, 25
Rodighiero, G., et al. 2007, A&A, 470, 21
Rowan-Robinson, M., et al. 2008, MNRAS, 386, 697
Salim, S., et al. 2007, ApJS, 173, 267
Santini, P., et al. 2009, A&A, 504, 751
Scoville, N., et al. 2007, ApJS, 172, 1
Steidel, C. C., Giavalisco, M., Pettini, M., Dickinson, M., & Adelberger, K. L. 1996, ApJ, 462, L17
Steidel, C. C., et al. 2003, ApJ, 592, 728
Villar, V., et al. 2008, ApJ, 677, 169
Walcher, C. J., et al. 2008, A&A, 491, 713
Wang, W., Cowie, L. L., Barger, A. J., Keenan, R. C., & Ting, H. 2010, ApJS, 187, 251
Williams, R. J., Quadri, R. F., Franx, M., van Dokkum, P., & Labbé, I. 2009, ApJ, 691, 1879
Williams, R. E., et al. 1996, AJ, 112, 1335
Wolf, C., et al. 2001, A&A, 377, 442
Wuyts, S., et al. 2007, ApJ, 655, 51
Wuyts, S., et al. 2008, ApJ, 682, 985
Yan, H., et al. 2004, ApJ, 616, 63
York, D. G., et al. 2000, AJ, 120, 1579
Zhao, Y., Huang, J., Ashby, M., Fazio, G., & Miyazaki, S. 2009, Res. Astron. Astrophys., 9, 1061

3

Estimate of the physical properties of *Spitzer*/IRAC galaxies in EGS

3.1 Introduction

In the previous chapter we have discussed the importance of multi-wavelength data to study in detail the physical properties of galaxies. The combined analysis of these resources offer a privileged view on the relative contribution of the different galaxy components to the overall SED. Nonetheless, in order to go from the observed SEDs of the galaxies to reliable estimates of their physical properties we need additional tools that allowed us to extract the information *imprinted* in the SED. This can be achieved using SED modeling techniques that establish a link between observational quantities and intrinsic properties using synthetic (or semi-empiric) models. These models are characterized with specific properties because they are created making assumptions on the physical processes that takes place inside the galaxy. SED modeling techniques are a very versatile tool that are nowadays used in multiple studies of galaxy evolution to get the maximum information out of the rapidly increasing volume of available data. Some of the relevant properties that can be estimated from this technique include an estimation of the stellar masses or the UV- and IR-SFRs. Nonetheless, SED modeling can be used for many other studies galaxy evolution.

In this context, **this chapter presents a multi-wavelength analysis of the SEDs of the galaxies computed in the previous chapter with the aim of estimating their physical properties**. In particular, we will characterize the optical-to-NIR and mid-to-far IR SEDs by fitting them to stellar population synthesis and dust emission models, respectively. The combination of both fits will allow us to reproduce with great detail the full SED of each galaxy and **obtain robust estimates of their redshifts, stellar masses and SFRs**. In addition we will perform an exhaustive analysis of the quality of each of these estimates to explore their overall accuracy and possible limitations. Some of the test carried out include: 1) a comparison of our estimates against values obtained with more accurate methods (e.g, photo-z versus spec-z) or computed by other authors with different techniques. 2) obtaining multiple estimates of the physical properties using different procedures or modeling assumptions. As we describe in this chapter, the procedures followed to carry out the different steps of the SED modeling and the estimate of the physical properties are essentially based on subroutines of the code *Rainbow* (Pérez-González et al. 2005, 2008). Nevertheless, there are significant improvements of the code and of the technique itself that has been specifically developed in this thesis work, and are discussed in this chapter. Some relevant examples are:

- A zero-point correction of the photometric bands based on the comparison to synthetic templates. This procedure reduce small systematic differences between the photometry of similar pass-bands improving the accuracy of the fitting of the observed photometry to the templates.

- The use of a template error function to improve the quality of the SED fitting procedure. This function essentially reduces the weight of certain wavelength ranges during the fitting procedure avoiding possible biases introduced by potentially uncertain regions that are not accurately represented by the models.

- The creation of new galaxy templates based on different stellar population modeling assumptions. Using this new templates we will be able to measure the impact of the modeling assumptions on the resulting estimated quantities, comparing for example the differences in the stellar masses obtained with each template set.

- The estimate of synthetic magnitudes based on the modeled SED. This values provide a reliable estimate of the magnitude of the galaxies in bands which has not been observed, and also allow us to estimate rest-frame magnitudes or luminosities.

This chapter is essentially devoted to describe SED modeling techniques and to compute physical properties of the galaxies based on the analysis of these results. Along the following introduction we will show that if the full SED is to be fully understood, care must be taken in modeling each of the components that originate the emission at different wavelengths, and combining them consistently. Given that most relevant components in the SED of the typical galaxy the stars, gas and dust, these are also the key contributions to the synthetic spectra of the models. Here we will briefly introduce the state-of-the-art techniques used to model both the stellar, gas and dust component. In addition, we will discuss the physics that lie beneath each of them and the current limitations of the method. In particular, we will specifically describe: 1) how photometric redshifts, stellar masses and SFRs can be obtained out of the best fitting models, 2) what are the different possible approaches to obtain them and 3) what are the assumptions made in the process.

3.2 SED modeling

3.2.1 Stellar population modeling

Stellar emission is generally the dominant component of the SED in UV-to-NIR wavelengths. The usual simplification adopted for the modeling of galactic SEDs is that their emission can be represented through a sum of spectra of simple stellar populations (SSPs) with different ages and element abundances. Each of these SSPs are then an idealized single age, single-abundance combination of stars whose distribution in mass depends on the assumed initial distribution and the chosen age. The technique that combines these ingredients in order to predict the spectrum of a galaxy is known as stellar population synthesis (SPS), and was pioneered in works by Tinsley (1972), Searle et al. (1973) and Larson & Tinsley (1978).

In a nutshell SPS models compute the emissivity (energy radiated per unit frequency per unit mass, L_ν), of an SSP of mass M, age t, and metallicity Z by adding the contribution from individual

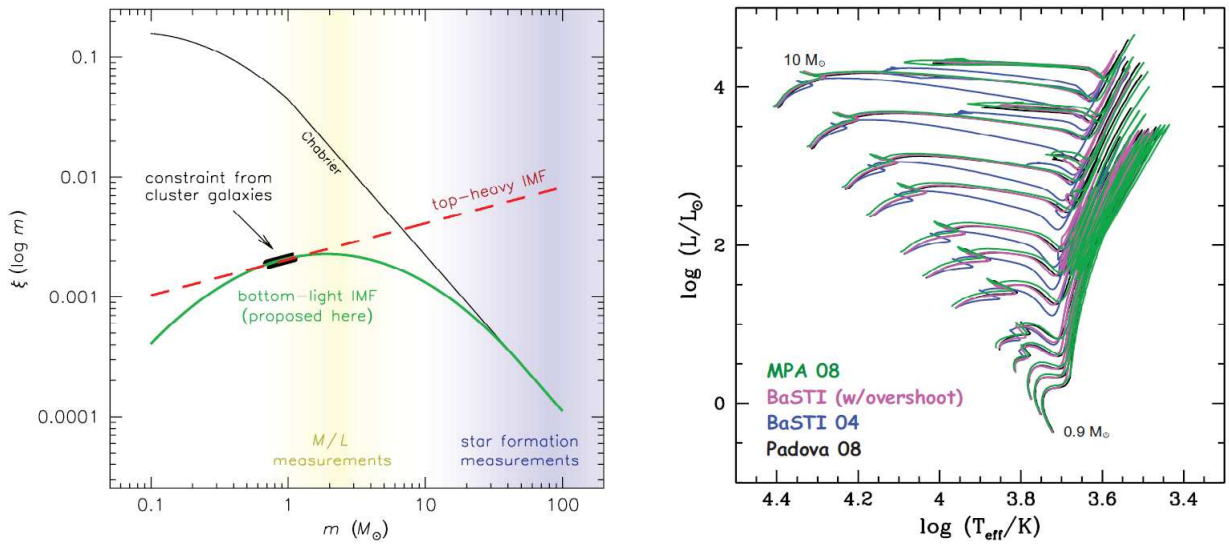

Figure 3.1: *Left:* Example of three initial mass functions that produce a different number of stars for a given mass (adapted from van Dokkum 2008). The colored regions indicate the different observational evidences that support these IMFs at different mass intervals. *Right:* Differences in the evolutionary paths of stars of a given mass in the theoretical isochrones developed by different authors (adapted from Walcher et al. 2008): MPA08 (Weiss and Schlattl 2008), BaSTI04 (with/without overshoot; Pietrinferni et al. 2009), and Padova08 (Marigo and Girardi 2007; Marigo et al. 2008)

stars:

$$L_\nu(t,Z) = \int_M \phi(M)_{t,Z} L_\nu(M,t,Z)$$

This formula essentially combines the stellar mass function, $\phi(M)$, and the spectra, L_ν, of each star with a given mass, age, and metallicity (M,t,Z).

The **stellar mass function** describes when stars of a given mass stop contributing to the spectra of the SSP because they end their lives, and it is computed from an IMF ($\phi_0(M)$) and stellar evolution. The IMF describes the distribution in mass (generally within given limits, M_{min}=0.05-1.0$M_\odot$; M_{max}=100-150$M_\odot$) of a zero-age main sequence stellar population (see left panel of Figure 3.1). The IMF combined with stellar evolution allows to trace the evolutionary tracks, i.e., the paths of the stars that constitute the SSP. The IMF is one of the key ingredients of the synthesis, and its shape is critical to determine the SED (e.g., the number of massive stars essentially determine the UV emission of the SPS). Some of the most common parametrizations include: a simple power-law model (Salpeter 1955; Massey & Hunter 1998), a broken power-law (Kroupa 2001), or a lognormal form (Chabrier 2003).

Evidently, the parametrization of the stellar evolution is also of paramount importance. The most commonly used method to compute the SPS is known as *isochrone synthesis* (the other common method being *fuel consumption*, see e.g. Buzzoni 1989; Maraston 1998, 2005 for a detailed description), which essentially means that the SED is computed from a combination of stars with the same age, i.e., an isochrone (Charlot & Bruzual 1991). The creation of stellar isochrones requires a large grid of evolutionary tracks for stars of a given (M,Z). Much work has been devoted into providing detailed sets of stellar tracks from different groups (right panel of Figure 3.1), e.g. Padova (Marigo & Girardi 2007; Marigo et al. 2008), Geneva (Lejeune & Schaerer 2001). Thanks to these efforts, current tracks now exist for a wide range of initial masses (Girardi et al. 2000;

Meynet & Maeder 2005) and metallicities (0.01 to $4Z_{\odot}$).

Nonetheless, the key component (and also the main issue) of SSPs is knowing **SEDs of single stars** characterized with precise stellar parameters, $L_{\nu}(M, t, Z)$. This ingredient is computed using libraries of stellar spectra, which similarly to the evolutionary tracks, has improved considerably in recent years. Both theoretical (e.g., Kurucz 1992; Coelho et al. 2005) and empirical (STELIB, Le Borgne et al. 2003; MILES, Sánchez-Blázquez et al. 2006, Cenarro et al. 2007; ELODIE, Prugniel & Soubiran 2001) libraries exist today covering a wide range of the parameter space (temperature, gravity, metallicity) with different spectral and parameter resolutions. A good coverage of the parameter space ensures the full mapping of the Hertprung-Russel diagram, which allows to reconstruct the isochrone minimizing the use of interpolation and reducing the uncertainties.

Even though significant improvements in the evolutionary tracks and stellar libraries have been made in the last decade, significant challenges remain, mainly because some parts of stellar evolution are only weakly understood, and hence poorly treated. The most important of these tend to be short lived very luminous phases such those of: massive stars, thermally pulsing asymptotic giant branch (TP-AGB) stars, extreme horizontal branch stars (EHB) and blue stragglers. But also, the effect of binaries in massive star evolution, evolutionary metallicity variations in a SSP (such us the α-enhancement), or the existence of a single, universal IMF (Meurer et al. 2009; van Dokkum 2008). Altogether, these uncertainties can in many cases dramatically impact our ability to convert observables into physical properties and vice–versa (see, e.g., recent studies by Maraston et al. 2006; Lee et al. 2007; Conroy et al. 2009, 2010; Conroy & Gunn 2010; Muzzin et al. 2009).

However, despite the unresolved issues, SSP modeling has advanced significantly in recent years, and a wide variety of SPS models predicting full spectra are available to the community: Fioc and Rocca- Volmerange (1997, PEGASE), Bressan et al. (1998, used in GRASIL) and Leitherer et al. (1999) and Vázquez et al. (2007) (both Starburst99), Bruzual and Charlot (2003, GALAXEV, also commonly referred to as BC03, and now CB10), Vazdekis (1999), Maraston (2005, M05, based on fuel consumption theorem), Mollá et al. (2009).

3.2.2 Dust attenuation and gas emission

The modeling of the UV-to-NIR SEDs would not be representative of the observed spectra of galaxies unless it includes the effect of dust attenuation in the stellar emission and, to a lesser extent (at least in modeling broad-band photometry) the contribution to the flux of emission lines and nebular continuum. A notably exception to this rule is the contribution of the nebular continuum in the NIR wavelengths (Fioc & Rocca-Volmerange 1997). Nonetheless, this is already an intrinsically difficult region of the SED to model, independently of the gas contribution.

The effects of dust attenuation are applied separately to the stellar emission, being often described by two parameters: reddening, and the total obscuration. The reddening parametrizes the wavelength dependence of the dust effects and takes into account the fact that shorter wavelength photons are more prone to be scattered and absorbed by dust. This is often parametrized by the color excess, E(B-V). The total obscuration is a measure of the total light absorbed by dust, generally in a reference band, and can be considered the normalization of the reddening. This is generally parametrized as A(V). For relative flux measurements correcting only for reddening is sufficient, however absolute quantities must be corrected for total obscuration.

When considering the integrated effects of dust over the whole of a galaxy the situation becomes more complex, depending on several factors such us the geometry of the stars and dust, the varying amounts of extinction due to the spatial distribution of stars and dust, or the scattering stellar light into our line of sight. All these effects tend to flatten the effects of dust on the spectrum, creating an average attenuation law, where the amount of reddening with extinction is less (or *greyer*) than we observe locally (see e.g., Cardelli et al. 1989, Witt et al. 1992).

In its simplest form, the effects of dust can be averaged into a single attenuation law (the functional dependence with wavelength e.g., Calzetti 1997; see left panel of Figure 3.2), and the total attenuation (in a particular band) can be expressed using a *screen* approximation, as if the dust was a layer between the galaxy and the observer, characterized only by the thickness of the screen. More sophisticated, (physically motivated) models consider a two phase attenuation in which young (age$<$10 Myr) stars suffer for stronger obscuration, being in the proximity of their birth cloud, whereas all stars suffer the effects of a diffuse dust component equally (Charlot & Fall 2000). Yet, these models do not account for the impact of the large structures such us bulges, bars or disk, or more importantly, the anisotropic scattering of light. A more realistic approach require complex radiative transfer calculations (see e.g., Baes & Dejonghe 2001) that make use of intensive calculations and thus are difficult to implement in large samples of galaxies. Nonetheless, averaged attenuation laws such us those from Calzetti et al. (2000) or Charlot & Fall (2000) have been shown to be accurate reproducing the effect of dust attenuation for whole galaxies (e.g., Noll et al. 2007; Noterdaeme et al. 2009)

As mentioned in the chapter 1, emission lines are especially important for young, actively star-forming galaxies, which emit a significant amount of ionizing photons. A fraction of these are absorbed locally by the neutral hydrogen in the ISM and then re-emitted in the hydrogen recombination lines. A similar process occur for other species. In first approximation the line strenght of the species can be modeled based on the amount of ionizing photons (from the stellar population modeling), the values of the recombination coefficients (depending on the temperature of the star forming region and on the element abundance) and theoretical-line ratios. A much detailed work would require a full consistent treatment of the energy balance using a ionizing code such as CLOUDY (Ferland et al. 1998).

3.2.3 Dust emission modeling

The same process responsible for the attenuation of the SED causes the dust grains to be heated and re-emit most of the energy in the mid-to-far IR wavelengths. This wavelength range overlaps with the region where the contribution of the stellar component is rapidly fading (Raighleigh-Jeans tail). Thus, stellar and dust components are mostly orthogonal and frequently one only requires subtracting a small stellar contribution at 3-8μm to attach the dust emission to the SED obtaining a consistent UV-to-FIR model.

As explained in chapter 1, excluding the mid-IR range at 3-20μm which is characterized by strong PAH ($\sim$ very small dust) emission and absorption lines/bands (Smith et al. 2007), the shape of the IR SED at longer wavelengths is almost featureless (at least at the resolution that we are able to probe), and can be described with a black body curve, an emissivity-modified black body (also called grey body), or the sum of 2-3 of these kind of curves. This assumes implicitly that there are an equivalent number of dust components characterized by different grain sizes and temperatures. Indeed, the ISM of galaxies is known to exhibit a wide range of temperatures,

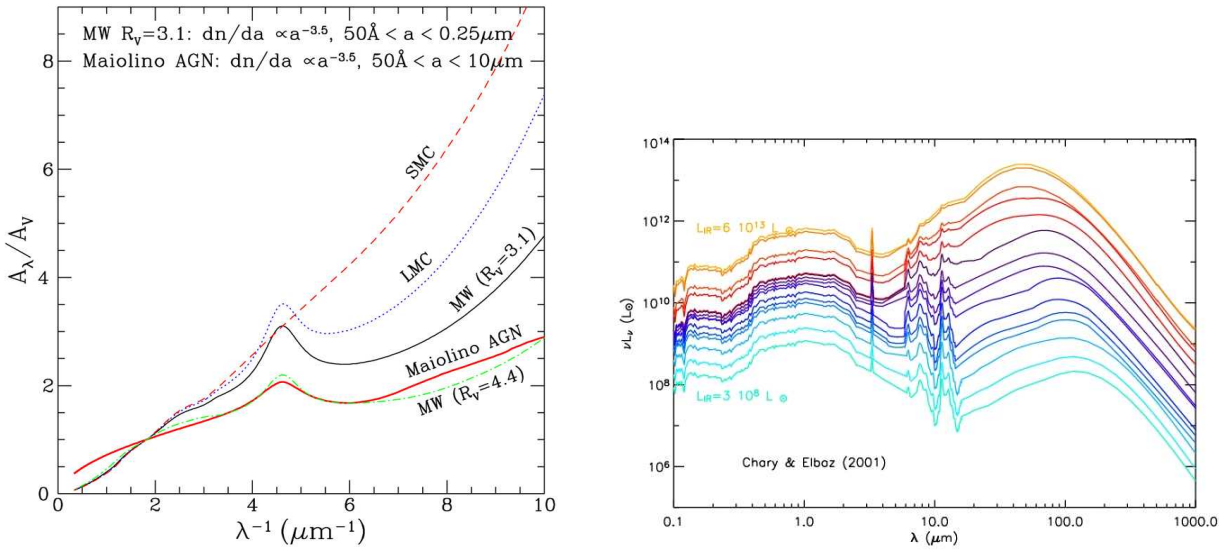

Figure 3.2: *Left:* Examples of interstellar extinction curves for the Milky Way, Small Magellanic Cloud (SMC), and Large Magellanic Cloud (LMC). Also plotted is the Maiolino-type extinction curve for AGNs (see Maiolino et al. 2000). Adapted from Li et al. 2007. *Right:* Example of the IR dust emission templates of Chary & Elbaz (2001). The Optical/NIR region is the same for all galaxies. The templates have been normalized by their total IR luminosity (i.e., the integrated luminosity from 8 to 1000 μm.

from the hot dust around young stars (e.g., HII regions, photo-dissociation regions) and galaxy outflows, to the coldest dust inside molecular cores. This variety of dust temperatures is the result of the different response to the strength of ionization field as a function of size (see e.g. the pioneer work of Desert et al. 1990). While, the largest dust grains are generally considered to have a single temperature, being in thermal equilibrium, the smallest grains are closer to an stochastic heating and respond to a increased radiation field by radiating at a faster rate instead of increasing their temperature (see e.g., Draine 2003).

Taking this into account, the modeled IR spectra is usually composed of a superposition of large-grains (warm), small grains (cold), and PAH emission curves, whose relative contributions are weighted over the radiation field. In the simplest approximation, the dependence of the mass distribution on the intensity of the radiation field (U) is assumed to be a power law ($dM_d = U^{-\alpha}dU$). For example, the combination of a diffuse radiation field following a inverse square root decay with the distance, and a uniformly distributed dust mass, whose contribution increases with the square of the distance, gives the parametrization $dM_d \propto U^{-2.5}dU$ (see e.g., Dale et al. 2001, Dale and Helou 2002 or Draine et al. 2007 for detailed description). Again, a more accurate modelization of dust emission would require detailed studies of the interplay between dust and photons using complex radiative transfer codes, but also an accurate representation of dust regions and their distribution in the galaxy. As a result of the large number of assumptions and variables implied in the characterization, there are multiple models in the literature which handle different layers of complexity. From a self-consistent simultaneous treatment of UV and FIR emission/absorption (da Cunha et al. 2008, Noll et al. 2009), to assuming different phase components, such as the cloud-disk-bulge components in the GRASIL model (Silva et al. 1998; Granato et al. 2000), or different implementations of radiative transfer calculations: e.g., Monte-Carlo methods such as SUNRISE (Jonsson 2006; Jonsson et al. 2010) or DIRTY (Gordon et al. 2001), or ray-tracing algorithms, such us Efstathiou et al. (2000), and Siebenmorgen & Krügel (2007).

In practice, due to the difficulty of accurately determining so many degrees of freedom, empirically-based templates are often used for representing the IR SED of galaxies, especially when IR data are limited due to sensitivity or confusion, which is frequently the case at high-z. These templates are obtained by taking dust models as described above and matching them to the observed IR colors of real galaxies. As a result, these templates then tend to have full galaxy properties such as the total IR luminosity (right panel of Figure 3.2). Well known examples of templates include: Chary and Elbaz (2001), Dale and Helou (2002), Lagache et al. (2004), and Rieke et al. (2009). Though these templates tend to be limited by the samples that define them, they provide a good alternative to models when no or very little information is available about the actual IR emission of a galaxy. In addition, due to the method used to derive the templates these are reasonably accurate reproducing the average IR emission of the galaxies. At least that of nearby galaxies that were used to compute them.

3.2.4 *Rainbow* SED modeling

In the context of the methods described in this section, the characterization of the UV-to-FIR SEDs of the galaxies in the IRAC catalog was carried out by combining the modeling of both the stellar populations and the dust emission. In particular, the code *Rainbow* estimates the SED of the stellar component by comparing (using a χ^2 fitting) the observed UV-to-NIR photometry with a set of templates characterized with a SPS modeling and a dust extinction law . This templates, presented in Pérez-González et al. (2008), are computed using the PEGASE models (Fioc and Rocca-Volmerange 1997) jointly with a Salpeter (1955) IMF and a Calzetti et al. (2000) extinction law. Nonetheless, as a part of this thesis we explore the effects of these modeling assumptions in the resulting SED by comparing the results obtained under the *default* modeling configuration with those obtained using different SPS models (e.g., BC03, M05), IMFs (e.g., Kroupa et al. 2001 or Chabrier et al. 2001) and extinction laws (e.g., Calzetti et al. 2001 or Charlot&Fall 2000). Similarly, *Rainbow* characterizes the dust emission of the galaxies (usually consisting on 1 or 2 flux measurements in the far IR from *Spitzer*/MIPS) fitting the observed fluxes at $\lambda_{\rm rest} > 5$ μm with different sets of templates (e.g., Chary and Elbaz 2001, Dale and Helou 2002 or Rieke et al. 2009). In this case, we investigate the effect of using different templates to model the IR emission, but we also asses the impact of characterizing such a large wavelength range ($\sim$5-1000 μm) based on relatively scarce data.

In the following section we present a brief summary of the usual techniques that allow us to estimate the physical properties of the galaxies from the analysis of their SED. In particular we focus on describing the parameters that we have computed for the IRAC galaxies in EGS as a part of this thesis.

3.3 What can we learn from SED fitting

Sophisticated SPS models have allowed an enormous body of work aimed at constraining physical parameters of galaxies. Physical parameters that are constrained by SPS include, but are not limited to: photometric redshifts (see e.g., Koo 1999 for a review); stellar masses (e.g. Bell et al. 2003; Kauffmann et al. 2003), star formation histories and rates (e.g. Kauffmann et al. 2003b; Pérez-González et al. 2003; Panter et al. 2007), and metallicities (e.g, Gallazzi et al. 2005). SPSs are also

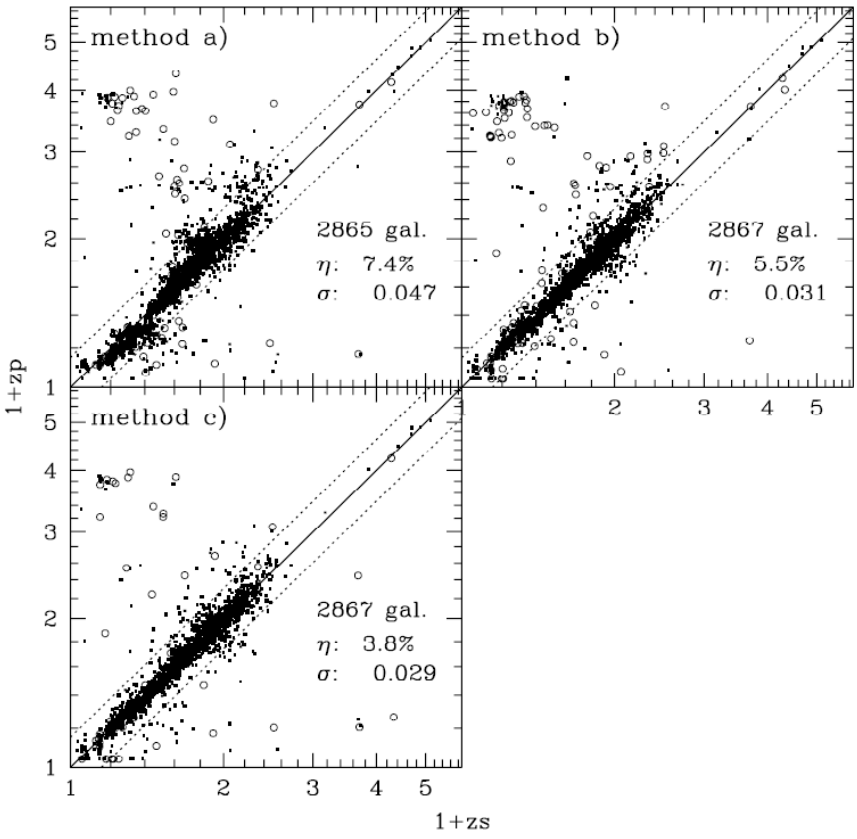

Figure 3.3: Photometric redshift versus spectroscopic redshift for a sample of i'-selected galaxies in Ilbert et al. (2006). Each panel corresponds to an additional step in the calibration method followed in the paper including: a) Pure χ^2 fitting; b) adding template optimization and a correction systematic offsets; c) adding Bayesian inference on the expected observed magnitude as a function of redshift.

routinely used to analyze the observed broad-band colors and spectra of galaxies (e.g., Shapley et al. 2005; Daddi et al. 2007b Kriek et al. 2006).

3.3.1 Photometric redshifts

An inherent problem in the SED analysis of distant extragalactic sources is the necessity to obtain a redshift estimation based on the observed photometry. A topic that is usually referred to as photometric redshifts. Indeed, the photo-z was one of the earliest forms of SED fitting, having been suggested as a manner to go beyond the limits of early spectroscopy (Baum 1957; see Koo et al. 1999 for a review). This particular problem is distinct from other estimates of the physical properties because contrary to stellar masses or SFRs it is a fundamental quantity that do not depend on empirical relations. In addition, large photometric surveys often count with a subset of spectroscopic galaxies and therefore the photo-z estimates can be tested extensively and even calibrated empirically.

Photometric redshift determinations are often divided into two major strategies: The first approach is based on purely **empirical methods**, i.e., on the observed properties of the galaxies. These methods assume that, with a sufficiently large spectroscopic *training* set, an empirical relation between redshift, observed magnitudes and colors of the galaxies can be determined (e.g.,

Connolly et al. 1995; Brunner et al. 1997; Wang et al. 1998). The other approach involves **fitting SED templates** to the observed photometry of galaxies. These galaxy templates may be empirical, synthetic, or hybrid, and may be completed with the inclusion of dust absorption and emission lines (e.g., Koo 1985; Lanzetta et al. 1996; Mobasher et al. 1996; Sawicki et al. 1997; Benítez et al. 1999; Fernández-Soto et al. 1999).The underlying concept behind the success of any of these methods is the identification of prominent spectral features in the SED of galaxies, such us the Lyman break or the 4000,Å break, that provides an accurate estimate of the redshift.

Current works based on **empirical methods** are frequently associated with the use of several machine learning algorithms (e.g. artificial neural networks, ANNs) in the redshift estimating routines. These algorithms relies on the empirical training set to build up a full relationship between magnitudes and colors and the redshift. As each individual parameter (e.g., one color) will have some spread with redshift, it is possible to use this interval as probability value for the redshift, constraining the distribution with the addition of each new parameter (Collister & Lahav 2004; Ball et al. 2008). Recently, these algorithms are increasingly being used based on inputs that are not limited only to photometry. Other properties such as the surface brightness (e.g. Kurtz et al. 2007), petrosian radii (e.g., Firth et al. 2003), or the concentration index (e.g., Collister & Lahav 2004) have all been used in association with the magnitudes and colors to constrain the redshift. One of the main drawbacks of this method is that the redshift estimation is only accurate when the objects in the training set have the same observables as the sources in question, being much more uncertain when used with objects fainter than the limit of the training sample. Furthermore, the training sample should be large enough so that magnitudes, colors, galaxy types and redshifts are well covered.

Unlike the empirical method, **template fitting** is essentially a form of SED fitting in the sense of SPS models. Basically, this technique use galaxy templates, that can be shifted to any redshift and convolved with the transmission curves of the filters used in the photometric survey, to match the observed fluxes. This creates a redshift fitting grid from which we can compare to the observed photometry and determine the most probable redshift using a maximum likelihood method, usually a χ^2 (as in HyperZ,Bolzonella et al. 2000; Le Phare, Ilbert et al. 2006; EAZY, Brammer et al. 2008). The primary advantage of this method is that it provides a full SED characterization of the source allowing straightforward estimates of their physical properties, but also a extrapolation/interpolation of the observed magnitudes in bands not included in the photometric survey. For obvious reasons, a critical step of this process is to make sure that the template set represent all, or at least the majority, of the galaxies detected in the survey. These often implies complementing the templates obtained with SPS with empirical templates of high-z galaxies (which can be different from their local analogous), or AGNs (which exhibit significantly different SEDs; see e.g. Polletta et al. 2007). A large template set is also important to gauge problems with degeneracies, i.e., where the template library estimate different redshifts for the same input colors. In order to avoid degeneracies, template fitting is often complemented with Bayesian inference techniques based on the inclusion of our prior knowledge of the galaxy distribution (e.g., Benitez 2000), such as the expected shape of the redshift distributions as a function of magnitude, or the evolution of the upper age limit with redshift (see Figure 3.3).

In the end, the accuracy of photo-z estimated from broad-band surveys appear to be limited to a redshift resolution of a few percent ($\sim$0.01·(1+z)) independently of the method used. This limit is inherited from the spectral resolution of broad band filters and the intrinsic variety of spectral properties in observed galaxies. Nonetheless, it is possible to trace spectral features with

higher accuracy using multiple (not redundant) deep band observations and/or higher resolution photometry, i.e., medium or narrow band photometry (e.g., Ilbert et al. 2009 or NEWFIRM; van Dokkum et al. 2009).

3.3.2 Stellar Masses

A rough estimate of the stellar masses can be obtained by multiplying a mass-to-light ratio (M/L), usually determined from single or multiple colors, by a rest-frame luminosity L (see e.g, Bell & de Jong 2001). However, when the galaxy SED is modeled using SPSs models (or in photo-z estimates based in SPSs derived templates), the stellar mass is estimated as a built-in part of the fitting process, just scaling of the observed photometry to the template luminosity (see left panel of Figure 3.4). This is possible because the output of SPSs models is frequently calibrated in luminosities per unit of stellar mass (see e.g., Bruzal&Charlot 2003).

The uncertainties on the stellar mass estimated with this method depend mainly on properties of the stellar population (age, metallicity, IMF) and the star-formation history (SFH; usually modeled with an exponentially declining burst) assumed for the template (or the SPS modeling; Maraston et al. 2006, Muzzin et al. 2009) but also on the overall quality of the photometric dataset. Frequent issues arising in the modeling of SEDs from a combination of several datasets are: a) are the observations deep enough to provide a continuous (without wavelength gaps) SED coverage?, b) do the observations probe the bands that better constraint the stellar mass (usually the NIR; Wuyts et al. 2007)?.

As described in the previous section, significant discrepancies can arise in the SEDs (and hence in the stellar masses) modeled with different IMFs or different parametrizations of the stellar evolutionary phases (see Conroy et al. 2009,2010ab for a detailed analysis). In principle, the IMF affects primarily to the normalization of the mass-to-light ratio, which would only imply a constant offset between stellar masses estimated with different IMFs. However, mass dependent effects can arise when significantly different IMFs (e.g. top-heavy, bottom-light) are considered (van Dokkum 2008; Marchesini et al. 2009). In turn, the impact of uncertain phases of stellar evolution is quite significant, as was highlighted recently by the different treatments of TP-AGBs in the models of Maraston (2005) and Bruzual&Charlot (2003). The use of one or the other in the modeling high-redshift galaxies, where light is dominated by 0.2 - 2 Gyr old populations, result in systematic factors of $\sim$2 differences in mass and age (Maraston et al. 2006; Bruzual 2007; Kannappan & Gawiser 2007). Other aspects of the modelization such as the metallicity range of the models or the extinction law have a relatively modest impact in the estimated stellar masses (Muzzin et al. 2009) although they play a more relevant role in the properties of the galaxies at shorter wavelengths (e.g., the un-obscured UV emission).

3.3.3 IR-based SFRs

The SFR of galaxies has been exhaustively studied using empirical calibrations for the UV and IR luminosities. As indicated in the previous section (and chapter 1), IR and UV wavelengths are ideal tracers for SFR in dust-obscured and unobscured galaxies, respectively. Although the full picture of the total (bolometric) SFR should incorporate the contributions from both (e.g., Bell et al. 2005; Papovich et al. 2006), with UV- and IR-bright galaxies dominating the two extremes. Nevertheless, considering the fact that the star-formation activity peaked at z=1-3, and that observations suggest

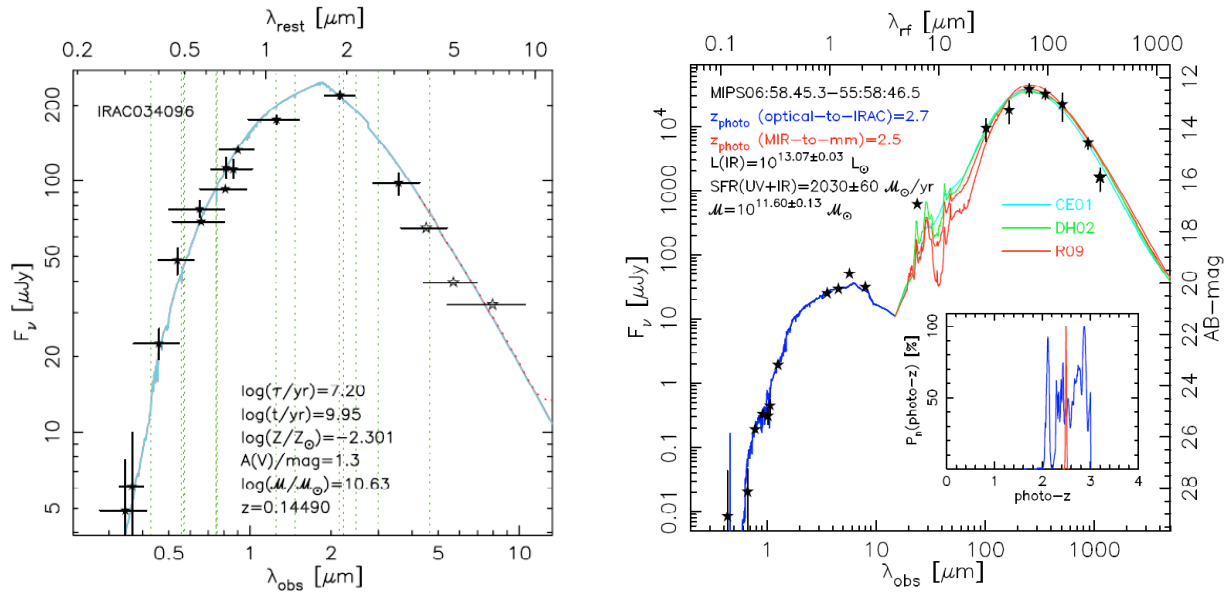

Figure 3.4: *Left:* Example of stellar population modeling for the SED of a galaxy at z=0.14490 in Pérez-González et al. (2008). The stellar mass (log(M/M$_\odot$)=10.63) was obtained as a part of the fitting process scaling the template to the observed rest-frame luminosities. *Right:* Example of the UV-to-FIR SED fitting of z=3.24 galaxy using stellar population modeling and dust templates (Pérez-González et al. 2010). The fitting of the IR-SED benefits from the use of FIR and (sub-)mm data from *Herschel*, LABOCA and AzTEC instead using only *Spitzer*/MIPS data.

that the amount of dust obscuration is in general substantial for the galaxies with the largest SFRs (Schmitt et al. 2006; Buat et al. 2007), one can conclude that the IR offers a relatively complete view (or a least a significant fraction) of SFR at intermediate and high redshifts.

As we have already mentioned, the majority of the IR-based analysis of the SFR are based on the assumption that all the absorbed UV photons are re-processed into the IR, which is often summarized in the widely-used Kennicutt (1998) relation between total IR luminosity (8–1000μm) and SFR. In reality, the situation is a slightly more complicated, and there can be deviations from this hypothesis if for example there are additional sources of dust heating such as obscured AGNs (Daddi et al. 2007ab), or older stellar populations (i.e., not necessarily young OB stars; Cortese et al. 2006, 2008). Nevertheless, this assumption seems to hold for the majority of the source (or at least excluding the most luminous) when sufficiently detailed data is available to fit the IR SED (Symeonidis et al. 2008; Huang et al. 2009; Kartaltepe et al. 2010).

In general, most of the studies at high-z working with mid-to-far IR data make use of dust emission templates to perform the SED fitting (e.g, Chary&Elbaz 2001; Dale&Helou et al. 2002; Siebenmorgen & Krügel 2007; Rieke et al. 2009). These models, although based on similar prescriptions, present slight differences in the treatment of some components (cold and warm dust and PAHs) and thus, similarly to what happen with SPS models, fitting the SED with one or the other results in systematic differences in the inferred SFR (typically of a factor $\sim$2; see e.g., Santini et al. 2009), specially when the fit is performed from very limited data-sets.

Under these circumstances, the advent of the *Spitzer* Space Telescope and other sub-mm and radio surveys (SCUBA, BLAST, VLA, etc; see e.g, Franceschini et al. 2009 for a review) has provided a substantial improvement in the quantity and quality of the IR data, specially for high redshift galaxies. Nevertheless, despite this observational development, the primary source of

uncertainties in the IR measurements is still the lack of data, and more precisely, the limited sensitivity and spatial resolution at longer wavelengths. Whereas Spitzer-MIPS 24μm observations has been extremely successful on characterizing the emission of high redshift sources (Pérez-González et al. 2005, 2008; Huang et al. 2005; Papovich et al. 2006; Rigopoulou et al. 2006), the data at 70μm and 160μm data are frequently limited to the very few most luminous sources, similarly to what happens with sub-mm and radio surveys. In the near future, when *Herschel* data becomes widely available we will be able to fill the gap between *Spitzer* and (sub-)mm/Radio observations with a significant improvement in both depth and resolution (see, e.g., the right panel of Figure 3.4).

As a result, and despite the relatively featureless shape of the FIR emission, it is very difficult to reliably fit the dust emission templates in the full IR range from such few data, which in many cases consist on just one flux measurement. These issues are aggravated by the fact that some measurements are frequently probing the rest-frame MIR which is plagued with prominent features (strong emissions/absorptions PAH at 3-12μm). This is the case for the MIPS-24μm data at z$\gtrsim$1.

In an effort to overcome this problem many time has been devoted to obtain empirical relations between total IR luminosity and monochromatic luminosities at a given wavelength (e.g., Bavouzet et al. 2008; Rieke et al. 2009) or even between monochromatic luminosities and other SFR tracers, such as Hα (Calzetti et al. 2007; Zhu et al. 2008) and Paα (Alonso-Herrero et al. 2006).

3.4 Barro et al. (2011b) ApJS, 193, 30

The Astrophysical Journal Supplement Series, 193:30 (34pp), 2011 April doi:10.1088/0067-0049/193/2/30

UV-TO-FIR ANALYSIS OF *SPITZER*/IRAC SOURCES IN THE EXTENDED GROTH STRIP. II. PHOTOMETRIC REDSHIFTS, STELLAR MASSES, AND STAR FORMATION RATES

G. Barro[1], P. G. Pérez-González[1,5], J. Gallego[1], M. L. N. Ashby[2], M. Kajisawa[3], S. Miyazaki[4], V. Villar[1], T. Yamada[3], and J. Zamorano[1]
[1] Departamento de Astrofísica, Facultad de CC. Físicas, Universidad Complutense de Madrid, E-28040 Madrid, Spain
[2] Harvard-Smithsonian Center for Astrophysics, 60 Garden St., Cambridge, MA 02138, USA
[3] Astronomical Institute, Tohoku University, Aramaki, Aoba, Sendai 9808578, Japan
[4] National Astronomical Observatory of Japan, Mitaka, Tokyo 181-8588, Japan
Received 2010 May 23; accepted 2011 February 19; published 2011 March 31

ABSTRACT

Based on the ultraviolet to far-infrared photometry already compiled and presented in a companion paper (Paper I), we present a detailed spectral energy distribution (SED) analysis of nearly 80,000 IRAC 3.6 + 4.5 μm selected galaxies in the Extended Groth Strip. We estimate photometric redshifts, stellar masses, and star formation rates (SFRs) separately for each galaxy in this large sample. The catalog includes 76,936 sources with $[3.6] \leqslant 23.75$ (85% completeness level of the IRAC survey) over 0.48 deg^2. The typical photometric redshift accuracy is $\Delta z/(1+z) = 0.034$, with a catastrophic outlier fraction of just 2%. We quantify the systematics introduced by the use of different stellar population synthesis libraries and initial mass functions in the calculation of stellar masses. We find systematic offsets ranging from 0.1 to 0.4 dex, with a typical scatter of 0.3 dex. We also provide UV- and IR-based SFRs for all sample galaxies, based on several sets of dust emission templates and SFR indicators. We evaluate the systematic differences and goodness of the different SFR estimations using the deep FIDEL 70 μm data available in the Extended Groth Strip. Typical random uncertainties of the IR-bases SFRs are a factor of two, with non-negligible systematic effects at $z \gtrsim 1.5$ observed when only MIPS 24 μm data are available. All data products (SEDs, postage stamps from imaging data, and different estimations of the photometric redshifts, stellar masses, and SFRs of each galaxy) described in this and the companion paper are publicly available, and they can be accessed through our the Web interface utility *Rainbow-navigator*.

Key words: galaxies: high-redshift – galaxies: photometry – galaxies: starburst – infrared: galaxies

Online-only material: color figures, machine-readable tables

1. INTRODUCTION

Multi-band catalogs are the fuel for studies aimed at exploring the global evolution of galaxies over cosmic history. They have been used to study the redshift evolution of the star formation rate (SFR) density (e.g., Hopkins & Beacom 2006; Reddy et al. 2008; Bouwens et al. 2009), and the stellar mass assembly process (e.g., Bundy et al. 2006; Fontana et al. 2006; Pérez-González et al. 2008; Marchesini et al. 2009).

The unprecedented sensitivity of modern surveys detect millions of distant galaxies to faint flux levels that for all practical purposes lie well beyond the capabilities of even the most recent multi-object spectrographs at the largest telescopes. As a consequence, their intrinsic properties must be estimated through multi-band photometric data using fitting techniques to stellar population templates, and/or empirical relations. Among the basic parameters needed to characterize a galaxy, arguably the most important is the redshift, which must be inferred from an analysis of its spectral energy distribution (SED). Photometric redshift techniques are now sufficiently accurate to derive statistically reliable conclusions for high-redshift galaxy populations (e.g., Silva et al. 1998; Wolf et al. 2003; Ilbert et al. 2009).

Many different codes have been developed to calculate photometric redshifts based in the same principle: finding the galaxy spectral template best fitting the observed photometry in several band-passes. Some examples include HYPERZ (Bolzonella et al. 2000), BPZ (Benítez 2000), or LePHARE (e.g., Arnouts & Ilbert; Ilbert et al. 2009). The implementation is very sensitive to the quality of the photometry and the capability of the observed bands to probe key continuum features of the spectra (e.g., the Lyman and Balmer breaks). It also depends strongly on the availability of templates that are statistically representative and successful in characterizing the emission of galaxies. The impact of these factors in the uncertainty of the estimations is not straightforward, and it can lead to catastrophic errors beyond the simple propagation of the statistical errors (Oyaizu et al. 2008; Hildebrandt et al. 2008). In recent years, several techniques have been developed to improve the reliability of the photometric redshifts (e.g., Bayesian priors (Benítez 2000), template-optimization procedures (Ilbert et al. 2006a), and machine-learning neural networks (Collister & Lahav 2004)). Recent work including some of these advances have achieved remarkable precision [e.g., $\Delta z/(1+z) < 0.012$ in Ilbert et al. 2009, and $\Delta z/(1+z) = 0.06$ at $z > 1.5$ in van Dokkum et al. 2009].

Once a galaxy's redshift has been estimated, the most significant physical properties that can then be derived from multi-wavelength photometry are the stellar mass and the SFR. However, estimates derived from modeling of the observed SEDs involve significant random and systematic uncertainties. The estimate of the stellar mass by fitting stellar population synthesis (SPS) models is a widespread technique (e.g., Bell et al. 2003; Panter et al. 2007; Walcher et al. 2008) that requires making some assumptions regarding the initial stellar mass function, the star formation history, or the extinction law. Moreover, there

[5] Associate Astronomer at Steward Observatory, The University of Arizona, USA.

exist significant differences among stellar population libraries. These differences can lead to discrepancies in the stellar mass estimation of a factor of a few (Maraston et al. 2006; Bruzual 2007).

SFR estimates based on UV and/or IR luminosities are considered reasonably robust for large galaxy samples with multi-wavelength photometry, where other tracers, such as spectroscopy, are unavailable (Reddy et al. 2006; Salim et al. 2007; Daddi et al. 2007). A major problem with SFRs estimated from UV data is the need for a extinction correction, which can be highly uncertain and redshift dependent (Iglesias-Páramo et al. 2007; Burgarella et al. 2007; Salim et al. 2009). On the other hand, IR-based SFRs estimated by fitting the MIR-to-mm fluxes with dust emission templates are model dependent (Papovich & Bell 2002; Dale et al. 2005; Caputi et al. 2006). Furthermore, these tracers are based on the assumption that the bulk of the IR emission traces warm dust heated by young star-forming regions. Thus, if a fraction of the energy heating the dust originates from an alternative source, such as deeply dust enshrouded active galactic nuclei (AGNs) or diffuse radiation fields (Daddi et al. 2007; Salim et al. 2009) the SFR will be overestimated. Nevertheless, despite these second-order effects, the uncertainties in the SFR are frequently driven by the absence of sufficient IR photometry to constrain the models robustly. In the last few years, the studies of SFRs at high redshift have often been based on the observed flux at MIPS 24 μm only and, although IR monochromatic luminosities are known to correlate well to total IR luminosity, recent works based on more detailed IR coverage have demonstrated that SFRs from MIPS 24 μm data may present significant systematics (Papovich et al. 2007; Daddi et al. 2007; Rigby et al. 2008).

In this context, Barro et al. (2011, hereafter Paper I) presented a multi-band photometric and spectroscopic catalog (including data from X-ray to radio wavelengths) in the Extended Groth Strip (EGS) that can be used as a starting point for detailed analysis of the galaxy population. That paper describes the method used to measure coherent multi-band photometry and presents the general properties of the merged catalog, including an analysis of the quality and reliability of the photometry. Paper I also presents *Rainbow Navigator*, a publicly available Web interface that provides access to all the multi-band data products.

In this paper, we focus on fitting the optical-to-NIR SEDs and IR emission of all the sources presented in Paper I using SPS models and dust emission templates. We then use the SEDs and fits to estimated photometric redshifts, stellar masses, and SFRs. We also quantify the uncertainties attending these estimations. In particular, we assess the quality of the photometric redshifts by comparing our results with spectroscopic redshifts and with other photometric redshift compilations found in the literature. We explore the systematic uncertainties in the stellar masses associated with the modeling assumptions, such as the choice of SPS models or the initial mass function (IMF). Finally, we study the systematic uncertainties in the IR-based SFRs estimated with different IR templates and indicators (e.g., different total IR luminosity-to-SFR calibrations).

The outline of this paper is as follows. Section 2 briefly reviews the available data and then summarizes the most relevant steps of the photometric measurement and band-merging procedure (presented in Paper I), as well as the overall photometric properties of the IRAC 3.6 + 4.5 μm selected catalog. Section 3 describes the techniques developed to perform the UV-to-IR SED fitting, and the methods used to estimate

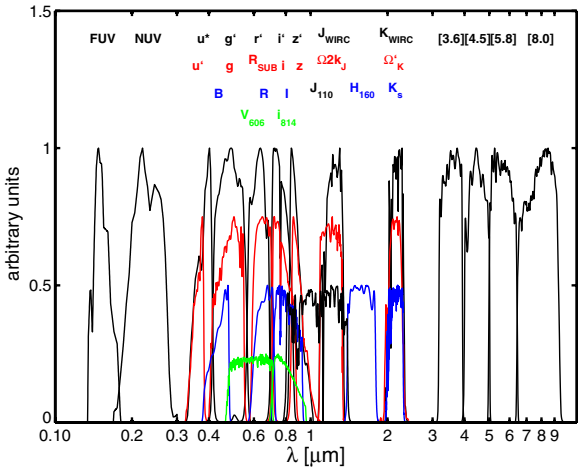

Figure 1. Filter transmission for the photometric bands included in the data set. The curves include the atmospheric transmission (for ground-based observations), quantum efficiency, and the transmission of the optical elements. The curves are normalized at the maximum value of the transmission and scaled arbitrarily for visualization. The color code for each filter corresponds to the labels shown above. The optical bands depicted from top to bottom are those of CFHTLS, MMT, and CFHT12k, respectively. The NIR bands, also shown from top-to-bottom are those of WIRC, CAHA, and *HST*/NICMOS. The *GALEX* (FUV, NUV) and IRAC ([3.6], [4.5], [5.8], [8.0]) filters are also listed in the top row.

(A color version of this figure is available in the online journal.)

redshifts. Section 4 describes the stellar masses estimation technique, and quantifies the uncertainties introduced by the modeling assumptions. Section 5 describes the methods used to fit the FIR emission to dust emission templates and the estimation of IR luminosities and SFRs. Section 6 presents tables containing all the data products presented in this paper, as well as the public database created to facilitate the access to these resources.

Throughout this paper we use AB magnitudes. We adopt the cosmology $H_0 = 70$ km^{-1} s^{-1} Mpc^{-1}, $\Omega_m = 0.3$, and $\Omega_\lambda = 0.7$. Our default choice of SED modeling parameters are the PEGASE (Fioc & Rocca-Volmerange 1997) library, a Salpeter (1955) IMF ($M \in [0.1\text{–}100]\ M_\odot$), and a Calzetti et al. (2000) extinction law.

2. MULTI-WAVELENGTH CATALOG

The present work is based on the multi-wavelength catalog of IRAC 3.6 + 4.5 μm selected galaxies in the EGS ($\alpha = 14^h14^m$, $\delta = +53°30'$) presented in Paper I. The catalog contains all the publicly available data provided by the All-Wavelength Extended Groth Strip International Survey (AEGIS) collaboration and some proprietary data including the following bands: *GALEX*, FUV, and NUV, CFHTLS $u^*g'r'i'z'$, MMT-$u'giz$, CFHT12k BRI, ACS $V_{606}i_{814}$, Subaru R, NICMOS $J_{110}H_{160}$, MOIRCS K_s, CAHA-JK_s, WIRC JK, the four IRAC bands at 3.6, 4.5, 5.8, and 8.0 μm, and lastly MIPS 24 and 70 μm. We cross-correlated our IRAC-selected catalog with the X-ray (*Chandra*) and radio (VLA/20 cm) catalogs of Laird et al. (2009) and Ivison et al. (2007), and with all the spectroscopic redshifts from DEEP2 DR3 and a small sample of 238 spectroscopically confirmed Lyman break galaxies (LBGs) from Steidel et al. (2003). The reader is referred to Paper I and Davis et al. 2007, and references therein, for a detailed description of all these data sets. Figure 1 illustrates the different

Table 1
Photometric Properties of the Data set

Filter (1)	$\lambda_{\rm eff}$ (2)	$m_{\rm lim}$[AB] (3)	FWHM (4)	Gal. Ext (5)	Offset (6)
GALEX–FUV	153.9 nm	25.6	5.″5	0.195	0.04
GALEX–NUV	231.6 nm	25.6	5.″5	0.101	0.08
MMT-u	362.5 nm	26.1	1.″0	0.049	−0.09
CFHTLS-u^*	381.1 nm	25.7	0.″9	0.045	−0.04
CFHT-B	439.0 nm	25.7	1.″2	0.036	0.04
MMT-g	481.4 nm	26.7	1.″3	0.031	−0.09
CFHTLS-g'	486.3 nm	26.5	0.″9	0.031	0.03
ACS-V_{606}	591.3 nm	26.1	0.″2	0.022	0.02
CFHTLS-r'	625.8 nm	26.3	0.″8	0.020	0.03
Subaru-R	651.8 nm	26.1	0.″7	0.019	0.00
CFHT-R	660.1 nm	25.3	1.″0	0.019	−0.03
CFHTLS-i'	769.0 nm	25.9	0.″8	0.015	0.03
MMT-i	781.5 nm	25.3	1.″0	0.015	0.00
ACS-i_{814}	813.2 nm	26.1	0.″2	0.014	0.00
CFHT-I	833.0 nm	24.9	1.″1	0.013	0.02
CFHTLS-z'	887.1 nm	24.7	0.″8	0.012	−0.02
MMT-z	907.0 nm	25.3	1.″2	0.011	−0.11
NICMOS-J_{110}	1.10 μm	23.5	0.″7	0.008	0.00
$\Omega 2k-J$	1.21 μm	22.9	1.″0	0.007	−0.16
WIRC-J[a]	1.24 μm	21.9	1.″0	0.007	0.01
NICMOS-H_{160}	1.59 μm	24.2	0.″8	0.005	0.00
$\Omega'-K$	2.11 μm	20.7	1.″5	0.003	−0.10
Subaru-MOIRCS-Ks	2.15 μm	23.7	0.″6	0.003	−0.04
WIRC-K[a]	2.16 μm	22.9	1.″0	0.003	0.00
IRAC-36	3.6 μm	23.7	2.″1	0.001	0.00
IRAC-45	4.5 μm	23.7	2.″1	0.001	0.00
IRAC-58	5.8 μm	22.1	2.″2	0.001	0.12
IRAC-80	8.0 μm	22.1	2.″2	0.000	0.12

Notes.
[a] The photometry was not measured, but taken from a published catalog.
Column 1: name of the observing band and instrument.
Column 2: effective wavelength of the filter calculated by convolving the Vega spectrum (Colina & Bohlin 1994) with the transmission curve of the filter+detector.
Column 3: limiting AB magnitude of the image estimated as the magnitude of a SNR = 5 detection (see Section 2.1 for details on the flux measurement).
Column 4: median FWHM of the PSF in arcseconds measured in a large number of stars (see Section 5.4 of Paper I for details on the stellarity criteria).
Column 5: galactic extinction estimated from the Schlegel et al. (1998) maps and assuming and average value of $E(B-V)=0.004$.
Column 6: zero-point corrections applied to the photometric bands, computed by comparing observed and synthetic magnitudes for spectroscopic galaxies (see Section 3.3).

filter transmission profiles for each band, and Table 1 presents the effective filter wavelengths, the survey depths, and image quality achieved in each band, and the (small) zero-point re-calibrations (Section 3.3).

The photometric coverage of the EGS is largely inhomogeneous, with each band covering a different portion of the IRAC mosaic (Davis et al. 2007). Fortunately, there is a natural way to divide the field into two smaller sub-regions. The main region, defined by the overlapping area of the CFHTLS and IRAC frames (0.35 deg^2), presents the densest coverage (∼19 bands, including *GALEX*, *Hubble Space Telescope* (*HST*), and MOIRCS). This region is essentially a field with the side edges following the contours of the IRAC image, i.e., inclined by 50° east of north, and upper and lower boundaries limited by $52.^\circ16 < \delta < 53.^\circ20$. The bottom-right side is also restricted to $\alpha > 214.^\circ04$ due to the intersection with the CFHTLS mosaic (a square field oriented north up, east left).

The 0.13 deg^2 outside of the main region (hereafter referred to as flanking regions) also have solid optical-to-NIR coverage. However, the overall data quality is slightly lower than in the main region. The median coverage includes only 11 bands, and for the most part lacks the deepest, highest-resolution imaging. As a result, the quality of the SED coverage in the flanking regions is significantly lower than in the main region. For these reasons we focus in this contribution on the main region.

2.1. Multi-band Identification and Photometry

The procedure followed to build consistent UV-to-FIR SEDs from the multiple data sets is described in detail in Paper I (see also Pérez-González et al. 2005 and Pérez-González et al. 2008, hereafter PG05 and PG08). This section summarizes the most relevant elements of the method, so that the impact of the photometric uncertainties on the parameters estimated from the SED modeling can be assessed (Sections 4 and 5).

First, multi-band identification is carried out by cross-correlating the 3.6 + 4.5 μm selection with all other optical/NIR catalogs (pre-computed with SExtractor; Bertin & Arnouts 1996) using a 2″ search radius. The MIPS, Radio, and X-ray catalogs required a different approach. For the MIPS and radio catalogs we used a 2.″5 and 3″ matching radius, respectively. For the X-ray catalog we used a 1″or 2″ radius depending on whether the X-ray sources were pre-identified in any other band (Laird et al. 2009). When two or more optical/NIR counterparts separated by >1″ (approximately half the FWHM in IRAC-3.6) are identified within the search radius, we apply a de-blending procedure to incorporate the multiple sources in the catalog (e.g., irac070100 would become irac070100_1 and irac070100_2). Roughly 10% of the IRAC sources present two or more counterparts in the ground-based images.

Once the sources are identified, the photometry was computed separately in all bands, to properly account for the significant differences in spatial resolution. The fluxes were then combined to derive the merged SED. The procedure is carried out using our custom software *Rainbow* based on the photometric apertures obtained from a previous SExtractor run.

For the optical and NIR bands, total fluxes were estimated using Kron (1980) elliptical apertures. The properties of the aperture are the same in all bands (although different between objects) and are defined from a *reference* image, which is chosen by sorting the bands according to depth and picking the first band with a counterpart positive detection. Thus, this image is usually among the deepest, and presents a spatial resolution representative of the entire data set (typically SUBARU-R or CFHTL-i'). Nevertheless, as a precaution, we established a minimum aperture size equal to the coarsest seeing in all bands (1.″5). Although the choice of reference band depends on the cross-identification, the flux is measured in all bands independently of the counterpart detection. If a source is detected by IRAC only (i.e., there is no optical/NIR reference image), we use a fixed circular aperture of minimum size. If the source is detected in just a few optical/NIR bands (e.g., it is detected in r but not in z) we still use the reference aperture in the un-detected bands. In this way, we recover fluxes for very faint sources not detected by SExtractor. If the forced measurements do not return a positive flux, the background flux from the sky rms within the aperture instead. These non-detections were not used for the subsequent SED fitting procedure.

The IRAC photometry was computed using circular apertures of 2″ radius and applying an aperture corrections estimated from empirical point-spread function (PSF) growth curves. The

measurement is carried our simultaneously in the four IRAC channels, using the 3.6 + 4.5 μm positions as priors for the 5.8 and 8.0 μm bands, which are much less sensitive. In the case of blended IRAC sources (i.e., those with multiple optical/NIR counterparts), we recomputed the photometry applying a deconvolution method similar to that used in Grazian et al. (2006a) or Wuyts et al. (2008), which essentially relies in using smaller 0.″9 radius apertures with larger aperture corrections. Paper I describes the accuracy of the deblending technique. For the *GALEX* (FUV, NUV) bands we drawn the photometry from the source catalog of the public data release GR3. This is computed with aperture photometry based on SExtractor (Morrissey et al. 2007). For the IRAC sources missed in this catalog (only ∼8% and 25% of the IRAC catalog is detected in the FUV and NUV bands, respectively; see Table 4 of Paper I) we used the forced measurement method described above. The photometry in the MIPS (24 μm, 70 μm) bands was carried out using PSF fitting with IRAF–DAOPHOT and aperture corrections (see PG05 and PG08 for more details).

The photometric uncertainties were computed simultaneously with the flux measurement. Although the *Rainbow* measurements are SExtractor-based, the SExtractor photometric errors were not used, because these are often underestimated due to correlated signal in adjacent pixels (Labbé et al. 2003; Gawiser et al. 2006). Instead, we used three different approach that range from a SExtractor-like method to a procedure similar to that described in Labbé et al. (2003, i.e., measuring the sky rms in empty photometric apertures at multiple positions). The photometric uncertainty was set to the largest value thereby derived.

The final multi-wavelength catalog contains 76,493 and 112,428 sources with [3.6] < 23.75 mag and [3.6] < 24.75 mag, respectively (these magnitude cuts correspond to the 85% and 75% completeness levels of the IRAC mosaics). Approximately 68% of the sources are located in the main region (52,453; [3.6] < 23.75). Spectroscopic redshifts have been assigned to 10% of the sample (only 120 are at $z > 1.5$). A total of 2913 stars have been identified based on several optical/NIR color criteria (see Section 5.4 of Paper I). A source was identified as a star only if three or more criteria were satisfied. The stellarity value (as the total number of criteria satisfied) is given in Table 7 (see Section 6). The fractions of IRAC sources detected at 24 μm and 70 μm are 20% and 2%, respectively. Finally, a total of 990 and 590 sources are detected in the X-ray and radio catalogs of Laird et al. (2009) and Ivison et al. (2007), respectively.

In the following, we analyze the SEDs and physical properties of the IRAC sources with [3.6] < 23.75 mag (typically SNR $\gtrsim$ 10). Nevertheless, the catalog contains sources up to [3.6] < 24.75 (3σ limiting magnitude). The complete catalog is available in the online version of the journal or through our Web interface *Rainbow navigator* (see Paper I for more details).

2.2. Galactic Extinction

The EGS field lies at high galactic latitude benefiting from low extinction and low galactic/zodiacal infrared emission. We derive an average $E(B-V) = 0.004$ based on the maps of Schlegel et al. (1998) based on several positions evenly spaced along the strip, centered at $\alpha = 241.^{\circ}80$, $\delta = 52.^{\circ}80$. In our analysis, a differential galactic extinction for each band is computed assuming a Cardelli et al. (1989) curve with $R = 3.1$. These corrections, summarized in Table 1, are not included in the photometric catalog (presented in Paper I) but these are applied before applying the SED fitting procedure.

3. SED ANALYSIS: PHOTOMETRIC REDSHIFTS

3.1. Rainbow Code

We computed photometric redshifts for all IRAC sources from the multi-color catalog presented in Paper I using our own dedicated template fitting code (*Rainbow* software hereafter; see PG05 and PG08). The program creates a grid of redshifted galaxy templates in steps of $\delta z = 0.01$ and then applies a χ^2 minimization algorithm to find the template best fitting the multi-band photometry. Upper limit detections and fluxes with uncertainties larger than 0.5 mag are not included in the fit. The χ^2 definition takes into account the flux uncertainties of each band, being defined as

$$\chi^2 = \sum_{i=0}^{N(\mathrm{band})} \left[\frac{F_{\mathrm{obs},i} - A \cdot F_{\mathrm{temp},i}}{\sigma_i} \right]^2, \quad (1)$$

where $F_{\mathrm{obs,i}}$ is the observed flux in the i filter and σ_i is its uncertainty, $F_{\mathrm{temp,i}}$ is the flux of the redshifted template in the i filter (obtained by convolving the template with the filter transmission curve). A scaling factor is applied to the input template to fit the observed photometry. This normalization parameter A is used to compute quantities such as the stellar masses, absolute magnitudes, or SFRs (see Sections 4.1 and 5.2).

Prior to the χ^2 minimization procedure, the *Rainbow* code gets rid of deviant and redundant photometric data points. The fluxes presenting a very steep gradient with respect to the surrounding bands are flagged and removed before attempting the final fit.

By analyzing the $\chi^2(z)$ distribution of the best fit in the model grid, we built the redshift probability distribution function (zPDF), from which we computed the most probable redshift and 1σ errors, z_{best} and σ_z. The single value that minimizes $\chi^2(z)$ is z_{peak}. We found that z_{best} provided the most accurate results presenting less outliers and a smaller scatter when compared with spectroscopic redshifts. The uncertainties in the photometric redshifts are used to compute the uncertainties in the stellar parameters derived from the best-fitting template.

The *Rainbow* code also analyzes the dust emission on sources with at least one flux measurement beyond rest-frame 8 μm, i.e., the MIPS 24 and 70 μm bands (see Section 5.2). Figure 2 shows the combined optical and IR SED along with the estimated physical parameters for a galaxy at $z \sim 1$ as an example of the optical and IR fitting techniques described here and in Section 5.2. The best-fit optical template to the data was used to estimate the photometric redshift, stellar mass (see Sections 3 and 4), and also the rest-frame UV flux. Moreover, IR luminosities and SFRs were obtained from the best-fit IR template to the data at rest-frame $\lambda > 5$ μm (see Section 5.1).

3.2. Stellar Population Templates

The stellar templates used by the minimization code are extracted from a library of synthetic templates built by fitting SPS and dust emission models to a representative sample of galaxies at different redshifts. This reference sample is drawn from the GOODS-N and GOODS-S IRAC surveys and have highly reliable spectroscopically confirmed redshifts ($0 < z < 3$) and at least 10 measurements of the SEDs from the UV to the MIR. A detailed description on the modeling of these templates is given in PG08. Here, we briefly summarized their most relevant characteristics.

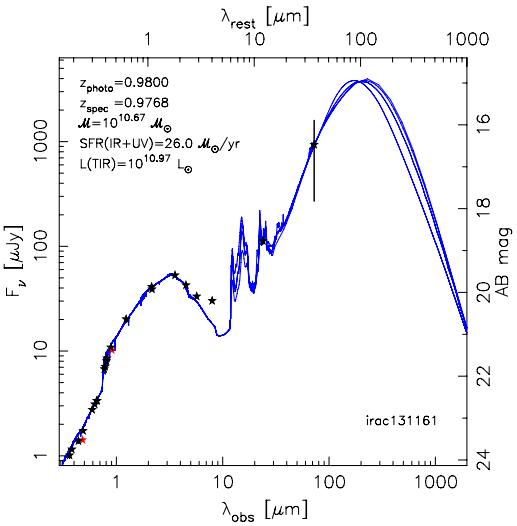

Figure 2. Example of the full Spectral Energy Distribution (SED) of a galaxy in our sample (black dots), and fit (blue lines) of the observed UV-to-MIR photometry to a set of empirical templates computed from PEGASE 2.0 models (Fioc & Rocca-Volmerange 1997) assuming a Salpeter IMF ($M \in [0.1\text{–}100]M_o$), and Calzetti et al. (2000) extinction law (see Section 3), and the FIR photometry (MIPS 24 and 70 μm) to dust emission models of Chary & Elbaz (2001), Dale & Helou (2002), and Rieke et al. (2009; see Section 5.1). The multiple lines in the FIR region correspond to best-fitting template from each of the dust emission models, and the average value of the three. In the upper left corner, we indicate the photometric redshift, and the stellar mass, IR-based SFR, and total IR luminosity estimated from fitting procedure.

(A color version of this figure is available in the online journal.)

The stellar emission of the reference template set was characterized using the PEGASE 2.0 models (Fioc & Rocca-Volmerange 1997) assuming a Salpeter IMF ($M \in [0.1\text{–}100]M_o$) and Calzetti et al. (2000) extinction law. We also considered the contribution from emission lines and the nebular continuum emitted by ionized gas. The models were obtained assuming a single population (1-POP models), characterized by an exponential star formation law. As a result, each template is characterized by four parameters in the 1-POP case, namely, the time scale τ, age t, metallicity z, and dust attenuation A(V). The MIR/FIR region of some templates includes a contribution from a hot dust component that was computed from dust emission models using a similar procedure to that described in Section 5.1 of this paper.

Defining a representative spectral library is a critical issue for photometric redshift codes, specially when NIR-selected samples are studied (Kriek et al. 2008). The reference sample should span a wide range of redshifts and galaxy colors that probe the parameter space of the magnitude limited sample in sufficient detail. This is why we included in the template set a few $z > 1.5$ galaxies which could not be fitted accurately with low-z templates. Furthermore, we complemented our synthetic templates with QSO and AGN empirical templates drawn from Polletta et al. (2007) that account for the galaxy population whose UV-to-NIR emission is not dominated by stars but by an AGN (see, e.g., Assef et al. 2010).

The template library contains a total of 1876 semi-empirical templates (see PG08 for more details and examples of the SEDs) spanning a wide range of colors and physical parameters. Figure 3 shows that the loci of the observed and template colors present an overall good agreement for the majority of the spectroscopic galaxies in a wide range of optical and NIR colors. The combination of colors based on the CFHTLS filters (Panels 1–4) is consistent with Figure 2 of Ilbert et al. (2006a) that presents the same colors for a sub-sample of i-band selected galaxies in the CFHTLS-D1 field.

On the other hand, we find small discrepancies between templates and observations in the [3.6]–[4.5] IRAC color at low redshift (Figure 3, Panel 6). This is not surprising considering that these bands are probing the rest-frame NIR (see, e.g., Huang et al. 2004; Brodwin et al. 2006 for similar examples), a wavelength region where the predictions from SPS models tend to be more uncertain (Maraston 2005). Furthermore, these differences tend to increase at $\lambda \gtrsim 3\,\mu$m rest-frame, where galaxies can exhibit a significant contribution from hot dust or polycyclic aromatic hydrocarbon (PAH) emission features that are not contemplated in the optical templates and therefore require more complicated modeling procedures (Magnelli et al. 2008; Mentuch et al. 2009).

3.3. Zero-point Corrections and Template Error Function

An improvement introduced in the current work on EGS over the previous *Rainbow* photometric redshifts in GOODS-N, GOODS-S, and Lockman Hole (PG05, PG08) is the fine-tuning of the photometric zero points and the use of a template error function. Both procedures are based on the comparison of the observed fluxes to synthetic photometry derived from the convolution of the filter transmission curves with the best-fitting templates for the galaxies with reliable spectroscopic redshifts. As demonstrated by Brodwin et al. (2006), Ilbert et al. (2006a), and Ilbert et al. (2009), the comparison between the observed apparent magnitudes and synthetic fluxes often shows small offsets that can lead to systematic errors in the calculation of the photometric redshifts. These offsets can be the result of small systematic errors in the absolute calibration, uncertainties in the filter transmission curves, or they can be the result of intrinsic limitations of the templates in reproducing the observed SEDs (Brammer et al. 2008).

To tackle these issues and improve the photometric redshift estimation, we fit the SEDs of the galaxies with secure spectroscopic redshift to our template set fixing the photometric redshift to the spectroscopic value. Then, we compute the difference between the observed fluxes and the template fluxes for each band, and we consider this residual value as a function of the rest-frame wavelength. The left panel of Figure 4 shows the result of applying this process to the sub-sample of galaxies with spectroscopic redshift and photometric fluxes with SNR > 5 in the main region. The median of the residuals (thick green line) shows an overall good agreement between templates and observations, with an rms (thin green lines) of $\sim$2 times the median value of the photometric uncertainty across all the wavelength range (red lines). However, significant deviations appear in the rest-frame wavelengths around 200 nm, the 500–1000 nm region, and the mid-IR ($\lambda > 3\,\mu$m).

To diminish the effect of these discrepancies, we considered two corrections: (1) we applied small calibration offsets in each band based on the residuals of the comparison with synthetic magnitudes (note that these corrections refer to observed wavelengths) and (2) we used a template error function such as that introduced in Brammer et al. (2008).

Figure 5 shows the comparison between observed and synthetic magnitudes for three different i-bands (ACS, CFHTLS, and MMT; left panel) and the $u*$, z', J, and K bands (from MMT, WIRC, and MOIRCS; right panel) as a function of redshift. The values in the parenthesis quote the median correction applied to

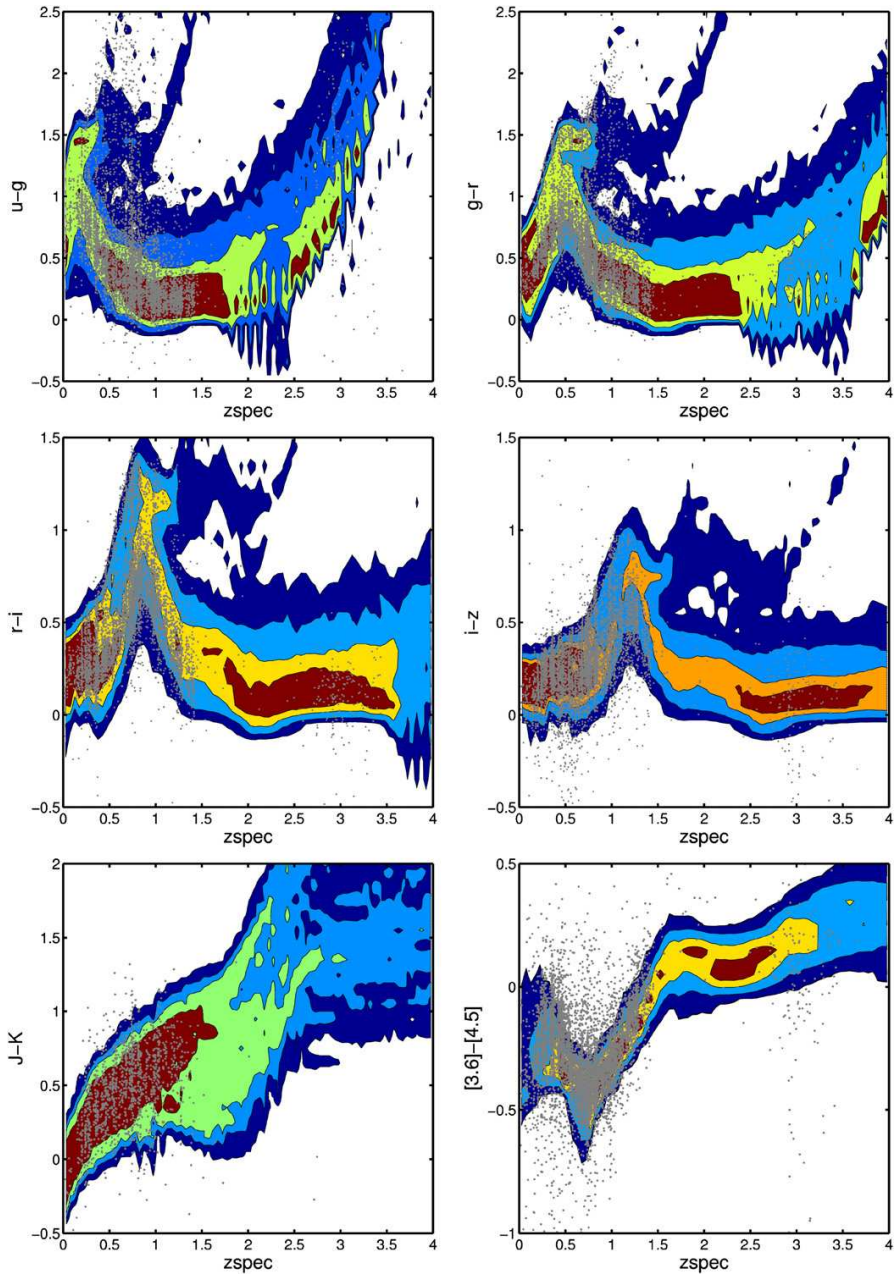

Figure 3. Comparison of different optical and NIR observed colors as a function of the spectroscopic redshift (gray dots) vs. the predicted colors for our 1876 galaxy templates (density map). Each density contour contains (from inside out) 25%, 50%, 75%, and 90% of the values.

each band to minimize the differences with respect to the synthetic fluxes. Note that the three *i*-bands present a similar trend at $z \gtrsim 1$, where the observations are slightly brighter than the predictions from the templates. This suggest that the feature is related to the templates and not to the absolute calibration of the bands. At $z \gtrsim 1$ the *i*-band ($\lambda_{\rm eff} \sim 800$ nm) probes rest-frame wavelengths around ∼300–400 nm, where the overall quality of the fit to templates is reduced.

The overall shape of the residual distribution, shown in the left panel of Figure 4, is very effective for identifying systematic deviations in the templates. This is because small zero-point errors in any of the individual bands are smoothed over the rest-frame wavelength range due to the mixed contribution from multiple bands. Therefore, based on the overall scatter in the residual with respect to the median photometric errors, we can compute a template error function that parameterizes the overall uncertainties in the templates as a function of wavelength. As demonstrated by Brammer et al. (2008), this function can be efficiently used as a weight term in the χ^2 function of the SED fitting procedure to minimize the impact of the template

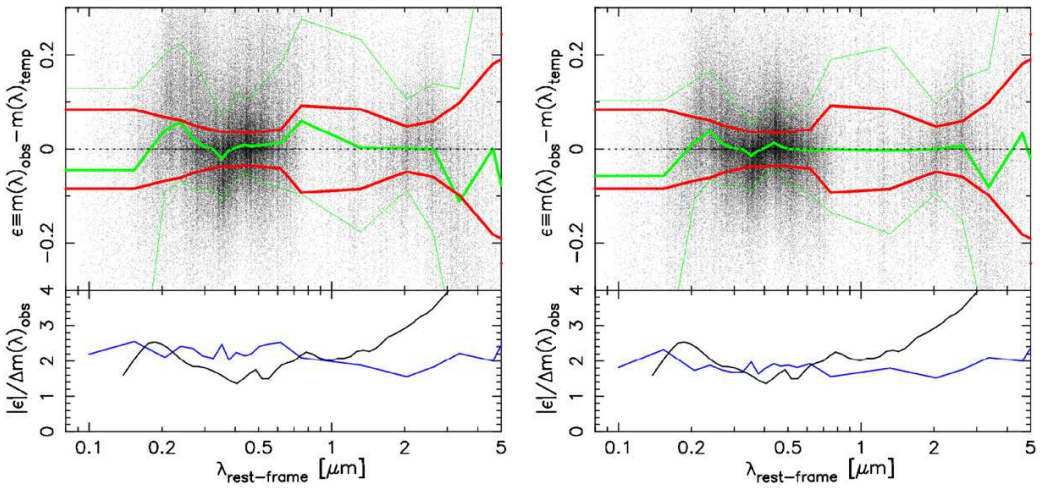

Figure 4. Top: residuals of the comparison between observed and synthetic magnitudes for a sub-sample of galaxies with spectroscopic redshift and SNR > 5 photometry in the main region. The residuals are shifted into rest-frame wavelengths based on the effective wavelength of the filters and the redshift. The figure on the left shows the raw residuals before applying the zero-point corrections nor the template error function to the fitting procedure. The figure on the right shows the final result of the iterative process to compute the zero-point corrections and the template error function. The thick green line depicts the median value of the residuals per redshift bin. The upper and lower red lines indicate the median value of the photometric error at each redshift. The upper and lower thin green lines encompasses 68% (1σ) of the residual distribution around the median value. Bottom: the blue line depicts the median absolute value of the residuals in the top panel divided by the photometric error and by 0.67 to scale the median (50%) to a 1σ(68%) confidence interval. The black line shows the template error function of Brammer et al. (2008) divided by the median photometric error (adapted from Figure 3 of their paper).

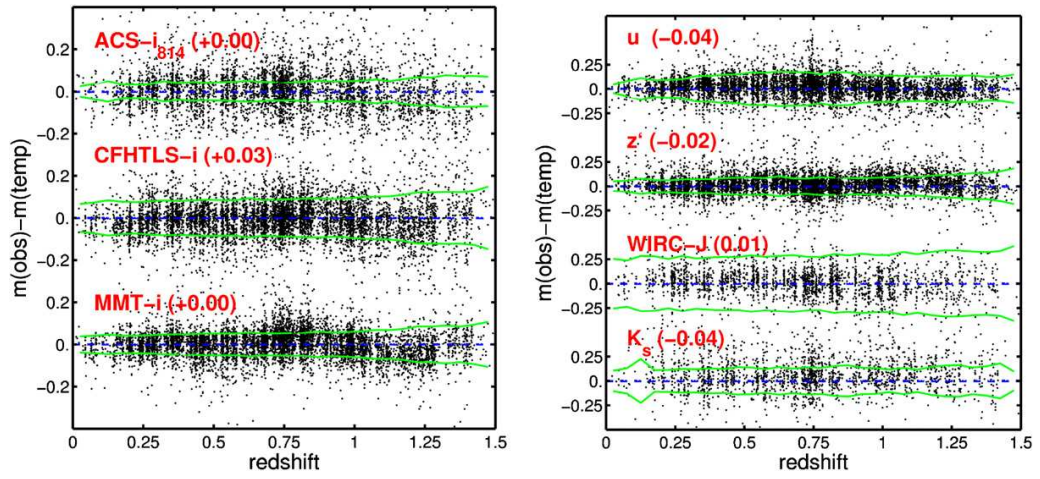

Figure 5. Left:differences between observed and synthetic magnitudes as a function of redshift in the ACS-i_{814}, CFHTLS-i', and MMT-i bands. The values quoted in the parenthesis indicate the zero-point correction applied to these bands. The dashed blue line depicts the median difference between observed and synthetic photometry after the zero-point correction has been applied. The green lines show the median photometric uncertainty in each band as a function of redshift multiplied by a factor two. At $z \sim 1$ the residuals are dominated by a systematic offset in the templates instead of deviations in the photometric calibration. Right: Same as the left panel for the MMT-u^*, MMT-z', WIRC-J, and MOIRCS-K_s bands.

uncertainties in some wavelength ranges. The bottom of the right panel of Figure 4 shows the median value of the absolute difference between observed and template fluxes divided by the photometric error and multiplied by 0.67 to scale the median (50%) to a 1σ(68%) confidence interval, as done in Brammer et al. (2008). Compared to the results of this work our combination of templates and filters present a slightly better agreement in the rest-frame UV and NIR (between 1 and 2 μm), probably as a result of our larger template set, which present more diversity in their spectral shapes.

In principle, the zero-point corrections and the effects of the template error function produce similar effects. Moreover, the re-calibration of adjacent (sometimes very similar) bands tend to modify the residual of both fits. Therefore, in order to obtain consistent results, both the template error function and the zero-point corrections are computed iteratively repeating the fitting process until we obtain variations smaller than 1%–2% (typically after a couple of iterations). The zero-point offsets are summarized in Table 1. Virtually all of the corrections are smaller than 0.1 mag, and some of them are exactly zero. The final results of the procedure are shown in the right panel of Figure 4. The application of the zero-point offsets results in the flattening of the median difference between observed and template magnitudes for the whole wavelength range in our

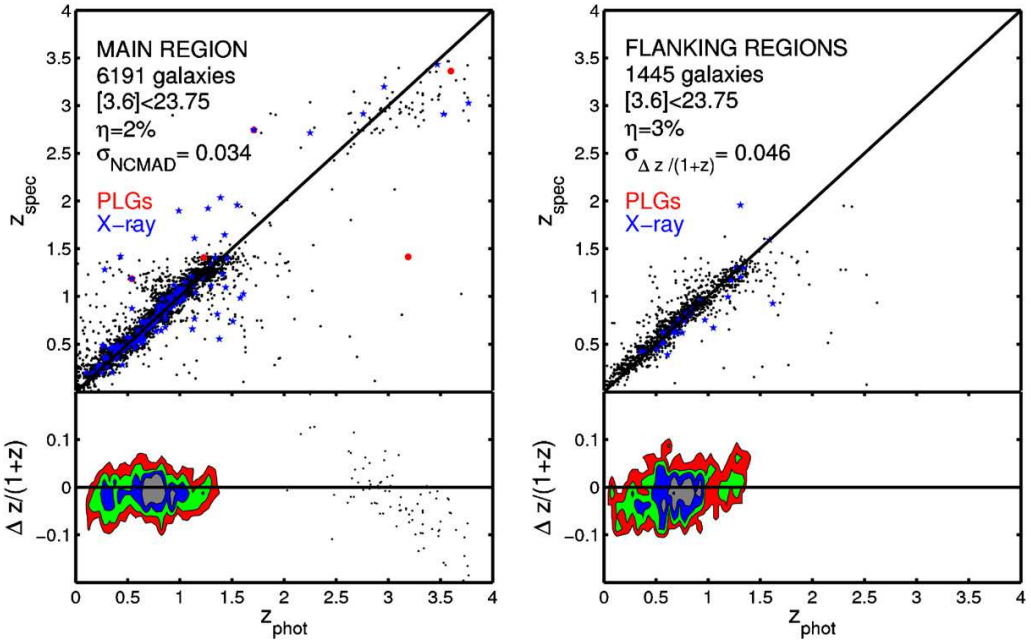

Figure 6. Top panels: photometric redshifts vs. spectroscopic redshifts for [3.6] < 23.75 mag sources in the main region (left) and flanking regions (right). Blue stars indicate sources detected in the X-ray catalog of Laird et al. (2009). Red dots correspond to galaxies with a power-law spectrum in the IRAC bands. This feature is frequently used to identify obscured AGNs (Alonso-Herrero et al. 2004; Donley et al. 2007) that usually underperform in the photometric redshift procedure. Bottom plots: density plots of the scatter in $\Delta z/(1+z)$ as a function of redshift for the main region (left) and flanking regions (right). Each contour contains (from the inside out) 25%, 50%, 75%, and 90% of the spectroscopic sample, respectively.

SEDs except in two regions, one around 200 nm and the other at ∼3 μm.

The poor agreement at 3 μm is most probably associated with limitations in the NIR–MIR range of stellar population templates and the contribution from PAH emission, which is also not properly taken into account in the SPS models nor the dust emission templates. In addition, there is a small peak/bump at ∼350–450 nm, which is very similar to the feature reported by Wild et al. (2007) and Walcher et al. (2008). In these papers, they explain this effect with an excess in the strength of the Balmer break in the models by Bruzual & Charlot (2003), relative to the observed values. The peak at 200 nm can be partly related with the use of a Calzetti et al. (2000) extinction curve in the modeling of the galaxy templates. This parameterization lacks the silicate absorption at 2175 Å, which appears in other extinction curves, such as that of Cardelli et al. (1989), which has been claimed to be produced by PAHs. The presence of this absorption bump has been reported on some studies of high-z galaxies (Noll et al. 2007; Noterdaeme et al. 2009).

As an additional check of the accuracy of the method we compare our photometry against the fluxes of a control sample of ∼300 bright unsaturated stars in common with the SDSS. In particular, we restrict the comparison to relatively blue sources ($u' - g = 1.2$, in the MMT bands) in order to avoid large color corrections in the filter transformations. These color terms were computed by convolving the filter transmissions with the spectra of F, G, and K class stars (Kurucz 1992), which makes up for most of our sample of stars. The transformation with respect to the MMT bands, which present a filter system similar to that of SDSS, are

$$u_{\rm MMT} = u_{\rm SDSS} - 0.095 \cdot [u - g]_{\rm SDSS} + 0.070$$
$$g_{\rm MMT} = g_{\rm SDSS} - 0.063 \cdot [g - i]_{\rm SDSS}$$
$$i_{\rm MMT} = i_{\rm SDSS} - 0.203 \cdot [i - z]_{\rm SDSS} - 0.002$$
$$z_{\rm MMT} = z_{\rm SDSS} - 0.087 \cdot [i - z]_{\rm SDSS} - 0.002.$$

After applying these corrections, we find zero-point offsets of $\Delta u' = -0.05$, $\Delta g = -0.10$, $\Delta i = -0.01$, and $\Delta z = -0.09$ with respect to the SDSS. The values are roughly consistent with our previous results based on galaxy templates. Only the u' and z bands present slightly lower values of the correction. These could be an additional effect of the template uncertainties (at 250 and 450 nm rest-frame), specially for the u' band. Also, it is worth noting that the zero-point offsets are estimated simultaneously and iteratively for all bands whereas the comparison to SDSS is done separately for each band.

3.4. Photometric Redshift Accuracy

In this section, we analyze the overall accuracy of the photometric redshifts ($z_{\rm phot}$) by comparing them against spectroscopic redshifts ($z_{\rm spec}$). In particular, we study the quality of our results as a function of the spectroscopic redshift and the observed magnitude in optical and NIR bands, and we provide specific results for different groups of galaxies such as X-ray, MIPS, or Radio sources. For the 76,936 galaxies ([3.6] < 23.75) in the sample we identify 7,636 (∼10%) spectroscopically confirmed sources from the DEEP2 catalog (mostly at $z < 1$) and from a small sample of LBGs ($z \sim 3$) presented in Steidel et al. (2003).

3.4.1. $z_{\rm phot}$ versus $z_{\rm spec}$: DEEP2 Sample

Figure 6 shows the comparison between $z_{\rm phot}$ and $z_{\rm spec}$ for 6,191 and 1,445 sources with reliable spectroscopic redshift in the main and flanking regions, respectively.

Following Ilbert et al. (2006b), we quantified the redshift accuracy using the normalized median absolute deviation ($\sigma_{\rm NMAD}$)

Table 2
Photometric Redshift Accuracy in the Main Region [3.6] < 23.75

		Rainbow				*EAZY*				
Redshift (1)	No. (2)	$\Delta z/(1+z)$ (3)	$\sigma_{\rm NCMAD}$ (4)	η (5)	$\Delta z_{\rm phot}$ (6)	$\Delta z/(1+z)$ (7)	$\sigma_{\rm NCMAD}$ (8)	η (9)	$\Delta z_{\rm phot}$ (10)	Qz (11)
All	6191	0.010	0.034	2%	0.068	0.019	0.029	2%	0.059	94%
$0. < z < 0.5$	1637	0.015	0.040	2%	0.070	0.019	0.031	1%	0.049	97%
$0.5 < z < 1.0$	3171	0.007	0.028	2%	0.061	0.018	0.025	2%	0.055	95%
$1.0 < z < 2.5$	1292	0.017	0.035	5%	0.083	0.021	0.032	4%	0.078	89%
$z > 2.5$ (LBGs)	91	−0.023	0.063	10%	0.110	−0.014	0.043	15%	0.107	42%
$z > 2.5$ (LBGs [3.6] < 24.75)	147	−0.027	0.069	12%	0.105	0.012	0.060	23%	0.119	33%
X-ray	142	0.003	0.038	10%	0.070	0.008	0.034	10%	0.057	82%
PLGs	8	0.031	0.142	50%	0.092	0.018	0.094	25%	0.108	50%
MIPS-24 μm	1955	0.010	0.033	3%	0.068	0.023	0.026	3%	0.055	94%
MIPS-70 μm	262	0.015	0.045	1%	0.071	0.031	0.028	2%	0.050	95%
Radio	85	−0.001	0.052	5%	0.066	0.017	0.032	2%	0.048	92%

Notes. Photometric redshift quality with the estimates with *Rainbow* and *EAZY* (see Section 3.5.2).
(1) Spectroscopic redshift range.
(2) Number of sources in the redshift bin.
(3, 7) Median systematic deviation in $\Delta z/(1+z)$; $\Delta z = z_{\rm phot} - z_{\rm spec}$.
(4, 8) Normalized median absolute deviation.
(5, 9) Percentage of catastrophic outliers ($|\Delta z|/(1+z) > 0.20$).
(6, 10) 68% confidence interval in the zPDF around the most probable $z_{\rm phot}$.
(11) Percentage of the sources with $Qz \leqslant 1$ in *EAZY* (high quality flag according to Brammer et al. 2008).

Table 3
Photometric Redshift Quality in the Flanking Regions [3.6] < 23.75

		Rainbow				*EAZY*				
Redshift (1)	No. (2)	$\Delta z/(1+z)$ (3)	$\sigma_{\rm NCMAD}$ (4)	η (5)	$\Delta z_{\rm phot}$ (6)	$\Delta z/(1+z)$ (7)	$\sigma_{\rm NCMAD}$ (8)	η (9)	$\Delta z_{\rm phot}$ (10)	Qz (11)
All	1445	0.013	0.046	3%	0.065	0.027	0.050	4%	0.073	87%
$0. < z < 0.5$	373	0.021	0.058	2%	0.065	0.037	0.058	5%	0.052	83%
$0.5 < z < 1.0$	785	0.015	0.040	3%	0.059	0.014	0.069	8%	0.077	75%
$1.0 < z < 2.5$	274	−0.001	0.058	8%	0.082	0.009	0.043	8%	0.079	70%
X-ray	33	−0.019	0.031	9%	0.057	0.000	0.035	9%	0.061	88%
PLGs	0	...	...	...	...	...	...	...	...	...
MIPS-24 μm	416	0.011	0.046	4%	0.061	0.028	0.048	5%	0.068	88%
MIPS-70 μm	66	0.008	0.050	2%	0.063	0.026	0.052	3%	0.055	89%
Radio	13	0.000	0.055	8%	0.071	0.035	0.015	0%	0.060	85%

Note. Same as Table 2.

of $\Delta z = z_{\rm phot} - z_{\rm spec}$

$$\sigma_{\rm NMAD} = 1.48 \times \text{median}\left(\left|\frac{\Delta z - \text{median}(\Delta z)}{1+z_{\rm spec}}\right|\right). \quad (2)$$

This quantity is equal to the rms for a Gaussian distribution and it is less sensitive to the outliers than the usual rms divided by $(1+z)$ (Ilbert et al. 2006b). We define η as the fraction of catastrophic outliers (those sources having $|\Delta z|/(1+z) > 0.20$).

Tables 2 and 3 summarize the quality of $z_{\rm phot}$ as a function of redshift in the main and flanking regions. The overall scatter and median systematic deviation are $\sigma_{\rm NMAD} = 0.034$ and 0.046, and $\Delta z/(1+z) = 0.010$ and 0.013 for each region, respectively. As expected, the rms in the flanking regions, where the overall photometric quality is slightly lower, is higher (∼20%) than in the main region. Nonetheless, the outlier fraction is only 1% worse.

The bottom panels of Figure 6 show the density plot of $\Delta z/(1+z)$ as a function of redshift. The subset of LBGs at $z_{\rm spec} > 2.5$ are shown as dots. These sources are explicitly discussed in the following section. The scatter distribution indicates that the accuracy of $z_{\rm phot}$ does not depend strongly on the redshift up to the limit of the DEEP2 sample. The systematics in both regions are fairly similar presenting a minimum scatter at $0.5 < z < 1$, around the peak of the $z_{\rm phot}$ distribution (see Section 3.7), and increasing by a factor of ∼1.3 at lower and higher redshifts ($z_{\rm spec} \lesssim 1.5$). We find that the slightly worse performance at $z < 0.5$ is associated with the use of four IRAC bands in the fitting of the SEDs. Although the template error out-weights the contribution of these bands (mostly at $\lambda > 3\,\mu$m rest-frame; see Section 3.3) their contribution cause a broadening of the zPDF that tends to increase the scatter. Nonetheless, this effect does not increase the outlier fraction at $z < 0.5$, which is comparatively lower than at $1 < z < 1.5$, for similar values of $\sigma_{\rm NMAD}$.

We also analyze the quality of $z_{\rm phot}$ as a function of the optical and NIR magnitudes. As the efficiency of $z_{\rm phot}$ mostly relies

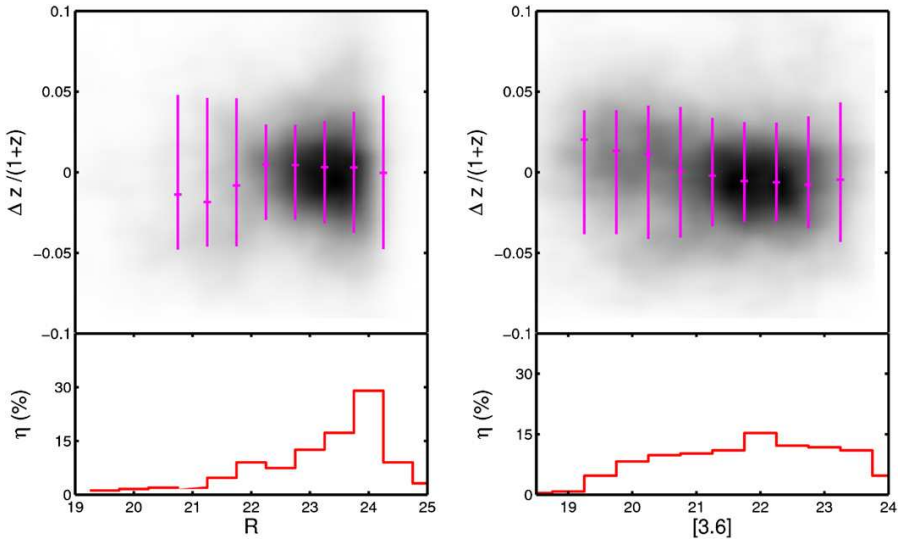

Figure 7. Density plot of the scatter in $\Delta z/(1+z)$ as a function of magnitude in the R (left) and [3.6] (right) bands. The magenta bars depict the median value of $\Delta z/(1+z)$ and $\sigma_{\rm NCMAD}$ (with respect zero) for each magnitude bin. The lower panel of each plot shows the fraction of photometric redshift outliers (η) as a function of magnitude.

(A color version of this figure is available in the online journal.)

on the detection of strong continuum features, the estimates are highly sensitive to overall consistency of the multi-band coverage. Figure 7 shows the scatter in $\Delta z/(1+z)$ as a function of the observed magnitudes in the R and [3.6] bands for sources in the main region. The results in the flanking fields are similar, but with a larger scatter. We choose these bands to be representative of the brightness of the sources in the optical and NIR, and ultimately of the overall band coverage. Note that, although this is NIR-selected sample, most of the photometric coverage consist of optical bands. Thus, galaxies with faint optical magnitudes tend to present worse photometric redshifts. The magenta bars depict the median deviation and $\sigma_{\rm NCMAD}$ per magnitude bin. We have corrected both plots by a median offset of $\Delta z/(1+z) = 0.01$. In the R-band, the scatter increases monotonically with the optical magnitude from $\sigma_{\rm NCMAD} = 0.03$–$0.06$ for $R = 22$–25 and >50% of the outliers are located at $R > 23.5$. The scatter is also wider at $R < 22$. However, since most of these bright galaxies lie at low-z, this trend is essentially the same as one mentioned above for sources at $z < 0.5$. Interestingly, there is weaker dependence in the scatter (and the outlier fraction) with the [3.6] mag than with the R-band magnitude. This is because the overall quality of the optical photometry is more relevant for constraining the shape of the SED and there is typically a wide range of optical brightnesses for any given [3.6] mag (see, e.g., Figure 6 of Paper I).

3.4.2. $z_{\rm phot}$ *versus* $z_{\rm spec}$: *LBGs Sample*

Given that the DEEP2 spectroscopic catalog consist mostly of low-redshift galaxies (68% is located at $z \lesssim 0.9$), we have included in our sample spectroscopic redshifts drawn from the LBG catalog of Steidel et al. (2003) to specifically study the accuracy of $z_{\rm phot}$ beyond the classic spectroscopic limit. This catalog contains 334 LBGs galaxies, 193 of them with confirmed spectroscopic redshift. To check the quality of our $z_{\rm phot}$ at $z > 2.5$, we first compare our results to their $z_{\rm spec}$, and then we check that the our photometric redshift distribution for the whole LBG sample is consistent with the average redshift of this population.

We identify IRAC counterparts for 91(147) of the spectroscopic LBGs with [3.6] < 23.75 mag (24.75). The rest were missed mainly because they lie out of the observed area in the IRAC survey; only 10 galaxies were lost due to their faintness in the IRAC bands. Note that, although these LBGs are relatively bright in the optical ($R < 25.5$ mag), most of them are intrinsically faint in the IRAC bands, ∼50% and 20% are fainter than [3.6] = 23.75 mag and 24.75 mag, respectively. In general, LBGs are known to span a wide range of IRAC magnitudes (Huang et al. 2005; Rigopoulou et al. 2006), and they exhibit a clear dichotomy in the R–[3.6] color, with red ($R-[3.6] > 1.5$) sources showing brighter IRAC magnitudes than blue sources (Magdis et al. 2008). We find that the median magnitudes and colors for the LBGs in our sample are [3.6] = 22.74, $R-[3.6] = 2.06$ and [3.6] = 23.80, $R-[3.6] = 0.88$ for red and blue galaxies, respectively, in good agreement with the values of Magdis et al. (2008) for a large sample of LBGs also drawn from the LBG catalog of Steidel et al. (2003).

The quality of $z_{\rm phot}$ for the spectroscopic LBGs is summarized in Table 2. For the galaxies with [3.6] < 23.75, both the scatter and the outlier fraction ($\sigma_{\rm NCMAD} = 0.063$, $\eta = 10\%$) are slightly worse than the median of the sample, as expected by their intrinsic faintness in several optical and NIR bands. Nonetheless, the statistics are similar to the results of other authors at high redshift (e.g., Wuyts et al. 2008) indicating that our $z_{\rm phot}$ still provide reasonably consistent values beyond $z > 1.5$. If we also consider the faintest sources ([3.6] < 24.75), the statistics do not degrade much ($\sigma_{\rm NCMAD} = 0.069$), even though we are including 60% more sources. We have visually inspected the outliers and at least four of them present flux contamination from close-by sources and another three are strong AGNs detected in the X-rays. The rest of them present a high-z solution in the zPDF, but the flux at [5.8] and [8.0] is too faint to reliably identify the rapid decline of the stellar

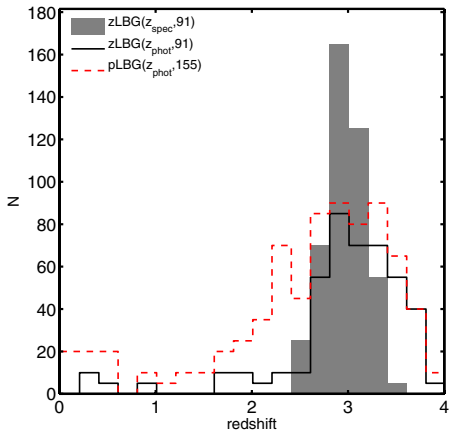

Figure 8. Photometric redshift distribution of the photometric (155, red dashed line) and spectroscopically confirmed (91, black line) LBGs (pLBG, zLBG) with [3.6] < 23.75 in common with the sample of Steidel et al. (2003). The spectroscopic redshift distribution for the zLBG is shown as a filled gray histogram for comparison.

(A color version of this figure is available in the online journal.)

component at $\lambda > 1.6\,\mu$m, which results on favoring the low-redshift solution.

We also compared the photometric redshift distribution of the 155 galaxies with [3.6] < 23.75 identified in the whole LBG catalog. Figure 8 shows the redshift distribution of the photometric and spectroscopic LBGs in our sample. The median value and quartiles for the photometric LBGs with [3.6] < 23.75 is $\tilde{z}_{\rm phot} = 2.8\pm^{0.4}_{0.6}$ consistent with the median redshift of the spectroscopic sample ($\tilde{z} = 2.95$) and with the typical width of the redshift distribution for the LBG criteria ($\tilde{z} = 3.0 \pm 0.3$; Steidel et al. 2004; Reddy et al. 2005). About 14% of these sources lie at redshift $z < 1.5$, similarly to the outlier fraction of the spectroscopic sample.

3.4.3. $z_{\rm phot}$ versus $z_{\rm spec}$: X-ray, Power Law, MIPS, and Radio Galaxies

We analyze in detail the quality of the $z_{\rm phot}$ for samples of galaxies that are known to present particularly different SEDs from the majority of the templates (e.g., X-ray or AGNs), which could cause a degradation of the redshift estimate. These sources are shown with different makers and colors in Figure 6 and their $z_{\rm phot}$ statistics are summarized in Tables 2 and 3.

The blue stars show galaxies identified in the X-Ray *Chandra*/ACIS catalog in EGS (Laird et al. 2009), probably indicating the presence of an AGN. The SED of these sources is likely affected by the AGN emission, which in principle should decrease the efficiency of the template fitting procedure. In spite of showing a larger outlier fraction (particularly at $z > 1.5$), the $z_{\rm phot}$ for X-ray sources are quite accurate, with a scatter similar to that of the full sample.

The red dots in Figure 6 depict galaxies satisfying the power-law criteria (PLG) commonly used to identify obscured AGNs (Alonso-Herrero et al. 2004; Donley et al. 2007), a good fraction of them being undetected in the X-rays. We find a surface density of 0.26 arcmin^{-2} for PLGs, in good agreement with the 0.22 arcmin^{-2} given in Donley et al. (2007, we apply a similar criteria restricted to $P_\chi > 0.1$ and a slope $\alpha < -0.5$). However, less than 2% of these sources present a spectroscopic redshift. Comparatively, PLGs present a lower accuracy and higher outlier fraction than the X-ray sources as a consequence of having their SED more contaminated by the AGN emission.

Similarly to the PLG, we find that sources with red colors in the IRAC bands ($f_{[3.6]} < f_{[4.5]} < f_{[5.8]} < f_{[8.0]}$), but not strictly satisfying the PLG criteria, make up for up to 15% of the total outliers. This is not surprising given that, for the typical galaxy at $z \leqslant 2$, the presence of the stellar bump (at 1.6 μm) causes the flux in the last two IRAC bands to be lower than in the previous two. Thus, for these sources, the code will try to assign incorrect high-redshift values of $z_{\rm phot}$.

Tables 2 and 3 also quote numbers and $z_{\rm phot}$ statistics for the spectroscopic sub-samples of galaxies detected in MIPS 24 μm ($f(24) > 60\,\mu$Jy), MIPS 70 μm ($f(70) > 3.5$ mJy), and in the catalog of Radio sources of Ivison et al. (2007). The latter present a slightly worse accuracy than the median of the sample, whereas the MIPS detected galaxies present essentially the same quality as the rest of the spectroscopic galaxies. This indicates that for most of them the IR emission does not contribute significantly to the NIR–MIR region fitted with the optical templates.

3.4.4. Error Analysis

The 1σ uncertainty of the photometric redshifts, $\Delta z_{\rm phot}$, is computed from the zPDF as the semi-width of the redshift range corresponding to a 68% confidence interval around the probability peak. This value allows to provide an estimate of the accuracy for sources without a spectroscopic redshift, which are >90% of the sample.

Tables 2 and 3 quote the values of $\Delta z_{\rm phot}$ as a function of redshift in the main and flanking regions. Based on these results, we find that 62% (approximately 1σ) of the galaxies present values of $\Delta z_{\rm phot} < |\Delta z|$. The median value and quartiles of $\Delta z_{\rm phot}/(1+z) = 0.036^{0.056}_{0.021}$ in the main region are consistent with the statistics for $\sigma_{\rm NCMAD}$ and also with $|\Delta z|/(1+z) = 0.027^{0.050}_{0.013}$. A similar agreement is found for the sources in the flanking regions. Note that as the $\Delta z_{\rm phot}$ is computed from the zPDF its minimum value is limited by the step size of the redshift grid ($\Delta z = 0.01$), and thus it tends to present larger values than $|\Delta z|$, specially for very accurate $z_{\rm phot}$. Therefore, it is not surprising that $\Delta z_{\rm phot}/(1+z)$ is on average larger than all the other scatter estimates. In fact, this indicates that $\Delta\ z_{\rm phot}$ provides a robust estimate of the uncertainty in $z_{\rm phot}$, which can be underestimated if it assumed to be equal to $\sigma_{\rm NCMAD}$ (see, e.g., Cardamone et al. 2010).

In order to obtain a better characterization of the catastrophic outliers caused by a poor fit to the data, we analyze the distribution of sources as a function of the reduced χ^2 of the SED fitting. Figure 9 shows the distribution of $-\log(\chi^2)$ for the full photometric sample, the spectroscopic sample, and the catastrophic outliers. Approximately 83% and 94% of the galaxies in the photometric and spectroscopic sample present values of χ^2 lower than the median of the outlier distribution ($-\log(\chi^2) < -0.6$), i.e., half of the outliers are located within the ~20% and 5% of the sources in the photometric and spectroscopic samples with the worse values of χ^2.

Finally, we also find that 58% of the sources with significantly different values of $z_{\rm best}$ and $z_{\rm peak}$ ($|z_{\rm best}\text{-}z_{\rm peak}|/(1+z) > 0.2$) are outliers. These sources account for only 1% of the spectroscopic sample, but they represent ~12% of the outliers. Therefore, the difference between both values is another useful indicator of possible outliers.

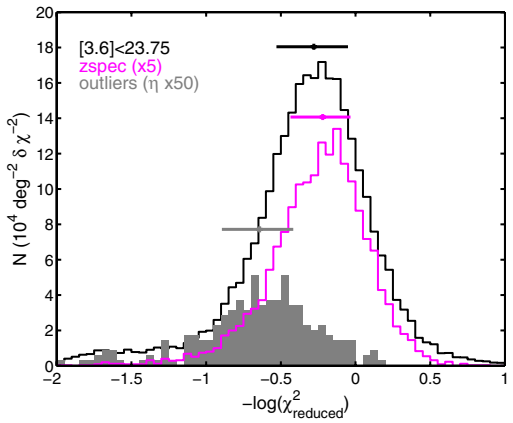

Figure 9. Distribution of the normalized χ^2 resulting from the fit of the data to the templates during the calculation of $z_{\rm phot}$. The black line is for the full sample ([3.6] < 23.75), and the magenta line and gray area are for the spectroscopic sample (×5) and photometric redshift outliers ($\eta \times 50$), respectively. The corresponding lines depict the median value and quartiles of each distribution.

3.5. Comparison of Photometric Redshift Catalogs

Here, we compare the $z_{\rm phot}$ computed with *Rainbow* to other previously published $z_{\rm phot}$ catalogs and to the estimates obtained with a different code. The alternative $z_{\rm phot}$ are also included in the our data release (see Section 6) in Table 7.

3.5.1. Rainbow versus Ilbert et al. (2006a)

We compare the $z_{\rm phot}$ presented in this paper with those derived by Ilbert et al. (2006a, hereafter I06) based on optical data from the CFHTLS. These authors used an i'-band selected sample with $i' < 24$ and obtained photometric redshifts for the four CFHTLS deep fields. The $z_{\rm phot}$ were computed using the template fitting code *Le phare* (Arnouts & Ilbert; e.g., Ilbert et al. 2009) for ∼500,000 sources observed in five bands $u*, g', r', i', z'$. Their template library is based on an upgrade of the empirical templates of Coleman et al. (1980) and Kinney et al. (1996) computed by applying zero-point corrections and interpolating between spectral types. Their $z_{\rm phot}$ also include a Bayesian prior on the redshift distribution. The accuracy of their results for the D3 field (the EGS) is $\sigma_{\rm NCMAD} = 0.035$ with $\eta = 4\%$ for sources with $i' < 24$ and $z < 1.5$. More recently, Coupon et al. (2009) repeated essentially the same exercise using the latest data release of the CFHTLS T004, obtaining $z_{\rm phot}$ of almost identical quality.

The source density in the i'-band selected sample of I06 is 25, 42, and 96 sources arcmin^{-2} up to limiting magnitudes of $i' = 24$, 25, and 26.5 (the estimated SNR ∼ 5 level). The source density of the IRAC selected catalog is ∼44 sources arcmin^{-2} at [3.6] < 23.75. This means that their source density at $i' < 25$, which is essentially the spectroscopic limit ($R = 25$), is similar to ours. However, at $i' < 24$, the limiting magnitude for their best performing $z_{\rm phot}$, the source density in i' is approximately 50% that in IRAC. At the faintest optical magnitudes, the source density in the i'-band selected catalog is larger, although the quality of these $z_{\rm phot}$ is worse than for the $i' < 24$ sample, given that many of the galaxies will also be undetected in the shallowest optical bands (u^*, z').

Even presenting similar source densities, the nature of the galaxies in an i' band and an IRAC-selected samples is different, and some of the sources in one selection will be missed by the other. We find that the optically bright galaxies missed by the IRAC catalog ([3.6] > 23.75) present a median and quartile redshifts $z_{\rm phot} = 1.0^{1.3}_{0.6}$, while the infrared bright galaxies undetected in the optical ($i' > 26.5$) present $z_{\rm phot} = 1.8^{1.1}_{2.3}$. The high-$z$ sources missed in the IR selection are typically low-mass galaxies (similar to LBGs), i.e., our catalog favors the detection of high-z massive galaxies, as expected.

Table 4
Rainbow $z_{\rm phot}$ vs. I06 at $i' < 25$ and [3.6] < 23.75

		Rainbow			I06		
Redshift	No.	$\sigma_{\rm NCMAD}$	η	$R(\eta)$	$\sigma_{\rm NCMAD}$	η	$R(\eta)$
(1)	(2)	(3)	(4)	(5)	(6)	(7)	(8)
All	5454	0.034	2%	82%	0.036	5%	55%
$0. < z < 0.5$	1444	0.040	2%	83%	0.032	5%	43%
$0.5 < z < 1.0$	2787	0.028	2%	80%	0.031	3%	53%
$1.0 < z < 2.5$	1143	0.035	4%	80%	0.054	8%	63%
$z > 2.5$ (LBGs)	80	0.063	9%	91%	0.345	46%	42%

Notes.
Photometric redshift quality in the estimates with *Rainbow* and in I06.
(1) Spectroscopic redshift range. (2) Number of sources in the redshift bin.
(3, 6) Normalized median absolute deviation.
(4, 7) Percentage of catastrophic outliers ($|\Delta z|/(1+z) > 0.20$).
(5, 8) Fraction of catastrophic outliers in the other code presenting an accurate $z_{\rm phot}$.

We cross-correlated the catalog of I06 to the IRAC selected sample using a search radius of 1.″5. Due to small differences in the extraction of the catalogs, the comparison is restricted to a slightly smaller portion of the main region (214.°09 < α < 215.°72 and 52.°20 < δ < 53.°16). Out of the 49605 IRAC sources, 40% and 88% are detected in I06 to $i' < 24$ and 26.5, respectively. The cross-match to the DEEP2 spectroscopic redshifts contains 5454 galaxies simultaneously identified in all three catalogs ([3.6] < 23.75, $i' < 26.5$). Approximately 6% of our spectroscopic subsample is missed due to a more conservative source removal around bright stars in I06.

The top panels of Figure 10 show the comparison of $z_{\rm phot}$ versus $z_{\rm spec}$ for the galaxies in common between the *Rainbow*, I06, and DEEP2 catalogs with [3.6] < 23.75 and $i' < 25$, without any other requirement of band coverage. Table 4 summarizes accuracy of the $z_{\rm phot}$ in *Rainbow* and I06 for these sources as a function of redshift. We also list the fraction of catastrophic outliers in each catalog that is recovered in the other (shown as green dots in Figure 10).

The overall scatter in I06 for the sources in common with the IRAC sample is consistent with their results for the whole D3 sample. The comparison as a function of redshift indicates that I06 estimates at lower redshift are slightly more precise, probably as a result of the template-optimization algorithm and the Bayesian prior (see Figure 6 of I06), but also because of our slightly lower performance at $z < 0.5$. On the contrary, the fraction of catastrophic outliers in I06 is larger than in *Rainbow* for all redshifts, and particularly at $z > 2.5$. Moreover, the $z_{\rm phot}$ *Rainbow* is able to recover ∼80% of these outliers. At $z > 1$, our larger band coverage, mostly in NIR bands, provides more accurate estimates. Note that the IRAC fluxes for the LBGs play a critical role in providing more accurate redshifts (and stellar parameters) for these sources.

3.5.2. Rainbow versus EAZY

Here, we check again the quality and overall consistency of our SEDs and $z_{\rm phot}$ by computing an independent estimation of

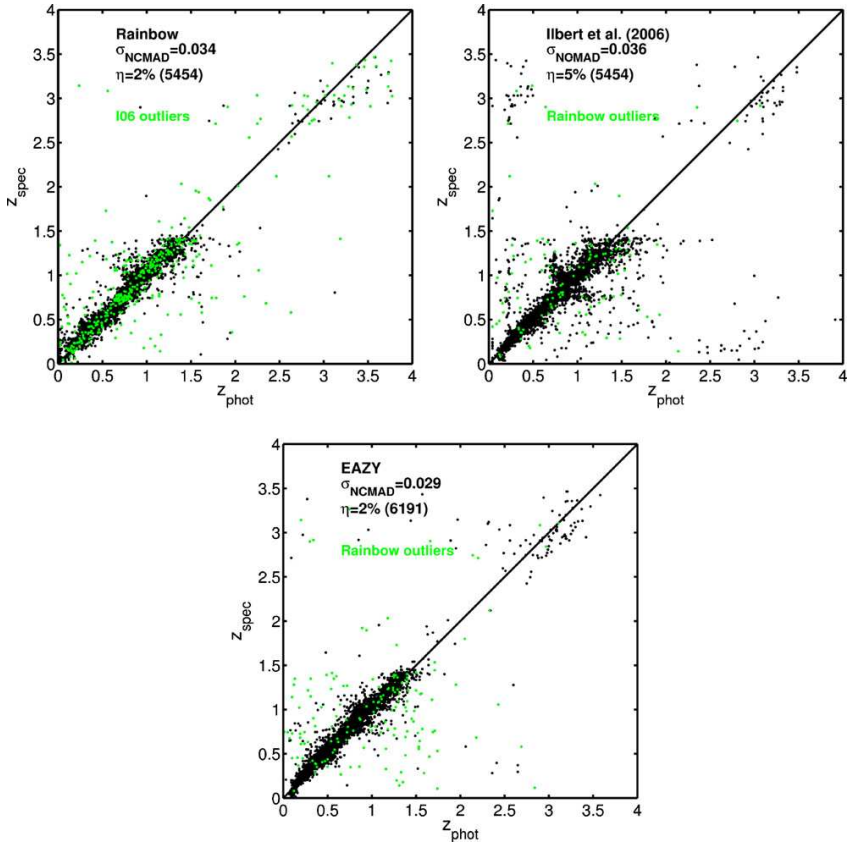

Figure 10. Top: comparison of $z_{\rm phot}$ vs. $z_{\rm spec}$ for the estimations presented in this paper (left) and the ones in I06 (right). The sample is drawn from the overlap region between the CFHTLS-D3 area and the IRAC mosaic (main region). Both figures contain the same 5454 sources simultaneously detected in both catalogs and in the DEEP2 sample at $[3.6] < 23.75$ and $i' < 24.5$. Green points depict $z_{\rm phot}$ in *Rainbow* for the outliers in I06 (left) and viceversa (right). Bottom: comparison of $z_{\rm phot}$ computed with *EAZY* vs. $z_{\rm spec}$ for sources in the main region. This figure is equivalent to the left panel of Figure 6 for estimates based in *EAZY*. Green dots depict catastrophic outliers in the $z_{\rm phot}$ estimated with *Rainbow*.

(A color version of this figure is available in the online journal.)

the $z_{\rm phot}$ with a different code. A successful result using a different fitting code based on different template sets would certify that the catalog reproduces accurately the observed SEDs and is therefore suitable for galaxy population studies.

We computed alternative $z_{\rm phot}$ using the photometric redshift code *EAZY* (Brammer et al. 2008). The advantage of *EAZY* is that it was conceived to provide accurate photometric redshift estimates for NIR-selected samples in absence of a representative calibration sample of spectroscopic redshifts. The code makes use of a new set of templates computed from a *K*-limited subsample of the Millennium Simulation (Springel et al. 2005; De Lucia & Blaizot 2007) and modeled by fitting the synthetic SEDs with PEGASE models and applying an optimization algorithm. The final result is set of six templates that essentially reproduces the principal components of the catalog. Furthermore, a template error function was introduced to account for systematic differences between the observed photometry and the template photometry at different wavelengths. After trying different configurations for the input parameters, we find that the best results in the $z_{\rm phot}$–$z_{\rm spec}$ comparison are obtained using the template error function and incorporating a Bayesian prior on the redshift distribution similar to that of Benítez (2000; see Brammer et al. 2008 for more details). The use of the template error function is decisive to weight the contribution of the IRAC bands at lower redshifts as we have also verified in our own $z_{\rm phot}$ (see Section 3.3).

In addition, we find that a critical issue to avoid a severe contamination from catastrophic $z_{\rm phot}$ is the use of the purged photometric catalog produced by *Rainbow*. Prior to the fitting procedure, *Rainbow* carries out a first pass on the catalog where potential photometric outliers are removed. If we use the resulting catalog as input for *EAZY* the outlier fraction is reduced by a factor $\sim$5, illustrating the relevance on the photometric errors not only in the overall quality of the $z_{\rm phot}$ but also in the catastrophic errors.

The bottom panel of Figure 10 depicts the comparison of the $z_{\rm phot}$ with *EAZY* versus spectroscopic redshifts for the galaxies in the main region (i.e., the same galaxies depicted in the left panel of Figure 6). As in the previous section green markers indicate outliers in $z_{\rm phot}$ *Rainbow*. Tables 2 and 3 summarize the quality of $z_{\rm phot}$ for *Rainbow* and *EAZY* in different redshift bins for the main and flanking regions, respectively. The overall scatter and outlier fractions of both estimates are roughly similar, with the estimates of *EAZY* presenting a slightly higher accuracy in the main region, but lower in the flanking fields. We also note that $z_{\rm phot}$ with *EAZY* perform better at $z < 0.5$, being less sensitive to the mild broadening of the zPDF present in *Rainbow*. The tables also quote the 68% confidence intervals of $z_{\rm phot}$, which

are similar for both codes and are in good agreement with other results based on *EAZY* (e.g., Cardamone et al. 2010). We show that the fraction of sources with a quality parameter $Qz \leqslant 1$ in *EAZY* (good photometric redshifts; Brammer et al. 2008) is typically >90% except for the highest redshift bin, where the photometry is more uncertain, due to the intrinsic faintness of these sources, and thus there is larger fraction of outliers. In addition, we find that roughly 40%–50% of the outliers in *EAZY* present a poor $z_{\rm phot}$ estimate in *Rainbow* and vice versa. Therefore, similarly to the galaxies with different values of $z_{\rm peak}$ and $z_{\rm prob}$, galaxies with significantly different estimates both catalogs are frequently (∼50%) outliers.

From the good agreement between the different $z_{\rm phot}$ estimates we conclude that the photometric catalog provides accurate SEDs suitable for studies of galaxy populations irrespective of the code used for the analysis.

3.6. Number Densities and Redshift Distribution of NIR-selected Galaxies

As an additional test of the accuracy of $z_{\rm phot}$ we compare the number densities and redshift distributions of NIR color-selected populations with the results from other authors. In order to facilitate the comparison to the references, the magnitudes in this section are given in Vega system.

Given the highly non-uniform band coverage of the field, we have chosen to compute galaxy colors based on synthetic magnitudes. An advantage of this method is that synthetic photometry behaves better than directly observed values when deep data are not available in some of the required bands, allowing us to assign robust fluxes for undetected sources in the shallower bands. This is the same procedure that we used in PG08, and is similar to that presented in Grazian et al. (2007) and Quadri et al. (2007). We restrict the analysis in this section to the 0.35 deg^2 of the main region which count with better photometry.

For obvious reasons, the success of this method depends critically on the quality of the synthetic fluxes. In Section 3.3, we showed that these fluxes provide an accurate representation of the observed values in the magnitude range covered by the observations. The median offsets are very small and the scatter is consistent within a factor ∼2 with the photometric errors at different magnitudes (see Figure 5).

In order to avoid possible selection effects, we restrict the analysis to NIR-selected galaxies which would be fully represented in the IRAC-selected sample. We selected distant red galaxies (DRGs; Franx et al. 2003) as galaxies with $[J-K] > 2.3$, and BzK galaxies, both star forming (s-BzK) and passively evolving (p-BzK), following the equations in Daddi et al. (2004). Both criteria were proposed to target massive galaxies at $z \sim 2$, although DRG and p-BzK are best at selecting galaxies with a significant fraction of evolved stars, whereas s-BzK select star-forming galaxies similar to those found by the low-redshift equivalent of the LBG criteria (LBG/BX; Steidel et al. 2004). For the DRG we convolved the templates with the VLT/ISAAC *J* and *K* filters, whereas for the BzK we used VLT/FORS B, *HST*/ACS *z*, and VLT/ISAAC *K* which are the same filters used in Daddi et al. (2004).

The top left panel of Figure 11 shows the *K*-band[6] number counts for the IRAC-selected catalog compared to other results from the bibliography. Our counts are in very good agreement with the values of Quadri et al. (2007) for the MUSYC survey, and with our previous results in Barro et al. (2009) for the south region of EGS (∼30% overlap with the IRAC sample). The overall agreement with the counts of the Palomar–WIRC catalog (Conselice et al. 2008) is slightly worse. However, the complete Palomar–WIRC catalog covers a total area of 1.47 deg^2 out of which EGS is only a small fraction (0.20 deg^2). At $K_{\rm VEGA} \sim 20$ our results are also consistent with those in Hartley et al. (2008), McCracken et al. (2010), and Förster Schreiber et al. (2006), following the same trend as the latter up to $K_{\rm VEGA} = 21$. From this comparison, we conclude that the IRAC catalog limited to $[3.6] = 23.75$ is a good proxy of a *K*-limited sample with at least $K_{\rm VEGA} < 21$ mag.

Table 5
Surface Density of DRG and BzKs

Criteria	$K_{\rm VEGA} < 21$		$K_{\rm VEGA} < 20$	
	$\rho^{\rm a}$	$z^{\rm b}$	$\rho^{\rm a}$	$z^{\rm b}$
DRG	1.4	2.47	0.5	2.24
s-BzK	5.0	1.89	1.5	1.70
p-BzK	0.5	1.85	0.3	1.73

Notes.
[a] Surface density of DRG and BzK in arcmin^{-2}.
[b] Median photometric redshift of each sub-sample.

The top right and the bottom panels of Figure 11 shows the comparison of the number counts for DRG and BzK (restricted to $z > 1.4$) galaxies with other values from the literature. There is good agreement within the typical scatter (0.1–0.2 dex), generally associated with cosmic variance. Our counts reproduce the most representative features of the overall distribution, namely, the plateau in DRG and p-BzK around $K_{\rm VEGA} \sim 20.5$ and the steep slope in the counts of s-BzK. We note that our s-BzK counts are slightly above those from Blanc et al. (2008) and McCracken et al. (2010) which count with very large surveyed areas (0.71 deg^2 and 2 deg^2, respectively). On the contrary, our results are in excellent agreement with Hartley et al. (2008, 0.63 deg^2). In McCracken et al. (2010) the authors argue that their disagreement with the counts of Hartley et al. (2008) is the result of an incorrect color correction in the filter system. However, for this work we used the exact same filters as in Daddi et al. (2004) obtaining similar results to Hartley et al. Thus, the most plausible explanation is that there is an excess of galaxies at $z \sim 1.5$ in our region.

For p-BzK, our results lie between those of Hartley et al. (2008) and McCracken et al. (2010). However, the counts of p-BzK exhibit the largest scatter of the three populations. This is not surprising given that p-BzK target a more constrained population, prone to stronger clustering (Grazian et al. 2006b; Kajisawa et al. 2006; Hartley et al. 2008; McCracken et al. 2010) and hence significantly affected by the large-scale structure (LSS). Table 5 summarizes the accumulated surface densities of DRG and BzK galaxies up to $K_{\rm VEGA} = 20$ and $K_{\rm VEGA} = 21$. The values are roughly consistent with the results of the studies shown in Figure 11, and with other values from the literature (0.89 DRG arcmin^{-2} in Quadri et al. 2007; 3.1 s-BzK arcmin^{-2} and 0.24 p-BzK arcmin^{-2} in Reddy et al. 2005; 3.2 s-BzK arcmin^{-2} and 0.65 p-BzK arcmin^{-2} in Grazian et al. 2007). As mentioned above, the excess of s-BzK by a factor of ∼1.5 could be caused by a source overdensity in the area. Note that this excess does not necessarily affect s-BzK and p-BzK in the same manner due to the different clustering properties of each population (Hartley et al. 2008; McCracken et al. 2010;

[6] We used the following transformations when required $\Delta K_{\rm VEGA-AB}$(UKIRT,CFHT,SOFI) = 1.90,1.85,1.87.

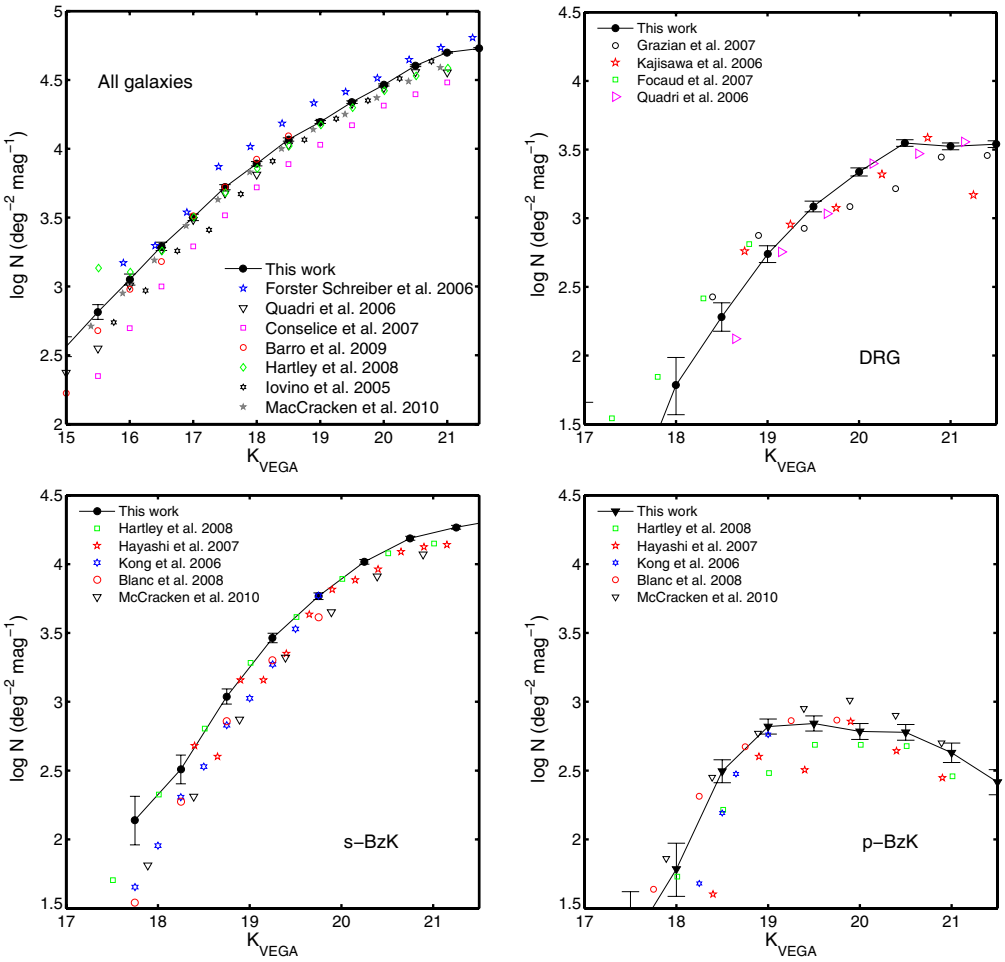

Figure 11. Galaxy number counts of our sample in the *K*-band, derived from synthetic observed magnitudes, compared to results from the literature. The black dots connected with a solid line depict the values derived in the present work. The other symbols show the results from other authors. Top left: number counts for the complete galaxy sample ([3.6] < 23.75) in the main region. Top right: number counts for DRG. Bottom left: number counts for s-BzK galaxies. Bottom right: number counts for p-BzK galaxies.

Hartley et al. 2010). In fact, our density of p-BzK is not among the lowest values.

Figure 12 shows the $z_{\rm phot}$ distribution of DRG, s-BzK, and p-BzK galaxies with $K_{\rm VEGA} < 20$ and $K_{\rm VEGA} < 21$, compared to some results from the literature. The distributions are convolved with a $\delta z = 0.1$ kernel in order to account for the $z_{\rm phot}$ uncertainties. The redshift range spanned by the different galaxy populations is in good agreement with the usual distributions observed in other studies, i.e., $z > 2$ for DRG and $1.4 < z < 2.5$ for BzKs (Daddi et al. 2004). DRG present a secondary redshift peak around $z \sim 1$, that accounts for a significant fraction of the total population at bright ($K_{\rm VEGA} < 20$) magnitudes (as already pointed out by other authors, e.g., Quadri et al. 2007; Conselice et al. 2007). Nevertheless, our surveyed area (0.35 deg^2) is not large enough to make (bright) low-z DRG the dominant fraction, as in the 0.70 deg^2 of the *K*-band Palomar survey where ∼70% of these galaxies are found at $z < 1.4$ Conselice et al. (2007). As expected, s-BzK and p-BzK present almost identical redshift distributions, although the latter seems to have a more extended high-redshift tail, being also less prone to low redshift interlopers (probably as a consequence of the more restrictive color criteria). In summary, our results about the number density and redshift distribution of color-selected $z > 1$ galaxy samples are consistent with previous studies (Reddy et al. 2005; Grazian et al. 2007; PG08), indicating that the photometric redshift estimates are generally robust at high redshift.

3.7. Photometric Redshift Distribution

Figure 13 shows the $z_{\rm phot}$ distribution for the IRAC selected sample in the main region, limited to [3.6] < 23.75. In addition, we also plot the redshift distributions of the galaxies detected at 24 μm, 70 μm, and the sub-sample with spectroscopic redshifts. In order to derive a realistic distribution, accounting for the uncertainties in $z_{\rm phot}$, the distribution was convolved with the typical width of the zPDFs. We used a conservative upper limit of $\Delta z/(1+z) = 0.07$. The shape of the distribution is consistent with that expected for a magnitude limited sample. At low redshift the number density increases as we probe larger volumes, and then an exponential decay is observed as the sources get fainter and the detection probability decreases.

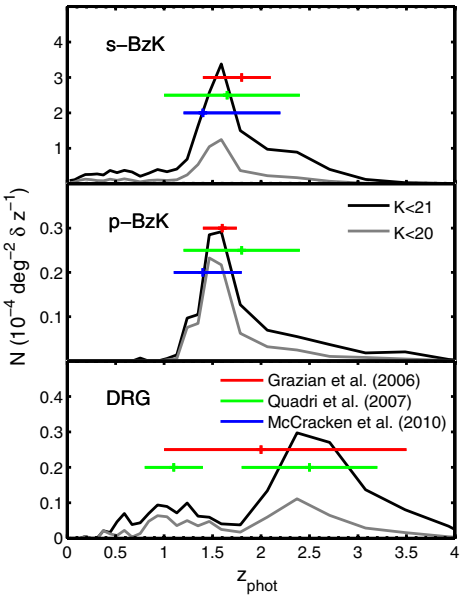

Figure 12. Photometric redshift distributions of s-BzK, p-BzK, and DRG galaxies (from top to bottom) drawn from the IRAC-selected sample with [3.6] < 23.75. The black line and gray line show the distributions at $K_{VEGA} < 21$ and $K_{VEGA} < 20$, respectively. Our results are compared with the median (and quartile) of the redshift distributions in Grazian et al. (2007, red), Quadri et al. (2007, green), and McCracken et al. (2010, blue; also top to bottom). The two (green) intervals in the redshift distribution of DRG indicate the median values of the distribution at redshifts lower and higher than $z = 1.5$ in the work Quadri et al. (2007).

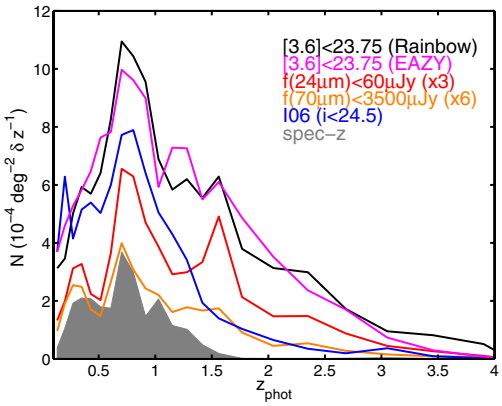

Figure 13. Photometric redshift distribution for the IRAC ([3.6] < 23.75; black), MIPS 24 μm (×3, red), MIPS 70 μm (×6, orange), and spectroscopic (gray area) samples in the main region of the EGS. The distribution of z_{phot} in I06 ($i' < 24.5$) for the overlapping area with the IRAC mosaic is shown in blue for comparison.

The positions of the minor prominences in the z_{phot} distribution are roughly consistent with the most remarkable peaks observed in the spectroscopic redshift distribution at $z \sim 0.3$, $z \sim 0.7$, $z \sim 1$. The median redshift of the photometric redshift distribution is $z = 1.2$, 75% of the sources are below $z = 2.1$, and 90% below $z = 2.7$. The median of the distribution is consistent with the results of Ilbert et al. (2009) in the COSMOS field for an $i' + 3.6\,\mu$m selected sample ($i' < 25, f(3.6) > 1\,\mu$Jy). Although the IRAC S-COSMOS catalog is shallower than ours, with a ∼50% completeness level at $f(3.6) = 1\,\mu$Jy, the median redshift limited to their faintest magnitude bin ($24.5 < i' < 25$), $z = 1.06$, is similar to ours. Note that the small differences could arise from the presence of underlying LSS in EGS, whereas this effect is largely reduced in the COSMOS sample due the larger area of field (∼1.73 deg^2). Finally, the distribution is also in good agreement with our results in PG08 for the averaged redshift distribution of a combination of IRAC-selected catalogs in the HDFN, CDFS, and Lockman Hole fields. The total combined area in PG08 is approximately that of the main region of EGS, and the limiting magnitude of the catalog was slightly lower ($f(3.6) < 1.6\,\mu$Jy). However, the redshift distribution also peaks around $z = 0.8$–1, consistently with ours.

4. SED ANALYSIS: STELLAR MASSES

In this section, we describe the method used to estimate stellar masses based on the SED fitting. In addition, we analyze the goodness of our stellar mass estimations quantifying the systematic and random errors linked to assumptions in the input parameters for the stellar population modeling. For the discussion in Section 4.2.1, we use only the spectroscopic sample in the main region (which count with better photometry) and we force the z_{phot} to the spectroscopic value.

4.1. Stellar Mass Estimates

The stellar mass of each galaxy is estimated from the wavelength-averaged scale factor required to match the template monochromatic luminosities to the observed fluxes. This is possible because our templates are obtained from SPS models which are expressed in energy density per stellar mass unit. Note that the stellar mass estimate is not obtained from a single rest-frame luminosity and its corresponding mass-to-light ratio, which has been a typical procedure seen in the literature, but from the whole SED. In our method, the fit to the multi-band data implicitly constraints the mass-to-light ratio by determining the most suitable template. Then, we estimate the mass from the averaged template normalization, weighted with the photometric errors. This approach is less sensitive to the effects of the star formation history (SFH) or the photometric and template uncertainties in a single band. Objects fitted with pure AGN templates have no stellar mass estimate, as their SED is dominated by non-stellar emission. The random uncertainty of the stellar mass is estimated with a bootstrap method by randomly varying the photometric redshift and observed fluxes based on their quoted errors.

4.2. Accuracy of the Stellar Masses

In addition to the uncertainties inherited from the probabilistic nature of z_{phot} and the intrinsic photometric errors, there is another source of systematic uncertainty associated with the assumptions in the SED modeling. Although significant effort has gone into providing accurate SPS models, key ingredients of the theoretical predictions are still poorly understood. As a result, there can be substantial differences in the physical properties estimated with many of the well-tested SPS models available in the literature. Most of these differences arise from the different parameterizations of potentially uncertain phases of the stellar evolution, such us the asymptotic giant branch (AGB) or the thermally pulsating AGB (Maraston 2005; Bruzual 2007; Kannappan & Gawiser 2007). Another critical aspect is the choice of an IMF. Although this is essentially assumed to

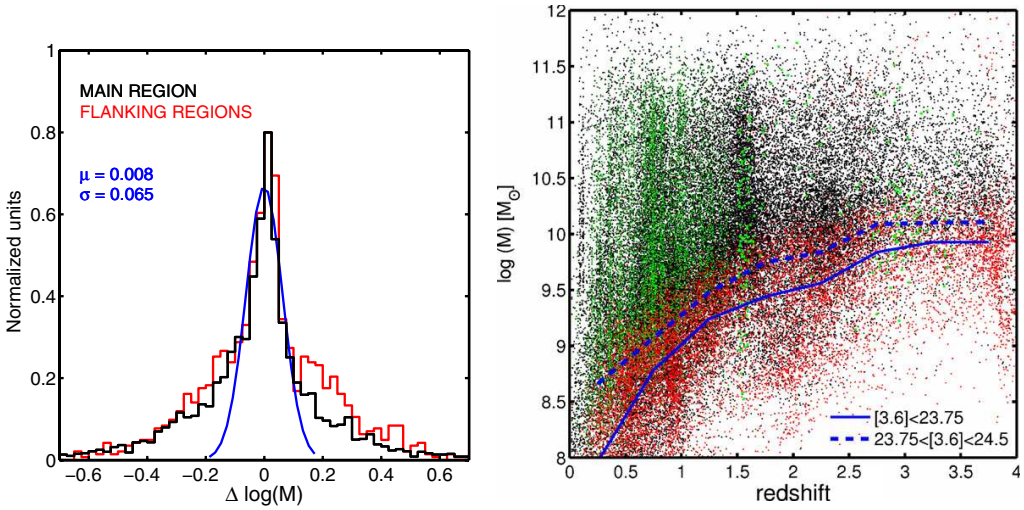

Figure 14. Left: comparison of the stellar masses estimated with [P01, SALP, CAL01] using spectroscopic and photometric redshifts in the main (black) and flanking (red) regions, respectively. The blue line indicates the best Gaussian fit to the central values of the main region distribution. Right: stellar masses of the galaxies in the sample as a function of redshift. The black dots depict galaxies with [3.6] < 23.75 (85% completeness level of the sample). The red dots depict galaxies 23.75 < [3.6] < 24.75 (3σ limiting magnitude). The green dots show galaxies with spectroscopic redshifts. The blue lines indicate the 90% and 10% percentiles of the mass distribution as a function of redshift for the galaxies with [3.6] < 23.75 (solid) and 23.75 < [3.6] < 24.75 (dashed), respectively.

introduce a change in the overall normalization of the stellar mass, there are additional effects attached, e.g., a change in the balance between low-mass and high-mass stars varies the relative fraction of stars in different points of the isochrones. Thus, modifying the colors and M/L of the modeled galaxies at different evolutionary stages (Maraston 1998; van Dokkum et al. 2008).

Apart from the choice of SPS models and IMF, additional effects might arise from the assumed SFH, usually parameterized with τ-models, or the choice of a dust extinction law and metallicity. As recently shown in Muzzin et al. (2009) (also Kriek et al. 2008 or Marchesini et al. 2009), due to all these effects, the physical properties of galaxies estimated from broadband photometry often presents large uncertainties (typically within a scatter of 0.2 dex for stellar masses), in addition to systematic offsets. Moreover, these uncertainties can be even larger (up to 0.6 dex) for particularly sensitive galaxy populations at high-z, such as bright red galaxies. See for example the series of paper by Conroy et al. (2009, 2010) and Conroy & Gunn (2010) for a detailed discussion of all these issues.

Taking these considerations into account, in the following sections, we analyze the accuracy of our stellar mass estimates quantifying the uncertainty budgets associated with different effects. First, we study the effect of photometric redshift uncertainties. Then, we evaluate the impact from the choice of SPS models, IMF, and dust extinction law restricting the analysis to the spectroscopic sample. For the sake of clarity, we refer all comparisons to a default choice of SED modeling parameters (as described in 3) characterized by SPS models, IMF, and extinction law [P01, SALP, CAL01]. Finally, we verify that our stellar masses provide realistic values by comparing them to other stellar mass catalogs available in the literature.

Note that although the a priori assumptions on the SFH can also introduce systematic effects in the estimated stellar masses, an in depth analysis of these issues is clearly beyond the scope of this paper (see, e.g., Maraston et al. 2010 for a detailed discussion). Nonetheless, a comparison of the results obtained with a single exponentially declining stellar population (1-POP) and with a single population plus a second burst (2-POP) is presented in PG08 (Appendix B) along with similar tests to the ones presented in the next section.

The catalog of stellar masses presented in this paper (see Section 6) contains the different values obtained with all the modeling configurations discussed in the next sections.

4.2.1. Effects of the Photometric Redshifts, SPS Models, IMF, and Extinction Law

The left panel of Figure 14 shows the scatter in the stellar masses estimated using $z_{\rm phot}$ and $z_{\rm spec}$ for the 7636 spectroscopic galaxies in the main (black) and flanking regions (red). Approximately 68% and 90% of the sources are confined within an rms of 0.16, 0.34 dex and 0.20, 0.39 dex in each region, respectively. Nonetheless, the distribution shows a pronounced central peak that it is well reproduced by a Gaussian distribution (blue line) with extended wings, indicating that for the most accurate redshifts, the scatter is substantially reduced ($\sim$0.065 dex). This is in good agreement with the results of Ilbert et al. (2010, see Figure 3) scaled to the overall accuracy of our photometric redshifts, which is slightly lower. The right panel of Figure 14 shows the range of stellar masses as a function of redshift for the whole sample (black). In order to illustrate the approximate limiting stellar mass inherited from the magnitude limit ([3.6] < 23.75; 85% completeness), we also depict the galaxies up to the 3σ limiting magnitude (23.75 < [3.6] < 24.75, red dots). Approximately 90% of the galaxies with [3.6] < 23.75 present $\log(M) > 10\ M_{\odot}$ at $z \gtrsim 2.5$ (blue line) in agreement with our results in PG08 for a similar limiting magnitude. Similarly, $\sim$10% of the faintest galaxies (23.75 < [3.6] < 24.75), absent in our main sample, present stellar masses larger than $\log(M) > 10\,M_{\odot}$ (blue dashed line). Note however that the completeness in stellar mass cannot be directly extraploted from these limits because for any given redshift, galaxies with different ages present different mass-to-light ratios. Hence, the completeness is an age (or color) dependent value. In particular, magnitude limited samples are known to be incomplete against the oldest (red) galaxies (see, e.g., Fontana

Table 6
Comparison of Stellar Masses Computed with Different Modeling Assumptions

IMFs (1)	SPS model (2)	Dust (3)	$\Delta\log(M)$ (4)	$\Delta\log(M)$ (5)
SALP−KROU	CB09	CAL01	$0.19\pm^{0.07}_{0.12}$	$0.19\pm^{0.12}_{0.10}$
SALP−KROU	P01	CAL01	$0.03\pm^{0.20}_{0.17}$	$0.13\pm^{0.19}_{0.21}$
KROU−CHAB	CB09	CAL01	$0.04\pm^{0.11}_{0.09}$	$0.07\pm^{0.24}_{0.10}$
SPS model	IMF	Dust	$\Delta\log(M)$	$\Delta\log(M)$
BC03−CB09	CHAB	CAL01	$0.04\pm^{0.28}_{0.15}$	$0.07\pm^{0.30}_{0.21}$
P01−CB09	KROU	CAL01	$0.15\pm^{0.23}_{0.29}$	$0.08\pm^{0.28}_{0.27}$
P01−M05	KROU	CAL01	$0.39\pm^{0.36}_{0.28}$	$0.30\pm^{0.35}_{0.27}$
CB09−M05	KROU	CAL01	$0.16\pm^{0.26}_{0.28}$	$0.20\pm^{0.27}_{0.29}$
Dust	IMF	SPS model	$\Delta\log(M)$	$\Delta\log(M)$
CAL01−CF00	SALP	P01	$-0.03\pm^{0.20}_{0.23}$	$0.00\pm^{0.20}_{0.21}$

Notes. Comparison of the stellar masses obtained under different combinations of the modeling assumptions.
(1), (2), and (3) SPS model, IMF, and dust extinction law, alternatively. The first column indicate the parameters being compared.
(4) Log of median value and quartiles of the difference for galaxies with $\log(M) < 10\ \mathcal{M}_\odot$.
(5) Same as (4) for galaxies with $\log(M) > 10\ \mathcal{M}_\odot$.

et al. 2006). A detailed analysis of the completeness limit as a function of the galaxy type will be included in a forthcoming paper.

The first test on the effect of the SED modeling assumptions consist of a comparison of the stellar masses computed with three different choices of the IMF: SALP, Kroupa (2001), and Chabrier (2003, hereafter KROU and CHAB, respectively) IMFs. The naive expectation is that the stellar masses obtained with a SALP IMF are on average larger than those obtained with the other two, as it predicts a larger number of low-mass stars. On the contrary, the IMFs of KROU and CHAB are quantitatively very similar and therefore the differences are expected to be small and mass independent. Table 6 summarizes the median value and quartiles of the comparison of stellar masses obtained with each IMF in combination with the P01 and S. Charlot & G. Bruzual (2011, in preparation, referred as CB09) models and a CAL01 extinction law against the reference values. The top panels in Figure 15 show this comparison for SALP or KROU IMFs (left) and a KROU or CHAB IMFs (right) and the CB09 models. In both cases the difference is essentially a constant value of factor ∼1.6 and 1.2, respectively, consistently with the results of the literature (e.g., Salimbeni et al. 2009; Muzzin et al. 2009; Marchesini et al. 2009). On the contrary, the difference in the values obtained with a SALP or KROU IMFs for the P01 models is significantly smaller than that for the CB09 models, showing also a larger scatter and a dependence on the stellar mass. This effect seems to be related with a difference in the age dependency of the mass-to-light ratio for each IMF in these particular models (see, e.g., Maraston 1998; van Dokkum et al. 2008 for a description of these effects).

The second test on the modeling parameters is the comparison of stellar masses obtained with the models of P01, Bruzual & Charlot (2003, BC03), Maraston (2005, M05), and CB09 for the same IMFs. The models of M05 were the first to account for the contribution of the TP-AGB phase in the SPSs, a consideration that is expected to lead to lower stellar masses compared to those obtained with P01 and BC03. However, this difference should be reduced in the CB09 models, the updated version of BC03, which include an improved treatment of this particular phase. The overall results of the comparison between models are also summarized in Table 6 and in the panels of Figure 16.

Interestingly, we find that the difference between [BC03, CHAB] and [CB09, CHAB] is relatively small, ∼0.04 dex, and mostly independent of the stellar mass. This suggests that, at least for the present sample, taking into account the TP-AGB phase does not introduce significant differences. A possible explanation could be that, since the spectroscopic sample consist mostly on $z < 1$ galaxies, the available photometric coverage is not probing the rest-frame NIR with sufficient detail. Only at higher redshifts ($z \gtrsim 1$) the IRAC bands would start probing the region of the SED that is heavily affected by the TP-AGB phases. Note also that the spectroscopic sample analyzed here might not be a critical population to constraint the effect of the TP-AGB, as, for example, the post-starburst galaxies studied in Conroy et al. (2010).

In addition, we find that the estimates with [P01, KROU] are larger than those obtained with [CB09, KROU] and [M05, KROU] with an average offset of 0.15 dex and 0.39 dex, respectively. The difference with respect to M05 is consistent with previous results (e.g., Maraston et al. 2006; van der Wel et al. 2006; Bruzual 2007) in spite of the slight dependence on the mass. However, the 0.16 dex offset between [CB09, KROU] and [M05, KROU] (illustrated for completeness in bottom-right panel of Figure 16) is larger than expected revealing a more complex relative difference between the two libraries beyond the treatment of the TP-AGB phase.

Finally, the bottom-right panel of Figure 15 shows the comparison of the stellar masses estimates obtained with a CAL01 and a Charlot & Fall (2000, CF00) dust extinction laws for the P01 models and a KROU IMF. The most relevant differences between CAL01 and CF00 extinction laws are that the latter presents a larger attenuation of the stellar component, which effectively leads to lower fluxes (mostly in the UV) for similar values of the extinction. Furthermore, the wavelength dependence of the attenuation in CF00 is grayer (i.e., shallower) than in CAL01. The overall result of the comparison is a small offset of −0.03 dex with a ∼0.2 dex rms, similar to what we found in PG08. This is also in good agreement with the results of Muzzin et al. (2009), indicating that the treatment of the extinction law does not play a major role in the estimate of the stellar mass (although it is more relevant for other estimated parameters).

In summary, we find that after accounting for the different systematic offsets, all models seem to be roughly consistent within a factor two (∼0.3 dex). However, there are mass dependent systematics that should be taken into account in the analysis of overall properties of galaxy samples (e.g., Marchesini et al. 2009; Taylor et al. 2009; Ilbert et al. 2010).

4.2.2. Comparison to other Stellar Mass Catalogs

In this section, we compare our stellar masses with the estimates from Bundy et al. (2006) and Trujillo et al. (2007). In the former, the authors derived stellar masses for a large sample of galaxies with spectroscopic redshifts from the DEEP2 survey in the EGS. In the latter, the authors combined spectroscopic and photometric redshifts to study the properties of a mass limited sample ($\log M > 11\ \mathcal{M}_\odot$). Both works used the same photometric data set consisting of five bands: *BRI* from the CFHT survey, and *JK* from the Palomar NIR survey. The stellar masses in both cases were essentially computed based

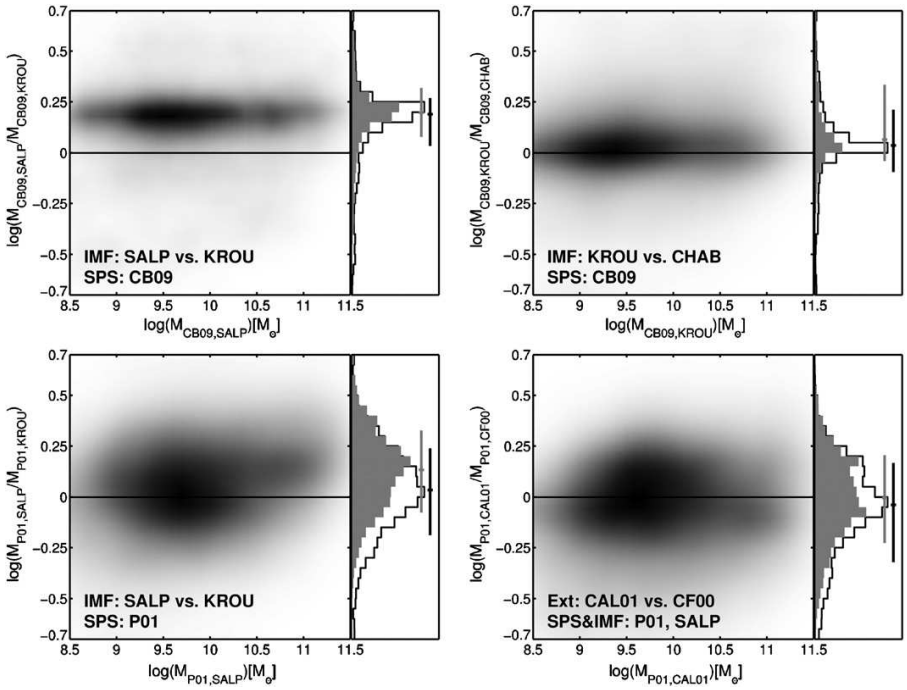

Figure 15. Comparison of the stellar masses obtained using different IMFs and dust extinction laws for a given SPS library. Top left: P01 models with a SALP and KROU IMFs. Top right: CB09 models with a SALP and KROU IMFs. Bottom: CB09 models with a KROU and CHAB IMFs. Bottom right: P01 models with a CAL01 and CF00 extinction laws. The histograms in the right part of the plot depict the ratio of the stellar masses obtained with each IMF for galaxies with $M_{\rm model} < 10\,\mathcal{M}_{\odot}$ (empty) and $M_{\rm model} > 10\,\mathcal{M}_{\odot}$ (filled). The solid lines above the histogram show the median value and 1σ of the distribution at both sides of the median.

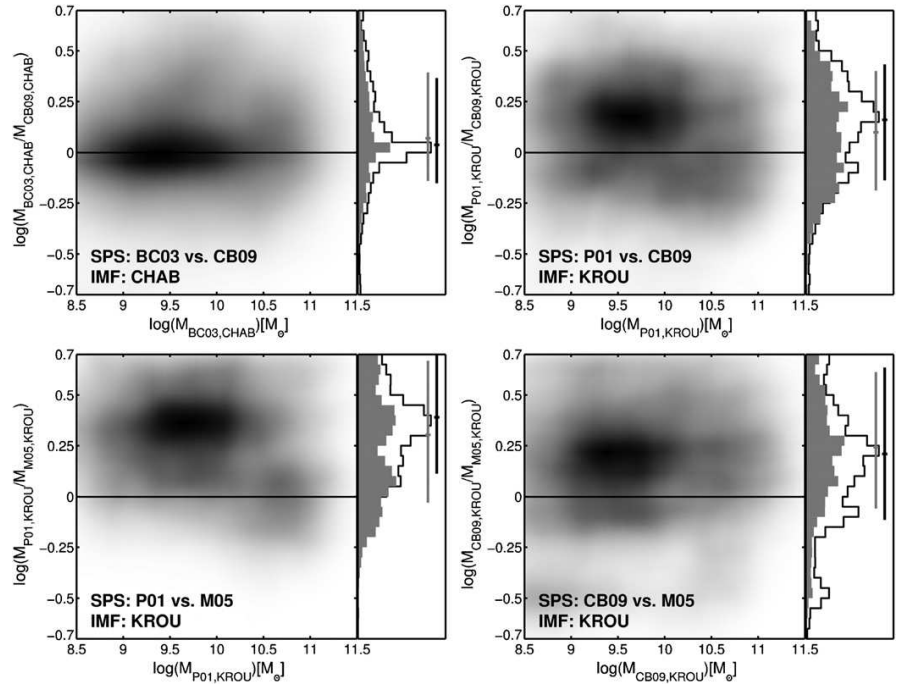

Figure 16. Comparison of the stellar masses obtained using different SPS models with the same IMF. Top left: BC03 and CB09 models with a CHAB IMF. Top right: P01 and CB09 models with a KROU IMF. Bottom left: P01 and M05 models with a KROU IMF. Bottom right: CB09 and M05 models with a KROU IMF. The histograms in the right part of the plot depict the ratio of the stellar masses obtained with each model for galaxies with $M_{\rm model} < 10\,\mathcal{M}_{\odot}$ (empty) and $M_{\rm model} > 10\,\mathcal{M}_{\odot}$ (filled). The solid lines above the histogram show the median value and 1σ of the distribution at both sides of the median.

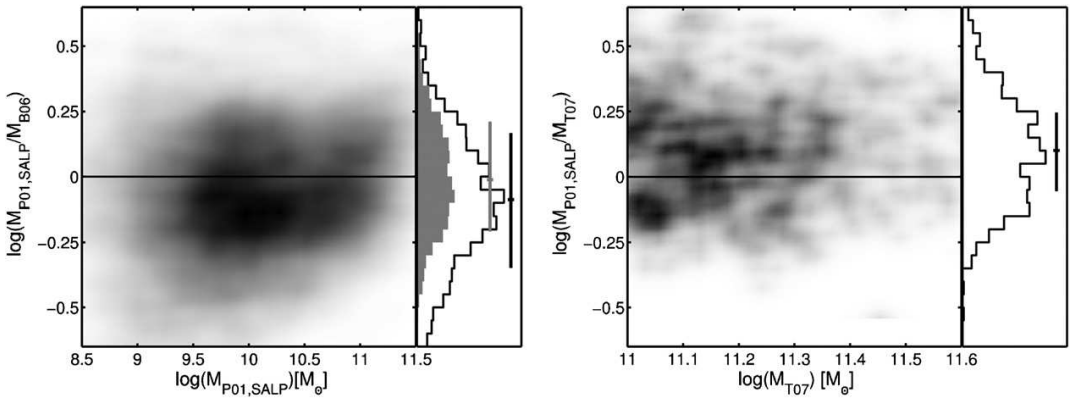

Figure 17. Difference between our best-fit stellar mass using [P01, SALP] and the stellar masses of Bundy et al. (2006) (left), and the mass limited sample (log $M >$ 11 $\mathcal{M}_{\odot}$) of Trujillo et al. (2007). The histograms in the right side are the same as in Figure 15. Note that the comparison to Trujillo et al. is limited to log $M > 11$ $\mathcal{M}_{\odot}$.

on the fitting of the SEDs to a grid of templates derived from BC03 models with a Chabrier (2003) IMF and exponentially decreasing SFHs. In particular, Bundy et al. used the rest-frame K-band luminosity and mass-to-light ratio to scale the templates and compute the probability distribution of the stellar mass and the most likely value. On the contrary, Trujillo et al. (based on the results of Conselice et al. 2007) did not renormalize the templates in a single band but used the whole SED to scale the fluxes, similarly to our approach but restricted to only five bands.

We cross-correlate the catalogs using a 2″ radius, and we double check the validity of the match ensuring that the spectroscopic redshifts (independently matched) are the same. The final sample contains 4706 and 791 galaxies detected in the catalogs of Bundy et al. and Trujillo et al., respectively. For the comparison to Bundy et al. the photometric redshifts were forced to the spectroscopic value and for the comparison to Trujillo et al. the photometric redshifts were forced to the values quoted in their paper.

The left panel of Figure 17 shows the comparison of the stellar masses with Bundy at al. for our default modeling assumptions. Our estimates are slightly lower with a median difference of $\Delta \log(M) = -0.07 \pm 0.21$ dex. Also, we find that the stellar masses computed with [P01,SALP] are in better agreement with Bundy et al. than those obtained using the same modeling configuration as in their work, [BC03, CHAB], which would increase the difference in smaller masses to $\Delta \log(M) = -0.12$ dex. We further investigate if this offset is caused by a difference in the photometry by comparing our K-band magnitudes to those of Bundy et al. that were computed using 2″ radius apertures (for the SED fitting). The sources in Bundy et al. are on average $\Delta\ K = 0.12$ mag fainter than in our catalog, which would imply a larger difference in the stellar masses if we simply scale their magnitudes to our photometry. Thus, the most plausible explanation for this small offset is the use of different techniques for estimating the stellar masses, and specifically the use of IRAC data in our study. The right panel of Figure 17 shows the comparison of the stellar masses with Trujillo at al. The overall comparison presents a good agreement with a median difference of $\Delta \log(M) = 0.10 \pm 0.25$ dex, slightly larger than the offset to masses of Bundy et al. However, the scatter of the distribution is quite similar to that of the comparison to Bundy et al. for the highest stellar masses $\log(M) > 11$ $\mathcal{M}_{\odot}$.

5. SED ANALYSIS: STAR FORMATION RATES

In this section, we present the estimations of the SFRs of the galaxies in our IRAC sample based on their UV-to-FIR SEDs. We also discuss the quality of these estimates as well as their associated systematic uncertainties.

The SFR of a galaxy is frequently computed from the UV and IR luminosities through theoretical or empirical calibrations. As young stellar populations emit predominantly in the UV, this wavelength range is highly sensitive to recent events of star formation. However, this UV emission is usually attenuated by dust, which re-emits the absorbed energy in the thermal IR. Consequently, the ongoing SFR can be estimated either by correcting the UV luminosity for extinction or combining the IR emission and the unobscured UV flux.

Here, we focus on the latter approach making use of the high quality FIR fluxes observed with MIPS at 24 and 70 μm. Thus, assuming that the total SFR of a galaxy can be estimated by summing up two components (see, e.g., Bell et al. 2005; Iglesias-Páramo et al. 2007): the part of the star formation that is probed by a tracer affected by dust attenuation, so we only are able to observe directly a fraction of it (i.e., the unobscured component), and the part of the star formation that is hidden by dust (obscured component). The unobscured star formation can be measured with the rest-frame UV emission, which can be estimated from the optical/NIR SEDs for the galaxies in our sample. The obscured component can be estimated from the total IR thermal emission (thus, we will refer to it as IR-SFR or IR-based SFR). However, its calculation is usually affected by the choice of template libraries fitting the IR part of the SED and, more significantly, by the photometric coverage in the MIR-to-mm spectral range. In this section, we will focus on the analysis of the IR-based SFR and the random and systematic uncertainties associated with the different procedures used to estimate it.

The structure of this section is as follows. First, we describe how we fit the IR part of the SEDs to dust emission models and present the different methods used to estimate an IR-based SFR from monochromatic and integrated luminosities in the MIR-to-mm range. Then, we compare these different methods and discuss the systematic and random uncertainties inherent to the calculation of IR-based SFRs.

In this section, the reader must have in mind that the most useful information to estimate IR-based SFRs comes from the

The Astrophysical Journal Supplement Series, 193:30 (34pp), 2011 April

MIPS 24 μm fluxes. The reason is simple: these observations are the deepest in the MIR-to-mm range, so we only have this SFR tracer for the vast majority of sources in our sample. Ideally, it would be desirable to have other fluxes in the IR to constrain the fits to dust emission models, but this is only possible for a very small fraction of galaxies which have MIPS 70 μm data, or other photometric points in the (sub)-mm. Even with *Herschel* data, there will be a significant population of galaxies that will only count with the MIPS 24 μm flux. Therefore, an important part of our discussion will be assessing the reliability of IR-based SFRs based only on MIPS 24 μm data. For that purpose, we will take advantage of the very deep observations carried out at 70 μm within the *Spitzer* FIDEL Legacy Project, studying the variations in the estimated IR-based SFRs fitting MIPS 24 μm and MIPS 70 μm simultaneously.

5.1. IR SED Fitting

Typically, IR-based SFR are computed either from the total IR luminosity, i.e., the integrated emission from 8 to 1000 μm [L(TIR)] or from monochromatic luminosities at different wavelengths. Both methods require a detailed characterization of the IR SED, which is usually obtained by fitting the observed fluxes to dust emission templates. However, as mentioned above, these estimates are largely dependent on the choice of templates. An issue that is usually aggravated by the fact that typically the only measurement of the MIR emission comes from the 24 μm data, and occasionally 70 μm, whereas the total IR luminosity is commonly dominated by the emission at longer wavelengths $\lambda \sim 100\,\mu$m.

Thus, in order to study in detail the intrinsic uncertainties in the IR-based SFRs arising from these issues, we follow two different approaches to fit the IR data to the dust templates: (1) we study the galaxies detected at MIPS 24 μm fitting only this flux to models of Chary & Elbaz (2001, CE01 hereafter), Dale & Helou (2002, DH02 hereafter), which is a usual scenario in studies of the IR-emission at high-z (see e.g., Santini et al. 2009; Wuyts et al. 2008). In this case, we asses the differences between IR-based SFR (hereafter SFR$_i$(24)) estimated with several methods, and the impact of using different models; (2) we restrict the analysis to galaxies simultaneously detected in IRAC and MIPS 24 and 70 μm, fitting all fluxes at rest-frame wavelengths $\lambda > 5\,\mu$m (where the luminosity of a galaxy must present a significant non-stellar contribution; see, e.g., Pérez-González et al. 2006; Smith et al. 2007) to the models of CE01, DH02, and also Rieke et al. (2009, R09 hereafter). We refer to these galaxies as the best-effort sample and their SFRs (8, 24, 70). The notation indicates that the fit essentially includes 8, 24, and 70 μm data up to $z \sim 0.6$, 24, and 70 μm data at higher redshift. Based on this sample we can study the impact of having a better constrained IR SED against the MIPS 24 μm only scenario (e.g., as in Kartaltepe et al. 2010). In both cases, the fitting is carried out by fixing the redshift to $z_{\rm phot}$ or $z_{\rm spec}$ (if available). Then, the excess resulting from subtracting the predicted contribution from the stellar flux (given by the best-fitting optical template) to the MIR bands is fitted to each set of models. In the case when only MIPS 24 μm data are used, the templates are not fitted but rather scaled, i.e., we obtain the rest-frame monochromatic luminosity for that flux and redshift and we select the most likely template based in their absolute normalization in the total IR luminosity (as in, e.g., Papovich et al. 2006; Santini et al. 2009). Moreover, for sources undetected in the 24 μm data, we set an upper limit of $f(24) = 60$ μJy, the approximate SNR = 5 level of the MIPS data in EGS (see Paper I for more details), which allows us to provide an upper limit of the IR-based SFR. Figure 2 shows an example of the IR SED fitting jointly with the optical template.

Based on the best-fitting templates, we computed several IR monochromatic and the integrated luminosities [$L(\lambda)$ and L(TIR), respectively] as the median value of all the fitted template sets. In the following, we describe various possibilities for IR-based SFRs based on $L(\lambda)$ at different wavelengths. These relations are calibrated from galaxy samples counting with extensive IR coverage (at least more than 3–4 bands), and provides an alternative estimate of the SFR based on milder template extrapolation than L(TIR), which in principle makes them more robust when only few bands are available for the fitting. Note however that the rest-frame wavelengths around 10–30 μm are wildly variable and thus extrapolating luminosities in this region involve significant uncertainties, e.g., $L(8)$ based on 24 μm data at $z \sim 2$ (see Section 5.3.2 for more details).

5.2. Total SFR and IR-based SFRs Estimates

Our method to estimate the total SFRs is based on a combination of the IR emission and the unobscured UV flux (similarly to Pérez-González et al. 2006; Kennicutt et al. 2009; Santini et al. 2009). In particular, we use the prescription of Bell et al. (2005, see also Papovich et al. 2007), which is based on the calibration for the total IR luminosity of Kennicutt (1998) and parameterizes the contribution of radiation that escapes directly in the UV:

$$\mathrm{SFR} = \mathrm{SFR_{TIR}} + \mathrm{SFR_{UV,obs}} \quad (3)$$

$$\mathrm{SFR}(M_\odot\,\mathrm{yr}^{-1}) = 1.8 \times 10^{-10}[L(\mathrm{TIR}) + 3.3 \times L(0.28)]/L_\odot, \quad (4)$$

where L(TIR) is the integrated total IR luminosity and $L(0.28)$ is the rest-frame monochromatic luminosity at 0.28 μm (uncorrected for extinction). The well-sampled SEDs of our galaxies at optical wavelengths allow a robust estimation of $L(0.28)$ by interpolating in the best-fitting optical template. However, as described in the previous section, the value of L(TIR) is strongly model dependent, as it is based on an extrapolation from one or a few MIR fluxes to the total emission from 8 to 1000 μm. An alternate possibility is to obtain other IR-based SFRs based on $L(\lambda)$, thus reducing the template dependence. In the following, we will refer to the IR-based SFR derived from L(TIR) as SFR$_{\rm TIR}$. In addition, we compute four other IR-based estimates.

The first estimate is based on rest-frame monochromatic luminosity at 8 μm (hereafter SFR$_{\rm B08}$). These estimate make use of the empirical relation between $L(8\,\mu\mathrm{m})$ and L(TIR) described in Bavouzet et al. (2008) and the Kennicutt factor to transform to SFR:

$$\mathrm{SFR_{B08}}(M_\odot\,\mathrm{yr}^{-1}) = 1.8 \times 10^{-10} \times (377.9 \times L(8)^{0.83})/L_\odot. \quad (5)$$

The second method in based on Equation (14) of Rieke et al. (2009) that relates the SFR (hereafter SFR$_{\rm R09}$) to the observed flux in the MIPS 24 μm band and the redshift. The redshift dependent coefficients of the relation were computed using averaged templates derived from a set of empirical IR–SEDs fitting local galaxies. This estimation of the SFR is independent of the rest, as it is based on different templates. The conversion from IR luminosities to SFRs is also computed through the Kennicutt factor. However, the authors scaled the factor to a Kroupa-like (2001) IMF (the original factor is for a SALP IMF)

multiplying it by 0.66 (a similar conversion is obtained in Salim et al. 2007). Here, we undo that change for consistency with the other methods that are computed using the factor for a SALP IMF.

The last method is not strictly an IR-based SFRs but an estimate the global SFR. It is based on the empirical relation given in Alonso-Herrero et al. (2006) between the rest-frame monochromatic luminosity at 24 μm and the SFR (hereafter, $SFR_{A\text{-}H06}$),

$$SFR_{A\text{-}H06}(M_\odot\ yr^{-1}) = 1.51 \times 10^{-8} \times L(24)^{0.871}/L_\odot. \quad (6)$$

This formula is based on the calibration of $L(Pa\alpha)$ versus $L(24\,\mu m)$ obtained for a set of local ULIRGS using the Kennicutt (1998) relation between $L(Pa\alpha)$ and SFR. A similar result was obtained by Calzetti et al. (2007) for resolved star-forming regions in local starburst (see also Kennicutt et al. 2009). This estimation refers to the global SFR, not the IR-based SFR, because the empirical relation in Alonso-Herrero et al. (2006) already takes into account the unobscured star formation (measured through the observed Paα emission) and the extinction correction (applied to calculate $L(Pa\alpha)$ in that paper).

5.3. Accuracy of the IR-based SFRs

In the following sections, we analyze the systematic uncertainties in the IR-based SFRs associated with the use of different models and indicators, and also the number of photometric bands available for IR SED fitting.

First, we compare the values obtained with each of the methods presented in the previous section for a sub-sample of MIPS 24 μm detected galaxies. In this case, the SED is fitted to 24 μm data only (Section 5.3.1). Note that we have chosen several methods for estimating the IR-based SFR that present intrinsically different approaches, using either integrated and monochromatic luminosities or observed fluxes. Here, we also test the differences introduced by the use of the CE01, DH02, or R09 models. For simplicity, in this case, the comparison to the R09 models is done through the SFRs obtained with their empirical relation (SFR_{R09}) instead of fitting the data to the three models.

Second, we study the differences in the SFRs obtained for MIPS 24 μm sample and the best-effort sample, which count with a better IR coverage based on IRAC-8.0 plus MIPS 24 and 70 μm data (Section 5.3.2). With this test we quantify the systematic effects associated with use of limited IR data. Finally, we repeat the comparison of values obtained with each method for the best-effort sample including also highly accurate SFRs drawn from other authors based on a more detailed IR coverage (Section 5.3.3). Based on this comparison we asses the goodness of our best-effort SFRs and the reliability of the different methods studied here.

For the sake of clarity, we will refer all the comparisons between the SFRs estimated with each method to SFR_{TIR} which, as explained in Section 5.1, is computed from the average total infrared luminosity of all the fitted template sets. In addition, we will refer to them just as SFRs (dropping the IR prefix). In the case of $SFR_{A\text{-}H06}$, the proper IR-based SFRs are obtained by subtracting the contribution of the $SFR_{UV,obs}$. Nevertheless, as our working samples are composed by strong IR-emitters, we are biased toward dust obscured galaxies where this contribution is presumably small. For example, Figure 18, which shows the ratio $SFR_{UV,obs}/SFR_{TIR}$, indicates that $SFR_{UV,obs}$ is lower than SFR_{TIR} (in most cases), with a clear trend for galaxies with intense star formation to present more and more extincted starbursts.

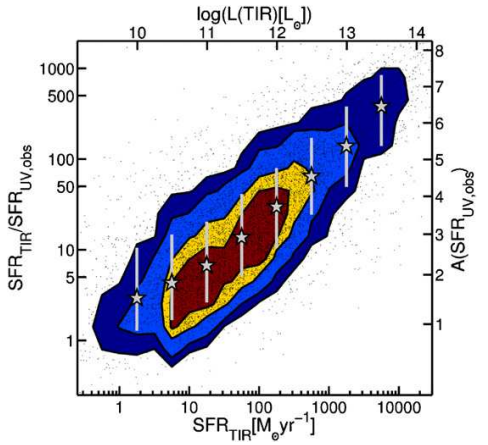

Figure 18. Ratio of the two components of the total SFR (SFR = $SFR_{UV,obs}$ + SFR_{IR}; Equation (4)) as a function of the SFR_{TIR} for a sub-sample galaxies detected in MIPS 24 μm ($f(24) > 60\,\mu$Jy). Each contour contains (from the inside out) 25%, 50%, 75%, and 90% of the sample, respectively. The underlying black dots depict the individual values of the ratio of SFRs. The gray stars with error bars depict the median and 1σ of the ratio of SFRs in bins of SFR_{TIR}.

5.3.1. Analysis of IR-based SFRs: MIPS 24 μm Sample

Figure 19 shows the comparison of the IR-based SFRs obtained with the different methods presented in Section 5.2 with respect to SFR_{TIR} as a function of SFR and redshift. All the estimates discussed in this section are based on 24 μm data only, i.e., $SFR_i(24)$. We omit the parentheses for simplicity. The SFR_{TIR} estimated separately with the models of CE01 (green dots) and DH02 (blue dots) are shown jointly with the median and rms of both values in several SFR and luminosity bins. The typical scatter of the SFRs estimated with both libraries is smaller than ~0.3 dex, consistent with the results by other authors (Marcillac et al. 2006; Papovich et al. 2007). When we compare the CE01 and DH02 libraries as a function of redshift, the maximum differences are observed for galaxies at $z = 1$–2. For these sources, the estimates with the DH02 models are larger than those with CE01 models, as found by Santini et al. (2009). In this redshift range, the 24 μm band is probing the spectral region where the 9.6 μm silicate absorption is found, jointly with the prominent PAHs around 7–9 μm. The shape of the models in CE01 and DH02 template sets is very different in this region, with the former presenting less prominent PAH features than the latter. In fact, all the DH02 models are identical below ~9 μm, while CE01 models present a wide variety of spectral shapes, with a rising warm-dust continuum hiding the PAH features between 6 and 20 μm as we move to models with higher IR luminosities.

The values of $SFR_{A\text{-}H06}$ are systematically smaller than SFR_{TIR}. For $SFR_{TIR} > 100\,M_\odot\ yr^{-1}$, we find $\Delta SFR = -0.18 \pm 0.05$ dex. For smaller values of the SFR, where the unobscured and obscured star formation are comparable, $SFR_{A\text{-}H06}$ is down to a factor of 0.6 dex smaller than SFR_{TIR}, with a larger scatter.

The comparison of SFR_{TIR} and SFR_{B08} clearly indicates that the empirical relations $L[8]$-to-L_{TIR} in Bavouzet et al. (2008) (Equation (5)) and in the models of CE01 and DH02 (see, e.g., Figure 8 of Daddi et al. 2007) are substantially different. The ratio of the two SFRs as a function of SFR_{TIR} is tilted

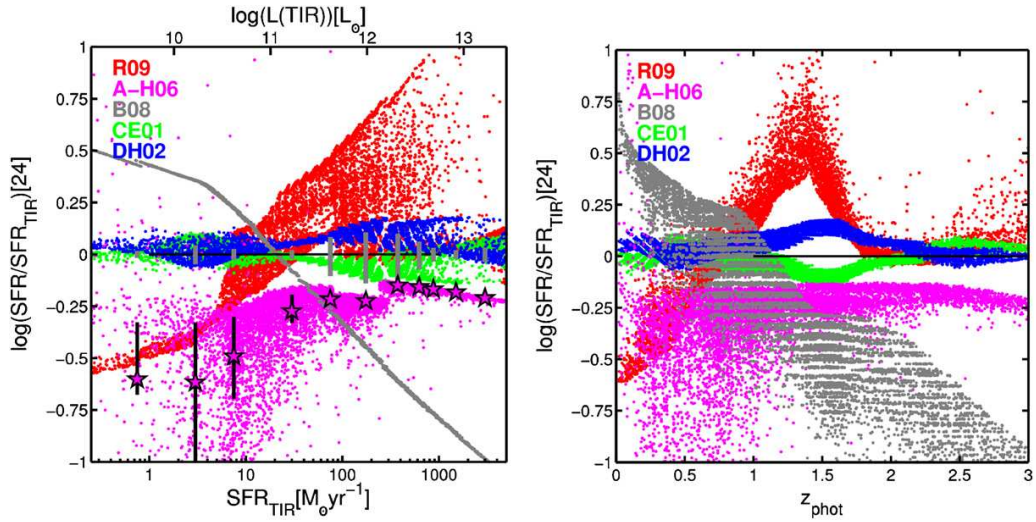

Figure 19. Comparison of different IR-based SFR indicators with respect to SFR_{TIR} as a function of SFR_{TIR} (left) and redshift (right) for galaxies detected in MIPS 24 μm ($f(24\,\mu m) > 60\,\mu$Jy). SFR_{TIR} is computed from the average value of L_{TIR} in the templates of CE01 and DH02 fitted to the flux at 24 μm. The magenta points show $SFR_{A\text{-}H06}$ estimated from the $L(24)$ using the relation of Alonso-Herrero et al. (2006); the magenta stars and error bars indicate the median value and 1σ per SFR bin. The gray points show SFR_{B08} estimated from $L(8)$ using the relation of Bavouzet et al. (2008). The red points show SFR_{R09} estimated from MIPS 24 μm using the calibration of Rieke et al. (2009). The green and blue points depict SFR_{TIR} estimated from the templates of CE01 and DH02, respectively. The gray error bars depict the 1σ uncertainty in SFR_{TIR} per SFR bin.

with respect to the unity line, and consequently, both estimates are only consistent within a narrow interval around SFR $\sim$ 20 $M_\odot$ yr^{-1} (or $z \sim 1$). For $SFR_{TIR} > 100$ and 1000 $M_\odot$ yr^{-1} (the latter being the typical value for the $z \sim 2$ galaxies detected by MIPS) the SFR_{B08} values are 0.3 and 0.8 dex lower than the SFR_{TIR} estimates, respectively. In contrast, for $SFR_{TIR} \lesssim 10\,M_\odot$ yr^{-1}, SFR_{B08} is larger than SFR_{TIR} by >0.2 dex.

The equation to calculate SFR_{R09} (Rieke et al. 2009) varies with redshift. Consequently, the SFR_{R09}/SFR_{TIR} ratio presents different trends as a function of both luminosity and redshift. In terms of redshift, we distinguish three regions: $0 < z < 1.4$, $1.4 < z \lesssim 1.75$, and $z \gtrsim 1.75$. At $z = 0$–1.4, the ratio increases with redshift from an average value of -0.5 dex at $z = 0$ to 0.5 dex at $z \sim 1.4$, being close to unity at $z \sim 0.75$. In the interval from $1.4 < z \lesssim 1.75$, the ratio decreases from 0.5 dex to nearly $\sim$0. Finally, at $z > 1.75$, SFR_{R09} values become roughly consistent with SFR_{TIR} with little scatter up to $z = 3$, $\Delta SFR = 0.02^{0.06}_{0.04}$ dex. These large differences are related to the distinct shapes of the R09 and CE01/DH02 templates. At $z \lesssim 0.5$, the 24 μm band probes a spectral range dominated by warm dust and emission features found by *Spitzer* at $\lambda \sim 17\,\mu$m and identified with PAH or nanoparticles (Werner et al. 2004). At these redshifts, our sample is dominated by galaxies with $L(TIR) \sim 10^{10}\,L_\odot$, and the CE01 models for these luminosities differ from the corresponding R09 templates by up to 0.5 dex in the $\lambda = 16$–20 μm. This explains the differences at low redshift in the right panel of Figure 19. At $z = 0.5$–1.0, our sample is dominated by LIRGs, and CE01 and R09 models for $L(TIR) \sim 10^{10.75}\,L_\odot$ and $L(TIR) \sim 10^{11.25}\,L_\odot$ are very similar (up to $\lambda = 1.5$ mm), resulting on very similar estimates of the SFR. At $z \sim 1.4$, the 24 μm band probes the spectral region around 10 μm, and the galaxies detected by MIPS in this range have $L(TIR) \gtrsim 10^{11.5}\,L_\odot$. For this luminosity, the CE01 and R09 models differ considerably due to the relative strength of the silicate absorption. For example, for an $L(TIR) \gtrsim 10^{12.25}\,L_\odot$, the R09 template predicts a luminosity at 10 μm which is a factor of $\sim$0.7 dex smaller than the CE01 model corresponding to the same $L(TIR)$. Below 8 μm, rest-frame, the CE01 and R09 models are almost identical for LIRGs and ULIRGs, explaining the good match between SFR_{TIR} and SFR_{R09} at $z \gtrsim 2$.

In summary, we conclude that whereas $SFR_{A\text{-}H06}$ and SFR_{TIR} are roughly consistent within $\sim$0.3 dex (modulo a constant offset), regardless of the models used to fit the IR-SED, the values of SFR_{B08} and SFR_{R09} present systematic deviations with respect to those that are not consistent within the typical rms. Moreover, these differences are not constant, but present a dependence of both redshift and SFR. As a result, large systematic offsets (of $\pm$0.5 dex) with respect to SFR_{TIR} are expected at certain redshifts, e.g., $\Delta SFR \sim +0.5$ and -0.5 dex for SFR_{R09} and SFR_{B08} at $z \sim 1.4$, respectively.

5.3.2. Analysis of IR-based SFRs: Best-effort versus MIPS 24 μm

Here, we study the impact on the IR-based SFRs of modeling the IR-SED with limited photometric data. For that matter, we quantify the differences in the SFRs estimated with each of methods compared in the previous section using the sample characterized with MIPS 24 μm data and with 8, 24, and 70 μm data, i.e., the best-effort sample (note that $\lesssim$2% of the sample in detected in MIPS 70 μm for $\sim$20% in MIPS 24 μm). In principle, the inclusion of additional mid-IR fluxes must improve the quality of the estimates given that there is a better sampling of the IR SED from which better k-corrections to the monochromatic luminosities can be obtained. On the downside, the spectral range probed by the MIPS bands gets narrower with redshift, and the 24 μm channel shifts progressively into PAH region, where models are more uncertain and different libraries differ significantly. Also, as the observed 70 μm moves further away from the tip of the IR-emission ($\sim$100 μm), the uncertainty in the extrapolated $L(TIR)$ increases.

Figure 20 shows the ratio SFR(24)/SFR(8, 24, 70) as a function of redshift for each of the different methods to estimate the SFR, except for SFR_{R09}, that only depends on the observed

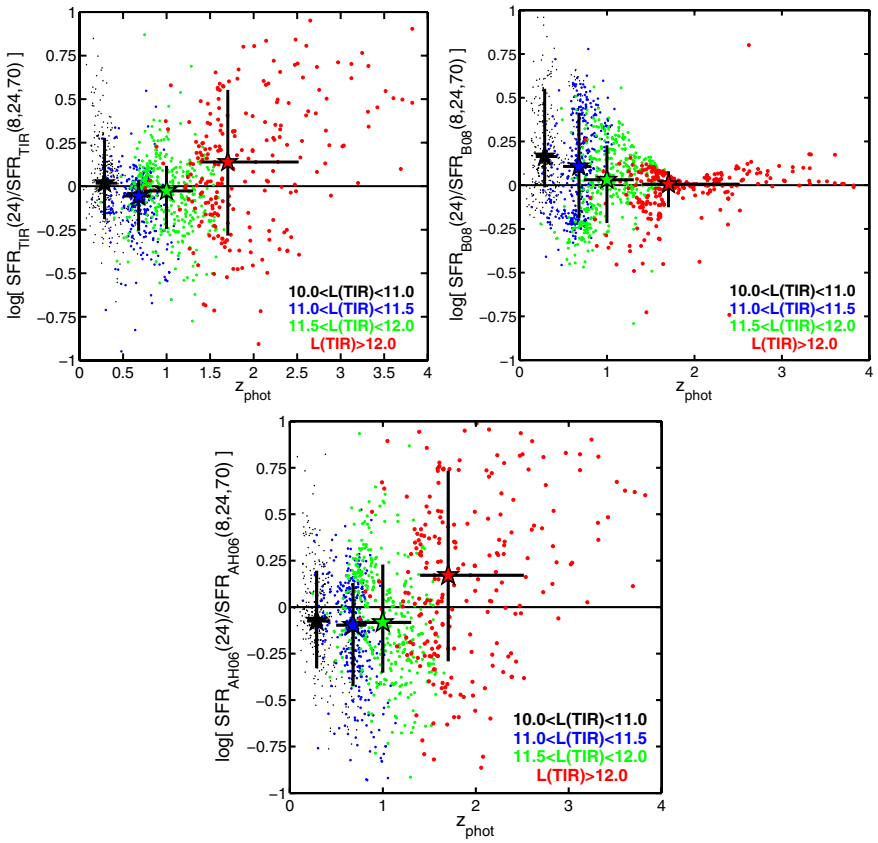

Figure 20. Ratio of SFR_{TIR}, SFR_{B08} (left and right), and $SFR_{A\text{-}H06}$ (bottom) estimated with 24 μm data only and with 8, 24, and 70 μm data as a function of redshift. The color code indicate increasing bins of IR luminosity from *normal* galaxies to ULIRGS. The colored stars with error bars depict the median value and 1σ of the ratio of SFRs and the redshift per luminosity bin.

flux at 24 μm and the redshift. The color code indicates four different bins of infrared luminosity. The colored stars with error bars depict the median value and 1σ of the redshift and the ratio of SFRs (24/8, 24, 70) for different luminosity bins.

The upper-left panel of Figure 20 shows that $SFR_{TIR}(24)$ and $SFR_{TIR}(8, 24, 70)$ are $\sim$1σ consistent within $\sim$0.20 dex up to ULIRG luminosities, showing a small offset (mostly at $z \gtrsim 0.5$) in $SFR_{TIR}(24)$ toward underestimating the SFR by $\Delta SFR = -0.05 \pm 0.20$ dex. On the other hand, ULIRGs (typically at $z \gtrsim 1.5$) present values of $SFR_{TIR}(24)$ larger than $SFR_{TIR}(8, 24, 70)$ with an average difference of $\Delta SFR = 0.15 \pm 0.40$ dex. This is consistent with the results found for ULIRGs at this redshift by several authors, who report excesses of a factor of 2–10 in the SFRs estimated from MIPS 24 μm only (Daddi et al. 2007; Papovich et al. 2007; Rigby et al. 2008). Note that estimating the IR-luminosities for these galaxies based on MIPS 24 μm data alone is intrinsically difficult as this band is probing the most variable region of the IR-SED, featuring emission from PAHs and silicate absorptions. In fact, further motive for these discrepancies could associated with a change in the relative strength of these components in high-z galaxies with respect to the local templates, particularly for the ULIRG templates.

Figure 21 presents further evidence of this issue. The left and right panels of the Figure show the rest-frame SED normalized to the flux at 24 μm for galaxies at $\tilde{z} = 0.7$ and $\tilde{z} = 1.5$ in different L(TIR) ranges. The red and black lines are the dust-emission templates of Rieke et al. (2009). The black templates are those corresponding to the IR-luminosity range shown in the legend. Note that we have selected the redshift ranges and template normalization with the specific aim of stressing the differences in warm-to-cold dust colors between the R09 models and the actual observations. The same differences apply to other template sets. The vertical line to the right of the MIPS 70 μm data depicts the median and 1σ of the distribution of MIPS 70 μm fluxes (normalized to 24 μm, i.e., the S_{70}/S_{24} color). At $z \sim 0.7$, the models for an $L(\mathrm{TIR}) = 10^{10.5}$–$10^{11.0}$ $L_{\odot}$ nicely predict the actual colors observed for galaxies (the templates plotted in black match the median and 1σ range of observed colors). However, at $z \sim 1.5$, galaxies present smaller colors than what the models for the appropriate luminosity range predict. This suggests that the excess in $SFR_{TIR}(24)$ could be related to a difference in spectral shapes for ULIRGs at high redshift in comparison with local ULIRGs either due to the strength of the PAH and the silicate features (Elbaz et al. 2010; Pérez-González et al. 2010) or due to additional continuum emission by an obscured AGN (Daddi et al. 2007).

The lower panel of Figure 20 shows SFR(24)/SFR(8, 24, 70) for the B08 recipe. The ratio of SFRs presents just the opposite trend of what we find for SFR_{TIR}, i.e., the offset and rms of the comparison are larger at lower redshifts and almost non-existent (< 0.1 dex) at high-z. This is not surprising considering that MIPS 24 μm shifts toward 8 μm with increasing redshifts,

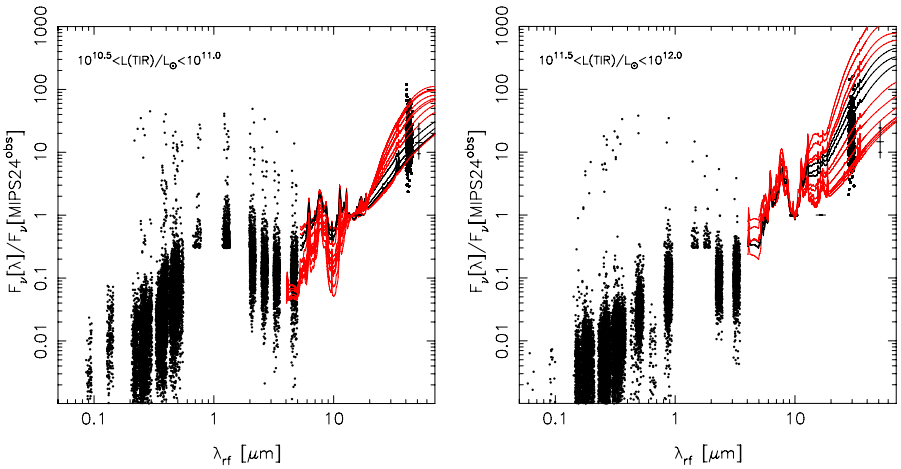

Figure 21. Rest-frame SEDs of galaxies detected in MIPS 24 and 70 μm at $0.6 < z < 0.8$ with $10^{10.5} < L(\mathrm{TIR}) < 10^{11.0}$ (left panel) and $1.3 < z < 1.6$ with $10^{11.5} < L(\mathrm{TIR}) < 10^{12}$ (LIRGS) (right panel). The fluxes are normalized to the flux in MIPS 24 μm. The solid lines depict the templates of Rieke et al. (2009): black lines are for templates with L(TIR) within the corresponding IR–luminosity range, red lines are for the rest of the templates. The vertical line and marks on the right of the MIPS 70 μm fluxes show the median, quartiles, and 1σ of the distribution of observed fluxes.

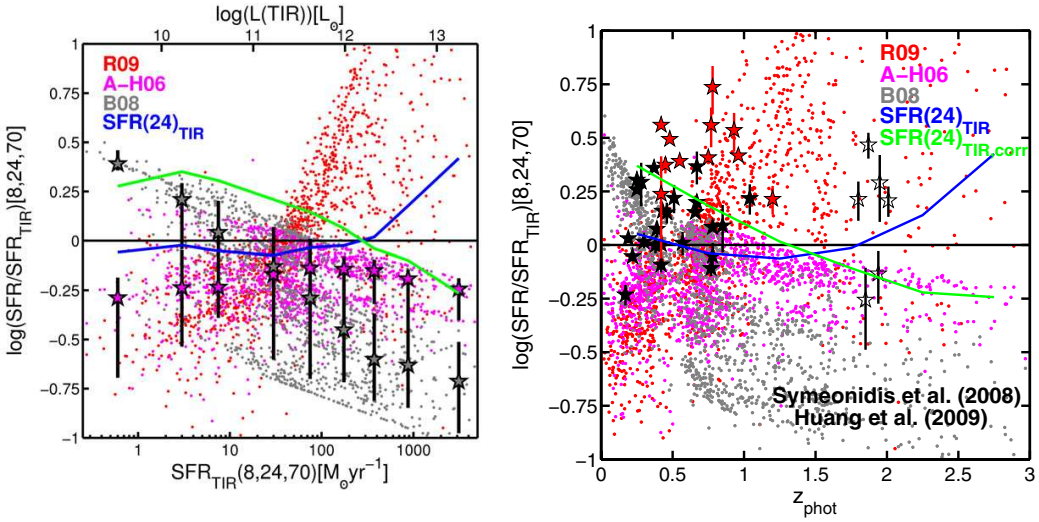

Figure 22. Comparison of different IR-based SFR(8, 24, 70) indicators with respect to SFR$_{TIR}$(8, 24, 70) as a function of SFR$_{TIR}$ (left) and redshift (right) for galaxies detected in MIPS 24 μm (f(24 μm) > 60 μJy) and MIPS 70 μm (f(70 μm) > 3500 μJy). The color code is the same as in Figure 19. Here we also show the median values and 1σ of the comparison to SFR$_{B08}$ (gray stars with error bars). The blue line joins the median values of SFR$_{TIR}$(24)/SFR$_{TIR}$(8, 24, 70) per luminosity bin (similarly to the colored stars in the top-left panel of Figure 19). The black stars depict the ratio of SFRs for galaxies in common with the sample of Symeonidis et al. (2008, filled stars at $z < 1.2$) and Huang et al. (2009, open stars at $z \sim 2$). The IR-based SFR for these sources is one of the most accurate available at the moment, and it is in overall good agreement with our estimates with SFR$_{TIR}$.

reducing the impact of the k-corrections. As a result, SFR$_{B08}$ is nearly insensitive to the inclusion of 70 μm data at $z \sim 2$. Note however that this does not mean that it is a better estimation of the SFR. At $z \lesssim 0.5$, SFR$_{B08}$(24) is larger than SFR$_{B08}$(8, 24, 70) by $\Delta\mathrm{SFR} = 0.18 \pm 0.23$ dex.

Finally, the right panel of Figure 20 shows the comparison of SFR(24)/SFR(8, 24, 70) for the A-H06 recipe. The overall trends are analogous to those observed for SFR$_{TIR}$ but with a larger scatter (∼0.30 dex), i.e., the offset and rms increases with redshift up from $\Delta\mathrm{SFR} = -0.10 \pm 0.26$ dex at $z < 1$ to $\Delta\mathrm{SFR} = 0.19 \pm 0.47$ dex at $z = 2$–4.

5.3.3. Analysis of IR-based SFRs: Best-effort Sample

In this Section, we compare again the IR-based SFRs obtained with different methods, but this time for the best-effort sample, i.e., with estimates based on 8, 24, and 70 μm data. We also present a comparison of IR-based SFRs to galaxies in common with other authors counting with better IR SED coverage (e.g., MIPS-160 or IR-spectroscopy) and therefore more reliable SFRs.

Figure 22 shows a comparison of the SFRs(8, 24, 70) obtained with each method with respect to SFR$_{TIR}$(8, 24, 70) (our

reference value), as a function of SFR (left panel) and redshift (right panel). The color code is the same as in Figure 19. To simplify the comparison to the results of the previous section, the Figure also shows the ratio of $SFR_{TIR}(24)$ to $SFR_{TIR}(8, 24, 70)$, i.e., basically the values shown in the upper-left panel of Figure 20. The blue line joins the median values of the ratio of SFRs per bin of luminosity (and redshift).

The relative differences with respect to $SFR_{TIR}(8, 24, 70)$ remain mostly unchanged with respect to what is shown in Figure 19 for estimates based on 24 μm data. For $SFR_{A\text{-}H06}$ the most noticeable differences are that the overall rms increases by $\sim$50% for the highest SFRs and the median ratio for $SFR_{TIR}(8, 24, 70) > 100\ M_{\odot}\ yr^{-1}$ decreases to $\Delta SFR = -0.12 \pm 0.12$ dex. For SFR_{B08}, the median ratio SFR_{B08}/SFR_{TIR} presents a smaller tilt and a significant increment of the rms with respect to the values in the MIPS 24 μm sample. Finally, SFR_{R09}, which only depends on the observed flux in MIPS 24 μm, presents the same trend at low-z as in Figure 19. However, at $z \sim 2$ it tends to overestimate $SFR_{TIR}(8, 24, 70)$ because the former present similar values to $SFR_{TIR}(24)$ that, as shown in the previous section, overpredicts $SFR_{TIR}(8, 24, 70)$ at $z \sim 2$.

As the relative trends between the estimates of the SFR(8, 24, 70) have barely changed, our conclusions from Section 5.3.1 still apply, i.e., the values of $SFR_{A\text{-}H06}$ are roughly consistent with those of SFR_{TIR}, but the SFR based on the calibrations of B08 and R09 presents systematic deviations with respect to these that can be significant (up to 0.75 dex) in certain SFR and redshift intervals. In addition, we find that the typical rms of the comparison of SFR(8, 24, 70) estimates is 20% larger with respect to the previous comparison based on 24 μm data. This is not surprising considering that Figure 19 shows only functional relation of each method but none of the uncertainties attached to the fit of data.

Note that the comparisons shown in Figures 19 and 22 only illustrate the expected uncertainty budget associated to the use of different SFR estimates, but they do not demonstrate that any of them provides intrinsically more accurate results. Nonetheless, having MIPS 70 μm data to constrain the shape of the IR SED, it is reasonable to assume that the values of $SFR_{TIR}(8, 24, 70)$ would provide more reliable values than the other three methods. In order to verify this statement and to asses the accuracy of $SFR_{TIR}(8, 24, 70)$, we compare the SFRs to the results from other authors based on better photometric data sets. In particular, we compare our SFRs against the values of Symeonidis et al. (2008, S08) and Huang et al. (2009). The latter studied the SFRs of a spectroscopic sample of high-z ($z \sim 1.9$) galaxies with strong IR-emission ($f(24) > 0.5$ mJy). For these galaxies, the authors provide accurate SFRs estimated from a very detailed coverage of the IR SED including *Spitzer*/IRS spectroscopy and data at 24, 70, and 160 μm, 1 mm, and 1.4 GHz. In S08 the authors describe the IR properties of a 70 μm selected sample restricted to galaxies detected at 160 μm and having reliable spectroscopic redshifts ranging from $0.1 < z < 1.2$ ($z = 0.5$).

The sources in common with S08 and Huang et al. (2009) are shown in the right panel of Figure 22 as black stars (open and closed, respectively). In addition, we show as red stars those sources which were poorly fitted to the models of CE01 and DH02 in the work of S08. We find that our values of $SFR_{TIR}(8, 24, 70)$ for the majority of the $z < 1.2$ galaxies tend to underestimate the SFRs of S08 with a median (considering only black stars) difference and scatter of $\Delta SFR = 0.09 \pm^{0.20}_{0.14}$ dex. However, there is small group of sources for which the SFRs are systematically underestimated by $\sim$0.5 dex or more (red stars). In S08, the authors showed that, for these galaxies, the IR SED fitting to the models of CE01 and DH02 severely underfitted the data at 160 μm, whereas the models of Siebenmorgen & Krügel (2007, SK07) allowed a better fit to the data (see also Symeonidis et al. 2010). As a result, the values of L(TIR) obtained from the fit to models of CE01 and DH02 would be systematically lower than the estimates for SK07. These strong discrepancies in the fitting of CE01 and DH02 models do not seem to be the usual scenario (e.g., Kartaltepe et al. 2010), although some issues fitting the MIPS 160 μm fluxes of local galaxies with the models of CE01 has been reported (Noll et al. 2009).

A possible explanation for this issue could be related to the fact that S08 makes use of the four IRAC bands in the SED fitting. As a result, these bands contribute significantly to the χ^2 (more than the MIPS bands), whereas they only represent a minimum fraction of the total IR luminosity. Nonetheless, some intrinsic differences in the IR–SED of MIPS 160 μm selected samples are expected, given that these are usually biased toward *cold* galaxies, i.e., galaxies with a relatively large (and probably not very frequent) cold dust content in comparison with the amount and emission of the warm dust featured in the models of CE01 and DH02. In summary, the differences in the SFR(8, 24, 70) with respect to the values of S08 for these sources are most likely the result of combined SED modeling issues and selection effects.

For the rest of the sources, the $\sim$0.10 dex offset in SFR(8, 24, 70) toward underestimating the values of S08 is in good agreement with the results of Kartaltepe et al. (2010, K10) for a sample of galaxies selected at 70 μm (and counting with 160 μm data for $\sim$20% them). The authors indicate that the estimates of L(TIR) for 160 μm detected sources computed without fitting that flux can be underestimated by up to 0.20 dex at $z < 1$ and $\sim$0.3 dex at higher redshifts. The authors also point out that these effect could be related to a bias in 160 μm selected samples toward selecting intrinsically cooler objects (as opposed to 70 μm selections). A similar statement is made in S08 based on the 160/70 flux ratios of their sample.

The comparison to the SFRs of Huang et al. (2009) for galaxies at $z \sim 2$ presents too few sources to provide a significant result. However, the overall results are in relatively good agreement within 0.3 dex. We find again that $SFR_{TIR}(8, 24, 70)$ slightly underpredicts the SFRs of some galaxies, consistently with the conclusions of K10 for 160 μm detected galaxies. Moreover, we find that the values of $SFR_{TIR}(24)$ for the galaxies of Huang et al. (2009) overestimates SFR(8, 24, 70) by a factor of $\sim$4, following the trend shown by the blue line.

Finally, we further check the accuracy of our estimates at high-z, comparing them to the values of $SFR_{TIR}(24)$ corrected with the empirical relation of Papovich et al. (2006). This correction was conceived to mitigate the excess in the IR-SFRs of high-redshift galaxies estimated from 24 μm data. The correction was computed by matching the SFR(24) to the SFRs estimated from the average stacked fluxes in MIPS 24, 70, and 160 μm of a sample of $z \sim 2$ galaxies. The green line in Figure 22 joins the median ratios of $SFR_{TIR,CORR}(24)/SFR_{TIR}(8, 24, 70)$ as a function of redshift. The overall results are that the values of $SFR_{TIR,CORR}(24)$ are a factor of $\sim$3–4 lower than $SFR_{TIR}(24)$ at $z \sim 2$. As a result these estimates are also slightly lower than our predictions for $SFR_{TIR}(8, 24, 70)$. Nonetheless, the values of $SFR_{TIR,CORR}(24)$ also agree within 0.3 dex with the SFRs of the galaxies in common with Huang et al. (2009).

Table 7
The IRAC-3.6 + 4.5 μm Sample: Photometric Redshifts

Object (1)	α (2)	δ (3)	zphot-best (4)	zphot-*EAZY* (5)	zphot-I06 (6)	zspec (7)	qflag (8)	zphot-err (9)	Qz (10)	N(band) (11)	Stellarity (12)
irac003270_1	215.43910540	53.08468920	1.09	1.06	1.04	0.00000	2	0.07	0.31	16	0
irac003278	215.42614011	53.09447161	0.49	0.39	0.58	0.00000	0	0.20	2.58	16	7
irac003291_1	215.44058360	53.08123980	0.83	0.80	0.84	0.85700	4	0.02	0.11	16	0
irac003310	215.42129738	53.09430607	0.08	0.14	0.15	0.00000	0	0.07	0.13	18	0
irac003313	215.43553774	53.08200958	1.06	1.01	1.09	0.00000	0	0.08	0.37	16	1

Notes. (1) Object unique identifier in the catalog.
(2, 3) Right Ascension and Declination (J2000) in degrees.
(4) Probability weighted photometric redshift. This is our default value of photometric redshift for SED fitting based estimates.
(5) Photometric redshift estimated with the code *EAZY* (Brammer et al. 2008) using the default template configuration and the *K*-band luminosity prior applied to the [3.6] band. The input photometric catalog is the same as for the other redshifts.
(6) Photometric redshifts as estimated in Ilbert et al. (2006a) from the (five band) i' selected catalog of the CFHTLS. This catalog overlaps with the IRAC sample in the central portion of the mosaic ($52.^{\circ}16 < \delta < 53.^{\circ}20$ & $214.^{\circ}04 < \alpha < 215.^{\circ}74$).
(7) Spectroscopic redshift determination drawn from DEEP2 (Davis et al. 2007; ~8000 galaxies) and (Steidel et al. 2003; LBGs at $z \gtrsim 3$).
(8) Quality flag of the spectroscopic redshift (4 = > 99.5%, 3 = > 90%, 2 = uncertain, 1 = bad quality). Only redshifts with qflag > 2 have been used in the analysis.
(9) Uncertainty in zphot-best(4) estimated from the 1 σ width of the probability distribution function.
(10) Reliability parameter of the photometric redshift estimated with *EAZY* (see Brammer et al. 2008 for more details); Good quality redshifts are in general $Q_z \leqslant 1$.
(11) Number of different photometric bands used in to estimate the photometric redshift with *Rainbow*, Column (4).
(12) Sum of all the stellarity criteria satisfied (see Section 5.4 of Paper I). A source is classified as star for Stellarity > 2.

(This table is available in its entirety in a machine-readable form in the online journal. A portion is shown here for guidance regarding its form and content.)

5.4. Summary of the SFRs

The accuracy of the SFRs estimated from IR tracers up to intermediate redshifts has been demonstrated by the good agreement with the estimates based on other tracers such us dust corrected UV/optical indicator (Iglesias-Páramo et al. 2007; Salim et al. 2007, 2009). On the other hand, the systematic effects in the IR-based SFRs of the most luminous galaxies (ULIRGS) at high redshift are quite significant. Some of these issues arise from the assumptions made in the estimation of IR-based SFRs, such as the validity of the local templates at high redshift or the contribution of obscured AGNs to the IR luminosity. However, the most relevant issues arise from the lack of enough data to constrain the full IR SED, particularly for studies based on 24 μm data alone. Nonetheless, the breadth and quality of the MIPS 24 μm data ensure that it will continue leading multiple studies of IR-based SFR for the foreseeable future. Thus, quantifying the systematic effects between the SFRs(24) computed with different methods, and the differences in the SFRs(24) with respect to the SFRs computed from more IR data, provides a useful information.

Our analysis shows that although the values of $SFR_{TIR}(24)$ are consistent with those of $SFR_{A\text{-}H06}(24)$ within 0.3 dex (the usual uncertainty quoted for IR-based SFRs) the values of $SFR_{B08}(24)$ and $SFR_{R09}(24)$ can be significantly deviated (up to $\pm$0.5 dex) with respect to $SFR_{TIR}(24)$ for certain redshift and luminosity ranges. The differences in the SFRs obtained with these methods remain mostly unchanged for SFR(8, 24, 70), and we find that the discrepancies in SFR_{B08} or SFR_{R09} with respect to $SFR_{TIR}(24)$ do not provide a better agreement to the SFRs of other authors computed from very detailed IR photometric data. Therefore, out of the four methods to estimate the IR-SFR discussed here, SFR_{TIR} present (after accounting for intrinsic systematics) the more accurate results.

From the analysis of sample of MIPS 70 μm detected galaxies, we find that $SFR_{TIR}(24)$ is reasonably consistent with the values of $SFR_{TIR}(8, 24, 70)$ up to ULIRG luminosities (typically at $z \lesssim 1.4$) showing only a small deviation toward underestimating SFR(8, 24, 70) by 0.05 dex with an rms of 0.2 dex. However, at $z > 1.5$ the agreement is significantly worse. The values of $SFR_{TIR}(24)$ tend to overestimate SFR(8, 24, 70) by a median value of 0.15 $\pm$ 0.40 dex. As already pointed out by other authors, the best approach to solve this issue is to apply a correction factor that reduces the estimated values at high-z (Papovich et al. 2006 or Santini et al. 2009).

The comparison of $SFR_{TIR}(8, 24, 70)$ (our best-effort SFRs) to the SFRs computed by other authors based on a better IR photometric coverage (including MIPS 160 μm) also shows an excellent agreement, proving that these estimates are robust. The overall results are consistent within 0.3 dex presenting only a small systematic deviation in $SFR_{TIR}(8, 24, 70)$ toward underestimating the values including MIPS 160 μm data by -0.09 dex (mostly $z < 1.2$ galaxies). Note that since this comparison is restricted to MIPS 160 μm detected sources there could be some selection effects, and thus this offset might not apply for all galaxies (see, e.g., the results of K10 based on stacked fluxes in MIPS 160 μm for a 70 μm selected sample).

6. DATA ACCESS

All the data products for the 76,936 IRAC 3.6 + 4.5 μm-selected ([3.6] < 23.75) sources in the EGS are presented here. These include (1) the photometric redshift catalog containing the estimates with *Rainbow*, *EAZY*, and from I06, when available (Table 7); (2) the stellar mass catalog containing the values estimated with each of the different modeling configurations described in Section 4 (Table 8); and (3) the SFR catalog containing the UV- and IR-based SFRs obtained with the different methods and calibrations discussed in Section 5 (Table 9). A table containing the UV-to-FIR SEDs for all these sources is presented in Paper I. The number of objects and unique identifier of this table and the tables presented in the following is the same.

A larger version of these catalogs containing all galaxies down [3.6] < 24.75 (3σ limiting magnitude) is available through the web utility *Rainbow Navigator*[7] (see Paper I for a more detailed description) that provides a query interface to the database containing all the data products of the multiple *Rainbow* tasks that we have used in the papers. *Rainbow Navigator* has been conceived to serve as a permanent repository for future versions of the data products in EGS, and also to similar results in other cosmological fields (such as GOODS-N and GOODS-S, presented in PG08).

6.1. Table 7: Photometric Redshift Catalog

These are the fields included in Table 7.

1. *Object*. Unique object identifier starting with irac000001. Objects labeled with an underscore plus a number (e.g., irac000356_1) are those identified as a single source in the IRAC catalog built with SExtractor, but deblended during the photometric measurement carried out with the *Rainbow* software (see Section 2.1). Note that, although the catalog contains 76,936 elements, the identifiers do not follow the sequence irac000001 to irac076185. This is because the catalog is extracted from a larger reference set by imposing coordinate and magnitude constraints. The table is sorted according to this unique identifier.
2. α, δ. J2000.0 right ascension and declination in degrees.
3. *zphot-peak*. Maximum likelihood photometric redshift.
4. *zphot-best*. Probability weighted mean photometric redshift. This is the value of $z_{\rm phot}$ used along the paper.
5. *zphot-err*. 1σ uncertainty in the photometric redshift as estimated from the zPDF.
6. *zphot-EAZY*. Photometric redshift estimated using the *EAZY* code (Brammer et al. 2008) on our SEDs with the default templates and including the K-band luminosity prior.
7. *Qz*. Estimate of the quality of the photometric redshifts computed with *EAZY*. Reliable photometric redshifts present values of $Qz \leqslant 1$ (Brammer et al. 2008).
8. *zphot-I06*. Photometric redshift from Ilbert et al. (2006a). These are only available for galaxies in the main region.
9. *zspec*. Spectroscopic redshift (set to -1 if not available).
10. *qflag*. Spectroscopic redshift quality flag from 1 to 4. Sources with *qflag* > 3 have a redshift reliability larger than 80%.
11. *N(bands)*. Number of photometric bands used to derive the photometric redshift.
12. *Stellarity*. Total number of stellarity criteria satisfied. A source is classified as a star if it satisfies three or more criteria. A description of all the stellarity criteria and the accuracy of the method is given in Section 5.4 of Paper I.

6.2. Table 8: Stellar Mass Catalog

The stellar masses are estimated from the same templates used to compute the photometric redshifts. These templates were computed using several combination of SPS library, IMFs, and extinction laws. Our reference stellar masses are those obtained with [P01, SALP, CAL01] (see Section 3). We provide two different stellar mass estimates based on these templates depending on the redshift used during the fitting procedure, namely, *zphot-best* and *zspec*. In addition, we obtained estimates with (1) the stellar population models of Bruzual & Charlot (2003, BC03), Maraston (2005, M05), and S. Charlot & G. Bruzual (2011, in preparation, CB09); (2) the IMFs of Kroupa (2001, KROU) and Chabrier (2003, CHAB); and (3) the dust extinction law of Charlot & Fall (2000, CF00). In Table 8, we give six additional stellar mass estimates obtained under different stellar population modeling assumptions, namely, [P01, KROU], [BC03, CHAB], [M05, KROU], [CB09, CHAB], [CB09, SALP], and [P01, SALP, CF00]. The extinction law in all cases except for the last is CAL01. For these stellar mass estimates we use *z-fit*, which is equal to *zphot-best* unless *zspec* is available.

These are the fields included in Table 8.

1. *Object*. Unique object identifier as in the photometric catalog.
2. α, δ. J2000.0 right ascension and declination in degrees.
3. *Mass (best)*. Stellar mass [log $M_{\odot}$] with the associated uncertainty estimated with *zphot-best* using our default modeling parameters [P01, SALP, CAL01].
4. *Mass (zspec)*. Stellar mass [log $M_{\odot}$] with the associated uncertainty, estimated with *zspec* using our default modeling parameters [P01, SALP, CAL01].
5. *z-fit*. Value of the photometric redshift used during the SED fitting with the [P01, KROU], [BC03, CHAB], [M05, KROU], [CB09, CHAB], [CB09, SALP], [P01, SALP, CF00] models. It is equal to *zphot-best* unless *zspec* is available.
6. *Mass (P01, KROU)*. Stellar mass [log $M_{\odot}$] with the associated uncertainty, estimated with the modeling parameters [P01, KROU, CAL01] and *zphot-fit*.
7. *Mass (BC03, CHAB)*. Stellar mass [log $M_{\odot}$] with the associated uncertainty, estimated with the modeling parameters [BC03, CHAB, CAL01] and *zphot-fit*.
8. *Mass (M05, KROU)*. Stellar mass [log $M_{\odot}$] with the associated uncertainty, estimated with the modeling parameters [M05, KROU, CAL01] and *zphot-fit*.
9. *Mass (CB09, CHAB)*. Stellar mass [log $M_{\odot}$] with the associated uncertainty, estimated with the modeling parameters [CB09, CHAB, CAL01] and *zphot-fit*.
10. *Mass (CB09, SALP)*. Stellar mass [log $M_{\odot}$] with the associated uncertainty, estimated with the modeling parameters [CB09, SALP, CAL01] and *zphot-fit*.
11. *Mass (P01, CF00)*. Stellar mass [log $M_{\odot}$] with the associated uncertainty, estimated with the modeling parameters [P01, SALP, CF00] and *zphot-fit*.

6.3. Table 9: SFR Catalog

The SFR catalog is presented in Table 9. The unobscured UV-SFR is obtained from the best-fitting optical template modeled with [P01, SALP, CAL01]. The rest-frame IR luminosities and IR-based SFRs are computed either from the average value of the best-fitting templates from the dust emission models of Chary & Elbaz (2001, CE01) and Dale & Helou (2002, DH02) to MIPS 24 μm data only, or the average value of the best-fitting dust emission models of CE01, DH02 and Rieke et al. (2009, R09) to IRAC-8.0, MIPS 24 and 70 μm data. Only fluxes at rest-frame $\lambda > 5$ μm are considered in this method. In both cases we use *zphot-fit*, which is equal to *zphot-best* unless *zspec* is available. For sources un-detected in MIPS 70 μm at $z \gtrsim 0.6$ both methods provide similar results modulo the effect of the R09 templates.

Note that the SFRs has been computed for all the MIPS 24 μm and 70 μm detections, but only sources with $f\,(24) > 60$ μJy and $f\,(70) > 3.5$ mJy (the 5σ detection limit) are discussed in Section 5. In addition, sources un-detected in MIPS 24 μm are

[7] http://rainbowx.fis.ucm.es

Table 8
The IRAC-3.6 + 4.5 μm Sample: Stellar Mass Estimates

Object	α	δ	M(best)	M(zspec)	z-fit	M(P01,KROU)	M(BC03,CHAB)	M(M05,KROU)	M(CB09,CHAB)	M(CB09,SALP)	M(P01,CF00)
			M-err	M-err		M-err	M-err	M-err	M-err	M-err	M-err
(1)	(2)	(3)	(4)	(5)	(6)	(7)	(8)	(9)	(10)	(11)	(12)
			(13)	(14)		(15)	(16)	(17)	(18)	(19)	(20)
irac003270_1	215.43892696	53.08455063	9.79	9.79	1.09	9.67	9.64	9.61	9.61	9.84	9.98
			0.05	0.05		0.04	0.08	0.07	0.08	0.08	0.07
irac003278	215.42614011	53.09447161	11.69	11.69	0.49	11.55	11.66	11.35	11.48	11.74	11.75
			0.15	0.15		0.14	0.17	0.16	0.18	0.15	0.17
irac003291_1	215.44043562	53.08128671	10.84	10.84	0.86	10.97	10.64	10.30	10.57	10.63	10.48
			0.03	0.04		0.04	0.04	0.03	0.03	0.04	0.04
irac003310	215.42129738	53.09430607	8.80	8.80	0.08	8.61	8.92	8.64	8.79	9.04	8.75
			0.06	0.06		0.06	0.08	0.08	0.05	0.05	0.06
irac003313	215.43553774	53.08200958	9.94	9.94	1.06	9.83	9.64	9.19	9.40	9.63	9.59
			0.04	0.04		0.05	0.04	0.05	0.07	0.07	0.04

Notes. (1) Object unique identifier in the catalog.
(2, 3) Right ascension and declination (J2000) in degrees.
(4–13) Stellar mass [log($M_{\odot}$)] with the associated uncertainty, estimated with our default modeling parameters, [P01, SALP, CAL01], and zphot-best.
(5–14) Stellar mass [log($M_{\odot}$)] with the associated uncertainty, estimated with our default modeling parameters, [P01, SALP, CAL01], forcing the photometric redshift to the spectroscopic value, when available.
(6) Redshift used in the fitting procedure of (8, 9, 10, 11 and 12). This redshift refer to zphot-best unless the spectroscopic redshift is available; in that case the redshift is forced to the spectroscopic value.
(7–15) Stellar mass [log($M_{\odot}$)] with the associated uncertainty, estimated with the modeling parameters, [P01, KROU, CAL01], and z-fit.
(8–16) Stellar mass [log($M_{\odot}$)] with the associated uncertainty, estimated with the modeling parameters, [BC03, CHAB, CAL01], and z-fit.
(9–17) Stellar mass [log($M_{\odot}$)] with the associated uncertainty, estimated with the modeling parameters, [M05, KROU, CAL01], and z-fit.
(10–18) Stellar mass [log($M_{\odot}$)] with the associated uncertainty, estimated with the modeling parameters, [CB09, CHAB, CAL01], and z-fit.
(11–19) Stellar mass [log($M_{\odot}$)] with the associated uncertainty, estimated with the modeling parameters, [CB09, SALP, CAL01], and z-fit.
(12–20) Stellar mass [log($M_{\odot}$)] with the associated uncertainty, estimated with the modeling parameters, [P01, SALP, CF00], and z-fit.

(This table is available in its entirety in a machine-readable form in the online journal. A portion is shown here for guidance regarding its form and content.)

Table 9
The IRAC-3.6 + 4.5 μm Sample: IR-Luminosities and Star Formation Rate Estimates

Object	α	δ	$f(24\,\mu\mathrm{m})$	$f(70\,\mu\mathrm{m})$	z-fit	SFR(0.28)	SFR(R09)	L(TIR,24)	SFR(TIR,24)	SFR(TIR,24,CE01)	SFR(B08,24)	SFR(AH06,24)
			err-f	err-f				L(TIR,best)	SFR(TIR,best)	SFR(TIR,CE01)	SFR(B08,best)	SFR(AH06,best)
(1)	(2)	(3)	(4)	(5)	(6)	(7)	(8)	(9)	(10)	(11)	(12)	(13)
			(14)	(15)				(16)	(17)	(18)	(19)	(20)
irac003270_1	215.43892696	53.08455063	55	...	1.09	6.0	21.8	10.93	14.6	15.1	17.5	9.4
			13	...				10.93	14.8	15.1	18.4	11.0
irac003278	215.42614011	53.09447161	...	...	0.49	2.0	1.7	−10.34	−3.8	−4.7	−8.1	−2.2
			...	...				...	...	...	...	...
irac003291_1	215.44043562	53.08128671	104	...	0.86	2.5	17.4	10.92	14.4	14.6	17.5	9.3
			12	...				10.94	14.9	14.6	18.5	10.7
irac003310	215.42129738	53.09430607	61	...	0.08	0.1	0.0	8.61	0.1	0.1	0.3	0.1
			10	...				8.51	0.1	0.0	0.2	0.1
irac003313	215.43553774	53.08200958	...	...	1.06	3.6	19.9	−10.90	−13.8	−14.5	−17.3	−8.6
			...	...				...	...	...	...	...

Notes. (1) Object unique identifier in the catalog.
(2, 3) Right Ascension and Declination (J2000) in degrees.
(4, 14) Observed flux and uncertainty in MIPS 24 μm [μJy].
(5, 15) Observed flux and uncertainty in MIPS 70 μm [μJy].
(6) Redshift used in the fitting procedure. This redshift refer to zphot-best unless the spectroscopic redshift is available; in that case the redshift is forced to the spectroscopic value.
(7) UV based SFR [$M_\odot$ yr^{-1}] estimated from the monochromatic luminosity at 2800 Å rest-frame using the calibration of Kennicutt (1998).We also refer to this value as $\mathrm{SFR_{UV,obs}}$
(8) IR based SFRs [$M_\odot$ yr^{-1}] estimated from the observed flux in MIPS 24 μm and the redshift using the formula of Rieke et al. (2009).
(9, 16) Total IR luminosity [$\log(L_\odot)$] obtained integrating (from 8–1000 μm) the average of the best-fitting templates.
(9) is computed from the fit of MIPS 24 μm data to the models of Chary & Elbaz (2001, CE01), Dale & Helou (2002, DH02);
(10) is computed from the fit of IRAC-8.0 and MIPS 24 and 70 μm (best effort) data to the models of CE01, DH02 and Rieke et al. (2009, R09).
(10, 17) IR based SFRs [$M_\odot$ yr^{-1}] estimated from L(TIR) using the calibration of Kennicutt (1998). (10) and (17) are computed using the same combination of data and models as (9) and (16), respectively.
(11, 18) Same as 10, but in this case the IR SED is fitted only with the models of CE01. (11) and (18) are computed from the fit of these models to MIPS-24 μm data only and IRAC-8.0 and MIPS 24 and 70 μm respectively.
(12, 19) IR based SFRs [$M_\odot$ yr^{-1})] estimated from the monochromatic luminosity at 8 μm rest-frame using the relation of Bavouzet et al. (2008). (12) and (19) are computed using the same combination of data and models as (9) and (16), respectively.
(13, 20) IR based SFRs [$M_\odot$ yr^{-1}] estimated from the monochromatic luminosity at 24 μm rest-frame using the relation of Alonso-Herrero et al. (2006). (13) and (20) are computed using the same combination of data and models as (9) and (16), respectively.
The uncertainties in the values of L(TIR) and the SFRs can be as high as a factor of two. The accuracy in (9, 16) is limited to two decimal places and one decimal place in (10–13, 17–20). Negative values in the columns (9–13) indicate that the sources are non-detected in MIPS 24 μm. In these cases, the corresponding IR luminosity is estimated from a upper limit of $f(24) = 60\,\mu$Jy, and the estimates in (16–20) are not computed.

(This table is available in its entirety in a machine-readable form in the online journal. A portion is shown here for guidance regarding its form and content.)

fitted using an upper limit value of $f(24) = 60\,\mu$Jy. In this cases the quoted L(TIR) and SFRs are negative values.

1. *Object*. Unique object identifier as in the photometric catalog.
2. α, δ. J2000.0 right ascension and declination in degrees.
3. *f(24), f(70)*. Observed flux [μJy] and uncertainties in MIPS 24 and 70 μm.
4. *z-fit*. Value of the redshift used during the IR SED fitting. It is equal to *zphot-best* unless *zspec* is available.
5. *L (TIR, 24)*. Total IR luminosity [log $M_\odot$ yr^{-1}], calculated by integrating the (average) dust emission model from 8 μm to 1000 μm. This value is computed by fitting the observed flux in MIPS 24 μm to the models of CE01 and DH02.
6. $SFR_{0.28}$. Unobscured UV-based SFR [$M_\odot$ yr^{-1}] estimated from the rest-frame luminosity at 0.28 μm interpolated in the best-fit optical template, $\nu L_\nu(0.28)$, using the Kennicutt (1998) calibration.
7. $SFR_{\rm TIR}(24)$. IR-based SFR [$M_\odot$ yr^{-1}], estimated from L(TIR) using the calibration of Kennicutt (1998). This value is computed by fitting the observed flux in MIPS 24 μm to the models of CE01 and DH02.
8. $SFR_{\rm CE01}(24)$. Same as $\rm SFR_{TIR}(24)$ but fitting the MIPS 24 μm data to the models of CE01 only.
9. $SFR_{\rm B08}(24)$. IR SFR [$M_\odot$ yr^{-1}] estimated from the rest-frame monochromatic luminosity at 8 μm using the calibration of Bavouzet et al. (2008). This value is computed by fitting the flux in MIPS 24 μm to the models of CE01 and DH02.
10. $SFR_{\rm A\text{-}H06}(24)$. Total SFR [$M_\odot$ yr^{-1}] estimated from the rest-frame monochromatic luminosity at 24 μm using the calibration of Alonso-Herrero et al. (2006). This value is computed by fitting the observed flux in MIPS 24 μm to the models of CE01 and DH02. Note that to obtain the IR-SFR part of this value, the unobscured UV-SFR must be subtracted according to Equation (4).
11. $SFR_{\rm R09}(24)$. IR SFR [$M_\odot$ yr^{-1}] estimated from the observed flux in MIPS 24 μm and the redshift using the formula of Rieke et al. (2009, Equation (14)).
12. $L(TIR)$, $SFR_{\rm TIR}$, $SFR_{\rm CE01}$, $SFR_{\rm B08}$, $SFR_{\rm A\text{-}H06}(8, 24, 70)$. Same as the previous values but fitting the IR SED with IRAC-8.0, MIPS 24 and 70 μm data to the models of CE01, DH02, and R09. Note that $\rm SFR_{R09}$ has been omitted because its value is independent of the flux in IRAC-8.0 nor MIPS 70 μm.

7. SUMMARY

In this paper, and in Paper I (Barro et al. 2011), we have presented an IRAC-3.6 + 4.5 μm selected sample in the Extended Groth Strip characterized with UV-to-FIR SEDs. The photometric catalog includes the following bands: far-UV and near-UV from *GALEX*, $u^*g'r'i'z'$ from the CFHTLS, $u'gRiz$ from MMT and Subaru observations, *BRI* from CFHT12k, V_{606}, i_{814}, J_{110} and H_{160} from *HST*, *JK* from Palomar Observatory, CAHA and Subaru data, and [3.6]-to-[8.0], 24 μm, and 70 μm data from *Spitzer* IRAC and MIPS surveys. Our catalog contains 76,936 sources down to a 85% completeness level ([3.6] < 23.75) over an area of 0.48 deg^2. In addition, we have cross-correlated our sample with the redshift catalog from DEEP2, and with X-ray and VLA 20 cm radio data.

Paper I presented the data, the procedure to measure consistent UV-to-FIR photometry using our own dedicated software (*Rainbow*), and the analysis of the multi-band properties of the sample. We showed that the SEDs present the level of consistency required to characterize the intrinsic stellar populations of the galaxy. In this paper, we have presented a galaxy-by-galaxy fitting of the UV-to-FIR SEDs to stellar population and dust emission models. From the best-fitting optical and IR templates, we have estimated: (1) photometric redshifts, (2) stellar masses, and (3) SFRs. Then, we have analyzed in detail their accuracy and reliability with respect to different parameters. In the following, we present the summary of the most important results of this analysis, organized by parameter.

Photometric redshifts ($z_{\rm phot}$) were estimated from the comparison of the UV-to-NIR SEDs to stellar population and AGN templates. This comparison was carried out with our own dedicated software (within the *Rainbow* package) using χ^2 minimization algorithm (see Pérez-González et al. 2008 for more details), and with the *EAZY* code (Brammer et al. 2008). These are our main results about photometric redshifts.

1. Two new features have been included in the *Rainbow* photometric redshift code over the previous implementation in Pérez-González et al. (2008) to improve the quality of the estimates: (a) a zero-point re-calibration of the observed photometry and (b) the use of template error function as a weight term in the SED fitting procedure. Both features are computed simultaneously and iteratively based on the comparison of observed and synthetic photometry in a spectroscopic control sample. The results show an overall good agreement between observations and templates. The zero-point corrections are typically $\lesssim$0.1 mag and converge after a few iterations. The overall rms in the residual is a factor of ∼2 the median photometric uncertainty. The most noticeable discrepancies present at $\lambda > 3\,\mu$m and (to a lesser extent) around 250 nm. These are the result of limitations in the stellar templates in the NIR range, and a possible excess in the strength of the dust attenuation with respect to a Calzetti et al. (2000) extinction law, respectively.
2. The comparison of our photometric redshifts to 7636 secure spectroscopic redshifts from DEEP2 and Steidel et al. (2003; LBGs at $z > 3$) shows an overall accuracy of $\sigma_{\rm NCMAD} \equiv 1.48 \times {\rm median}(|\frac{\Delta z - {\rm median}(\Delta z)}{1+z_{\rm spec}}|) = 0.034$ (where $\Delta z = z_{\rm phot} - z_{\rm spec}$) and $\sigma_{\rm NCMAD} = 0.046$, with $\eta = 2\%$ and 3% catastrophic outliers (η defined as the fraction of galaxies presenting $\sigma_{\rm NCMAD} > 0.2$) in the EGS main region (covered by the CFHTLS) and flanking regions (covered with fewer and shallower bands), respectively. The overall scatter in $z_{\rm phot}$ does not depend strongly on the redshift, presenting a minimum value around $z = 0.5$–1 ($\sigma_{\rm NCMAD} = 0.028$ and 0.040 in the main and flanking regions, respectively), and increasing by a factor of ∼1.3 at lower and higher redshifts (up to $z < 1.5$). At $z \sim 3$, the $z_{\rm phot}$ accuracy for 91 LBGs with secure spectroscopy is reduced to $\sigma_{\rm NCMAD} = 0.063$ and $\eta = 10\%$.
3. The accuracy of the $z_{\rm phot}$ is mostly independent of the [3.6] mag. However, it decreases with the optical magnitude from $\sigma_{\rm NCMAD} = 0.030$ at $R = 22$ to $\sigma_{\rm NCMAD} = 0.060$ at $R = 25$. Approximately 50% of the catastrophic outliers have $R > 23.5$ and $\log(\chi^2) > 0.6$. Approximately 60% of the sources with significantly different values of $z_{\rm best}$ and $z_{\rm peak}$ ($|z_{\rm best}\text{-}z_{\rm peak}|/(1+z) > 0.2$) are catastrophic outliers.
4. The $z_{\rm phot}$ statistics for the 1995 and 262 spectroscopic galaxies detected in MIPS 24 μm ($f(24) > 60\,\mu$Jy) and 70 μm ($f(70) > 3.5$ mJy) in the main region are similar to the rest of the sample with $\sigma_{\rm NCMAD} = 0.033$, $\eta = 3\%$, and

$\sigma_{\rm NCMAD} = 0.045$, $\eta = 1\%$, respectively. The accuracy for the 142 X-ray sources is similar ($\sigma_{\rm NCMAD} = 0.038$) although with larger fraction of outliers ($\eta = 10\%$), probably as a result of some degree of contamination by the AGN, for which reliable $z_{\rm phot}$ are difficult to estimate based on stellar templates. The worst results are found for a very few (12) power-law galaxies (PLGs, identified as obscured AGNs): $\sigma_{\rm NCMAD} = 0.052$ ($\eta = 17\%$). We also note that sources with increasing fluxes in the IRAC bands ($f_{[3.6]} < f_{[4.5]} < f_{[5.8]} < f_{[8.0]}$) make up for up to 15% of the total number of outliers.

5. The $z_{\rm phot}$ *Rainbow* are in good agreement with those from the i'-band-selected catalog of Ilbert et al. (2006a, I06), which overlaps with our sample in the main region. For the 5454 galaxies in common between the two catalogs with $[3.6] < 23.75$ and $i' < 24.5$, the accuracy of the $z_{\rm phot}$ at $z < 1$ is roughly the same, $\sigma_{\rm NCMAD} = 0.035$. At higher redshifts, our larger band coverage (mostly in the NIR) provides more accurate results and less severe systematic errors and uncertainties. In particular, for galaxies at $z \sim 3$ (the LBG sub-sample), the outlier fraction in I06 is 46% for only 9% in *Rainbow*. Our $z_{\rm phot}$ catalog and the one presented in I06 are complementary: whereas the NIR-selected sample detected more galaxies at high-z, which are too faint in the optical to be included in the I06 catalog, the IRAC catalog misses a population of low-mass galaxies at $z < 1$ which are recovered by the i'-band selection in I06.
6. We showed that the photometric catalog provides robust SEDs by obtaining a different realization of the $z_{\rm phot}$ catalog with similar quality using the code *EAZY* (Brammer et al. 2008). In particular, these alternative photometric redshifts are slightly more accurate for the sources in the main region, particularly at $z < 0.5$, whereas they present a larger scatter in the flanking regions. Moreover, these $z_{\rm phot}$ exhibit a slightly larger systematic deviation ($\Delta z/(1+z) = 0.019$ and 0.027 in the main and flanking regions, respectively) than the $z_{\rm phot}$ computed with *Rainbow*.
7. We further tested the accuracy of our $z_{\rm phot}$ by checking the number densities and $z_{\rm phot}$ distributions of a sub-sample of (NIR-selected) s-BzK ($\rho = 5.0$ arcmin^2; $\tilde{z} = 1.89$), p-BzK ($\rho = 0.5$ arcmin^2; $\tilde{z} = 1.85$), and DRG ($\rho = 1.4$ arcmin^2; $\tilde{z} = 2.47$). These are in relatively good agreement with the results from the literature down to $K_{\rm VEGA} < 21$. The most significant difference is an excess of $\sim$1.5 in the density s-BzKs, which could be caused by an overdensity of galaxies at $z \sim 1.5$.
8. The median redshift of the ($[3.6] < 23.75$) sample, $\tilde{z} = 1.2$, is consistent with that of the flux limited samples of Pérez-González et al. (2008) and Ilbert et al. (2009) in different fields.

Stellar masses for the whole sample were obtained in a galaxy-by-galaxy basis by fitting the optical-to-NIR SEDs to SPS models. In addition, we analyzed the effects of the choice of different SPS libraries, IMFs, and dust extinction laws on our estimations. For that we considered a reference set of assumptions to which several combinations of input parameters were compared. This reference stellar masses were obtained with the PEGASE 2.0 (Fioc & Rocca-Volmerange 1997) SPS models (P01), a Salpeter (1955) IMF (SALP), and the Calzetti et al. (2000, CALZ01) extinction law. We compared these estimations with those obtained with: (1) the stellar population models of Bruzual & Charlot (2003, BC03), Maraston (2005, M05), and S. Charlot & G. Bruzual (2011, in preparation, CB09); (2) the IMFs of Kroupa (2001, KROU) and Chabrier (2003, CHAB); (3) the dust extinction law of Charlot & Fall (2000, CF00). These are our main results about stellar masses.

1. From the comparison of the stellar masses estimated with photometric and spectroscopic redshifts we find a 1σ uncertainty of $\sim$0.2 dex. The distribution of stellar masses as a function of redshift for our default modeling assumptions shows that 90% of the galaxies present $\log(M) > 10\ M_{\odot}$ at $z > 2$, at the limiting magnitude of our sample ($[3.6] < 23.75$).
2. We quantified the impact of the choice of different IMFs in the estimated stellar masses. For the CB09 models, we found that the use of a SALP, KROU, or CHAB IMF introduces constant offsets (with a very small scatter) in the estimated stellar masses: $\Delta\log(M)$[SALP$-$KROU] = 0.19 dex and $\Delta\log$(M)[CHAB$-$KROU] = -0.04 dex. For the models of P01, the difference for a SALP and KROU IMFs depends on the mass, ranging from $\Delta\log(M) = 0.03$ dex for masses lower than $\log(M) = 10\ \mathcal{M}_{\odot}$ to 0.13 dex above that threshold.
3. We quantified the impact of using different SPS codes in the estimated stellar masses. We found that the new CB09 models predict slightly lower masses than the older version, BC03, by $\Delta\log(M) = 0.04\ ^{+0.28}_{-0.15}$ dex. Our stellar masses estimated with the P01 models are on average larger than those obtained with the CB09 models (for a KROU IMF) by $\Delta\log(M) = 0.15 \pm 0.26$ dex. The estimates with the P01 library are also larger than those with the M05 SPS by $\Delta\log(M) = 0.39 \pm 0.34$ dex. We found slightly lower values of this offset for galaxies with $\log(M) > 10\ \mathcal{M}_{\odot}$ ($\sim$0.30 dex). Our default modeling assumptions, [P01, SALP, CAL01], predict comparatively the largest stellar masses. Accounting for all systematic offsets, all models are roughly consistent within a factor of 2–3.
4. We quantified the effect of using different treatments of the dust extinction by comparing the stellar masses estimated with a CAL01 and CF00 extinction laws. The median result is a small systematic deviation of 0.03 dex toward smaller values when using CAL01, and an rms of $\sim$0.20 dex. This suggest that the different treatments of the dust attenuation do not play a major role in the estimate of the stellar masses.
5. The comparison of our results with several stellar mass catalogs already published in EGS revealed a good agreement despite the differences in the modeling technique and in the photometric data set. We found a median offset and scatter of $\Delta\log(M) = -0.07 \pm 0.21$ dex and $\Delta\log(M) = 0.10 \pm 0.25$ dex with respect to the catalogs of stellar masses published by Bundy et al. (2006) and Trujillo et al. (2007), respectively.

SFRs were estimated for all galaxies in our sample following a variety of procedures. First, we calculated the unobscured SFR (the star formation which is directly observable in the UV/optical) from the observed luminosity at 280 nm ($\rm SFR_{UV,obs}$). To get the total SFR of a galaxy, the former value must be added to the SFR which is not directly measurable in the UV/optical because of the extinction by dust. We calculated this SFR from the IR data taken by *Spitzer*/IRAC and MIPS at 24 μm and 70 μm (if available). The general procedure consists on fitting the IR photometry at rest-frame wavelengths $\lambda > 5\ \mu$m (usually involving 8, 24, and 70 μm data) to the dust emission templates of Chary & Elbaz (2001, CE01) and Dale & Helou (2002, DH02) and Rieke et al. (2009), but we also performed some test by fitting only MIPS 24 μm data to the models of CE01 and DH02.

From the best fit to the models, the IR-based SFR for each object was estimated with four different methods: (1) the total infrared luminosity, L(TIR), integrated from 8 to 1000 μm transformed to an SFR with the factor published by Kennicutt (1998). (2) The rest-frame monochromatic luminosity at 8 μm (SFR_{B08}) transformed to L(TIR) and SFR using the empirical relation described in Bavouzet et al. (2008) and the Kennicutt factor. (3) The empirical relation given in Alonso-Herrero et al. (2006) between the rest-frame monochromatic luminosity at 24 μm and the SFR ($SFR_{A\text{-}H06}$). (4) Using Equation (14) of Rieke et al. (2009) that relates the SFR (SFR_{R09}) to the observed flux in the MIPS 24 μm band and the redshift. The monochromatic and integrated luminosities were computed from the average value of the best-fit templates. These are our main results about SFRs.

1. We quantified the differences in the IR-based SFRs obtained with the four methods based on the fit to MIPS 24 μm data only. The SFR estimates with the models of CE01 and DH02 are compatible within a factor of two, presenting a maximum difference around $z \sim 1.5$. The estimates of SFR_{TIR} and $SFR_{A\text{-}H06}$ are roughly consistent ($\Delta SFR \sim -0.18 \pm 0.05$ dex) when the contribution of $SFR_{UV,obs}$ is small. SFR_{B08} gives systematically lower values than SFR_{TIR} for $SFR > 20\,M_{\odot}$ yr^{-1} and $z > 1$, and higher values for lower redshifts and SFRs. The difference exceeds a factor of five for $SFR > 1000\,M_{\odot}$ yr^{-1}. The overall agreement between SFR_{TIR} and SFR_{R09} is rather poor, except at $z > 1.8$ where the differences are lower than 0.05 dex. The reasons for these discrepancies can be found in the differences in the relative emission of the cold and warm dust, and in the strength of the PAH and silicate absorption. These characteristics can vary by up to a factor of ∼5 from one set of templates to the other.
2. For each of the methods to estimate the SFR, we studied the effect having a better constrained IR SED comparing the SFRs computed from IRAC+MIPS, SFR(8, 24, 70), and just MIPS 24 μm, SFR(24). At low-z, the median values of $SFR_{TIR}(24)$ and $SFR_{A\text{-}H06}(24)$ tend to underestimate SFR(8, 24, 70) by 0.05 and 0.10 dex, respectively, with an rms of ∼0.2–0.3 dex. At $z \sim 2$, the estimates from these two methods based on 24 μm data are only on average ∼0.20 dex larger than those obtained with SFR(8, 24, 70). $SFR_{B08}(24)$ presents the opposite trend, giving larger values than SFR_{B08}(8, 24, 70) at $z \leqslant 1$ (up to 0.18 dex), but remaining mostly unchanged at higher redshifts.
3. The relative differences between each of the methods to estimate the IR-based SFRs with respect SFR_{TIR} (described in the first item) remain mostly unchanged when using SFRs(8, 24, 70). The values of SFR_{TIR}(8, 24, 70) (best-effort estimate) for a sample of galaxies in common with Symeonidis et al. (2008) and Huang et al. (2009), who counted with more photometric fluxes in the FIR and (sub-)mm range, presented a relatively good agreement within ∼0.3 dex. At $z < 1.2$ we find a small deviation of 0.09 dex in SFR_{TIR}(8, 24, 70) toward underestimating the SFR of MIPS-160 detected galaxies. Larger discrepancies, up to 0.5 dex, might arise for individual galaxies due to the use of different template sets.

In the context of studies of galaxy evolution, our catalog provides a self-consistent sample with a very detailed characterization of the systematic uncertainties suitable for multiple scientific purposes. It is also an alternative to other catalogs providing only photometry, redshifts, or stellar parameters alone. Furthermore, our photometric catalog itself provides a reference point for independent analysis of the stellar populations.

The multi-band photometric catalog presented in Paper I, jointly with the photometric redshifts and estimated stellar parameters presented here are publicly available. We have developed a Web interface, named *Rainbow Navigator*[8], that provides full access to the imaging data and estimated parameters and allows several other data handling functionalities.

We thank the referee for providing constructive comments and help in improving the contents of this paper. We thank G. Bruzual and S. Charlot for allowing us to use their models prior to publication. We acknowledge support from the Spanish Programa Nacional de Astronomía y Astrofísica under grants AYA 2006-02358 and AYA 2006-15698-C02-02. P.G.P.-G. acknowledges support from the Ramón y Cajal Program financed by the Spanish Government and the European Union. Partially funded by the Spanish MICINN under the Consolider-Ingenio 2010 Program grant CSD2006-00070: First Science with the GTC. Support was also provided by NASA through contract no. 1255094 issued by JPL/Caltech. This work is based in part on observations made with the *Spitzer* Space Telescope, which is operated by the Jet Propulsion Laboratory, Caltech under NASA contract 1407. Observations reported here were obtained at the MMT Observatory, a joint facility of the Smithsonian Institution and the University of Arizona. *GALEX* is a NASA Small Explorer launched in 2003 April. We gratefully acknowledge NASA's support for construction, operation, and scientific analysis of the *GALEX* mission. This research has made use of the NASA/IPAC Extragalactic Database (NED) which is operated by the Jet Propulsion Laboratory, California Institute of Technology, under contract with the National Aeronautics and Space Administration. Based in part on data collected at Subaru Telescope and obtained from the SMOKA, which is operated by the Astronomy Data Center, National Astronomical Observatory of Japan.

REFERENCES

Alonso-Herrero, A., et al. 2004, ApJS, 154, 155
Alonso-Herrero, A., et al. 2006, ApJ, 650, 835
Assef, R. J., et al. 2010, ApJ, 713, 970
Barro, G., et al. 2011, ApJS, 193, 13
Bavouzet, N., et al. 2008, A&A, 479, 83
Bell, E. F., McIntosh, D. H., Katz, N., & Weinberg, M. D. 2003, ApJ, 585, L117
Bell, E. F., et al. 2005, ApJ, 625, 23
Benítez, N. 2000, ApJ, 536, 571
Bertin, E., & Arnouts, S. 1996, A&AS, 117, 393
Blanc, G. A., et al. 2008, ApJ, 681, 1099
Bolzonella, M., Miralles, J., & Pelló, R. 2000, A&A, 363, 476
Bouwens, R. J., et al. 2009, ApJ, 705, 936
Brammer, G. B., van Dokkum, P. G., & Coppi, P. 2008, ApJ, 686, 1503
Brodwin, M., et al. 2006, ApJ, 651, 791
Bruzual, G. 2007, in ASP Conf. Ser. 374, From Stars to Galaxies: Building the Pieces to Build Up the Universe, ed. A. Vallenari et al. (San Francisco, CA: ASP), 303
Bruzual, G., & Charlot, S. 2003, MNRAS, 344, 1000
Bundy, K., et al. 2006, ApJ, 651, 120
Burgarella, D., et al. 2007, MNRAS, 380, 986
Barro, G., et al. 2009, A&A, 494, 63
Calzetti, D., et al. 2000, ApJ, 533, 682
Calzetti, D., et al. 2007, ApJ, 666, 870
Caputi, K. I., et al. 2006, ApJ, 637, 727
Cardamone, C. N., et al. 2010, ApJS, 189, 270
Cardelli, J. A., Clayton, G. C., & Mathis, J. S. 1989, ApJ, 345, 245

[8] http://rainbowx.fis.ucm.es

Chabrier, G. 2003, PASP, 115, 763
Charlot, S., & Fall, S. M. 2000, ApJ, 539, 718
Chary, R., & Elbaz, D. 2001, ApJ, 556, 562
Coleman, G. D., Wu, C., & Weedman, D. W. 1980, ApJS, 43, 393
Colina, L., & Bohlin, R. C. 1994, AJ, 108, 1931
Collister, A. A., & Lahav, O. 2004, PASP, 116, 345
Conroy, C., & Gunn, J. E. 2010, ApJ, 712, 833
Conroy, C., Gunn, J. E., & White, M. 2009, ApJ, 699, 486
Conroy, C., White, M., & Gunn, J. E. 2010, ApJ, 708, 58
Conselice, C. J., et al. 2007, ApJ, 660, L55
Conselice, C. J., et al. 2008, MNRAS, 383, 1366
Coupon, J., et al. 2009, A&A, 500, 981
Daddi, E., et al. 2004, ApJ, 617, 746
Daddi, E., et al. 2007, ApJ, 670, 156
Dale, D. A., & Helou, G. 2002, ApJ, 576, 159
Dale, D. A., et al. 2005, ApJ, 633, 857
Davis, M., et al. 2007, ApJ, 660, L1
De Lucia, G., & Blaizot, J. 2007, MNRAS, 375, 2
Donley, J. L., Rieke, G. H., Pérez-González, P. G., Rigby, J. R., & Alonso-Herrero, A. 2007, ApJ, 660, 167
Elbaz, D., et al. 2010, A&A, 518, L29
Fioc, M., & Rocca-Volmerange, B. 1997, A&A, 326, 950
Fontana, A., et al. 2006, A&A, 459, 745
Förster Schreiber, N. M., et al. 2006, AJ, 131, 1891
Franx, M., et al. 2003, ApJ, 587, L79
Gawiser, E., et al. 2006, ApJS, 162, 1
Grazian, A., et al. 2006a, A&A, 449, 951
Grazian, A., et al. 2006b, A&A, 453, 507
Grazian, A., et al. 2007, A&A, 465, 393
Hartley, W. G., et al. 2008, MNRAS, 391, 1301
Hartley, W. G., et al. 2010, MNRAS, 407, 1212
Hildebrandt, H., Wolf, C., & Benítez, N. 2008, A&A, 480, 703
Hopkins, A. M., & Beacom, J. F. 2006, ApJ, 651, 142
Huang, J., et al. 2004, ApJS, 154, 44
Huang, J., et al. 2005, ApJ, 634, 137
Huang, J., et al. 2009, ApJ, 700, 183
Iglesias-Páramo, J., et al. 2007, ApJ, 670, 279
Ilbert, O., et al. 2006a, A&A, 457, 841
Ilbert, O., et al. 2006b, A&A, 453, 809
Ilbert, O., et al. 2009, ApJ, 690, 1236
Ilbert, O., et al. 2010, ApJ, 709, 644
Ivison, R. J., et al. 2007, ApJ, 660, L77
Kajisawa, M. 2006, PASJ, 58, 951
Kannappan, S. J., & Gawiser, E. 2007, ApJ, 657, L5
Kartaltepe, J. S., et al. 2010, ApJ, 709, 572
Kennicutt, R. C., Jr. 1998, ARA&A, 36, 189
Kennicutt, R. C., et al. 2009, ApJ, 703, 1672
Kinney, A. L., et al. 1996, ApJ, 467, 38
Kriek, M., et al. 2008, ApJ, 677, 219
Kron, R. G. 1980, ApJS, 43, 305
Kroupa, P. 2001, MNRAS, 322, 231
Kurucz, R. L. 1992, in IAU Symp. 149, The Stellar Populations of Galaxies, ed. B. Barbuy & A. Renzini (Cambridge: Cambridge Univ. Press), 225
Labbé, I., et al. 2003, AJ, 125, 1107
Laird, E. S., et al. 2009, ApJS, 180, 102
Magdis, G. E., et al. 2008, MNRAS, 386, 11
Magnelli, B., et al. 2008, ApJ, 681, 258
Maraston, C. 1998, MNRAS, 300, 872
Maraston, C. 2005, MNRAS, 362, 799
Maraston, C., et al. 2006, ApJ, 652, 85
Maraston, C., et al. 2010, MNRAS, 407, 830
Marchesini, D., et al. 2009, ApJ, 701, 1765
Marcillac, D., et al. 2006, A&A, 451, 57
McCracken, H. J., et al. 2010, ApJ, 708, 202
Mentuch, E., et al. 2009, ApJ, 706, 1020
Morrissey, P., et al. 2007, ApJS, 173, 682
Muzzin, A., et al. 2009, ApJ, 701, 1839
Noll, S., Pierini, D., Pannella, M., & Savaglio, S. 2007, A&A, 472, 455
Noll, S., et al. 2009, A&A, 507, 1793
Noterdaeme, P., Ledoux, C., Srianand, R., Petitjean, P., & Lopez, S. 2009, A&A, 503, 765
Oyaizu, H., Lima, M., Cunha, C. E., Lin, H., & Frieman, J. 2008, ApJ, 689, 709
Panter, B., Jimenez, R., Heavens, A. F., & Charlot, S. 2007, MNRAS, 378, 1550
Papovich, C., & Bell, E. F. 2002, ApJ, 579, L1
Papovich, C., et al. 2006, ApJ, 640, 92
Papovich, C., et al. 2007, ApJ, 668, 45
Pérez-González, P. G., et al. 2005, ApJ, 630, 82
Pérez-González, P. G., et al. 2006, ApJ, 648, 987
Pérez-González, P. G., et al. 2008, ApJ, 675, 234
Pérez-González, P. G., et al. 2010, A&A, 518, L15
Polletta, M., et al. 2007, ApJ, 663, 81
Quadri, R., et al. 2007, AJ, 134, 1103
Reddy, N. A., Steidel, C. C., Erb, D. K., Shapley, A. E., & Pettini, M. 2006, ApJ, 653, 1004
Reddy, N. A., et al. 2005, ApJ, 633, 748
Reddy, N. A., et al. 2008, ApJS, 175, 48
Rieke, G. H., et al. 2009, ApJ, 692, 556
Rigby, J. R., et al. 2008, ApJ, 675, 262
Rigopoulou, D., et al. 2006, ApJ, 648, 81
Salim, S., et al. 2007, ApJS, 173, 267
Salim, S., et al. 2009, ApJ, 700, 161
Salimbeni, S., Fontana, A., Giallongo, E., Grazian, A., Menci, N., Pentericci, L., & Santini, P. 2009, in AIP Conf. Ser. 1111, ed. G. Giobbi et al. (Melville, NY: AIP), 207
Salpeter, E. E. 1955, ApJ, 121, 161
Santini, P., et al. 2009, A&A, 504, 751
Schlegel, D. J., Finkbeiner, D. P., & Davis, M. 1998, ApJ, 500, 525
Siebenmorgen, R., & Krügel, E. 2007, A&A, 461, 445
Silva, L., Granato, G. L., Bressan, A., & Danese, L. 1998, ApJ, 509, 103
Smith, J. D. T., et al. 2007, ApJ, 656, 770
Springel, V., et al. 2005, Nature, 435, 629
Steidel, C. C., et al. 2003, ApJ, 592, 728
Steidel, C. C., et al. 2004, ApJ, 604, 534
Symeonidis, M., et al. 2008, MNRAS, 385, 1015
Symeonidis, M., et al. 2010, MNRAS, 403, 1474
Taylor, E. N., et al. 2009, ApJ, 694, 1171
Trujillo, I., et al. 2007, MNRAS, 382, 109
van der Wel, A., et al. 2006, ApJ, 652, 97
van Dokkum, P. G., et al. 2008, ApJ, 677, L5
van Dokkum, P. G., et al. 2009, PASP, 121, 2
Walcher, C. J., et al. 2008, A&A, 491, 713
Werner, M. W., et al. 2004, ApJS, 154, 309
Wild, V., et al. 2007, MNRAS, 381, 543
Wolf, C., et al. 2003, A&A, 401, 73
Wuyts, S., et al. 2008, ApJ, 682, 985

4

Scientific explotation of multi-wavelength catalogs I: The nature of extragalactic number counts in the K-band

4.1 Introduction

In the previous two Chapters we have presented a detailed characterization of the SEDs and the physical properties of a large sample of galaxies in the cosmological field EGS. In this Chapter, we aim to present a work focused on addressing a more concise astrophysical question, thus illustrating the vast possibilities of characterizing the galaxies with accurate physical properties. Although the previous Chapters presented relevant conclusions on the properties of the galaxies in the EGS, our main goal was to develop and characterize a galaxy catalog. Therefore, in this Chapter we will focus on the particular problem of analyzing the nature of the galaxy number counts (NCs) in the K-band.

Chronologically, the analysis presented in this Chapter was performed prior to the studies of previous Chapters and therefore it is does not make use of the *Spitzer*/IRAC selected sample. However, the analysis carried out is fundamentally sustained in the same principles introduced in the previous chapters, i.e, exploiting the multi-wavelength characterization of SEDs and physical properties of galaxy sample. The main difference is that in this Chapter the description of the technical details on the creation of a merged catalog and the estimate of the relevant properties of the galaxies is briefly summarized in favor of a more detailed discussion on the implications of these results and how these can be used to solve a particular question.

In particular, this studies presented in this Chapter are based on the analysis of a K-band selected sample in the EGS. The characterization of the galaxy sample followed essentially the same steps described in the previous Chapters consisting on: 1) gathering all the available spectro-photometric data in the area. In particular, the K-band data in which the study is based was obtained by our group in 2002 and it was reduced and processed for this thesis; 2) performing a multi-band identification of the K-band sources; 3) obtaining consistent multi-band photometry; 4) model the resulting UV and IR SEDs fitting them with SPS models and dust emission templates; 5) Derive photometric redshifts and rest-frame luminosities in several wavelengths out of the best-fitting templates. An specific sub-routine to obtain rest-frame magnitudes and luminosities from the synthetic spectra in any given band was developed and included in the suite of programs that conform the whole *Rainbow* package as a part of this work. Now it is available for any subsequent study that makes use of *Rainbow*.

As a result to the techniques applied to develop this catalog, all galaxies were also characterized with stellar masses and SFRs. However, as these were not required to address the questions raised in this Chapter, we do not discussed them here. Nonetheless, it is worth mentioning that realizing the vast amount of resources that can be obtained from *Rainbow* was a fundamental motivation to perform the exhaustive analysis described in Chapters 2 and 3. This is because, by describing the basis of the *Rainbow* methodology and discussing the accuracy and limitations of the estimated properties we allow a more straightforward use of all these resources in future studies.

Based on the estimated properties for the K-band selected sample we will explore the nature of the K-band NCs. In particular, we will disentangle the relative contribution of galaxies at different redshifts to identify what is the cause for the shape of the NCs. To achieve this goal we will assume that NCs can be explained in terms of a set of LFs at different rest-frame magnitudes and redshift intervals. Based on that characterization we will identify three different regimes in the galaxy NCs as a function of magnitude which are related to key parameters of the LFs, and thus to intrinsic properties of the galaxies. To conclude our analysis we will compute multiple LFs that, combined with other results from the literature, will allow us to interpret the overall shape of the NCs (and particular features) in terms of LFs. Thus, linking the NCs to the intrinsic properties of the galaxies at different redshifts.

Along the following introduction we give a brief overview on the studies of galactic number counts describing the kind of insight that they can provide on the properties of the underlying galaxy populations. Then, we will conclude presenting some particular issues posed by the results of these studies that still remains un-solved.

4.1.1 The Number Counts view on galaxy evolution

As we described in the introduction to this work, the first studies of distant galaxies were focused on constraining the values of the cosmological parameters rather than to analyze galaxies themselves (see e.g., Sandage 1960; Tinsley 1977). In the dawn of observational cosmology, before multi-band catalogs and redshift surveys appeared, little was known about the values of the cosmological parameters, but even less about galaxy evolution. As a result, simple test such us counting the surface density of galaxies on the sky as a function of apparent magnitude became one of the classic cosmological tests. The idea is fairly simple, and it only requires taking a very deep wide-field image at any place on the sky, counting afterward the number of galaxies per unit of area and magnitude bin.

Then, making reasonable, but simple, assumptions on the properties of galaxies and their evolution with cosmic time the shape of these number counts would be exclusively dependent on the underlying geometry of the universe which is determined by the cosmological parameters. The initial assumptions on galaxy evolution were based on the few properties of local galaxies that were already known, such as the different Hubble types, their characteristic SEDs and distribution on luminosity (cf. luminosity functions). Upon that, the simplest parametrizations, so-called *no evolution* models, frequently assumed that the luminosity and characteristic density of galaxies remained constant with time i.e., no they do not age nor suffer mergers. The first papers on NC, soon revealed that these models were too simplistic to reproduce the counts (Brown & Tinsley 1974; Bruzual A. & Kron 1980; Koo 1986; Babul & Rees 1992), particularly at faint magnitudes, were there seemed to be an excess of galaxies. The discrepancies were aggravated with the advent

of deeper surveys which showed even larger differences compared to the models, being the largest in the blue bands (cf. the excess of faint blue galaxies; Babul & Ferguson 1996). In contrast, the first works on NIR NCs showed a comparatively flatness relative to optical counts, and a distinctive change of slope that made the interpretation even more puzzling (see, e.g., Cowie et al. 1990; Gardner et al. 1993; Gronwall & Koo 1995; Djorgovski et al. 1995; Bershady et al. 1998).

More detailed models appeared introducing luminosity evolution, detailed SED modeling (based on SPS), mergers, and assumptions on the formation time of different populations (see e.g., Kauffmann et al. 1994; Gardner et al. 1996; Pozzetti et al. 1996; Nakata et al. 1999; McCracken et al. 2000). The use of more sophisticated models improved the fitting to the observed NCs allowing a more challenging simultaneous fitting of NCs in different bands. The development of more detailed galaxy evolution models set the basis of the techniques that are currently ΛCDM simulations and semi-analytical models.

The change of paradigm for NC modeling started with the first rigorous proofs of an accelerating, closed, dark energy dominated universe (ΛCDM), presented in the results of WMAP (Spergel et al. 2003). Nowadays, our knowledge of the cosmological parameters has improved to a precision inconceivable in the 1970s. In addition, we also have proof of a substantial and complex, galaxy evolution with cosmic time, that must affect significantly to the shape of NCs. However, NCs are still widely used in combination with other key parameters (such as luminosity functions and mass functions) to test galaxy evolution models (both numerical and semi-analytical). The availability of NCs down to very faint magnitude limits over large sky areas is used to test the predictions of different theoretical models without being strongly affected by the cosmic variance (see e.g., Kitzbichler & White 2007; Monaco et al. 2007). In addition, as NCs are an almost unbiased measurement that do not require further assumptions (unlike e.g., luminosity/mass functions), these are commonly used as a validation test for deep multi-band surveys, being only subject to the effects of cosmic variance (i.e, clustering effects at small scales that affects the expected homogeneity of the galaxy distribution).

It is also worth mentioning that, despite our improved knowledge in both cosmology and galaxy evolution, it is still challenging reproducing the shape of NCs from its first principles, i.e., associating particular features to the properties of galaxies. Thus, even a widely used assumption such us that the faintest NCs are dominated by distant high-z galaxies can be potentially wrong (Bershady 2003). The main cause of uncertainties is the difficulty of interpreting galaxy counts (see, e.g., Koo 1990, and references therein), which represent sums of luminosity functions modulated by shifts in apparent magnitude (due to cosmological luminosity-distance effects, K-corrections and evolutionary corrections) and in apparent number (due to changes in the volume element with redshift). Thus, despite the conceptual simplicity of NCs, the large number of contributing parameters makes difficult the interpretation of galaxy counts only in terms of evolutionary effects in galaxy populations. However, our current knowledge of luminosity functions and galaxy redshift distributions allows us to do the opposite, i.e., reverse engineerer the NCs analyzing the relative effect of its components and revealing the underlying causes to their shape.

4.2 Barro et al. (2009) A&A 703, 1569

On the nature of the extragalactic number counts in the K-band

G. Barro[1], J. Gallego[1], P.G. Pérez-González[1], C. Eliche-Moral[1], M. Balcells[2], V. Villar[1], N. Cardiel[1], D. Cristobal-Hornillos[5], A. Gil de Paz[1], R. Gúzman[3], R. Pelló[4], M. Prieto[2], and J. Zamorano[1]

[1] Departamento de Astrofísica, Universidad Complutense de Madrid, 28040 Madrid, Spain
[2] Instituto de Astrofísica de Canarias, Vía Lactea, 38200 La Laguna, Canary Islands, Spain
[3] Department of Astronomy, 477 Bryant Space Center, University of Florida, Gainesville, FL
[4] Laboratoire d'Astrophysique de Toulouse-Tarbes, CNRS, Université de Toulouse, 14 Avenue Edouard Belin, 31400-Toulouse, France
[5] Instituto de Astrofísica de Andalucía, 18080 Granada, Spain

Preprint online version: November 19, 2008

ABSTRACT

Context. The galaxy number counts has been traditionally used to test models of galaxy evolution. However, the origin of significant differences in the shape of number counts at different wavelengths is still unclear. By relating the most remarkable features in the number counts with the underlying galaxy population it is possible to introduce further constraints on galaxy evolution.
Aims. We aim to investigate the causes of the different shape of the K-band number counts when compared to other bands, analyzing in detail the presence of a change in the slope around $K \sim 17.5$.
Methods. We present a near-infrared imaging survey, conducted at the 3.5m telescope of the Calar Alto Spanish-German Astronomical Center (CAHA), covering two separated fields centered on the HFDN and the Groth field, with a total combined area of $\sim 0.27\mathrm{deg}^2$ to a depth of $K \sim 19$ (3σ,Vega). By combining our data with public deep K-band images in the CDFS (GOODS/ISAAC) and high quality imaging in multiple bands, we extract K-selected catalogs characterized with highly reliable photometric redshift estimates. We derive redshift binned number counts, comparing the results in our three fields to sample the effects of cosmic variance. We derive luminosity functions from the observed K-band in the redshift range [0.25-1.25], that are combined with data from the references in multiple bands and redshifts, to build up the K-band number count distribution.
Results. The overall shape of the number counts can be grouped into three regimes: the classic Euclidean slope regime ($d\log N/dm \sim 0.6$) at bright magnitudes; a transition regime at intermediate magnitudes, dominated by M^* galaxies at the redshift that maximizes the product $\phi^* \frac{dV_c}{d\Omega}$; and an α dominated regime at faint magnitudes, where the slope asymptotically approaches -0.4(α+1) controlled by post-M^* galaxies. The slope of the K-band number counts presents an averaged decrement of $\sim 50\%$ in the range $15.5 < K < 18.5$ ($d\log N/dm \sim 0.6 - 0.30$). The rate of change in the slope is highly sensitive to cosmic variance effects. The decreasing trend is the consequence of a prominent decrease of the characteristic density $\phi^*_{K,obs}$ ($\sim 60\%$ from $z = 0.5$ to $z = 1.5$) and an almost flat evolution of $M^*_{K,obs}$ (1σ compatible with $M^*_{K,obs} = -22.89 \pm 0.25$ in the same redshift range).

Key words. galaxies: evolution — galaxies: high redshift — infrared: galaxies

1. Introduction

With the advent of the large photometric surveys (such as COSMOS - Scoville et al. 2006; UKIDDS - Lawrence et al. 2007, etc), the coverage of the extragalactic number counts (hereafter, NCs) on multiple bandpasses has greatly improved. Benefiting from the new generation of wide area cameras and dedicated telescope facilities, these surveys have provided large galaxy samples with a significant improvement in efficiency (Gabasch et al. 2008; McCracken et al. 2003). Even the traditionally more problematic NIR surveys have made considerable progress in covering areas close to a square degree, up to limiting magnitudes hardly reachable a few years ago (Simpson et al. 2006; Conselice et al. 2008).

The NIR galaxy counts usually have been considered a particularly useful method to constrain galaxy evolution and cosmology, providing a simpler, less biased, test of galaxy evolution models. However, although the overall shape of the NCs is well defined, published counts still exhibit a considerable scatter, making it difficult to narrow down the evolution in a small magnitude interval. Additionally, the apparent simplicity of the NCs hides a mixture of evolving galaxy properties that complicates the interpretation of the observed features in terms of a single physical origin. Thus, it is not surprising that the explanation for the flatness of the K-band counts (relative to the optical NCs) or the presence of a sharp break in the slope around $16 < K < 18$ are still a matter of debate (Gardner et al. 1993; Cristóbal-Hornillos et al. 2003; Quadri et al. 2007; Iovino et al. 2005; Temporin et al. 2008).

The change in the slope of the NCs is a direct consequence of galactic evolution. Indeed, any feature in the shape of the NCs is closely related to the luminosity distribution of galaxies at a given epoch. By disentangling the relative contribution from the luminosity functions (hereafter, LFs) at different redshift ranges, we will be able to identify the driving force behind the shape of the NCs.

Therefore, we aim to refine our understanding of the K-band NCs in the light of galaxy evolution by reconstructing the NCs in the K-band from rest-frame LFs in the multiple bandpasses probed by the observed K-band at different epochs. We benefit from the substantial amount of work done on deriving accurate LFs at different redshifts in the optical bands (Wolf et al. 2003;Blanton et al. 2003; Chen et al. 2003; Ilbert et al. 2005; Gabasch et al. 2006; Marchesini et al. 2007) and NIR bands (Kochanek et al. 2001; Cole et al. 2001; Pozzetti et al. 2003; Feulner et al. 2003; Cirasuolo et al. 2007; Arnouts et al. 2007) to disentangle the multiple galactic populations at different redshift that assemble together to create the observed NCs, and to discern the true nature of the reported features on that distribution.

The purpose of this paper is two-fold. First we present a NIR survey conceived to serve as reference for future spectroscopic follow up. Second, we use these datasets and high quality photometric redshifts to derive NCs and LFs in the observed K-band, allowing us to analyze the underlying galaxy population responsible for the observed shape of the K-band NCs. The paper is organized as follows: In §2 we describe the observations, data reduction and the compilation of complementary data sets. Sections 3 and 4 show the multi-wavelength characterization of the K-selected samples and the procedure to derive photometric redshifts. In §5 we investigate the reliability of these photometric redshift estimates. Then, we use these K-selected samples in §6 and §7, presenting K-band NCs in three different fields and making use of the photometric redshifts to explore the redshift distribution and to probe the impact of cosmic variance in the NCs. In §8 we discuss the connection between NCs and LFs, and present our LF estimates along with previously published results in multiple bands and redshifts. In §9 we derive the expected NCs distribution from the corresponding LFs. Section §10 summarizes the conclusions of the paper.

Throughout this paper we use Vega magnitudes unless noted otherwise and adopt the current standard cosmology $H_0 = 70$ km^{-1}s^{-1}Mpc^{-1}, $\Omega_M = 0.3$ and $\Omega_\Lambda = 0.7$.

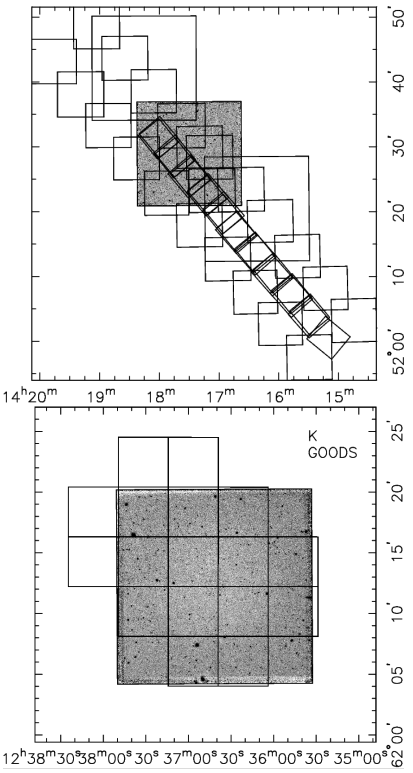

Fig. 1. Sky coverage maps of the NIR datasets in the Groth and HDFN fields. The outlines represent. *Top.*- The CAHA-Ω' K'-band flanking fields at both sides of the WHT-INGRID K-band coverage of the original Groth strip (Cristóbal-Hornillos et al. 2003), and the $\Omega 2k$ J-band pointings of Villar et al. (2008). The J-band central image is shown for comparison with the HDFN K-band image covering the same area ($\sim$ 225arcmin^2). *Bottom.*- The CAHA-Ω2k K-band coverage of the HDFN. The GOODS-HST footprints are also shown for comparison.

2. NIR observations

K-band observations were carried out on two separate fields: one covering the flanking fields of the original Groth strip (Groth et al. 1994) at $\alpha(J2000.0) = 14^h17^m43^s$, $\delta(J2000.0) = 52°28'41''$ (hereafter, Groth-FF), and the second centered at the Great Observatories Origins Deep Survey north field (HFDN; Giavalisco et al. 2004), $\alpha(J2000.0) = 12^h36^m49^s$, $\delta(J2000.0) = 62°12'58''$. Additionally, we made use of complementary infrared imaging which includes a full mapping of the Groth strip in the J and Ks bands (Cristóbal-Hornillos et al. 2003; hereafter, CH03), and J-band observations in the Groth and HDFN fields (Villar et al. 2008; hereafter V08), consisting of three pointings covering at least $\sim$ 60% of the K surveyed area in Groth, and a single pointing in HDFN completely overlapping with the K exposure. Details of the observations are shown in Table 1. Fig. 1 shows the layout of the two areas covered.

The Groth-FF infrared observations in the K'-band were obtained using OMEGA-PRIME (hereafter, Ω'), mounted on the prime focus of the 3.5m telescope at Calar Alto Spanish-German Astronomical Center (CAHA) during three runs in 2000 May 15-17, 2002 March 28-31 and 2002 August 19-23. The K' filter was preferred to Ks for a better removal of thermal background. No significant difference in $\langle K' - Ks \rangle$ galaxy photometry was found (see Section 2.2).

The Ω' camera was equipped a 1k×1k HgCdTe Rockwell array that provides a field of view of $7' \times 7'$ with $0.396''$/pixel scale. In the first runs, a small misalignment on the secondary mirror caused the PSF to be slightly asymmetric. This problem was enhanced in the 2002 run, causing the FWHM to be noticeably higher, and reducing the depth of the observations. The seeing conditions were generally average, with the FWHM ranging from $1.10''$ to $1.50''$ except for a few pointings with a higher seeing ($\sim 1.9''$). The background emission in the NIR is bright, non-uniform and highly variable. Therefore, in order to perform an accurate sky subtraction, sky dithered exposures are required. We used a hexagonal dithering pattern of $20''$ side, repeated 12 times, shifting the center $3''$ each time to create the final exposure. After excluding the edges (having a lower coverage), each pointing in the Groth-FF covers 47 arcmin^2. The integration times were chosen to keep the count levels

within the linear regime of the detector. Typical exposure times were 31×2 s per dithered position (co-adds $\times$ individual exposure time), rejecting the first frame each time to avoid charge persistency problems. Total integration times were around 84 minutes per pixel. Note that the integration time for the last run was increased to alleviate the alignment problem.

The whole Groth-FF mosaic comprises 22 pointings of about $7' \times 7'$, for a total of 822 arcmin^2. $\sim$ 80% of the total area is above the average exposure time per frame ($\sim$ 80 min), with relatively shallow limiting magnitudes of $K \sim 19.1 - 19.8$ (3σ). The CH03 Groth strip observations covered $\sim$180 arcmin^2 in eleven $4' \times 4'$ pointings, carried out with the INGRID instrument and K-band filter in the William Herschel Telescope, to a deeper limiting magnitude of $K \sim 20.5$ (3σ). The V08 central Groth strip observations covered 702 arcmin^2 in three $15' \times 15'$ pointings taken using the OMEGA 2000 ($\Omega 2k$) instrument at 3.5m CAHA to a limiting depth of $J \sim 22.5$ (3σ). The combination of the Groth NIR observations leads to a total area of 955 arcmin^2 in the K-band and at least 462 arcmin^2 simultaneously observed in both the J and K bands.

The HDFN infrared observations in the Ks-band were performed with the CAHA 3.5m telescope using $\Omega 2k$, which is an improvement over the previous Ω' instrument. The detector is a 2k$\times$2k HgCdTe HAWAII-2 Array, with a $0.450''$/pixel and a $15.4' \times 15.4'$ field of view. Observations were performed over the course of one observing run in 2006 May 15-17. The seeing conditions were slightly better than in Groth-FF, ranging from $0.9''$ to $1.1''$. The typical exposure times at each dithered position were 50×3 s. The total exposure time is 1.7 h. After excluding the noisy edges, we obtained a final image of 232 arcmin^2 to a $K \sim 19.5$ depth (3σ). The same area is covered in V08 J-band observations of HDFN to a limiting magnitude $J \sim 21.9$ (3σ).

2.1. Data reduction

The data were reduced in a standard way using a combination of the UCM NIR reduction software (Cardiel et al.) and the IRAF[1] software package XDIMSUM. The basic methods are outlined below.

First, an average dark image with the same exposure time and number of co-adds is subtracted from the science images. Second, each science frame is flat-field corrected and the background emission is removed. Finally, all the frames are combined using an iterative method.

The skyflat image employed in the second step is built from the science frames by combining all the images with a median filter to remove sources. The background emission image is created for each science image using the median combination of the same pixel in the 3 previous images and the 3 next images. The positions of several stars are used to determine the relative shifts between background-subtracted images. The images are aligned to a common reference using integer pixel shifts, to preserve the Poisson nature of the noise. Since the PSF is well sampled, we do not expect an increase in the average seeing. Object masks in the combined image are constructed using SExtractor (Bertin & Arnouts 1996). In a second step (and following iterations), the construction of the skyflat and the background estimation is repeated (and improved), this time masking out the sources detected in the previous step.

Several additional reduction procedures are carried out to improve the quality of the final images. We create a mask of bad pixels in each image. An initial cosmetic defect mask is created using the dark images. We then inspect each background subtracted image individually; images with severe artifacts, significantly higher seeing or very poor transparency are discarded, while others with localized artifacts (e.g. satellite trails) are masked using a custom procedure. Additional bad pixels in each image are identified using a cosmic ray detection procedure or are removed with a sigma-clipping algorithm during image combination.

2.2. Photometric calibration

Photometric calibration was performed comparing aperture photometry from Two Micron All Sky Survey (2MASS) (Skrutskie et al. 2006) bright stars in the final mosaic after rejecting those with poor quality flags in the 2MASS catalog. Despite the different K-band filters, the integrated K_s fluxes are essentially preserved, as the color transformations (Eq.1) are typically smaller than a few 0.01 mag, due to the smooth behavior of NIR SEDs. The Ω'-K' and 2MASS-K_s magnitudes are related by the following equations (Wainscoat & Cowie 1992);

$$\begin{aligned} K_s &= K + 0.005(J-K) \\ K &= K' - (0.22 \pm 0.03)(H-K). \end{aligned} \quad (1)$$

We find that the same equations apply for $\Omega 2k$ with no significant dispersion.

The number of stars employed for each field calibration ranges from 7 to 15, leading to a zero-point rms between 0.04 and 0.08 in Groth-FF, and $\sim$ 0.05 in HDFN, which should only be considered as a lower bound to cumulative uncertainties introduced by the color transformations. To check the quality of the Groth-FF photometric calibrations we compared them to CH03 INGRID K-band observations inside an $\sim$80 arcmin^2 overlapping region. Using standard stars (Persson et al. 1998), they found their photometric uncertainty to be less than 0.03-0.05 mag. The median offset of the comparison is less than 0.07 mag for bright objects, so we do not attempt to readjust the zero-points to their calibration.

Note that the shift in effective wavelength between the K' and K_s filters is small, and much less than the filter widths. In the discussion that follows we do not distinguish between the different K filter sets.

2.3. Catalog completeness

We estimated the completeness of our catalogs by simulating the detection and photometry of fake sources. The fake sources were created by extracting a bright source from the image, scaling it to the desired flux level, and injecting it at random locations in the central well-exposed regions of the images. We then attempt to detect these objects by running SExtractor under the same parameters as in the original frame. Figure 2 shows the resulting completeness curves for point sources as a function of magnitude for some of the pointings. Because the simulated sources are not required to fall on empty regions, the confusion to real sources may slightly lower our detection efficiency. Nonetheless, given

[1] http://iraf.noao.edu/

Pointing (1)	R.A. (J2000.0) (2)	Decl (J2000.0) (3)	Exposure (s) (4)	FWHM (arcsec) (5)	m(80%eff) (mag) (6)	$m_{lim}(5\sigma)$ (mag) (7)	Area ($arcmin^2$) (8)
groth11	14:14:43.515	+52:03:14.76	4800	1.15	19.1	19.3	47.2
$groth12^{\dagger}$	14:15:28.298	+51:57:35.62	5820	1.53	18.7	19.3	48.7
groth21	14:15:11.712	+52:08:13.31	4680	1.20	18.8	19.2	47.1
$groth22^{\dagger}$	14:15:56.989	+52:02:48.05	7500	1.50	18.8	19.3	45.4
groth31	14:15:39.456	+52:13:11.31	3720	1.50	18.7	19.2	47.4
groth32	14:16:21.756	+52:07:41.58	2520	1.30	18.7	19.1	46.6
groth41	14:16:06.669	+52:18:38.36	3240	1.16	18.3	18.5	47.2
groth42	14:16:49.262	+52:12:49.23	5040	1.31	19.1	19.4	48.6
groth51	14:16:35.898	+52:23:32.60	5040	1.00	19.1	19.5	49.6
groth52	14:17:17.680	+52:18:02.82	5040	1.14	19.2	19.5	48.5
groth61	14:17:07.477	+52:28:30.29	4680	1.30	19.2	19.7	48.9
$groth62^{\dagger}$	14:17:50.812	+52:22:59.62	6180	1.50	18.7	19.3	47.0
groth63	14:17:04.981	+52:23:23.18	5040	1.14	18.8	19.1	49.1
groth64	14:17:17.456	+52:30:05.59	5040	1.07	19.2	19.5	46.8
groth71	14:17:35.943	+52:33:22.61	5040	1.42	18.9	19.6	50.9
groth72	14:18:21.179	+52:28:19.52	4920	1.80	19.0	19.8	47.4
groth81	14:18:03.943	+52:38:41.66	5040	1.30	19.2	19.8	47.4
groth82	14:18:49.704	+52:33:22.23	2940	1.90	18.4	19.3	48.2
groth91	14:18:33.323	+52:43:46.63	4560	1.50	19.2	19.7	48.7
groth92	14:19:17.913	+52:38:09.21	4920	1.60	18.9	19.5	50.7
groth101	14:19:02.220	+52:48:38.00	4800	1.90	18.5	19.7	49.4
$groth102^{\dagger}$	14:19:45.792	+52:43:11.56	6300	1.50	18.9	19.5	49.6
gooodsn	12:36:49	+62:12:58	6300	1.1	19.2	19.5	232.2

Table 1. Units of right ascension are hours, minutes and seconds, and units of declination are degrees, arcminutes and arcseconds.(†) Pointing observed during secondary mirror misalignment problem. Col. (7) is the 5σ limiting magnitude measured inside a 1" radius circular aperture.

the uncrowded nature of our K-band images, we expect the confusion to affect our completeness values by less than 5% at the $\sim 80\%$ level.

For a more realistic depth estimation, we have simulated extended sources as well as point like sources. Extended sources are considered when the effective radius is 20% greater than the typical radius of the stars on that frame. As expected, the efficiency for extended sources lowers the estimation from point-like sources by 0.2 to 0.3 magnitudes. A precise determination of the completeness correction would require measuring the detection efficiency over a wider range of effective radius. Nevertheless, for the purpose of our investigation, we can establish a conservative magnitude threshold of K=18.5 in the HDFN and Groth-FF without affecting our conclusions. Hence, excluding the shallowest fields (groth32, groth41, groth82, groth101) from the final catalog, we obtain a galaxy sample of reasonably homogeneous depth in both fields, avoiding the use of completeness corrections. The estimated 80% completeness and limiting magnitudes for each pointing are given in Table 1. For the Groth strip data, CH03 carried out simulations finding insignificant completeness corrections below $K = 19$. We will adopt that value as the limiting magnitude.

2.4. Complementary data

In addition to our NIR survey, high-quality imaging and photometry are publicly available for both fields. For the Groth field, we made use of some of the panchromatic data sets that have been acquired as a part of the All-wavelength Extended Groth Strip International Survey (AEGIS, see Davis et al. 2007 for a detailed data description), including ground based *ugriz* deep imaging from the Canada-France Hawaii Telescope Large Survey (CFHTLS-D03-, Gwyn et al. in preparation), observed with MegaCam at the 4 m CFTH; *BRI* wide field ($0.70^{\circ}\times0.47^{\circ}$) observations using the CFHT12K mosaic camera; *Spitzer* mid-IR data covering the wavelength range $3.6\mu m$ to $8.0\mu m$ (GTO program) and a deep R-band image from Subaru-SuprimeCam (Miyazaki et al. 2007).

Band (1)	$\lambda_{eff}(\mu m)$ (2)	m_{lim} (3)	Source (4)
IRAC-3.6..	3.561	21.6	*Spitzer* GTO
IRAC-4.5..	4.510	21.8	*Spitzer* GTO
IRAC-5.8..	5.689	21.8	*Spitzer* GTO
IRAC-8.0..	7.958	21.7	*Spitzer* GTO
U.....	0.358	25.2	Subaru deep *imaging*[a]
B.....	0.442	25.2	Subaru deep *imaging*[a]
V.....	0.546	24.9	Subaru deep *imaging*[a]
R.....	0.652	24.4	Subaru deep *imaging*[a]
I.....	0.795	23.9	Subaru deep *imaging*[a]
z.....	0.909	23.6	Subaru deep *imaging*[a]
b.....	0.430	25.7	*GOODS*[b]
v.....	0.592	24.9	*GOODS*[b]
i.....	0.770	24.3	*GOODS*[b]
z.....	0.906	23.9	*GOODS*[b]
HK_s ..	2.127	21.3	QUIRC deep *imaging*[a]
b,spectra..	0.430	24.4	*TKRS*[c]

Table 2. Main characteristics of the datasets in HDFN. Col. (1): Observing band. Col. (2): Effective wavelength of the filter calculated by convolving the Vega spectrum (Colina & Bohlin 1994) with the transmission curve of the filter+detector. Col. (3): Limiting AB magnitude. Col. (4): Source from where the data were obtained. [a] Publicly available ultra-deep optical and NIR data from Capak et al.(2004). [b] The Great Observatories Origins Deep Survey (GOODS; Giavalisco et al. 2004a). [c] Team Keck Treasury Redshift Survey (TKRS; Wirth et al. 2004) and Cowie et al. (2004).

In the HDFN, we used ultra-deep optical and NIR data spanning from the U to the HK-band ($UBVRIzHKs$, Capak et al. 2004), together with HST-ACS *bviz* imaging published by the GOODS Team (Giavalisco et al. 2004). The main characteristics of each data set are given in Table 2 and Table 3.

Band	$\lambda_{eff}(\mu m)$	m_{lim}	Source
(1)	(2)	(3)	(4)
Kp.....	2.114	20.3	CAHA-Oprime
R.....	0.652	-	Subaru deep imaging
u.....	0.381	27	CFHTLS
g.....	0.486	28.3	CFHTLS
r.....	0.626	27.5	CFHTLS
i.....	0.769	27	CFHTLS
z.....	0.887	26.4	CFHTLS
B.....	0.437	24.5	CFHT-12k
R.....	0.660	24.2	CFHT-12k
I.....	0.813	23.5	CFHT-12k
J.....	1.255	22	WHT-INGRID
K.....	2.170	21.8	WHT-INGRID
IRAC-3.6.....	3.561	21.6	*Spitzer* GTO
IRAC-4.5.....	4.510	21.8	*Spitzer* GTO
IRAC-5.8.....	5.690	21.8	*Spitzer* GTO
IRAC-8.0.....	7.957	21.7	*Spitzer* GTO
nuv.....	0.232	24.5	GALEX GTO
fuv.....	0.154	24.5	GALEX GTO
U.....	0.361	24.8	INT-WFC
B.....	0.436	25.5	INT-WFC
R,redshift....	0.660	24.2	DEEP2

Table 3. Main characteristics of the datasets in Groth. Col. (1): Observing band. Col. (2): Effective wavelength of the filter calculated by convolving the Vega spectrum (Colina & Bohlin 1994) with the transmission curve of the filter+detector. Col. (3): Limiting AB magnitude. Col. (4): Source from where the data were obtained.

At the time of writing, the CFHT12k fully reduced images were not publicly available. Instead, raw images and calibration files were downloaded from the CFHT-CADC archive and the Elixir website[2], and were reduced using the IRAF MSCRED package. Precise astrometry and photometry calibrations were carried out by comparison to the CFHT12k public catalogs, and the CFHTLS and Subaru imaging in overlapping regions.

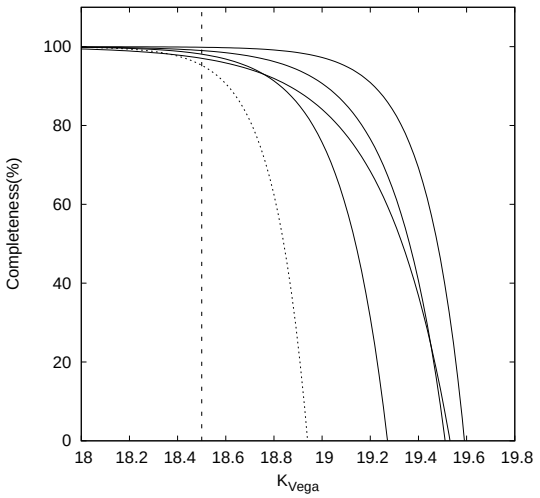

Fig. 2. The K-band best fit to the point source completeness curves. Point-like sources were inserted at random locations in the images. The completeness is defined as the fraction of recovered sources in each image. The short dashed line shows the completeness curve for the Groth32 pointing, the shallowest frame employed computing the number counts. The vertical long dashed line at $K = 18.5$ depicts the magnitude threshold to which our catalog is $\sim 100\%$ complete.

To complement the imaging data we have compiled a set of spectroscopic redshifts obtained by several surveys on these fields. For the HDFN we have 1699 spectroscopic redshifts from Wirth et al. (2004), Cowie et al. (2004), and Reddy et al. (2006). Most of these sources are below $z \sim 1$ and have a high reliability flag ($\sim$ 80%). In the Groth field we have $\sim$15000 redshifts from the DEEP2 collaboration (Davis 2006). Only a small fraction of those are found within our surveyed area.

3. Source characterization

3.1. Multi-wavelength photometry

Multicolor photometry in all available bands was obtained employing a similar method to the one described in Pérez-González et al. (2008, Appendix A). Briefly, the K-band source catalog, obtained with SExtractor, was cross-correlated in a $2''$ radius to each one of the UV, optical and NIR catalogs. Sources detected in fewer than 3 bands were rejected. Given the relatively shallow limiting magnitude of the K-band images, fully covered by deep optical and IRAC images, this is a safe method to reject spurious sources. Then, aperture matched photometry was performed using elliptical Kron-like apertures. The aperture size and orientation is determined by the K-band image and translated to all the other optical and NIR images except for the IRAC bands.

For our typical seeing values the aperture is large enough to enclose the PSF in all these bands. For the IRAC bands, where the resolution is slightly worse ($\sim 2''$; Fazio et al. 2004), the flux was measured in small circular apertures (typically $3''$) and corrected using stellar PSF growth curves (similarly to Huang et al. 2004; Barmby et al. 2008). In addition, we have also applied a deblending algorithm for the sources with multiple K-band counterparts associated with a single IRAC source and separated by more than $1''$ (the approximate limit of the astrometric resolution). The K-band positions of the sources were used to re-align the position of the aperture in the IRAC band. Then, the IRAC PSF is convolved with the K-band PSF and the flux is measured again inside a $0.9''$ aperture, applying the corresponding aperture correction. For source separations larger than $1''$, the flux contamination with this method is lower than 10% (Pérez-González et al. 2008).

For GALEX and HST data, we took the SExtractor MAG_BEST magnitude of the closest source. Consequently, we do not use these data in the photometric redshift determination. For the rest of the bands, the procedure allows us to obtain accurate colors, since we measure a similar fraction of the flux from an object in each filter.

Uncertainties in the measured flux were derived taking into account the background noise, photon statistics, readout noise and scatter in the WCS. The standard method of determining the background noise from pixel-to-pixel variations of adjacent sky pixels often underestimates the

[2] http://www.cfht.hawaii.edu/Instruments/Elixir/

real value due to correlated signal effects introduced during the data reduction (Labbé et al. 2003;Gawiser et al. 2006). To obtain a more accurate determination of the background noise we followed the method described in Pérez-González et al. (2008), which is similar to that of Labbé et al. (2003). For each source, the sky flux was measured in randomly distributed apertures with the same size as the photometric aperture. Then, we estimated the background noise from the width of the flux histogram, approximated by a Gaussian distribution. The comparison to the sky background measured with SExtractor shows that the latter tends to underestimate (10%-15%) the noise even in the K-band images, where integer pixel shifts were used during the frame combination.

3.2. Photometric redshift

We calculate photometric redshifts using the methods described in detail in Peréz González et al. (2005,2008). Briefly, a reference set of galaxy templates is fitted to the observed spectral energy distributions (SEDs), taking into account the flux uncertainties. The galaxy templates are composed of a sample of galaxy spectra from HDFN and CDFS with highly reliable redshift determinations, including some $z > 1.5$ galaxies, and well-covered SEDs (with more than 10 different photometric data points). The set is fitted with models of single, and composed stellar populations (1-POP and 2-POP) and models of dust emission. The comparison between data and models is done using a maximum likehood estimator that takes into account the uncertainties in each data point. The resulting 1-POP templates are characterized by four parameters: The star formation time scale τ, age t (assuming exponentially declining star formation history), metallicity Z, and extinction A(V). For the 2-POP we have twice the same family of parameters to characterize both the young (instantaneous burst) and the old populations. The final set comprises 3624 models (1666 1-POP+dust, 1958 2-POP+dust). The photometric redshift estimation and uncertainty is derived from the minimization of the χ^2 probability distribution obtained from the fitting of the observed data to a grid of redshifted models (using $\delta z = 0.01$). In addition, we include AGN templates from Polletta et al. (2007) to provide a better fit of the very few AGN dominated SEDs.

Furthermore, it is possible to use the best fitting SED to estimate rest-frame fluxes, luminosities and also observed fluxes in bands that might be missing due to shallow imaging or differences in the covered area. The use of these synthetic magnitudes allows a consistent calculation of colors for all sources in the sample.

3.3. Star-galaxy separation

Stars are separated from galaxies using a combination of morphological and color criteria. Following Pérez-González et al. (2008), all secured objects (with detection in more than 3 photometric bands) are classified as stars if they satisfy at least 3 of 9 morphological and color criteria. The first one is the all-band weighted SExtractor STELLARITY parameter. When available, the STELLARITY estimations from HST images are given a higher weight in the comparison. The other criteria are based on nIR and IRAC color-color criteria and comparisons between magnitudes derived from isophotal and circular apertures extracted from Eisenhardt et al. (2004) and Rowan-Robinson et al. (2005) (see Pérez-González et al. 2005, 2008 for a detailed description). We also consider the BzK criteria by Daddi et al. (2004), to isolate the stellar locus: $(z-K)_{AB} < 0.3 \times (B-z)_{AB} - 0.5$. In Fig. 3 we compare the efficiency of the latter to the other color-morphology criteria. Sources classified as galaxies are required to satisfy fewer than three different criteria. We find that almost all the stars satisfy the BzK criteria with only a few objects below our star threshold, probably being galaxies scattered into the stellar boundary due to photometric errors as already reported by other authors (Kong et al. 2006).

We also classify as stars a very small fraction of objects whose best fit to a spectral template is the Vega SED, and that does not have a reliable spectroscopic redshift. These objects typically satisfy at least 2 of the other criteria, and after visual inspection, it is most likely that they are stars.

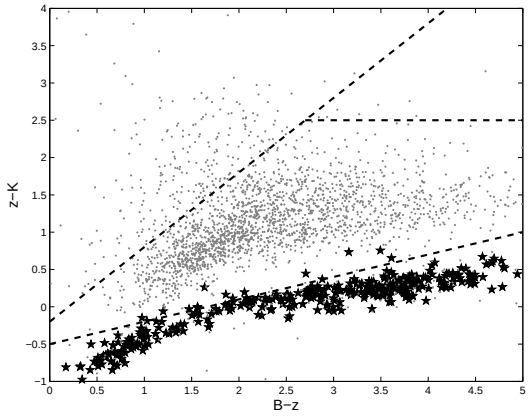

Fig. 3. Efficiency of the BzK color-color diagram to identify stars, compared to the combination of the other 9 criteria applied to isolate stars. The dashed lines depict the regions defined by the BzK criteria. The bottom line isolates the stellar locus, while the other two select sources at z>1.4. Black stars show the sources that satisfy three or more stellarity criteria.

4. Composite sample

Our final K-selected sample is comprised of 1313 sources in the 223 arcmin^2 of HFDN, 4660 sources in the 648 arcmin^2 of the Groth-FF, and 1957 sources in the 161 arcmin^2 of Groth strip. Out of these, less than 15% are identified as stars in each field. We merged both Groth samples into a single catalog with 5948 sources. To avoid repeated sources, the two samples were cross-correlated in a $1''$ radius removing duplicate sources with lower S/N.

Additionally, to complement the low depth samples, we have created a K-band selected sample in the Chandra Deep Field South (CDFS, $\alpha(J2000.0) = 03^h32^m28^s, \delta(J2000.0) = -27°48'30''$). The reference image was drawn from the latest data release of the GOODS/ISAAC observations (Retzlaff et al. in preparation). This final release adds two new frames in the K-band,

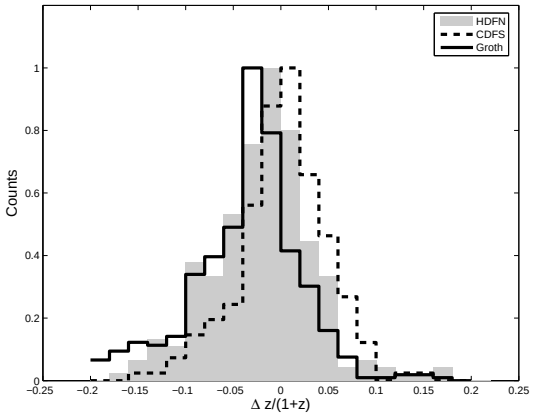

Fig. 4. Comparison of the scattering in the photometric redshift estimates $(z_{\rm spec} - z_{\rm phot})/(1 + z_{\rm phot})$ for the three fields.

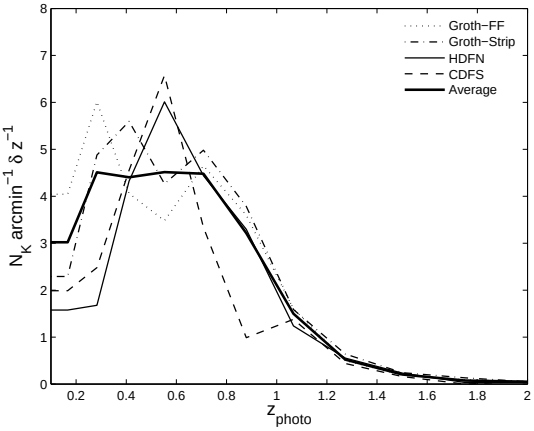

Fig. 5. Photometric redshift distributions of the K-band selected galaxies in the HDFN, CDFS and Groth fields.

increasing the total surveyed area to 172 arcmin^2. The combined mosaic covers the region with a variety of exposure times, with an average depth of $K \sim 22.7$ and a maximum of $K \sim 24.2$. Consequently, we can safely consider the whole sample to be complete below $K = 20$ (see also the area-depth estimations from Grazian et al. 2006 for the v1.5 data). The CDFS has also been the target of extensive multi-wavelength observations. We make use of all the public and proprietary data compiled in Pérez-González et al. (2005) to create the multicolor sample, following the procedures described in section §3. After excluding a small portion of the mosaic with very low S/N regions, the sample contains 6810 galaxies in an area of 168 arcmin^2.

5. Photometric redshift distribution

We have checked the quality of our photometric redshifts with all the available spectroscopic data compiled for the three fields (Fig. 4). For HDFN there are 287 sources (36% of the sample) with highly reliable spectroscopy. The average redshift difference ($\delta z = z_{\rm spec} - z_{\rm photo}$) is 0.001, 70% of the sample present values of $\sigma_z/(1 + z) < 0.05$ (where σ_z is the absolute value of δz), and 91% have $\sigma_z/(1 + z) < 0.1$. In the CDFS 232 sources (53% of the sample) have spectroscopic redshift with a high quality flag. The mean value of δz is 0.014. 72% of the sample present values of $\sigma_z/(1+z) < 0.05$ and 91% have $\sigma_z/(1+z) < 0.1$. In the Groth-FF we find 846 sources with high quality flag (35%). The average $\delta z = 0.036$. 59% of the sample present values of $\sigma_z/(1+z) < 0.05$ and 85% have $\sigma_z/(1+z) < 0.1$. Finally, there are 334 spectroscopically measured sources in the Groth strip with an average $\delta z = 0.010$. The 68% and 89% have values of $\sigma_z/(1 + z)$ below 0.05 and 0.10 respectively.

Figure 5 shows the photometric redshift distribution for the samples in Groth, HDFN and CDFS to a limiting magnitude of $K = 18.5$. The distributions have been derived taking into account the typical photometric redshift error. Although the shape of the distributions are typical for a flux limited sample, field-to-field differences reveal the effects of large scale structure. The peak of the redshift distribution depends on the luminosity function of the galaxies at different redshifts. At $K < 18.5$ the majority of the sources are found at $z < 0.7$ (see next section), leading to an exponentially decreasing tail at higher redshifts. The prominent density peak in HDFN at $z \sim 0.5$ is in good agreement with the redshift distribution found by the Team Keck spectroscopic survey (Wirth et al. 2004). The less pronounced feature in CDFS at approximately the same redshift also coincides with a spectroscopically confirmed overdensity at $z = 0.7$ (Vanzella et al. 2006), if we take into account the broadening caused by the photometric redshift uncertainties and the decreasing selection function at high redshift. Finally, there appears to be a slight underdensity at $z \sim 0.4$ and a small peak at $z \sim 0.2$ in the Groth field. This alternation of peaks and voids between fields highlights the impact of field-to-field variance in the small area surveys, especially at $z \leq 1$.

6. K-band number counts

Figure 6 shows the K-band NCs for the three fields, as well as the NCs from CH03, for comparison. The NCs in 0.5 magnitude bins, up to K=18.5 for Groth and HDFN, and up to K=20.0 for CDFS are summarized in Table 4. Within these limits, detection efficiencies for point sources are well above 90% (see Fig. 2, and completeness estimates in §2.3 and §4). Hence, we do not apply completeness corrections to the NCs. Our counts do not need corrections for spurious sources either; spurious sources typically appear at brightness levels where the efficiency drops significantly below 100% (CH03;Eliche-Moral et al. 2006), and the fraction of spurious sources in our catalogs must be negligible given that each source is required to be detected in at least three bands (§3.1). NCs are tabulated in Table 4. The error calculation assumes Poisson statistics for low numbers (Gehrels 1986) added in quadrature to the standard deviation derived from bootstrapping the source magnitudes convolved with a Gaussian error kernel.

In the Groth field, our counts are in good agreement with those of CH03. Differences are 1σ compatible in the range $16.0 < K < 18.5$. The overall agreement provides an external check on the quality of both sets of K-band number counts in the Groth field. As we move to brighter magnitudes, our counts are systematically above those of CH03

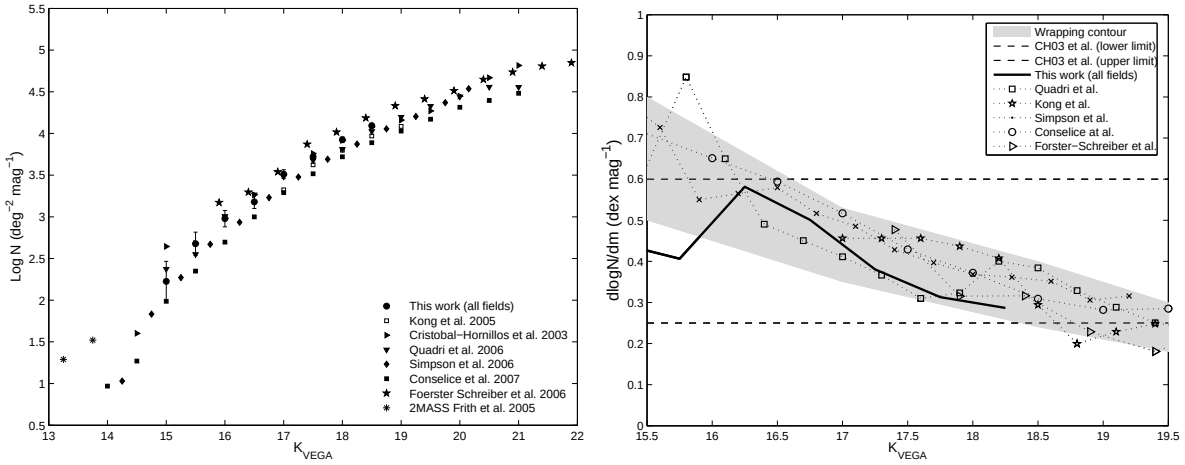

Fig. 7. *Left*: Averaged K-band number counts from Groth, HDFN and CDFS compared with a compilation of results taken from various sources. *Right*: Slope for the differential number counts in our three fields, along with data from the literature. The horizontal dashed lines indicates the value of the slope at both sides of $K = 17.5$ reported in CH03.

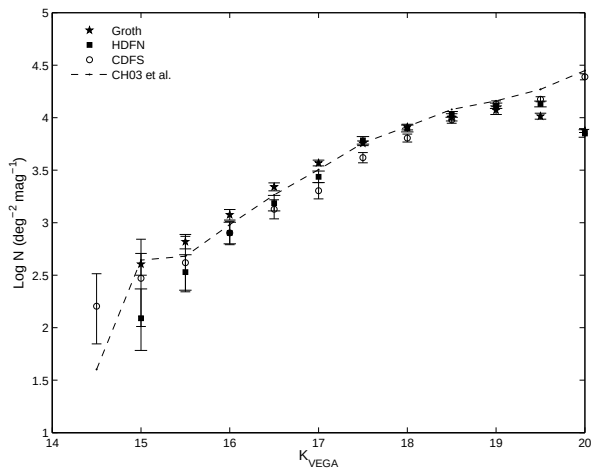

Fig. 6. The raw number counts in our three fields (HDFN, CDFS, Groth) and counts from CH03 obtained in an small portion of our total area in the Groth field. Error bars are derived from a combination of Poisson errors and bootstrapping. No completeness corrections have been made.

	Groth	HDFN	CDFS
K Bin Center	log(N)	log(N)	log(N)
16.00	$3.07^{0.05}_{0.05}$	$2.90^{0.10}_{0.10}$	$2.90^{0.11}_{0.11}$
16.50	$3.34^{0.04}_{0.04}$	$3.18^{0.07}_{0.07}$	$3.13^{0.10}_{0.09}$
17.00	$3.56^{0.03}_{0.03}$	$3.44^{0.06}_{0.05}$	$3.30^{0.08}_{0.08}$
17.50	$3.75^{0.02}_{0.02}$	$3.78^{0.04}_{0.04}$	$3.62^{0.05}_{0.05}$
18.00	$3.91^{0.03}_{0.03}$	$3.89^{0.03}_{0.03}$	$3.81^{0.04}_{0.04}$
18.50	$4.00^{0.03}_{0.03}$	$4.03^{0.03}_{0.03}$	$3.97^{0.03}_{0.03}$
19.00	-	-	$4.13^{0.03}_{0.03}$
19.50	-	-	$4.18^{0.02}_{0.02}$
20.00	-	-	$4.38^{0.03}_{0.03}$

Table 4. Differential number counts in 0.5 magnitude bins for the K-selected samples in HDFN, CDFS and the Groth field, uncorrected for completeness. Only the NCs up to the completeness limit of each field are shown.

and HDFN. Such an offset is likely due to the smaller area mapped in these two surveys (∼5 times smaller in the case of CH03). Nevertheless, NCs below $K < 16$ probe very low redshift populations (see next section) that would require larger areas to be studied accurately.

The NCs in the Groth and HDFN fields at $K > 18.5$ are shown in Fig. 6 for comparison to the deeper CDFS counts and the completeness corrected counts of CH03. The fact that the shallower NCs do not fall abruptly until K ∼19 supports our efficiency estimates for the Groth and HDFN images. In addition, it is noteworthy that the scatter in the brighter counts ($K < 17$) is on average greater than the typical uncertainties for the NCs in any of the fields. The most plausible cause of this discrepancy is cosmic variance. As we showed in the previous section (Fig. 5), there might be significant overdensities at some redshifts that lead to these differences. Additionally, the effect is accentuated by the fact that bright counts come mainly from low redshift sources, which are poorly sampled in small area surveys, like HDFN and CDFS. We will further discuss field-to-field variance effects in the next section.

The left panel of Fig. 7 shows the averaged NCs of the 3 fields along with counts from the literature. We have compiled measurements from large area surveys to mitigate the effects of cosmic variance on the shape of the NCs. That is the case of the 1.47 deg^2 of the DEEP2/Palomar survey (Conselice et al. 2008), the 0.70 deg^2 of the UKIDDS-UDS (Simpson et al. 2006), the 0.17 deg^2 of the Daddi-F (Kong et al. 2006) and the combined ∼0.11 deg^2 of the MUSYC survey (Quadri et al. 2007). Additionally, we compared our results with the deeper NCs of Förster Schreiber et al. (2006) in the MS1054-03 galaxy cluster to illustrate the asymptotic behavior of faint counts and also the impact on the NCs of a very prominent overdensity such as a cluster at z=0.83. It can be seen in Fig. 7 that the density peak dominates the bright counts. This is comparable, to a lesser extent, to the effect at $K < 17$ of the low redshift peak in CDFS.

The logarithmic derivative of the differential NCs (i.e., the slope of the NCs) is shown in the right panel of Fig. 7. The horizontal lines at 0.25 and 0.6 indicate the value of the slope on both sides of $K = 17.5$ reported in CH03. The thick black line shows the evolution of the slope for the combined NCs of our three fields. We confirm that the logarithmic slope decreases rather sharply from 0.6 at $K = 16.25$ to $\sim$0.3 at K =18.0, a similar result to CH03. However, it appears that the evolution of the slope is best described by a continous decreasing trend, rather than by fixed values on both sides of $K \sim 17.5$; i.e., the slope of K-band NCs decreases monotonically over the $16.0 < K < 19.0$ range. The logarithmic slopes derived from counts by other authors are bound by the same upper and lower limits as in our data, except at $K < 16.0$. However, they show a more gentle variation with magnitude, as well as a greater dispersion. Such variations among different surveys may be driven by two processes. First, completeness and reliability of the photometry are treated with varying degrees of rigor by different authors, which contributes to the scatter in the NCs (see CH03). Second is cosmic variance. Substructure in the redshift distribution can cause significant fluctuations in the characteristic density, and hence slope variations, that might lead either to a sharp break or to a smoother evolution in the slope of NCs. These density peaks are clearly recognizable in the right panel of Fig. 7 at $K = 16.5$ and $K \sim 18$ when comparing the NCs of HDFN and CDFS. To strengthen this idea we have created 100 Millennium simulation mock catalogs from Kitzbichler & White (2007) selected over a 0.25 deg^2 area, similar to that of our Groth field, to sample the extent of field-to-field variance effects. Although the K-band NCs from Kitzbichler & White (2007) do not accurately reproduce the observed distribution at $K > 17$ (mainly because the $z > 1$ galaxy population is overestimated compared to the observations), their results on clustering analysis are consistent with observations. Thus, the simulation is suitable to mimic the effects of cosmic variance. As can be seen in Fig. 8, the broadening effect in the slope of the bright counts is similar to ours, whereas the confidence interval for the faint counts is significantly narrower, probably because at that point our NCs are dominated by photometric errors and depth effects, and not by large scale structure (LSS).

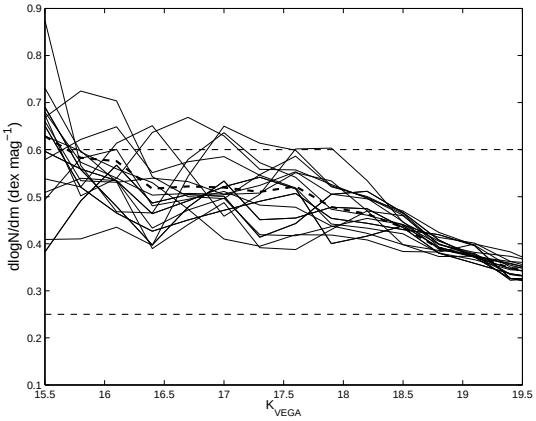

Fig. 8. Slope for the differential number counts in the 100 samples of the Millennium simulation drawn from the mock catalogs of Kitzbichler & White (2007). The thick dashed line shows the averaged NCs combining all the samples.

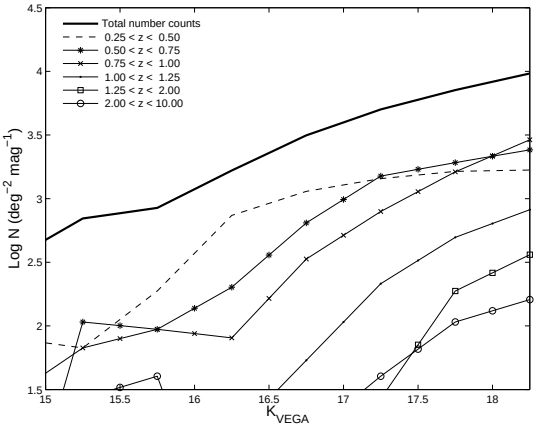

Fig. 9. NCs in the K-band for the CDFS field alone (thick black line) and NCs in several photo-redshift ranges. At bright magnitudes ($K\sim$17) the contribution to the NCs is limited to only a few low redshift bins, whereas at $K\sim$18 the total number counts becomes a mixture of several low and high redshift bins ($z > 1.5$)

7. Redshift distribution of K-band number counts

The change in the slope of NCs is an indirect effect of galactic evolution. Indeed, any feature in the shape of NCs is closely related to the luminosity distribution of galaxies at a given epoch. By disentangling the relative contribution to the NCs of the LFs at different redshift ranges, we will be able to identify the main effect responsible for shape of the NCs.

Fig. 9 depicts the K-band NCs in the CDFS, the deepest sample. We have used the photometric redshift estimation to split the total number counts into redshifts bins. The binned NCs tend to resemble the shape of a (Schechter) LF. The evolution of the comoving distance with redshift causes an effective shift in the successive redshift bins towards fainter magnitudes, and the posterior accumulation of the higher redshift NCs. In addition, despite the likely greater effects of cosmic variance on a single field, it seems clear that for $K > 18$ the total number counts tend to become a mixture of very different redshifts ranges, with a growing contribution of high redshift galaxies ($z > 1.5$) absent at brighter magnitudes, where 2-3 low redshift bins account for 90% of the total NCs (Conselice et al. 2008). Furthermore, it can be seen that for $K < 16$ the counts sample the bright part of the LFs at $z < 1$, causing values to be highly sensitive to both volume effects and LSS.

The four panels of Fig. 10 show the relative contribution to NCs in HDFN, CDFS and the Groth field divided in four redshift bins: [0.25-0.50],[0.50-0.75],[0.75-1] and [1-1.25]. Below $z < 0.25$ the averaged contribution is small enough ($< 10\%$) to be neglected. The next three bins are responsible for most of the total counts up to $K \sim 18$. However, the exact proportion might differ by up to a factor of 2 due to LSS. The alternate peaks and valleys between HDFN/CDFS and the Groth fields between $z = 0.4 - 0.9$ (see Fig. 5) cause the most prominent differences around

$K = 17.0 - 17.5$ in the first panel of Fig. 10, similarly to the underdensity in CDFS at $z \sim 0.8$ which leads to the significantly lower NCs around $K \sim 17.5 - 18$ in the third panel.

8. Number counts & luminosity functions

In the previous section, we showed evidence for a mild decreasing trend in the slope of the NCs. In this section, we will try to find the origin of such a decreasing trend by studying the LF at several redshift intervals (benefiting from the estimation of photometric redshifts for the entire sample). The calculation of LFs must take into account that the observed K-band probes progressively bluer rest-frame bands with increasing redshift. By $z \sim 0.75$, the K-band central wavelength shifts to $1.25\mu m$(J-band), and for $z > 1.5$ it begins to probe the optical bands. Therefore, in order to derive NCs from LFs it is necessary to select different rest-frame bands at each redshift bin.

In §8.1, we present the functional relation between the NCs and LFs, parametrized using a Schechter (1976) function, that we will use to derive the K-band NCs. In §8.2, we derive LFs from the observed K-band, in the redshift range [0.25-1.25], using our three galaxies samples. In §8.3 we combine our LFs with LFs from the literature to explore the general picture of luminosity evolution in the optical and NIR. Finally, in §8.4, we summarize the multi-wavelength LFs probed by the observed K-band at different redshifts, that gives rise to the K-band NCs distribution.

8.1. Number counts from Schechter functions

The distribution of observed galaxy counts is a consequence of the LFs and the cosmological framework. Hence, any feature in the NC distribution could be explained in terms of the evolution of the LFs assuming a cosmological context. Here we will adopt a ΛCDM framework, and assume that the galaxy LF can be described by means of a Schechter function,

$$\phi(M) = 0.4\ln(10)\phi^* 10^{0.4(M^*-M)(\alpha+1)} \exp\left(10^{0.4(M^*-M)}\right) \quad (2)$$

where M^* is the characteristic absolute magnitude, α the faint-end slope, and ϕ^* the normalization of the luminosity function. Although a Schechter function might not be appropriate to fully describe the faint end population of the LF (Blanton et al. 2005), this is not the case for the bright NCs, which will be mostly dominated by M^* galaxies (see next section). The NCs represent the distribution of galaxies per apparent magnitude and sky area. Assuming a parametrization for the LF, the functional form of the NCs becomes

$$\mathbf{N}(m_{\lambda_0}, [M,\phi,\alpha]_{\frac{\lambda_0}{(1+z)}}) = \int_{z_i}^{z_f} \phi(m, z, [M,\phi,\alpha]_{\frac{\lambda_0}{(1+z)}}) \frac{dV_c}{d\Omega} dz \quad (3)$$

where z_i and z_f are the lower and upper limit of the redshift bin, $dV_c/d\Omega$ is the differential comoving volume, and $m[M,\phi,\alpha]_{\frac{\lambda_0}{(1+z)}}$ represents the Schechter parameters of a LF in a band with effective wavelength $\frac{\lambda_0}{(1+z)}$. This indicates the explicit dependence of the NCs in the K-band on bluer LFs with increasing redshifts. Note that even if we assume that the Schechter parameters are constant in the redshift bin $(z_i, z_f]$, the expression 3 still depends on LFs at different wavelengths. When Δz is small, we can approximate the NCs from single LFs in a photometric band at $\frac{\lambda_0}{(1+\bar{z})}$, where $\bar{z}$ is the mean value of the redshift bin $(z_i, z_f]$.

Additionally, Eq. 3 can be interpreted as a sum of LFs at different redshift bins, weighted by the corresponding comoving volumes. Hence, the shape of the NCs would be the result of the LF parameters at a given epoch and their evolution with redshifts modulated by the volume element. Furthermore, the slope of the total NCs is the sum of the slope from each redshift bin weighted by the normalized NCs.

$$\ln\left(\frac{dN}{dmd\Omega}\right) = \frac{1}{N}\frac{dN}{dm} = \sum_{i=0}^{\infty} \frac{\mathbf{N_i}}{N}\left(\frac{1}{\mathbf{N_i}}\frac{d\mathbf{N_i}}{dm}\right) \quad (4)$$

where $\mathbf{N_i}$ are the NCs in the redshift bin i, and N is the sum of all the redshift bins. The slope of the NCs presents some interesting properties. First, it is independent of the absolute value of ϕ^*, but it does depend on the relative change of this parameter (i.e., it depends only on the evolution of ϕ^*), which can be normalized arbitrarily. Second, in addition to the low redshift Euclidean limit ($d\log N/dm$ =0.6), it can be shown that, at very faint magnitudes, the slope approximates asymptotically to $-0.4(\alpha+1)$.

$$\ln\left(\frac{dN}{dmd\Omega}\right)\Big|_{m\gg} = 0.4\left(\frac{I(\alpha, M(m))}{\hat{I}(\alpha, M(m))} 10^{-0.4m} - (\alpha+1)\right) \quad (5)$$

where $I(\alpha, M(m))$ accounts for all other terms except $10^{-0.4m}$, including the integral over redshift and the exponential term in the Schechter equation, and $M(m)$ indicates the relation between absolute and apparent magnitudes through the luminosity distance. The $I(\alpha, M(m))$ in the numerator differs from the denominator only in the derivative of the exponential term, which also outputs the $10^{-0.4m}$ term, indicated explicitly. At faint magnitudes the first term of the Eq. 5 tends to zero, dominated by the faster decrement of $10^{-0.4m}$, yielding the asymptotic limit $-0.4(\alpha+1)$. More intuitively, it can be understood as a regime where the NCs are mostly dominated by the faint end of a single LF. Hence, the slope of the NCs necessarily becomes the slope of this LF. For any given variation with redshift of the Schechter parameters, there will always be a maximum value of the product $\phi^* \frac{dV_c}{d\Omega}$. The LF at that redshift will be favored among the others (suppressed smaller values of the product) and, at sufficiently faint magnitudes, it will be the main contributor to the NCs.

A very interesting result that emerges from the analysis of the NCs in the full magnitude range is that the evolution of the slope can be summarized in three main regimes, namely:

- (1) *The Euclidean regime.* The classical low redshift approximation, that yields the well-known result $d\log N/dm = 0.6$. The NCs in this regime are mostly populated by M$\leq M^*$ at very low redshift (z< 0.2).
- (2) *The transition regime.* The slope departs from the Euclidean limit into a weighted sum of the slopes of LFs at low-mid redshifts. The dominant contribution would come from the LF at the redshift that maximizes the product $\phi^* \frac{dV_c}{d\Omega}$ (the factors controlling the normalization of Eq. 3). In this regime, the slope decreases rapidly

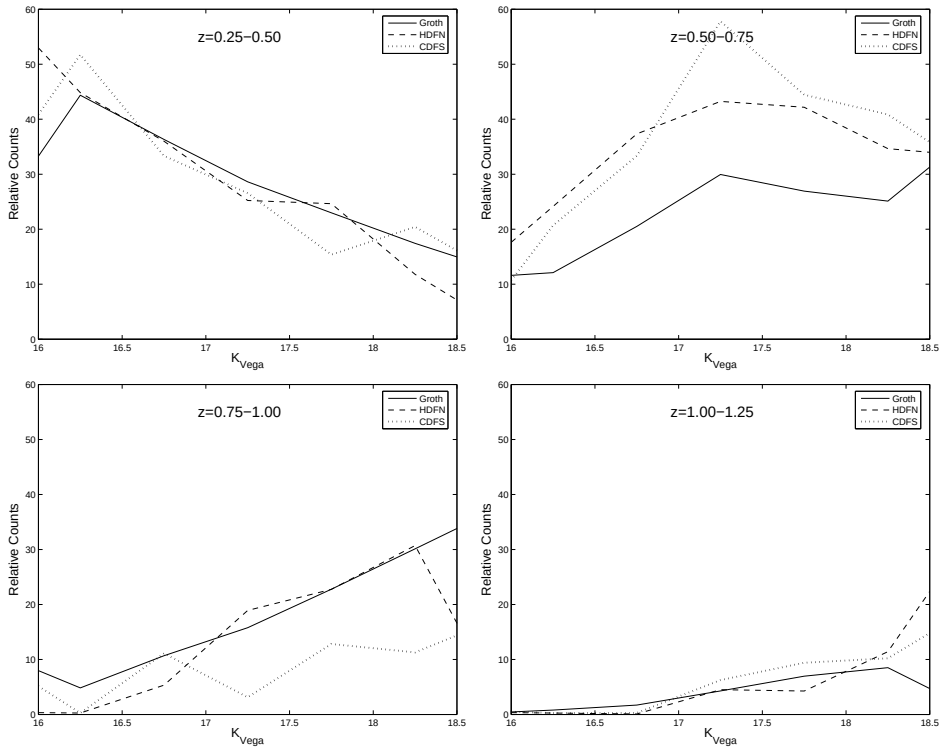

Fig. 10. Relative contribution to the K-band number counts in redshift bins for the samples in the HFDN, CDFS and Groth field. Field-to-field differences can reach the 40% for the most prominent LSS features.

around the apparent magnitude of M^* at the dominant LF (i.e. at the knee of the LF). In the absence of a significant evolution in ϕ^*, the maximum would take place at the peak of the volume element at z∼2 (Bershady 2003).

– (3) *The "α regime"*. In this regime, the majority of the LFs dominating the NCs contribute with galaxies at the faint end. Therefore, the slope will be a combination of individual slopes approaching the minimum value (∼-0.4(α+1)). As a consequence of the previous regime, this phase should be controlled by the same LF as in the previous phase. However, other LFs, not strongly suppressed by the $\phi^* \frac{dV_c}{d\Omega}$ factor, and having a significantly larger α, might dominate this phase.

We will further discuss the evolution of the slope in terms of this schema in §9.1.

8.2. LFs from the observed K-band

In order to derive NCs in the K-band using Eq. 3 we need to feed the equation with LFs in different bands at different redshifts. More precisely, we are interested in the LFs from the observed K-band. Thus, we have obtained LFs in several redshift bins at decreasing rest-frame wavelengths centered at $2.16\mu m/(1+\bar{z})$, where $\bar{z}$ is the mean redshift of the bin $(z_i, z_f]$.

8.2.1. Methodology

To estimate the observed LF we have applied the $1/V_{\rm max}$ method (Schmidt 1968). We associate the Poisson errors to each magnitude bin (Gehrels 1986) added in quadrature to photometric errors. Since we have not applied k-corrections, Δm translates directly into ΔM. Additionally, in order to quantify the uncertainties due to the photometric redshift errors, we have performed Monte Carlo simulations at each redshift bin, assuming an uncertainty characterized by the width of a Gaussian distribution derived fitting the histogram of $\sigma_z/(1+z)$ for each redshift bin.

Additionally, we measured the LF from the STY (Sandage et al. 1979) estimator, which is a parametric maximum likelihood method. The STY is not as sensitive to large-scale fluctuations as the $1/V_{\rm max}$ method, but requires a priori fixing the functional form of the LF. Nevertheless, the assumption that $\phi(M)$ is well described by a Schechter function suits our purpose of explaining the NCs in terms of LFs, as we have described in the previous section.

To check the effect of photometric redshift errors in the STY method, we perform the same Monte Carlo simulations as for the $1/V_{\rm max}$. Since the probability of galaxies existing at redshift z grows rapidly until $z \sim 2.5$, a larger fraction of intrinsically faint sources are shifted to the bright end than viceversa. This can potentially bias the determination of the LF introducing large systematic effects when Δz is large and the distance modulus grows rapidly (Chen et al. 2003; Marchesini et al. 2007). Nevertheless, the combination of the typical values of $\sigma_z \sim 0.05 - 0.07$ with the relatively shallow limiting magnitude of our LFs

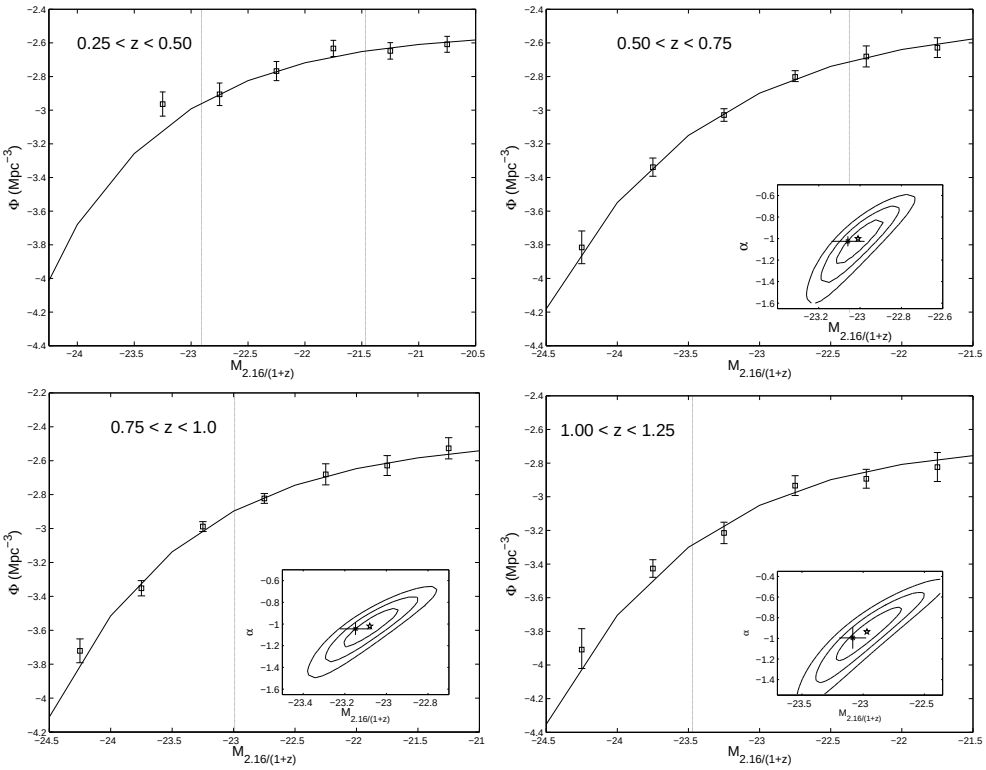

Fig. 11. LFs derived from the observed K-band in different redshift slices. The LF with the $V_{\rm max}$ method are shown as open squares with error bars (including Poisson, photometric and photometric redshift uncertainties).The continuous line depicts the best fit from the STY method. The inset shows the best fitting (M,α) values (star) with 1,2 and 3σ confidence contours, and also the mean value (cross) with error bars derived from the photometric redshift simulations. The vertical line shows the photometric threshold for the shallowest fields, $K_{\rm Vega} = 18.5$. The additional vertical line in the first panel shows the lower threshold at bright magnitudes.

(less than ~ 1 mag deeper than M^*) cause only a moderate offset in the Schechter parameters ($\Delta M < 0.2$,$\Delta\alpha < 0.1$). It can be seen from the inset of Fig. 11 that the mean and standard deviation resulting from the simulations (star) lie always within the 1σ-2σ confidence level derived from the best fitting result of the STY method.

8.2.2. Observed luminosity functions

The LFs, $\phi(M)dM$, of the combined samples were computed in four redshift bins of width $\Delta z = 0.5$ using the methods described above.

redshift bin	$M^*_{K,obs}$(AB)	$\alpha_{K,obs}$	$\phi^*_{K,obs}(10^{-3}{\rm Mpc}^{-3})$
0.25 - 0.50	-22.95(fixed)	$-1.15^{0.20}_{0.20}$	$3.4^{2.10}_{1.70}$
0.50 - 0.75	$-23.01^{0.13}_{0.12}$	$-1.00^{0.18}_{0.23}$	$3.4^{0.22}_{0.18}$
0.75 - 1.00	$-23.08^{0.14}_{0.12}$	$-1.02^{0.19}_{0.17}$	$3.2^{0.17}_{0.24}$
1.00 - 1.25	$-22.96^{0.28}_{0.26}$	$-0.93^{0.23}_{0.29}$	$2.3^{0.31}_{0.26}$

Table 5. Best fitting Schechter parameters for the STY LFs from our combined samples. The 1σ errors were derived from Monte Carlo simulations

Table 5 summarizes the best fitting values of the Schechter function for each redshift. Fig. 11 shows the estimates from the $V_{\rm max}$ method (open squares) with 1σ error bars (from Poisson statistics and photometric redshift simulations), and the LF from the maximum likelihood method at different redshifts. The inset shows the 1, 2 and 3σ confidence levels for the α and M^* parameters (open star), together with the mean value derived from the photometric redshift simulations (cross). The vertical line indicates the photometric threshold of the shallowest sample (K=18.5). For fainter luminosities, the values of the LFs are derived exclusively from the CDFS sample. Note that the completeness limit of our samples translates into luminosities very close to or even fainter than M^* for the higher redshift bins. This means that galaxies fainter than M^* will not contribute significantly to the NCs up to $K < 18.5$. Nevertheless, the deeper coverage of the CDFS allow us to properly fit the LFs that will be employed to derive the NC function (see section §8.4).

In order to properly account for cosmic variance, the values of ϕ_i for the $V_{\rm max}$ method derived exclusively from the CDFS data (those above the photometric threshold; vertical line of Fig. 11) have been corrected by a scale factor. This scale factor has been derived from the median value of all fields in the magnitude bins in common, weighted by the area covered by each field. Also, only the magnitude bins with more than 100 galaxies in the CDFS sample have been considered in the calculation.

Finally, for the $0.25 < z < 0.50$ bin, the bright extremity of the LF is poorly constrained even in the total combined area of the three fields. Nevertheless, since the faint end is properly sampled, we decided to fit the LF fixing the value of M^* and setting a threshold on the bright ($K < 16$) magnitudes. The value of M^* was taken from the literature. At $z \sim 0.38$ the rest-frame wavelength probed by the K-band is close to the H-band. However, no references for H-band LFs at that redshift were available then, and we decided to use M^* from the rest-frame K-band LF at $z \sim 0.4$ published by Arnouts et al. (2007).Then, we corrected that value by applying an H-K color term. The mean value of that color at $z \sim 0.4$ derived from our data is $\langle H - K)(AB) = -0.21 \pm 0.11$, very similar to the local value (∼-0.20; Jarrett et al. 2003).

8.3. LFs evolution in rest-frame bands

Analyzing the evolution of the LFs directly derived from the observed K-band requires exploring LFs in shorter rest-frame wavelengths at different redshifts. For this purpose we compiled LF estimates from the literature in optical and NIR bands. We have compiled the local LFs in the J and K-bands from Cole et al. (2001) and Kochanek et al. (2001) respectively, whereas for the H-band we estimated a value of M^* by applying a color correction to the K-band value, following the same procedure as in the previous section. The local optical LFs in the i,z and R bands were drawn from Blanton et al. (2003).

At higher redshift, the K-band LFs were drawn from Arnouts et al. (2007). Their LFs for the SWIRE-VVDS-CFHTLS survey predicts an evolution in the Schechter parameters which is consistent with previous results from Cirasuolo et al. (2007) in the UKIDDS-UDS. For the J-band we considered the LF estimates from Pozzetti et al. (2003) (K20 survey, 52 arcmin^2), Feulner et al. (2003) (MUNICS survey, 0.17 deg^2), and Dahlen et al. (2005) (GOODS-CDFS, 130 arcmin^2). Their results are compared in Figure 15 of the latter, showing that, despite the apparent inconsistency in the Schechter parameters, there is good agreement in the data points. The different observational constraints of each survey lead to different best fitting values for a distribution with a very similar shape. We have taken the LF in the J-band at $z \sim 0.48$ from Feulner et al. (2003) and from Dahlen et al. (2005) at $z \sim 0.9$. The larger area of the first is better to constraint the bright end at low redshift, while the depth of the latter is more suitable at higher redshifts.

We find the same apparent inconsistencies due to the $\alpha - M^*$ degeneracy in the LFs of optical bands. Ilbert et al. (2005) (VVDS, 0.6 deg^2) and Gabasch et al. (2006) (FORS Deep Field Survey, FDF, 35 armin^2) derived very different values of the Schechter parameters that nevertheless produce $1 - 2\sigma$ compatible LFs when comparing both estimates under a common limiting magnitude and using Monte Carlo simulations (Gabasch et al. 2006). For our purposes we are more interested in the high-redshift optical LFs ($z > 1.5$). Thus, we preferred the estimates from Gabasch et al. (2006) that, despite the smaller area, are able to probe the LF 3-4 magnitudes deeper. In addition to the LFs at $z = 1.60$ and $z = 2.26$, we derived some values for M^* and ϕ^* at other redshifts using the evolutionary parametrization also given in Gabasch et al. (2006; as $(1 + z)^\gamma$). Finally, the LF in the R-band at $z \sim 2.3$ was drawn from Marchesini et al. (2007). The authors derive high redshift LFs in optical bands from a combination of very deep nIR infrared observations (including 51arcmin^2 to $K \sim 23$). Table 6 summarizes the Schechter parameters of the LFs in the different bands and redshifts.

The two panels of Fig. 12 show the evolution with redshift of M^* and ϕ^* in several NIR and optical bands. Vertical dotted lines indicate the effective rest-frame wavelength of each band. The open circles show the values of M^* and ϕ^* in each band at different redshifts increasing from top to bottom. For clarity, the local values have been plotted with small black dots. The dashed lines connect the values of the Schechter parameters for the different bands at the same redshift (continuous grey line at z=0). Finally, the large black dots show our estimates of the LFs at $z \sim 0.4, 0.6, 0.9, 1.1$. These estimates do not match exactly any standard photometric band. However, the value at $z \sim 0.4$ is almost centered in the H-band, and the LFs at $z \sim 0.6$ and $z \sim 0.9$ should be consistent with the estimates in the J-band. Comparing our values with the results for these bands of Dahlen et al. and Feulner et al., we find a very a good agreement in the characteristic luminosity, whereas the values of ϕ^* are poorly consistent. A possible explanation for this discrepancy is that the values of Dahlen et al. at $z \sim 0.9$ might be affected by an underdensity peak between $z = 0.7 - 1.1$, while our results present a slight overdensity around that redshift (see Fig. 5). Nevertheless, the comparison to the values of Feulner et al. is 2σ compatible, and is also consistent with the results of Pozzetti et al. (2003). Wider areas are necessary to reduce the field-to-field variations and obtain more reliable estimates.

It can be seen from the left panel of Fig. 12 that the multi-band values of M^* at $z = 0$ resemble the shape of a galactic SED, with the absolute magnitude peaking around the H band, close to the $1.6\mu m$ stellar bump. At higher redshifts, the shape is not preserved due to the different luminosity evolution in each band; i.e., in the K-band, a substantial brightening of ~ 1 mag between the local universe and $z \sim 2$ has been reported by several authors (Caputi et al. 2006; Cirasuolo et al. 2007; Saracco et al. 2006). In the J-band, Saracco et al. find $\Delta M^* \sim -0.7$ to $z \sim 3$, and the results from Marchesini et al. (2007) indicate a similar or slightly higher brightening ($\Delta M^* \sim 1.7$) in the optical LFs up to the same epoch. However, it is not surprising that the brightening is faster in the optical bands than in the NIR since they are more affected by the light coming from younger stellar populations (Dahlen et al. 2005; Ilbert et al. 2005; Wolf et al. 2003).

In the right panel of Fig. 12 we can see that the characteristic density, ϕ^*, follows a decreasing trend in every band. The average estimates for optical LFs indicate a decrease of $\sim 50\%$ in the number density from the local value to $z \sim 1$ (Gabasch et al. 2006, Ilbert et al. 2005), whereas the evolution in the NIR LFs seems to be slightly weaker ($\sim 30\%$). Also, the results in the K-band from Arnouts et al. (2007) and Cirasuolo et al. (2007) suggest a mild decreasing trend from $z = 0.4 - 1.25$. Finally, the LFs of Marchesini et al. (2007) in optical bands confirm the decreasing trend at high redshift finding a decrement of the $\sim 70 - 80\%$ in ϕ^* from the local value to z$\sim$ 3.

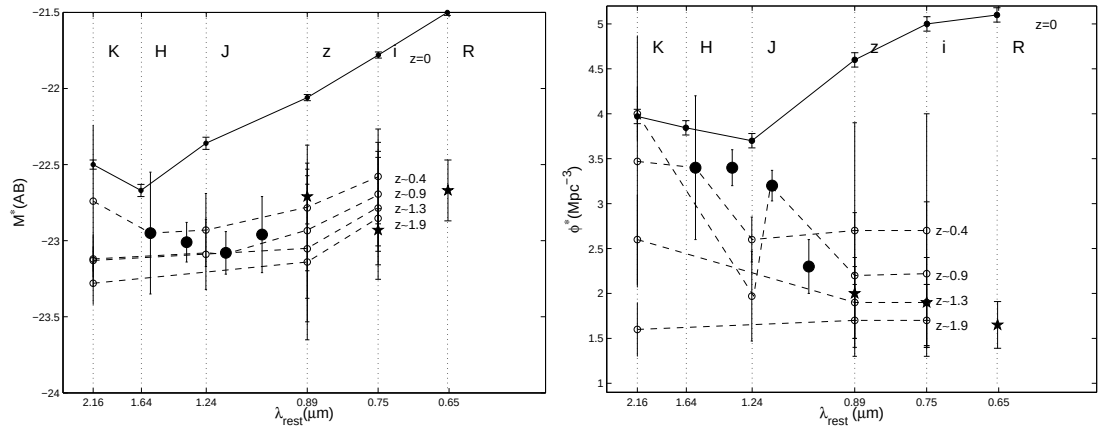

Fig. 12. Evolution with redshift of the Schechter parameters M^*(left panel), ϕ^*(right panel) in the $RizJK$ rest-frame bands. For each photometric band (RizJK, vertical dotted lines) the empty circles depict the redshift evolution of the parameter at $z \sim 0.4$, 0.9, 1.3 and 1.9, drawn from different authors (see Table 5). The long dashed lines connect the values of the parameter at the same redshift in different bands. The black stars shows the value of the parameter at $z = 1.70$, $z = 2.26$ and $z = 2.25$ in the i, z and R bands respectively. The black dots indicate the LF parameters at $\bar{z} = 0.38, 0.62, 0.88, 1.12$ derived in this work.

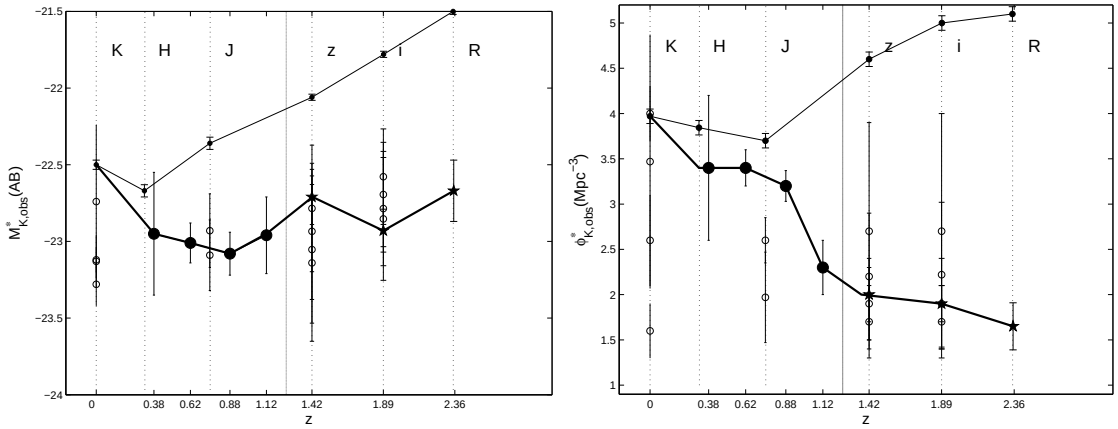

Fig. 13. Multi-wavelength evolution of the Schechter parameters $M^*_{K,obs}$ (left panel), $\phi^*_{K,obs}$ (right panel) as probed by the observed K-band. For each photometric band (RizJK, vertical dotted lines) the empty circles depict the redshift evolution of the parameter at $z \sim 0.4$, 0.9, 1.3 and 1.9, drawn from different authors (see Table 5). The black stars show the value of the parameter at $z = 1.70$, $z = 2.26$ and $z = 2.25$ in the i, z and R bands respectively. The grey vertical line at $z = 1.25$ is the estimated redshift from which the contribution of the sources to the NCs up to $K = 18.5$ is less than 10%. The black dots indicate the LF parameters at $\bar{z} = 0.38, 0.62, 0.88, 1.12$ derived in this work. The thick black line shows the approximated evolution of the Schechter parameters as probed by the observed K-band at growing redshifts.

8.4. LF evolution from the observed K-band

The two panels of Fig. 13 shows the multi-wavelength evolution of the Schechter parameters as probed by the observed K-band (thick black line); i.e, LFs at progressively shorter rest-frame wavelengths for growing redshifts. This is essentially the same plot as in Fig. 12 except that now the x-axis indicates the redshift where the K-band probes the different rest-frame bands. The vertical grey line centered at $z = 1.25$ indicates the approximate redshift limit where the contribution to the K-band NCs ($K < 19$) becomes smaller than 10%. Althought this means that the impact of the optical LFs on the bright counts is negligible, they illustrate the process of construction of NCs from LFs, allowing us to estimate the NCs to fainter magnitudes.

Note that in the optical bands, we have no references for the LFs at the precise redshift. Therefore, together with the estimated value of the z-band LF at $\bar{z} = 1.42$ (open circle), derived from the Gabash et al. parametrization (see previous section), we show the measured value at $\bar{z} = 1.7$ (black star), which presents an M^* significantly fainter than their estimates at lower redshift. The same applies for the LF in the i-band at $\bar{z} = 2.26$ (instead of $\bar{z} = 1.89$) and the R-band at $\bar{z} = 2.25$ (instead of $\bar{z} = 2.36$).

Source	Limit [mag]	Area [$\mathbf{deg}^2$]	Band	z	$M^* - 5\log h_{70}$ [AB]	ϕ^* $[10^{-3}h_{70}^3 Mpc^{-3}]$	α
Kochanek et al. (2001)	K< 11.25	< 7000	K	0.02	-22.36 ± 0.05	3.97 ± 0.34	-1.09 ± 0.06
Arnouts et al. (2007)	F(3.6μm) > 9μJy	0.85	K	0.50	-22.83 ± 0.30	3.47 ± 1.4	-1.1 ± 0.2
Arnouts et al. (2007)	F(3.6μm) > 9μJy	0.85	K	0.90	-23.12 ± 0.08	4.00 ± 0.3	-1.11 ± 0.06
Arnouts et al. (2007)	F(3.6μm) > 9μJy	0.85	K	1.35	-23.13 ± 0.17	2.60 ± 0.5	-1.1 ± 0.2
Arnouts et al. (2007)	F(3.6μm) > 9μJy	0.85	K	1.75	-23.28 ± 0.14	1.62 ± 0.3	-1.1 ± 0.2
Feulner et al. (2003)	K< 17.50	0.18	J	0.30..0.60	-22.93 ± 0.24	2.60 ± 0.80	-1.00 fixed
Dahlen et al. (2005)		0.036	J	0.75..1.00	$-23.09 \pm^{0.24}_{0.22}$	$1.97 \pm^{0.60}_{0.40}$	$-1.31 \pm^{0.10}_{0.09}$
Gabasch at al. (2006)	I(AB)< 26.8	0.01	z	0.4	-22.78 ± 0.41	2.7 ± 1.2	-1.33(fixed)
Gabasch at al. (2006)	I(AB)< 26.8	0.01	z	0.9	-22.93 ± 0.44	2.2 ± 0.7	-1.33(fixed)
Gabasch at al. (2006)	I(AB)< 26.8	0.01	z	1.32	-23.05 ± 0.48	1.9 ± 0.5	-1.33(fixed)
Gabasch at al. (2006)	I(AB)< 26.8	0.01	z	1.31..1.91	-22.71 ± 0.18	2.0 ± 0.3	-1.33(fixed)
Gabasch at al. (2006)	I(AB)< 26.8	0.01	z	1.89	-23.14 ± 0.51	1.70 ± 0.4	-1.33(fixed)
Gabasch at al. (2006)	I(AB)< 26.8	0.01	i	0.4	-22.58 ± 0.31	2.7 ± 1.3	-1.33(fixed)
Gabasch at al. (2006)	I(AB)< 26.8	0.01	i	0.9	-22.69 ± 0.34	2.2 ± 0.8	-1.33(fixed)
Gabasch at al. (2006)	I(AB)< 26.8	0.01	i	1.32	-23.78 ± 0.37	1.9 ± 0.5	-1.33(fixed)
Gabasch at al. (2006)	I(AB)< 26.8	0.01	i	1.89	-22.85 ± 0.40	1.7 ± 0.4	-1.33(fixed)
Gabasch at al. (2006)	I(AB)< 26.8	0.01	i	1.91..2.61	-22.93 ± 0.14	1.9 ± 0.2	-1.33(fixed)
Marchesini et al. (2007)	$K < 23$(max)	0.65	R	2.0..2.5	$-22.67 \pm^{0.20}_{0.22}$	$1.07 \pm^{0.27}_{0.27}$	$-1.01 \pm^{0.21}_{0.20}$

Table 6. Summary of the derived parameters of the LF parameters obtained by various authors by fitting them with Schechter functions, in several rest-frame bands, in different redshift bins, and from different samples of field galaxies.

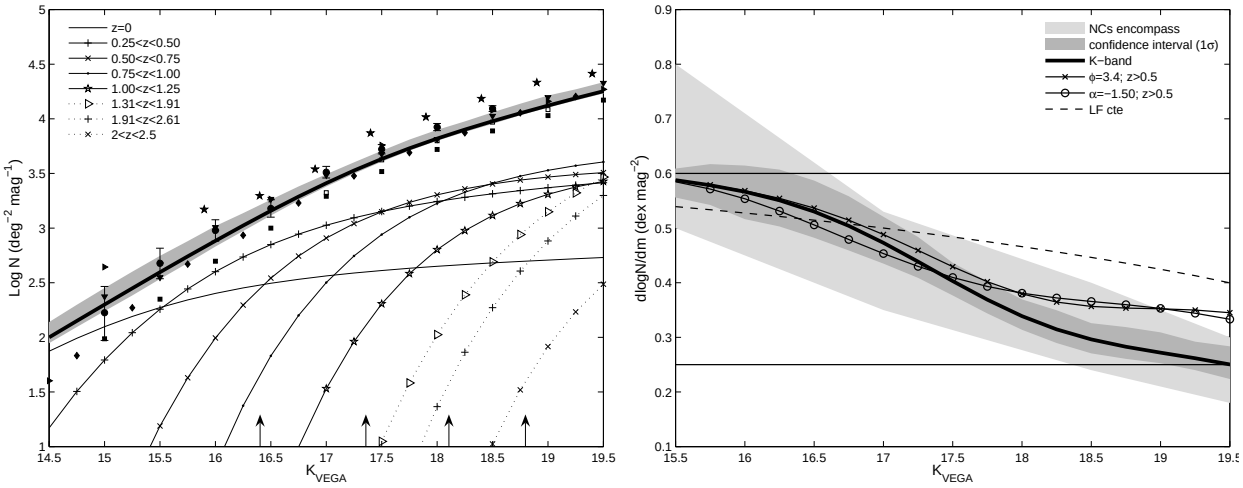

Fig. 14. *Left:* K-band NCs derived from the LFs (thick black line) compared to data from other authors (the legend as in the left panel of Fig. 7). The shaded region indicates the 1σ confidence interval derived from the simulations on the uncertainties of the Schechter parameters. The continuous lines with different symbols show the redshift binned number counts at $\bar{z} = 0.32, 0.62, 0.88, 1.12$ derived from the LFs in the present work. The dashed lines with different symbols show the redshift binned number counts at higher redshifts from Gabasch et al. (2006) (in the i and z rest-frame bands) and Marchesini et al. (2007) (in the R rest-frame band). These NCs have a negligible effect on the on the total NCs at K<18. The arrows depict the best-fit value of $M^*_{K,obs}$ for the LFs at $\bar{z} = 0.32, 0.62, 0.88, 1.12$. Note that to derive the total NCs we have also used LFs at higher redshift from the literature. *Right:* Slope of the NCs derived from the LFs (thick black line). The dark grey shaded region represents the 1σ confidence interval derived from the simulations on the uncertainties of the Schechter parameters. The light grey shaded region shows the region encompassing the slopes derived from the references. The dashed line shows the predicted slope derived from a single LF constant through all redshifts. The circled line shows the predicted slope fixing $\alpha = -1.50$ for the LFs at $z > 0.5$, The crossed line shows the predicted slope fixing $\phi^*_{K,obs} = 3.4 \times 10^{-3} h_{70}^3 Mpc^{-3}$ for the LFs at $z = 0.5$.

8.5. Summary

In this section we presented the tools and measurements required to recover the NCs in terms of LFs at different bands and redshifts. As outlined at the beginning of this section, our motivation here is to determine the family of LFs at different redshifts that constitutes the NCs in the K-band, a result which is easily summarized in the thick black lines of Fig. 13.

As it can be seen from the left panel of that figure, the characteristic luminosity $M^*_{K,obs}$ shows an almost flat evolution beyond $z = 0.4$. In fact, it is 1σ compatible with a constant evolution: $M^*_{K,obs} = -22.89 \pm 0.25$. On the other hand, $\phi^*_{K,obs}$ shows a progressive decline of the $\sim 60\%$ from the local value in the rest-frame K-band to the high redshift value in the R-band, with a significant decrease around $z \gtrsim 1$. A number of recent results seem to confirm the existence of this decline, suggesting that it is mostly driven by a steeper decrement in the number density of

quiescent galaxies (Zucca et al. 2006; Arnouts et al. 2007; Faber et al. 2007). This trend is usually interpreted as an indicator of the beginning of an epoch of major build-up for these populations. Nevertheless, a deeper analysis of the evolution with redshift of the color bimodality is beyond the scope of this paper.

The evolution described by the (K, obs) quantities has no direct physical meaning regarding galaxy evolution. However, it is crucial to describing how galaxy evolution is encrypted in the K-band NCs, and provides an interpretation for the shape of the NCs in terms of meaningful quantities, as we will show in the next section.

K Bin Center	log(N)	dlog(N)/dm
15.0000	2.3005	0.6013
15.5000	2.5959	0.5877
16.0000	2.8835	0.5666
16.5000	3.1584	0.5301
17.0000	3.4114	0.4730
17.5000	3.6327	0.4030
18.0000	3.8193	0.3388
18.5000	3.9783	0.2962
19.0000	4.1209	0.2720
19.5000	4.2530	0.2504

Table 7. Theoretical K-band NCs and NCs slope in 0.5 magnitude bins derived from the LF of section 8.

9. K-band NCs from evolving LFs

Using the multi-wavelength evolution of $M^*_{K,obs}$, $\phi^*_{K,obs}$ presented in the previous section (thick black line of Fig. 13) and their corresponding values for the α parameter (see Table 5), we have derived the NCs in the K-band and its slope up to $K < 19$ (these results are summarized in Table 7). Additionally, we have calculated the 68% confidence interval for both using Monte Carlo simulations on the Schechter function parameters. The random values of M^* and α for each LF were taken from the error ellipses calculated with the STY method. When the ellipse parameters were not available, such as for the optical bands, we used a Gaussian distribution with a median equal to the given value and σ equal to the 1σ deviation.

In the left panel of Fig. 14 we compare the K-band NCs derived from the LFs (solid black line) with the observational results shown in the left panel of Fig. 7 (the legend is the same). The remarkably good agreement proves the validity of the method applied to relate both quantities, and allows us to interpret the variation of the slope in terms of LFs. Therefore, we can consistently argue that the main causes of the shape of the K-band NCs are: the almost flat evolution with redshif of $M^*_{K,obs}$ and the significant decline of $\phi^*_{K,obs}$ with redshift. The former causes the redshift binned NCs to become progressively concentrated at fainter magnitudes due to the variation with redshift of the distance modulus (higher at low redshift but decreasing rapidly at higher redshifts). However, the dominant effect is the decrease of the characteristic density, which opposes the growing comoving volume. The relative growth in the comoving volume per redshift bin ($\Delta z = 0.25$) progressively decreases from a factor of 2 at z=0.32 to 1.3 at z=1.12 (as we approach the peak at z$\sim$2). Simultaneously, $\phi^*_{K,obs}$ presents a decreasing trend that matchs the growth of the volume element at z=1.12, *freezing* the contribution of the LFs at higher redshifts, that otherwise would continue to increase to the peak of the volume element.

In terms of luminosity, it can be seen in the left panel of Fig. 14 that the decline of $\phi^*_{K,obs}$ leads to a smooth transition between the intrinsically faint galaxies at $z < 0.5$ and the $\sim M^*_{K,obs}$ galaxies at $0.5 < z < 1$ around $K \sim 17.5$ (the second and third arrows of the panel represent $M^*_{K,obs}$ at those redshifts). Hence, since the slope of the LFs (and therefore of the NCs) decreases rapidly after the knee, the transition leads to more flattening compared to the slope at $K = 16$, where the $\sim M^*$ galaxies at $z < 0.5$ clearly dominate the NCs.

To help us clarify the relevance of $M^*_{K,obs}$ and $\phi^*_{K,obs}$ for the modeling of the slope, in the right panel Fig. 14 we show the slope of the K-band NCs resulting from assuming the local K-band LF through all redshift bins (constant LF; dashed line). Despite the poor resemblance to the slope derived from the observed LFs (i.e., the slope of NCs in the left panel; solid black line), the decreasing trend is indicative that a gradual change in the slope is a natural consequence of the shape of the LFs modeled by the volume element. However, a precise evolution in the LFs is required to reproduce the change in the slope in the appropriate place.

To strengthen this idea we have also explored the scenario of no density evolution, fixing the value of $\phi^*_{K,obs}$ at $z > 0.5$ (crossed line). In the absence of a decreasing characteristic density, the weigth of the M$\geq M^*$ galaxies up to z$\sim$2 would lead to a slope systematically larger than our 1σ prediction at $K > 17.5$, and clearly out of the envelope of the observed NCs at $K > 18.5$.

Finally, we have tested the role of α in the shape of the NCs. As can be seen from both panels of Fig. 14, the rather flat values of α in the low redshift LFs accentuates the decreasing trend of the slope. However, these values might be slightly underestimated due to the relatively shallow depth of the samples. The line with open circles in the right panel of Fig. 14 shows the predicted slope with $\alpha = -1.50$ fixed in the LFs at $z > 0.5$. As expected, the steeper faint end does not significantly affect the NCs around $K \sim 17.5$, which are dominated by M^* galaxies. However, it does predict a higher slope at fainter magnitudes that falls outside the region defined by the observations. This test poses a restriction against high values of $\alpha > -1.5$ in the low redshift (z=0.5-1) NIR LFs.

9.1. Summary and predictions for fainter magnitudes

Within the three regime schema for the evolution of the slope proposed in section §8.1, it can be seen that the slope of the K-band NCs leaves the Euclidean limit around $K \sim 15.5$. It reachs the (M^* dominated) transition regime faster (K$\sim$17.5) than in a no evolution scenario (K$\geq$19) due to a significant decrease in $\phi^*_{K,obs}$ that *freezes* the contribution from bright $z > 1$ galaxies. The migration into the α regime is harder to determine. The relatively low ($\alpha = -0.9, -1$) faint end slope at z$\sim$1 might cause LFs with larger values of α to dominate the faint counts. These LFs would not be severely suppressed if the decreasing trend in $\phi^*_{K,obs}$ stabilizes at $z > 1.5$, given that the volume element evolves smoothly between z=1.5-4. Therefore, for any $\alpha <$-1 the high-z LFs could eventually dominate the NCs at sufficiently faint magnitudes.

For the set of LFs that we have compiled, Gabash et al. propose a fixed α =-1.33 for the LFs at z=1.3-2.6 in the i, z bands, whereas Marchesini et al. give $\alpha = -1.07$ in the R-band at z=2.35. Interestingly, several authors report significantly larger values of α for the optical LFs at high-z (Marchesini et al. 2007, α =-1.40 in the B-band at z=3; Reddy et al. 2008, α =-1.80 at 1700$\AA$ at z=3). Based on these numbers, we predict a slowly decreasing slope from $d\log N/dm \sim 0.3 - 0.2$ in the magnitude range K =19.5-22, due to the dominant contribution from the z$\sim$2 bin (α=-1.33). However, the slope in this range is not purely in the asymptotic α regime (that would lead to $d\log N/dm \sim 0.13$). The resulting value is a weighted sum of slopes which includes a contribution from $z > 2$ (around $K \sim 20$) M^* galaxies. This contribution from larger slopes lowers the rate of approach to the asymptotic limit. Furthermore, if the slope of the high-z LFs grows rapidly to large values ($\alpha \sim -1.8$) we could measure an increase in the slope around $K >$23.

9.2. NCs in other NIR bands

The procedure to derive NCs from LFs described in section 8 can be used to reproduce the NCs in any other band using the appropriate LFs and redshifts. Nevertheless, based on the multiwavelength LFs probed by the observed K-band (summarized in Fig.13 for the K-band) it is possible to predict the approximate shape of the NCs in the closest NIR bands; e.g., IRAC-3.6 or H ($1.65\mu m$).

Firstly, if the NCs in different bands are referred to AB magnitudes, the results can be compared in a more meaningful context, avoiding the offset introduced by the AB-Vega transformation. In the AB-system, the magnitude range where the NCs fall in the Euclidean regime ($d\log N/dm \sim$0.6) is determined by the local value of M^* and ϕ^* in that band. Therefore, similar values of the local LFs will result in similar NCs at bright magnitudes.

Furthermore, if the multiwavelength evolution of M^* and ϕ^* probed by the different bands exhibits a similar evolution, the slope of the NCs should change around the same magnitude range. That is the case of the H and K bands. At z=0, we have derived the H-band LF directly from the K-band applying a color term. At higher redshifts, the multiwavelength LFs probed by the observed H-band (J-band at z=0.32 and z-band at z=0.83) presents similar values to the LFs probed by the K-band at the same redshifts (see Fig. 13). As a consequence, the NCs in the H-band also present a flattening in the slope around m[AB]$\sim$19-19.5 (see Metcalfe et al. 2006 and references therein). In addition, Magdis et al. (2008) have shown that the NCs in the IRAC-3.6 band exhibit a significant flattening at slightly fainter magnitudes (m[3.6]$\sim$20). This suggests that IRAC-3.6 and K probe a similar evolution in the LFs. If we estimate the [3.6] local LF following the same approximation as for the H-band, the shift in the slope flattening is consistent with applying the typical color K-[3.6]$\sim$-0.6 mag (Dale et al. 2007) to the K-band local LF.

A detailed study of the change in the slope would depend on the multi-band LFs probed by the given band. Nevertheless, this simple calculation provides a rough estimate of the magnitude where the change in the slope begins to be appreciable.

10. Summary and conclusions

In this paper we present the data of a NIR photometric survey in the HDFN and Groth fields. Combining this data with the panchromatic sets available we have extracted a K-band selected sample up to K = 18.5 in a combined area of $\sim$ 0.27 deg^2. Additionally, we made use of the deep NIR public survey conducted by ESO in the CDFS (172 arcmin^2) to complement our relatively shallow survey and increase the surveyed area. We have derived high quality photometric redshifts for the whole sample, taking advantage of the excellent coverage of the SED. K-band galaxy NCs have been derived in the three fields covering the range $16 < K < 18.5$. The comparison to a compilation of shallow wide-area and deep pencil-beam surveys shows a general good agreement in spite of the considerable scatter, a consequence of the cosmic variance. We have studied the redshift distribution of the NCs finding that the 90% of the galaxy counts up to $K \sim 18.5$ come from the low-redshift population ($z < 1$). Additionally, we have measured the effects of cosmic variance by comparing the redshift binned NCs in our three fields, finding that field-to-field differences reach 40% at a certain magnitude, with consequent impact on the NC distribution.

We have provided evidence of an average decreasing trend in the slope of the K-band NCs, $\sim$ 50% in the $15.5 < K < 18.5$ range, evolving from $d\log N/dm = 0.6 - 0.3$. The comparison to 100 synthetic catalogs from the Millennium simulation reveals that cosmic variance in areas ~ 0.25deg^2 leads to significant scatter in the observed flattening rate of the slope.

We have studied the composition of the NCs in terms of LF building blocks, concluding that the change in the slope with observed magnitude can be summarized in three main regimes. Firstly, at bright magnitudes, the classical Euclidean regime ($d\log N/dm = 0.6$) is dominated by low redshift M^* galaxies. Then, at intermediate magnitudes, the transition regime is dominated by the LF at the redshift that maximizes $\phi^* \frac{dV_c}{d\Omega}$. Here the slope decreases rapidly around the apparent magnitude of M^* at that redshift. Finally, at faint magnitudes, the "α regime" is populated by galaxies at the faint end of a combination of LFs. Here the slope asymptotically approaches a minimum value at $\sim$-0.4(1+α). The value of α will typically be given by the LF at the maximum of $\phi^* \frac{dV_c}{d\Omega}$ or a close LF with a much larger faint end slope.

We have explored the evolution of the K-band NCs by deriving LFs in the observed K-band as a function of redshift (at a mean rest-frame wavelength $2.16\mu m/(1+\bar{z})$), and complementing our data with optical and NIR LFs from the literature. In terms of the multi-wavelength LFs, we find that the flattening of the slope is the consequence of a prominent decrease of the characteristic density $\phi^*_{K,obs}$ ($\sim$ 60% from $z = 0.5$ to $z = 1.5$) and the almost flat evolution of $M^*_{K,obs}$ (1σ compatible with $M^*_{K,obs} = -22.89 \pm 0.25$). The combination of both effects forces a transition to the α regime at $K \sim 17.5$ that otherwise would have taken place $1 - 2$ magnitudes later.

Our predictions for $K \gtrsim 20$, based on LFs from the literature, suggest that the slope will continue to decrease steadily to $d\log N/dm \lesssim 0.2$ dominated by intrinsically faint galaxies from a mixture of LFs at z=1.5-2 and a minor contribution from bright galaxies at z>2. However, if optical LFs at $z > 3$ present an even larger faint end, as

suggested by some authors, there might be a slope increase to a higher asymptotic limit around $K \gtrsim 22.5$.

Acknowledgments

We thank the referee M. Bershady for his useful and constructive comments. We acknowledge support from the Spanish Programa Nacional de Astronomía y Astrofísica under grant AYA 2006–02358. Partially funded by the Spanish MEC under the Consolider-Ingenio 2010 Program grant CSD2006-00070: First Science with the GTC (http://www.iac.es/consolider-ingenio-gtc/) Based on observations collected at the Centro Astronómico Hispano Alemán (CAHA) at Calar Alto, operated jointlyby the Max-Planck Institut fur Astronomie and the Instituto de Astrofísica de Andalucía (CSIC). This article is based on observations made with the WHT operated on the island of La Palma by the Instituto Astrofísico de Canarias in the Spanish Observatorio del Roque de los Muchachos. This work is based in part on observations made with the *Spitzer* Space Telescope, which is operated by the Jet Propulsion Laboratory, Caltech under NASA contract 1407. GALEX is a NASA Small Explorer launched in 2003 April. We gratefully acknowledge NASA's support for construction, operation, and scientific analysis of the GALEX mission. Based in part on data collected at Subaru Telescope and obtained from the SMOKA, which is operated by the Astronomy Data Center, National Astronomical Observatory of Japan. This publication makes use of data products from the Two Micron All Sky Survey, which is a joint project of the University of Massachusetts and the Infrared Processing and Analysis Center/California Institute of Technology, funded by the National Aeronautics and Space Administration and the National Science Foundation. Based on observations obtained with MegaPrime/MegaCam, a joint project of CFHT and CEA/DAPNIA, at the Canada-France-Hawaii Telescope (CFHT) which is operated by the National Research Council (NRC) of Canada, the Institut National des Science de l'Univers of the Centre National de la Recherche Scientifique (CNRS) of France, and the University of Hawaii.

References

Arnouts, S., Walcher, C. J., Le Fevre, O., et al. 2007, ArXiv e-prints, 705
Barmby, P., Huang, J. ., Ashby, M. L. N., et al. 2008, ArXiv e-prints, 803
Bershady, M. A. 2003, in Revista Mexicana de Astronomia y Astrofisica, vol. 27, Vol. 16, Revista Mexicana de Astronomia y Astrofisica Conference Series, ed. J. M. Rodriguez Espinoza, F. Garzon Lopez, & V. Melo Martin, 203–208
Bertin, E. & Arnouts, S. 1996, A&AS, 117, 393
Blanton, M. R., Hogg, D. W., Bahcall, N. A., et al. 2003, ApJ, 592, 819
Blanton, M. R., Lupton, R. H., Schlegel, D. J., et al. 2005, ApJ, 631, 208
Capak, P., Cowie, L. L., Hu, E. M., et al. 2004, AJ, 127, 180
Caputi, K. I., McLure, R. J., Dunlop, J. S., Cirasuolo, M., & Schael, A. M. 2006, MNRAS, 366, 609
Chen, H.-W., Marzke, R. O., McCarthy, P. J., et al. 2003, ApJ, 586, 745
Cirasuolo, M., McLure, R. J., Dunlop, J. S., et al. 2007, MNRAS, 380, 585
Cole, S., Norberg, P., Baugh, C. M., et al. 2001, MNRAS, 326, 255
Conselice, C. J., Bundy, K., U, V., et al. 2008, MNRAS, 383, 1366
Cowie, L. L., Barger, A. J., Hu, E. M., Capak, P., & Songaila, A. 2004, AJ, 127, 3137
Cristóbal-Hornillos, D., Balcells, M., Prieto, M., et al. 2003, ApJ, 595, 71
Daddi, E., Cimatti, A., Renzini, A., et al. 2004, ApJ, 617, 746
Dahlen, T., Mobasher, B., Somerville, R. S., et al. 2005, ApJ, 631, 126
Dale, D. A., Gil de Paz, A., Gordon, K. D., et al. 2007, ApJ, 655, 863
Davis, M. 2006, in American Astronomical Society Meeting Abstracts, Vol. 209, American Astronomical Society Meeting Abstracts, 190.01–+
Davis, M., Guhathakurta, P., Konidaris, N. P., et al. 2007, ApJ, 660, L1
Eisenhardt, P. R., Stern, D., Brodwin, M., et al. 2004, ApJS, 154, 48
Eliche-Moral, M. C., Balcells, M., Prieto, M., et al. 2006, ApJ, 639, 644
Faber, S. M., Willmer, C. N. A., Wolf, C., et al. 2007, ApJ, 665, 265
Fazio, G. G., Ashby, M. L. N., Barmby, P., et al. 2004, ApJS, 154, 39
Feulner, G., Bender, R., Drory, N., et al. 2003, MNRAS, 342, 605
Förster Schreiber, N. M., Franx, M., Labbé, I., et al. 2006, AJ, 131, 1891
Gabasch, A., Goranova, Y., Hopp, U., Noll, S., & Pannella, M. 2008, MNRAS, 383, 1319
Gabasch, A., Hopp, U., Feulner, G., et al. 2006, A&A, 448, 101
Gardner, J. P., Cowie, L. L., & Wainscoat, R. J. 1993, ApJ, 415, L9
Gawiser, E., van Dokkum, P. G., Herrera, D., et al. 2006, ApJS, 162, 1
Gehrels, N. 1986, ApJ, 303, 336
Giavalisco, M., Ferguson, H. C., Koekemoer, A. M., et al. 2004, ApJ, 600, L93
Grazian, A., Fontana, A., de Santis, C., et al. 2006, A&A, 449, 951
Huang, J.-S., Barmby, P., Fazio, G. G., et al. 2004, ApJS, 154, 44
Ilbert, O., Tresse, L., Zucca, E., et al. 2005, A&A, 439, 863
Iovino, A., McCracken, H. J., Garilli, B., et al. 2005, A&A, 442, 423
Jarrett, T. H., Chester, T., Cutri, R., Schneider, S. E., & Huchra, J. P. 2003, AJ, 125, 525
Kitzbichler, M. G. & White, S. D. M. 2007, MNRAS, 376, 2
Kochanek, C. S., Pahre, M. A., Falco, E. E., et al. 2001, ApJ, 560, 566
Kong, X., Daddi, E., Arimoto, N., et al. 2006, ApJ, 638, 72
Labbé, I., Franx, M., Rudnick, G., et al. 2003, AJ, 125, 1107
Lawrence, A., Warren, S. J., Almaini, O., et al. 2007, MNRAS, 379, 1599
Magdis, G. E., Rigopoulou, D., Huang, J.-S., et al. 2008, MNRAS, 386, 11
Marchesini, D., van Dokkum, P., Quadri, R., et al. 2007, ApJ, 656, 42
McCracken, H. J., Radovich, M., Bertin, E., et al. 2003, A&A, 410, 17
Metcalfe, N., Shanks, T., Weilbacher, P. M., et al. 2006, MNRAS, 370, 1257
Miyazaki, S., Hamana, T., Ellis, R. S., et al. 2007, ApJ, 669, 714
Pérez-González, P. G., Rieke, G. H., Egami, E., et al. 2005, ApJ, 630, 82
Pérez-González, P. G., Rieke, G. H., Villar, V., et al. 2008, ApJ, 675, 234
Persson, S. E., Murphy, D. C., Krzeminski, W., Roth, M., & Rieke, M. J. 1998, AJ, 116, 2475
Polletta, M., Tajer, M., Maraschi, L., et al. 2007, ApJ, 663, 81
Pozzetti, L., Cimatti, A., Zamorani, G., et al. 2003, A&A, 402, 837
Quadri, R., Marchesini, D., van Dokkum, P., et al. 2007, AJ, 134, 1103
Reddy, N. A., Steidel, C. C., Erb, D. K., Shapley, A. E., & Pettini, M. 2006, ApJ, 653, 1004
Reddy, N. A., Steidel, C. C., Pettini, M., et al. 2008, ApJS, 175, 48
Rowan-Robinson, M., Babbedge, T., Surace, J., et al. 2005, AJ, 129, 1183
Sandage, A., Tammann, G. A., & Yahil, A. 1979, ApJ, 232, 352
Saracco, P., Fiano, A., Chincarini, G., et al. 2006, MNRAS, 367, 349
Schechter, P. 1976, ApJ, 203, 297
Schmidt, M. 1968, ApJ, 151, 393
Scoville, N., Aussel, H., Brusa, M., et al. 2006, ArXiv Astrophysics e-prints
Simpson, C., Almaini, O., Cirasuolo, M., et al. 2006, MNRAS, 373, L21
Skrutskie, M. F., Cutri, R. M., Stiening, R., et al. 2006, AJ, 131, 1163
Temporin, S., Iovino, A., Bolzonella, M., et al. 2008, A&A, 482, 81
Vanzella, E., Cristiani, S., Dickinson, M., et al. 2006, A&A, 454, 423
Villar, V., Gallego, J., Pérez-González, P. G., et al. 2008, ApJ, 677,

169
Wainscoat, R. J. & Cowie, L. L. 1992, AJ, 103, 332
Wirth, G. D., Willmer, C. N. A., Amico, P., et al. 2004, AJ, 127, 3121
Wolf, C., Meisenheimer, K., Rix, H.-W., et al. 2003, A&A, 401, 73
Zucca, E., Ilbert, O., Bardelli, S., et al. 2006, A&A, 455, 879

5

Scientific explotation of multi-wavelength catalogs II: Further examples

Following the motivation of Chapter 4, this Chapter is focused on presenting specific results on the properties of the galaxies at different epochs of the Universe. In particular, we will present an overview of the main purpose and relevant conclusions of several works of different nature in which I have collaborated. The common denominator of all of these projects, and my major contribution to them, is that they all based their conclusions on the analysis of fundamental galaxy properties derived from a detailed modeling of their multi-wavelength SEDs, featuring to higher or lesser degree resources contained within the *Rainbow* database. The studies described in this Chapter include: an analysis of the evolution of the SMD and SFRD from $0<z<4$; exploring the accuracy of different methods to select AGNs in galaxy samples; quantifying the evolutive pattern of the most massive galaxies at $z\sim2$; determining the nature of X-ray sources detected in the FIR. All these studies are published in refereed journals, and are presented following an affinity order.

We will finish this Chapter with the description of a project to study properties of red, passively evolving galaxies at $z\sim2$. This project constitutes our current work to exploit the resources presented in Chapters 2 and 3 to address a more concise scientific question. Nevertheless, the study is still on its early stages and thus we will only outline the more relevant lines of work.

5.1 The stellar mass assembly in the last 12 Gyr (Pérez-González et al. 2008, ApJ 432; 30-47)

This work follows the efforts started with (Pérez-González et al. 2005) to exploit *Spitzer* IRAC and MIPS data to characterize the SFRs and stellar masses of galaxies at different redshifts, and thus analyze the evolution of the SMD and SFRD over the last 12 Gyr of the Universe. Aside from the fundamental conclusions, the technical work developed for this paper constitutes the seed for many of the methods and procedures that are now the body of the *Rainbow* package, as explicitly mentioned in Chapters 2 and 3. Consequently, the characterization of the properties of the galaxies that are analyzed in this work follows essentially the same procedures described in detail in these Chapters.

This study is based on the analysis of a combined sample of 30,000 galaxies in three of the most relevant cosmological fields, namely the HDFN, CDFS and Lockman Hole, counting with high quality multi-wavelength photometric and data and spectroscopy. To study in detail the evolution of the mass tracking the most massive objects, this sample of galaxies is selected rest-frame

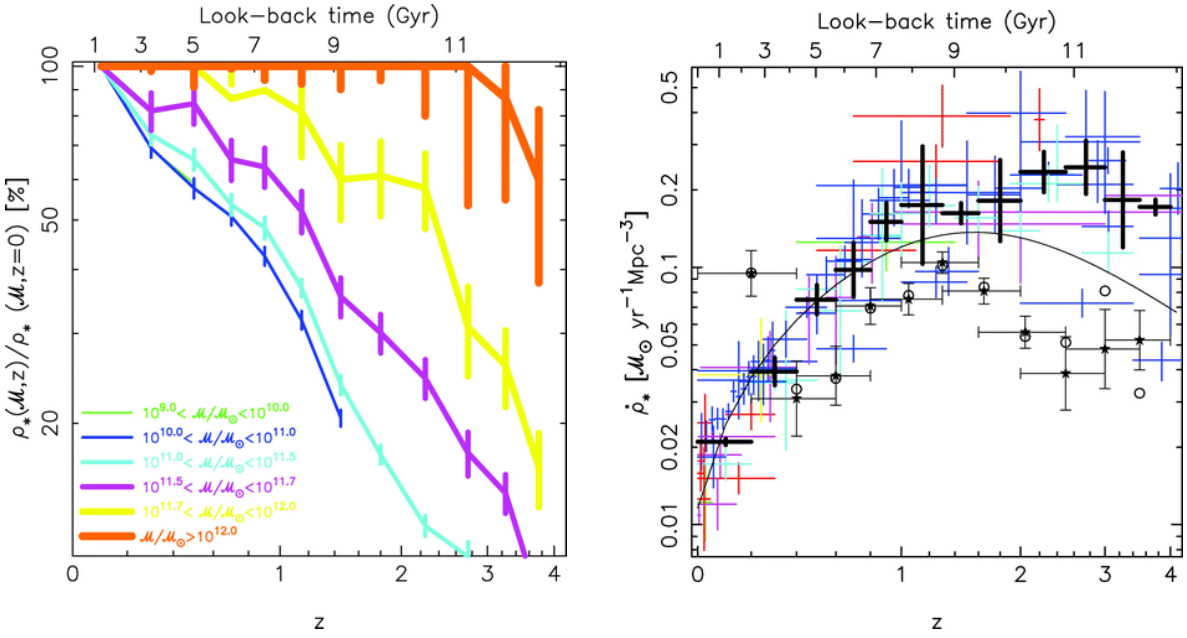

Figure 5.1: *Left:* Fraction of the local stellar mass density already assembled at a given redshift for several mass intervals (wider lines referring to more massive systems). Only results for masses above the 75% completeness level at each redshift are shown. *Right:* Evolution of the comoving SFR density of the universe (Lilly- Madau plot; Lilly et al. 1996; Madau et al. 1996). Filled stars and thin error bars show the SFR density estimations based on the time derivative of the stellar mass density evolution. Open circles show the derivative for the observed values of the stellar mass density. The colored points (shown with error bars) are extracted from different sources in the literature (using different SFR tracers), compiled and normalized to the same cosmology by Hopkins (2004) and Hopkins & Beacom (2006). Thick black error bars show weighted averages and standard deviations of the literature data points for the 12 redshift intervals considered for the stellar mass functions in Pérez-González et al. (2008). The black line shows the evolution of the cosmic SFR density as parametrized in Cole et al. (2001).

NIR using IRAC as reference sample, as done for the EGS sample presented in Chapters 2 and 3. The sample is 75% complete down to 1.6 μJy ([3.6]=23.4), which translates to an approximate stellar mass completeness level of at least 10^9M$_\odot$ up to z=0.5, 10^{10}M$_\odot$ up to z=1.0, and 10^{11}M$_\odot$ to z=4.0. However, to avoid incompleteness at lower masses (due to lower depth of the IRAC survey compared to optical ones), the primary IRAC selection is complemented with an optically (I<25.5) selected sample of a similar size. For the purpose of the analysis, photo-z's were computed comparing to same templates as in Chapter 2. Similarly the total SFR is also obtained fundamentally from IR data traced with Spitzer MIPS complemented with the unobscured SFR in the UV traced from the optical/NIR best fitting model.

Figure 5.1 summarizes some of the most relevant results of these paper. The left panel depicts the fraction of the local stellar mass density that was already in place at different redshifts for several intervals of stellar mass, i.e., the number of galaxies of a given mass that were already formed at a certain redshift with respect to the number of these galaxies observed in the local Universe. It follows from the different evolution with redshift of each mass interval that the bulk of the massive systems formed first whereas less massive systems continued their build up until recent epochs. More precisely, the most massive systems (M> $10^{12.0}$ M$_\odot$) assembled most of their stellar mass very fast at early epochs ($\sim$40% of their mass was assembled in 1 Gyr between z=4 and z=3) , closer to the monolithic collapse than to the hierarchical growth. Intermediate mass systems with $10^{11.0} < M < 10^{12.0}$ M$_\odot$ formed more slowly, assembling half of their stellar mass in

the time interval between z$\sim$2.5 and z$\sim$1 (about 4 Gyr), and most of their mass (80%) not before z$\sim$0.5. The more dilated time span for these galaxies allows an scenario where merging could have play a more relevant role. Finally the less massive systems (with $10^{9.0} < M < 10^{11.0}$ M$_{\odot}$) followed an even slower evolution reaching the local density at very recent epochs, the 20%–40% was assembled in the last 4 Gyr (z$<$0.4) probably by dry accretion of small satellite galaxies. If we consider the whole stellar mass density of the Universe as a function of redshift (instead of the mass binned intervals), we find that approximately half of the total local stellar mass density was already formed at z$\sim$1 (8 Gyr ago).

The differential evolution as a function of stellar mass is consistent with the *downsizing* scenario for galaxy formation, where the galaxies hosting the most intense events of star formation present smaller characteristic masses with decreasing redshift. In this picture, the most massive galaxies formed the bulk of their mass at z > 3 in very intense and rapid episodes of star formation, presenting high specific SFRs, whereas less massive systems assembled more slowly, presenting specific SFRs which would double their mass in timescales comparable to the look-back time of the universe at each redshift. Another consecuence of the *downsizing* scenario is that the typical mass limit above which galaxies have their star formation events significantly supressed (the so-called quenching stellar mass) decreases with redshift. If we consider quenched those galaxies that have already assembled $\sim$70% of their local mass density at a given redshift (e.g., M$\sim 10^{10.5}$ M$_{\odot}$ reached that level at z=0.2, whereas systems with M$\sim 10^{11.75}$ M$_{\odot}$ did it around z=0.7) we find an evolution of the quenching mass consistent with that estimated in Bundy et al. (2006, $\propto$(1+z)$^{3.5}$).

The right panel of Figure 5.1 illustrates the strong disagreement (a factor of $\sim$1.7 up to z$\sim$2) between the the SFRD obtained by differentiating the evolution of the SMD (open circles) and a compilation of values from the literature (different markers; drawn from Hopkins&Beacom 2006). This issue, that was already outlined in the introduction to this thesis, could be explained by changing the IMF to a Chabrier (2003) IMF (instead of a Salpeter 1955 IMF, the default used in this paper). However, the discrepancy at z$>$2 is larger (a factor of 4–5), and it can only be solved if the IMF is completely different (e.g., top-heavy; Van Dokkum et al. 2008) and/or if the SFRs of the most massive galaxies at z=3–4 calculated with different star formation tracers were all overestimated due, for example, to the presence of strong obscured AGN in most of these sources (see e.g., Daddi et al. 2007ab). The topic of the next two papers discussed in this Chapter are intimately related with fraction of obscured AGNs hidden in mid-IR selected samples.

5.2 Reliable identification of the AGN population from mid-to-far IR data (Donley et al. 2008, ApJ 687; 111-132)

Identifying complete and reliable samples of AGNs has become a critical necessity for extragalactic surveys. As outlined in Chapter 1, the role of the AGN as a fundamental mechanism to regulate the formation and evolution of galaxies is a critical test for the majority of the current evolutionary theories (see e.g., Croton et al. 2006 or Bower et al. 2006). Simultaneously, accurately determining the contribution of the AGN obscured accretion (that heats the dust) to the IR emission is essential for obtaining reliable measurements of the SFRD at different redshifts, thus solving the existing discrepancies with the values derived from SMD (Hopkins & Beacom 2006).

The aim of this study is to determine the potential of IR-based selection criteria to comple-

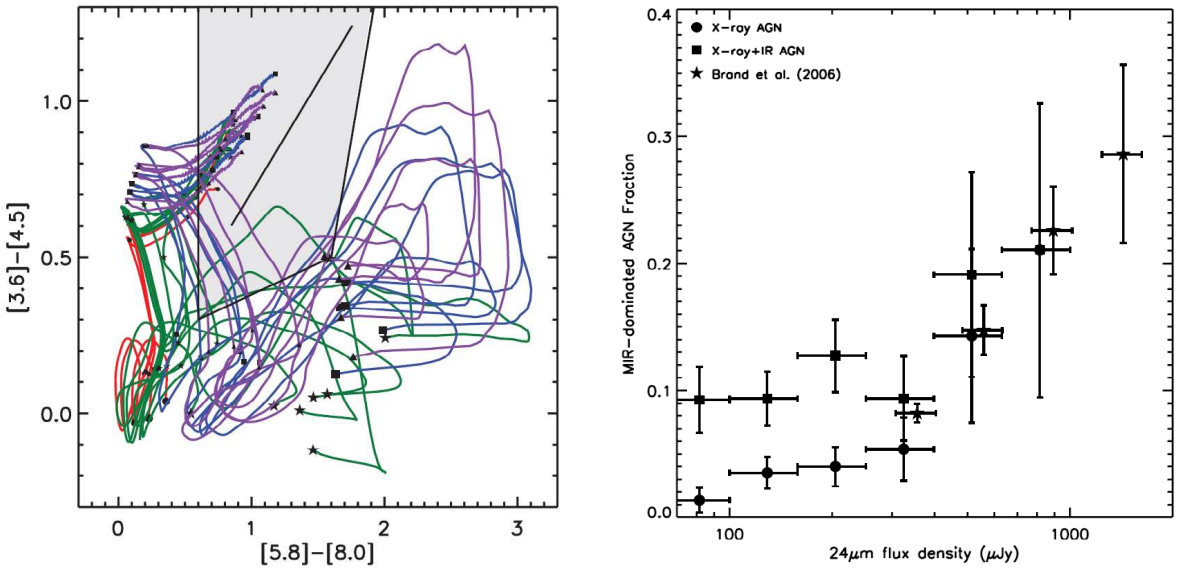

Figure 5.2: Left:Tracks in color-space of the purely star-forming SEDs of ULIRGS (purple triangles), LIRGS (blue squares), spirals and starbursts (green stars), and elliptical galaxies (red circles), from redshifts of z=0 (large symbols) to z=4. Small symbols mark redshift intervals of 1. The power-law locus with α =-0.5 to α =-3.0 is shown as a line inside the shaded AGN selection regions. Right: Fraction of MIR-dominated AGNs, and all AGNs (regardless of their contribution to the MIR light), as a function of 24 μm flux density. Error bars represent the 1 σ errors on the source number counts, and the width of the bins.

ment traditional AGN selection methods and to yield a more complete census of AGN activity. While traditionally X-ray surveys are capable of detecting unobscured AGNs, they miss many of the obscured AGNs and nearly all of the Compton-thick AGNs (e.g., Gilli et al. 2007; Daddi et al. 2007ab). On the other hand, IR selection criteria face the risk of suffering from significant contamination by star-forming galaxies in the AGN candidates.

This work test the reliability and completeness of three infrared AGN selection methods: (1) IRAC color-color selection, (2) IRAC power-law selection, and (3) IR-excess selection (IRX). The first selection method employs color cuts in two representations of IRAC four-band mid-infrared (MIR) color-color space (Lacy et al. 2004; Stern et al. 2005), the second identifies AGNs whose IRAC spectral energy distributions (SEDs) are well fit by a power law (PLGs, Alonso- Herrero et al. 2006; Donley et al. 2007) of slope α <-0.5, and the third selects red galaxies with large infrared to UV/optical flux ratios (Daddi et al. 2007a; Dey et al. 2008; Fiore et al. 2008; Polletta 2008).

The analysis of these criteria is based on the study of the multi-wavelength properties of a MIPS 24 μm selected ($f_{24\mu m}$ >80.0 μJy) sample in the CDFS. In particular, this work exploits the X-ray, mid-IR and radio photometry for these sources, but it also makes use of the full SEDs of the galaxies in the *Rainbow* database for the GOODS-S field (Pérez-González et al. 2008) to estimate optical/NIR colors and photometric redshifts. The later are particularly critical for this study since the majority of the contaminants in the different selection methods satisfy the color criteria only for specific redshifts. In addition, obscured AGNs tend to be very faint in the optical, thus only an accurate multi-wavelength characterization of the IRAC selected galaxies (in which I have worked) can ensure reliable photometric redshifts (and by extension colors and rest-frame luminosities) for these sources.

Figure 5.2 illustrates some of the most relevant results of this study. The left panel depict the color-color criteria of Stern et al. (2005) to identify AGNs. The shaded region represent the AGN selection region, and the diagonal line within are the loci of perfect power laws with α =-0.5 to α =-3.0, i.e., the region where PLGs are located. Tracks in color-space show the purely star-forming SEDs of ULIRGS (purple triangles), LIRGS (blue squares), spirals and starbursts (green stars), and elliptical galaxies (red circles), from redshifts of z=0 (large symbols) to z=4. While the star-forming templates generally avoid the powerlaw locus itself, they enter the selection region of Stern et al. at both low and high redshifts, tracing out the same regions in color space occupied by many of the color-selected AGNs (same applies for the criteria of Lacy et al.). The templates therefore suggest potential star-forming galaxy contamination of the color-selected AGNs, as previously predicted by Barmby et al. (2006), Donley et al. (2007), and Cardamone et al. (2008). The contamination depends strongly on the IR-flux being more likely at lower 24 μm observed fluxes (Treister & Urry 2006; Brandt et al. 2006). For the Stern criteria we consider as contaminants those candidates within 1 σ of the probability contours defined by star-forming templates. On the other hand, PLG selection criterion identifies the majority of secure AGN candidates in IRAC color-space presenting an increasing detection fraction in the X-ray with decreasing α: 30%, 45%, 67%, 88%, and 80% at α=0.0, -0.5, -1.0, -1.5, and -2.0. The PLG criteria is however more sensitive to contamination by high-z star-forming galaxies. At z$>$2.5 ULIRGs start to verify the PLG selection criteria. With regard to IRX sources, a re-examination of the stacked X-ray properties, including a careful characterization of faint detections, suggest that although this technique successfully identifies a number of severely obscured (Compton-thick) AGNs, particularly for the most IR luminous (e.g., Alexander et al. 2008), there may be a contamination by star-forming galaxies. Daddi et al. (2007b,a) argues that 50% of their IRX galaxies are Compton-thick AGNs. However, attending to the X-ray luminosities and photon index derived from the stacking of weakly detected IRX galaxies there are other plausible explanations, particularly if a few marginal detections in the X-ray dominate the contribution of the stacked flux. More precisely, 1) the Compton-thin possibility can not by ruled out if the soft X-ray emission is not entirely originated by star formation, and 2) the star-formation scenario is also possible if the X-ray emission is dominated by low- and high-mass X-ray binaries (LMXBs, HMXBs), which could be responsible for the hard (Γ =1.0-1.5) X-ray spectrum. We expand more on this topic in the study described in the next section of this Chapter.

The sum of all candidates detected with the different criteria, considering only the most reliable cases (i.e., requiring at least marginal 2 σ X-ray detections in the 0.2-5 KeV band), would increase the sample of extrictly X-ray detected AGNs by $\sim$54%-77%. The analysis of the IR emission of this (more complete) sample, shown in the right panel of Figure 5.2, indicates that the fraction of MIR sources dominated by an AGN decreases with decreasing flux density, but only down to a 24 μm flux density of $\sim$300 μJy. Below this limit, the AGN fraction levels out at 10%. This indicates that a non negligible fraction of faint 24 μm sources are primarily powered not by star formation, but by the central engine.

5.3 On the nature of IRX sources (Georgakakis et al. 2010, MNRAS 406; 420-433)

The purpose of this work is to shed some light into the true nature of IRX sources. These galaxies has attracted much attention recently as they are proposed as a very efficient method to select highly obscured (Compton-thick) AGNs. Although there is not a unique criteria for selecting

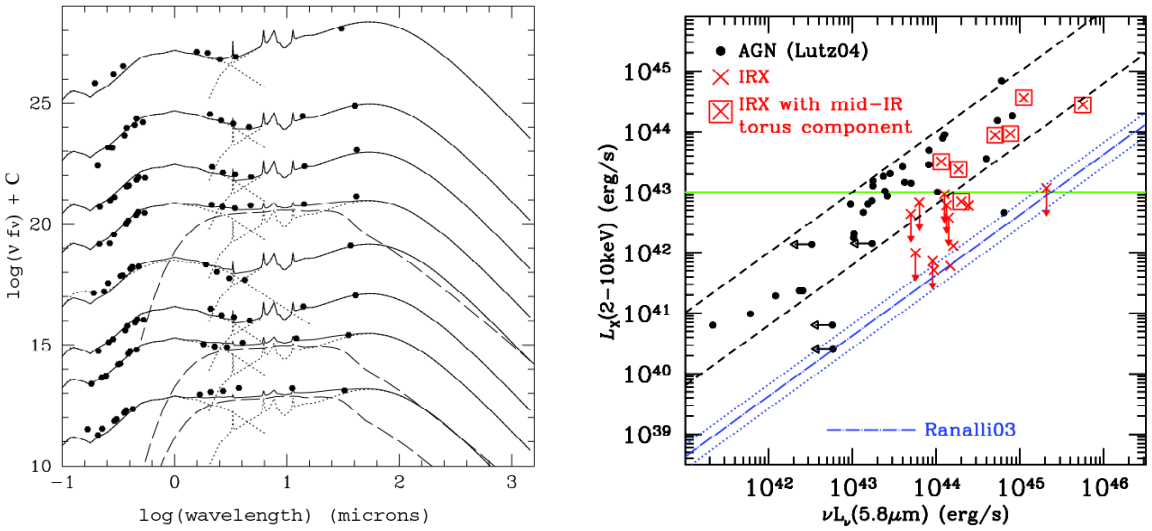

Figure 5.3: *Left:* Examples of template fits to the SEDs of the IRX selected galaxies in the EGS field. The UV-to-FIR photometry (black dots) was extracted from the analysis described in Chapters 2 and 3. The continuous lines are the best-fitting models. Different sources are offset by an arbitrary constant for clarity. The dashed curves correspond to the hot dust torus component, which is needed to fit the IR-SED of all X-ray detected sources. The dotted lines at infrared wavelengths are the starburst components. *Right*: X-ray (2–10 keV) luminosity versus the 5.8 μm luminosity. The black circles and dashed lines are local AGN from the sample of Lutz et al. (2004) and the scatter of the correlation. The blue lines show the correlation for star-forming galaxies adapted from (Ranalli et al. 2003; see Fiore et al. 2009). The IRX sources of this work are shown as red crosses. Upper limits in the X-ray data are depicted with arrows and sources which require a torus component to fit their infrared SEDs a marked with a square.

IRX galaxies, the idea behind the method is essentially the same in all cases (e.g., Daddi et al. 2007ab; Dey et al. 2008): selecting sources that are faint at optical and bright at mid-IR wavelengths. In its simplest version this method applies a cut in the 24 μm over R-band flux density ratio, $f_{24\mu m}/f_R > 1000$ to identify dust obscured galaxies (DOGs; Dey et al. 2008) at a mean redshift z$\sim$2. Additional restrictions such us red optical colors (R$-K$ >4.5; Fiore et al. 2008,2009) are sometimes required to ensure higher degree of dust obscuration. In general, the properties of the galaxies selected in these studies are roughly similar: high redshift (z$\sim$2), massive galaxies (M$\sim$10^{10}-10^{11}M$_\odot$; Treister et al. 2009; Bussmann et al. 2009) with relatively uniform X-ray properties and mid-IR luminosities (L$_X$=10^{43}ergs^{-1}; Daddi et al. 2007b). In addition, they all feature two key properties that are frequently interpreted as evidence for Compton-thick AGNs: their hard mean X-ray spectrum, and their faintness at X-ray wavelengths relative to the mid-IR (L$_X$(2-10 keV)/νL$_\nu$(5.8 μm)) by 2-3 dex relative to local AGN samples (e.g., Lutz et al. 2004). Nevertheless, given the faint X-ray properties of these sources (being undetected mostly undetected even in the deepest surveys), and the relatively limited data in the mid-to-fir IR that we have for them, the evidence regarding their Compton-thick nature is far from conclusive. In fact, the two key properties of IRX sources may also be consistent with Compton thin AGNs of lower luminosity. Only under the strong assumption that the bulk of the mid-IR luminosity is associated with reprocessed radiation from accretion on the central SBH, can one infer that these sources are Compton thick.

Unveiling the true nature of IRX sources has relevant implications for characterizing galaxy evolutionary models, or for studying the relative black hole/galaxy growth. Furthermore, a precise identification of Compton-thick sources is also relevant to test the relative contribution of X-ray sources to the diffuse X-ray background at the highest energies (e.g., Gilly et al. 2007,

Draper&Ballantine 2009).

This work explores the nature of IRX galaxies by analyzing the properties of lower redshift analogues at z=1. Thus, taking advantage of the far better (brighter) spectro-photometric data available for lower redshift sources to analyze in depth the accuracy of different hypothesis on the nature of these sources. To achieve this goal, this study combines all the available resources in the *Rainbow* database for the EGS (see Chapters 2 and 3) and GOODS-N (Pérez-González et al. 2008) fields. In particular, it makes use of the merged UV-to-FIR SEDs and spectroscopic redshifts of IRAC-3.6 μm selected sources to isolate a sample of galaxies which at z=2 that would have *observed* SEDs that satisfy the IRX criteria ($f_{24\mu m}/f_R >$900, R-[3.6]>3.7). This is possible because the best-fitting templates (fitted to the spec-z) can be artificially redshifted to z=2 to compute their *observed* colors. In particular, the specific task to compute synthetic magnitudes developed for this thesis was critical for the estimate of reliable *observed* colors at different redshifts. In addition, similarly to the preceeding paper, this work targets heavily obscured optically faint galaxies that are much brighter in the NIR (and particularly in the FIR). Therefore, it greatly benefits from the work presented in this thesis that characterizes IRAC selected galaxies with multi-wavelength photometry.

A total of 19 sources (14 in EGS and 5 in the GOODS-N) are selected at a median redshift z=1. The left panel of Figure 5.3 present and example of the combined optical/NIR and mid-to-far IR SED fitting procedures. To obtain information on the dominant emission mechanism in the infrared (AGN versus star formation) the fitting of the IR SED is performed with a mixture of four different templates: cirrus (Efstathiou & Rowan-Robinson 2003), AGN dust tori (Rowan-Robinson 1995; Efstathiou & Rowan-Robinson 1995), M82 and Arp 220 starbursts (Efstathiou, Rowan-Robinson & Siebenmorgen 2000). The analysis of the dust emission shows that the far-IR SEDs of IRX sources are better described by warm-dust templates (e.g., similar to M82 or Mrk 231) being inconsistent with cold dust templates (e.g. Arp 220). Only 3 (of 8) sources required an additional QSO torus component to fit the mid-IR (first, second and fifth SEDs in Figure 5.3, from bottom to top). Interestingly, this component is needed only for those sources which are detected at X-ray wavelengths and which have large intrinsic X-ray luminosities, $L_X >10^{43}$ ergs^{-1}.

When the observed SED is combined with X-ray spectroscopic observations we find that that about 35% per cent of the sources in the AEGIS (5/14) and 80% in the CDF-North (4/5) fields are associated with hard (2–7 keV) X-ray detection. These fractions increase to 43% (6/14) and 100% (5/5) per cent in the AEGIS and CDF-N, respectively, if lower significance sources are included. This suggests a high AGN identification rate in samples selected using the infrared excess criteria. However, the fit of the spectra to a model of AGN power-law emission (Γ =1.9; Nandra & Pounds 1994) plus a reflection component (emission that intersects a optically thick material) suggest that the hard X-ray spectral properties are consistent with Compton thin column densities, $N_H \sim 10^{22}-5\times10^{23}$cm^{-2}. Only 4 of them shows tentative evidence for Compton thick obscuration. In addition, the IRX sources un-detected in the X-rays shows no indication for a hot dust component associated with a powerful AGN. The right panel of Figure 5.3 demonstrates that a QSO torus component is required to fit the mid-IR part of the SED of only X-ray detected sources. Thus, if some of the X-ray undetected sources were associated with heavily obscured and powerful AGNs with X-ray emission suppressed by the intervening dust and gas clouds, we would have identified them in the mid-IR as sources with a QSO torus component.

This result has implications on the nature of the z $\approx$ 2 IRX population detected in deep

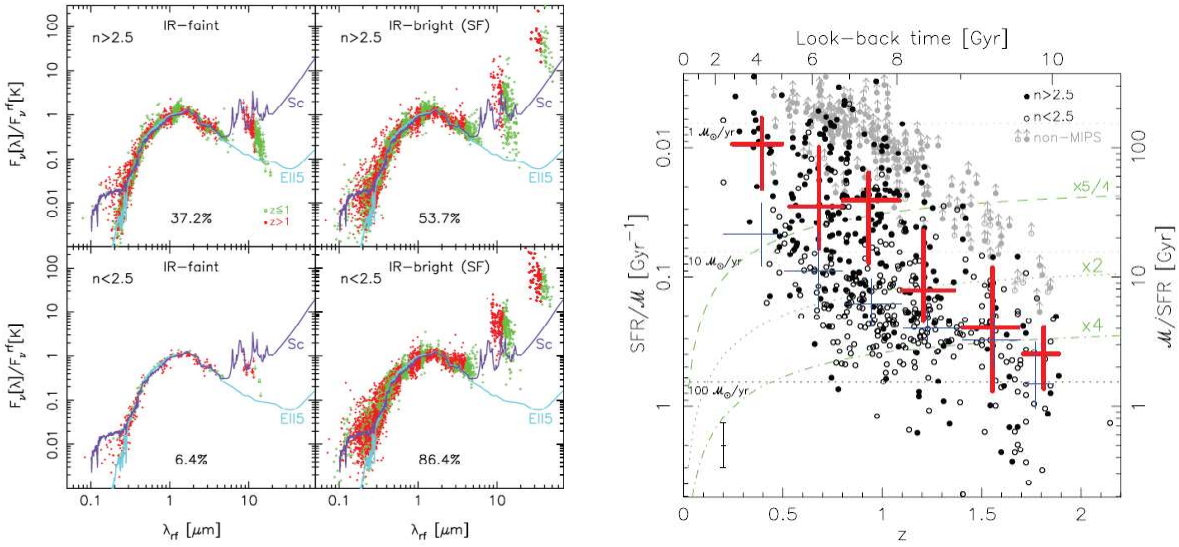

Figure 5.4: *Left: Right*:Specific SFRs as a function of redshift and morphology for galaxies not identified as AGN. Galaxies detected at 24 μm are plotted with open (disks) and filled (spheroids) black circles, while gray symbols show upper limits for sources not detected by MIPS. Red and blue crosses represent the median and quartiles for the distribution of specific SFRs in different redshift ranges. The red widest lines refer to spheroids and the blue narrowest lines to disky galaxies. Green curves show the expected positions of galaxies which would multiply their stellar mass by 5/4, 2, and 4 between their redshift and z=0 if they maintained a constant SFR. Horizontal dashed lines show constant SFR values for the median stellar mass of our sample ($1.6\times10^{11}M_{\odot}$).

surveys. There is no doubt that some of these sources are Compton thick QSOs. Georgantopoulos et al. (2009), for example, identified Compton thick QSOs among X-ray sources in the CDF-North through X-ray spectroscopy and showed that some of them satisfy the infrared excess selection criteria. This analysis, however, shows that a potentially large fraction of the IRX population at z$\sim$2 are not luminous Compton thick QSOs but lower luminosity equivalents (L_X $<10^{43}$ergs^{-1}), possibly Compton thin AGNs and/or starbursts.

5.4 Evolutionary paths of the most massive systems (Pérez-González et al. 2008, ApJ 687; 50)

Following the lines of the study discussed in the first section of this Chapter, this work focus on the analysis of the stellar mass assembly of massive (M$>10^{11}M_{\odot}$) galaxies at z$<$2. As shown in Figure 5.1 a significant fraction of the most massive galaxies were already in place at early epochs of the Universe (z$\gtrsim$2). In addition, some of these galaxies seen to have assembled most of their mass content by that time, thus evolving passively (Kriek et al. 2006, 2008, Cimatti et al. 2008). The sole presence of this massive objects at the highest redshifts is in apparent contradiction with a hierarchical growth of structures which predicts that these galaxies should form latter via merging of smaller galaxies (e.g., De Lucia et al. 2006). Interestingly, recent observational evidence indicates that some of these galaxies, which are supposedly at relatively late evolutionary stages, are extremely compact a factor of $\sim$4 smaller than local analogs of the same mass (Daddi et al. 2005; Trujillo et al. 2006). This puzzling scenario raises the question of what possible evolutive paths could lead these objects to their present shape.

The main goal of this work is exploring the evolution of the most massive galaxies and their dependence on the morphology. To do this, we quantify the growth in stellar mass via star formation events of massive (M>10^{11}M$_{\odot}$) galaxies as a function of size and brightness profile shape up to z$\sim$2. The analysis presented in this work is fundamentally based on the characterization of the UV- and IR-SFRs of the IRAC sample in EGS described in Chapters 2 and 3 of this thesis. This estimates allowed us to provide robust SFRs for a sample of 831 K-band selected galaxies presented in Trujillo et al. (2007) which count with accurate photometric redshifts and stellar masses estimates computed from a multi-wavelength SED fitting similar to that described in the Chapter 3 of this thesis. In addition, Trujillo et al. (2007) estimated (circularized) half-light radius (r_e) and Sérsic (1968) indices (n) for all galaxies. They used i-band *HST* ACS images to fit surface brightness profiles and divided the sample in disk-like (n <2.5) and spheroid-like (n >2.5) galaxies according to the value of the Sérsic (1963) index.

The left panel of Figure 5.4 shows the composite de-redshifted SEDs (normalized in the rest-frame K-band) of all galaxies in the sample grouped into morphological (Sérsic index) and IR activity (detection at F(24 μm)>15 μJy). Interestingly, not only most (more than 90%) disk-like (n <2.5) massive galaxies are detected by MIPS (revealing MIR emission consistent with a PAH features i.e, dust-enshrouded star formation), but also around 50% of spheroids (n >2.5) have MIPS counterparts, even when rest-frame optical colors reveal that they are dead and evolving passively (more similar to a elliptical spectral template). Nonetheless, the IR detection does not play an important role in the position occupied by these galaxies in the stellar mass-size plane. Except perhaps for spheroid-like objects which at a given stellar mass, tend to be brighter in the IR for larger sizes (r_e >5 kpc).

The right panel of Figure 5.4 shows the specific SFRs of massive galaxies as a function of redshift and morphology. Red and blue crosses represent the median and quartiles for the distribution of specific SFRs in different redshift ranges for disk- and spheroid-like galaxies, respectively. The specific SFRs of spheroid galaxies evolve as $(1+z)^{5.5\pm0.6}$ from z=0 to z=2, while the evolution for disk-like galaxies goes as $(1+z)^{3.6\pm0.3}$. Below z=1 spheroid-like galaxies present very low specific SFRs. On average, they would increase their stellar mass by less than 25% at 0<z<1 if they maintained a constant SFR. At z>1, the specific SFRs of massive galaxies are higher than 0.1 Gyr^{-1}. Both the active spheroid-like (note that there are 40% of spheroids which are not detected by MIPS) and disky systems are forming stars at approximately the same rate, and the number of quiescent galaxies (those not detected by MIPS) is less than 50% for both types. For typical burst durations, and even for star-forming events with a constant SFR and lasting up to 1 Gyr, the maximum increase in stellar mass would be $\sim$15% at 1.1< z <1.4, $\sim$ 25% at 1.4< z <1.7, and $\sim$50% at 1.7< z <2.0, for both spheroids and disks. This means that a significant fraction (more than 50%) of the stellar mass of z > 1 massive galaxies was assembled at z>2 (Pérez-González et al. 2008; Marchesini et al. 2009).

Summarizing the full redshift interval, spheroid-like galaxies have doubled (at the most, depending on the burst durations) their stellar mass due to newly-born stars alone from z=2 to z=0.2. Most of this mass increase (60%) occurs at z>1, where specific SFRs are as high as 0.4 Gyr^{-1}. Disk-like galaxies have tripled (at the most) their stellar mass by newly-formed stars at z<2, with a more steady growth rate as a function of redshift.

The moderate mass growth for these galaxies (especially for spheroids) contrast with the size increments measured by Trujillo et al. (2007) for the same sample: massive spheroid-like galaxies

have increased their size up to a factor of ∼5.5 from z=2 to z=0 (10 Gyr), while massive disks have increased their size by a ∼2.5 factor in the same period. If star formation works in the same way in making both spheroid and disk-like galaxies grow in size, clearly there should be another mechanism (mergers?, adiabatic expansion?) helping (more noticeably) the spheroids (which form less new stars than disks between z=2 and the present, but grow more) to increase their size.

The next section describes our current project to further explore the nature of these galaxies and unveil their evolutionary paths. In this study we do not limit the analysis to a small (∼800) sample in the EGS, but we exploit the full possibilities of the catalog described in Chapters 2 and 3 and similar catalogs in other fields described in Pérez-González et al. (2008). The main advantage of the IRAC sample is that it is much deeper and encompasses a larger area than that of the sample described in this section. The enhanced capabilities of the IRAC catalog would allow us to carry out a similar study as the one present in this section (i.e., analyze the masses and SFRs of the galaxies), but focused on obtaining an accurate sample of passively evolving galaxies at 1.5>z>2.5.

5.5 Red and Dead galaxies at high-redshift (Barro et al. 2011 in preparation)

Understanding the red, passively evolving, galaxies at intermediate redshifts (z∼2) is one of the outstanding challenges of galaxy evolution studies. Red galaxies with typically very low UV fluxes make up for 80% of the mass contained in the most massive galaxies (van Dokkum et al. 2006) and 25-75% of the total mass in galaxies at 2<z<3 (Papovich et al. 2006; Marchesini et al. 2006), and thus provide critical constraints for studies of galaxy formation and mass assembly.

The general consensus is that the process of mass assembly at z>1 is much faster than at lower redshifts (e.g. Bell et al. 2006; Faber et al. 2007). Recent measurements at z<4 show a strong evolution with redshift of the stellar mass function of galaxies, as well as a dependency on the stellar mass, with the low-mass end evolving more rapidly than the high-mass end (e.g., Pérez-González et al. 2008; Marchesini et al. 2009). In particular, the number density of the most massive galaxies (M>$10^{11} M_{\odot}$) seems to evolve very little from z=4 to z=1.5 (Pérez González et al. 2008), suggesting that the most massive galaxies in the universe were mostly in place already at z∼2.5, and implying potentially severe disagreements with the predictions from the latest generations of semi-analytic models of galaxy formation.

Deep spectroscopic studies of massive red galaxies at z>1.5 (e.g., McCarthy et al. 2004; Cimatti et al. 2004, 2008 estimated stellar ages consistent with early formation redshifts (z_{form} ∼4), which is potentially inconsistent with the rapid evolution in stellar mass density at these epochs. It is however clear that the red sequence was in place at fairly early epochs (Bell et al. 2004; Taylor et al. 2009; Brammer et al. 2009), and that density of red galaxies evolved strongly in the 1<z<3 era (e.g., Arnouts et al. 2007, Van Dokkum et al. 2009; Demarco et al. 2010), while the stellar mass in blue galaxies remains roughly constant over the same redshift range. This indicates a fast rate of blue objects entering the red sequence controlled by feedback processes that regulate star formation (e.g., Schawinski et al. 2007).

Since the growth of a central black hole and the growth of a bulge or spheroid dominated galaxy are intimately connected (Novak et al. 2006a), models based on AGN feedback for quench-

ing the star formation in the host galaxy are frequently advocated as the main mechanism to stop the galaxy growth (Bower et al. 2006; Croton et al. 2006). Nonetheless, an emerging picture in which massive galaxies are assembled via mergers followed by a rapid quenching of star formation could address many of the observed properties of the red sequence galaxies (Faber et al. 2007).

In addition to being compatible with the observed evolution of the stellar mass function, the quenching mechanisms must be able to deal with the closely related issue of the striking compactness of massive red galaxies at these redshifts. High spatial resolution studies showed that the passive red galaxies at intermediate redshifts are systematically smaller than their likely present-day counterparts (e.g. Daddi et al. 2005; Trujillo et al. 2006, Cenarro & Trujillo 2009). In order to match their equivalents at z=0, these galaxies would require a factor of $\sim$3 growth in size during an epoch in which the stellar masses, population ages, and overall morphologies show little or no evolution. This puzzling scenario has fueled several competing models, currently under discussion: Dry merging (e.g, Hopkins et al. 2009c; Lopez-SanJuan et al. 2010), AGN puffing-up (Fan et al. 2008, 2010; Damjanov et al. 2009) or late satelite accretion (Naab et al. 2007,2009; Bezanson et al. 2009);

In order to observationally verify either scenario, compelling evidence must be found that supports any of them. Recent observational efforts has been done in order to obtain: robust estimates of the velocity dispersion (σ; a direct probe of stellar mass and kinematics) from accurate spectroscopy (van Dokum et al. 2009; van Dokkum&Brammer 2010; Onodera et al. 2010; Newman et al. 2010); ultra deep NIR imaging (Szomoru et al. 2010; Ryan et al. 2010) to study their morphology and verify their compactness or to compute accurate physical properties such us their masses (Marchesini et al. 2010). However, in order to obtain meaningful results on the properties and evolution of these sources at high redshift it is of critical importance to accurately identify the most massive red galaxies at z$>$1.5.

5.5.1 A census of Red and Dead galaxies at z$>$1.5

As mentioned above, there is some evidence that the red sequence is already in place at z$=$2.5 (Labbé et al. 2007; Cenarro & Trujillo 2009), although the contrast separating the red and blue sequences is low. This is either because spectroscopic samples that span a broad range of colors are small (Cassata et al. 2008; Kriek et al. 2008) or because larger photometric samples suffer from uncertain photometric redshifts at z$>$1.5, which leads to uncertain rest-frame colors (Taylor et al. 2009a).

A wide variety of criteria has been proposed to effectively isolate quiescent galaxies at high redshift based on their intrinsically red colors. However, in addition to the issues mentioned above, there is a strong intrinsic degeneracy in the optical colors of quiescent and heavily enshrouded galaxies. As a result, the samples of galaxies selected with many of the classic color-criteria, such as EROs (Elston et al. 1988; McCarthy et al. 1992) or DRGs (Franx et al. 2003; Rudnick et al. 2003), present an undetermined mixture of dusty and passive galaxy populations. Other techniques based on more restrictive color-color criteria, such as the BzK (Daddi et al. 2004), Optical/NIR rest-frame colors (Wuyts et al. 2007, Williams et al. 2009), or SED fitting methods, seem to have been more successful breaking the degeneracy up to z=2 by getting a better grip on the subtle differences between SEDs of dusty and passive galaxies.

Nevertheless, the most reliable approach to disentangling these two population is through

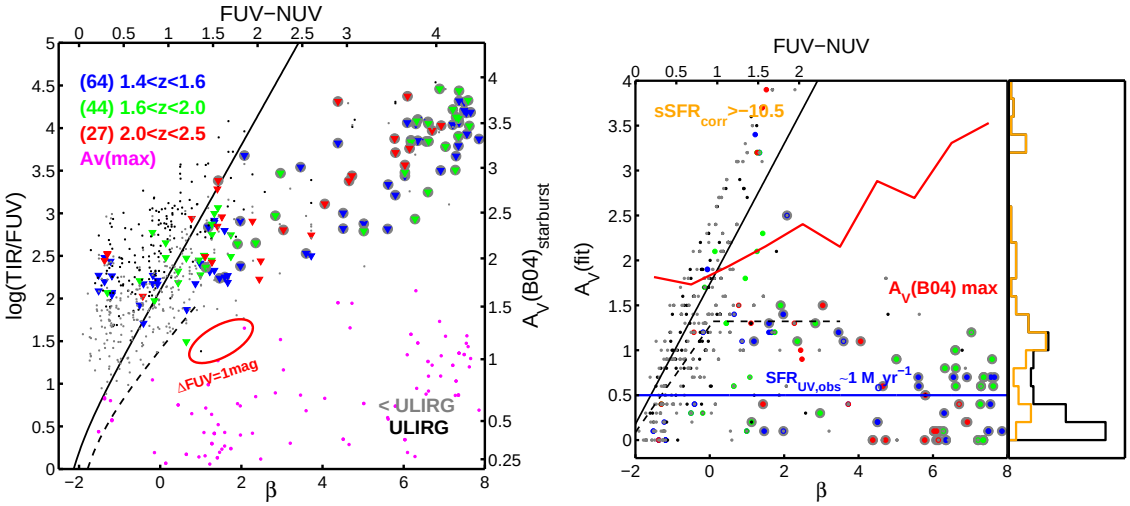

Figure 5.5: *Left* Ratio of the total IR-luminosity to the UV-luminosity as a function of the UV-slope. The colored triangles depict the candidates to quiescent galaxies (sSFR$\gtrsim$-10.5 yr^{-1}) in different redshift bins. The grey and black dots depict sources detected in MIPS 24μm (F(24)>60μJy) with $\log$M>10.5$M_{\odot}$ and having $L_{IR}<10^{12}L_{\odot}$ and $L_{IR}>10^{12}L_{\odot}$ (ULIRGS), respectively. The solid and dashed lines show the IRX-β relation for local starburst galaxies Meurer et al. (1999) and local *normal* star-forming galaxies Muñoz-mateos et al. (2009). The values in the rightmost axis are based on the IRX-A(FUV) relation of Buat et al. (2005) and the extinction law of Calzetti et al. (2000). *Right* Attenuation in the V-band derived from best fitting optical template (A(V)) versus the UV-slope. The colored markers are the same as in the left panel. The candidates to quiescent galaxies with $\mathrm{sSFR}_{\mathrm{corr}}\gtrsim$-10.5 yr^{-1}, after correcting the SFR_{UV} for extinction using the model A(V) are depicted as colored markers above grey circles.

the analysis of their IR-SEDs in which the red-dusty galaxies present a very strong emission in comparison with the almost non-existent emission of quiescent galaxies. Unfortunately this has proven to be a difficult task, as the results are often limited by the depth of the FIR surveys which are frequently restricted to the most luminous IR-galaxies (U-, Hy- LIRGS).

5.5.2 Sample selection and methodology

We combine the IRAC 3.6+4.5 μm selected samples in EGS, HDFN and CDFS. The sample in EGS is the shallowest of the three with a 85% completeness at [3.6]<23.75, whereas the average exposure times in the GOODS fields is more than a factor of $\sim$2 larger than in EGS.

All three fields count with extensive multi-wavelength photometry that has been processed using the *Rainbow* methodology. The merged catalogs and estimated parameters for the sources in the GOODS and EGS fields are presented in Pérez-González et al. (2005, 2008) and Barro et al. (2011ab). The three fields count with very deep, high quality data in MIPS 24 μm, which are the cornerstone of our study. For this work we combine all the available MIPS data in these fields from the GTO and FIDEL surveys in order to create the deepest mosaic available from public data.

The relevant properties of the sources under study are obtained following a modeling procedure of both the SEDs and the physical properties, similar to that described in Chapters 2 and 3 of this thesis. In particular, our analysis focuses on the estimated stellar masses and SFRs (UV- and IR- based). Based on these, we select a sample of quiescent galaxies at 1.5<z<2.5 using a specific star-formation rate (sSFR) criterion. An sSFR criterion is in general more robust than a single color-color criteria as it computed from a combination of parameters that requires an analysis of

the whole SED. Moreover, the sSFR is closely related to the SFR history of the galaxy. In fact, the inverse of the sSFR provide a natural time-scale for the time of the last major star-formation event in the galaxy.

Although the choice of a sSFR limit for discriminating active and quiescent galaxies can be somewhat arbitrary, the completeness limit in the stellar mass ($\log$M$\gtrsim$10.5 [$M_{\odot}$]) and the average limiting magnitude of the optical bands and FIR bands: 27-28 mag, i.e., a SFR$_{UV}$ $\sim 1 M_{\odot}\mathrm{yr}^{-1}$ at z$\sim$2 for zero UV extinction; F(24)$>$60μJy (5 σ), i.e. , SFR$_{TIR}$ $\gtrsim$70[$M_{\odot}\mathrm{yr}^{-1}$] at z$\sim$2, provides a natural threshold for the sSFR of the typical quiescent galaxy ($\sim$ optical drop-outs). Thus, we establish a primary criteria for selecting candidates to quiescent galaxies which requires sSFR$\gtrsim$-10.5 yr^{-1} and MIPS 24 μm undetection ($>$5 σ). This implies that the prototypical candidate would be a galaxy characterized with a faint ($\lesssim$5 σ) detection in the B-band ($\sim$FUV rest-frame), un-detected in MIPS 24 μm and presenting stellar mass equal to the our completeness limit in stellar mass. Similar criteria has been proposed to discriminate quiescent based on the sSFRs or equivalent quantities (see e.g., Brichmann et al. 2004, Grazian et al. 2006, Fontana et al. 2009). In this work we will also show that the sample obtained with this threshold is consistent with other color-color and SED-fitting based criteria.

Nonetheless, the sSFR criterion face at least two main issues: (1) how many of these red harbor an ongoing burst of with SFR(IR)$\sim$10-70[$M_{\odot}\mathrm{yr}^{-1}$] (i.e, MIPS 24 μm $<$5 σ)?. Does an un-detection in MIPS 24 μm (at any significance level) suffice to ensure that these galaxies are not star-forming?; (2) how accurate are the estimated dust-extinctions for these optically faint galaxies?. These issues tend to induce opposite biases. Whereas the former lead us to include mildly enshrouded starburst in the sample, particularly for the highest redshift candidates, the latter could cause us to remove real passive galaxies if the extinction obtained from the best fitting template is the result of a wrong match to a highly extinguished young stellar population instead of a old population. The best approach to tackle both issues simultaneously is to treat the UV and IR emission in a self-consistent manner. As the amount of IR-emission and the dust-obscuration present a tight correlation, the comparison of observed and expected UV and IR luminosities can be use to efficiently narrow down the confidence intervals of the selection.

As an example of the kind of analysis that we are performing on the sample, the left panel of Figure 5.5 shows the ratio of the total IR-luminosity to the UV-luminosity as a function of the UV-slope, β, usually referred as IRX-β diagram. The value of β, is computed from the rest-frame FUV$-$NUV color of the best fitting template. The IR-luminosity of the quiescent candidates (un-detected in MIPS 24 μm) is obtained by fitting the dust emission models to an upper limit flux of F(24 μm)=60μJy. The solid and dashed lines show the IRX-β relation for local starburst galaxies Meurer et al. (1999) and local *normal* star-forming galaxies Muñoz-Mateos et al. (2009), respectively. The triangles depict the candidates to quiescent galaxies. These are color coded according to their redshift. The gray and black dots depict sources detected in MIPS 24μm (F(24)$>$60μJy) with $\log$M$>$10.5$M_{\odot}$ and having L$_{IR}<10^{12}$L$_{\odot}$ and L$_{IR}>10^{12}$L$_{\odot}$ (ULIRGS), respectively. The values in the rightmost axis are based on the IRX-A(FUV) relation of Buat et al. (2005) for starburst galaxies. The values of A(FUV) are converted to A(V) using the extinction curve of Calzetti et al.(2001). The right panel of Figure 5.5 shows the attenuation in the V-band obtained from best fitting optical template (i.e., the extinction applied in the modeling of the template) versus the UV slope. The colored markers are the same as in the left panel of the Figure. The candidates to quiescent galaxies with sSFR$_{\mathrm{corr}}$ $\gtrsim$-10.5 yr^{-1}, after correcting the SFR$_{UV}$ for extinction using the model A(V) are depicted as colored markers above grey circles. The solid and dashed black

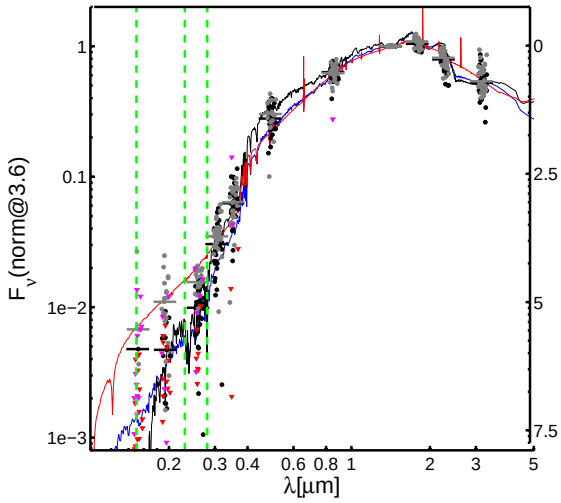

Figure 5.6: Rest-frame SEDs of the candidates to quiescent galaxies at 1.5<z<2.5 normalized at 1.6 μm. The black and red markers depict the observed flux and forced detections (<3σ) in multiple bands for galaxies with β >1.5. The grey and magenta markers depict the same kind of photometric measurements but for galaxies with β <1.5. The solid lines show the best fitting templates to some of these galaxies featuring different properties but similar colors in some regions of the spectra: an old galaxy (t$\sim$9Gyr) with super-solar metallicity (x2.5$Z_{\odot}$) and A(V)=0.7 mag (black line); an old galaxy (t>9Gyr), sub-solar metallicity (x0.005$Z_{\odot}$) and A(V)=2 mag (red line); an old galaxy (t=9Gyr), solar metallicity and A(V)=0.5 mag (blue line). The green lines depict the central wavelength of the FUV, NUV bands and 2800 Årest-frame (the flux at this wavelength is used to compute SFR_{UV})

lines depict the relations by Meurer et al.(1999) and Salim et al. (2007). Note that in the latter the attenuation *saturates* for β>0, i.e., in their local sample galaxies redder than this slope do not present higher extinctions.

Both panels show that MIPS 24 μm detected sources (black and grey markers) follows (or slightly exceed in the case of ULIRGs) the IRX-β relation of Meurer et al. (1999) quite nicely. Approximately 1 σ (68.1%) of these galaxies are confined within β =-0.6-1.02, i.e, we find no evidence of highly enshrouded, UV opaque galaxies with extremely high values of β >>, i.e, whose SED are fitted to very red galaxy templates. Thus, we expect that, as it happens with local galaxies, past some red color, the UV-slope is no longer tracing large amounts of dust, but older stellar populations (see e.g. Cortese et al. 2008).

If the UV color of the candidates with β >>1 is entirely caused by dust these would extremely IR-luminous galaxies. Hence the most likely possibility is that these are quiescent galaxies. On the contrary, we can not rule out the moderate starburst scenario for candidates at $\beta\sim$0.5 given the uncertainty in estimated β or the detection limit in MIPS 24 μm. Nonetheless, the fact that we are not picking up these sources in MIPS even at 2 σ suggest that β could be redder. Attending to the left panel of Figure 5.5 it seems that galaxies with $\beta \gtrsim$1 present a transition in the extinction trend, with the attenuation dropping abruptly from the highest values (A(V)>2.5) to the lowest (A(V)<0.5) ones. A change in the extinction properties of the reddest galaxies is consistent with a migration from the blue-cloud to red-sequence. At $\beta \sim$0-1 dusty galaxies and passive galaxies (in terms of A(V)) coexist in the green valley with a similar density, whereas for $\beta \gtrsim$1, the galaxies transit completely into the red-sequence, entering a domain where the fraction of dusty-to-passive galaxies decreases significantly. See, e.g, a similar argument by Brammer et al.(2009) based on very accurate A(V) estimates derived from narrow-band photometry.

Note that, following a similar reasoning as for the quiescent candidates with $\beta >> 1$, there are some galaxies for which the model extinction A(V) is clearly overestimated (those above the red line in the right panel of Figure 5.5). A detailed analysis of the SEDs and the estimated SFH and A(V) of the candidates to quiescent is galaxies is being conducted. This study would allow us to reduce the error in the estimated extinction values for galaxies with potentially uncertain values (e.g, at $\beta \sim 1$). Figure 5.6 shows an example of the observed and best fitting SEDs for the candidates to quiescent galaxies normalized at 1.6μm rest-frame. The black and red markers depict the reliable detections and limiting detections ($<3\sigma$) in multiple observed bands for galaxies with $\beta > 1.5$. The grey and magenta markers depict the same kind of photometric detections but for galaxies with $\beta < 1.5$. As it can be seen there are intrinsic differences in their observed fluxes of the two groups.

Once we obtain a reliable sample of quiescent galaxies we can compute the fraction of these galaxies relative to the total number of massive galaxies in the $1.5<z<2.5$ range, effectively quantifying the evolution of the stellar mass assembly for this galaxies, which are known to dominate the population of massive galaxies at low redshifts ($z \lesssim 1$). It would also be particularly interesting to check whether theoretical models agree with the observational evidences, comparing our results of purely semi-analytic models (e.g., Fontanot et al. 2007), semi-analytical dark-matter simulations (e.g., Millenium: Kitzbichler&White 2007) and hydrodynamical simulations (e.g., Nagamine et al. 2006). Although all models predict the decrease with cosmic time of the fraction of massive quiescent galaxies, this value is a particularly sensitive constraint (particularly at $z>2$) and thus it is a robust method to emphasize the differences between them, and consequently the differences in the intrinsic mechanisms that regulate the star-formation in each of them.

6

Resumen, conclusiones y trabajo futuro

En esta tesis se ha presentado un catálogo fotométrico multi-banda para fuentes seleccionadas en IRAC-3.6-4.5μm en el campo cosmológico EGS (**Capítulo 2**). Este catálogo contiene una gran cantidad de datos fotométricos cubriendo el rango espectral desde el UV hasta el infrarrojo lejano, lo que nos permite caracterizar la SED de las galaxias con el nivel de la consistencia necesario para para analizar en detalle sus propiedades físicas intrínsecas. Basandonos en este extepcional conjunto de datos hemos podido realizar un ajuste individualizado de la fotometría multi-longitud de onda a modelos de poblaciones estelares y de emisión de polvo, obteniendo de ellos *redshifts* precisos, masas estelares y SFRs junto con otras propiedades de las galaxias (**Capítulo 3**). Hemos explicado en detalle los métodos utilizados para ajustar los datos fotométricos a los modelos de síntesis de poblaciones estelares y a los *templates* de emisión de polvo, y se ha discutido en detalle las incertidumbres asociadas a la estimación de los parámetros físicos a partir del ajuste de SEDs. Además, el catalogo fotométrico, junto con los *redshift* fotométricos y los parámetros estelares presentados en esta tesis han sido puestos a disposición pública. Para ello, hemos desarrollado un interfaz web llamado *Rainbow Navigator*, que proporciona acceso completo a los datos de imagen y a parámetros estimados, permitiendo además otras funcionalidades para el manejo de datos.

En el contexto de los estudios de evolución de las galaxias, nuestro catálogo ofrece una muestra auto-consistente con una caracterización muy detallada de las incertidumbres sistemáticas, lo que lo convierte en una herramienta apta para múltiples fines científicos. Como se ha discutido ampliamente en esta tesis, contar con un gigantesco volumen de datos para miles de galaxias a diferentes épocas del Universo proporciona una base sólida para llevar a cabo estudios científicos centrados en diferentes objetivos. En particular, en el **Capítulo 4** se han aprovechado estos datos para llevar a cabo un análisis detallado de las funciones de luminosidad de galaxias a z$<$1 midiendo la contribución relativa de cada una de estas poblaciones de galaxias a distintos *redshifts* a las cuentas de galaxias en banda K. En el **Capítulo 5** se presenta un resumen de los resultados mas importantes obtenidos en varios trabajos científicos diferentes en los cuales he colaborado. Todos ellos hacen un uso exhaustivo de los recursos multi-longitud de onda presentados en el **Capítulo 2 y 3**. Entre estos trabajos se incluyen, estudios sobre la evolución de la SMD, las propiedades de galaxias AGNs e IRX seleccionados con diferentes métodos, o una caracterización de la evolución de las galaxias mas masivas a z$\sim$2.

A continuación se resumen los resultados más importantes y las conclusiones obtenidas en cada capítulo de esta tesis.

En el **Capítulo 2** presentamos una muestra de galaxias caracterizada con fotometría multi-longitud de onda seleccionada en IRAC-3.6-4.5μm en el campo EGS. Dicha muestra contiene 76,936 galaxias con [3.6]$<$23.75 (85% de completitud) cubriendo una superficie de 0.48 deg^2. Las

fuentes están caracterizadas con fotometría en las bandas FUV NUV $u^*g'r'i'z'$ $u'gRiz$ BRI $V_{606}i_{814}$ $J_{110}H_{160}$ JK [3.6]-[8.0]. Además, estos datos se han cruzado los datos disponibles en rayos X, infrarrojo lejano de *Spitzer*/MIPS 24 μm y 70 μm, y radio en VLA-20 cm. Además, *redshifts* espectroscópicos muy fiables para 7636 fuentes, han sido obtenidos a través de los catálogos de los *surveys* de DEEP2 y de Steidel et al. (2003; LBGs).

Se realizó una extracción cuidadosa de las fuentes IRAC disponibles en el mosaico del campo EGS limitándonos exclusivamente a las regiones con tiempos de exposición mas altos (t>4 ks) y eliminando aquellas detecciones espurias mediante mascaras alrededor de estrellas brillantes. Validamos la calidad del catálogo IRAC mediante la comparación de nuestros resultados fotométricos con el catálogo publicado en Barmby et al. (2008), encontrando un buen acuerdo de ambas magnitudes ($\lesssim 0.05$ mag) y en sus incertidumbres.

Utilizando nuestro procedimiento fotométrico personalizado (*Rainbow*) se realizo un correlación cruzada de la muestra IRAC con todos los otros datos fotométricos. A partir de estos resultados se obtuvo una fotometría consistente basada en mediciones en aperturas fijas, para un amplio rango de bandas fotométricas tomadas desde telescopios terrestres y espaciales con diferentes profundidades y resoluciones. Algunas de las características más relevantes de nuestro método son: la re-calibración de la solución astrométrica local para mejorar el correlación cruzada, la de-convolución de fuentes de IRAC no resueltas, las mediciones de flujo forzadas y los límites superiores para fuentes muy débiles. Debido a la cobertura inhomogena del mosaico IRAC, el catálogo final se compone de dos áreas complementarias, la principal (0.35 deg^2) y la adyacente (0.13 deg^2), que cuentan con una cobertura promedio de 19 y 11 bandas observadas, respectivamente.

En este capítulo también se presenta el interfaz web *Rainbow Navigator* que permite acceder a la base de datos con todos los datos presentados en esta tesis. El interfaz permite además el acceso a los datos mediante consultas personalizadas sobre los datos fotométricos y los parámetros derivados, y esta disponible online para toda la comunidad científica.

Las principales conclusiones de este capítulo son las siguientes:

- Aproximadamente un $\sim$16% de los objetos seleccionados en IRAC-3.6 μm hasta [3,6] $<$ 23.75 presentan confusión de fuentes con al menos dos contra-partes en las imágenes ópticas/NIR. No obstante, fotometría de precisión (0.03-0.10 mag) puede obtenerse mediante el uso de fotometría de apertura.

- Cerca de un 20$\%$ y 2 $\%$ de las fuentes IRAC-3.6 μm seleccionadas hasta [3.6]$<$ 23.75 son detectadas en MIPS 24 y 70 μm (f(24)>60 μJy, f(70)>3500 μJy), respectivamente. Independientemente, cerca del 20$\%$ y el 54$\%$ de las fuentes detectadas en MIPS 24 y 70 μm presentan varias contrapartidas en la imagen IRAC (normalmente 2-3).

- La probabilidad de detección de las fuentes de IRAC ([3.6]$<$23.75) en otras bandas es alta: más del 85% de las fuentes se detectan (con SNR $>$ 5) en los datos ópticos mas profundos (bandas R$-$ o $i'-$) y el 70% en las imágenes en banda K_s mas profundas (MOIRCS). Las detecciones fotométricas forzadas, especialmente desarrolladas para este trabajo, son capaces de recuperar un 10-20% de fuentes adicionales a niveles de significancia bajos ($<2\,\sigma$) en el imágenes menos profundas.

- Las fuentes débiles en IRAC son en promedio mas azules que las más brillantes para los colores óptico−IRAC. La mediana del color óptico/IRAC para las galaxias más débiles de la muestra ($22.50 < [3.6] < 23.75$) es de $R - [3.6] = 1.6$ y $i'-[3.6]$=1.4. Estos colores son similares a los de galaxias observadas estereoscópicamente a 1<z<1.5, lo cual es consistente con el hecho de que la mediana del *redshift* para la muestra seleccionada en IRAC es z∼1.

- Las galaxias presentan un color óptico−IRAC mas rojo para *redshifts* mayores debido a que las bandas ópticas tienden a desplazarse hacia el UV en reposo (que es mas débil) mientras que la magnitud [3.6] se vuelve más brillante al acercase al pico de la SED (a 1.6 μm en reposo) hasta z$\lesssim$1.2. Como consecuencia, la mediana del color en banda u^* ($u^*-[3.6]$=2.1) es más roja que en otras bandas ópticas. Por el contrario, el color $K-[3.6]$ presenta un valor casi constante en función de la magnitud [3.6], pero tiende a hacerse más rojo con el *redshift*: $K-[3.6]<0$ a z<0.5 y $K-[3.6]>0$ a z>1. Esto es consistente con el hecho de que tanto la banda K como [3.6] transitan por el pico de la SED a (a 1.6 μm en reposo) para *redshifts* menores que z<1.

- Existe un número no despreciable de fuentes débiles en IRAC pero ópticamente brillantes con detecciones en más de 19 bandas fotométricos (∼37% de las fuentes con $[3.6] > 23.75$). Estos objetos constituyen una población de galaxias enanas azules un *redshift* intermedio que son fáciles de detectar en el óptico, pero con contrapartidas débiles en IRAC (es decir, no muy masivas). Además un ∼3% de las galaxias de la muestra con [3.6]<23.75, son detectadas exclusivamente en las bandas de IRAC. Estas galaxias son probablemente objetos a alto *redshift* u objetos muy oscurecidas a *redshifts* mas bajos.

En el **Capítulo 3** presentamos un ajuste galaxia por galaxia de las SED observadas desde el UV hasta el infrarrojo lejano presentadas en el **Capítulo 2**. A partir de los resultados del mejor ajuste se han estimado: (1) *redshifts* fotométricos, (2) masas estelares, y (3) SFRs. Los *redshifts* fotométricos ($z_{\rm PHOT}$) se estimaron a partir de la comparación de las SEDs con modelos de poblaciones estelares y *templates* de AGN. Esta comparación se llevó a cabo usando nuestro propio software dedicado (dentro del paquete de programas *Rainbow*) consistente en un algoritmo de minimización de χ^2. Se obtuvieron también masas estelares para todas las galaxias de la muestra mediante el ajuste de la SED desde el óptico al NIR con modelos de síntesis de poblaciones estelares. Además, se analizaron los efectos en nuestras estimaciones de la elección de diferentes bibliotecas de síntesis de poblaciones estelares (SPS del ingles Stellar Population Synthesis), IMFs y leyes de extinción del polvo. Se estimaron SFRs para todas las galaxias de nuestra muestra siguiendo una serie de procedimientos centrados en el análisis de las SFR infrarrojas (IR-SFRs) obtenidas mediante el ajuste de la fotometría de infrarroja observada con *Spitzer*/IRAC y MIPS a 24 μm y 70 μm a diferentes *templates* de emisión de polvo. Se estudió la precisión de estas IR-SFRs mediante la comparación de los resultados obtenidos con diferentes métodos y varias configuraciones de datos observados. Además, se utilizaron magnitudes sintéticas (consistentes con las magnitudes observadas dentro de un factor $\times 2$ el error fotométrico) para seleccionar s-BzK, p BzK y DRG en la muestra IRAC hasta $K_{\rm VEGA}$<21.

Las principales conclusiones de este capítulo son las siguientes:

- Encontramos limitaciones específicas en los modelos SPS de Fioc & Rocca-Volmerange (1997) para reproducir la fotometría observada de galaxias. En particular, la comparación

entre las SED observadas y sintéticas (basados en el mejor de ajuste a los *templates*) revelan pequeñas desviaciones sistemáticas del orden del <10% en ciertas longitudes de onda. Las discrepancias más relevantes se aprecian en $\lambda > 3$ μm, y en menor medida en torno a 250 nm. Estas diferencias están probablemente asociadas con un exceso en la atenuación de polvo observada con respecto a ley de extinción de Calzetti et al. (2000) aplicada en los modelos.

- Los *redshifts* fotométricos para las fuentes de IRAC estimados a partir de SED consistentes en 11-19 flujos fotométricas diferentes presentan una precisión de $\sigma_{\rm NCMAD} \equiv 1.48 \times \mathrm{median}\left(\left|\frac{\Delta z - \mathrm{median}(\Delta z)}{1+z_{\rm spec}}\right|\right)$=0.034 (donde $\Delta z = z_{\rm phot} - z_{\rm spec}$) y $\sigma_{\rm NCMAD}$=0.046 en la región central y en la anexa, respectivamente. Ademas los *redshifts* presentan un η=2% y 3% de resultados catastróficos (definidos como la fracción de galaxias presenta $\sigma_{\rm NCMAD} > 0.2$) en cada uno de estos campos. La precisión de los $z_{\rm PHOT}$ es prácticamente independiente de magnitud en [3.6]. Sin embargo, esta disminuye con la magnitud óptica pasando de $\sigma_{\rm NCMAD}$=0.030 a R =22, a $\sigma_{\rm NCMAD}$=0.060 a R= 25.

- La probabilidad de detección de la muestra seleccionada en IRAC ([3.6]< 23.75) es máxima en torno a z=0.8-1.0. Para z< 0.6 la detección de las fuentes está dominado por el volumen de observado, y mas allá de z>1.0, la probabilidad de detección disminuye exponencialmente hasta z=4. Alrededor de la mitad de la muestra se encuentra a z<0.9, 40% a z> 1, y 20% a z > 1.5. La mayor parte de las galaxias en este estudio (90%) se encuentran en z<2.

- La densidad de objetos en la muestra seleccionada en banda i' de Ilbert et al. (2006) (que solapa con el catálogo IRAC en la región principal) es de 25, 42 y 96 fuentes/arcmin^2 hasta magnitudes limite de $i' = 24$, 25 y 26.5 (siendo esta ultima la magnitud de las detecciones a SNR$\sim$5). La densidad de fuentes en la selección en IRAC es de $\sim$44 fuentes/arcmin^2 a [3.6]<23.75. Aunque ambos catálogos presentan densidades similares a [3.6]<23.75 y i' =25, la naturaleza de las galaxias seleccionadas en cada muestra es diferente. Encontramos que para la muestra de galaxias brillante en el óptico pero no detectadas en IRAC ([3,6]>23.75) la mediana y cuartiles del *redshift* es $z_{\rm phot}$ $=1.0^{1.3}_{0.6}$, mientras que para las galaxias brillantes en el infrarrojo no detectadas en el óptico ($i'>$ 26,5) los valores son de $z_{\rm phot}$ $=1.8^{1.1}_{2.3}$. Las fuentes a alto z no detectadas en el infrarrojo son típicamente galaxias de baja masa (similares a LBGs), es decir, nuestro catálogo favorece la detección de galaxias masivas a alto *redshift*.

- Las 91 (147) LBGs con espectroscopía (Steidel et al. 2003) a [3.6]<23.75 mag (24,75) identificadas en el catálogo IRAC son intrínsecamente débiles en las bandas de IRAC, el $\sim$50% y 20% de ellas son mas débiles [3.6]>23.75 y 24.75 mag, respectivamente. Las LBGs muestran además una clara dicotomía en el color [3.6]$-$R, siendo las fuentes rojas (R$-$[3.6]> 1.5) más brillantes en IRAC que las azules. La mediana de la magnitud IRAC y de los colores para las 155 LBGs fotométricas en la muestra IRAC es [3.6]=22.74, R-[3.6]=2.06 y [3.6]=23.80, R-[3.6]=0.88 para las galaxias rojas y azules, respectivamente, en buen acuerdo con los valores de Magdis et al. (2008). La mediana de su *redshift* fotométrico $\tilde{z}_{\rm phot}$=2.8$\pm^{0.4}_{0.6}$ es consistente con la mediana del *redshift* para la muestra espectroscópica ($\tilde{z}$=2.95) y con la anchura típica para distribución en *redshift* de las galaxias seleccionadas con el criterio LBG ($\tilde{z}$=3.0$\pm$0.3; Steidel et al. 2004, Reddy et al. 2005).

- El número de cuentas de galaxias s-BZK presenta una pendiente creciente hasta la magnitud límite de las observaciones, mientras que las p-BZK y DRG presentan una meseta en

sus cuentas de galaxias alrededor de $K_{\rm VEGA}$ $\sim$19 y 20, respectivamente. Las densidades numéricas y la mediana del *redshift* fotométrico para estas poblaciones son ρ =5.0 arcmin^2; $\tilde{z}$ =1.89 (s-BzK), ρ =0.5 arcmin^2; $\tilde{z}$ =1.85 (p-BzK) y ρ =1.4 arcmin^2; $\tilde{z}$ =2.47 (DRG), en buen acuerdo con los resultados de la literatura. La diferencia mas significativa en estos resultados es un exceso de un factor $\sim$1.5 en la densidad de s-BzKs, lo que podría estar relacionado con una sobre densidad de las galaxias a z$\sim$ 1.5.

- La distribución de las masas estelares en función del *redshift* para la muestra seleccionada en IRAC ([3.6]$<$ 23.75) muestra que un $\sim$90% de las galaxias presentan log(M)$>$10 M$_\odot$ a z$>$2.5. Esta estimación esta basada en los resultado obtenidos con nuestros valores de modelado por defecto, que son: los modelos SPS de PEGASE 2.0 (Fioc & Rocca-Volmerange 1997, P01), una IMF de Salpeter (1955; SALP) y una ley de extinción de Calzetti et al. (2000, CALZ01).

- El uso de las IMF de Kroupa (2001, KROU) y Chabrier (2003, CHAB) (en lugar de SALP) para la estimación de las masas estelares introduce unas desviaciones constantes en los valores resultantes. Para los modelos de Charlot & Bruzual (2009; CB09) encontramos: $\Delta\log$(M)[SALP-KROU]=0.19$\pm^{0.07}_{0.12}$ dex y $\Delta\log$(M)[KROU-CHAB]=0.04$\pm^{0.11}_{0.09}$ dex. Para los modelos de P01, la diferencia entre las masas obtenidas con las IMF de SALP o KROU depende de la masa, variando entre $\Delta\log$(M) = 0.03$\pm^{0.20}_{0.17}$ dex y $\Delta\log$(M)=0.13$^{0.19}_{0.21}$ dex para masas menores y mayores de log(M)=10 $M_\odot$, , respectivamente.

- El uso de diferentes códigos SPS para la estimación de las masas estelares causa desviaciones aproximadamente constantes los resultados estimados. Encontramos que las masas estimadas con los nuevos modelos de CB09 son ligeramente menores que aquellas obtenidas con la versión anterior de los modelos Bruzual & Charlot (2003, BC03); para la IMF de CHAB esta diferencia es de $\Delta\log$(M)[CHAB]=0.04$\pm^{0.28}_{0.15}$ dex. Las masas estelares estimadas con los modelos P01 son en promedio mayores que aquellas obtenidas con los modelos de CB09; para una IMF de KROU la diferencia es $\Delta\log$(M)[KROU]=0.15$\pm^{0.23}_{0.29}$ dex. Las estimaciones obtenidas con P01 son también mayores que aquellas basadas en los modelos SPS de M05; para una IMF de KROU la diferencia es $\Delta\log$(M)[KROU]=0.39$\pm^{0.36}_{0.28}$ dex. Encontramos también que esta diferencia es ligeramente menor para galaxias $\log$(M)$>$10 $\mathcal{M}_\odot$ ($\sim$0.30 dex). En resumen, las masas estelares calculadas con [P01, SALP, CAL01], son comparativamente las mas altas. No obstante, teniendo en cuenta todas la diferencias sistemáticas, la dispersión entre los resultados obtenidos con los diferentes modelos es dentro de un factor de 2-3.

- El uso de diferentes parametrizaciones para la ley de extinción del polvo tiene un impacto reducido en la estimación de las masas estelares para galaxias lejanas (z$\gtrsim$0.2). Los valores obtenidos con las leyes de extinción de CAL01 y Charlot & Fall (2000, CF00) presentan tan solo una pequeña desviación sistemática $\Delta\log$(M)[CAL01$-$CF00]=-0.03$\pm^{0.20}_{0.23}$ dex.

- Las SFRs estimadas a partir de la luminosidad infrarroja total (SFR$_{\rm TIR}$) calculada mediante el ajuste de los datos MIPS 24 μm a los modelos de Chary & Elbaz (2001, CE01) y Dale & Helou (2002, DH02) son consistentes dentro de un factor 2, presentando una diferencia máxima alrededor de z=1.5. Las estimaciones obtenidas con SFR$_{\rm TIR}$ y la relación empírica de Alonso-Herrero et al. (2006, SFR$_{\rm A-H06}$) para la luminosidad monocromática en 24 μm en reposo, son relativamente consistentes (ΔSFR$\sim-0.18\pm0.05$ dex) cuando la contribución de la tasa de formación estelar en el UV no oscurecido (SFR$_{UV,obs}$) es pequeña.

Los valores estimados con la calibración de Bavouzet et al. (2008, SFR_{B08}) para la luminosidad monocromatica en 8 μm en reposo, son sistemáticamente menores que los resultados obtenidos con SFR_{TIR} para SFR$>$20 $M_{\odot}yr^{-1}$ y z$>$1; por otro lado, los valores de SFR_{B08} son mayores para valores mas bajos de la SFR y el *redshift*. La diferencia excede un factor 5 para SFR$>$1000 $M_{\odot}yr^{-1}$. El acuerdo entre SFR_{TIR} y la SFR estimada a través del flujo observado en 24 μm usando la relación de Rieke et al. (2009, SFR_{R09}) es bastante pobre excepto a partir de *redshift* z$>$1.8 donde las discrepancias se reducen a un factor constante de 0.05 dex. Las razones de estas discrepancias se pueden encontrar en las diferentes emisiones relativas del polvo caliente y frio, y diferentes intensidades de la absorción de los silicatos y los PAH en los modelos de R09 frente a CE01 y DH02. Estas características pueden presentar diferencias de hasta un factor 5 entre modelos.

- Las SFRs infrarrojas estimadas con datos IRAC y MIPS a 8, 24 y 70 μm, SFR(8,24,70) presentan diferencias sistemáticas con respecto de los valores estimados usando solo MIPS 24 μm, SFR(24). A bajo *redshift*, la mediana del valor de SFR_{TIR} (y también SFR_{A-H06})) tiende a subestimar SFR_{TIR}(8,24,70) por 0.05 y 0.10 dex, respectivamente, con un *rms* de $\sim$0.2-0.3 dex. A *redshift* z$\sim$2, la diferencia aumenta hasta un valor medio de $\sim$0.20 dex. SFR_{B08}(24) presenta la tendencia opuesta obteniendo valores mayores que SFR_{B08}(8,24,70) a z$\leq$1, pero siendo muy similar para *redshifts* mayores.

- El análisis de una muestra de galaxias en común con Symeonidis et al. (2008) y Huang et al. (2009), que cuentan con mas y mejores flujos fotométricos en el infrarrojo lejano y (sub)-mm, indica que para las galaxias a z$<$ 1.2, SFR_{TIR}(8,24,70) tiende a subestimar la SFR de las galaxias detectadas en MIPS 160 μm con una diferencia promedio de 0,09 dex. Discrepancias aun mayores, hasta 0.5 dex, pueden aparecer para galaxias concretas debido al uso de distintos *templates* de emisión del polvo para ajustar la SED infrarroja.

Los resultados presentados en estos dos Capítulos constituyen el grueso de esta tesis, cuyo principal objetivo es la creación de catalogo multi-longitud de onda exhaustivo que nos permita a la vez obtener SEDs muy detalladas y propiedades físicas precisas para miles de galaxias en un amplio rango de *redshift*. Como se ha mencionado en esta tesis, los catálogos de este tipo son la piedra angular de la mayoría de los estudios de evolución de galaxias basados en grandes muestras de fuentes extragalácticas, y el catálogo presentado en esta tesis es uno de los pocos ejemplos que pone a disposición de la comunidad astrofísica una compilación consistente de fotometría (SEDs) y propiedades físicas (*redshifts*, masas, SFRs y más). Por último, pero no por ello menos importante, se ha realizado un esfuerzo considerable para mejorar las posibilidades de explotación de todos estos recursos incluyendo todos los resultados de este trabajo en una base de datos (*Rainbow*) y creando un interfaz web que permite multiples posibilidades de acceso a los datos (*Rainbow Navigator*).

Ejemplos específicos de la explotación de catálogos multi-longitud se han descrito en los Capítulos 4 y 5. En particular, el **Capítulo 4** describe en detalle un estudio basado en estos datos que se ha llevado a cabo como parte de esta tesis; por otro lado, el **Capítulo 5** presenta los resultados más relevantes de una recopilación de varios trabajos en los que he colaborado y que hacen un uso extensivo del catálogo presentado en los Capítulos 2 y 3. Este capítulo contiene también una breve introducción al trabajo en curso que se llevando a cabo actualmente para aprovechar las posibilidades del catálogo multi-longitud de onda.

El **Capítulo 4** se centra en una cuestión científica más concreta mediante el estudio de la naturaleza de las cuentas de galaxias (NCs) en la banda-K. Este trabajo se basa en la explotación de un catalogo multi-longitud de onda seleccionado en la banda K en los campos cosmológicos EGS y HDFN caracterizado con *redshifts* y luminosidades en reposo muy precisas calculadas siguiendo los procedimientos descritos en los capítulos 2 y 3. En base a estas propiedades se realizo un estudió de la contribución relativa de las galaxias a diferentes redshifts a las cuentas de galaxias en la banda K. Además, se obtuvieron funciones de luminosidad (LFs) que nos permitieron explicar las características observadas en la forma de las NCs en base a las características fundamentales de las poblaciones de galaxias a diferentes *redshifts*.

Las principales conclusiones de este capítulo son las siguientes:

- Para magnitudes $K > 18.5$ las NCs tienden a ser una mezcla de galaxias a *redshifts* muy diferentes. En particular, encontramos una contribución creciente de galaxias a alto *redshift* (z>1.5) que no se observan a magnitudes mas brillantes, donde las galaxias a bajo *redshift* (z<1) constituyen la mayor parte (90%) de las NCs. Para K <16, las NCs muestrean la parte brillante de la LF a z<1 lo que hace que los valores observados sean muy sensibles a efectos de volumen y de estructura a gran escala. Por debajo de z<0.25 la contribución de las galaxias a las NCs es prácticamente despreciable (<10%). Las NCs estimadas en áreas relativamente pequeñas (∼100 arcmin^2) pueden presentar diferencias campo-a-campo de hasta un 40$\%$ dependiendo de la magnitud, lo que puede afectar sensiblemente a la forma de las NCs.

- La pendiente de las NCs en la banda K disminuye un $\sim 50\%$ en el intervalo de magnitudes $15.5 < K < 18.5$, produciéndose una variación en el valor de la pendiente de $d\log N/dm = 0.6 - 0.3$. La comparación de 100 catálogos sintéticos a partir de la simulación *Millenium* muestra que la varianza cósmica en áreas de ∼0.25 deg^2 puede causar una dispersión significativa en la variación observada en la pendiente de las NCs.

- La composición de las NCs en términos de LFs (como bloques constituyentes) indica que el cambio en la pendiente de las NCs con la magnitud observada se puede describir en tres regímenes principales: 1) a magnitudes brillantes, el régimen Euclideo clásico ($d\log N/dm = 0.6$) dominado por galaxias a bajo *redshift* con luminosidades M^*; 2) a magnitudes intermedias, el régimen de transición, dominado por la LF al *redshift* que maximiza la función producto $\phi^* \frac{dV_c}{d\Omega}$. Aquí la pendiente disminuye rápidamente alrededor de la magnitud aparente correspondiente al M^* en ese *redshift*, 3) a magnitudes débiles, el régimen-α, poblado principalmente por galaxias en el extremo débil las LFs a varios *redshifts*. En este intervalo la pendiente varía asintoticamente hacia un valor de ∼-0.4(1+α). Donde el valor de α será típicamente el de la LF al redshift que maximiza $\phi^* \frac{dV_c}{d\Omega}$ o una LF a un redshift próximo con un valor de α sensiblemente mayor.

- Se obtuvieron LFs en la banda K observada para diferentes *redshifts* (a una longitud de onda en reposo de $2.16\mu m/(1+\bar{z})$) con las siguientes características:
(z=0.25-0.50) $\phi^*_{K,obs}$ =3.4$\pm^{2.10}_{1.70}\times 10^{-3}$Mpc^{-3} $M^*_{K,obs} = -22.95$(fixed) $\alpha_{K,obs} = -1.15\pm^{0.20}_{0.20}$
(z=0.50-0.75) $\phi^*_{K,obs}$ =3.4$\pm^{0.22}_{0.18} \times 10^{-3}$Mpc^{-3} $M^*_{K,obs} = -23.01\pm^{0.13}_{0.12}$ $\alpha_{K,obs} = -1.00\pm^{0.18}_{0.23}$
(z=0.75-1.00) $\phi^*_{K,obs}$ =3.2$\pm^{0.17}_{0.24} \times 10^{-3}$Mpc^{-3} $M^*_{K,obs} = -23.08\pm^{0.14}_{0.12}$ $\alpha_{K,obs} = -1.02\pm^{0.19}_{0.17}$
(z=1.00-1.25) $\phi^*_{K,obs}$ =2.3$\pm^{0.31}_{0.26} \times 10^{-3}$Mpc^{-3} $M^*_{K,obs} = -22.96\pm^{0.28}_{0.26}$ $\alpha_{K,obs} = -0.93\pm^{0.23}_{0.29}$

- En términos de estas LFs y otros valores de la literatura, encontramos que el aplanamiento de la pendiente es consecuencia de una disminución importante de la densidad característica $\phi^*_{K,obs}$ ($\sim 60\%$ de $z = 0.5$ a $z = 1.5$) y una evolución prácticamente nula de $M^*_{K,obs}$ (compatible a 1σ con $M^*_{K,obs} = -22.89 \pm 0.25$). La combinación de ambos efectos causa la transición al régimen α de la pendiente a K ∼17.5, un evento que de otro modo habría tenido lugar a $K = 20 - 21$ mag.

- Las predicciones para las NCs a $K \gtrsim$20 basadas en la LFS de la literatura, sugieren que la pendiente sigue disminuyendo asintoticamente hasta $d \log N/dm \lesssim$0.2 dominada por galaxias intrínsecamente débiles en un intervalo de *redshift* z=1.5-2 y con una contribución menor de galaxias brillantes a z$>$ 2. No obstante, si las LFs ópticas a $z > 3$ presentan un valor de la pendiente débil de la LF mayor de lo estimado, como sugieren algunos autores, podría producirse un incremento en el valor de pendiente hasta un valor asintótico mayor alrededor de $K \gtrsim 22.5$.

Como se mencionó anteriormente, el capítulo 5 contiene un breve resumen de las principales conclusiones de varios trabajos en los que he colaborado. Como estos no se han discutido en detalle como parte de esta tesis no se incluye aquí una descripción detallada de los principales resultados. Sin embargo, queremos subrayar que el objetivo principal de dicho capítulo es poner de relieve las amplias posibilidades científicas de catálogo cuya descripción constituye la mayor parte de esta tesis, y sin el cual estos trabajos no se podrían haber llevado a cabo.

6.1 Trabajo futuro

En esta sección se describen algunos de los temas más interesantes que nos permitirán continuar y ampliar los resultados presentados en esta tesis. Algunos de ellos son ya proyectos en curso.

Como se describe en la sección final del capítulo 5, ya existe un proyecto en desarrollo cuyo objetivo es ampliar los resultados obtenidos en Pérez-González et al. (2008) mediante la obtención de una muestra muy precisa de galaxias masivas quiescentes en el intervalo de *redshift* 1.5$<$z$<$2.5 con la que caracterizar la densidad de fuentes tanto absoluta como relativa a otras galaxias masivas activas. Este proyecto sera mi objetivo prioritario durante los próximos meses.

Relacionado con este tema, nuestro interés en el estudio de estas galaxias quiescentes nos llevó a proponer el proyecto SHARDS (Survey For High Redshift Red And Dead Sources). Dicho *survey* es un proyecto ESO/GTC cuyo propósito es llevar a cabo un estudio fotométrico de las galaxias quiescentes en el intervalo de *redshift* 1.0$<$z$<$2.5 mediante la medición directa de una intensa línea de absorción presente en el espectro UV en reposo de las galaxias de este tipo. Los resultados obtenidos con este *survey* serán directamente complementarios con los obtenidos en nuestro actual trabajo en desarrollo sobre galaxias quiescentes. Este estudio hace uso de 25 filtros de anchura intermedia (FWHM$\sim$ 17 nm) en GTC/OSIRIS que cubren el rango en longitud de onda entre 5000 y 9500Å lo que nos permite explorar en detalle el rango UV de las galaxias en el rango de *redshift* de interés. SHARDS ya está observando el campo HDFN y ha obtenido alrededor del ∼20% del total de los datos. Junto al proyecto descrito anteriormente, este *survey* será mi prioridad a medio plazo.

Existen propiedades fundamentales de estas galaxias que no podemos estudiar a partir de los datos disponibles en la actualidad y que serian de gran importancia para mejorar significativamente su caracterización. De estos datos, los mas relevantes serían su cinemática (velocidad de dispersión) y su morfología. La combinación de estos dos datos permitiría verificar con exactitud las masas estelares estimadas con datos fotométricos y confirmar la sorprendente compacidad estas galaxias. Para medir estas propiedades se requiere espectroscopia muy profunda e imagen de alta resolución en una banda fotométrica que muestree el óptico en reposo de estos objetos (es decir, el NIR observado). Estudios recientes han demostrado que la espectroscopia óptica es posible (aunque muy costosa en tiempo de observación) para los objetos mas brillantes a z$\sim$1.5 (Newman et al. 2010). Del mismo modo, la espectroscopia IR ofrecería la posibilidad de ampliar este estudio a *redshifts* mas altos z$>$ 1.5 (Onodera et al. 2010; Van Dokkum et al. 2009). En este sentido, podemos aprovechar las posibilidades de GTC/OSIRIS, Gemini Flamingos II o GTC/EMIR (en el futuro) para la obtención de espectroscopia multi-objeto de estas galaxias tanto en el óptico como en el NIR. Los datos espectroscópicos se pueden complementar con las imágenes del *survey* mas profundo y de mejor resolución que esta siendo llevado a cabo con *HST*/WFC3 en los campos cosmológicos mas importantes, incluyendo EGS.

La excelente calidad de los datos NIR de WFC3 también nos permitiría seguir un proyecto muy interesante basado en los resultados obtenidos con el catálogo IRAC presentado en esta tesis. Este proyecto consistiría en la caracterización del $\sim$3% de las fuentes que sólo se detectan en las bandas de IRAC, pero que probablemente se detectarían en otras imágenes NIR muy profundas. Aunque es difícil de precisar debido a los pocos datos disponibles, estas fuentes son candidatos interesantes a galaxias masivas a z$>$3 (ver por ejemplo, Mancini et al. 2009; Marchesini et al. 2010) o incluso *redshifts* mas altos (aunque estos serian también muy débiles en IRAC; ver por ejemplo Labbe et al. 2010).

Otro tema interesante que puede aumentar significativamente nuestro conocimiento sobre el proceso de formación y evolución de galaxias es la precisión en nuestras estimaciones de las SFRs para galaxias a alto *redshift*, sobre todo aquellas basadas en datos IR. Como hemos discutido en esta tesis, el principal problema en nuestra comprensión actual de las SFR basadas en datos IR para galaxias a z$\gtrsim$2 es en realidad la falta de datos suficientes para acotar con precisión la forma de la SED en el infrarrojo, y particularmente en longitudes de onda (sub)mm y radio donde estos datos nos permitirían determinar con mas precisión la posición del máximo de la emisión infrarroja (alrededor de $\sim$100 μm en reposo). Aunque las observaciones actuales en estas longitudes de onda existen, los catálogos de fuentes se limitan tan sólo a unos pocos objetos (en comparación con los datos MIPS 24 μm) y suelen estar afectados por un alto nivel de confusión de fuentes debido a la baja resolución. En este sentido, los datos que empiezan a llegarnos desde el observatorio espacial *Herschel* (Pilbratt et al. 2010) nos ayudarán a llenar el vacio existente entre los datos MIPS y los datos (sub)mm/radio mejorando además tanto la sensibilidad como la resolución. En el futuro, revisaremos las estimaciones de SFRs obtenidas en esta tesis, que se basan fundamentalmente en datos *Spitzer*/MIPS, incluyendo en el nuevo análisis los flujos disponibles en *Herschel* que incluyen hasta 5 bandas fotométricas diferentes en el infrarrojo lejano: PACS 100 y 160 μm, y SPIRE 250, 350, y 500 μm. (ver por ejemplo en Pérez-González et al. 2010 o Elbaz et al. 2010 el tipo de mejora que se puede alcanzar).

6

Summary, conclusions and future work

In this thesis we have presented a multi-band photometric catalog for IRAC-3.6+4.5 μm selected sources in the EGS (Chapter 2). This catalog contains extensive UV-to-FIR data that allow us to characterize the SEDs of the galaxies with the level of consistency required to analyze in detail their intrinsic physical properties. Thus, based on this exceptional dataset we have been able to perform a galaxy-by-galaxy fitting of the multi-wavelength data to stellar population and dust emission models, obtaining accurate photometric redshifts, stellar masses and SFRs along with other properties of the galaxies (Chapter 3). We have explained in detail the methods used to fit the photometric data to stellar population synthesis models, and dust emission templates, and we have discussed at length the systematic uncertainties associated to the physical parameters estimated from the SED fitting. In addition, the multi-band photometric catalog jointly with the photometric redshifts and estimated stellar parameters presented here has been made publicly available. To that end, we have developed a web-interface, named *Rainbow Navigator*, that provides full access to the imaging data and estimated parameters and allows several other data handling functionalities.

In the context of studies of galaxy evolution, our catalog provides a self consistent sample with a very detailed characterization of the systematic uncertainties, suitable for multiple scientific purposes. As extensively discussed in this thesis having a colossal body of data for thousands of galaxies at different epochs of the Universe provide a solid ground for further scientific studies aimed at different goals. In particular, in Chapter 4 we have exploited these data products to carry out an analysis of the luminosity functions of z$<$1 galaxies measuring the relative contribution of these galaxy populations at different redshift to the observed K-band number counts. Chapter 5 presents a summary of the most important results obtained in several different papers in which I have collaborated, that makes extensive use of the multi-wavelength resources presented in Chapter 2 and 3. These include, studies of the evolution of the SMD, the properties of AGNs and IRX galaxies selected with different methods, or a characterization of the evolution of massive galaxies at z$\sim$2.

In the following we summarize the most important results and conclusion obtained in each Chapter of this thesis.

In Chapter 2 we presented an IRAC-3.6+4.5μm selected catalog in the EGS characterized with multi-wavelength photometry. The sample contains 76,936 galaxies with [3.6]$<$23.75 (85$\%$ completeness of the sample) covering an area of 0.48 deg^2. The sources are characterized with FUV NUV $u^*g'r'i'z'$ $u'gRiz$ BRI $V_{606}i_{814}$ $J_{110}H_{160}$ JK [3.6]-[8.0] photometry. In addition, we have cross-correlated the sample with X-ray data, *Spitzer*/MIPS 24 μm and 70 μm FIR photometry, and VLA-20cm radio data. Secure spectroscopic redshifts are also included in the catalog for 7,636 sources, obtained from the DEEP2 Survey and Steidel et al. (2003; LBGs).

We performed a careful extraction of the IRAC sources limiting the sample only to the regions with high exposure times (>4 ks), and removing spurious detections by masking areas around bright stars. The quality of the IRAC catalog was validated by comparing our results with the catalog of Barmby et al. (2008), finding good agreement in both magnitudes ($\lesssim$ 0.05 mag) and uncertainties.

Using our custom photometric procedure *Rainbow* we cross-correlated the IRAC sample with all other photometric data measuring consistent aperture matched photometry for a wide range of ground− and space− based observations, with different depths and resolutions. Some of the most relevant characteristics of our method include: a re-calibration of the local astrometric solution to improve the cross-match, a de-convolution of IRAC blended sources or obtaining (forced) flux measurements and upper limits for faint sources. Due to the inhomogeneous coverage of the IRAC mosaic, the final catalog comprises two complementary areas, the main (0.35 deg^2) and flanking (0.13 deg^2) regions which count with an average coverage of 19 and 11 observed bands, respectively.

In this Chapter we also presented a publicly available web-interface, *Rainbow Navigator*, to the database containing all the data presented in this thesis. The interface allows the access to the data using customizable queries on the photometry and derived parameters.

The main conclusions of this chapter are as follows:

- A ∼16% of the IRAC-3.6 μm selected sources up to [3.6]<23.75 are blended, presenting at least 2 counterparts in optical/NIR ground based images. IRAC photometry with an accuracy of 0.03-0.10 mag can be obtained using aperture photometry.
- Nearly 20% and 2% of the IRAC-3.6 μm selected sources up to [3.6]<23.75 are detected in MIPS 24 and 70 μm data (f(24)>60 μJy, f(70)>3500 μJy), respectively. Independently, about 20% and 54% of the sources detected in MIPS 24 and 70 μm present a multiple IRAC counterparts (typically 2-3).
- The detection probability of IRAC sources ([3.6]<23.75) in other bands is high: more than 85% of the sources are detected (with SNR>5) in the deepest optical data (R- or i'-bands) and 70% in the deepest (MOIRCS) K_s-band images. The *forced* photometric measurement developed in this work is able to recover a 10–20% additional sources in the shallowest images at the lowest significance levels (<2 σ).
- Faint IRAC sources are on average bluer in optical−IRAC colors than brighter ones. The median colors for the faintest galaxies in the sample (22.50<[3.6]<23.75) are R−[3.6]=1.6 and i'−[3.6]=1.4. These colors are similar to those of spectroscopic galaxies at 1<z<1.5, which is consistent with the fact that the median redshift of the IRAC sample is z∼1.
- Galaxies present redder optical−IRAC colors with increasing redshifts due to the optical bands shifting into the (fainter) rest-frame UV whereas the [3.6] mag becomes brighter as it approaches the stellar bump (at 1.6 μm rest-frame) for z$\lesssim$1.2). As a consequence the median color in the u^* band (u^*−[3.6]=2.1) is redder than in other optical bands. On the contrary, the K−[3.6] color presents an almost constant value as a function of [3.6] mag but becomes redder for increasing redshifts: K−[3.6]<0 at z<0.5 and K−[3.6]>0 at z>1. This is consistent with the fact that both K and [3.6] transit through the peak of the stellar bump for z<1.

- There exist a non-negligible number of IRAC-faint but optically-bright sources with more than 19 photometric data points (37% at [3.6]>23.75). These constitute a population of blue dwarf galaxies at intermediate redshift easily detected in the optical but with faint IRAC counterparts (i.e., not very massive). In addition ∼3% of the galaxies in the sample with [3.6]<23.75 are exclusively but accurately detected in the IRAC bands only. These are probably very high redshift sources or highly obscured galaxies slightly lower redshifts.

In Chapter 3 we presented a galaxy-by-galaxy fitting of the UV-to-FIR SEDs of Chapter 2. From the best fitting results, we have estimated: (1) photometric redshifts, (2) stellar masses, and (3) SFRs. Photometric redshifts ($z_{\rm phot}$) were estimated from the comparison of the UV-to-NIR SEDs to stellar population and AGN templates. This comparison was carried out with our own dedicated software (within the *Rainbow* package) using a χ^2 minimization algorithm. Stellar masses for all galaxies in our sample were obtained by fitting the optical-to-NIR SEDs to stellar population synthesis models. In addition, we analyzed the effects of the choice of different stellar population synthesis (SPS) libraries, IMFs and dust extinction laws on our estimations. SFRs were estimated for all galaxies in our sample following a variety of procedures focusing on the analysis of the IR-SFRs obtained fitting the IR photometry taken by *Spitzer*/IRAC and MIPS at 24 μm and 70 μm to different dust emission templates. We studied the accuracy of these IR-SFRs by comparing the results obtained with different methods and data configurations. In addition, we used synthetic magnitudes (consistent with observed magnitudes within $\times 2$ the photometric errors) to select s-BzK, p-BzK and DRGs in the IRAC sample down to $K_{\rm VEGA}$<21.

The main conclusions of this chapter are as follows:

- There are specific limitations in the SPS models of Fioc & Rocca-Volmerange (1997) to reproduce the observed photometry of galaxies. The comparison between observed and synthetic (from the best-fitting templates) SEDs reveal small systematic deviations of a few percent level (<10%) at certain wavelengths. The most relevant discrepancies present at λ>3 μm and (to a lesser extent) around 250nm. These are probably associated with an excess in the strength of the dust attenuation with respect to a Calzetti et al. (2000) extinction law, respectively.

- Photometric redshifts for IRAC sources estimated from SEDs 11 to 19 different photometric fluxes present an overall accuracy of $\sigma_{\rm NCMAD} \equiv 1.48 \times {\rm median}\left(\left|\frac{\Delta z - {\rm median}(\Delta z)}{1+z_{\rm spec}}\right|\right)$=0.034 (where $\Delta z = z_{\rm phot} - z_{\rm spec}$) and $\sigma_{\rm NCMAD}$=0.046, with η=2% and 3% catastrophic outliers (η defined as the fraction of galaxies presenting $\sigma_{\rm NCMAD}$>0.2) in the main region and flanking regions, respectively. The accuracy of the $z_{\rm phot}$ is mostly independent of the [3.6] magnitude. However, it decreases with the optical magnitude from $\sigma_{\rm NCMAD}$=0.030 at R=22 to $\sigma_{\rm NCMAD}$=0.060 at R=25.

- The detection probability of the IRAC sample ([3.6]<23.75) peaks at around z=0.8-1.0. For z< 0.6, the detection of sources is dominated by the surveyed volume, and after z>1.0, the detection probability decreases exponentially up to z=4. About half of our sample lies at z<0.9, 40% at z>1, and 20% at z>1.5. The bulk of the galaxies in this study (90%) lie at z<2.

- The source density in the i'-band selected sample of Ilbert et al. (2006) (overlapping with the IRAC catalog in the Main region) present source densities of 25, 42 and 96 sources/arcmin^2

up to limiting magnitudes of i' =24, 25 and 26.5 (the estimated SNR∼5 level). The source density of the IRAC selected catalog is ∼44 sources/arcmin^2 at [3.6]<23.75. Even both catalogs presents similar source densities at [3.6]<23.75 and i' =25, the nature of the galaxies selected in each sample is different. We find that the optically bright galaxies missed by the IRAC catalog ([3.6]>23.75) present a median and quartile redshifts $z_{\rm phot}$ =$1.0^{1.3}_{0.6}$, while the infrared bright galaxies undetected in the optical (i'>26.5) present $z_{\rm phot}$ =$1.8^{1.1}_{2.3}$. The high-z sources missed in the IR selection are typically low-mass galaxies (similar to LBGs), i.e., our catalog favors the detection of high-z massive galaxies.

- The 91(147) spectroscopic LBGs (Steidel et al. 2003) with [3.6]<23.75 mag (24.75) identified in the IRAC catalog are intrinsically faint in the IRAC bands, ∼50% and 20% are fainter than [3.6]=23.75 mag and 24.75 mag, respectively. LBGs exhibit a clear dichotomy in the R-[3.6] color, with red (R−[3.6]>1.5) sources showing brighter IRAC magnitudes than blue sources. The median magnitudes and colors for the 155 photometric LBGs in the IRAC sample are [3.6]=22.74, R-[3.6]=2.06 and [3.6]=23.80, R-[3.6]=0.88 for red and blue galaxies, respectively, in good agreement with the values of Magdis et al. (2008). Their median photometric redshift $\tilde{z}_{\rm phot}$=$2.8\pm^{0.4}_{0.6}$ is consistent with the median redshift of the spectroscopic sample ($\tilde{z}$=2.95) and with the typical width of the redshift distribution for the LBG criteria ($\tilde{z}$=3.0±0.3; Steidel et al. 2004, Reddy et al. 2005).

- The differential number counts of s-BzK present a steep slope up to the limiting magnitude, whereas p-BzK and DRGs show a plateau around $K_{\rm VEGA}$∼19 and 20, respectively. The number densities and median $z_{\rm phot}$ of these populations are: ρ =5.0 arcmin^2; $\tilde{z}$ =1.89 (s-BzK), ρ =0.5 arcmin^2; $\tilde{z}$ =1.85 (p-BzK) and ρ =1.4 arcmin^2; $\tilde{z}$ =2.47 (DRG), in good agreement with the results from the literature. The most significant difference is an excess of ∼1.5 in the density s-BzKs, which could be caused by an overdensity of galaxies at z∼1.5.

- The distribution of stellar masses in the IRAC sample [3.6]<23.75 as a function of redshift, for our default modeling assumption, PEGASE 2.0 (Fioc & Rocca-Volmerange 1997, P01) stellar population synthesis models, a Salpeter (1955; SALP) IMF and the Calzetti et al. (2000, CALZ01) extinction law, shows that ∼90% of the galaxies with [3.6]<23.75 present log(M)>10M$_\odot$ at z>2.5.

- The use of the IMFs of Kroupa (2001, KROU) and Chabrier (2003, CHAB) (instead of SALP) for the estimate of stellar masses introduces constant offsets in the estimated stellar masses. For the models of Charlot & Bruzual (2009; CB09) we find: $\Delta\log$(M)[SALP-KROU]=$0.19\pm^{0.07}_{0.12}$ dex and $\Delta\log$(M)[KROU-CHAB]=$0.04\pm^{0.11}_{0.09}$ dex. For the models of P01, the difference for a SALP and KROU IMFs depends on the mass, ranging from $\Delta\log$(M) = $0.03\pm^{0.20}_{0.17}$ dex for masses lower than $\log$(M)=10 $M_\odot$ to $\Delta\log$(M)=$0.13^{0.19}_{0.21}$ dex above that threshold.

- The use of different SPS codes for the estimate stellar masses introduces constant offsets in the estimated stellar masses. We find that the new CB09 models predict slightly lower masses than the older version, Bruzual & Charlot (2003, BC03), by $\Delta\log$(M)[CHAB]=$0.04\pm^{0.28}_{0.15}$ dex. The stellar masses estimated with the P01 models are on average larger than those obtained with the CB09 models by $\Delta\log$(M)[KROU]=$0.15\pm^{0.23}_{0.29}$ dex. The stellar masses estimated with the P01 models are also larger than those obtained with the M05 models by $\Delta\log$(M)[KROU]=$0.39\pm^{0.36}_{0.28}$ dex. We found slightly lower values of this offset for galaxies with $\log$(M)>10 $\mathcal{M}_\odot$ (∼0.30 dex). In summary, the stellar masses computed with [P01,

SALP, CAL01], predicts comparatively the largest stellar masses. Accounting for all systematic offsets, all models are roughly consistent within a factor of 2-3.

- The use of different parametrization of the dust extinction law has little impact in the estimate of the stellar masses for distant galaxies (z$\gtrsim$0.2). The values estimated with a CAL01 and a Charlot & Fall (2000, CF00) extinction laws present a small systematic deviation $\Delta\log$(M)[CAL01$-$CF00]=-0.03$\pm^{0.20}_{0.23}$ dex.

- The IR-based SFRs estimated from the total IR-luminosity (SFR_{TIR}) and the fit of MIPS 24 μm data to the models of Chary & Elbaz (2001, CE01) and Dale & Helou (2002, DH02) are compatible within a factor of 2, presenting a maximum difference around z$\sim$1.5. The estimates of based on SFR_{TIR} and the empirical relation of Alonso-Herrero et al. (2006, SFR_{A-H06}) for the monochromatic luminosity at 24 μm rest-frame are roughly consistent (ΔSFR$\sim-0.18\pm0.05$ dex) when the contribution of the unobscured UV-SFR ($SFR_{UV,obs}$) is small. The values estimated with the calibration of Bavouzet et al. (2008, SFR_{B08}) for the monochromatic luminosity at 8 μm rest-frame gives systematically lower values than SFR_{TIR} for SFR$>$20 $M_{\odot}yr^{-1}$ and z$>$1, and higher values for lower redshifts and SFRs. The difference exceeds a factor of 5 for SFR$>$1000 $M_{\odot}yr^{-1}$. The overall agreement between SFR_{TIR} and the estimate based on the empirical relation for the observed flux at 24 μm of Rieke et al. (2009, SFR_{R09}) is rather poor, except at z$>$1.8 where the differences are lower than 0.05 dex. The reasons for these discrepancies can be found in the differences in the relative emission of the cold and warm dust, and in the strength of the PAH and silicate absorption. These characteristics can vary by up to a factor of $\sim$5 from one set of templates to the other.

- The IR-based SFR, estimated from IRAC+MIPS data at 8, 24 and 70 μm, SFR(8,24,70), and just MIPS 24 μm, SFR(24), data present systematic differences. At low-z, the median values of SFR_{TIR}(24) (also SFR_{A-H06}(24)) tend to underestimate SFR_{TIR}(8,24,70) by 0.05 and 0.10 dex, respectively, with an *rms* of $\sim$0.2-0.3 dex. At z$\sim$2, the difference increases up to an average value of $\sim$0.20 dex. SFR_{B08}(24) presents the opposite trend, estimating larger values than SFR_{B08}(8,24,70) at z$\leq$1 (up to 0.18 dex), but remaining mostly unchanged at higher redshifts.

- The analysis of a sample of galaxies in common with Symeonidis et al. (2008) and Huang et al. (2009), who counted with more photometric fluxes in the FIR and (sub-)mm range, indicates that, for galaxies at z$<$1.2, SFR_{TIR}(8,24,70) tend to underestimate the SFR of MIPS-160 detected galaxies by 0.09 dex. Larger discrepancies, up to 0.5 dex, might arise for individual galaxies due to the use of different template sets.

The results presented in these two Chapters constitute the bulk of this thesis whose main goal was the creation of a exhaustive multi-wavelength catalog simultaneously containing very detailed SEDs and accurate physical properties for thousands of galaxies in a wide range of redshifts. As mentioned in this thesis, catalogs like this are the cornerstone of most studies of galaxy evolution based on large samples of extragalactic sources, and the catalog presented in thesis is one of the very few examples making publicly available an integral compilation of both photometry (SEDs) and physical properties (photo-z's, masses, SFRs and more) for the whole scientific community. Last but not least, a significant effort has been made to enhance the most useful exploitation of these

resources including all these data into a database (*Rainbow*, and creating a web-based interface that allows multiple data handling possibilities (*Rainbow Navigator*).

Specific examples of the exploitation of multi-wavelength catalogs are described in Chapter 4 and 5. In particular: Chapter 4 described in detail a study that I have led as a part of this thesis; Chapter 5 presented the most relevant results from a compilation of several works in which I have collaborated and that makes extensive use of the catalog presented in Chapters 2 and 3. This chapter also contains a brief introduction to the current work that I'm carrying out to further exploit the possibilities of the catalog.

In Chapter 4 we focused in a more specific scientific question by studying the nature of the extragalactic NCs in the K-band. This work is based on the exploitation of a multi-wavelength K-band selected catalog in the EGS and the HDFN characterized with accurate photometric redshifts and rest-frame luminosities computed following the procedures described in Chapters 2 and 3. Based on these properties we studied the relative contribution of galaxies at different redshifts to the K-band NCs and we obtained LFs that allowed us to explain observed features in the shape of the NCs in terms of fundamental characteristics of the galaxy populations at different redshifts.

The main conclusions of this chapter are as follows:

- For K >18.5 the total number counts tend to become a mixture of very different redshifts ranges, with a growing contribution of high redshift galaxies (z>1.5) absent at brighter magnitudes, where low redshift galaxies (z<1) account for 90% of the total NCs. For K <16 the counts sample the bright part of the LFs at z<1, causing values to be highly sensitive to both volume effects and large scale structure. Below z<0.25 the averaged contribution of galaxies to the NCs is small enough (<10%) to be neglected. NCs estimated from relatively small areas (∼100 arcmin^2) can present field-to-field differences reach 40% at a certain magnitude, with consequent impact on the NC distribution.

- The slope of the K-band NCs decreases $\sim 50\%$ in the $15.5 < K < 18.5$ range, evolving from a slope of $d\log N/dm = 0.6 - 0.3$. The comparison to 100 synthetic catalogs from the Millennium simulation reveals that cosmic variance in areas ~ 0.25 deg^2 leads to significant scatter in the observed flattening rate of the slope.

- The composition of the NCs in terms of LF building blocks indicates that the change in the slope of NCs with observed magnitude can be summarized in three main regimes: 1) at bright magnitudes, the classical Euclidean regime ($d\log N/dm = 0.6$) is dominated by low redshift M^* galaxies; 2) at intermediate magnitudes, the transition regime is dominated by the LF at the redshift that maximizes $\phi^* \frac{dV_c}{d\Omega}$. Here the slope decreases rapidly around the apparent magnitude of M^* at that redshift; 3) at faint magnitudes, the "α regime" is populated by galaxies at the faint end of a combination of LFs. Here the slope asymptotically approaches a minimum value at ∼-0.4(1+α). The value of α will typically be given by the LF at the maximum of $\phi^* \frac{dV_c}{d\Omega}$ or a close LF with a much larger faint end slope.

- LFs in the observed K-band as a function of redshift (at a mean rest-frame wavelength $2.16\mu m/(1+\bar{z})$) has been obtained with the following characteristics:
(z=0.25-0.50) $\phi^*_{K,obs}$ =3.4$\pm^{2.10}_{1.70}\times 10^{-3}$Mpc^{-3} $M^*_{K,obs} = -22.95$(fixed) $\alpha_{K,obs} = -1.15\pm^{0.20}_{0.20}$
(z=0.50-0.75) $\phi^*_{K,obs}$ =3.4$\pm^{0.22}_{0.18} \times 10^{-3}$Mpc^{-3} $M^*_{K,obs} = -23.01\pm^{0.13}_{0.12}$ $\alpha_{K,obs} = -1.00\pm^{0.18}_{0.23}$

(z=0.75-1.00) $\phi^*_{K,obs}$ =3.2$\pm^{0.17}_{0.24} \times 10^{-3}$Mpc^{-3} $M^*_{K,obs} = -23.08\pm^{0.14}_{0.12}$ $\alpha_{K,obs} = -1.02\pm^{0.19}_{0.17}$
(z=1.00-1.25) $\phi^*_{K,obs}$ =2.3$\pm^{0.31}_{0.26} \times 10^{-3}$Mpc^{-3} $M^*_{K,obs} = -22.96\pm^{0.28}_{0.26}$ $\alpha_{K,obs} = -0.93\pm^{0.23}_{0.29}$

- In terms of these LFs and other values from the literature, we find that the flattening of the slope is the consequence of a prominent decrease of the characteristic density $\phi^*_{K,obs}$ ($\sim 60\%$ from $z = 0.5$ to $z = 1.5$) and the almost flat evolution of $M^*_{K,obs}$ (1σ compatible with $M^*_{K,obs} = -22.89 \pm 0.25$). The combination of both effects forces a transition to the α regime at $K \sim 17.5$ that otherwise would have taken place $1 - 2$ magnitudes later.

- The predictions for NCs at $K \gtrsim 20$, based on LFs from the literature, suggest that the slope will continue to decrease steadily to $d\log N/dm \lesssim$0.2 dominated by intrinsically faint galaxies from a mixture of LFs at z=1.5-2 and a minor contribution from bright galaxies at z>2. However, if optical LFs at $z > 3$ present an even larger faint end, as suggested by some authors, there might be a slope increase to a higher asymptotic limit around $K \gtrsim 22.5$.

As mentioned above, Chapter 5 contains a brief summary of the main conclusions of several works in which I have collaborated. As these has not been discussed in detail as a part of this thesis we do not include here a description of that results. However, we want to stress that the main goal of Chapter 5 is to highlight the science capabilities of the catalog which constitute the bulk of this thesis and without which these works could not have been carried out.

6.1 Future work

In this section we describe the most relevant topics that would allow us to continue and expand the results presented in this thesis. Some of the them are already ongoing projects.

As described in the final section of Chapter 5 we are currently working on a project to expand the results obtained in Pérez-González et al. (2008) by obtaining a very accurate sample of massive quiescent galaxies at 1.5<z<2.5 to characterize their absolute and relative densities with respect to other massive galaxies. This project will be my immediate goal for the next months.

On a closely related topic, our interest on the study of these galaxies led us to propose SHARDS (Survey For High Redshift Red And Dead Sources). This is an ambitious ESO/GTC project whose purpose is to carry out a photometric survey of quiescent galaxies at 1.0<z<2.5 through the direct measurement of a strong absorption feature in the rest-frame UV. The results obtained with this survey will be directly complementary to that obtained in our current of quiescent galaxies. The survey makes use of 25 medium-band (FWHM$\sim$17 nm) filters with GTC/OSIRIS, covering the wavelength range between 5000 and 9500Å which allows us to explore the rest-frame UV of the galaxies at the redshift of interest. SHARDS is currently observing the GOODS-N field and has obtained $\sim$20% of the data. Next to the project described above this will be my long term priority.

There are fundamental properties of these galaxies that we can not study from currently available datasets and that would greatly strengthen the significance of their characterization. These are the kinematic (velocity dispersions) and morphological properties (mass radial distributions). Combining these data we could verify the accuracy of the stellar masses estimated with photometric data and striking compactness of these galaxies. To measure these properties we will require

very deep spectroscopy and high resolution imaging in a band the probes the rest-frame optical (i.e., the observed NIR). Recent studies has demonstrated that optical spectroscopy is feasible (although time consuming) for the brightest of these galaxies at z$\sim$1.5 (Newman et al. 2010). Similarly, the NIR offers the possibility to extend this study at higher redshifts z$>$1.5 (Onodera et al. 2010; Van Dokkum et al. 2009). In this respect, we can exploit the capabilities of GTC/OSIRIS, Gemini/Flamingos II or the GTC/EMIR (in the future) to obtain multi-object spectroscopy of these galaxies in the optical and NIR. The spectroscopic data can be complemented using the imaging data by the deepest and highest resolution survey in the NIR that is being conducted by the *HST*/WFC3 in the most important cosmological fields, including the EGS.

The excellent quality of the WFC3 NIR data would also allow us to pursue a very interesting project which arise from the results of the IRAC catalog presented in this thesis. The characterization of the $\sim$3% of the sources which are only detected in the IRAC bands but that will be likely detected in very deep NIR images. Although it is hard to determine from the absence of sufficient data, these sources are candidates to very massive galaxies at z$>$3 (e.g., Mancini et al. 2009; Marchesini et al. 2010) or even higher redshifts (these only marginally detected in the IRAC bands; e.g., Labbe et al. 2010).

Another interesting topic that can significantly increase our knowledge of the process of galaxy formation and evolution is the accuracy of the estimated SFRs for high redshift galaxies, particularly in the IR-SFRs. As we have discussed in this thesis, the major drawback in our current understanding of the IR-based SFR properties for galaxies at z$\gtrsim$2 is the lack of enough data to accurately constraint the IR-SEDs, particularly at (sub-)mm and radio wavelengths that would allow us to better constraint the peak of the IR emission (at $\sim$100 μm). Although current observations at these wavelengths exist, source catalogs are restricted to only a few sources (compared to MIPS 24μm data) and severely affected by confusion. In this regard, the incoming data from the *Herschel* Space Observatory (Pilbratt et al. 2010) will help to us fill the gap between MIPS and (sub-)mm/radio observations improving both in sensitivity and resolution. In the future, we will revisit the estimates obtained in this thesis based on *Spitzer*/MIPS data and we will complement the analysis with the addition of *Herschel* data in five bands: PACS 100 and 160 μm, and SPIRE 250, 350, and 500 μm. (see e.g., Pérez-González et al. 2010,Elbaz et al. 2010).

A

The Rainbow Database

Most of the results of this thesis are based on the successful exploitation of a vast amount of data gathered from multiple sources. All the data has been homogeneously merged and processed to extract the maximum information for a large number of galaxies observed in different areas of the sky. As detailed in Chapters 2 and 3, multiple tasks must be carried out before obtaining the most relevant parameters of the galaxies that will the basis of the scientific analysis. During the processing, special care was taken in order to keep a permanent and clear register of the different procedures applied to process to data from individual telescope images to the final properties of the objects. To fully achieve these transparency and organizational goals all the data processing has been carried out within the context of the *Rainbow Database*. The purpose of this database is twofold. From a functional point of view, it serves as a large repository that allow us not only to store all the data products but also to keep a detailed record of the multiple steps of the data processing. From a scientific point of view, the *Rainbow* database is the perfect tool to exploit and distribute the final data products. Note that the collective efforts to gather and properly process the data were not intended only for the benefit a small scientific community, but to become the basis of a data mining program specifically designed for the benefit of the extragalactic astrophysics community.

In the following we briefly describe the scheme and structure of the astronomical data that constitute the bulk of the *Rainbow* database. All the data processing described in the different chapters of this thesis has been carried using *Rainbow* compliant tools, and the final results has been included in the database. This has allowed us a more efficient analysis of the results and has created a lasting legacy for future scientific exploitation.

A.1 Database structure

Although we refer to the whole data structure as *Rainbow* database, this is actually the name of the server that contains multiple databases. The constituent element of each of these databases is what we usually called a cosmological field, thus referring to all data, usually images, spectra, catalogs, on a certain region of the sky (e.g., EGS or GOODS) regardless of the source or category of them.

Although data for a certain cosmological field can encompass many different types, the *Rainbow* database is based essentially on photometric data. Therefore, the tables that constitute the database will contain information regarding images of the fields taken with different instruments. A common way to extract photometric information about the resources contained in an image is, as indicated in Chapter 2, using SExtractor. This program produces an output table listing all sources

detected in the image jointly with a set of parameters that can be customized in the configuration file. Although our ultimate goal is to use a custom program within the *Rainbow* software package to extract the photometry of an object in different bands (as described in Chapter 2), we will use SExtractor tables as a first level of processing to generate catalogs of sources that provide the position of the sources in each image. From these catalogs we define the smallest unit of information that can be found in a table of the database, in this case, a source (e.g, a galaxy or star). Using these sources as constituent elements, each table of the database will contain different information for these objects in a given cosmological field.

A.1.1 Database tables

The tables are the natural way to group different information about the objects. We describe here their organization within each database. In principle, tables are grouped into two different families: the Single Band Data tables (SBD) and Rainbow Processed Data tables (RPD). The main difference between them is whether the data in the table has been processed using a program from the *Rainbow* software package or not. More precisely:

- Single Band Data (SBD) Tables

  SBD tables contain information about objects derived from a single image in a given photometric band (e.g., B, V, K.. etc). Generally, these data are the result of grouping the various parameters of the output of the SExtractor table. Thus, each image of the field in a given band will have its associated catalog. This will be the result of running SExtractor under a given configuration file. The resulting catalog is usually subdivided into individual tables according to type of information. Table A.1 lists some of these tables and their content.

Name	Description
SEXTRACTOR_band	Full SExtractor catalog
sources_band	Source IDs and details of the image
spectros_band	Spectroscopic information on the sources
opticalphotom_band	Optical photometry of the sources
nir_photom_band	NIR photometry of the sources
mir_photom_band	MIR photometry of the sources
fir_photom_band	FIR photometry of the sources
faruv_photom_band	far UV photometry of the sources
radiophotom_band	Radio photometry of the sources
xrayphotom_band	X-ray photometry of the sources
mips_key_band	Description of the columns in the SEXTRACTOR table
crosscor_band	ID of the source in other bands
coord_band	Sky/Images coordinates of the sources in the image

Table A.1: Brief description of the SBD tables in the *Rainbow* database.

  It is worth mentioning that, although the usual procedure is that the information in SBDs is associated with the output of SExtractor running on a given image, it is possible to include in the SBD data from tables whose images are not available or do not exist (e.g., a table with spectrosocopic data).

  It is important to note at this point that since the tables are generated by running SExtractor on images at different wavelengths and with different depths, the number of objects in each table will be different (for example, the B-band image might have 100 objects, while another may have R-band 200). Therefore, although all the information in the SBD tables focuses on the same field, it is not sufficient to characterize the multi-wavelength properties of a

particular object in the region. That is the purpose of the RPD, and primarily of the *Rainbow* software package.

- *Rainbow* Processed Data (RPD) tables

  RPD tables contain the final data results resulting from running the programs in the *Rainbow* software package (described in Chapters 2 and 3; also Pérez-González et al. 2008) on a set of tables/images containing multi-wavelength data. The first step of the procedure is to choose a *selection* band, which consist essentially on a single image and the associated SBD tables. Then, the *Rainbow* photometric code measures the photometry in that band, finds the counterparts of these sources in all other images and also measures the photometry on them. The output of this program is therefore a compilation of multi-wavelength data on all sources in the selection band source catalog. The output file containing the photometry is ready to serve as input for the rest of programs in the package, so that the successive execution of the programs proceeds efficiently. Since a detailed description of how each of the programs in the *Rainbow* package works has been given along the thesis, we just provide in table A.2 a summary of the name and the purpose of these programs.

Name	Description
Rainbow	Cross-correlation of the sources and measurement of multi-wavelength photometry
Pzeta	Estimate of photometric redshifts and physical properties of the galaxies
IR fitting	Modeling of the dust emission of the galaxies in the mid-to-far IR
Detect stars	Star/Galaxy classification
Synthcolor	Estimate of synthetic magnitudes

Table A.2: Brief description of the programs contained in the *Rainbow* software package.

  As explained above, the RPD tables will be the result of storing separately the output of running all the programs in the *Rainbow* software package. As a result, each RPD table contains information of a different kind regarding the same set of sources that was chosen as the *selection* band.

  The RPD tables that exist in each database are identified using the following nomenclature: (1) the root name *merged*,indicating that the information is the result of combining several images, (2) the table type RPD, and (3) the photometric band that was chosen as a reference (e.g. i, K, IRAC-3.6 μm. In the following we briefly describe the content of each RPD table.

- *merged*KEY-*band* This table contains a description of the content in all other RPD columns. It provides the name of the table, the name of the columns and a brief description, e.g., the physical units (if it is a measurement) or relevant comments if needed (for example, ALPHA_GR and DELTA_GR, degrees J2000, Right Ascension and Declination).

- *merged*ID-*band* This table contains all the information regarding the cross-correlation between the reference catalog and all the other catalogs in the different photometric bands. Based on a given cross-match radius (typically a few arc seconds), the table indicates the nearest neighbor for each source in the selection band in the rest of the bands (in other words, its counterpart). Since the same source in the sky has been named differently in each band, this table is the reference index that will allow us to identify each object in all wavelengths (for example, irac360014 will also be K00312 and B001124). Additionally, the tables reports the version of the source catalog using in the cross-match. This is done to avoid cross-correlation problems that might arise if one (or many) of the SBD tables is updated.

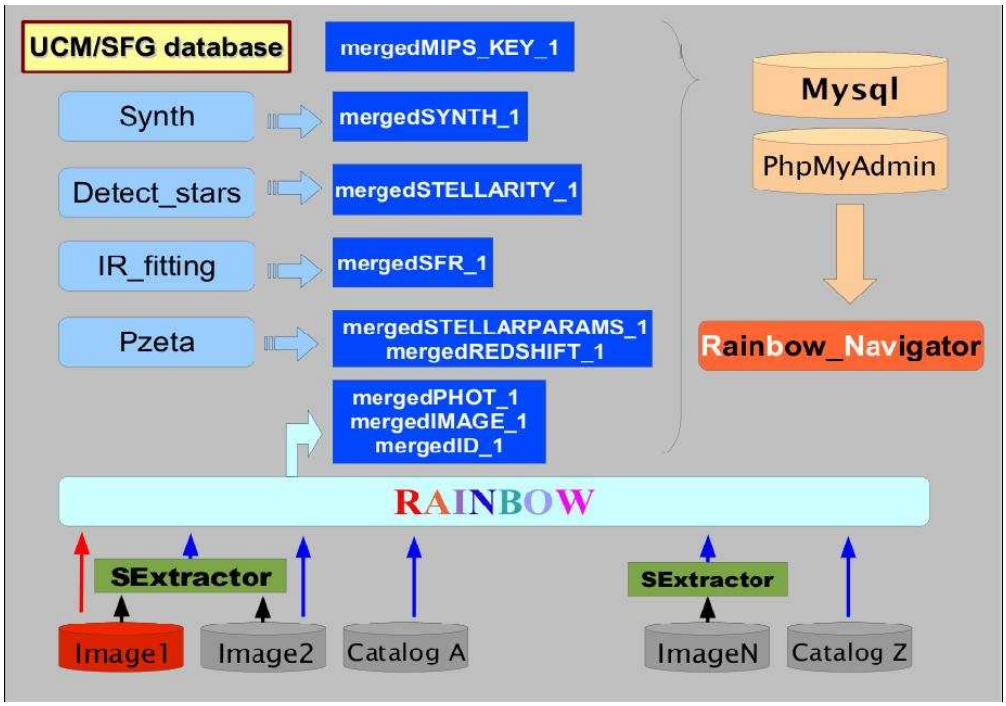

Figure A.1: Schematic diagram of the data flow within the *Rainbow* database

- *merged*IMAGE-*band* This table shows the name of the source images in different bands for the objects in the reference catalog. This information depends on the result of the cross-correlation which is stored in *merged*ID-*band*. Once each object in the reference catalog has been identified with a source in other band, the name of the reference image in that band is stored in the table. Additionally, this table also stores the name of the folder where the images are located on the server.

- *merged*PHOT-*band* This table contains all the multi-wavelength photometric data (as fluxes in μJy) for the sources in the reference catalog. This table contains as many columns as photometric bands has been measured by the Rainbow program. The photometric uncertainty and the effective wavelength of the photometric filter in each band are also given.

- *merged*REDSHIFTS-*band* This table stores the information about the spectroscopic and photometric redshift for each source in the reference catalog. To include spectroscopic data a SBD table with the spectroscopic data must exist so that it can cross-matched with the reference catalog. On the other hand, the photometric redshifts are the result of running the program Pzeta on the output of the photometric measurement program and should be available for the majority of the sources, if these are observed in a sufficiently large number of bands. As described in Chapter 2 the quality of the photometric redshift depends on the quality and quantity of the photometric data. The table provides two estimates of the photometric redshift (the most likely and the probability weighted estimate), the associated uncertainty, several parameters with the probability distribution, the number of photometric bands used in the SED fitting, the name of the templates that best fits the observed SED at the two possible photometric redshift solutions, and the scale factor required to match the observed photometry to the template.

- *merged*SFR-*band* This table contains different estimates of the UV- and IR- based SFR as

well as rest-frame luminosities for the sources in the reference catalog. These values depends on the estimated photometric redshift and the corresponding best fitting template. The UV luminosities and SFRs are computed from the best fitting optical template. However, as explained in Chapter 3, the IR-based SFRs (and luminosities) are based on the fitting of the IR emission of the galaxy with dust emission templates. Thus, only if the galaxy has been observed at a rest-frame wavelength $\lambda > 5$ μm (typically in the *Spitzer*/MIPS bands), the program IR-fitting will estimate IR-based SFRs using different methods.

- *merged*STELLARITY-*band* This table provides information on stellar or galactic nature of the sources detected in the reference catalog. These results are the output of the program detect-stars, which computes a total of 8 different stellarity criteria (see Chapter 2) for each source. The columns of this table shows whether an object satisfies a certain criterion, the total number of criteria satisfied and the final star/galaxy classification.

- *merged*STELLARPARAMS-*band* This table stores the values of the stellar parameters for the sources in the reference catalog. These parameters refer to different properties of a galaxy, as the stellar mass, age, metallicity or dust extinction. As described in Chapter 3, this values are estimated as a by-product of the SED fitting procedure (performed with Pzeta) used to estimate the photometric redshift. The physical properties thus are inherited from the parameters that characterize the best fitting galaxy template used in the SED fitting (prior to that, the templates has been modeled using of a certain combination of SPS models, IMF and a dust extinction law).

A.2 Web Connectivity, Rainbow Navigator

The inclusion of detailed information on a given sample of galaxies in a database is a powerful tool that can potentially improve the analysis of the data. However, nearly as important as improving the data access is to simplify the user interface to handle the data. In this regard, the SQL language (which is the standard language to work with databases) is highly flexible, but expensive in terms of writing the code. One option is to sacrifice some of this flexibility to simplify the queries for the typical user. In general, the database user interested in working with extragalactic sources will typically prioritize the searches over a certain parameter (e.g., redshifts, luminosities, etc). This implies that by creating a template search form we can greatly simplify the access to the data. In the case of *Rainbow*, we decided to implement the search form in a web interface not only improve the searches but also to make the database accessible through any browser. This was the idea behind the development of *Rainbow Navigator*, a highly interactive query web-interface designed to browse the data products in the *Rainbow* database. In the following we present several captions showing the multiple capabilities of *Rainbow Navigator*.

Figure A.2 shows the main interface of *Rainbow Navigator*. The left column present the principal options to browse the data: first, the user has to select the Database (i.e., the cosmological field) and the selection band (the reference catalog for which the multi-wavelength photometry a physical properties were computed); then, it is possible to enter the name of the source or alternatively perform a proximity search by coordinates (R.A, DEC and a search radius). Below this search menus, the interface presents some configuration options that modify the display in the output page (Figure A.5). For example, it allows to change the size and color of the object captions or

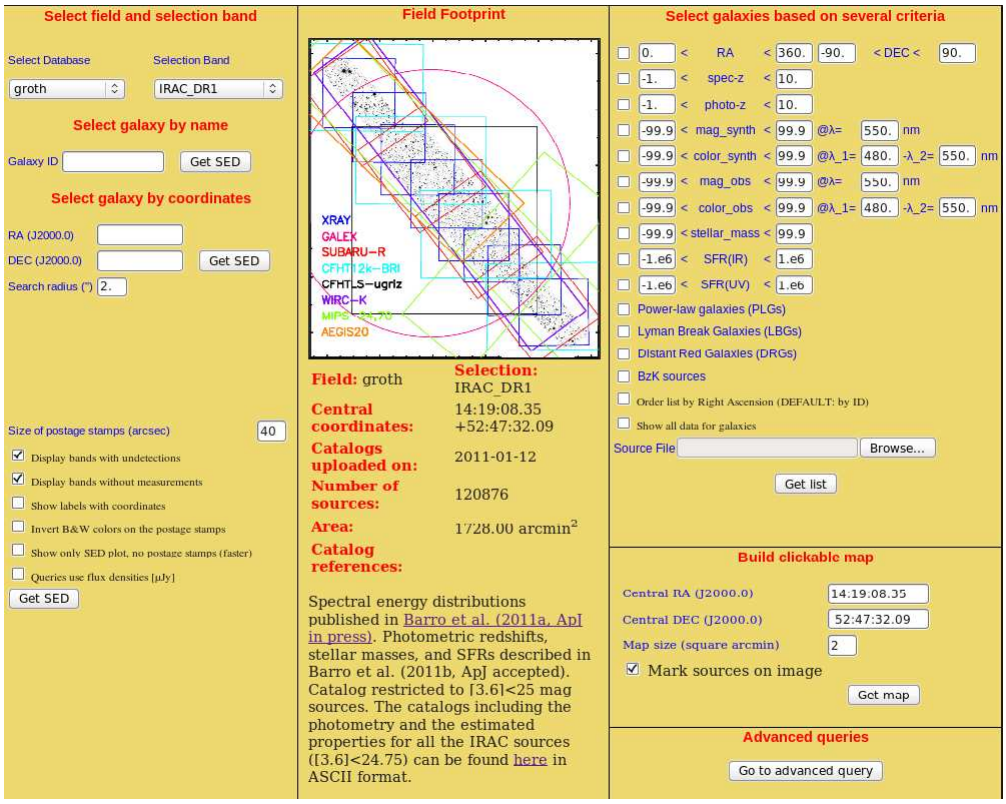

Figure A.2: Main access page to *Rainbow Navigator*. The user can chose any of the cosmological fields available in the server and any selection band for which the *Rainbow* software has been executed. Once the scheme has been selected the central column displays an image of the field coverage together with some other relevant information. From this interface the user can perform a search based on the ID, celestial coordinates (left menu) or physical properties of the source (right menu). A clickable map around displaying all sources around a given position can also be generated (bottom-right menu).

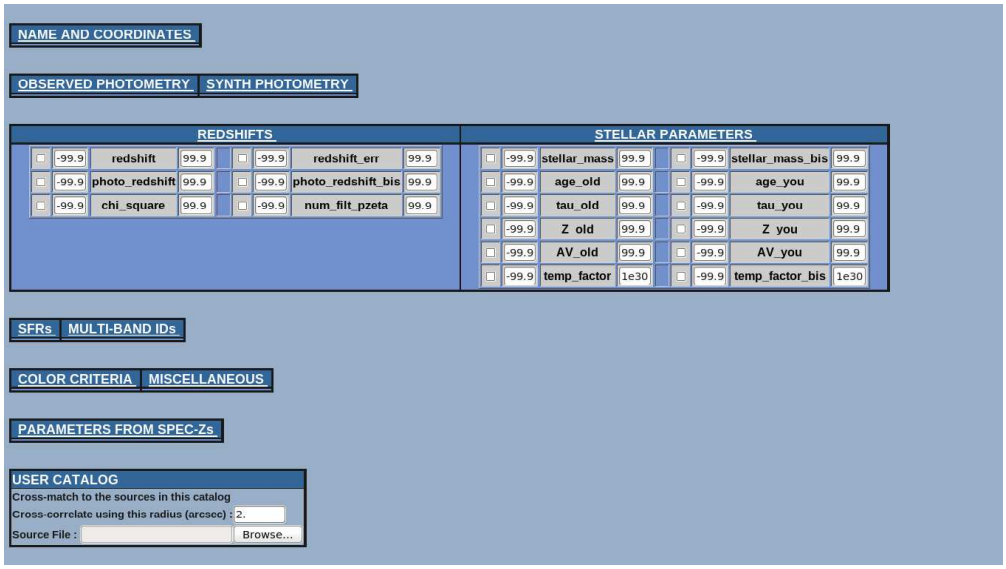

Figure A.3: Display of the Advanced Queries menu in *Rainbow Navigator*. Similarly to the menu in the right column of the main interface, this menu allows to perform searches based on multiple different parameters. However, this interface allows queries in mostly all the available parameters in the database. To facilitate the access, these parameters are grouped in tables that summarize different pieces of information, e.g., observed photometry, synthetic photometry, redshifts, stellar parameters, etc. This menu also allows the user to perform an on-the-fly cross-match of his own catalog to the reference catalog.

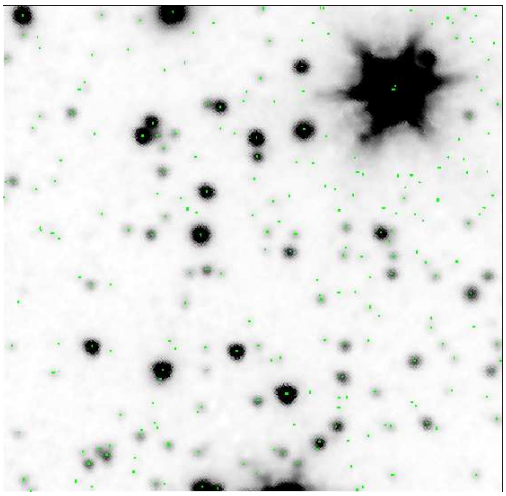

#	Source ID	RA (J2000.0)	DEC (J2000.0)
1	irac134516	214.77448370	+52.77518170
2	irac132796	214.81181150	+52.77530430
3	irac132929	214.80909390	+52.77580740
4	irac134597	214.77314470	+52.77586280
5	irac133874	214.78851420	+52.77594960
6	irac133794	214.79024340	+52.77605500
7	irac133608	214.79435150	+52.77624950
8	irac133218_1	214.80241700	+52.77608040
9	irac133519_2	214.79435150	+52.77624950
10	irac133519_1	214.79533420	+52.77626180
11	irac133111	214.80414210	+52.77643350
12	irac132823	214.80990000	+52.77656460
13	irac134596	214.77249490	+52.77600930
14	irac134730	214.76923400	+52.77683310
15	irac135193	214.76003370	+52.77684970
16	irac133366	214.79776980	+52.77706830
17	irac134466	214.77381820	+52.77740240

Figure A.4: *Left:* Image of a 1'×1' clickable map generated from the main interface of *Rainbow Navigator*. The background image correspond to the selection band (IRAC-3.6 μm) and the detected sources are depicted as green dots. *Right:* Output table associated to the clickable map indicating the name of all the sources present in the image. By clicking the name of a source a new page depicting all the information about the source will open.

simply hide them. Once the main options have been chosen, the central column displays an image of the cosmological field depicting the footprints of all the different observational data available in the database. In addition, some practical information about the field (e.g., celestial coordinates, total number of sources in the catalog) is shown below the figure. The top right menu present a menu that allows the user to create on-the-fly clickable maps of the merged photometric catalog around a given position. An example of the resulting map is shown in Figure A.4 . Detected sources (green dots) on the region are displayed over the selection band image (in this case IRAC-3.6 μm). Clicking on the object a new page with the source information will appear (Figure A.5). Below the clickable map option, there is a menu that allows the user to design queries selecting samples based on multiple parameters, e.g., coordinates, observed magnitudes, photo-z, spec-z, ..etc. The menu also allows to use some of the most popular color criteria for selecting high redshift galaxies or AGN. In addition, it is possible to upload user created catalogs to obtain a list of the closest neighbors (on-the-fly cross-match) in the reference sample selected by the user.

As a result of any of the searches performed in the main interface, *Rainbow Navigator* will display a dedicated webpage with detailed information about the selected source. Figure A.5 presents an example of these pages for a particular source. The tables on the left present a summary of several different parameters: the first table contain the source coordinates, the band where the photometric aperture is defined, the kron radius, the field and selection band, the (total) number of photometric bands in the field, and the number of bands used in the SED fitting; the second table shows the observed magnitudes (AB) in a few representative bands and the source classification attending to some color criteria used to select high redshift sources (LBG, ERO, etc..); the third table shows the spectroscopic redshift and quality flag (from 1-4) and summarizes the main stellar parameters derived from the SED fitting analysis. Namely, the photometric redshift, stellar mass, (UV- and IR- based) SFRs, age, metallicity, etc...; the fourth table quotes the closest neighbors of the source in a $10''$ radius, clicking on the ID of these sources will open the specific page for each source. In addition, clicking on the name of the selected source in any of the four tables described above will open a new table containing all the information available in the database for that source. This is basically a one line result of all the RPD tables for that source. The Figure

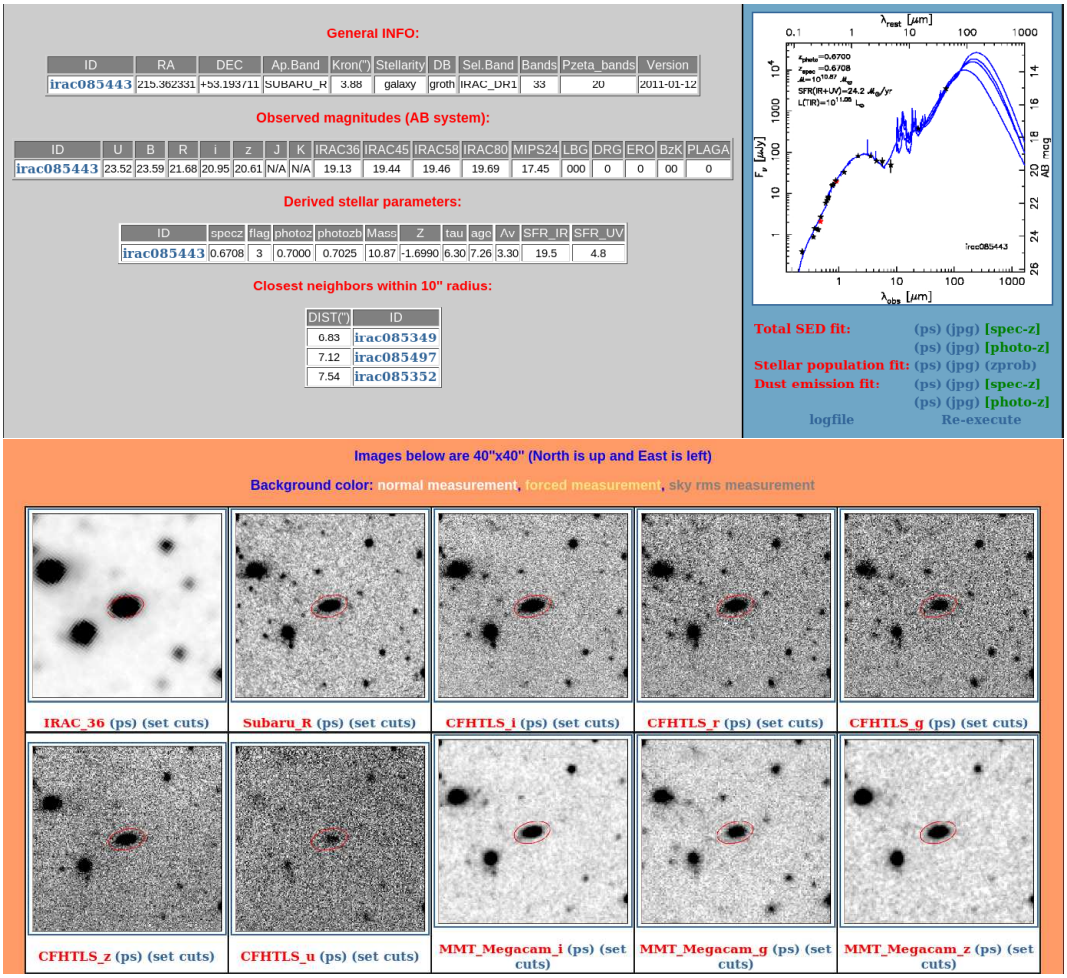

Figure A.5: Individual webpage for a given source in the *Rainbow* database. The top-left tables present a summary of the most relevant photometric and physical properties (e.g., observed magnitudes, redshifts, stellar mass or SFRs) of the source jointly with the names of the closest neighbors. The figure on the right shows the observed SED and the best fitting UV-to-FIR template resulting from the merged of the stellar population and dust templates. Finally, the figures at the bottom depict the image of the source in all the different observed bands. The size and appearance of this figures can be modified interactively from the webpage.

on the right displays the observed SED (colored stars) jointly with the best fitting model resulting from the combination of the stellar population and dust emission templates. The options below the figure present similar figures (available in different forms) depicting either the best fitting stellar population or dust emission template. The former also shows the photometric redshift probability distribution. The postage stamps below the tables depict the source in all the photometric bands where it was detected (white background) or undetected, but an image existed at the given position and: a flux was measured (yellow background) the sky rms was measured (cyan background) or the measurement failed (grey background). The aperture used to measure the integrated photometry is shown in all the stamps. Clicking in the image open a new page where it is possible to create on-the-fly postages customizing with the image cuts and its size; if HST data are available RGB color stamps can be generated combining data from different bands. When spectroscopic data are available for the source, a 1D spectra is also displayed in the last postage. The 1D spectra can be checked interactively with the possibility of setting the redshift. In addition, this postage shows a set of reference spectral features.

Glossary

2MASS Two Micron All Sky Survey. Survey of the whole sky in the J, H and K_S bands (1.2 μm, 1.6 μm and 2.2 μm, respectively).

AEGIS the All-Wavelength Extended Groth Strip International Survey. A multi-wavelength astronomical survey focused on observing the Extended Groth Strip area.

AGB Asymptotic Giant Branch. A late stage in stellar evolution undertaken by low- to intermediate-mass stars.

AGN Active Galactic Nucleus. Very luminous and compact source in the center of a galaxy, possibly hosting a supermassive black hole.

ALMA Atacama Large Millimeter/Submillimeter Array. Interferometer being built in the Atacama desert (Chile), that will observe in the spectral range between 0.3 mm to 9.6 mm.

BzK A type of galaxy selected using a combination of optical and NIR colors, B$-$z and z$-K$, hence its name.

CCD A charge-coupled device employed in astronomy to take images.

CDFS Chandra Deep Field South. Also refered as GOODS-S; One of the most important cosmological fields, observed in multi-wavelength photometry and spectroscopy.

COSMOS The Cosmological Evolution Survey. A multi-wavelenght survey centered in 2 square degree equatorial field.

CMB Cosmic Microwave Background. Relic radiation of the Big Bang observed today at microwave wavelengths.

DEEP The Deep Evolutionary Extragalactic Probe, a highly ambitious spectroscopic survey.

DEIMOS The DEep Imaging Multi-Object Spectrograph , a multi-slit optical spectrograph at Keck.

DRG Distant Red Galaxy. A type of galaxy selected using a NIR (J$-K$) color criteria.

ESO European Southern Observatory (also ESO/Uppsala Survey of the ESO(B) Atlas).

EGS Extended Groth Strip. A cosmological field observed in the northen hemisphere.

ERO Extremely Red Object. A type of galaxy selected using a NIR (R$-K$) color criteria.

EW Equivalent Width. In a spectral feature, width of a rectangle whose height is equal to the continuum level, and whose area is the same as that encompassed by the spectral feature.

EHB The hottest variety of stars on the horizontal branch of the Hertzsprung-Russell diagram.

FITS Flexible Image Transport System. Standard image format used in astronomy.

FIR Far-Infrared (from 25-40 μm to 200-350 μm).

FUV Far-Ultraviolet (1350-1750 Å).

FWHM Full Width at Half Maximum. Measurement of the width of a function (such as a spectral line or a PSF), defined as the difference between the two values of the x variable when the y one is equal to half of its maximum value.

GALEX Galaxy Evolution Explorer. Space telescope that observes in the FUV and NUV bands.

GOODS The Great Observatories Origins Deep Survey a multi-wavelength photometric and spectroscopic survey centered around two areas of the sky in different hemispheres.

HB Horizontal Branch. A stage in stellar evolution that follows the asymptotic giant branch in the Hertzsprung-Russell diagram.

HST Hubble Space Telescope.

HDF/HDF-N,-S Hubble Ultra Deep Field. Deepest image of the distant universe taken by the Hubble Space Telescope. Also used to refer to the field itself in the northern hemisphere and its counterpart in the south.

IPAC Infrared Processing and Analysis Center.

IMF Initial Mass Function. Mass distribution of a population of stars in terms of their theoretical initial mass.

IRAC Infrared Array Camera. Mid-infrared instrument onboard *Spitzer*, providing images at 3.6 μm, 4.5 μm, 5.8 μm and 8.0 μm.

IRAF Image Reduction and Analysis Facility. Software to reduce and analyze astronomical data.

IRS Infrared Spectrograph. Instrument onboard *Spitzer* that provides low- and high-resolution mid-infrared spectra from 5.2 μm to 38 μm.

IRX Infrared Excess Galaxies. Galaxies featuring a strong far IR emission with respect to their optical fluxes.

IRX-β Relation between the total-infrared to UV ratio (or infrared excess, IRX) and the slope of the UV spectrum (β).

ISM Interstellar medium. The gas and dust pervading space between stars.

ΛCDM Lambda Cold Dark Matter. Cosmological model that includes dark energy (in the form of a cosmological constant Λ) and non-baryonic dark matter moving at non-relativistic speeds.

JCMT James Clerk Maxwell Telescope radio telescope in Hawaii.

JWST James Webb Space Telescope, a large infrared-optimized space telescope, scheduled for launch in 2014.

KPNO Kitt Peak National Observatory.

LAE Lyman-α Emitters.

LIRG Luminous Infrared Galaxy. Galaxy whose total infrared luminosity is larger than 10^{11} solar luminosities.

LBG Lyman Break Galaxies.

LF Luminosity Funtion. Volume density of galaxies as a function of their luminosity.

LRIS Low Resolution Imaging Spectrometer, an optical spectrograph mounted at the Keck telescopes.

ULIRG Ultra-Luminous Infrared Galaxy. Galaxy whose total infrared luminosity is larger than 10^{12} solar luminosities.

MIPS Multiband Imaging Photometer. Camera onboard *Spitzer* observing in the far-infrared, at 24 μm, 70 μm and 160 μm.

MIR Mid-Infrared (from 5 μm to 25-40 μm).

NASA National Aeronautics and Space Administration.

NC Number Counts, short name for Galaxy Number Counts; the number of galaxies per unit of sky area and observed magnitude.

NED NASA/IPAC Extragalactic Database. Database that compiles positions, basic data and bibliographic references for millions of extragalactic objects.

NIR Near-infrared (from 0.7-1 μm to 5 μm).

NUV Near-Ultraviolet (1750-2750 Å).

PAH Polycyclic Aromatic Hydrocarbon. Very large and flat molecules consisting of an hexagonal grid of carbon atoms surrounded by hydrogen ones.

PLG Power Law Galaxies. Galaxies featuring a strong mid-to-far IR emission that can characterized with a power law functional form.

PSF Point Spread Function. Image of a point source yielded by an optical system.

SCUBA Submillimeter Common-User Bolometer Array. Submillimeter array detector at 450 μm and 850 μm, operating at the James Clerk Maxwell Telescope.

SDSS Sloan Digital Sky Survey. Photometric and spectroscopic survey of more than a quarter of the sky in the optical range.

SED Spectral Energy Distribution. Variation with wavelength of an object's luminosity.

SFH Star Formation History. Temporal evolution of the star formation rate.

SFR Star Formation Rate. Mass of gas transformed into stars per unit of time.

SFRD Star Formation Rate Density. The density of SFR per unit of cosmological volume.

SNR Signal-to-noise ratio.

SMD Stellar Mass Density. Volume density of galaxies as a function of their stellar mass.

SPS Stellar Population Synthesis. A modeling technique aimed at characterizing the spectral energy distribution of the stellar population of the galaxies.

SSP Single Stellar Population. A galaxy composed of a single generation of stars formed at the same time with the same properties.

TIR Total Infrared (8-1100 μm).

UV Ultraviolet wavelength range, $\sim$2000-3000 Å).

VIMOS Visible Multi-Object Spectrograph. Imager, multi-object spectrograph and integral field unit in the optical range, mounted on one of the telescopes (unit 3) of the Very Large Telescope facility.

VLA Very Large Array. Radio interferometer in New Mexico.

VLT Very Large Telescope. Array of four fixed 8.2 m telescopes and four movable 1.8 m ones at Cerro Paranal (Chile).

Bibliography

Alexander, D. M., Chary, R., Pope, A., et al. 2008, ApJ, 687, 835

Alonso-Herrero, A., Rieke, G. H., Rieke, M. J., et al. 2006, ApJ, 650, 835

Arnouts, S., Schiminovich, D., Ilbert, O., et al. 2005, ApJL, 619, L43

Arnouts, S., Walcher, C. J., Le Fevre, O., et al. 2007, ArXiv e-prints, 705

Babul, A. & Ferguson, H. C. 1996, ApJ, 458, 100

Babul, A. & Rees, M. J. 1992, MNRAS, 255, 346

Baes, M. & Dejonghe, H. 2001, MNRAS, 326, 722

Baldwin, J. A., Phillips, M. M., & Terlevich, R. 1981, PASP, 93, 5

Ball, N. M., Brunner, R. J., Myers, A. D., et al. 2008, ApJ, 683, 12

Balogh, M. L., Morris, S. L., Yee, H. K. C., Carlberg, R. G., & Ellingson, E. 1999, ApJ, 527, 54

Barmby, P., Alonso-Herrero, A., Donley, J. L., et al. 2006, ApJ, 642, 126

Baugh, C. M. 2006, Reports on Progress in Physics, 69, 3101

Baum, W. A. 1957, AJ, 62, 6

Bavouzet, N., Dole, H., Le Floc'h, E., et al. 2008, A&A, 479, 83

Bell, E., Davis, M., Dey, A., et al. 2009, in ArXiv Astrophysics e-prints, Vol. 2010, astro2010: The Astronomy and Astrophysics Decadal Survey, 106–+

Bell, E. F. 2003, ApJ, 586, 794

Bell, E. F. & de Jong, R. S. 2001, ApJ, 550, 212

Bell, E. F., McIntosh, D. H., Katz, N., & Weinberg, M. D. 2003, ApJL, 585, L117

Bell, E. F., Naab, T., McIntosh, D. H., et al. 2006, ApJ, 640, 241

Bell, E. F., Papovich, C., Wolf, C., et al. 2005, ApJ, 625, 23

Bell, E. F., Wolf, C., Meisenheimer, K., et al. 2004, ApJ, 608, 752

Benítez, N., Broadhurst, T., Bouwens, R., Silk, J., & Rosati, P. 1999, ApJL, 515, L65

Bennett, A. S. 1962, MmRAS, 68, 163

Bershady, M. A. 2003, in Revista Mexicana de Astronomia y Astrofisica, vol. 27, Vol. 16, Revista Mexicana de Astronomia y Astrofisica Conference Series, ed. J. M. Rodriguez Espinoza, F. Garzon Lopez, & V. Melo Martin, 203–208

Bershady, M. A., Lowenthal, J. D., & Koo, D. C. 1998, ApJ, 505, 50

Bolzonella, M., Miralles, J., & Pelló, R. 2000, A&A, 363, 476

Bouwens, R. J., Illingworth, G. D., Blakeslee, J. P., & Franx, M. 2006, ApJ, 653, 53

Bouwens, R. J., Illingworth, G. D., González, V., et al. 2010a, ApJ, 725, 1587

Bouwens, R. J., Illingworth, G. D., Oesch, P. A., et al. 2010b, ApJL, 709, L133

Bower, R. G., Benson, A. J., Malbon, R., et al. 2006, MNRAS, 370, 645

Brammer, G. B., van Dokkum, P. G., & Coppi, P. 2008, ApJ, 686, 1503

Brammer, G. B., Whitaker, K. E., van Dokkum, P. G., et al. 2009, ApJL, 706, L173

Brandt, W. N., Alexander, D. M., Bauer, F. E., & Vignali, C. 2006, in Lecture Notes in Physics, Berlin Springer Verlag, Vol. 693, Physics of Active Galactic Nuclei at all Scales, ed. D. Alloin, 185–+

Bressan, A., Granato, G. L., & Silva, L. 1998, A&A, 332, 135

Brinchmann, J. & Ellis, R. S. 2000, ApJL, 536, L77

Brown, G. S. & Tinsley, B. M. 1974, ApJ, 194, 555

Brunner, R. J., Connolly, A. J., Szalay, A. S., & Bershady, M. A. 1997, ApJL, 482, L21+

Bruzual, G. 2007, in Astronomical Society of the Pacific Conference Series, Vol. 374, From Stars to Galaxies: Building the Pieces to Build Up the Universe, ed. A. Vallenari, R. Tantalo, L. Portinari, & A. Moretti, 303–+

Bruzual, G. & Charlot, S. 2003, MNRAS, 344, 1000

Bruzual A., G. 1983, ApJ, 273, 105

Bruzual A., G. & Kron, R. G. 1980, ApJ, 241, 25

Buat, V., Deharveng, J. M., & Donas, J. 1989, A&A, 223, 42

Buat, V., Iglesias-Páramo, J., Seibert, M., et al. 2005, ApJL, 619, L51

Buat, V., Marcillac, D., Burgarella, D., et al. 2007, A&A, 469, 19

Bundy, K., Ellis, R. S., Conselice, C. J., et al. 2006, ApJ, 651, 120

Bussmann, R. S., Dey, A., Borys, C., et al. 2009, ApJ, 705, 184

Buzzoni, A. 1989, ApJS, 71, 817

Calzetti, D. 1997, AJ, 113, 162

Calzetti, D., Armus, L., Bohlin, R. C., et al. 2000, ApJ, 533, 682

Calzetti, D., Kennicutt, R. C., Engelbracht, C. W., et al. 2007, ApJ, 666, 870

Caputi, K. I., Lagache, G., Yan, L., et al. 2007, ApJ, 660, 97

Cardamone, C. N., Urry, C. M., Damen, M., et al. 2008, ApJ, 680, 130

Cardelli, J. A., Clayton, G. C., & Mathis, J. S. 1989, ApJ, 345, 245

Cassata, P., Cimatti, A., Kurk, J., et al. 2008, A&A, 483, L39

Cenarro, A. J., Peletier, R. F., Sánchez-Blázquez, P., et al. 2007, MNRAS, 374, 664

Cenarro, A. J. & Trujillo, I. 2009, ApJL, 696, L43

Chabrier, G. 2003, PASP, 115, 763

Charlot, S. & Bruzual, A. G. 1991, ApJ, 367, 126

Charlot, S. & Fall, S. M. 2000, ApJ, 539, 718

Chary, R. & Elbaz, D. 2001, ApJ, 556, 562

Cimatti, A., Cassata, P., Pozzetti, L., et al. 2008, A&A, 482, 21

Cimatti, A., Daddi, E., Renzini, A., et al. 2004, Nature, 430, 184

Coelho, P., Barbuy, B., Meléndez, J., Schiavon, R. P., & Castilho, B. V. 2005, A&A, 443, 735

Cole, S., Lacey, C. G., Baugh, C. M., & Frenk, C. S. 2000, MNRAS, 319, 168

Cole, S., Norberg, P., Baugh, C. M., et al. 2001, MNRAS, 326, 255

Coleman, G. D., Wu, C., & Weedman, D. W. 1980, ApJS, 43, 393

Collister, A. A. & Lahav, O. 2004, PASP, 116, 345

Condon, J. J. 1992, ARA&A, 30, 575

Connolly, A. J., Csabai, I., Szalay, A. S., et al. 1995, AJ, 110, 2655

Conroy, C. & Gunn, J. E. 2010, ApJ, 712, 833

Conroy, C., Gunn, J. E., & White, M. 2009, ApJ, 699, 486

Conroy, C., White, M., & Gunn, J. E. 2010, ApJ, 708, 58

Conselice, C. J., Bershady, M. A., Dickinson, M., & Papovich, C. 2003, AJ, 126, 1183

Conselice, C. J., Rajgor, S., & Myers, R. 2008, MNRAS, 386, 909

Conselice, C. J., Yang, C., & Bluck, A. F. L. 2009, MNRAS, 394, 1956

Cortese, L., Boselli, A., Buat, V., et al. 2006, ApJ, 637, 242

Cortese, L., Boselli, A., Franzetti, P., et al. 2008, MNRAS, 386, 1157

Cowie, L. L., Gardner, J. P., Lilly, S. J., & McLean, I. 1990, ApJL, 360, L1

Cowie, L. L., Songaila, A., Hu, E. M., & Cohen, J. G. 1996, AJ, 112, 839

Croton, D. J., Springel, V., White, S. D. M., et al. 2006, MNRAS, 365, 11

da Cunha, E., Charlot, S., & Elbaz, D. 2008, MNRAS, 388, 1595

Daddi, E., Alexander, D. M., Dickinson, M., et al. 2007a, ApJ, 670, 173

Daddi, E., Cimatti, A., Renzini, A., et al. 2004, ApJ, 617, 746

Daddi, E., Dickinson, M., Morrison, G., et al. 2007b, ApJ, 670, 156

Daddi, E., Renzini, A., Pirzkal, N., et al. 2005, ApJ, 626, 680

Dale, D. A. & Helou, G. 2002, ApJ, 576, 159

Dale, D. A., Helou, G., Contursi, A., Silbermann, N. A., & Kolhatkar, S. 2001, ApJ, 549, 215

Davis, M., Efstathiou, G., Frenk, C. S., & White, S. D. M. 1985, ApJ, 292, 371

Davis, M., Faber, S. M., Newman, J., et al. 2003, in Presented at the Society of Photo-Optical Instrumentation Engineers (SPIE) Conference, Vol. 4834, Society of Photo-Optical Instrumentation Engineers (SPIE) Conference Series, ed. P. Guhathakurta, 161–172

Davis, M., Guhathakurta, P., Konidaris, N. P., et al. 2007, ApJL, 660, L1

Davis, M. & Wilkinson, D. T. 1974, ApJ, 192, 251

De Lucia, G., Kauffmann, G., & White, S. D. M. 2004, MNRAS, 349, 1101

De Lucia, G., Springel, V., White, S. D. M., Croton, D., & Kauffmann, G. 2006, MNRAS, 366, 499

de Propris, R., Pritchet, C. J., Hartwick, F. D. A., & Hickson, P. 1993, AJ, 105, 1243

Dekel, A., Sari, R., & Ceverino, D. 2009, ApJ, 703, 785

Desert, F., Boulanger, F., & Puget, J. L. 1990, A&A, 237, 215

Dey, A., Soifer, B. T., Desai, V., et al. 2008, ApJ, 677, 943

Djorgovski, S., Soifer, B. T., Pahre, M. A., et al. 1995, ApJL, 438, L13

Donley, J. L., Rieke, G. H., Pérez-González, P. G., Rigby, J. R., & Alonso-Herrero, A. 2007, ApJ, 660, 167

Draine, B. T. 2003, ARA&A, 41, 241

Draine, B. T., Dale, D. A., Bendo, G., et al. 2007, ApJ, 663, 866

Drory, N. & Alvarez, M. 2008, ApJ, 680, 41

Drozdovsky, I., Yan, L., Chen, H., et al. 2005, AJ, 130, 1324

Efstathiou, A. & Rowan-Robinson, M. 1995, MNRAS, 273, 649

—. 2003, MNRAS, 343, 322

Efstathiou, A., Rowan-Robinson, M., & Siebenmorgen, R. 2000, MNRAS, 313, 734

Egami, E., Dole, H., Huang, J., et al. 2004, ApJS, 154, 130

Eke, V. R., Baugh, C. M., Cole, S., et al. 2005, MNRAS, 362, 1233

Elbaz, D., Hwang, H. S., Magnelli, B., et al. 2010, A&A, 518, L29+

Elsner, F., Feulner, G., & Hopp, U. 2008, A&A, 477, 503

Elston, R., Rieke, G. H., & Rieke, M. J. 1988, ApJL, 331, L77

Fabbiano, G. 1989, ARA&A, 27, 87

Faber, S. M., Phillips, A. C., Kibrick, R. I., et al. 2003, in Society of Photo-Optical Instrumentation Engineers (SPIE) Conference Series, Vol. 4841, Society of Photo-Optical Instrumentation Engineers (SPIE) Conference Series, ed. M. Iye & A. F. M. Moorwood, 1657–1669

Faber, S. M., Willmer, C. N. A., Wolf, C., et al. 2007, ApJ, 665, 265

Fardal, M. A., Katz, N., Weinberg, D. H., & Davé, R. 2007, MNRAS, 379, 985

Feldmann, R., Mayer, L., & Carollo, C. M. 2008, ApJ, 684, 1062

Ferland, G. J., Korista, K. T., Verner, D. A., et al. 1998, PASP, 110, 761

Fernández-Soto, A., Lanzetta, K. M., & Yahil, A. 1999, ApJ, 513, 34

Ferreras, I., Lisker, T., Pasquali, A., Khochfar, S., & Kaviraj, S. 2009, MNRAS, 396, 1573

Fioc, M. & Rocca-Volmerange, B. 1997, A&A, 326, 950

Fiore, F., Grazian, A., Santini, P., et al. 2008, ApJ, 672, 94

Firth, A. E., Lahav, O., & Somerville, R. S. 2003, MNRAS, 339, 1195

Fontana, A., Salimbeni, S., Grazian, A., et al. 2006, A&A, 459, 745

Fontana, A., Santini, P., Grazian, A., et al. 2009, A&A, 501, 15

Fontanot, F., De Lucia, G., Monaco, P., Somerville, R. S., & Santini, P. 2009, MNRAS, 397, 1776

Fontanot, F., Monaco, P., Silva, L., & Grazian, A. 2007, MNRAS, 382, 903

Franceschini, A., Rodighiero, G., Vaccari, M., et al. 2009, ArXiv e-prints

Franx, M., Labbé, I., Rudnick, G., et al. 2003, ApJL, 587, L79

Gallazzi, A., Charlot, S., Brinchmann, J., White, S. D. M., & Tremonti, C. A. 2005, MNRAS, 362, 41

Gallego, J., Zamorano, J., Aragon-Salamanca, A., & Rego, M. 1995, ApJL, 455, L1+

Gardner, J. P., Cowie, L. L., & Wainscoat, R. J. 1993, ApJL, 415, L9

Gardner, J. P., Sharples, R. M., Carrasco, B. E., & Frenk, C. S. 1996, MNRAS, 282, L1

Garrett, M. A. 2002, ArXiv Astrophysics e-prints

Gavazzi, G., Boselli, A., Donati, A., Franzetti, P., & Scodeggio, M. 2003, A&A, 400, 451

Georgantopoulos, I., Akylas, A., Georgakakis, A., & Rowan-Robinson, M. 2009, A&A, 507, 747

Giavalisco, M., Ferguson, H. C., Koekemoer, A. M., et al. 2004, ApJL, 600, L93

Gilli, R., Daddi, E., Chary, R., et al. 2007, A&A, 475, 83

Girardi, L., Bressan, A., Bertelli, G., & Chiosi, C. 2000, A&AS, 141, 371

Glazebrook, K., Blake, C., Economou, F., Lilly, S., & Colless, M. 1999, MNRAS, 306, 843

Gordon, K. D., Clayton, G. C., Witt, A. N., & Misselt, K. A. 2000, ApJ, 533, 236

Gordon, K. D., Misselt, K. A., Witt, A. N., & Clayton, G. C. 2001, ApJ, 551, 269

Granato, G. L., De Zotti, G., Silva, L., Bressan, A., & Danese, L. 2004, ApJ, 600, 580

Granato, G. L., Lacey, C. G., Silva, L., et al. 2000, ApJ, 542, 710

Grazian, A., Fontana, A., de Santis, C., et al. 2006, A&A, 449, 951

Gronwall, C. & Koo, D. C. 1995, ApJL, 440, L1

Gunn, J. E. & Peterson, B. A. 1965, ApJ, 142, 1633

Hippelein, H., Haas, M., Tuffs, R. J., et al. 2003, A&A, 407, 137

Hopkins, A. M. 2004, ApJ, 615, 209

Hopkins, A. M. & Beacom, J. F. 2006, ApJ, 651, 142

Hopkins, A. M., Miller, C. J., Nichol, R. C., et al. 2003, ApJ, 599, 971

Hu, E. M. & Cowie, L. L. 1987, ApJL, 317, L7

Huang, J., Faber, S. M., Daddi, E., et al. 2009, ApJ, 700, 183

Huang, J., Rigopoulou, D., Willner, S. P., et al. 2005, ApJ, 634, 137

Ilbert, O., Arnouts, S., McCracken, H. J., et al. 2006, A&A, 457, 841

Ilbert, O., Capak, P., Salvato, M., et al. 2009, ApJ, 690, 1236

Jonsson, P. 2006, MNRAS, 372, 2

Jonsson, P., Groves, B. A., & Cox, T. J. 2010, MNRAS, 403, 17

Kannappan, S. J. & Gawiser, E. 2007, ApJL, 657, L5

Kartaltepe, J. S., Sanders, D. B., Le Floc'h, E., et al. 2010, ApJ, 709, 572

Kauffmann, G., Guiderdoni, B., & White, S. D. M. 1994, MNRAS, 267, 981

Kauffmann, G. & Haehnelt, M. 2000, MNRAS, 311, 576

Kauffmann, G., Heckman, T. M., White, S. D. M., et al. 2003, MNRAS, 341, 54

Kauffmann, G., White, S. D. M., & Guiderdoni, B. 1993, MNRAS, 264, 201

Kennicutt, R. C., Hao, C., Calzetti, D., et al. 2009, ApJ, 703, 1672

Kennicutt, Jr., R. C. 1998, ARA&A, 36, 189

Kitzbichler, M. G. & White, S. D. M. 2007, MNRAS, 376, 2

Komatsu, E., Smith, K. M., Dunkley, J., et al. 2010, ArXiv e-prints

Koo, D. C. 1985, AJ, 90, 418

—. 1986, ApJ, 311, 651

Koo, D. C. 1990, in Astronomical Society of the Pacific Conference Series, Vol. 10, Evolution of the Universe of Galaxies, ed. R. G. Kron, 268–285

Koo, D. C. 1999, in Astronomical Society of the Pacific Conference Series, Vol. 191, Photometric Redshifts and the Detection of High Redshift Galaxies, ed. R. Weymann, L. Storrie-Lombardi, M. Sawicki, & R. Brunner, 3–+

Koo, D. C. & Kron, R. T. 1980, PASP, 92, 537

Kriek, M., van Dokkum, P. G., Franx, M., et al. 2006, ApJ, 645, 44

—. 2008, ApJ, 677, 219

Kroupa, P. 2001, MNRAS, 322, 231

Kurtz, M. J., Geller, M. J., Fabricant, D. G., Wyatt, W. F., & Dell'Antonio, I. P. 2007, AJ, 134, 1360

Kurucz, R. L. 1992, in IAU Symposium, Vol. 149, The Stellar Populations of Galaxies, ed. B. Barbuy & A. Renzini, 225–+

Labbé, I., Franx, M., Rudnick, G., et al. 2007, ApJ, 665, 944

Lacy, M., Storrie-Lombardi, L. J., Sajina, A., et al. 2004, ApJS, 154, 166

Lagache, G., Dole, H., Puget, J., et al. 2004, ApJS, 154, 112

Lanzetta, K. M., Yahil, A., & Fernández-Soto, A. 1996, Nature, 381, 759

Larson, R. B. & Tinsley, B. M. 1978, ApJ, 219, 46

Le Borgne, J., Bruzual, G., Pelló, R., et al. 2003, A&A, 402, 433

Le Fèvre, O., Saisse, M., Mancini, D., et al. 2003, in Society of Photo-Optical Instrumentation Engineers (SPIE) Conference Series, Vol. 4841, Society of Photo-Optical Instrumentation Engineers (SPIE) Conference Series, ed. M. Iye & A. F. M. Moorwood, 1670–1681

Le Fèvre, O., Vettolani, G., Garilli, B., et al. 2005, A&A, 439, 845

Le Floc'h, E., Papovich, C., Dole, H., et al. 2005, ApJ, 632, 169

Lee, Y., Gim, H. B., & Casetti-Dinescu, D. I. 2007, ApJL, 661, L49

Leitherer, C. & Heckman, T. M. 1995, ApJS, 96, 9

Leitherer, C., Schaerer, D., Goldader, J. D., et al. 1999, ApJS, 123, 3

Lejeune, T. & Schaerer, D. 2001, A&A, 366, 538

Lilly, S. J., Le Fevre, O., Hammer, F., & Crampton, D. 1996, ApJL, 460, L1+

Lilly, S. J., Le Fèvre, O., Renzini, A., et al. 2007, ApJS, 172, 70

Loeb, A. & Barkana, R. 2001, ARA&A, 39, 19

Lowenthal, J. D., Hogan, C. J., Leach, R. W., Schmidt, G. D., & Foltz, C. B. 1990, ApJ, 357, 3

Madau, P., Ferguson, H. C., Dickinson, M. E., et al. 1996, MNRAS, 283, 1388

Madau, P., Pozzetti, L., & Dickinson, M. 1998, ApJ, 498, 106

Magdis, G. E., Rigopoulou, D., Huang, J.-S., et al. 2008, MNRAS, 386, 11

Maraston, C. 1998, MNRAS, 300, 872

—. 2005, MNRAS, 362, 799

Maraston, C., Daddi, E., Renzini, A., et al. 2006, ApJ, 652, 85

Marchesini, D., van Dokkum, P., Quadri, R., et al. 2007, ApJ, 656, 42

Marchesini, D., van Dokkum, P. G., Förster Schreiber, N. M., et al. 2009, ApJ, 701, 1765

Marigo, P. & Girardi, L. 2007, A&A, 469, 239

Marigo, P., Girardi, L., Bressan, A., et al. 2008, A&A, 482, 883

Massey, P. & Hunter, D. A. 1998, ApJ, 493, 180

Mateo, M. L. 1998, ARA&A, 36, 435

McCarthy, P. J., Le Borgne, D., Crampton, D., et al. 2004, ApJL, 614, L9

McCracken, H. J., Metcalfe, N., Shanks, T., et al. 2000, MNRAS, 311, 707

Meurer, G. R., Heckman, T. M., & Calzetti, D. 1999, ApJ, 521, 64

Meurer, G. R., Wong, O. I., Kim, J. H., et al. 2009, ApJ, 695, 765

Meynet, G. & Maeder, A. 2005, A&A, 429, 581

Mobasher, B., Rowan-Robinson, M., Georgakakis, A., & Eaton, N. 1996, MNRAS, 282, L7

Mollá, M., García-Vargas, M. L., & Bressan, A. 2009, MNRAS, 398, 451

Monaco, P., Fontanot, F., & Taffoni, G. 2007, MNRAS, 375, 1189

Moore, B., Ghigna, S., Governato, F., et al. 1999, ApJL, 524, L19

Moustakas, J., Kennicutt, Jr., R. C., & Tremonti, C. A. 2006, ApJ, 642, 775

Muñoz-Mateos, J. C., Gil de Paz, A., Boissier, S., et al. 2009, ApJ, 701, 1965

Muzzin, A., Marchesini, D., van Dokkum, P. G., et al. 2009, ApJ, 701, 1839

Naab, T., Johansson, P. H., Ostriker, J. P., & Efstathiou, G. 2007, ApJ, 658, 710

Nagamine, K., Ostriker, J. P., Fukugita, M., & Cen, R. 2006, ApJ, 653, 881

Nakata, F., Shimasaku, K., Doi, M., et al. 1999, MNRAS, 309, L25

Noll, S., Burgarella, D., Giovannoli, E., et al. 2009, A&A, 507, 1793

Noll, S., Pierini, D., Pannella, M., & Savaglio, S. 2007, A&A, 472, 455

Noterdaeme, P., Ledoux, C., Srianand, R., Petitjean, P., & Lopez, S. 2009, A&A, 503, 765

Panter, B., Jimenez, R., Heavens, A. F., & Charlot, S. 2007, MNRAS, 378, 1550

Papovich, C., Moustakas, L. A., Dickinson, M., et al. 2006, ApJ, 640, 92

Partridge, R. B. & Peebles, P. J. E. 1967a, ApJ, 147, 868

—. 1967b, ApJ, 148, 377

Pascual, S., Gallego, J., Aragón-Salamanca, A., & Zamorano, J. 2001, A&A, 379, 798

Peebles, P. J. E. 1982, ApJL, 263, L1

Pei, Y. C., Fall, S. M., & Hauser, M. G. 1999, ApJ, 522, 604

Pérez-González, P. G., Egami, E., Rex, M., et al. 2010, A&A, 518, L15+

Pérez-González, P. G., Gallego, J., Zamorano, J., et al. 2003, ApJL, 587, L27

Pérez-González, P. G., Rieke, G. H., Egami, E., et al. 2005, ApJ, 630, 82

Pérez-González, P. G., Rieke, G. H., Villar, V., et al. 2008, ApJ, 675, 234

Persic, M. & Rephaeli, Y. 2002, A&A, 382, 843

Polletta, M. 2008, A&A, 480, L41

Polletta, M., Tajer, M., Maraschi, L., et al. 2007, ApJ, 663, 81

Popescu, C. C., Tuffs, R. J., Volk, H. J., Pierini, D., & Madore, B. F. 2002, ApJ, 567, 221

Pozzetti, L., Bruzual A., G., & Zamorani, G. 1996, MNRAS, 281, 953

Pozzetti, L., Cimatti, A., Zamorani, G., et al. 2003, A&A, 402, 837

Prugniel, P. & Soubiran, C. 2001, A&A, 369, 1048

Reddy, N. A., Erb, D. K., Steidel, C. C., et al. 2005, ApJ, 633, 748

Reddy, N. A. & Steidel, C. C. 2009, ApJ, 692, 778

Reddy, N. A., Steidel, C. C., Pettini, M., et al. 2008, ApJS, 175, 48

Rieke, G. H., Alonso-Herrero, A., Weiner, B. J., et al. 2009, ApJ, 692, 556

Rigopoulou, D., Huang, J., Papovich, C., et al. 2006, ApJ, 648, 81

Rowan-Robinson, M. 1995, MNRAS, 272, 737

—. 2003, MNRAS, 345, 819

Rudnick, G., Rix, H., Franx, M., et al. 2003, ApJ, 599, 847

Salim, S., Rich, R. M., Charlot, S., et al. 2007, ApJS, 173, 267

Salimbeni, S., Giallongo, E., Menci, N., et al. 2008, A&A, 477, 763

Salpeter, E. E. 1955, ApJ, 121, 161

Sánchez-Blázquez, P., Gorgas, J., Cardiel, N., & González, J. J. 2006, A&A, 457, 787

Sandage, A. 1960, ApJ, 131, 610

Santini, P., Fontana, A., Grazian, A., et al. 2009, A&A, 504, 751

Sauvage, M., Tuffs, R. J., & Popescu, C. C. 2005, ApJ, 119, 313

Sawicki, M. J., Lin, H., & Yee, H. K. C. 1997, AJ, 113, 1

Schaerer, D., Guseva, N. G., Izotov, Y. I., & Thuan, T. X. 2000, A&A, 362, 53

Schawinski, K., Kaviraj, S., Khochfar, S., et al. 2007, ApJS, 173, 512

Schiminovich, D., Ilbert, O., Arnouts, S., et al. 2005, ApJL, 619, L47

Schmitt, H. R., Calzetti, D., Armus, L., et al. 2006, ApJ, 643, 173

Schneider, D. P., Gunn, J. E., Turner, E. L., et al. 1986, AJ, 91, 991

Scoville, N., Aussel, H., Brusa, M., et al. 2007, ApJS, 172, 1

Searle, L., Sargent, W. L. W., & Bagnuolo, W. G. 1973, ApJ, 179, 427

Sérsic, J. L. 1963, Boletin de la Asociacion Argentina de Astronomia La Plata Argentina, 6, 41

Shapley, A. E., Steidel, C. C., Erb, D. K., et al. 2005, ApJ, 626, 698

Siebenmorgen, R. & Krügel, E. 2007, A&A, 461, 445

Silva, L., Granato, G. L., Bressan, A., & Danese, L. 1998, ApJ, 509, 103

Simpson, C. & Eisenhardt, P. 1999, PASP, 111, 691

Smith, J. D. T., Draine, B. T., Dale, D. A., et al. 2007, ApJ, 656, 770

Smoot, G. F., Bennett, C. L., Kogut, A., et al. 1992, ApJL, 396, L1

Sobral, D., Best, P. N., Geach, J. E., et al. 2009, MNRAS, 398, 75

Somerville, R. S., Hopkins, P. F., Cox, T. J., Robertson, B. E., & Hernquist, L. 2008, MNRAS, 391, 481

Somerville, R. S. & Primack, J. R. 1999, MNRAS, 310, 1087

Spergel, D. N., Verde, L., Peiris, H. V., et al. 2003, ApJS, 148, 175

Spinrad, H. & Djorgovski, S. 1984a, ApJL, 280, L9

—. 1984b, ApJL, 285, L49

Spinrad, H., Marr, J., Aguilar, L., & Djorgovski, S. 1985, PASP, 97, 932

Springel, V., Di Matteo, T., & Hernquist, L. 2005a, MNRAS, 361, 776

Springel, V., White, S. D. M., Jenkins, A., et al. 2005b, Nature, 435, 629

Stasińska, G., Mateus, Jr., A., Sodré, Jr., L., & Szczerba, R. 2004, A&A, 420, 475

Steidel, C. C., Adelberger, K. L., Giavalisco, M., Dickinson, M., & Pettini, M. 1999, ApJ, 519, 1

Steidel, C. C., Adelberger, K. L., Shapley, A. E., et al. 2003, ApJ, 592, 728

Steidel, C. C., Giavalisco, M., Pettini, M., Dickinson, M., & Adelberger, K. L. 1996, ApJL, 462, L17+

Steidel, C. C., Shapley, A. E., Pettini, M., et al. 2004, ApJ, 604, 534

Stern, D., Eisenhardt, P., Gorjian, V., et al. 2005, ApJ, 631, 163

Sullivan, M., Treyer, M. A., Ellis, R. S., et al. 2000, MNRAS, 312, 442

Symeonidis, M., Willner, S. P., Rigopoulou, D., et al. 2008, MNRAS, 385, 1015

Taylor, E. N., Franx, M., van Dokkum, P. G., et al. 2009, ApJ, 694, 1171

Thompson, D., Djorgovski, S., & Trauger, J. 1995, AJ, 110, 963

Tinsley, B. M. 1972, A&A, 20, 383

—. 1977, ApJ, 211, 621

Treister, E. & Urry, C. M. 2006, ApJL, 652, L79

Treister, E., Urry, C. M., & Virani, S. 2009, ApJ, 696, 110

Trujillo, I., Conselice, C. J., Bundy, K., et al. 2007, MNRAS, 382, 109

Trujillo, I., Feulner, G., Goranova, Y., et al. 2006, MNRAS, 373, L36

van Dokkum, P. G. 2008, ApJ, 674, 29

van Dokkum, P. G., Labbé, I., Marchesini, D., et al. 2009, PASP, 121, 2

Vazdekis, A. 1999, ApJ, 513, 224

Vázquez, G. A., Leitherer, C., Schaerer, D., Meynet, G., & Maeder, A. 2007, ApJ, 663, 995

Villar, V., Gallego, J., Pérez-González, P. G., et al. 2008, ApJ, 677, 169

Wang, Y., Bahcall, N., & Turner, E. L. 1998, AJ, 116, 2081

White, N. E., Swank, J. H., & Holt, S. S. 1983, ApJ, 270, 711

White, S. D. M. & Frenk, C. S. 1991, ApJ, 379, 52

White, S. D. M. & Rees, M. J. 1978, MNRAS, 183, 341

Wilkins, S. M., Trentham, N., & Hopkins, A. M. 2008, MNRAS, 385, 687

Williams, R. E., Blacker, B., Dickinson, M., et al. 1996, AJ, 112, 1335

Witt, A. N., Thronson, Jr., H. A., & Capuano, Jr., J. M. 1992, ApJ, 393, 611

Wolf, C., Meisenheimer, K., Rix, H.-W., et al. 2003, A&A, 401, 73

Wuyts, S., Labbé, I., Franx, M., et al. 2007, ApJ, 655, 51

Yan, H., Dickinson, M., Eisenhardt, P. R. M., et al. 2004, ApJ, 616, 63

York, D. G., Adelman, J., Anderson, Jr., J. E., et al. 2000, AJ, 120, 1579

Young, J. S. & Scoville, N. Z. 1991, ARA&A, 29, 581

Zhu, Y., Wu, H., Cao, C., & Li, H. 2008, ApJ, 686, 155